Control Complexity of Nonlinear Chaotic Systems and its Applications

Lead Guest Editor: Chun-Lai Li
Guest Editors: Shao-Bo He, Karthikeyan Rajagopal, and Nikolay Kuznetsov

Control Complexity of Nonlinear Chaotic Systems and its Applications

Control Complexity of Nonlinear Chaotic Systems and its Applications

Lead Guest Editor: Chun-Lai Li
Guest Editors: Shao-Bo He, Karthikeyan Rajagopal, and Nikolay Kuznetsov
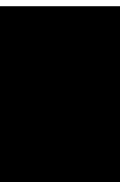
Contents

Contents

WILEY | Hindawi

Corrigendum

Corrigendum to "Introducing a Chaotic Component in the Control System of Soil Respiration"

Peng An [ID],[1] Wen-Feng Wang [ID],[1,2,3] Xi Chen,[3,4,5,6] Jing Qian [ID],[3,7] and Yunzhu Pan [ID][2,8]

[1]Laboratory of Pattern Analysis and Machine Intelligence, School of Electronic and Information Engineering,
Ningbo University of Technology, Ningbo 315211, China
[2]Research Institute of Intelligent Engineering and Data Applications, School of Electronic and Electrical Engineering,
Shanghai Institute of Technology, Shanghai 200235, China
[3]State Key Laboratory of Desert and Oasis Ecology, Xinjiang Institute of Ecology and Geography, Chinese Academy of Sciences,
Urumqi 830011, China
[4]University of Chinese Academy of Sciences, Beijing 100049, China
[5]Sino-Belgian Joint Laboratory of Geo-information, Urumqi 830011, China
[6]CAS Research Centre for Ecology and Environment of Central Asia, Urumqi 830011, China
[7]Center for Geo-Spatial Information, Shenzhen Institutes of Advanced Technology, Chinese Academy of Sciences,
Shenzhen 518055, China
[8]School of Management, Cranfield University, Cranfield MK43 0AL, UK

Correspondence should be addressed to Wen-Feng Wang; wangwenfeng@sit.edu.cn and Xi Chen; chenxi@ms.xjb.ac.cn

In the article titled "Introducing a Chaotic Component in the Control System of Soil Respiration" [1], the corresponding author's e-mail address has been corrected as shown above.

In addition, Tables 1 and 2 were omitted in error, which correspond to Figures 4–6.

In Section 3.2 (Control Complexity of the System), the following sentence should be revised to reflect the above: "We further examined the variability of Q_{10} values, as seen in Figures 4 and 5" to "We further examined the variability of Q_{10} values with T and WC_s, utilizing four exponential functions, as seen in Table 1 and Figures 4–5."

In Section 4 (Treating the Control Complexity), the following sentence should also be revised from "Overall, the nonlinear chaotic system is simplified and can be further developed" to "The model performance and corresponding weathering parameters are shown in Table 2."

TABLE 1: Four coupling functions of (T_a, WC$_s$) were employed in the analyses of Q_{10} with T_a and WC$_s$, with the fitted parameters and the statistics in model performance.

Models	R^2	RMSE	F-stat	p value
$Q_{10} = 0.0186\text{WC}_s - 0.0028T_s + 1.389$	0.134	0.502	1.47	0.254
$Q_{10} = 1.4151e^{0.0101\text{WC}_s - 0.0016T_s}$	0.133	0.503	1.45	0.259
$Q_{10} = 1.3258e^{(-0.002T_s + 0.0175)\text{WC}_s}$	0.136	0.502	1.49	0.250
$Q_{10} = 1.4151e^{0.0101\text{WC}_s - 0.0016T_s}$	0.120	0.506	1.30	0.297

Note: $n = 21$; T_a: air temperature 10 cm above the soil surface; WC$_s$: soil volumetric water content at 5 cm depth; F-stat: F-statistic vs. constant model; error degrees of freedom = 18.

TABLE 2: Performance of equation (3) with weathering parameters after rainfall.

Rainfall (time)	λ	μ	R^2	RMSE
~1 mm				
3 days after	1.2972	0.2688	0.91	0.12
4 days after	0.0740	0.0543	0.86	0.10
7 days after	1.1437	0.2840	0.90	0.09
0.6–3.6 mm				
5 days after	1.1321	0.2575	0.95	0.07
9 days after	1.1922	−0.0797	0.93	0.11
~1.7 mm				
1 day after	0.9915	0.1741	0.90	0.10

References

[1] P. An, W.-F. Wang, X. Chen, J. Qian, and Y. Pan, "Introducing a chaotic component in the control system of soil respiration," *Complexity*, vol. 2020, Article ID 5310247, 8 pages, 2020.

Research Article

Dynamics and Complexity Analysis of Fractional-Order Chaotic Systems with Line Equilibrium Based on Adomian Decomposition

Heng Chen,[1] Tengfei Lei [ID],[2,3] Su Lu,[4] WenPeng Dai,[2] Lijun Qiu,[1] and Lin Zhong[1]

[1]*Shaanxi Engineering Research Center of Controllable Neutron Source, School of Science, Xijing University, Xi'an 710123, China*
[2]*Collaborative Innovation Center of Memristive Computing Application, Qilu Institute of Technology, Jinan 250200, Shandong, China*
[3]*Shandong Engineering Research Center of China-Germany Smart Factory Applied, Jinan 250200, Shandong, China*
[4]*School of Civil Engineering, Inner Mongolia University of Technology, Inner Mongolia, Huhehot 010051, China*

Correspondence should be addressed to Tengfei Lei; leitengfeicanhe@126.com

In this paper, the Adomian decomposition method (ADM) is applied to solve the fractional-order system with line equilibrium. The dynamics of the system is analyzed by means of the Lyapunov exponent spectrum, bifurcations, chaotic attractor, and largest Lyapunov exponent diagram. At the same time, through the Lyapunov exponent spectrum and bifurcation graph of the system under the change of the initial value, the influence of fractional order q on the system state can be observed. That is, integer-order systems do not have the phenomenon of attractors coexistence, while fractional-order systems have it.

1. Introduction

Three hundred years ago, fractional-order calculation was proposed as a classical mathematical problem. Fractional calculation has no practical background and has not been applied in engineering. Therefore, researchers and scientists are not interested in fractional research. Recently, it has been found that many engineering and physical systems, electronic systems, etc. exhibit their own fractional-order characteristics, and the fractional order can more accurately reflect natural phenomena, such as material memory and damping characteristics [1–4]. In recent years, with the deepening and perfection of chaotic theory research, fractional-order chaotic systems have become a hot topic in the field. In particular, the complexity of fractional-order chaotic systems is not only related to the parameters of the system itself, but also related to the fractional order of the system. Many scholars have proposed several fractional-order chaotic systems based on integer-order chaotic systems: fractional-order Lorenz system [5], factional-order

Lorenz hyperchaotic system [6], four-wing fractional-order chaotic system [7], and so on [8, 9].

In the numerical calculation of fractional chaotic systems, namely, discretization of fractional chaotic systems, many scholars have made some achievements based on frequency-domain method (FDM) [10], Adomian decomposition method (ADM) [5–7, 9, 11], and Adams–Bashforth–Moulton (ABM) algorithm [12, 13]. Among them, FDM uses high-dimensional system close to fractional-order system through Laplace change, but the error is relatively large [14]. ABM is the most commonly used method, but its operation speed is slow. ADM scheme, on the other hand, has more accuracy and requires less computational resources compared with ABM algorithm [5–7, 9]. Reference [15] shows that fractional-order chaotic systems show more complex chaotic behaviors than integer-order chaotic systems, which can be seen from complexity, Lyapunov index, bifurcation diagram, and other aspects. When the system order is smaller, the system is more complicated [9, 16].

On the other hand, hot research on chaotic systems mainly focuses on chaos control [17–20], Lyapunov exponent calculation and analysis [21, 22], and doubling and growth of attractors [23, 24], and chaotic systems with hidden attractors are also hot research topics, because such systems are extremely prone to multistable phenomenon, which is a common phenomenon in nature. Hidden attractors originate from several types of dynamical systems; the dynamical systems with one stable equilibrium [25], a line or plane equilibrium [26, 27], or no equilibrium [28] can all have hidden attractors. Hidden attractors are even found in some special chaotic systems, which have both unstable and stable equilibria. However, the fractional-order chaotic system with hidden attractor, which can be easily obtained by combining the hidden attractor with fractional-order systems, is rarely studied [29]. The system has high complexity, so it plays an important role in the field of communication encryption.

In this paper, we propose a new fractional-order chaotic system with line equilibrium. Discretization of the proposed system is performed using Adomian decomposition scheme. The rest of the paper is organized as follows. In Section 2, the equilibrium point and dynamic analysis of the integer-order chaotic equilibrium point system are presented. In Section 3, the fractional-order chaotic system is numerically calculated and simulated by Adomian decomposition method. In Section 4, the bifurcation diagram, phase diagrams, and Lyapunov exponents spectrum are employed to analyze the dynamics of the system. In Section 5, complexity of fractional-order chaotic system is analyzed. Finally, the obtained results are summarized in Section 6.

2. Integer-Order Chaotic System with Line Equilibrium

2.1. Analysis of Equilibrium Points of Systems.

Reference [29] proposes a class of T chaotic systems defined by

$$\begin{cases} \dot{x} = a(y - x), \\ \dot{y} = cx - axz, \\ \dot{z} = xy - bz. \end{cases} \tag{1}$$

A 3D integer-order chaotic system is defined by

$$\begin{cases} \dot{x} = yz - ax, \\ \dot{y} = cx - axz, \\ \dot{z} = xy - bz, \end{cases} \tag{2}$$

where, a, b, and c are system (2) parameters and x, y, and z are three state variables of system (2). When parameters $a = 5$, $b = 2$, and $c = 34$, the system has two equilibrium points: $E_1 ((c\sqrt{ab})/a^2, \sqrt{ab}, (c/a))$, $E_2 (-(c\sqrt{ab}/a^2), -\sqrt{ab}, (c/a))$, and $E_3 (0, h, 0)$. The eigenvalues at E_1 and E_2 are

$\lambda_{11} = -6.0739$, $\lambda_{12} = -0.4631 + 21.3673$, and $\lambda_{13} = 0$; $E_3 (0, h, 0)$ is the line equilibrium point; and h is any real number. The Jacobian matrix linearized under equilibrium E_3 is as follows:

$$J = \begin{bmatrix} -a & 0 & h \\ c & 0 & 0 \\ h & 0 & -b \end{bmatrix}. \tag{3}$$

The characteristic equation of matrix is

$$\lambda^3 + (a + b)\lambda^2 + (ab - h^2)\lambda = 0. \tag{4}$$

The eigenvalue at the line equilibrium point E_3 is as follows:

$$\lambda_1 = 0,$$

$$\lambda_2 = -\frac{(a + b)}{2} - \frac{\sqrt{(a - b)^2 + 4h^2}}{2}, \tag{5}$$

$$\lambda_3 = -\frac{(a + b)}{2} + \frac{\sqrt{(a - b)^2 + 4h^2}}{2}.$$

Case 1. If $h^2 < ab$, then $\lambda_3 = -((a + b)/2) + (\sqrt{(a - b)^2 + 4h^2}/2) < 0$; according to Routh–Hurwitz criterion, the equilibrium E_3 is stable.

Case 2. If $h^2 < ab$, then $\lambda_3 = -((a + b)/2) + (\sqrt{(a - b)^2 + 4h^2}/2) > 0$; according to Routh–Hurwitz criterion, the equilibrium E_3 is unstable.

Case 3. If $h^2 = ab$, then $\lambda_3 = -((a + b)/2) + (\sqrt{(a - b)^2 + 4h^2}/2) = 0$; according to Routh–Hurwitz criterion, we obtain that the equilibrium E_3 is critical stable.

When $a = 5$, $b = 2$, and $c = 34$, using ODE45 function in MATLAB software to simulate (2), the chaotic attractor is shown in Figure 1. The orbits marked by the blue and red colors emerge form initial (1, 2, 3) and (1, 2, −1), and the red attractor is periodic. The blue attractors are shown in chaotic states.

2.2. Dynamics Analysis of the Chaotic System.

Fix $a = 5$, $b = 2$, and $c = 34$; initial values of state variables $[x_0, y_0, z_0] = [1, 2, z_0]$; let the z_0 vary from −15 to 15 with step size of 0.01. Bifurcation diagram and Lyapunov exponents spectrum of system (2) are shown in Figure 2. As can be seen from the bifurcation diagram of the system in Figure 2(a), when $z_0 \in [-15, -0.6]$, the system is in a periodic state and

(a)

(b)

(c)

FIGURE 1: Phase diagrams in different projections of chaotic systems (2) from initial values (1, 2, 3), red, and (1, 2, −1). (a) Phase portraits in the x-y plane. (b) Phase portraits in the x-z plane. (c) Phase portraits in the y-z plane.

stable at $(0, 0, 0)$. When $z_0 \in (-0.6, 15]$, the system is in a chaos state. When $z_0 \in [-15, -0.6]$, the maximum Lyapunov exponent is equal to 0. When $z_0 \in (-0.6, 15]$, the largest Lyapunov exponent is positive, as shown in Figure 2(b).

Fix $a = 5$, $b = 2$, and $c = 34$; initial values of state variables $[x_0, y_0, z_0] = [1, 2, z_0]$; let the $z(0)$ vary from -15 to 15 with step size of 0.3 and $y(0)$ vary from -20 to 20 with step size of 0.4. In the $z(0) - y(0)$ plane, the chaos diagram of the largest LEs is calculated and shown in Figure 3. In Figure 3 the chaotic region is green (labeled "C") and the periodic

region is red (labeled "P"). We can see from Figure 3 that the system state is mainly affected by the initial condition z_0.

3. Solution of Fractional Chaotic System Based on Adomian Decomposition

System (2) can generate complex chaotic attractors with line equilibrium point, and it has three typical parameter sets. Change the above system equations to the following fractional-order form:

(a)

(b)
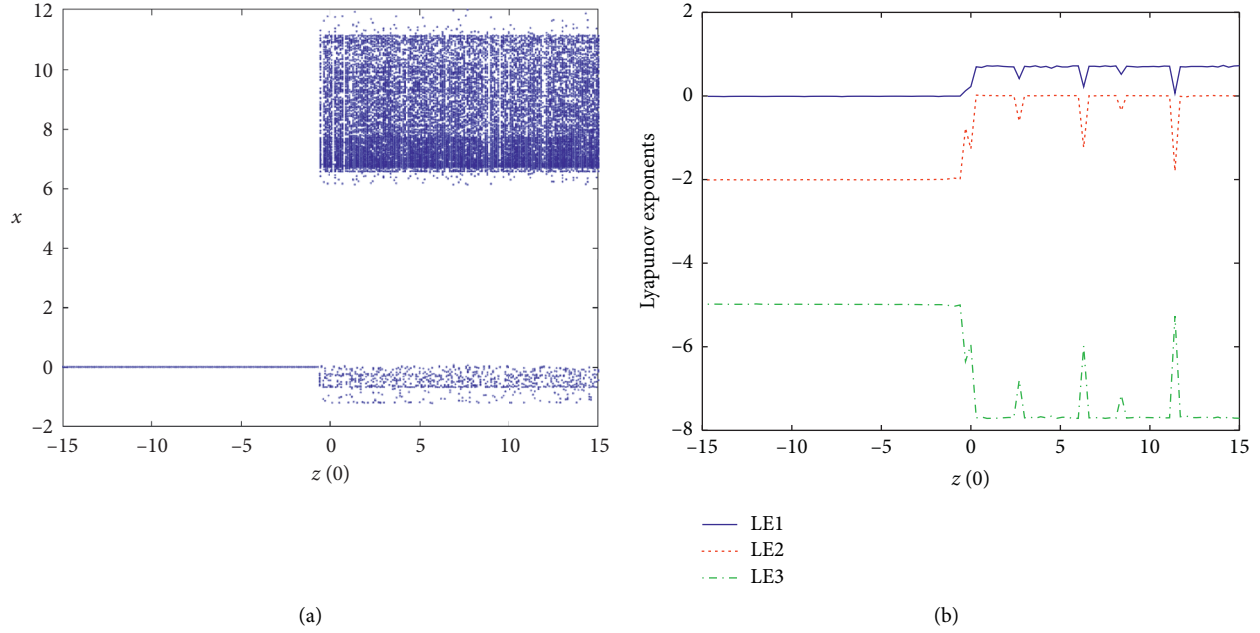
FIGURE 2: Bifurcation diagram and Lyapunov exponents spectrum of system (2) with initial conditional $[x_0, y_0, z_0] = [1, 2, z_0]$. (a) Bifurcation diagram. (b) Lyapunov exponents (LEs).
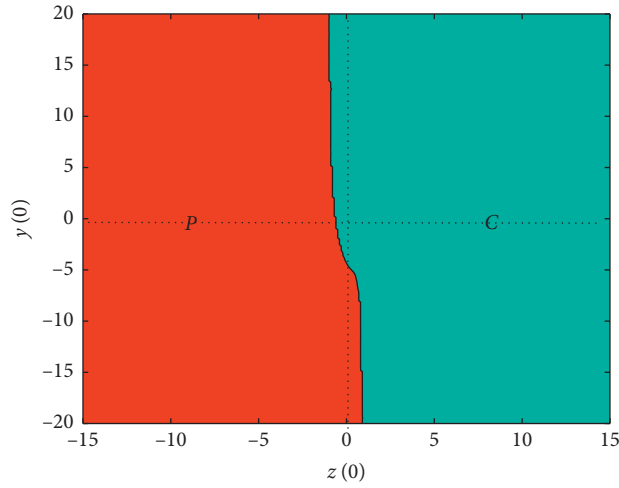
FIGURE 3: The chaos diagram of the largest Lyapunov exponents with $z_0 \in [-15, 15]$ and $y_0 \in [-20, 20]$.

$$
\begin{cases}
\dfrac{\mathrm{d}x^q}{\mathrm{d}^q t} = yz - ax, \\[2mm]
\dfrac{\mathrm{d}y^q}{\mathrm{d}^q t} = cx - axz, \\[2mm]
\dfrac{\mathrm{d}z^q}{\mathrm{d}^q t} = xy - bz.
\end{cases}
\tag{6}
$$

The initial condition is $\begin{cases} x^0 = x(t_0) = c_1^0 \\ y^0 = y(t_0) = c_2^0 \\ z^0 = z(t_0) = c_3^0 \end{cases}$. According to

domains decomposition method [30] and fractional calculus properties, the following properties are obtained:

$$
\begin{cases}
x^1 = \left(c_2^0 c_3^0 - ac_1^0\right) \dfrac{h^q}{\Gamma(q+1)}, \\[3mm]
y^1 = \left[cc_1^0 - ac_1^0 c_3^0\right] \dfrac{h^q}{\Gamma(q+1)}, \\[3mm]
z^1 = \left(c_1^0 c_2^0 - bc_3^0\right) \dfrac{h^q}{\Gamma(q+1)},
\end{cases}
\tag{7}
$$

where x^1, y^1, z^1 are the values of systems (3). $h_s = t - t_0$ is iteration step size. $\Gamma(\cdot)$ is Gamma function. The corresponding variables are assigned to the corresponding value; let

$$\begin{cases} c_1^1 = c_2^0 c_3^0 - a c_1^0, \\ c_2^1 = c c_1^0 - a c_1^0 c_3^0, \\ c_3^1 = c_1^0 c_2^0 - b c_3^0, \end{cases} \tag{8}$$

$$\begin{cases} c_1^2 = c_2^0 c_3^1 + c_2^1 c_3^0 - a c_1^1, \\ c_2^2 = c c_2^1 - a\left(c_1^1 c_3^0 + c_1^0 c_3^1\right), \\ c_3^2 = c_1^1 c_2^0 + c_1^0 c_2^1 - b c_3^1, \end{cases} \tag{9}$$

$$\begin{cases} c_1^3 = c_2^2 c_3^0 + c_2^0 c_3^2 + c_2^1 c_3^1 \dfrac{\Gamma(2q+1)}{\Gamma^2(q+1)} - a c_1^2, \\[2mm] c_2^3 = c c_1^2 - a c_1^2 c_3^0 - a c_1^0 c_3^2 - a c_1^1 c_3^1 \dfrac{\Gamma(2q+1)}{\Gamma^2(q+1)}, \\[2mm] c_3^3 = c_1^2 c_2^0 + c_1^0 c_2^2 + c_1^1 c_2^1 \dfrac{\Gamma(2q+1)}{\Gamma^2(q+1)} - b c_3^2, \end{cases} \tag{10}$$

$$\begin{cases} c_1^4 = c_2^3 c_3^0 + c_2^0 c_3^3 + \left(c_2^1 c_3^2 + c_2^2 c_3^1\right) \dfrac{\Gamma(3q+1)}{\Gamma(2q+1)\Gamma(q+1)} - a c_1^3), \\[2mm] c_2^4 = c c_1^3 - a c_1^3 c_3^0 - a c_1^0 c_3^3 - a\left(c_1^1 c_3^2 + c_1^2 c_3^1\right) \dfrac{\Gamma(3q+1)}{\Gamma(2q+1)\Gamma(q+1)}, \\[2mm] c_3^4 = c_1^3 c_2^0 + c_1^0 c_2^3 + \left(c_1^1 c_2^2 + c_1^2 c_2^1\right) \dfrac{\Gamma(3q+1)}{\Gamma(2q+1)\Gamma(q+1)} - b c_3^3, \end{cases} \tag{11}$$

$$\begin{cases} c_1^5 = c_2^4 c_3^0 + c_2^0 c_3^4 + \left(c_2^1 c_3^3 + c_2^3 c_3^1\right) \dfrac{\Gamma(4q+1)}{\Gamma(3q+1)\Gamma(q+1)} + c_2^2 c_3^2 \dfrac{\Gamma(4q+1)}{\Gamma^2(2q+1)} - a c_1^4, \\[2mm] c_2^5 = c c_1^4 - a c_1^4 c_3^0 - a c_1^0 c_3^4 - a\left(c_1^1 c_3^3 + c_1^3 c_3^1\right) \dfrac{\Gamma(4q+1)}{\Gamma(3q+1)\Gamma(q+1)} - a c_1^2 c_3^2 \dfrac{\Gamma(4q+1)}{\Gamma^2(2q+1)}, \\[2mm] c_3^5 = c_1^4 c_2^0 + c_1^0 c_2^4 + \left(c_1^1 c_3^3 + c_1^3 c_2^1\right) \dfrac{\Gamma(4q+1)}{\Gamma(3q+1)\Gamma(q+1)} + c_1^2 c_2^2 \dfrac{\Gamma(4q+1)}{\Gamma^2(2q+1)} - b c_3^4, \end{cases} \tag{12}$$

$$\begin{cases} c_1^6 = c_2^5 c_3^0 + c_2^0 c_3^5 + \left(c_2^2 c_3^3 + c_2^3 c_3^3\right) \dfrac{\Gamma(5q+1)}{\Gamma(3q+1)\Gamma(2q+1)} + \left(c_2^1 c_3^4 + c_2^4 c_3^1\right) \dfrac{\Gamma(5q+1)}{\Gamma(4q+1)\Gamma(q+1)} - a c_1^5, \\[2mm] c_2^6 = c c_1^5 - a c_1^5 c_3^0 - a c_1^0 c_3^5 - a\left(c_1^2 c_3^3 + c_1^3 c_3^2\right) \dfrac{\Gamma(5q+1)}{\Gamma(3q+1)\Gamma(2q+1)} - a\left(c_1^1 c_3^4 + c_1^4 c_3^1\right) \dfrac{\Gamma(5q+1)}{\Gamma(4q+1)\Gamma(q+1)}, \\[2mm] c_3^6 = c_1^5 c_2^0 + c_1^0 c_2^5 + \left(c_1^2 c_2^3 + c_1^3 c_2^3\right) \dfrac{\Gamma(5q+1)}{\Gamma(3q+1)\Gamma(2q+1)} + \left(c_1^1 c_2^4 + c_1^4 c_2^1\right) \dfrac{\Gamma(5q+1)}{\Gamma(4q+1)\Gamma(q+1)} - b c_3^4. \end{cases} \tag{13}$$

Thus, the solution of systems (5) is defined as

$$
\begin{cases}
x(t) = c_1^0 + c_1^1 \dfrac{h^q}{\Gamma(q+1)} + c_1^2 \dfrac{h^{2q}}{\Gamma(2q+1)} + c_1^3 \dfrac{h^{3q}}{\Gamma(3q+1)} + c_1^4 \dfrac{h^{4q}}{\Gamma(4q+1)} + c_1^5 \dfrac{h^{5q}}{\Gamma(5q+1)} + c_1^6 \dfrac{h^{6q}}{\Gamma(6q+1)}, \\[3mm]
y(t) = c_2^0 + c_2^1 \dfrac{h^q}{\Gamma(q+1)} + c_2^2 \dfrac{h^{2q}}{\Gamma(2q+1)} + c_2^3 \dfrac{h^{3q}}{\Gamma(3q+1)} + c_2^4 \dfrac{h^{4q}}{\Gamma(4q+1)} + c_2^5 \dfrac{h^{5q}}{\Gamma(5q+1)} + c_2^6 \dfrac{h^{6q}}{\Gamma(6q+1)}, \\[3mm]
z(t) = c_3^0 + c_3^1 \dfrac{h^q}{\Gamma(q+1)} + c_3^2 \dfrac{h^{2q}}{\Gamma(2q+1)} + c_3^3 \dfrac{h^{3q}}{\Gamma(3q+1)} + c_3^4 \dfrac{h^{4q}}{\Gamma(4q+1)} + c_3^5 \dfrac{h^{5q}}{\Gamma(5q+1)} + c_3^6 \dfrac{h^{6q}}{\Gamma(6q+1)}.
\end{cases}
\tag{14}
$$

When $a = 5$, $b = 2$, and $c = 34$, system (5) has stable equilibrium with line $(0, h, 0)$. The analytical solution of the system can be obtained according to (14). Using MATLAB to simulate (14), the chaotic attractor is shown in Figure 4. The orbits marked by the blue and red colors emerge form initial $(1, 2, 3)$ and $(1, 2, -1)$, and the red attractor is periodic. The blue attractors are shown in chaotic states.

4. Dynamical Analysis

Based on the ADM solution of the fractional-order chaotic system, we focus on the analysis of the influence of parameters on the system. In this paper, the system bifurcation diagram and Lyapunov exponent are used to analyze the dynamic system. The bifurcation diagram is obtained by using the maximum value of state variables. In this section, the influence of three parameters on the system is studied.

4.1. Dynamics with z(0) Varying. Fix $a = 5$, $b = 2$, $c = 34$, and $q = 0.8$; initial values of state variables $[x_0, y_0, z_0] = [1, 2, z_0]$; let the z_0 vary from -15 to 15 with step size of 0.01. Bifurcation diagram and Lyapunov exponents spectrum of the system (5) are shown in Figure 5. As can be seen from the bifurcation diagram of the system in Figure 5(a), when $z_0 \in [-15, -0.7]$, the system is in a periodic state and stable at $(0, 0, 0)$. When $z_0 \in (-0.7, 15]$, the system is in a chaos state. When $z_0 \in [-15, -0.7]$, the largest Lyapunov exponents is equal to 0. When $z_0 \in (-0.7, 15]$, the largest Lyapunov exponents is positive, as shown in Figure 5(b).

4.2. Dynamics with q Varying. Fix $a = 5$, $b = 2$, and $c = 34$; let the derivative order q vary from 0.6 to 1 with step size of 0.002 and the initial values of state variables $[x_0, y_0, z_0] = [1, 2, 3]$. It can be seen from Figure 6(a) that, under the variation of derivative order q, the system chaos and periodic variation are repeated and crossed and are not a process from period to chaos directly. At the same time, Figure 6 shows that the system is chaotic over the interval $q \in [0.678, 0.824) \cap [0.876, 1]$. However, $q \in [0.876, 1]$ also has a periodic window. It can be seen clearly that the maximum Lyapunov exponent decreases with the increase of derivative order $q \in [0.678, 0.824]$. In this case, the minimum order for chaos is $q = 0.678$. The maximum Lyapunov exponent value at this point ($q = 0.678$) is the largest. With the change of parameter q, the bifurcation

diagram of the system is consistent with the Lyapunov exponent spectrum of the system.

For further research, influence of coexistence of attractors in fractional derivative q system. In this paper, the phase diagram is used to introduce. It is found that $a = 5$, $b = 2$, and $c = 34$. The integer-order system ($q = 1$) is different from the fractional-order system ($q = 0.98$). The attractors of the integer-order system are almost the same, while the attractors of the fractional-order system coexist. As shown in Figure 7, the red initial values are $[1, 2, 3]$. The blue initial values are $[1, 2, 20]$.

4.3. Dynamics with a and b Varying. The fractional chaotic system (5) has three system parameters besides the fractional derivative q. In this paper, the dynamic properties of the system parameters with a and b varying are analyzed. Firstly, bifurcation diagrams of the fractional-order system with $a \in [3, 10]$ is investigated as shown in Figure 8(a), where the step size of a is 0.05, $q = 0.8$, $b = 2$, and the initial conditional is $[x_0, y_0, z_0] = [1, 2, 3]$. Obviously, it can be seen that $a \in [3.3, 4.1] \cup [4.3, 4.7] \cup [8.4, 8.5]$ is in a periodic state; phase diagrams of the systems with different a values are shown in Figure 9. Other regions are in chaotic state with periodic windows.

Secondly, bifurcation diagrams of the fractional-order system (5) with $b \in [0, 6]$ is investigated as shown in Figure 8(b), where the step size of b is 0.05, $a = 5$, and the initial conditional is $[x_0, y_0, z_0] = [1, 2, 3]$. Obviously, it can be seen that $b \in [3.16, 3.38] \cup [3.92, 6]$ is in a periodic state, and other regions are in chaotic state with periodic windows.

QR decomposition method [6, 15] is effective in calculating the LEs, and its computational process is shown by

$$
\begin{aligned}
\mathrm{qr}\left[\mathbf{J}_m \mathbf{J}_{m-1}, \ldots, \mathbf{J}_2 \mathbf{J}_1\right] &= \mathrm{qr}\left[\mathbf{J}_m \mathbf{J}_{m-1}, \ldots, \mathbf{J}_2\left(\mathbf{J}_1 \mathbf{Q}_0\right)\right] \\
&= \mathrm{qr}\left[\mathbf{J}_m \mathbf{J}_{m-1}, \ldots, \mathbf{J}_3\left(\mathbf{J}_2 \mathbf{Q}_1\right)\right] \times \left[\mathbf{R}_1\right] \\
&= \mathrm{qr}\left[\mathbf{J}_m \mathbf{J}_{m-1}, \ldots, \mathbf{J}_4\left(\mathbf{J}_3 \mathbf{Q}_2\right)\right] \times \left[\mathbf{R}_2 \mathbf{R}_1\right] \\
&= \cdots \\
&= \mathrm{qr}\left[\mathbf{J}_m \mathbf{J}_{m-1}, \ldots, \mathbf{J}_{i+1}\left(\mathbf{J}_i \mathbf{Q}_{i-1}\right)\right] \\
&\quad \times \left[\mathbf{R}_{i-1} \mathbf{R}_{i-2}, \ldots, \mathbf{R}_1\right] \\
&= \mathbf{Q}_m\left[\mathbf{R}_m \mathbf{R}_{m-1}, \ldots, \mathbf{R}_1\right] = \mathbf{Q}_m \mathbf{R}.
\end{aligned}
\tag{15}
$$

Here, qr( ) represents QR decomposition function, m is the maximum iteration number, and J is the Jacobian matrix of

(a)

(b)

(c)
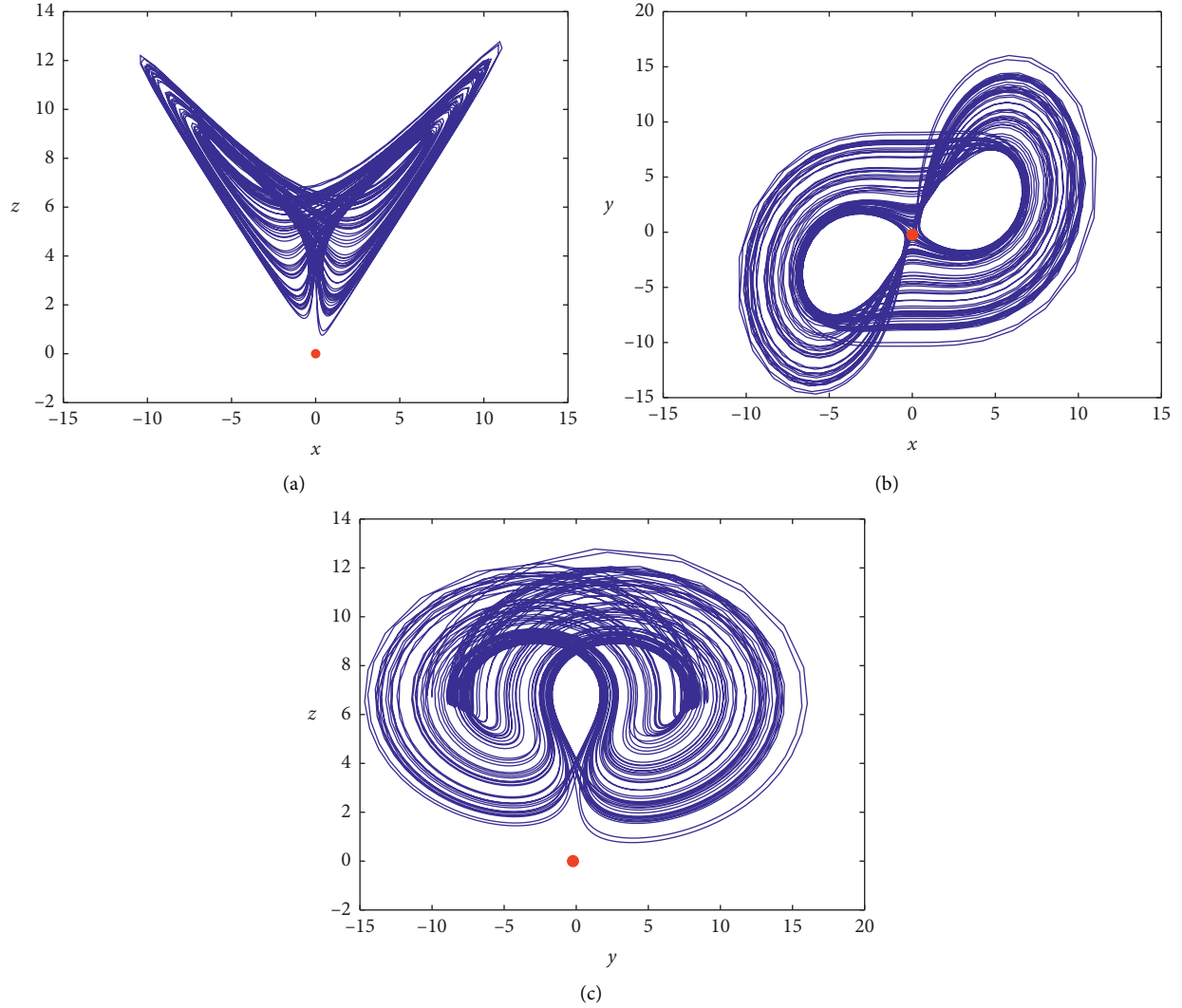
FIGURE 4: Phase diagrams in different projections of fractional-order chaotic systems from initial values (1, 2, 3), red, and (1, 2, −1). (a) Phase portraits in the (x)-(z) plane. (b) Phase portraits in the (x)-(y) plane. (c) Phase portraits in the (y)-(z) plane.

the given discrete formula as presented in (14). LCEs are calculated by

$$\lambda_k = \frac{1}{mh} \ln \left| \mathbf{R}_i (k, k) \right|. \tag{16}$$

Here, $k = 1, 2, n$ (system dimension); n is the maximum number of iterations; and h is the iteration time step. According to the above basic formula, make $n = 4$, $n = 7000$, and $h = 0.01$, and use MATLAB to draw the Lyapunov exponent under parameter changes.

Fix $b = 2$, $q = 0.8$; initial conditional is $[x_0, y_0, z_0] = [1, 2, 3]$; and let a vary. Lyapunov exponents spectrum of system (5) is shown in Figure 10(a), which is consistent with the bifurcation diagram; namely, $a \in [3.3, 4.1] \cup [4.3, 4.7] \cup [8.4, 8.5]$; the largest Lyapunov exponent of the system is equal to 0 (not positive), and the maximum Lyapunov exponent in other regions is greater than 0 (positive).

Fix $a = 5$, $q = 0.8$; initial conditional is $[x_0, y_0, z_0] = [1, 2, 3]$; and let b vary. Lyapunov exponents spectrum of system (5) is shown in Figure 10(b), which is consistent with the bifurcation

diagram; namely, $b \in [3.16, 3.38] \cup [3.92, 6]$; the largest Lyapunov exponent of the system is less than 0 (the phase diagram is a collection point), and the maximum Lyapunov exponent in other regions is greater than 0 (positive).

5. Complexity Analysis of the Fractional-Order System

5.1. Completeness Calculation. By calculating the energy distribution in the Fourier transform domain and combining it with the Shannon entropy, spectral entropy is obtained [31]. C0 complexity [32] is mainly to decompose the time series into regular and irregular parts and to test the proportion of irregular parts in the sequence. In practical applications, the chaos diagram of SE and C0 complexity can provide a basis to select parameter better.

Sample entropy (SampEn) [16] measures the complexity of time series by measuring the probability of generating new patterns in signals. The greater the probability of generation, the greater the value of the complexity of the sequence.

(a)

(b)
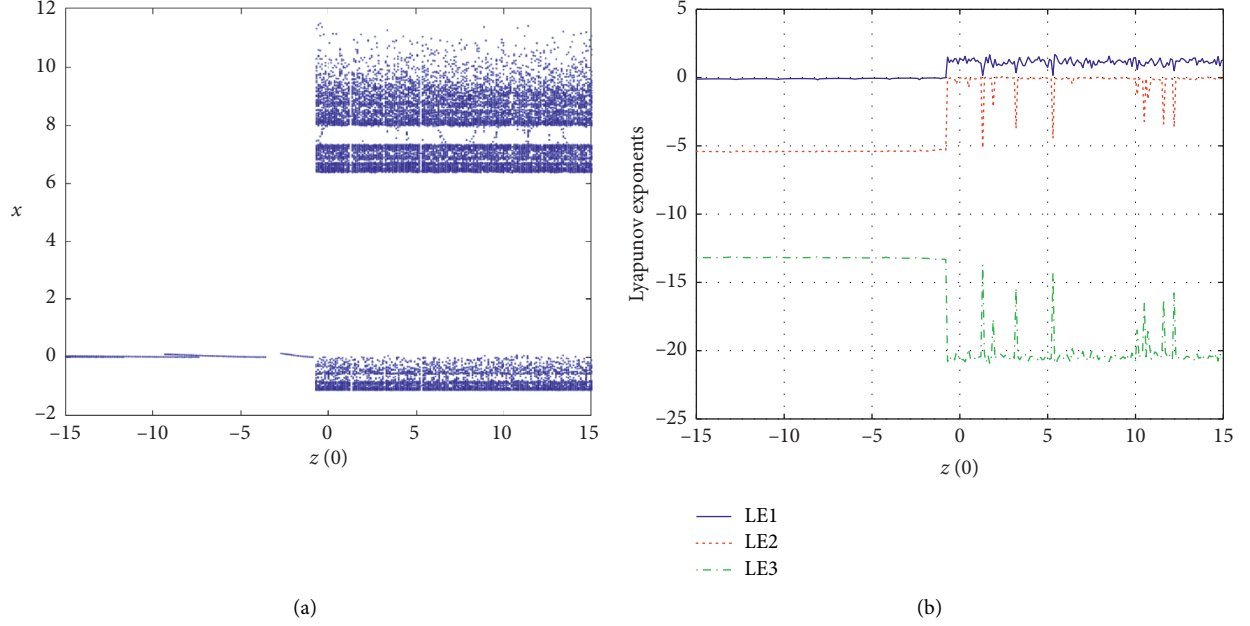
Figure 5: Bifurcation diagram and Lyapunov exponents spectrum of the fractional-order chaotic system (5) with initial conditional $[x_0, y_0, z_0] = [1, 2, z_0]$. (a) Bifurcation diagram. (b) Lyapunov exponents (LEs).

(a)

(b)
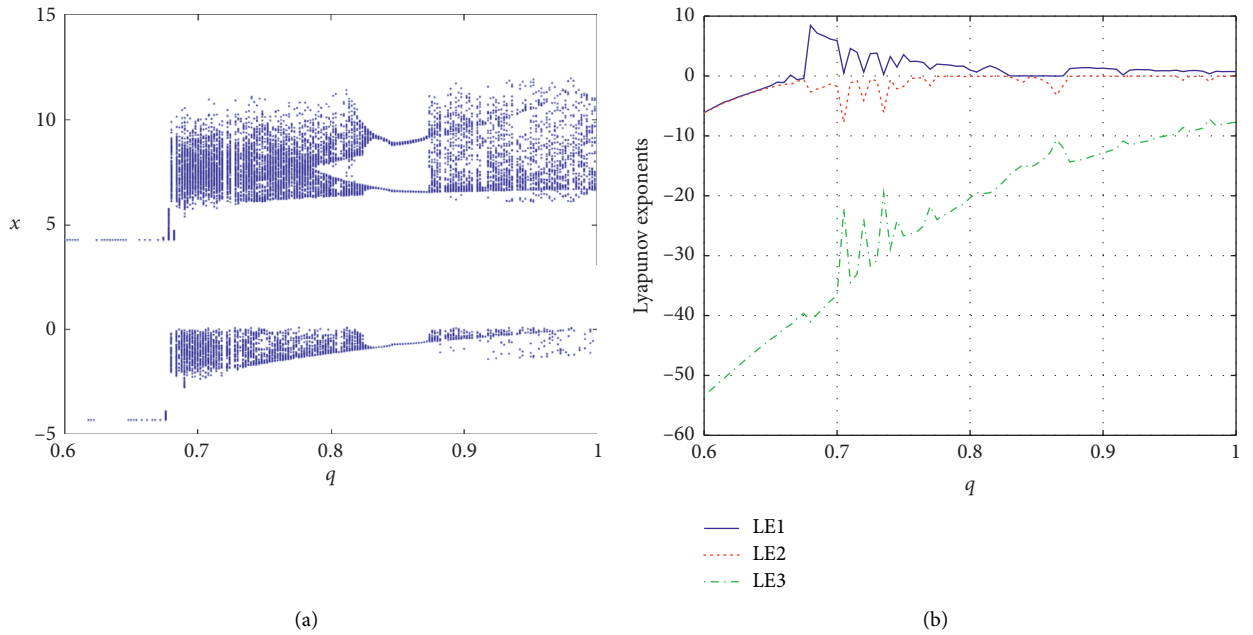
Figure 6: Bifurcation diagram and Lyapunov exponents spectrum of system (11) with $a = 5$, $b = 2$, and $c = 34$. (a) Bifurcation diagram. (b) Lyapunov exponents (LEs).

In general, for the specific calculation method of sample entropy of time series $\{x(n)\}$ composed of N data, the specific steps are as follows:

(i) $S1$: according to the serial number to form a one-dimensional m vector sequence, $\{X_m(1), \ldots, X_m(N-m+1)\}$, where $X_m(1) = \{x(i), x(i+1), \ldots, x(i+m-1)\}$, $1 \le i \le N - m + 1$. These vectors are m consecutive x values starting from point 1.

(ii) $S2$: define the distance between $X_m(i)$ and $X_m(j)$ as $d[X_m(i) X_m(j)]$, as the difference between the maximum absolute values of the corresponding elements.

(iii) $S3$: define the criterion of similarity r. Count the number of $d[X_m(i), X_m(j)] < r$ $(1 \le j \le N - m, 1 \le i \le N - m)$, and its ratio to total distance $N - m$ is denoted as $B_i^m(r) = B_i/(N - m - 1)$.
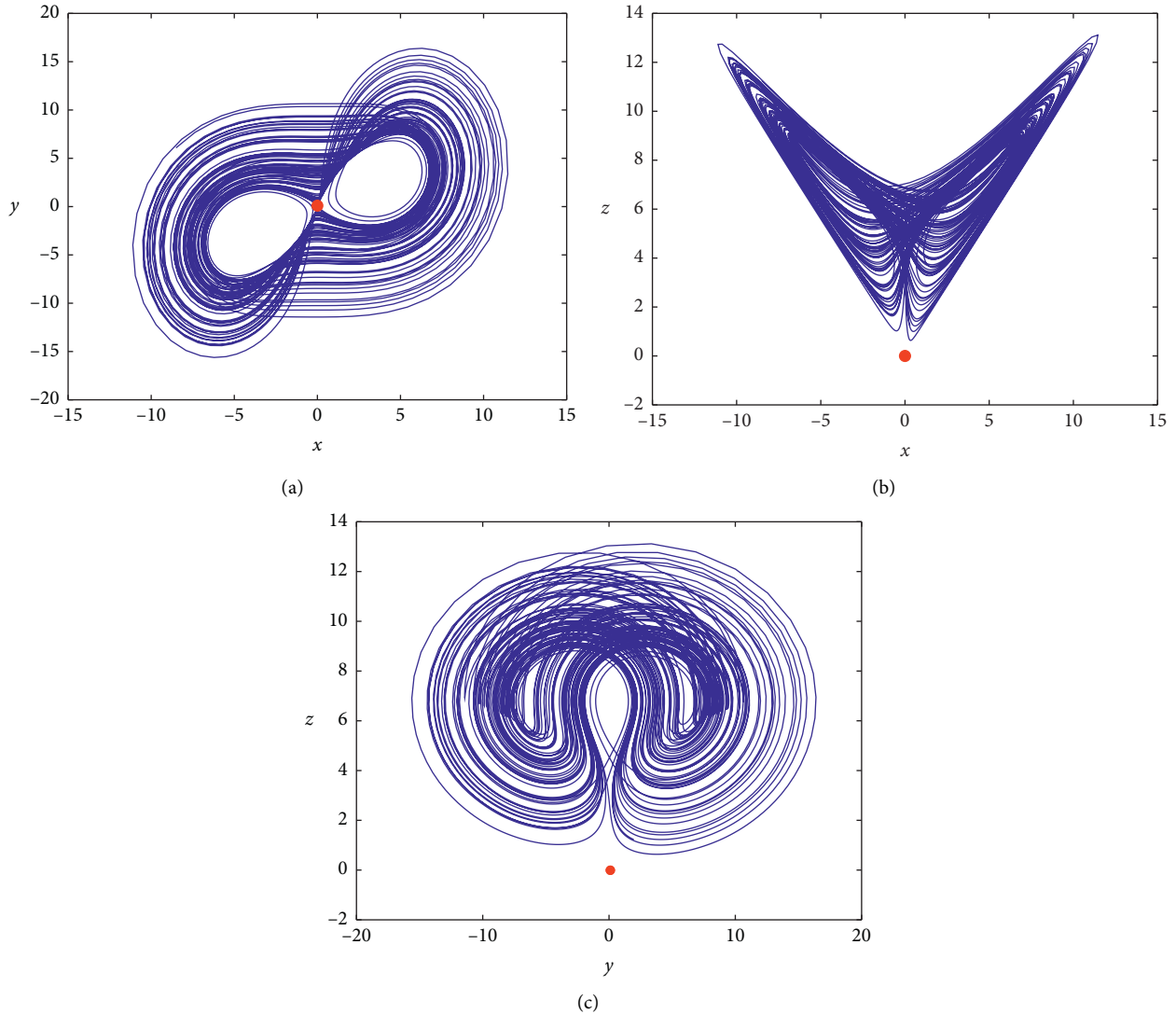
(a)

(b)
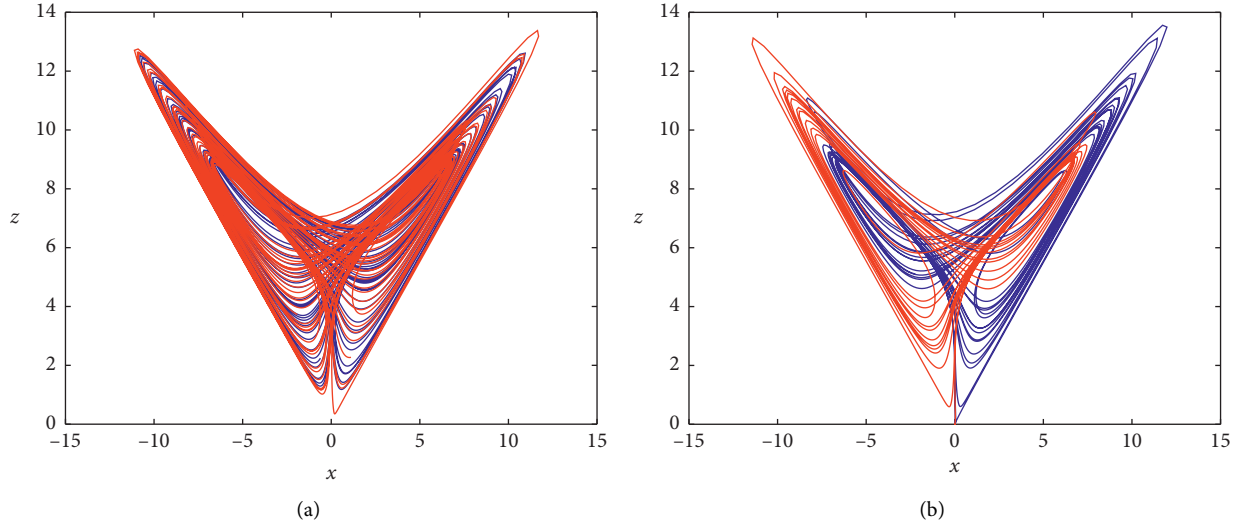
FIGURE 7: Phase diagrams in different projections of chaotic systems from initial values (1, 2, 20) and (1, 2, 3). (a) Phase diagrams in integer-order system (2). (b) Phase diagrams in fractional-order system (5).

(a)

(b)
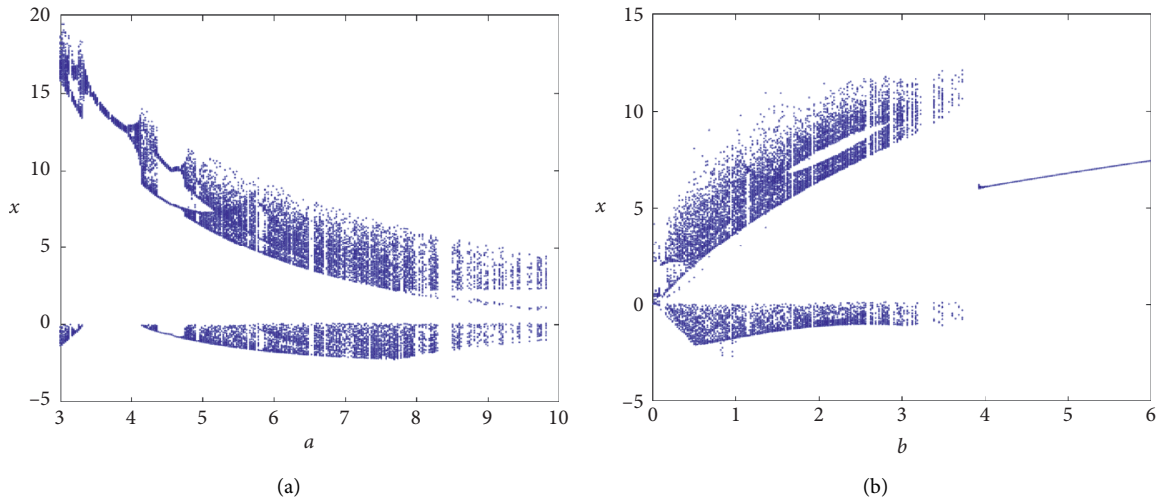
FIGURE 8: Dynamical properties of the fractional-order system with a and b varying. (a) a varying. (b) b varying.

(iv) $S4$: the average value of $B_i^m(r)$ can be calculated as

$$B^m(r) = \frac{1}{N-m} \sum_{i=1}^{N-m} B_i^m(r). \quad (17)$$

(v) $S5$: similarly, change m to $m+1$ and repeat step one with step three; get $A^m(r)$.

(vi) $S6$: theoretically, the SampEn complexity can be calculated by

$$\text{SampEn}(m, r) = \lim_{N \longrightarrow \infty} \left\{ -\ln \frac{A^m(r)}{B^m(r)} \right\}. \quad (18)$$

5.2. Complexity Analysis. Fix $a = 5$, $b = 2$, $c = 34$; let q change from 0.6 to 1; step size is 0.002; and the initial value of state variables $[x_0, y_0, z_0] = [1, 2, 3]$. The complexity of the system is shown in Figure 11(a). We can see that the complexity decreases with the increase of q, and the change of complexity is consistent with the change of Lyapunov exponent in Figure 6(b).

Fixed $b = 2$, $q = 0.8$; initial conditional is $[x_0, y_0, z_0] = [1, 2, 3]$; and let a vary. The complexity of the system is shown in Figure 11(b). The change of complexity is consistent with the change of Lyapunov exponent in Figure 10(a).

Fix $a = 2$, $q = 0.8$; initial conditional is $[x_0, y_0, z_0] = [1, 2, 3]$; and let b vary. The complexity of the system is shown in

(a)

(b)

(c)
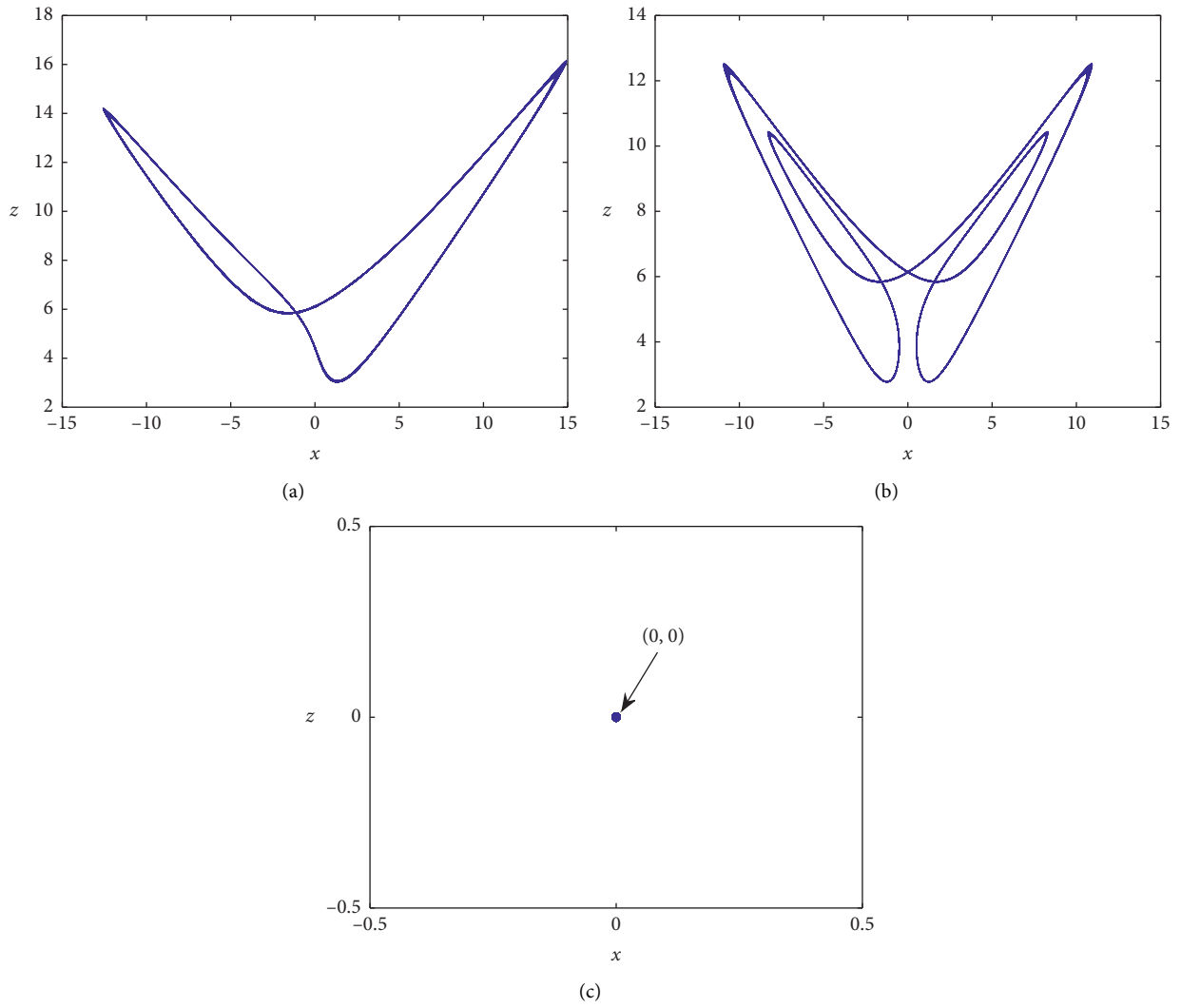
FIGURE 9: Phase diagrams of the systems with different a values. (a) $a = 3.5$. (b) $a = 4.4$. (c) $a = 8.46$.

(a)

(b)
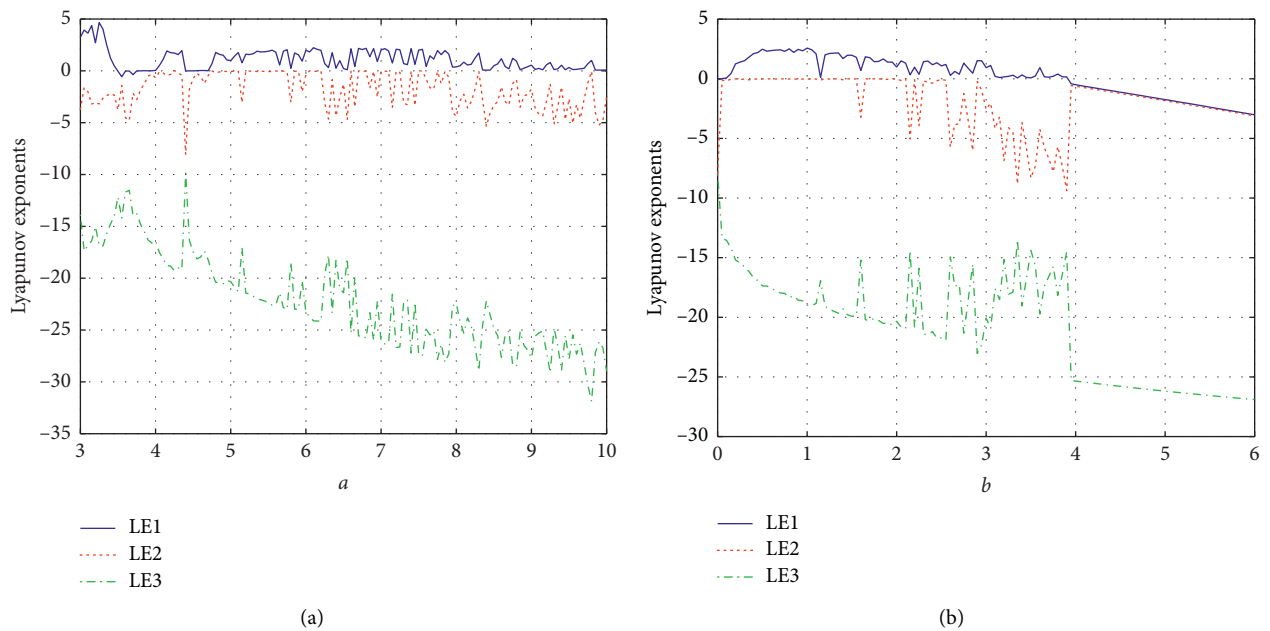
FIGURE 10: Lyapunov exponents spectrum of fractional order with a and b varying. (a) a varying. (b) b varying.

(a)

(b)

(c)
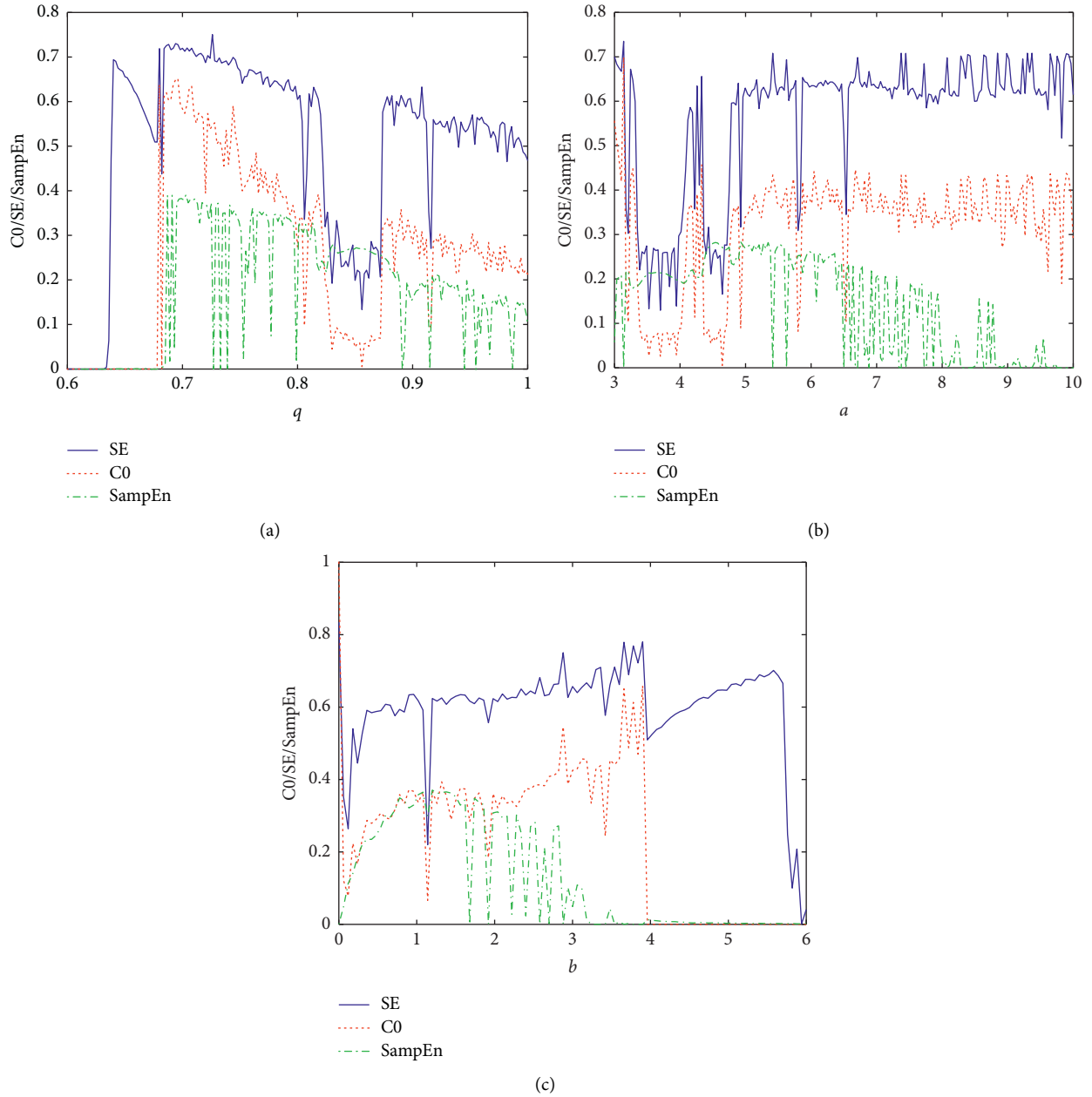
Figure 11: Complexity of the system with parameter varying. (a) q varying. (b) a varying. (c) b varying.

Figure 11(c). The change of complexity is consistent with the change of Lyapunov exponent in Figure 10(b).

Complexity is consistent with Lyapunov exponent, but Figure 11 also shows that sample entropy complexity is small; SE complexity is not obvious when some bifurcation points change; C_0 complexity is accurate; and C_0 complexity is faster than Lyapunov exponent, consumes less resources, and provides a good idea for analysis of chaotic systems.

Fix $a = 5$, $b = 2$, and $c = 34$; initial values of state variables $[x_0, y_0, z_0] = [1, 2, z0]$; let the $z(0)$ vary from 0 to 25 with step

size of 0.2 and q vary from 0.6 to 1 with step size of 0.004. The C_0 complexity in the $z(0)$-q plane is shown in Figure 12. It can be seen that, in the fractional-order region, the system complexity under the change of $z(0)$ is more complex than that of the integer order.

The complexity of the system is calculated by the time sequence of a certain state variable. Compared with Lyapunov exponent calculation, the calculation of complexity is faster and saves resources, but there are also some errors in complexity, especially when SE complexity is in a periodic state.
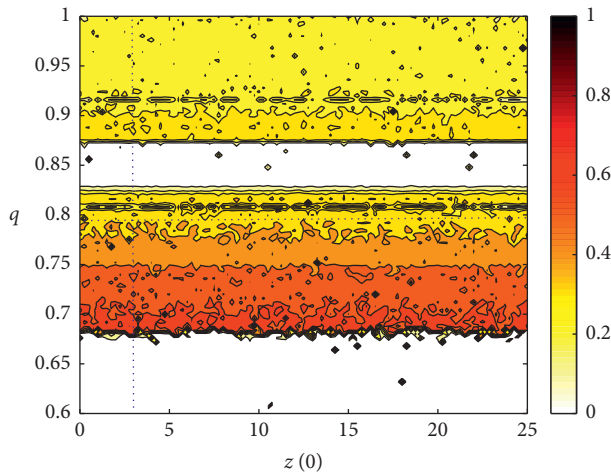
FIGURE 12: C_0 complexity in the $z\,(0)$-q plane.

6. Conclusion

In this paper, the accurate approximate solution for the fractional-order system with line equilibrium is obtained based on the Adomian decomposition method. Dynamical behaviors of the systems are analyzed using the chaotic attractor, bifurcation diagram, Lyapunov exponent spectrum, and largest Lyapunov exponent diagram. Chaotic range and periodic windows are determined. Both the system parameter and the fractional order can be taken as bifurcation parameters, which shows that the fractional-order system has more complex and abundant dynamics than its integral-order counterpart. Besides, integer-order systems do not have the phenomenon of attractors coexistence, while fractional-order systems have it, so fractional-order systems have better effects when applied to communication security systems.

Data Availability

The data used to support the findings of this study are available from the corresponding author upon request.

Conflicts of Interest

The authors declare that they have no conflicts of interest.

Acknowledgments

References

[1] K. I. Bolotin, F. Ghahari, M. D. Shulman, H. L. Stormer, and P. Kim, "Observation of the fractional quantum hall effect in graphene," *Nature*, vol. 462, no. 7270, p. 196, 2009.

[2] V. E. Tarasov and G. M. Zaslavsky, "Fractional dynamics of coupled oscillators with long-range interaction," *Chaos: An Interdisciplinary Journal of Nonlinear Science*, vol. 16, no. 2, Article ID 023110, 580 pages, 2006.

[3] O. P. Agrawal, "A general formulation and solution scheme for fractional optimal control problems," *Nonlinear Dynamics*, vol. 38, no. 1–4, pp. 323–337, 2004.

[4] P. J. Torvik and R. L. Bagley, "On the appearance of the fractional derivative in the behavior of real materials," *Journal of Applied Mechanics*, vol. 51, no. 2, pp. 725–728, 1984.

[5] Y. Wang, K. Sun, S. He, and H. Wang, "Dynamics of fractional-order sinusoidally forced simplified Lorenz system and its synchronization," *The European Physical Journal Special Topics*, vol. 223, no. 8, pp. 1591–1600, 2014.

[6] S. He, K. Sun, and H. Wang, "Complexity analysis and DSP implementation of the fractional-order Lorenz hyperchaotic system," *Entropy*, vol. 17, no. 12, pp. 8299–8311, 2015.

[7] H. Jia, Z. Guo, G. Qi, and Z. Chen, "Analysis of a four-wing fractional-order chaotic system via frequency-domain and time-domain approaches and circuit implementation for secure communication," *Optik*, vol. 155, pp. 233–241, 2018.

[8] S. He, K. Sun, H. Wang, X. Mei, and Y. Sun, "Generalized synchronization of fractional-order hyperchaotic systems and its DSP implementation," *Nonlinear Dynamics*, vol. 92, no. 1, pp. 85–96, 2018.

[9] C. Li, K. Su, Y. Tong, and H. Li, "Robust synchronization for a class of fractional-order chaotic and hyperchaotic systems," *Optik - International Journal for Light and Electron Optics*, vol. 124, no. 18, pp. 3242–3245, 2013.

[10] S. B. He, S. Banerjee, and B. Yan, "Chaos and symbol complexity in a conformable fractional-order memcapacitor system," *Complexity*, vol. 2018, Article ID 4140762, 15 pages, 2018.

[11] A. Charef, H. H. Sun, Y. Y. Tsao, and B. Onaral, "Fractal system as represented by singularity function," *IEEE Transactions on Automatic Control*, vol. 37, no. 9, pp. 1465–1470, 1992.

[12] G. Adomian, "A review of the decomposition method and some recent results for nonlinear equations," *Mathematical and Computer Modelling*, vol. 13, no. 7, pp. 17–43, 1990.

[13] W. Deng, "Short memory principle and a predictor-corrector approach for fractional differential equations," *Journal of Computational and Applied Mathematics*, vol. 206, no. 1, pp. 174–188, 2007.

[14] K. Diethelm, N. J. Ford, and A. D. Freed, "A predictor-corrector approach for the numerical solution of fractional differential equations," *Nonlinear Dynamics*, vol. 29, no. 1–4, pp. 3–22, 2002.

[15] M. S. Tavazoei and M. Haeri, "Unreliability of frequency-domain approximation in recognising chaos in fractional-order systems," *IET Signal Processing*, vol. 1, no. 4, pp. 171–181, 2007.

[16] H. Shao-Bo, S. Ke-Hui, and W. Hui-Hai, "Solution of the fractional-order chaotic system based on Adomian decomposition algorithm and its complexity analysis," *Acta Physica Sinica*, vol. 63, no. 3, Article ID 030502, 8 pages, 2014.

[17] B. Yan and S. He, "Dynamics and complexity analysis of the conformable fractional-order two-machine interconnected

power system," *Mathematical Methods in the Applied Sciences*, vol. 7270, pp. 1–16, 2019.

[18] S. Zhou and X. Wang, "Identifying the linear region based on machine learning to calculate the largest Lyapunov exponent from chaotic time series," *Chaos: An Interdisciplinary Journal of Nonlinear Science*, vol. 28, no. 12, Article ID 123118, 2018.

[19] S. Zhou, X. Wang, Z. Wang, and C. Zhang, "A novel method based on the pseudo-orbits to calculate the largest Lyapunov exponent from chaotic equations," *Chaos: An Interdisciplinary Journal of Nonlinear Science*, vol. 29, no. 3, Article ID 033125, 2019.

[20] C. Li, T. Lu, G. Chen, and H. Xing, "Doubling the coexisting attractors," *Chaos: An Interdisciplinary Journal of Nonlinear Science*, vol. 29, no. 5, Article ID 051102, 2019.

[21] C. Li, Y. Xu, G. Chen, Y. Liu, and J. Zheng, "Conditional symmetry: Bond for attractor growing," *Nonlinear Dynamics*, vol. 95, no. 2, pp. 1245–1256, 2018.

[22] X. Wang and G. Chen, "A chaotic system with only one stable equilibrium," *Communications in Nonlinear Science and Numerical Simulation*, vol. 17, no. 3, pp. 1264–1272, 2012.

[23] S. Jafari, J. C. Sprott, and M. Molaie, "A simple chaotic flow with a plane of equilibria," *International Journal of Bifurcation and Chaos*, vol. 26, no. 6, Article ID 1650098, 2016.

[24] S. Jafari, A. Ahmadi, A. J. M. Khalaf, H. Reza Abdolmohammadi, V.-T. Pham, and F. E. Alsaadi, "A new hidden chaotic attractor with extreme multi-stability," *AEU International Journal of Electronics & Communications*, vol. 89, pp. 131–135, 2018.

[25] B. Hamdi and S. Hassen, "A new hypersensitive hyperchaotic system with No equilibria," *International Journal of Bifurcation and Chaos*, vol. 27, no. 5, Article ID 1750064, 2017.

[26] X. Y. Hu, C. X. Liu, L. Liu, Y. P. Yao, and G. C. Zheng, "Multiscroll hidden attractors and multi-wing hidden attractors in a 5-dimensional memristive system," *Chinese Physics B*, vol. 26, no. 11, 130 pages, Article ID 110502, 2017.

[27] K. E. Chlouverakis and J. C. Sprott, "Chaotic hyperjerk systems," *Chaos, Solitons & Fractals*, vol. 28, no. 3, pp. 739–746, 2006.

[28] C. Li, J. C. Sprott, and W. Thio, *Linearization of the Lorenz systemPhysics Letters A*, vol. 379, no. 10-11, pp. 888-889, 2015.

[29] Z. Wang, "Existence of attractor and control of a 3D differential system," *Nonlinear Dynamics*, vol. 60, no. 3, pp. 369–373, 2009.

[30] G. Adomian, "A new approach to nonlinear partial differential equations," *Journal of Mathematical Analysis and Applications*, vol. 102, no. 2, pp. 420–434, 1984.

[31] P. A. Phillip, F. L. Chiu, and S. J. Nick, "Rapidly detecting disorder in rhythmic biological signals: a spectral entropy measure to identify cardiac arrhythmias," *Physical Review E*, vol. 79, no. 1, Article ID 011915, 2009.

[32] E. H. Shen, Z. J. Cai, and F. J. Gu, "Mathematical foundation of a new complexity measure," *Applied Mathematics & Mechanics*, vol. 26, no. 9, pp. 1188–1196, 2005.

Research Article

A Four-Zone Model and Nonlinear Dynamic Analysis of Solution Multiplicity of Buoyancy Ventilation in Underground Building

Yuxing Wang [iD] **and Chunyu Wei**

School of Architecture, Hunan University, Changsha 410082, Hunan, China

Correspondence should be addressed to Yuxing Wang; yuxingwang@hnu.edu.cn

The solution multiplicity of natural ventilation in buildings is very important to personnel safety and ventilation design. In this paper, a four-zone model of buoyancy ventilation in typical underground building is proposed. The underground structure is divided to four zones, a differential equation is established in each zone, and therefore, there are four differential equations in the underground structure. By solving and analyzing the equilibrium points and characteristic roots of the differential equations, we analyze the stability of three scenarios and obtain the criterions to determine the stability and existence of solutions for two scenarios. According to these criterions, the multiple steady states of buoyancy ventilation in any four-zone underground buildings for different stack height ratios and the strength ratios of the heat sources can be obtained. These criteria can be used to design buoyancy ventilation or natural exhaust ventilation systems in underground buildings. Compared with the two-zone model in (Liu et al. 2020), the results of the proposed four-zone model are more consistent with CFD results in (Liu et al. 2018). In addition, the results of proposed four-zone model are more specific and more detailed in the unstable equilibrium point interval. We find that the unstable equilibrium point interval is divided into two different subintervals corresponding to the saddle point of index 2 and the saddle focal equilibrium point of index 2, respectively. Finally, the phase portraits and vector field diagrams for the two scenarios are given.

1. Introduction

Nonlinear characteristics exist in systems with various research directions, such as neural network [1–3], chaotic circuit [4–12], and information security [13–15]. Building natural ventilation also has nonlinear characteristics. The solution multiplicity of natural ventilation in buildings is very important to personnel safety and ventilation design [16]. In the last decade, the multisolution problem of natural ventilation in buildings has attracted wide attention. Many papers have been published on the problem of multiple solutions to building natural ventilation [17–23]. These studies can be divided into three categories according to the number of building zones and vents. The first kind research is about the solution multiplicity of single-zone and double-opening buildings under the combined effect of wind pressure and thermal pressure [19, 24–27]. For example, Heiselberg et al. [24] studied the multiple steady-state

properties of single-zone and double-opening buildings under the action of wind pressure and buoyancy through a salt water experiment and CFD simulation; Lishman and Woods [25] reported solution multiplicity in both inclined tunnels and two-story aboveground buildings, and the study focused on the confrontation of wind pressure and buoyancy in a single-story building; Yuan and Glicksman [19, 26] researched the effects of different initial conditions on the generation of multiple steady states in single-zone buildings under the combined action of wind pressure and buoyancy; Pulat and Ersan [27] found that different turbulence parameters may produce multiple solutions through CFD simulation. The second kind research is about the solution multiplicity of single-zone and multiple opening buildings [28, 29]. For example, Durrani et al. [28] researched the multiple solutions in a typical aboveground building with one zone and three openings by CFD simulations; through theoretical analysis, Chen and Li [29] researched the

buoyancy ventilation of a single-zone building with three horizontal openings. The third kind research is about the solution multiplicity of two-zone buildings [30–33]. For example, Yang et al. [30, 31] analyzed in detail multiple steady states in a two-zone building by theoretical analyses and CFD simulations; Li et al. [32] studied the buoyancy ventilation in a two-story building with two heat sources and three openings by establishing a mathematical model of nonlinear ordinary differential equation; Yang et al. [33] analyzed the smoke exhaust spread of the three entrance tunnel in the fire scenarios and obtained six possible equilibrium states.

Recently, there are some reports on the multiplicity of ventilation solutions of underground structures [34, 35]. The study of the multiplicity of solutions for the natural ventilation of underground buildings is different from that of overground buildings. Because the underground buildings are not exposed to the outdoor environment, it is mainly thermal pressure ventilation (or buoyancy ventilation) rather than wind pressure ventilation which exist in the under structure. Liu et al. [34] investigated the formation process of multiple steady states in an underground building with two tunnel connecting to the outdoor environment. The heights of two tunnels are same, and one heat source is located in the corner of the buried space. Using the CFD method reproduces the two steady states of the buoyancy ventilation in the underground building. In 2020, Liu et al. [35] made nonlinear dynamic analysis of solution multiplicity of buoyancy ventilation in a typical underground structure. They gave a description of mathematical model of second-order nonlinear differential equation to underground structure with two zones and two tunnel connecting to the outdoor environment. Two heat sources are located in the two zones, respectively, and the heights of the two tunnels are not necessarily the same. By solving the equilibrium points and characteristic roots of the second order differential equation, the solution multiplicity can be determined when the strength ratio of two heat sources and height ratio of two tunnels were changed. However, in the literatures [34, 35], the underground structure has only two zones. The deeply burred room and tunnel were treated as one zone, which is just a very simple model. In the real underground structure, the deeply burred room and tunnel are different in temperature, mass flow rate, and air density. So, the deeply burred room and tunnel should not be treated as one zone if a more accurate model is needed. In this paper, we propose a new model, where the buried rooms and tunnels are treated as different zones. Thus, the underground structure consists of four zones, two zones for two tunnels, and two zones for deeply buried room. In this paper, the nomenclature of every variables and constants are shown in abbreviation section.

2. Proposed New Mathematical Model and Analysis

In order to study the nonlinear dynamics of typical deep-buried underground buildings with two openings, we first established the mathematical mode. Some assumptions were made: (i) each zone is well mixed; (ii) thermal mass is 1; (iii)

$E_1 > 0$; (iv) the mass flow impedance coefficient of the geometry is constant. Because the driving force is from thermal pressure, as illustrated in Figure 1, we divide the building into four zones: we can assume the heat source in the left side as positive, and the heat source of the right side could be either negative or positive, such that we could discuss the scenarios of two heat sources (the heat source in the left and right sides both are positive and the heat source in the left side is positive, the heat source in the right side is negative) and the scenario of one heat source.

2.1. Description of Mathematical Model. The proposed new schematics of underground structure is shown as Figure 1, which contains four zones, zone 1 and zone 2 for deeply burred room and zone 3 and zone 4 for two tunnels. The heights of two tunnels are H_1 and H_2 respectively, the T_i, q_i ($i = 1 \sim 4$) denote the temperature, and mass flow rate of four zones, respectively. Heat sources E_1 and E_2 are located in zone 1 and zone 2. As shown in Figure 1, two realizations are considered: for realization 1, the air flow enters from zone 1 to zone 2; for realization 2, the air flow enters from zone 2 to zone 1.

For realization 1, the heat gain of the internal thermal mass should be equal to the heat released by the heat sources minus the heat loss through airflows. Therefore, we can obtain the heat balance equations of the four zones shown in the following equations:

$$M_1 C_P \frac{dT_1}{dt} = -q_1 C_P (T_1 - T_3) + E_1, \tag{1}$$

$$M_2 C_P \frac{dT_2}{dt} = -q_2 C_P (T_2 - T_1) + E_2, \tag{2}$$

$$M_3 C_P \frac{dT_3}{dt} = -q_3 C_P (T_3 - T_a), \tag{3}$$

$$M_4 C_P \frac{dT_4}{dt} = -q_4 C_P (T_4 - T_2). \tag{4}$$

According to the flow loop method, the total pressure loss at ventilation vents on the flow loop is balanced by sum of the buoyancy pressure [35]. The pressure balance equation can be obtained as follows:

$$-\frac{T_1 - T_a}{T_a} \rho_a g H_1 + \frac{T_2 - T_a}{T_a} \rho_a g H_2$$
$$= S_1 q_1^2 + S_2 q_2^2 + S_3 q_3^2 + S_4 q_4^2. \tag{5}$$

According to the conservation of mass, we can obtain

$$q_1 = q_2 = q_3 = q_4. \tag{6}$$

Combining equations (5) and (6), mass flow rate can be obtained as follows:

$$q_1 = q_2 = q_3 = q_4 = q$$
$$= \sqrt{\frac{-((T_1 - T_a)/T_a)\rho_a g H_1 + ((T_2 - T_a)/T_a)\rho_a g H_2}{S_1 + S_2 + S_3 + S_4}}. \tag{7}$$
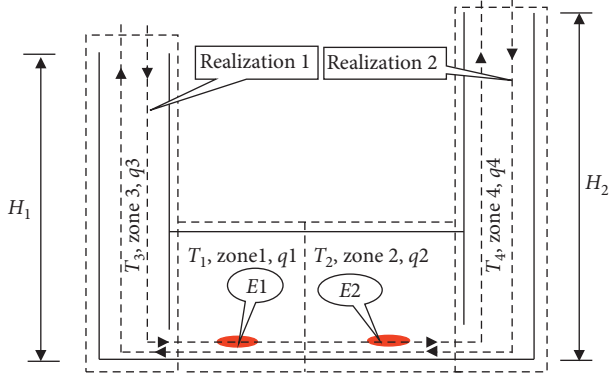
FIGURE 1: Proposed schematics of four-zone underground structure.

For realization 2, similarly, we can obtain the heat balance equations of the four zones as follows:

$$M_1 C_P \frac{dT_1}{dt} = -q_1 C_P (T_1 - T_2) + E_1, \quad (8)$$

$$M_2 C_P \frac{dT_2}{dt} = -q_2 C_P (T_2 - T_4) + E_2, \quad (9)$$

$$M_3 C_P \frac{dT_3}{dt} = -q_3 C_P (T_3 - T_1), \quad (10)$$

$$M_4 C_P \frac{dT_4}{dt} = -q_4 C_P (T_4 - T_a). \quad (11)$$

Based on the flow loop method, the total pressure loss at ventilation vents on the flow loop is balanced by sum of the buoyancy pressure, and we can obtain the pressure balance equation as follows:

$$\frac{T_1 - T_a}{T_a} \rho_a g H_1 - \frac{T_2 - T_a}{T_a} \rho_a g H_2 = S_1 q_1^2 + S_2 q_2^2 + S_3 q_3^2 + S_4 q_4^2. \quad (12)$$

According to the conservation of mass, we can obtain following equations about air flow rate:

$$q_1 = q_2 = q_3 = q_4 = q. \quad (13)$$

By combining equations (11) and (12), we can obtain

$$q_1 = q_2 = q_3 = q_4$$

$$= \sqrt{\frac{((T_1 - T_a)/T_a)\rho_a g H_1 - ((T_2 - T_a)/T_a)\rho_a g H_2}{S_1 + S_2 + S_3 + S_4}}. \quad (14)$$

2.2. Transformation of Variables and Parameters in Differential Equations.
Assuming $k = E_2/E_1$, $\Delta T_1 = T_1 - T_a$, $\Delta T_2 = T_2 - T_a$, $\Delta T_3 = T_3 - T_a$, $\Delta T_4 = T_4 - T_a$, $n = \sqrt{(\rho_a g H_1/(S_1 + S_2 + S_3 + S_4))}$, $\alpha = H_2/H_1$, $M_1 = M_2 = M$, $M_3 = M_4 = M/\xi$, and $\tau = t/(MC_p)$, we can obtain simplified nonlinear differential equations.

For realization 1, according to equations (1)~(4), (7) and above assumptions about variables and parameters, the simplified differential equations can be obtained as follows:

$$f_1 = \frac{d\Delta T_1}{d\tau} = -n\sqrt{\alpha \Delta T_2 - \Delta T_1}(\Delta T_1 - \Delta T_3) + E_1, \quad (15)$$

$$f_2 = \frac{d\Delta T_2}{d\tau} = -n\sqrt{\alpha \Delta T_2 - \Delta T_1}(\Delta T_2 - \Delta T_1) + E_2, \quad (16)$$

$$f_3 = \frac{d\Delta T_3}{d\tau} = -\xi n\sqrt{\alpha \Delta T_2 - \Delta T_1} \Delta T_3, \quad (17)$$

$$f_4 = \frac{d\Delta T_4}{d\tau} = -\xi n\sqrt{\alpha \Delta T_2 - \Delta T_1}(\Delta T_4 - \Delta T_2). \quad (18)$$

For realization 2, according to equations (8)~(11) and (14) and above assumptions about variables and parameters, the simplified differential equations can be obtained as follows:

$$f_1 = \frac{d\Delta T_1}{d\tau} = -n\sqrt{\Delta T_1 - \alpha \Delta T_2}(\Delta T_1 - \Delta T_2) + E_1, \quad (19)$$

$$f_2 = \frac{d\Delta T_2}{d\tau} = -n\sqrt{\Delta T_1 - \alpha \Delta T_2}(\Delta T_2 - \Delta T_4) + E_2, \quad (20)$$

$$f_3 = \frac{d\Delta T_3}{d\tau} = -\xi n\sqrt{\Delta T_1 - \alpha \Delta T_2}(\Delta T_3 - \Delta T_1), \quad (21)$$

$$f_4 = \frac{d\Delta T_4}{d\tau} = -\xi n\sqrt{\Delta T_1 - \alpha \Delta T_2} \Delta T_4. \quad (22)$$

2.3. Nonlinear Dynamic Analysis.
We can assume the heat source in the left side as positive and the heat source of the right side could be either negative or positive, such that we could discuss the scenarios of two heat sources (the heat source in the left and right sides both are positive and the heat source in the left side is positive, the heat source in the right side is negative) and the scenario of one heat source.

2.3.1. Stability Analysis for Scenario 1 (k Is Fixed and α Is Control Parameter).
Here, two conditions $k > 0$ (the heat source in the left and right sides both are positive) and $k < 0$ (the heat source in the left side is positive, and the heat source in the right side is negative) are discussed at the same time. We should solve equilibrium points and characteristic roots before stability analysis:

(1) Analysis of Equilibrium Points and Characteristic Roots for Realization 1.
The steady state solutions (equilibrium points) of realization 1 equations (15)~(18) are denoted as $(\Delta T_{01}, \Delta T_{02}, \Delta T_{03}, \Delta T_{04})$. In order to solve the equilibrium points, we can make that the right sides of equations (15)~(18) equal to zero; and the following equations hold:

$$-n\sqrt{\alpha\Delta T_2 - \Delta T_1}\left(\Delta T_1 - \Delta T_3\right) + E_1 = 0, \qquad (23)$$

$$-n\sqrt{\alpha\Delta T_2 - \Delta T_1}\left(\Delta T_2 - \Delta T_1\right) + E_2 = 0, \qquad (24)$$

$$-\xi n\sqrt{\alpha\Delta T_2 - \Delta T_1}\,\Delta T_3 = 0, \qquad (25)$$

$$-\xi n\sqrt{\alpha\Delta T_2 - \Delta T_1}\left(\Delta T_4 - \Delta T_2\right) = 0. \qquad (26)$$

By solving equations (23)~(26), we can obtain the equilibrium points as follows:

$$\Delta T_{01} = \frac{E_1}{n^{2/3}\left(-E_1 + E_1\alpha + E_2\alpha\right)^{1/3}} = \frac{E_1^{2/3}}{n^{2/3}\left(\alpha k - 1 + \alpha\right)^{1/3}}, \qquad (27)$$

$$\Delta T_{02} = \Delta T_{04} = (1 + k)\Delta T_{01}$$
$$= \frac{(1 + k)E_1}{n^{2/3}\left(-E_1 + E_1\alpha + E_2\alpha\right)^{1/3}} = \frac{(1 + k)E_1^{2/3}}{n^{2/3}\left(\alpha k - 1 + \alpha\right)^{1/3}}, \qquad (28)$$

$$\Delta T_{03} = 0. \qquad (29)$$

According to the characteristic determinant equal to 0, the solution of the differential equation can be discussed. The characteristic determinant equation is shown as follows. The expression of characteristic determinant is that

$$|J(Q) - \lambda E| = \begin{vmatrix} \dfrac{\partial f_1}{\partial \Delta T_1} - \lambda & \dfrac{\partial f_1}{\partial \Delta T_2} & \dfrac{\partial f_1}{\partial \Delta T_3} & \dfrac{\partial f_1}{\partial \Delta T_4} \\[2mm] \dfrac{\partial f_2}{\partial \Delta T_1} & \dfrac{\partial f_2}{\partial \Delta T_2} - \lambda & \dfrac{\partial f_2}{\partial \Delta T_3} & \dfrac{\partial f_2}{\partial \Delta T_4} \\[2mm] \dfrac{\partial f_3}{\partial \Delta T_1} & \dfrac{\partial f_3}{\partial \Delta T_2} & \dfrac{\partial f_3}{\partial \Delta T_3} - \lambda & \dfrac{\partial f_3}{\partial \Delta T_4} \\[2mm] \dfrac{\partial f_4}{\partial \Delta T_1} & \dfrac{\partial f_4}{\partial \Delta T_2} & \dfrac{\partial f_4}{\partial \Delta T_3} & \dfrac{\partial f_4}{\partial \Delta T_4} - \lambda \end{vmatrix} = 0. \qquad (30)$$

Combining equations (15)~(18), we can obtain the following expression:

$$\begin{vmatrix} \dfrac{n\left(\Delta T_{01} - \Delta T_{03}\right)}{2A} - nA - \lambda & -\dfrac{n\alpha\left(\Delta T_{01} - \Delta T_{03}\right)}{2A} & nA & 0 \\[3mm] \dfrac{n\left(\Delta T_{02} - \Delta T_{01}\right)}{2A} + nA & -\dfrac{n\alpha\left(\Delta T_{02} - \Delta T_{01}\right)}{2A} - nA - \lambda & 0 & 0 \\[3mm] \dfrac{\xi n\Delta T_{03}}{2A} & -\dfrac{\xi n\alpha\Delta T_{03}}{2A} & -\xi nA - \lambda & 0 \\[3mm] \dfrac{\xi n\left(\Delta T_{04} - \Delta T_{02}\right)}{2A} & -\dfrac{\xi n\alpha\left(\Delta T_{04} - \Delta T_{02}\right)}{2A} + \xi nA & 0 & -\xi nA - \lambda \end{vmatrix} = 0, \qquad (31)$$

where $J(Q)$ is the Jacobian matrix of equilibrium point Q, λ is the characteristic root, E is the identity matrix, and

$$A = \sqrt{\alpha\Delta T_{02} - \Delta T_{01}} = \frac{(\alpha k - 1 + \alpha)^{1/3}E_1^{1/3}}{n^{1/3}}, \qquad (32)$$

$$B = \Delta T_{01} - \Delta T_{03} = \frac{E_1^{2/3}}{n^{2/3}\left(\alpha k - 1 + \alpha\right)^{1/3}}, \qquad (33)$$

$$C = \Delta T_{02} - \Delta T_{01} = \frac{kE_1^{2/3}}{n^{2/3}\left(\alpha k - 1 + \alpha\right)^{1/3}}. \qquad (34)$$

Combining equations (31)~(34), we can obtain characteristic roots as follows:

$$\lambda_1 = \lambda_2 = -\xi nA = -\xi n\sqrt{\alpha\Delta T_{02} - \Delta T_{01}}$$
$$= -\xi n^{2/3}E_1^{1/3}\left(\alpha k - 1 + \alpha\right)^{1/3}. \qquad (35)$$

Assuming $k = E_2/E_1$, $\alpha = H_2/H_1$, to ensure that a real solution exists for equations (27) and (28), we have

$$\alpha k - 1 + \alpha > 0. \qquad (36)$$

Two other characteristic roots can be obtained according to a quadratic formula:

$$\lambda_{3,4} = \frac{-b \pm \sqrt{b^2 - 4ac}}{2a}$$

$$= \frac{-(n(\alpha C - B)/2A) - 2nA \pm \sqrt{[(n(\alpha C - B)/2A) + 2nA]^2 - 4n^2\left[(\alpha(B + C)/2) + A^2 - (B/2)\right]}}{2}, \qquad (37)$$

where

$$\begin{cases} a = 1; \\ b = \dfrac{n(\alpha C - B)}{2A} + 2nA = \dfrac{n^{2/3}E_1^{1/3}(5\alpha k - 5 + 4\alpha)}{2(\alpha k - 1 + \alpha)^{2/3}}, \\ c = n^2\left[\dfrac{\alpha(B+C)}{2} + A^2 - \dfrac{B}{2}\right] = \dfrac{3E_1^{2/3}(\alpha k - 1 + \alpha)^{2/3}n^{4/3}}{2} > 0, \\ \Delta = b^2 - 4ac = \dfrac{n^{4/3}E_1^{2/3}(5\alpha k - 5 + 4\alpha)^2}{4(\alpha k - 1 + \alpha)^{4/3}} - 6E_1^{2/3}(\alpha k - 1 + \alpha)^{2/3}n^{4/3}. \end{cases}$$

(38)

For convenience, the characteristic roots are set as follows: the real root are γ_i ($i = 1,2,3,4$); the complex roots are $\sigma_i + j\omega_i$ ($i = 1,2,3,4$). It is easy to know that $\lambda_{1,2}$ are always real number, $\lambda_1 = \gamma_1 = \lambda_2 = \gamma_2$.

If the discriminant Δ is greater than 0, both characteristic roots are real number, namely, $\lambda_3 = \gamma_3$ and $\lambda_4 = \gamma_4$. From equations (37) and (38), we can know that when $\Delta > 0$, the following expression holds:

$$n^{4/3}E_1^{2/3}(5\alpha k - 5 + 4\alpha)^2 > 24n^{4/3}E_1^{2/3}(\alpha k - 1 + \alpha)^2. \quad (39)$$

It is clear that

$$|5\alpha k - 5 + 4\alpha| > |2\sqrt{6}\,(\alpha k - 1 + \alpha)|. \quad (40)$$

When the discriminant Δ is less than 0, conjugate complex roots exist, namely, $\lambda_{3,4} = \sigma_{3,4} \pm j\omega_{3,4}$. From equations (37) and (38), we can know that when $\Delta < 0$, the following expression holds:

$$|5\alpha k - 5 + 4\alpha| < |2\sqrt{6}\,(\alpha k - 1 + \alpha)|. \quad (41)$$

(2) Stability Analysis for Realization 1 (k Is Fixed and α Is Control Parameter)

(1) No equilibrium point exists in realization 1

If no equilibrium point exists in realization 1, from equation (36), it is known that the following expression is satisfied:

$$\alpha k - 1 + \alpha < 0. \quad (42)$$

Therefore from expression (42), when $k < -1$, it is clear that $\alpha > (1/(k + 1))$ and when $k > -1$, we know that $0 < \alpha < (1/(k + 1))$.

(2) A stable equilibrium point exists in realization 1

(2.1) Assuming there are all negative real characteristic roots

In this case, λ_1, λ_2, λ_3, and λ_4 are all less than 0, and the system has a stable solution.

We know that owing to $\alpha k - 1 + \alpha > 0$, from equation (35), it is clear that λ_1 and λ_2 are always less than 0. To make $\lambda_{3,4} < 0$, according to Vieta theorem, we know that $\lambda_3 + \lambda_4 = -b$ and $\lambda_3\lambda_4 = c$. From equation (38), it

is known that always $c > 0$, and owing to $\alpha k - 1 + \alpha > 0$, from equation (38), if $5\alpha k - 5 + 4\alpha > 0$, we have $-b < 0$, then $\lambda_{3,4} < 0$. In this case, the absolute value sign in equation (40) can be removed; therefore, the following expression (43) can be obtained:

$$5\alpha k - 5 + 4\alpha > 2\sqrt{6}\,(\alpha k - 1 + \alpha). \quad (43)$$

From expression (43), we can obtain the following expression:

$$\alpha[k(5 - 2\sqrt{6}) + 4 - 2\sqrt{6}] > 5 - 2\sqrt{6}. \quad (44)$$

In summary, if there are all negative real characteristic roots, the system is stable when the following inequalities are satisfied:

$$\begin{cases} \alpha(k+1) - 1 > 0, \\ \alpha(5k+4) - 5 > 0, \\ \alpha[k(5 - 2\sqrt{6}) + 4 - 2\sqrt{6}] > 5 - 2\sqrt{6}. \end{cases} \quad (45)$$

(2.2) Assuming two negative real roots and two conjugate complex roots

In this case, the four characteristic roots behave as $\lambda_1 = \gamma_1 = \lambda_2 = \gamma_2$, $\lambda_{3,4} = \sigma_{3,4} \pm j\omega_{3,4}$, where λ_1 and λ_2 are two negative real roots and λ_3, λ_4 are two conjugate complex roots. When λ_1, λ_2, σ_3, and σ_4 are all less than 0, the system has a stable solution.

From equation (37), we know $\sigma_{3,4} = -b/2$. Owing to $\lambda_{1,2} < 0$, to make $\sigma_{3,4} < 0$, we need $-b < 0$, and from equation (38), we can obtain $5\alpha k + 4\alpha - 5 > 0$.

In this case, the absolute value sign in expression (41) can be removed; therefore, the following expression can be obtained:

$$5\alpha k - 5 + 4\alpha < 2\sqrt{6}\,(\alpha k - 1 + \alpha). \quad (46)$$

From (46), we can obtain that

$$\alpha[k(5 - 2\sqrt{6}) + 4 - 2\sqrt{6}] < 5 - 2\sqrt{6}. \quad (47)$$

In summary, λ_1, λ_2, σ_3, and σ_4 are all less than 0, the system is stable when the following inequalities are satisfied:

$$\begin{cases} \alpha(k+1) - 1 > 0, \\ \alpha(5k+4) - 5 > 0, \\ \alpha[k(5 - 2\sqrt{6}) + 4 - 2\sqrt{6}] < 5 - 2\sqrt{6}. \end{cases} \quad (48)$$

Combining expressions (45) and (48), a stable equilibrium point exists in realization 1, when the following expression is satisfied:

$$\begin{cases} \alpha(k+1) - 1 > 0, \\ \alpha(5k+4) - 5 > 0. \end{cases} \tag{49}$$

Case 1: when $k > -4/5$, it is easy to know that $5k + 4 > 0$ and $k + 1 > 0$, then expression (49) can be simplified to

$$\begin{cases} \alpha > \dfrac{1}{k+1}, \\ \alpha > \dfrac{5}{5k+4}. \end{cases} \tag{50}$$

From $5k + 4 > 0$ and $k + 1 > 0$, it is clear that $(1/(k+1)) - (5/(5k+4)) < 0$ and $0 < (1/(k+1)) < (5/(5k+4))$,

Therefore, from expression (49), it can be known that, when $k > -(4/5)$, $\alpha > (5/(5k+4))$

Case 2: when $-1 < k < -(4/5)$, it is easy to know that $5k + 4 < 0$ and $k + 1 > 0$.

Expression (49) can be simplified to

$$\begin{cases} \alpha > \dfrac{1}{k+1}, \\ \alpha < \dfrac{5}{5k+4}. \end{cases} \tag{51}$$

Owing to $5k + 4 < 0$ and $k + 1 > 0$, it is clear that $(5/(5k+4)) < 0$ and $(1/(k+1)) > 0$. Therefore, when $-1 < k < -(4/5)$, α does not exist.

Case 3: when $k < -1$, it is easy to know that $5k + 4 < 0$ and $k + 1 < 0$.

Expression (49) can be simplified to

$$\begin{cases} \alpha < \dfrac{1}{k+1}, \\ \alpha < \dfrac{5}{5k+4}. \end{cases} \tag{52}$$

Owing to $5k + 4 < 0$ and $k + 1 < 0$, it is clear that $(1/(k+1)) - (5/(5k+4)) < 0$. Thus we can obtain that $(5/(5k+4)) < (1/(k+1)) < 0$. Therefore, when $k < -1$, α does not exist.

In conclusion, we can obtain following several cases:

Case 1: $k > -(4/5)$ and $\alpha > (5/(5k+4))$

Case 2: $-1 < k < -(4/5)$ and α does not exist

Case 3: $k < -1$ and α does not exist

(3) An unstable equilibrium point exists in realization 1

(3.1) Assuming characteristic roots are all real and at least one is a positive

As long as one characteristic root is greater than 0, the equilibrium point of the system is unstable.

Owing to $\alpha k - 1 + \alpha > 0$, λ_1 and λ_2 are always less than 0 and only λ_3 or λ_4 is greater than 0. According to Vieta theorem, $\lambda_3 + \lambda_4 = -b$ and $\lambda_3 \lambda_4 = c$; it is known that $c > 0$, and owing to $\alpha k - 1 + \alpha > 0$, from equation (38), if $5\alpha k - 5 + 4\alpha < 0$, we can obtain $-b > 0$, then $\lambda_{3,4} > 0$.

In this case, the number in the left absolute value sign of expression (40) is less than zero, right absolute value sign of equation (40) is greater than zero, the absolute value signs are removed, and expression (40) can be transformed as follows:

$$5 - 4\alpha - 5\alpha k > 2\sqrt{6}(\alpha k - 1 + \alpha). \tag{53}$$

From expression (53), we can obtain

$$\alpha[k(2\sqrt{6} + 5) + 2\sqrt{6} + 4] < 5 + 2\sqrt{6}. \tag{54}$$

In summary, λ_1 and λ_2 are less than 0 and λ_3 and λ_4 are greater than 0. The system equilibrium point is unstable, and it is the saddle point of index 2, when the following inequalities are satisfied:

$$\begin{cases} \alpha k + \alpha - 1 > 0, \\ 5\alpha k + 4\alpha - 5 < 0, \\ \alpha[k(2\sqrt{6} + 5) + 2\sqrt{6} + 4] < 5 + 2\sqrt{6}. \end{cases} \tag{55}$$

Firstly, we consider the coefficient of α on the left side of third equation in expression (55) is greater than 0, namely, $k(2\sqrt{6} + 5) + 2\sqrt{6} + 4 > 0$, we can obtain $k > ((-2\sqrt{6} - 4)/(2\sqrt{6} + 5))$.

Then, we consider the coefficient of α on the left side of the third equation in expression (55) is less than 0, namely, $k(2\sqrt{6} + 5) + 2\sqrt{6} + 4 < 0$, we can obtain $k < ((-2\sqrt{6} - 4)/(2\sqrt{6} + 5))$.

It is easy to know that $-1 < ((-2\sqrt{6} - 4)/(2\sqrt{6} + 5)) < -(4/5)$. We discuss following several cases:

Case 1: when $((-2\sqrt{6} - 4)/(2\sqrt{6} + 5)) < k < -(4/5)$, owing to $-1 < ((-2\sqrt{6} - 4)/(2\sqrt{6} + 5)) < -(4/5)$, it is easy to know that $5k + 4 < 0$, $k + 1 > 0$ and $k(2\sqrt{6} + 5) + 2\sqrt{6} + 4 > 0$. Expression (55) is simplified as

$$\begin{cases} \alpha > \dfrac{1}{k+1}, \\ \alpha > \dfrac{5}{5k+4}, \\ \alpha < \dfrac{5 + 2\sqrt{6}}{k(2\sqrt{6} + 5) + 2\sqrt{6} + 4}. \end{cases} \tag{56}$$

From $5k + 4 < 0$, $k + 1 > 0$, $k(2\sqrt{6} + 5) + 2\sqrt{6} + 4 > 0$, it is clear that $(1/(k+1)) - ((5 + 2\sqrt{6})/(k(2\sqrt{6} + 5) + 2\sqrt{6} + 4)) < 0$ and $(5/(5k + 4)) - (1/(k + 1)) < 0$. So we have $0 < (1/(k + 1)) < ((5 + 2\sqrt{6})/(k(2\sqrt{6} + 5) + 2\sqrt{6} + 4))$ and $(5/(5k + 4)) < 0$.

Therefore, when $((-2\sqrt{6} - 4)/(2\sqrt{6} + 5)) < k < -(4/5)$, it can be obtained that $(1/(k + 1)) < \alpha < ((2\sqrt{6} + 5)/(k(2\sqrt{6} + 5) + 2\sqrt{6} + 4))$.

Case 2: when $-(4/5) < k$, owing to $-1 < ((-2\sqrt{6} - 4)/(2\sqrt{6} + 5)) < -(4/5)$, it is easy to know that $5k + 4 > 0$, $k + 1 > 0$ and $k(2\sqrt{6} + 5) + 2\sqrt{6} + 4 > 0$. Expression (55) can be simplified to

$$
\begin{cases}
\alpha > \dfrac{1}{k + 1}, \\[2mm]
\alpha < \dfrac{5}{5k + 4}, \\[2mm]
\alpha < \dfrac{5 + 2\sqrt{6}}{k(2\sqrt{6} + 5) + 2\sqrt{6} + 4}.
\end{cases}
\tag{57}
$$

From $5k + 4 > 0$, $k + 1 > 0$, $k(2\sqrt{6} + 5) + 2\sqrt{6} + 4 > 0$, it is clear that $(5/(5k + 4)) - ((5 + 2\sqrt{6})/(k(2\sqrt{6} + 5) + 2\sqrt{6} + 4)) > 0$ and $((5 + 2\sqrt{6})/(k(2\sqrt{6} + 5) + 2\sqrt{6} + 4)) - (1/(k + 1)) > 0$. So we have $0 < (1/(k + 1)) < ((5 + 2\sqrt{6})/(k(2\sqrt{6} + 5) + 2\sqrt{6} + 4)) < (5/(5k + 4))$. Therefore, when $-(4/5) < k$, we have $(1/(k + 1)) < \alpha < ((2\sqrt{6} + 5)/(k(2\sqrt{6} + 5) + 2\sqrt{6} + 4))$.

Case 3: when $-1 < k < ((-2\sqrt{6} - 4)/(2\sqrt{6} + 5))$, owing to $-1 < ((-2\sqrt{6} - 4)/(2\sqrt{6} + 5)) < -(4/5)$, it is easy to know that $5k + 4 < 0$, $k + 1 > 0$, and $k(2\sqrt{6} + 5) + 2\sqrt{6} + 4 < 0$.

Expression (55) can be simplified to

$$
\begin{cases}
\alpha > \dfrac{1}{k + 1}, \\[2mm]
\alpha > \dfrac{5}{5k + 4}, \\[2mm]
\alpha > \dfrac{5 + 2\sqrt{6}}{k(2\sqrt{6} + 5) + 2\sqrt{6} + 4}.
\end{cases}
\tag{58}
$$

From $5k + 4 < 0$, $k + 1 > 0$, $k(2\sqrt{6} + 5) + 2\sqrt{6} + 4 < 0$, it is easy to know that $((5 + 2\sqrt{6})/(k(2\sqrt{6} + 5) + 2\sqrt{6} + 4)) - (5/(5k + 4)) < 0$, so we have $((5 + 2\sqrt{6})/(k(2\sqrt{6} + 5) + 2\sqrt{6} + 4)) < (5/(5k + 4)) < 0$ and $0 < (1/(k + 1))$

Therefore, when $-1 < k < ((-2\sqrt{6} - 4)/(2\sqrt{6} + 5))$, we can obtain that $(1/(k + 1)) < \alpha$.

Case 4: when $k < -1$, owing to $-1 < ((-2\sqrt{6} - 4)/(2\sqrt{6} + 5)) < -(4/5)$, it is easy to know that $5k + 4 < 0$, $k + 1 < 0$, and $k(2\sqrt{6} + 5) + 2\sqrt{6} + 4 < 0$. Equation (55) can be simplified to

$$
\begin{cases}
\alpha < \dfrac{1}{k + 1}, \\[2mm]
\alpha > \dfrac{5}{5k + 4}, \\[2mm]
\alpha > \dfrac{5 + 2\sqrt{6}}{k(2\sqrt{6} + 5) + 2\sqrt{6} + 4}.
\end{cases}
\tag{59}
$$

From $5k + 4 < 0$, $k + 1 < 0$ and $k(2\sqrt{6} + 5) + 2\sqrt{6} + 4 < 0$, it is clear that $((5 + 2\sqrt{6})/(k(2\sqrt{6} + 5) + 2\sqrt{6} + 4)) - (5/(5k + 4)) < 0$ and $(1/(k + 1)) - ((5 + 2\sqrt{6})/(k(2\sqrt{6} + 5) + 2\sqrt{6} + 4)) < 0$, so we have $(1/(k + 1)) < ((5 + 2\sqrt{6})/(k(2\sqrt{6} + 5) + 2\sqrt{6} + 4)) < (5/(5k + 4)) < 0$. Therefore, when $k < -1$, α does not exist.

From what has been discussed above, we can obtain following relation between k and α:

Case 1: $((-2\sqrt{6} - 4)/(2\sqrt{6} + 5)) < k < -(4/5)$ and $(1/(k + 1)) < \alpha < ((2\sqrt{6} + 5)/(k(2\sqrt{6} + 5) + 2\sqrt{6} + 4))$

Case 2: $-(4/5) < k$ and $(1/(k + 1)) < \alpha < ((2\sqrt{6} + 5)/(k(2\sqrt{6} + 5) + 2\sqrt{6} + 4))$

Case 3: $-1 < k < ((-2\sqrt{6} - 4)/(2\sqrt{6} + 5))$ and $(1/(k + 1)) < \alpha$

Case 4: $k < -1$ and α does not exist.

(3.2) Assuming two negative real roots and two conjugate complex roots

In this case, the four characteristic roots behave as $\lambda_1 = \gamma_1 = \lambda_2 = \gamma_2$, $\lambda_{3,4} = \sigma_{3,4} \pm j\omega_{3,4}$, where λ_1 and λ_2 are two negative real roots and λ_3 and λ_4 are two conjugate complex roots.

Owing to λ_1 and λ_2 are always less than 0, when $\sigma_{3,4}$ is greater than 0, the equilibrium point of the system is unstable and it is the saddle-focus point of index 2. From (37), we know $\sigma_{3,4} = -b/2$. To make $\sigma_{3,4} > 0$, we need $-b > 0$, and from equation (38), we can obtain $5\alpha k + 4\alpha - 5 < 0$.

In this case, the absolute value sign in Expression (41) can be removed; therefore, the following expression can be obtained:

$$
5 - 5\alpha k - 4\alpha < 2\sqrt{6}(\alpha k - 1 + \alpha).
\tag{60}
$$

From expression (60), we can obtain that

$$
\alpha[k(5 + 2\sqrt{6}) + 4 + 2\sqrt{6}] > 2\sqrt{6} + 5.
\tag{61}
$$

In summary, λ_1 and λ_2 are less than 0, σ_3 and σ_4 are greater than 0, the system equilibrium point is unstable, and it is the saddle-focus point of index 2, when the following inequalities are satisfied:

$$\begin{cases} \alpha(k+1) - 1 > 0, \\ \alpha(5k+4) - 5 < 0, \\ \alpha[k(5 + 2\sqrt{6}) + 4 + 2\sqrt{6}] > 2\sqrt{6} + 5. \end{cases} \tag{62}$$

According to above discussion, we can obtain the following several cases:

Case 1: $((-4 - 2\sqrt{6})/(5 + 2\sqrt{6})) < k < -(4/5)$ and $\alpha > ((5 + 2\sqrt{6})/(k(5 + 2\sqrt{6}) + 4 + 2\sqrt{6}))$

Case 2: $-(4/5) < k$ and $((5 + 2\sqrt{6})/(k(5 + 2\sqrt{6}) + 4 + 2\sqrt{6})) < \alpha < (5/(5k+4))$

Case 3: $-1 < k < ((-4 - 2\sqrt{6})/(5 + 2\sqrt{6}))$ and α does not exist

Case 4: $k < -1$ and α does not exist

If k and α satisfy the above relation, the system equilibrium point is the saddle-focus point of index 2, which is unstable.

(3) Analysis of Equilibrium Points and Characteristic Roots for Realization 2. The steady state solution (equilibrium points) of realization 2, equations (19)~(22), is denoted as $(\Delta T_{01}, \Delta T_{02}, \Delta T_{03}, \Delta T_{04})$. In order to solve the equilibrium points, we can make that the right sides of equations (19)~(22) equal to zero; the following equations hold:

$$-n\sqrt{\Delta T_1 - \alpha\Delta T_2}(\Delta T_1 - \Delta T_2) + E_1 = 0, \tag{63}$$

$$-n\sqrt{\Delta T_1 - \alpha\Delta T_2}(\Delta T_2 - \Delta T_4) + E_2 = 0, \tag{64}$$

$$-\xi n\sqrt{\Delta T_1 - \alpha\Delta T_2}(\Delta T_3 - \Delta T_1) = 0, \tag{65}$$

$$-\xi n\sqrt{\Delta T_1 - \alpha\Delta T_2}\Delta T_4 = 0. \tag{66}$$

By solving equations (63)~(66), we can obtain the equilibrium points as follows:

$$\Delta T_{02} = \frac{E_2}{n^{2/3}(E_2 + E_1 - E_1\alpha k)^{1/3}} = \frac{kE_1^{2/3}}{n^{2/3}(k + 1 - \alpha k)^{1/3}}, \tag{67}$$

$$\Delta T_{01} = \Delta T_{03} = \frac{1+k}{k}\Delta T_{02} = \frac{(1+k)E_1}{n^{2/3}(E_2 + E_1 - E_1\alpha k)^{1/3}}$$
$$= \frac{(1+k)E_1^{2/3}}{n^{2/3}(k + 1 - \alpha k)^{1/3}}, \tag{68}$$

$$\Delta T_{04} = 0. \tag{69}$$

According to the characteristic determinant equal to 0, the solution of the differential equation can be discussed. The characteristic determinant equation is that

$$|J(Q) - \lambda E| = \begin{vmatrix} \dfrac{\partial f_1}{\partial \Delta T_1} - \lambda & \dfrac{\partial f_1}{\partial \Delta T_2} & \dfrac{\partial f_1}{\partial \Delta T_3} & \dfrac{\partial f_1}{\partial \Delta T_4} \\[2mm] \dfrac{\partial f_2}{\partial \Delta T_1} & \dfrac{\partial f_2}{\partial \Delta T_2} - \lambda & \dfrac{\partial f_2}{\partial \Delta T_3} & \dfrac{\partial f_2}{\partial \Delta T_4} \\[2mm] \dfrac{\partial f_3}{\partial \Delta T_1} & \dfrac{\partial f_3}{\partial \Delta T_2} & \dfrac{\partial f_3}{\partial \Delta T_3} - \lambda & \dfrac{\partial f_3}{\partial \Delta T_4} \\[2mm] \dfrac{\partial f_4}{\partial \Delta T_1} & \dfrac{\partial f_4}{\partial \Delta T_2} & \dfrac{\partial f_4}{\partial \Delta T_3} & \dfrac{\partial f_4}{\partial \Delta T_4} - \lambda \end{vmatrix} = 0. \tag{70}$$

Combining equations (19)~(22), we can obtain the following expression as follows:

$$\begin{vmatrix} -\dfrac{n(\Delta T_{01} - \Delta T_{02})}{2A} - nA - \lambda & \dfrac{n\alpha(\Delta T_{01} - \Delta T_{02})}{2A} + nA & 0 & 0 \\[2mm] -\dfrac{n(\Delta T_{02} - \Delta T_{04})}{2A} & \dfrac{n\alpha(\Delta T_{02} - \Delta T_{04})}{2A} - nA - \lambda & 0 & nA \\[2mm] -\dfrac{\xi n(\Delta T_{03} - \Delta T_{01})}{2A} + \xi nA & \dfrac{\xi n\alpha(\Delta T_{03} - \Delta T_{01})}{2A} & -\xi nA - \lambda & 0 \\[2mm] -\dfrac{\xi n\Delta T_{04}}{2A} & \dfrac{\xi n\alpha\Delta T_{04}}{2A} & 0 & -\xi nA - \lambda \end{vmatrix} = 0, \tag{71}$$

$$A = \sqrt{\Delta T_{01} - \alpha\Delta T_{02}} = \frac{(k + 1 - \alpha k)^{1/3}E_1^{1/3}}{n^{1/3}}, \tag{72}$$

$$B = \Delta T_{01} - \Delta T_{02} = \frac{E_1^{2/3}}{n^{2/3}(k + 1 - \alpha k)^{1/3}}, \tag{73}$$

$$C = \Delta T_{02} - \Delta T_{04} = \frac{kE_1^{2/3}}{n^{2/3}(k + 1 - \alpha k)^{1/3}}, \tag{74}$$

Combining equations (71)~(74), we can obtain characteristic roots as follows:

$$\lambda_1 = \lambda_2 = -\xi nA = -\xi n\sqrt{\Delta T_{01} - \alpha \Delta T_{02}}$$
$$= -\xi n^{2/3} E_1^{1/3} (k + 1 - \alpha k)^{1/3}. \tag{75}$$

$$\lambda_{3,4} = \frac{-b \pm \sqrt{b^2 - 4ac}}{2a}$$

$$= \frac{-(n(B - \alpha C)/2A) - 2nA \pm \sqrt{[(n(B - \alpha C)/2A) + 2nA]^2 - 4n^2[((B + C)/2) + A^2 - (\alpha C/2)]}}{2}, \tag{77}$$

where

$$\begin{cases} a = 1, \\[2mm] b = \dfrac{n(B - \alpha C)}{2A} + 2nA = \dfrac{n^{2/3} E_1^{1/3} (4k + 5 - 5\alpha k)}{2(k + 1 - \alpha k)^{2/3}}, \\[4mm] c = n^2 \left[\dfrac{(B + C)}{2} + A^2 - \dfrac{\alpha C}{2} \right] = \dfrac{3n^{4/3} E_1^{2/3} (k + 1 - \alpha k)^{2/3}}{2}, \\[4mm] \Delta = b^2 - 4ac = \dfrac{n^{4/3} E_1^{2/3} (4k + 5 - 5\alpha k)^2}{4(k + 1 - \alpha k)^{4/3}} - 6n^{4/3} E_1^{2/3} (k + 1 - \alpha k)^{2/3}. \end{cases} \tag{78}$$

Therefore, it is easy to know that $\lambda_{1,2}$ are always a real number, $\lambda_1 = \gamma_1 = \lambda_2 = \gamma_2$. If the discriminant Δ is greater than 0, both characteristic roots are real number: $\lambda_3 = \gamma_3$, $\lambda_4 = \gamma_4$. From equations (77) and (78), we can know that when $\Delta > 0$, the following expression holds:

$$n^{4/3} E_1^{2/3} (4k + 5 - 5\alpha k)^2 > 24n^{4/3} E_1^{2/3} (k + 1 - \alpha k)^2. \tag{79}$$

It is clear that

$$|4k + 5 - 5\alpha k| > |2\sqrt{6}(k + 1 - \alpha k)|. \tag{80}$$

When the discriminant Δ is less than 0, conjugate complex roots exist, namely, $\lambda_{3,4} = \sigma_{3,4} \pm j\omega_{3,4}$. From equations (77) and (78), we can know that when $\Delta < 0$, the following expression holds:

$$|4k + 5 - 5\alpha k| < |2\sqrt{6}(k + 1 - \alpha k)|. \tag{81}$$

(4) Stability Analysis for Realization 2 (k Is Fixed and α Is Control Parameter)

(1) No equilibrium point exists in realization 2

If no equilibrium point exists in realization 2, from equations (67)~(68), it is known that the following expression is satisfied:

$$k + 1 - \alpha k < 0. \tag{82}$$

To ensure that a real solution exists for equations (67) and (68), we have

$$k + 1 - \alpha k > 0. \tag{76}$$

Two other characteristic roots can be obtained according to the quadratic formula:

Therefore, from equation (82), when $k < -1$, it is clear that $0 < \alpha < ((k + 1)/k)$ and when $-1 < k < 0$, we know that α does not exist, or when $0 < k$, we know that $\alpha > ((k + 1)/k)$.

(2) A stable equilibrium point exists in realization 2

(2.1) Assuming there are all negative real characteristic roots

In this case, λ_1, λ_2, λ_3, and λ_4 are all less than 0, and the system has a stable solution. We know that, owing to $k + 1 - \alpha k > 0$, from equation (75), it is clear that λ_1 and λ_2 are always less than 0. To make $\lambda_{3,4} < 0$, according to Vieta theorem, we know that $\lambda_3 + \lambda_4 = -b$ and $\lambda_3 \lambda_4 = c$. From equation (78), it is known that always $c > 0$, and owing to $k + 1 - \alpha k > 0$, from equation (78), if $4k + 5 - 5\alpha k > 0$, we have $-b < 0$, then $\lambda_{3,4} < 0$. In this case, the absolute value sign in equation (80) can be removed; therefore, the following expression can be obtained:

$$4k + 5 - 5\alpha k > 2\sqrt{6}(k + 1 - \alpha k). \tag{83}$$

From expression (83), we can obtain the following expression:

$$\alpha k(5 - 2\sqrt{6}) < k(4 - 2\sqrt{6}) + 5 - 2\sqrt{6}. \tag{84}$$

In summary, if there are all negative real characteristic roots, the system is stable when the following inequalities are satisfied:

$$\begin{cases} \alpha k < k + 1, \\ 5\alpha k < 4k + 5, \\ \alpha k(5 - 2\sqrt{6}) < k(4 - 2\sqrt{6}) + 5 - 2\sqrt{6}. \end{cases} \tag{85}$$

(2.2) Assuming two real roots and two conjugate complex roots

In this case, the four characteristic roots behave as $\lambda_1 = \gamma_1 = \lambda_2 = \gamma_2$ and $\lambda_{3,4} = \sigma_{3,4} \pm j\omega_{3,4}$, where λ_1 and λ_2 are two negative real roots and λ_3 and λ_4 are two conjugate complex roots. When λ_1, λ_2, σ_3, and σ_4 are all less than 0, the system has a stable solution.

From equation (77), we know $\sigma_{3,4} = -b/2$. Owing to $\lambda_{1,2} < 0$, to make $\sigma_{3,4} < 0$, we have $-b < 0$, from equation (78), we can obtain $4k + 5 - 5\alpha k > 0$.

In this case, the absolute value sign in expression (81) can be removed; therefore, the following expression (86) can be obtained:

$$4k + 5 - 5\alpha k < 2\sqrt{6}\,(k + 1 - \alpha k). \tag{86}$$

From expression (86), we can obtain that

$$\alpha k\,(5 - 2\sqrt{6}\,) > k\,(4 - .2\sqrt{6}\,) + 5 - 2\sqrt{6}. \tag{87}$$

In summary, the system is stable when the following inequalities are satisfied:

$$\begin{cases} \alpha k < k + 1, \\ 5\alpha k < 4k + 5, \\ \alpha k\,(5 - 2\sqrt{6}\,) > k\,(4 - .2\sqrt{6}\,) + 5 - 2\sqrt{6}\,. \end{cases} \tag{88}$$

Combining expressions (85) and (88), a stable equilibrium point exists in realization 2, and the following equations are satisfied:

$$\begin{cases} \alpha k < k + 1, \\ 5\alpha k < 4k + 5. \end{cases} \tag{89}$$

Case 1: when $k > 0$, expression (89) can be simplified to

$$\begin{cases} \alpha < \dfrac{k + 1}{k}, \\ \alpha < \dfrac{4k + 5}{5k}. \end{cases} \tag{90}$$

When $k > 0$, it is easy to know that $((4k + 5)/5k) > 0$ and $((k + 1)/k) > 0$, and it is clear that $((k + 1)/k) - ((4k + 5)/5k) > 0$ and $0 < ((4k + 5)/5k) < ((k + 1)/k)$. Therefore, from expression (90), when $k > 0$, we know that $0 < \alpha < ((4k + 5)/5k)$.

Case 2: when $k < 0$, expression (89) can be simplified to

$$\begin{cases} \alpha > \dfrac{k + 1}{k}, \\ \alpha > \dfrac{4k + 5}{5k}. \end{cases} \tag{91}$$

It is clear that $((k + 1)/k) - ((4k + 5)/5k) > 0$ and $((4k + 5)/5k) < ((k + 1)/k)$. Owing to $\alpha > 0$, when $-1 < k < 0$, it clear that $((k + 1)/k) < 0$. Therefore, from expression (91), when $-1 < k < 0$, we know that $\alpha > 0$.

When $k < -1$, it clear that $((k + 1)/k) > 0$. Therefore, from expression (91), when $k < -1$, we know that $\alpha > ((k + 1)/k)$.

In conclusion, we can obtain following several cases:

Case 1: $k > 0$ and $0 < \alpha < ((4k + 5)/5k)$

Case 2: $-1 < k < 0$ and $\alpha > 0$

Case 3: $k < -1$ and $\alpha > ((k + 1)/k)$

(3) An unstable equilibrium point exists in realization 1

(3.1) Assuming characteristic roots are all real and at least one is a positive

As long as one characteristic root is greater than 0, the equilibrium point of the system is unstable. Owing to $k + 1 - \alpha k > 0$, λ_1 and λ_2 are always less than 0 and only λ_3 or λ_4 are greater than 0. According to Vieta theorem, it is known that $c > 0$, and owing to $k + 1 - \alpha k > 0$, from equation (78), if $4k + 5 - 5\alpha k < 0$, we have $-b > 0$, then $\lambda_{3,4} > 0$.

In this case, the number in the left absolute value sign of expression (80) is less than zero, right absolute value sign of expression (80) is greater than zero, and the absolute value signs are removed; expression (92) can be derived as follows:

$$5\alpha k - 5 - 4k > 2\sqrt{6}\,(k + 1 - \alpha k). \tag{92}$$

From expression (92), we can obtain

$$\alpha k\,(5 + 2\sqrt{6}\,) > k\,(4 + 2\sqrt{6}\,) + 5 + 2\sqrt{6}. \tag{93}$$

In summary, λ_1 and λ_2 are less than 0 and λ_3 and λ_4 greater than 0. The system equilibrium point is the saddle point of index 2, when the following inequalities are satisfied:

$$\begin{cases} \alpha k < k + 1, \\ 5\alpha k > 4k + 5, \\ \alpha k\,(5 + 2\sqrt{6}\,) > k\,(4 + 2\sqrt{6}\,) + 5 + 2\sqrt{6}\,. \end{cases} \tag{94}$$

It is easy to know that for any k, $((k\,(4 + 2\sqrt{6}\,) + 5 + 2\sqrt{6}\,)/k\,(5 + 2\sqrt{6}\,)) - ((k + 1)/k) < 0$ and $((4k + 5)/5k) - ((k\,(4 + 2\sqrt{6}\,) + 5 + 2\sqrt{6}\,)/k\,(5 + 2\sqrt{6}\,)) < 0$, so we have $((4k + 5)/5k) < ((k\,(4 + 2\sqrt{6}\,) + 5 + 2\sqrt{6}\,)/k\,(5 + 2\sqrt{6}\,)) < ((k + 1)/k)$. We discuss following several cases:

Case 1: when $k > 0$, expression (94) is simplified as

$$\begin{cases} \alpha < \dfrac{k+1}{k}, \\\\ \alpha > \dfrac{4k+5}{5k}, \\\\ \alpha > \dfrac{k(4+2\sqrt{6})+5+2\sqrt{6}}{k(5+2\sqrt{6})}. \end{cases} \tag{95}$$

Therefore, when $k > 0$, we have $((k(4+2\sqrt{6})+5+2\sqrt{6})/k(5+2\sqrt{6})) < \alpha < ((1+k)/k)$.

Case 2: when $k < 0$, expression (94) is simplified as

$$\begin{cases} \alpha > \dfrac{k+1}{k}, \\\\ \alpha < \dfrac{4k+5}{5k}, \\\\ \alpha < \dfrac{k(4+2\sqrt{6})+5+2\sqrt{6}}{k(5+2\sqrt{6})}. \end{cases} \tag{96}$$

Therefore, when $k < 0$, α does not exist.

In conclusion, we can obtain following several cases:

Case 1: $k > 0$ and $((k(4+2\sqrt{6})+5+2\sqrt{6})/k(5+2\sqrt{6})) < \alpha < ((1+k)/k)$

Case 2: $k < 0$ and α does not exist

If k and α satisfy above relation, the system equilibrium point is the saddle point of index 2, which is unstable.

(3.2) Assuming two negative real roots and two conjugate complex roots

In this case, the four characteristic roots behave as $\lambda_1 = \gamma_1 = \lambda_2 = \gamma_2$ and $\lambda_{3,4} = \sigma_{3,4} \pm j\omega_{3,4}$, where λ_1 and λ_2 are two negative real roots and λ_3 and λ_4 are two conjugate complex roots.

Owing to λ_1 and λ_2 are always less than 0, when σ_3 and σ_4 are greater than 0, the equilibrium point of the system is unstable and it is the saddle-focus point of index 2. From (77), we know $\sigma_{3,4} = -b/2$. To make $\sigma_{3,4} > 0$, we have $-b > 0$. From equation (78), it is known that $4\alpha - 5 + 5\alpha k < 0$.

In this case, the absolute value sign in expression (81) can be removed; therefore, the following expression (97) can be obtained:

$$5\alpha k - 5 - 4k < 2\sqrt{6}(k+1-\alpha k). \tag{97}$$

From expression (97), we can obtain that

$$\alpha k(5+2\sqrt{6}) < k(4+2\sqrt{6})+5+2\sqrt{6}. \tag{98}$$

In summary, λ_1 and λ_2 are less than 0 and σ_3 and σ_4 are greater than 0; the system equilibrium point is unstable and it is the saddle-focus point of index 2 when the following inequalities are satisfied:

$$\begin{cases} \alpha k < k+1, \\\\ 5\alpha k > 4k+5, \\\\ \alpha k(5+2\sqrt{6}) < k(4+2\sqrt{6})+5+2\sqrt{6}. \end{cases} \tag{99}$$

By referring the classification results of expression (94), we can obtain the following several cases:

Case 1: $k > 0$ and $((4k+5)/5k) < \alpha < ((k(4+2\sqrt{6})+5+2\sqrt{6})/k(5+2\sqrt{6}))$

Case 2: $k < 0$ and α does not exist

If k and α satisfy above relation, the system equilibrium point is the saddle-focus point of index 2, which is unstable.

In brief, for the scenario of the heat source in the left and right sides both are positive $(k > 0)$, from the above discussion, we can form a criterion shown in Table 1 to determine the stability of the system shown in Figure 1 when K is fixed, α is the control parameter, and $k > 0$. According to the values of α in Table 1, we can know whether there is an equilibrium point and the equilibrium point is stable or not.

We compared Table 1 with the part $k > 0$ of Table 1 in [35]. From these two tables, we can know that the results (whether the equilibrium point is stable or not) are roughly the same as those of [35]. However, our results are more specific and more detailed when the equilibrium points are unstable. In the unstable equilibrium point interval corresponding [35], we obtain two different subintervals corresponding to the saddle point of index 2 and the saddle focal equilibrium point of index 2, respectively. This is because our model has four characteristic roots and only two in [35]. The brief description is as follows. The equilibrium point is unstable in realization 1, when α is in the interval of $((1/(1+k)), (5/(5k+4)))$, and this interval can be divided into two parts, namely, $\alpha \in ((1/(k+1)), ((5+2\sqrt{6})/(k(5+2\sqrt{6})+4+2\sqrt{6})))$, where the unstable equilibrium point is the saddle point of index 2 and $\alpha \in (((5+2\sqrt{6})/(k(5+2\sqrt{6})+4+2\sqrt{6})), (5/(5k+4)))$, where the unstable equilibrium point is the saddle-focus point of index 2. The equilibrium point is unstable in realization 2, when α is in the interval of $(((4k+5)/5k), ((k+1)/k))$, and we divide this interval into two parts, namely, $\alpha \in (((4k+5)/5k), ((k(4+2\sqrt{6})+5+2\sqrt{6})/k(5+2\sqrt{6})))$, where the unstable equilibrium point is the saddle point of index 2 and $\alpha \in (((k(4+2\sqrt{6})+5+2\sqrt{6})/(k(5+2\sqrt{6}))), ((k+1)/k))$, where the unstable equilibrium point the saddle-focus point of index 2.

TABLE 1: Criterion for scenario 1 ((k is fixed, α is control parameter, and $k > 0$).

k	α	Realization 1	Realization 2
	$(0, (1/(k+1)))$	No	Stable
	$((1/(k+1)), ((5 + 2\sqrt{6})/(k(5 + 2\sqrt{6}) + 4 + 2\sqrt{6})))$	Saddle point of index 2	Stable
	$(((5 + 2\sqrt{6})/(k(5 + 2\sqrt{6}) + 4 + 2\sqrt{6})), (5/(5k+4)))$	Saddle-focus point of index 2	Stable
$(0, +\infty)$	$((5/(5k+4)), ((4k+5)/5k))$	Stable	Stable
	$(((4k+5)/5k), ((k(4 + 2\sqrt{6}) + 5 + 2\sqrt{6})/k(5 + 2\sqrt{6})))$	Stable	Saddle-focus point of index 2
	$(((k(4 + 2\sqrt{6}) + 5 + 2\sqrt{6})/k(5 + 2\sqrt{6})), ((k+1)/k))$	Stable	Saddle point of index 2
	$(((k+1)/k), +\infty)$	Stable	No

For the scenario of the heat source in the left is positive and the right is negative ($k < 0$), from the above discussion, we can form a criterion as shown in Table 2 to determine the stability of the system shown in Figure 1 when K is fixed, α is the control parameter, and $k < 0$. According to the values of α in Table 2, we can know whether there is an equilibrium point and the equilibrium point is stable or not.

We compared Table 2 with the part $k < 0$ of Table 1 in [35]. From these two tables, we can know the results (whether the equilibrium point is stable or not) are roughly the same as those in [35]. However, similarly, our results are more specific and more detailed when the equilibrium points are unstable. In the unstable equilibrium interval corresponding to literature [35], we obtain two different subintervals corresponding to the saddle point of index 2 and the saddle focal equilibrium point of index 2, respectively. This is because our model has four characteristic roots and only two in [35].

2.3.2. Stability Analysis for Scenario 2 (α Is Fixed and k Is Control Parameter)

(1) Stability Analysis for Realization 1 (α Is Fixed and k Is Control Parameter). In this scenario, the characteristic equation is the same as that of scenario 1.

(1) No equilibrium point exists in realization 1

In point (1) of Section 2.3.1, we already know that no equilibrium point exists in realization 1, when the following inequalities (equation (42) in Section 2.3.1) are satisfied:

$$\alpha k - 1 + \alpha < 0. \tag{100}$$

Therefore, from expression (98), when $\alpha > 0$, it is clear that $k < ((1 - \alpha)/\alpha)$.

(2) A stable equilibrium point exists in realization 1

In point (2) of Section 2.3.1, we already know that the system was stable, when the following inequalities (expression (49) in Section 2.3.1) are satisfied:

$$\begin{cases} \alpha(k+1) - 1 > 0, \\ \alpha(5k+4) - 5 > 0. \end{cases} \tag{101}$$

Taking out the coefficient k of expression (101), we can obtain expression (102):

$$\begin{cases} k\alpha > 1 - \alpha, \\ 5k\alpha > 5 - 4\alpha. \end{cases} \tag{102}$$

Owing to $\alpha > 0$, expression (102) are simplified as

$$\begin{cases} k > \dfrac{1 - \alpha}{\alpha}, \\ k > \dfrac{5 - 4\alpha}{5\alpha}. \end{cases} \tag{103}$$

Owing to $\alpha > 0$, it is clear that $((5 - 4\alpha)/5\alpha) - ((1 - \alpha)/\alpha) > 0$ and $((5 - 4\alpha)/5\alpha) > ((1 - \alpha)/\alpha)$; therefore, from expression (101), when $\alpha > 0$, we know that $((5 - 4\alpha)/5\alpha) < k$.

(3) An unstable equilibrium point exists in realization 1

(3.1) Assuming characteristic roots are all real and at least one is a positive

In point (3.1) of Section 2.3.1, we already know that the equilibrium point of the system is unstable and it is the saddle point of index 2, when the following inequalities (expression (55) in Section 2.3.1) are satisfied:

$$\begin{cases} \alpha k + \alpha - 1 > 0, \\ 5\alpha k + 4\alpha - 5 < 0, \\ \alpha[k(2\sqrt{6} + 5) + 2\sqrt{6} + 4] < 5 + 2\sqrt{6}. \end{cases} \tag{104}$$

Taking out the coefficient k of expression (104), we can obtain the following expression:

$$\begin{cases} k\alpha > 1 - \alpha, \\ 5k\alpha < 5 - 4\alpha, \\ (5 + 2\sqrt{6})k\alpha < 5 + 2\sqrt{6} - \alpha(4 + 2\sqrt{6}). \end{cases} \tag{105}$$

Owing to $\alpha > 0$, expression (105) is simplified:

Table 2: Criterion for scenario 1 (k is fixed, α is control parameter and $k < 0$).

k	α	Realization 1	Realization 2
$(-(4/5), 0)$	$(0, (1/(k+1)))$	No	Stable
	$((1/(k+1)), ((2\sqrt{6}+5)/(k(2\sqrt{6}+5)+2\sqrt{6}+4)))$	Saddle point of index 2	Stable
	$(((2\sqrt{6}+5)/(k(2\sqrt{6}+5)+2\sqrt{6}+4)), (5/(5k+4)))$	Saddle-focus point of index 2	Stable
	$((5/(5k+4)), +\infty)$	Stable	Stable
$(((-2\sqrt{6}-4)/(2\sqrt{6}+5)), -(4/5))$	$(0, (1/(k+1)))$	No	Stable
	$((1/(k+1)), ((5+2\sqrt{6})/(k(5+2\sqrt{6})+4+2\sqrt{6})))$	Saddle point of index 2	Stable
	$(((5+2\sqrt{6})/(k(5+2\sqrt{6})+4+2\sqrt{6})), +\infty)$	Saddle-focus point of index 2	Stable
$(-1, ((-2\sqrt{6}-4)/(2\sqrt{6}+5)))$	$(0, (1/(k+1)))$	No	Stable
	$((1/(k+1)), +\infty)$	Saddle point of index 2	Stable
$(-\infty, -1)$	$(0, ((1+k)/k))$	No	No
	$(((1+k)/k), +\infty)$	No	Stable

$$\begin{cases} k > \dfrac{1-\alpha}{\alpha}, \\[2mm] k < \dfrac{5-4\alpha}{5\alpha}, \\[2mm] k < \dfrac{5+2\sqrt{6}-\alpha(4+2\sqrt{6})}{(5+2\sqrt{6})\alpha}. \end{cases} \tag{106}$$

It is easy to know that, for any $\alpha > 0$, $((1-\alpha)/\alpha) - ((5+2\sqrt{6}-\alpha(4+2\sqrt{6}))/(\alpha(5+2\sqrt{6}))) < 0$ and $((5+2\sqrt{6}-\alpha(4+2\sqrt{6}))/\alpha(5+2\sqrt{6})) - ((5-4\alpha)/5\alpha) < 0$, so we have $((1-\alpha)/\alpha) < ((5+2\sqrt{6}-\alpha(4+2\sqrt{6}))/\alpha(5+2\sqrt{6})) < ((5-4\alpha)/5\alpha)$. Therefore, from expression (106), it can be known that, when $\alpha > 0$, we know that $((1-\alpha)/\alpha) < k < ((5+2\sqrt{6}-\alpha(4+2\sqrt{6}))/\alpha(5+2\sqrt{6}))$.

If α and k satisfy above relation, the system equilibrium point is the saddle point of index 2, which is unstable.

(3.2) Assuming two negative real roots and two conjugate complex roots

In point (3.2) of Section 2.3.1, we already know that the equilibrium point of the system is unstable and it is the saddle-focus point of index 2, when the following inequalities (expression (62) in Section 2.3.1) are satisfied:

$$\begin{cases} \alpha(k+1) - 1 > 0, \\ \alpha(5k+4) - 5 < 0, \\ \alpha[k(5+2\sqrt{6})+4+2\sqrt{6}] > 2\sqrt{6}+5. \end{cases} \tag{107}$$

Taking out the coefficient k of expression (107), we can obtain the following expression:

$$\begin{cases} k\alpha > 1 - \alpha, \\ 5k\alpha < 5 - 4\alpha, \\ (5+2\sqrt{6})k\alpha > 5 + 2\sqrt{6} - \alpha(4+2\sqrt{6}). \end{cases} \tag{108}$$

Owing to $\alpha > 0$, expression (108) is simplified:

$$\begin{cases} k > \dfrac{1-\alpha}{\alpha}, \\[2mm] k < \dfrac{5-4\alpha}{5\alpha}, \\[2mm] k > \dfrac{5+2\sqrt{6}-\alpha(4+2\sqrt{6})}{(5+2\sqrt{6})\alpha}. \end{cases} \tag{109}$$

By referring the solution procedure of expression (104), we can obtain the following result. When $\alpha > 0$, we know that $((5+2\sqrt{6}-\alpha(4+2\sqrt{6}))/\alpha(5+2\sqrt{6})) < k < ((5-4\alpha)/5\alpha)$.

If α and k satisfy the above relation, the system equilibrium point is the saddle-focus point of index 2, which is unstable.

(2) Stability Analysis for Realization 2 (α Is Fixed, k Is Control Parameter)

(1) No equilibrium point exists in realization 2

In point (1) of (4) of Section 2.3.1, we already know that no equilibrium point exists in realization 2, when the following inequalities (expression (82) in Section 2.3.1) are satisfied:

$$k + 1 - \alpha k < 0. \tag{110}$$

Therefore, from expression (110), when $0 < \alpha < 1$, it is clear that $k < (1/(\alpha - 1))$ and when $\alpha > 1$, we know that $k > (1/(\alpha - 1))$.

(2) A stable equilibrium point exists in realization 2

In point (2) of (4) of Section 2.3.1, we already know that the system was stable, when the following inequalities (expression (89) in (4) of Section 2.3.1) are satisfied:

$$\begin{cases} \alpha k < k + 1, \\ 5\alpha k < 4k + 5. \end{cases} \tag{111}$$

Taking out the coefficient k of expression (111), we can obtain the following expression:

$$\begin{cases} k(\alpha - 1) < 1, \\ k(5\alpha - 4) < 5. \end{cases} \tag{112}$$

Case 1: when $\alpha > 1$, it is easy to know that $\alpha - 1 > 0$ and $5\alpha - 4 > 0$, and then expression (112) can be simplified to

$$\begin{cases} k < \dfrac{1}{\alpha - 1}, \\ k < \dfrac{5}{5\alpha - 4}. \end{cases} \tag{113}$$

From $\alpha - 1 > 0$ and $5\alpha - 4 > 0$, it is clear that $(5/(5\alpha - 4)) - (1/(\alpha - 1)) < 0$ and $0 < (5/(5\alpha - 4)) < (1/(\alpha - 1))$. Therefore, from expression (113), when $\alpha > 1$, we know that $k < (-5/(4 - 5\alpha))$.

Case 2: when $(4/5) < \alpha < 1$, it is easy to know that $\alpha - 1 < 0$ and $5\alpha - 4 > 0$; then expression (112) can be simplified to

$$\begin{cases} k > \dfrac{1}{\alpha - 1}, \\ k < \dfrac{5}{5\alpha - 4}. \end{cases} \tag{114}$$

From $\alpha - 1 < 0$ and $5\alpha - 4 > 0$, it is clear that $(5/(5\alpha - 4)) - (1/(\alpha - 1)) > 0$, $(1/(\alpha - 1)) < 0$ and $0 < (5/(5\alpha - 4))$. Therefore, from expression (112), when $(4/5) < \alpha < 1$, we know that $(1/(\alpha - 1)) < k < (5/(5\alpha - 4))$.

Case 3: when $0 < \alpha < (4/5)$, it is easy to know that $\alpha - 1 < 0$ and $5\alpha - 4 < 0$, then expression (112) can be simplified to

$$\begin{cases} k > \dfrac{1}{\alpha - 1}, \\ k > \dfrac{5}{5\alpha - 4}. \end{cases} \tag{115}$$

From $\alpha - 1 < 0$ and $5\alpha - 4 < 0$, it is clear that $(5/(5\alpha - 4)) - (1/(\alpha - 1)) < 0$ and $(5/(5\alpha - 4)) < (1/(\alpha - 1)) < 0$, Therefore, from expression (115), when $0 < \alpha < (4/5)$, we know that $(1/(\alpha - 1)) < k$. In conclusion, we can obtain following several cases:

Case 1: $\alpha > 1$ and $k < (-5/(4 - 5\alpha))$

Case 2: $(4/5) < \alpha < 1$ and $(1/(\alpha - 1)) < k < (5/(5\alpha - 4))$

Case 3: $0 < \alpha < (4/5)$ and $(1/(\alpha - 1)) < k$

(3) An unstable equilibrium point exists in realization 2

(3.1) Assuming characteristic roots are all real and at least one is a positive

In point (3.1) of Section 2.3.1, we already know that the equilibrium point of the system is unstable and it is the saddle point of index 2, when the following inequalities (expression (94) in Section 2.3.1) are satisfied:

$$\begin{cases} \alpha k < k + 1, \\ 5\alpha k > 4k + 5, \\ \alpha k(5 + 2\sqrt{6}) > k(4 + 2\sqrt{6}) + 5 + 2\sqrt{6}. \end{cases} \tag{116}$$

Taking out the coefficient k of expression (116), we can obtain the following expression:

$$\begin{cases} k(1 - \alpha) + 1 > 0, \\ k(4 - 5\alpha) + 5 < 0, \\ k[\alpha(5 + 2\sqrt{6}) + (-2\sqrt{6} - 4)] > 5 + 2\sqrt{6}. \end{cases} \tag{117}$$

Firstly, we consider the coefficient of k on the left side of third inequality in expression (117) is greater than 0, namely, $\alpha(5 + 2\sqrt{6}) + (-2\sqrt{6} - 4) > 0$, and we can obtain $\alpha > ((4 + 2\sqrt{6})/(5 + 2\sqrt{6}))$. Then, we consider the coefficient of α on the left side of third inequality in (117) is less than 0, namely, $\alpha(5 + 2\sqrt{6}) + (-2\sqrt{6} - 4) < 0$, and we can obtain $\alpha < ((4 + 2\sqrt{6})/(5 + 2\sqrt{6}))$. It is easy to know that $0 < (4/5) < ((4 + 2\sqrt{6})/(5 + 2\sqrt{6})) < 1$. We discuss following several cases:

Case 1: when $((4 + 2\sqrt{6})/(5 + 2\sqrt{6})) < \alpha < 1$, owing to $0 < (4/5) < ((4 + 2\sqrt{6})/(5 + 2\sqrt{6})) < 1$, it is easy to know that $4 - 5\alpha < 0$, $1 - \alpha > 0$, and $\alpha(5 + 2\sqrt{6}) + (-2\sqrt{6} - 4) > 0$; equation (117) is simplified as

$$\begin{cases} k > \dfrac{-1}{1 - \alpha}, \\ k > \dfrac{-5}{4 - 5\alpha}, \\ k > \dfrac{5 + 2\sqrt{6}}{\alpha(5 + 2\sqrt{6}) - 4 - 2\sqrt{6}}. \end{cases} \tag{118}$$

From $4 - 5\alpha < 0$, $1 - \alpha > 0$, and $\alpha(5 + 2\sqrt{6}) + (-2\sqrt{6} - 4) > 0$, it is clear that $(-1/(1 - \alpha)) - (-5/(4 - 5\alpha)) < 0$, $(-5/(4 - 5\alpha)) - ((5 + 2\sqrt{6})/(\alpha(5 + 2\sqrt{6}) - 4 - 2\sqrt{6})) < 0$, and $(-1/(1 - \alpha)) < (-5/(4 - 5\alpha)) < ((5 + 2\sqrt{6})/(\alpha(5 + 2\sqrt{6}) - 4 - 2\sqrt{6}))$. Therefore, when $((4 + 2\sqrt{6})/(5 + 2\sqrt{6})) < \alpha < 1$, we know that $k > ((5 + 2\sqrt{6})/(\alpha(5 + 2\sqrt{6}) - 4 - 2\sqrt{6}))$.

Case 2: when $\alpha > 1$, owing to $0 < (4/5) < ((4 + 2\sqrt{6})/(5 + 2\sqrt{6})) < 1$, it is easy to know that $4 - 5\alpha < 0$,

$1 - \alpha < 0$, and $\alpha(5 + 2\sqrt{6}) + (-2\sqrt{6} - 4) > 0$; expression (117) is simplified as

$$\begin{cases} k < \dfrac{-1}{1 - \alpha}, \\[2mm] k > \dfrac{-5}{4 - 5\alpha}, \\[2mm] k > \dfrac{5 + 2\sqrt{6}}{\alpha(5 + 2\sqrt{6}) - 4 - 2\sqrt{6}}. \end{cases} \tag{119}$$

From $4 - 5\alpha < 0$, $1 - \alpha < 0$, and $\alpha(5 + 2\sqrt{6}) + (-2\sqrt{6} - 4) > 0$, it is clear that $(-5/(4 - 5\alpha)) - ((5 + 2\sqrt{6})/(\alpha(5 + 2\sqrt{6}) - 4 - 2\sqrt{6})) < 0$, $((5 + 2\sqrt{6})/(\alpha(5 + 2\sqrt{6}) - 4 - 2\sqrt{6})) - (-1/(1 - \alpha)) < 0$, and $(-5/(4 - 5\alpha)) < ((5 + 2\sqrt{6})/(\alpha(5 + 2\sqrt{6}) - 4 - 2\sqrt{6})) < (-1/(1 - \alpha))$. Therefore, when $\alpha > 1$, we know that $((5 + 2\sqrt{6})/(\alpha(5 + 2\sqrt{6}) - 4 - 2\sqrt{6})) < k < (-1/(1 - \alpha))$.

Case 3: when $(4/5) < \alpha < ((4 + 2\sqrt{6})/(5 + 2\sqrt{6}))$, owing to $0 < (4/5) < ((4 + 2\sqrt{6})/(5 + 2\sqrt{6})) < 1$, it is easy to know that $4 - 5\alpha < 0$, $1 - \alpha > 0$, and $\alpha(5 + 2\sqrt{6}) + (-2\sqrt{6} - 4) < 0$; expression (117) are simplified as

$$\begin{cases} k > \dfrac{-1}{1 - \alpha}, \\[2mm] k > \dfrac{-5}{4 - 5\alpha}, \\[2mm] k < \dfrac{5 + 2\sqrt{6}}{\alpha(5 + 2\sqrt{6}) - 4 - 2\sqrt{6}}. \end{cases} \tag{120}$$

From $4 - 5\alpha < 0$, $1 - \alpha > 0$, and $\alpha(5 + 2\sqrt{6}) + (-2\sqrt{6} - 4) < 0$, it is clear that $((5 + 2\sqrt{6})/(\alpha(5 + 2\sqrt{6}) - 4 - 2\sqrt{6})) - (-1/(1 - \alpha)) < 0$, $(-1/(1 - \alpha)) - (-5/(4 - 5\alpha)) < 0$ $0 < (-5/(4 - 5\alpha))$, and $((5 + 2\sqrt{6})/(\alpha(5 + 2\sqrt{6}) - 4 - 2\sqrt{6})) < (-1/(1 - \alpha)) < 0$. Therefore, when $(4/5) < \alpha < ((4 + 2\sqrt{6})/(5 + 2\sqrt{6}))$, we know that k does not exist.

Case 4: when $0 < \alpha < (4/5)$, owing to $0 < (4/5) < ((4 + 2\sqrt{6})/(5 + 2\sqrt{6})) < 1$, it is easy to know that $4 - 5\alpha > 0$, $1 - \alpha > 0$, and $\alpha(5 + 2\sqrt{6}) + (-2\sqrt{6} - 4) < 0$; expression (117) is simplified as

$$\begin{cases} k > \dfrac{-1}{1 - \alpha}, \\[2mm] k < \dfrac{-5}{4 - 5\alpha}, \\[2mm] k < \dfrac{5 + 2\sqrt{6}}{\alpha(5 + 2\sqrt{6}) - 4 - 2\sqrt{6}}. \end{cases} \tag{121}$$

From $4 - 5\alpha > 0$, $1 - \alpha > 0$, and $\alpha(5 + 2\sqrt{6}) + (-2\sqrt{6} - 4) < 0$, it is clear that $(-5/(4 - 5\alpha)) - ((5 + 2\sqrt{6})/(\alpha(5 + 2\sqrt{6}) - 4 - 2\sqrt{6})) < 0$, $((5 + 2\sqrt{6})/(\alpha(5 + 2\sqrt{6}) - 4 - 2\sqrt{6})) - (-1/(1 - \alpha)) < 0$, and $(-5/(4 -$

$5\alpha)) < ((5 + 2\sqrt{6})/(\alpha(5 + 2\sqrt{6}) - 4 - 2\sqrt{6})) < (-1/(1 - \alpha)) < 0$. Therefore, when $0 < \alpha < (4/5)$, we know that k does not exist.

From what has been discussed above, we can obtain following relations between α and k.

Case 1: $((4 + 2\sqrt{6})/(5 + 2\sqrt{6})) < \alpha < 1$ and $k > ((5 + 2\sqrt{6})/(\alpha(5 + 2\sqrt{6}) - 4 - 2\sqrt{6}))$

Case 2: $\alpha > 1$ and $((5 + 2\sqrt{6})/(\alpha(5 + 2\sqrt{6}) - 4 - 2\sqrt{6})) < k < (-1/(1 - \alpha))$

Case 3: $0 < \alpha < (4/5)$ and k does not exist.

Case 4: $(4/5) < \alpha < ((4 + 2\sqrt{6})/(5 + 2\sqrt{6}))$ and k does not exist.

If α and k satisfy above relation, the system equilibrium point is the saddle point of index 2, which is unstable.

(3.2) Assuming two negative real roots and two conjugate complex roots

In point (3.2) of Section 2.3.1, we already know that the equilibrium point of the system is unstable and it is the saddle-focus point of index 2, when the following inequalities (expression (96) in Section 2.3.1) are satisfied:

$$\begin{cases} \alpha k < k + 1, \\ 5\alpha k > 4k + 5, \\ \alpha k(5 + 2\sqrt{6}) < k(4 + 2\sqrt{6}) + 5 + 2\sqrt{6}. \end{cases} \tag{122}$$

Taking out the coefficient k of expression (122), we can obtain the following expression:

$$\begin{cases} k(1 - \alpha) + 1 > 0, \\ k(4 - 5\alpha) + 5 < 0, \\ k[\alpha(5 + 2\sqrt{6}) + (-2\sqrt{6} - 4)] < 5 + 2\sqrt{6}. \end{cases} \tag{123}$$

By referring the classification results of expression (117), we can obtain the following several cases:

Case 1: $((4 + 2\sqrt{6})/(5 + 2\sqrt{6})) < \alpha < 1$ and $(-5/(4 - 5\alpha)) < k < ((5 + 2\sqrt{6})/(\alpha(5 + 2\sqrt{6}) - 4 - 2\sqrt{6}))$

Case 2: $\alpha > 1$ and $(-5/(4 - 5\alpha)) < k < ((5 + 2\sqrt{6})/(\alpha(5 + 2\sqrt{6}) - 4 - 2\sqrt{6}))$

Case 3: $0 < \alpha < (4/5)$ and k does not exist

Case 4: $(4/5) < \alpha < ((4 + 2\sqrt{6})/(5 + 2\sqrt{6}))$ and $k > (-5/(4 - 5\alpha))$

If k and α satisfy above relation, the system equilibrium point is the saddle-focus point of index 2, which is unstable.

In brief, for the scenario 2, α can be discussed in the following sections: $0 < \alpha < (4/5)$, $(4/5) < \alpha < ((4 + 2\sqrt{6})/(5 + 2\sqrt{6}))$, and $((4 + 2\sqrt{6})/(5 + 2\sqrt{6})) < \alpha < 1$ and $1 < \alpha$.

From the above discussion, we can form a criterion shown in Table 3 to determine the stability of the system shown in Figure 1; when α is fixed, k is the control parameter. According to the values of k in Table 3, we can know

TABLE 3: Criterion for scenario 2 (α is fixed and k is control parameter).

α	k	Realization 1	Realization 2
	$(-\infty, (-1/(1-\alpha)))$	No	No
	$((-1/(1-\alpha)), ((5-2\sqrt{6})/(\alpha(5-2\sqrt{6})+(2\sqrt{6}-4))))$	No	Stable
	$(((5-2\sqrt{6})/(\alpha(5-2\sqrt{6})+(2\sqrt{6}-4))), ((1-\alpha)/\alpha))$	No	Stable
$(0, (4/5))$	$(((1-\alpha)/\alpha), ((5+2\sqrt{6}-\alpha(4+2\sqrt{6}))/\alpha(5+2\sqrt{6})))$	Saddle point of index 2	Stable
	$(((5+2\sqrt{6}-\alpha(4+2\sqrt{6}))/\alpha(5+2\sqrt{6})), ((5-4\alpha)/5\alpha))$	Saddle-focus point of index 2	Stable
	$(((5-4\alpha)/5\alpha), +\infty)$	Stable	Stable
	$(-\infty, (-1/(1-\alpha)))$	No	No
	$((-1/(1-\alpha)), ((1-\alpha)/\alpha))$	No	Stable
	$(((1-\alpha)/\alpha), ((5+2\sqrt{6}-\alpha(4+2\sqrt{6}))/\alpha(5+2\sqrt{6})))$	Saddle point of index 2	Stable
$((4/5), ((4+2\sqrt{6})/(5+2\sqrt{6})))$	$(((5+2\sqrt{6}-\alpha(4+2\sqrt{6}))/\alpha(5+2\sqrt{6})), ((5-4\alpha)/5\alpha))$	Saddle-focus point of index 2	Stable
	$(((5-4\alpha)/5\alpha), ((4-5\alpha)/-5))$	Stable	Stable
	$((-5/(4-5\alpha)), +\infty)$	Stable	Saddle-focus point of index 2
	$(-\infty, (-1/(1-\alpha)))$	No	No
	$((-1/(1-\alpha)), ((1-\alpha)/\alpha))$	No	Stable
	$(((1-\alpha)/\alpha), ((5+2\sqrt{6}-\alpha(4+2\sqrt{6}))/\alpha(5+2\sqrt{6})))$	Saddle point of index 2	Stable
$(((4+2\sqrt{6})/(5+2\sqrt{6})), 1)$	$(((5+2\sqrt{6}-\alpha(4+2\sqrt{6}))/\alpha(5+2\sqrt{6})), ((5-4\alpha)/5\alpha))$	Saddle-focus point of index 2	Stable
	$(((5-4\alpha)/5\alpha), (-5/(4-5\alpha)))$	Stable	Stable
	$((-5/(4-5\alpha)), ((5+2\sqrt{6})/(\alpha(5+2\sqrt{6})-4-2\sqrt{6})))$	Stable	Saddle-focus point of index 2
	$(((5+2\sqrt{6})/(\alpha(5+2\sqrt{6})-4-2\sqrt{6})), +\infty)$	Stable	Saddle point of index 2
	$(-\infty, ((1-\alpha)/\alpha))$	No	Stable
	$(((1-\alpha)/\alpha), ((5+2\sqrt{6}-\alpha(4+2\sqrt{6}))/\alpha(5+2\sqrt{6})))$	Saddle point of index 2	Stable
	$(((5+2\sqrt{6}-\alpha(4+2\sqrt{6}))/\alpha(5+2\sqrt{6})), ((5-4\alpha)/5\alpha))$	Saddle-focus point of index 2	Stable
$(1, +\infty)$	$(((5-4\alpha)/5\alpha), (-5/(4-5\alpha)))$	Stable	Stable
	$((-5/(4-5\alpha)), ((5+2\sqrt{6})/(\alpha(5+2\sqrt{6})-4-2\sqrt{6})))$	Stable	Saddle-focus point of index 2
	$(((5+2\sqrt{6})/(\alpha(5+2\sqrt{6})-4-2\sqrt{6})), (-1/(1-\alpha)))$	Stable	Saddle point of index 2
	$((-1/(1-\alpha)), +\infty)$	Stable	No

whether there is an equilibrium point and the equilibrium point is stable or not.

We compared Table 3 with Table 2 in [35]. From these two tables, we can know the results (whether the equilibrium point is stable or not) are roughly the same as those in [35]. However, our results are more specific and more detailed when the equilibrium points are unstable. In the unstable equilibrium point interval corresponding to [35], we can obtain two different subintervals corresponding to the saddle point of index 2 and the saddle focal equilibrium point of index 2, respectively. This is because our model has four characteristic roots and only two in [35].

2.3.3. Stability Analysis for Scenario 3 (One Heat Sink and One Heat Source). For realization 1, the heat at the bottom releases to the right side. Therefore, we can obtain following equations:

$$f_1 = \frac{d\Delta T_1}{d\tau} = -n\sqrt{\alpha\Delta T_2 - \Delta T_1}(\Delta T_1 - \Delta T_3), \quad (124)$$

$$f_2 = \frac{d\Delta T_2}{d\tau} = -n\sqrt{\alpha\Delta T_2 - \Delta T_1}(\Delta T_2 - \Delta T_1) + E_1, \quad (125)$$

$$f_3 = \frac{d\Delta T_3}{d\tau} = -\xi n\sqrt{\alpha\Delta T_2 - \Delta T_1}\Delta T_3, \quad (126)$$

$$f_4 = \frac{d\Delta T_4}{d\tau} = -\xi n\sqrt{\alpha\Delta T_2 - \Delta T_1}(\Delta T_4 - \Delta T_2). \quad (127)$$

For realization 2, the heat at the bottom releases to zone 1. Therefore,

$$f_1 = \frac{d\Delta T_1}{d\tau} = -n\sqrt{\Delta T_1 - \alpha\Delta T_2}(\Delta T_1 - \Delta T_2) + E_1, \quad (128)$$

$$f_2 = \frac{d\Delta T_2}{d\tau} = -n\sqrt{\Delta T_1 - \alpha\Delta T_2}(\Delta T_2 - \Delta T_4), \quad (129)$$

$$f_3 = \frac{d\Delta T_3}{d\tau} = -\xi n \sqrt{\Delta T_1 - \alpha \Delta T_2} (\Delta T_3 - \Delta T_1), \quad (130)$$

$$f_4 = \frac{d\Delta T_4}{d\tau} = -\xi n \sqrt{\Delta T_1 - \alpha \Delta T_2} \Delta T_4. \quad (131)$$

(1) Stability Analysis for Realization 1. The steady state solution (equilibrium points) of realization 1 with equations (124)~(127) is denoted as $(\Delta T_{01}, \Delta T_{02}, \Delta T_{03}, \Delta T_{04})$; in order to solve the equilibrium points, we can make that the right sides of equations (124)~(127) equal to zero; the following equations hold:

$$-n\sqrt{\alpha \Delta T_2 - \Delta T_1} (\Delta T_1 - \Delta T_3) = 0, \quad (132)$$

$$-n\sqrt{\alpha \Delta T_2 - \Delta T_1} (\Delta T_2 - \Delta T_1) + E_1 = 0, \quad (133)$$

$$-\xi n \sqrt{\alpha \Delta T_2 - \Delta T_1} \Delta T_3 = 0, \quad (134)$$

$$-\xi n \sqrt{\alpha \Delta T_2 - \Delta T_1} (\Delta T_4 - \Delta T_2) = 0. \quad (135)$$

By solving equations (132)~(135), we can obtain the value of equilibrium points as follows:

$$\Delta T_{01} = \Delta T_{03} = 0, \quad (136)$$

$$\Delta T_{02} = \Delta T_{04} = \frac{E_1^{2/3}}{n^{2/3} \alpha^{1/3}}. \quad (137)$$

According to the characteristic determinant equal to 0, the solution of the differential equation can be discussed. The characteristic determinant equation is that

$$|J(Q) - \lambda E| = \begin{vmatrix} \dfrac{\partial f_1}{\partial \Delta T_1} - \lambda & \dfrac{\partial f_1}{\partial \Delta T_2} & \dfrac{\partial f_1}{\partial \Delta T_3} & \dfrac{\partial f_1}{\partial \Delta T_4} \\[2mm] \dfrac{\partial f_2}{\partial \Delta T_1} & \dfrac{\partial f_2}{\partial \Delta T_2} - \lambda & \dfrac{\partial f_2}{\partial \Delta T_3} & \dfrac{\partial f_2}{\partial \Delta T_4} \\[2mm] \dfrac{\partial f_3}{\partial \Delta T_1} & \dfrac{\partial f_3}{\partial \Delta T_2} & \dfrac{\partial f_3}{\partial \Delta T_3} - \lambda & \dfrac{\partial f_3}{\partial \Delta T_4} \\[2mm] \dfrac{\partial f_4}{\partial \Delta T_1} & \dfrac{\partial f_4}{\partial \Delta T_2} & \dfrac{\partial f_4}{\partial \Delta T_3} & \dfrac{\partial f_4}{\partial \Delta T_4} - \lambda \end{vmatrix} = 0. \quad (138)$$

Combining equations (124)~(127), we can obtain the following expression:

$$\begin{vmatrix} \dfrac{n(\Delta T_{01} - \Delta T_{03})}{2A} - nA - \lambda & -\dfrac{n\alpha(\Delta T_{01} - \Delta T_{03})}{2A} & nA & 0 \\[3mm] \dfrac{n(\Delta T_{02} - \Delta T_{01})}{2A} + nA & -\dfrac{n\alpha(\Delta T_{02} - \Delta T_{01})}{2A} - nA - \lambda & 0 & 0 \\[3mm] \dfrac{\xi n \Delta T_{03}}{2A} & -\dfrac{\xi n \alpha \Delta T_{03}}{2A} & -\xi nA - \lambda & 0 \\[3mm] \dfrac{\xi n(\Delta T_{04} - \Delta T_{02})}{2A} & -\dfrac{\xi n \alpha(\Delta T_{04} - \Delta T_{02})}{2A} + \xi nA & 0 & -\xi nA - \lambda \end{vmatrix} = 0, \quad (139)$$

$$A = \sqrt{\alpha \Delta T_{02} - \Delta T_{01}} = \frac{\alpha^{1/3} E_1^{1/3}}{n^{1/3}}, \quad (140)$$

$$B = \Delta T_{01} - \Delta T_{03} = 0, \quad (141)$$

$$C = \Delta T_{02} - \Delta T_{01} = \frac{E_1^{2/3}}{n^{2/3} \alpha^{1/3}}. \quad (142)$$

Combining equations (139)~(142), we can obtain characteristic root as follows:

$$\lambda_1 = \lambda_2 = -\xi nA = -\xi n \sqrt{\alpha \Delta T_{02} - \Delta T_{01}} = -\xi n^{2/3} E_1^{1/3} \alpha^{1/3}. \quad (143)$$

Two other eigenvalues can be obtained according to the quadratic formula:

$$\lambda_{3,4} = \frac{-b \pm \sqrt{b^2 - 4ac}}{2a} = \frac{-(n\alpha C/2A) - 2nA \pm \sqrt{[(n\alpha C/2A) + 2nA]^2 - 4n^2[(\alpha C/2) + A^2]}}{2}, \quad (144)$$

where

$$
\begin{cases}
a = 1, \\[2mm]
b = \dfrac{n\alpha C}{2A} + 2nA = \dfrac{3n^{2/3}E_1^{1/3}\alpha^{1/3}}{2}, \\[3mm]
c = n^2\left[\dfrac{\alpha C}{2} + A^2\right] = \dfrac{3E_1^{2/3}\alpha^{2/3}n^{4/3}}{2}, \\[3mm]
\Delta = b^2 - 4ac = \dfrac{9n^{4/3}E_1^{2/3}\alpha^{2/3}}{4} - 6E_1^{2/3}\alpha^{2/3}n^{4/3} = -\dfrac{15n^{4/3}E_1^{2/3}\alpha^{2/3}}{4}.
\end{cases}
\tag{145}
$$

It is easy to know that $\lambda_{1,2}$ are always real number $\lambda_1 = \gamma_1 = \lambda_2 = \gamma_2$. Owing to $\alpha > 0$, $E_1 > 0$, and $n > 0$, from equation (143), it is clear that $\lambda_{1,2}$ are always less than 0. From equation (145), we know that $\Delta < 0$. Since the discriminant $\Delta < 0$, we know that λ_3 and λ_4 are always conjugate complex numbers $\lambda_{3,4} = \sigma_{3,4} \pm j\omega_{3,4}$. Hence, the stability related with $\lambda_{3,4}$ is determined by the real part $\sigma_{3,4}$. Owing to $\alpha > 0$, $E_1 > 0$, $n > 0$, from equations (144) and (145), we know that $\sigma_{3,4} = -b < 0$. As a result, λ_1, λ_2, and $\sigma_{3,4}$ are negative. It is clear that the equilibrium point is stable in realization 1.

(2) Stability Analysis for Realization 2. The steady state solution (equilibrium points) of realization 2 with equations (127)~(130) is denoted as $(\Delta T_{01}, \Delta T_{02}, \Delta T_{03}, \Delta T_{04})$. In order to solve the equilibrium points, we can make that the right sides of equations (127)~(130) equal to zero; the following equations hold:

$$
-n\sqrt{\Delta T_1 - \alpha\Delta T_2}\,(\Delta T_1 - \Delta T_2) + E_1 = 0,
\tag{146}
$$

$$
-n\sqrt{\Delta T_1 - \alpha\Delta T_2}\,(\Delta T_2 - \Delta T_4) = 0,
\tag{147}
$$

$$
-\xi n\sqrt{\Delta T_1 - \alpha\Delta T_2}\,(\Delta T_3 - \Delta T_1) = 0,
\tag{148}
$$

$$
-\xi n\sqrt{\Delta T_1 - \alpha\Delta T_2}\,\Delta T_4 = 0.
\tag{149}
$$

By solving equations (146)~(149), we can obtain the value of equilibrium point as follows:

$$
\Delta T_{01} = \Delta T_{03} = \frac{E_1^{2/3}}{n^{2/3}},
\tag{150}
$$

$$
\Delta T_{02} = \Delta T_{04} = 0.
\tag{151}
$$

According to the characteristic determinant equal to 0, the solution of the differential equation can be discussed. The characteristic determinant equation is that

$$
|J(Q) - \lambda E| =
\begin{vmatrix}
\dfrac{\partial f_1}{\partial \Delta T_1} - \lambda & \dfrac{\partial f_1}{\partial \Delta T_2} & \dfrac{\partial f_1}{\partial \Delta T_3} & \dfrac{\partial f_1}{\partial \Delta T_4} \\[3mm]
\dfrac{\partial f_2}{\partial \Delta T_1} & \dfrac{\partial f_2}{\partial \Delta T_2} - \lambda & \dfrac{\partial f_2}{\partial \Delta T_3} & \dfrac{\partial f_2}{\partial \Delta T_4} \\[3mm]
\dfrac{\partial f_3}{\partial \Delta T_1} & \dfrac{\partial f_3}{\partial \Delta T_2} & \dfrac{\partial f_3}{\partial \Delta T_3} - \lambda & \dfrac{\partial f_3}{\partial \Delta T_4} \\[3mm]
\dfrac{\partial f_4}{\partial \Delta T_1} & \dfrac{\partial f_4}{\partial \Delta T_2} & \dfrac{\partial f_4}{\partial \Delta T_3} & \dfrac{\partial f_4}{\partial \Delta T_4} - \lambda
\end{vmatrix}
= 0.
\tag{152}
$$

Combining equations (128)~(131), we can obtain the following expression:

$$
\begin{vmatrix}
-\dfrac{n(\Delta T_{01} - \Delta T_{02})}{2A} - nA - \lambda & \dfrac{n\alpha(\Delta T_{01} - \Delta T_{02})}{2A} + nA & 0 & 0 \\[3mm]
-\dfrac{n(\Delta T_{02} - \Delta T_{04})}{2A} & \dfrac{n\alpha(\Delta T_{02} - \Delta T_{04})}{2A} - nA - \lambda & 0 & nA \\[3mm]
-\dfrac{\xi n(\Delta T_{03} - \Delta T_{01})}{2A} + \xi nA & \dfrac{\xi n\alpha(\Delta T_{03} - \Delta T_{01})}{2A} & -\xi nA - \lambda & 0 \\[3mm]
-\dfrac{\xi n\Delta T_{04}}{2A} & \dfrac{\xi n\alpha\Delta T_{04}}{2A} & 0 & -\xi nA - \lambda
\end{vmatrix}
= 0,
\tag{153}
$$

$$
A = \sqrt{\Delta T_{01} - \alpha\Delta T_{02}} = \frac{E_1^{1/3}}{n^{1/3}},
\tag{154}
$$

$$
B = \Delta T_{01} - \Delta T_{02} = \frac{E_1^{2/3}}{n^{2/3}},
\tag{155}
$$

$$
C = \Delta T_{02} - \Delta T_{04} = 0.
\tag{156}
$$

Combining equations (153)~(156), we can obtain characteristic roots as follows:

$$\lambda_1 = \lambda_2 = -\xi nA = -\xi n\sqrt{\Delta T_{01} - \alpha\Delta T_{02}} = -\xi n^{2/3}E_1^{1/3}. \tag{157}$$

Two other eigenvalues can be obtained according to the quadratic formula:

$$\lambda_{3,4} = \frac{-b \pm \sqrt{b^2 - 4ac}}{2a} = \frac{-(nB/2A) - 2nA \pm \sqrt{[(nB/2A) + 2nA]^2 - 4n^2[(B/2) + A^2]}}{2}, \tag{158}$$

where

$$\begin{cases} a = 1, \\[2mm] b = \dfrac{nB}{2A} + 2nA = \dfrac{5n^{2/3}E_1^{1/3}}{2}, \\[2mm] c = n^2\left[\dfrac{B}{2} + A^2\right] = \dfrac{3n^{4/3}E_1^{2/3}}{2}, \\[2mm] \Delta = b^2 - 4ac = \dfrac{25n^{4/3}E_1^{2/3}}{4} - 6n^{4/3}E_1^{2/3} = \dfrac{n^{4/3}E_1^{2/3}}{4}. \end{cases} \tag{159}$$

It is easy to know that $\lambda_{1,2}$ are always real number $\lambda_1 = \gamma_1 = \lambda_2 = \gamma_2$. Owing to $E_1 > 0$ and $n > 0$, from equation (157), we know that $\lambda_{1,2}$ are always less than 0; from equation (159), we know that $\Delta > 0$, and thus λ_3 and λ_4 are always real numbers $\lambda_3 = \gamma_3$ and $\lambda_4 = \gamma_4$. Combining equations (158) and (159), we can obtain that $\lambda_3 = -n^{2/3}E_1^{1/3}$ and $\lambda4 = -((3n^{2/3}E_1^{1/3})/2)$. Owing to $E_1 > 0$ and $n > 0$, we can know that λ_3 and λ_4 are less than 0. In conclusion, four eigenvalues λ_1, λ_2, λ_3, and λ_4 are less than 0, and it is clear that the equilibrium point is stable in realization 2.

In brief, for the scenario 3 of one heat source at the bottom of the building, because the heat can enter either the left or the right side, two steady states always exist for this scenario. The parameter α will not affect the stability and existence of solution of buoyancy ventilation of this building configuration.

3. Model Validation

Reference [35] showed the comparison results with [34], which is the literature studying the structure of one heat source at the bottom with two adiabatic tunnels. In order to verify the validity and accuracy of our model, similarly, we compared the scenario 3 results with those of [34]. The outdoor temperature is 288 K, the air density 1.225 kg/m³, C_p 1.0 kJ/(kg·K), heat source 1 kW, H_1 5.5 m, H_2 5.5 m, $S_{1+2+3+4}$ 37.2933 kg⁻¹/m⁻¹, and gravity acceleration g 9.81 m/s².

The comparison in temperature difference between the proposed model and the validated results from [34] is illustrated in Figure 2(a). The comparison in flow rate between the proposed model and the validated results from [34] is illustrated in Figure 2(b). In [35], we know the maximum

relative error for the temperature difference is 13.2% and the maximum relative error for the flow rate is 15.9%, when the strength of the local heat source is 100 W. While in our results, the maximum relative error for the temperature difference is 2.16% and the maximum relative error for the flow rate is 3.23%. These show that our results are closer to the CFD simulation results in [34] than in [35], which means that the proposed 4-zone model in our paper is more reasonable than 2-zone model in [35].

Referring to method of [35], we rectify our model and obtain the rectified results of temperature and flow rate. Here, we give rectified results in zone 2 for the realization 1. Tunnel H_1 on the left remains unchanged to 5.5 m, and tunnel H_2 on the right is subtracted from room height. In order to compare with [34, 35], the height of the room is 0.5 m, so after adjustment, $H_2 = 5$ m. After improvement, the maximum relative error of flow rate is 1.0% and the maximum relative error of temperature is 1.58% when our results are compared with the ones in [34]. While in [35], the maximum relative error of flow rate is 12.31% and the maximum relative error of temperature is 10.39%. Therefore, the results of the model we proposed are closer to the CFD results of [34].

4. Representation of Phase Portraits

We compare the formation process of the system from different initial conditions to the steady state under different control parameter a by means of the vector field and phase portrait. Based on the analysis of stability of equilibrium points for scenario 1, we fix control parameter k to 10 and four typical values of α are selected, which are 0.05, 0.5, 1, and 2. We make phase portrait and vector field for scenario 1 ($k > 0$) through MATLAB, and the results are shown in Figure 3. Figure 3(a) denotes the phase portrait and vector field for $k = 10$ and $\alpha = 0.05$ of realization 2; Figure 3(b) denotes phase portrait and vector field for $k = 10$ and $\alpha = 0.5$, where the red point and blue point denote the equilibrium point of realization 1 and realization 2, respectively. Figures 3(c) and 3(d) display the vector field and phase portrait of realization 1 and realization 2, respectively, when the control parameter α is equal to 1. The red dot in Figure 3(c) represents the stable equilibrium point of realization 1, and the initial condition around the equilibrium point converges to stable equilibrium point. The blue dot in Figure 3(d) represents the unstable equilibrium point of realization 2, and the initial condition around the unstable

(a)

(b)
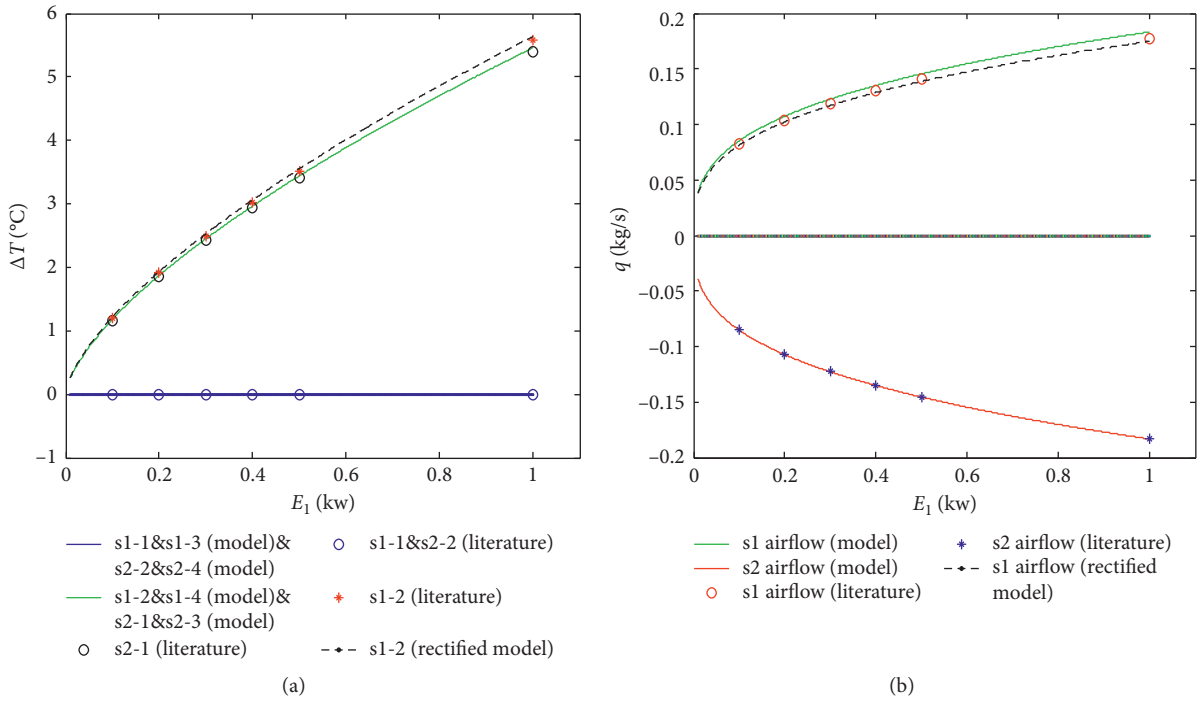
Figure 2: Modeled results validation. (a) Temperature comparison between the four-zone model and previous CFD results. (b) Mass flow rates comparison between the four-zone model and previous CFD results (S1 indicates status1/realization 1; 1, 2, etc. indicates zone serial number).

(a)

(b)

(c)

(d)
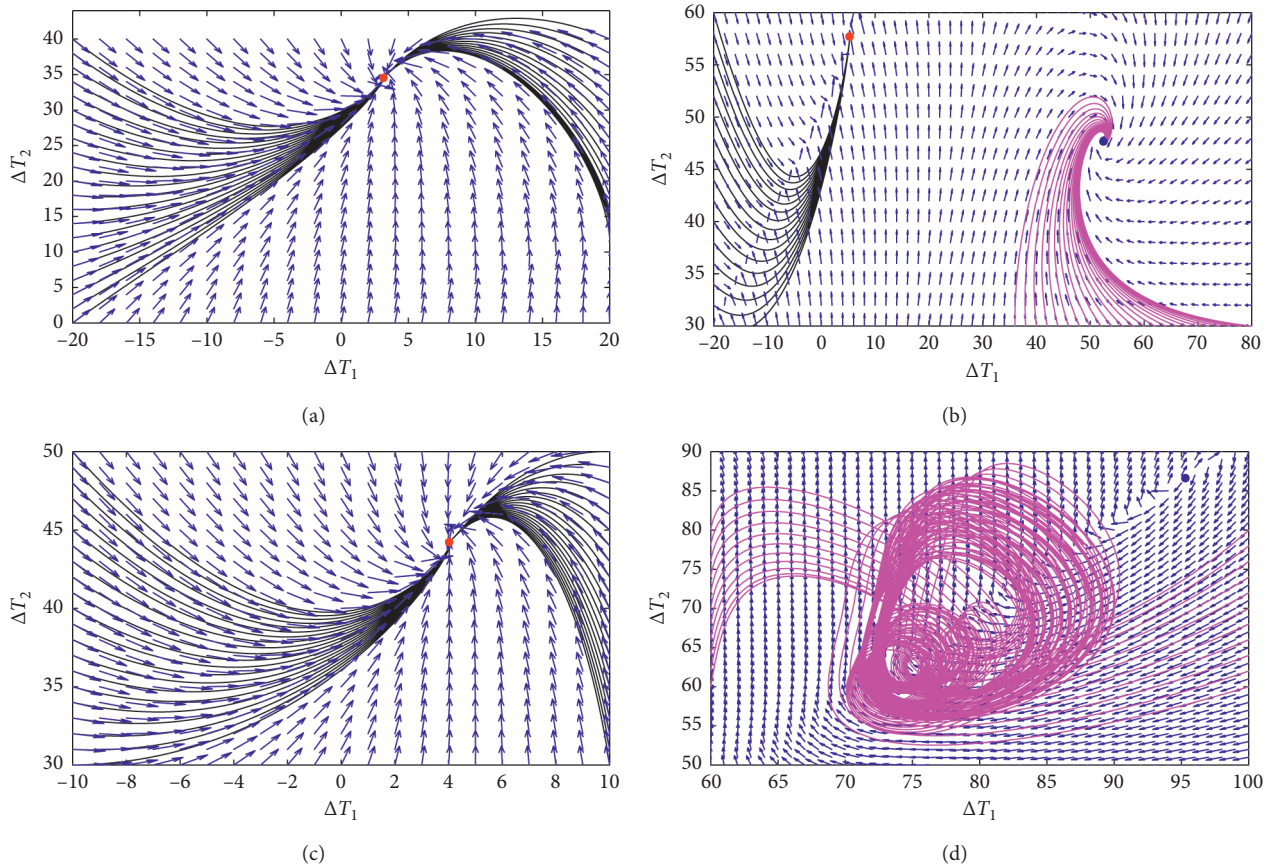
Figure 3: Continued.

(e)
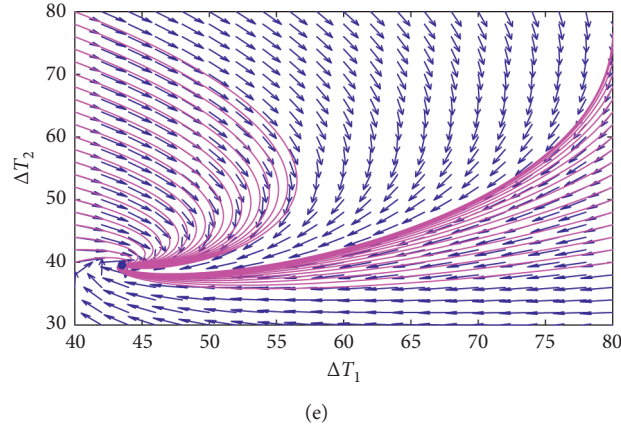
FIGURE 3: Phase portrait and vector field for scenario 1 ($k > 0$): (a) $k = 10$ and $\alpha = 0.05$ of realization 2; (b) $k = 10$ and $\alpha = 0.5$, where the red point and blue point denote the equilibrium point of realization 1 and realization 2, respectively; (c) $k = 10$ and $\alpha = 1$ of realization 1; (d) $k = 10$ and $\alpha = 1$ of realization 2; (e) $k = 10$ and $\alpha = 2$ of realization 1.

(a)

(b)

(c)
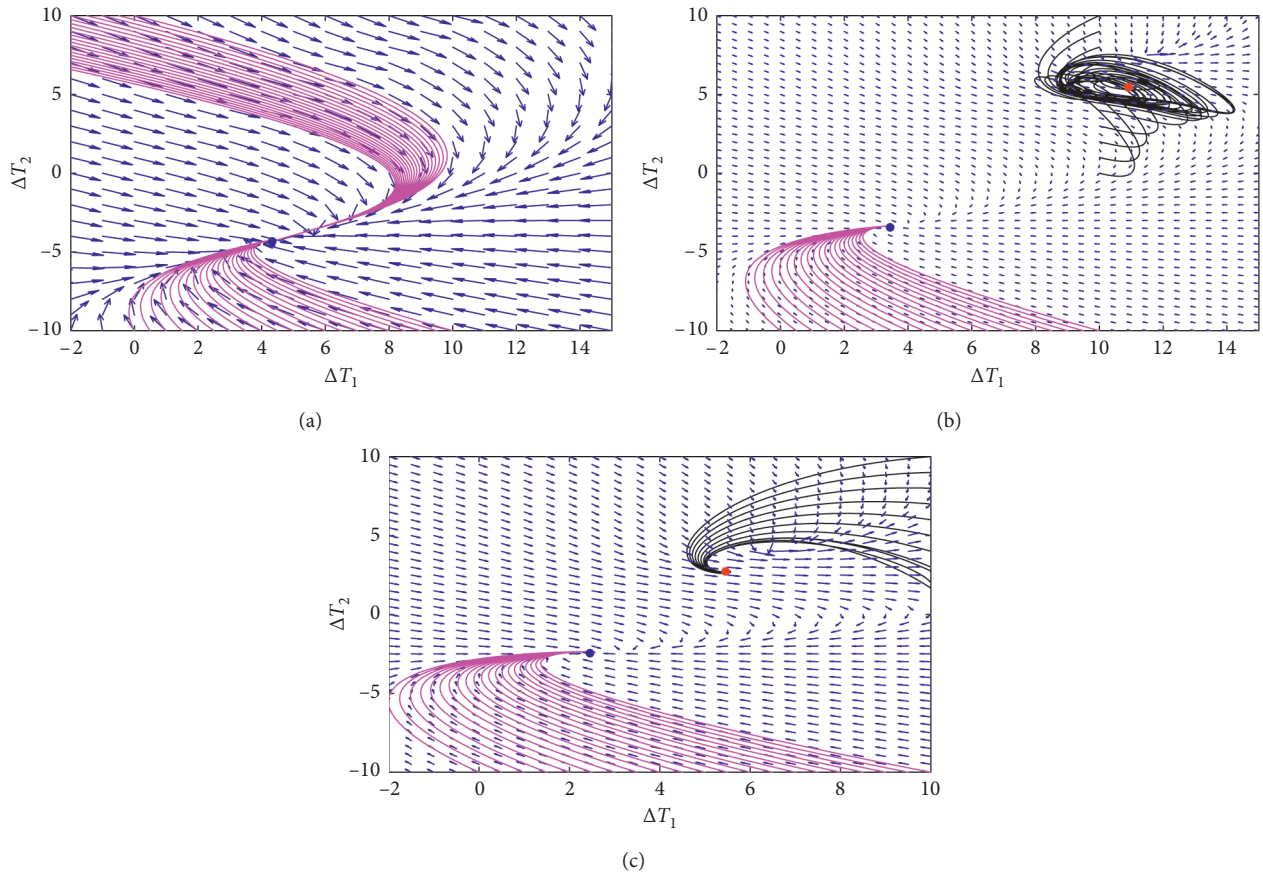
FIGURE 4: Phase portrait and vector field for scenario 1 ($k < 0$). (a) $k = -0.5$ and $\alpha = 1$ of realization 2; (b) $k = -0.5$ and $\alpha = 3$, where the red dot indicates the equilibrium point of realization 1 and the blue dot represents the equilibrium point of realization 2; (c) $k = -0.5$ and $\alpha = 10$, where the red dot indicates the equilibrium point of realization 1 and the blue dot represents the equilibrium point of realization 2.

equilibrium point forms the periodic motion. Figure 3(e) denotes the phase portrait and vector field for $k = 10$ and $\alpha = 2$ of realization 1. In Figure 3(e), there is only one stable equilibrium point of realization 1, and all different initial states converge to the same steady state.

Based on the analysis of stability of equilibrium points for scenario 1, we fix control parameter k to -0.5, and three typical values of α are selected, which are 1, 3, and 10. We make phase portrait and vector field for scenario 1 ($k < 0$), and the results are shown in Figure 4. Figure 4(a) denotes the
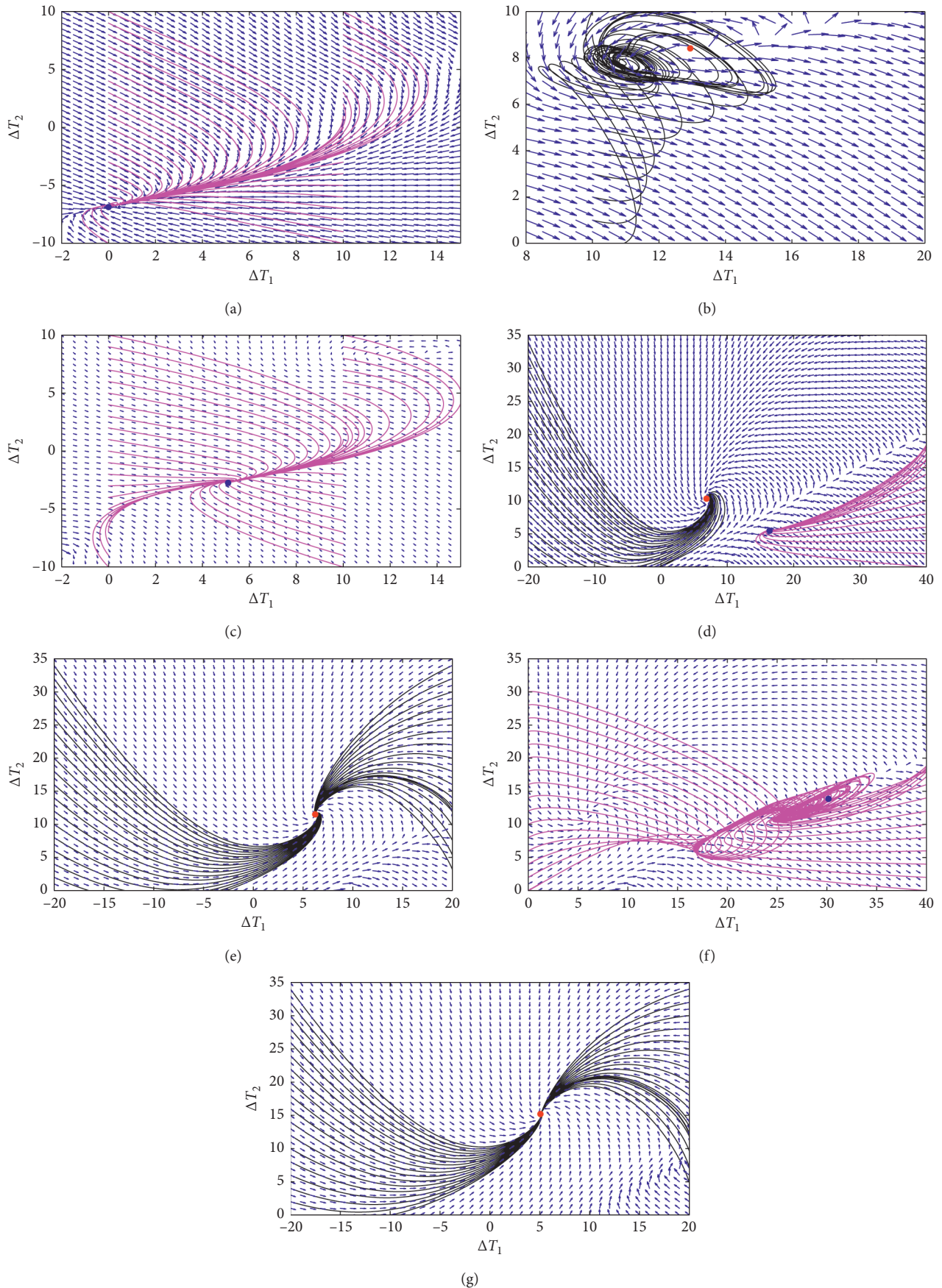
FIGURE 5: Phase portrait and vector field for scenario 2. (a) $\alpha = 2$ and $k = -1$ of realization 2; (b) $\alpha = 2$ and $k = -0.35$ of realization 1; (c) $\alpha = 2$ and $k = -0.35$ of realization 2; (d) $\alpha = 2$ and $k = 0.5$, where the red dot indicates the equilibrium point of realization 1 and the blue dot represents the equilibrium point of realization 2; (e) $\alpha = 2$ and $k = 0.85$ of realization 1; (f) $\alpha = 2$ and $k = 0.85$ of realization 2; (g) $\alpha = 2$ and $k = 2$ of realization 1.

phase portrait and vector field for $k = -0.5$ and $\alpha = 1$ of realization 2. In Figure 4(a), only one stable equilibrium point appeared, and all different initial states converge to the same steady state. Figure 4(b) denotes the phase portrait and vector field for $k = -0.5$ and $\alpha = 3$. In Figure 4(b), the red dot represents the unstable equilibrium point of realization 1, and the initial condition around the unstable equilibrium point converges to periodic motion. And, the blue dot represents stable equilibrium point of realization 2, and the initial conditions around the stable equilibrium point converge to the equilibrium point. Figure 4(c) denotes phase portrait and vector field for $k = -0.5$, $\alpha = 10$. The red dot and blue dot in Figure 4(c) represent the stable equilibrium point of realization 1 and realization 2, respectively. The initial condition around the red dot converges to the stable equilibrium point of realization 1, and the initial condition around the blue dot converges to the equilibrium point of realization 2.

Based on the analysis of stability of equilibrium points for scenario 2, we fixed control parameter α to 2, and five typical values of k were selected, which were -1, -0.35, 0.5, 0.85, and 2. We make phase portrait and vector field for scenario 2, and the results are shown in Figure 5. In Figure 5(a), only one stable equilibrium point of realization 2 appeared, when k is equal to -1, and all different initial states converge to the same steady state. Figures 5(b) and 5(c) display the vector field and phase portrait of realization 1 and realization 2, respectively, when the control parameter k is equal to -0.35. The red dot in Figure 5(b) represents the unstable equilibrium point of realization 1, and the initial condition around the unstable equilibrium point forms the periodic motion. The blue dot in Figure 5(c) represents the stable equilibrium point of realization 2, and the initial condition around the equilibrium point converges to stable equilibrium point. Figure 5(d) denotes the phase portrait and vector field for $\alpha = 2$ and $k = 0.5$, where the red dot indicates the equilibrium point of realization 1 and the blue dot represents the equilibrium point of realization 2. Figures 5(e) and 5(f) display the vector field and phase portrait of realization 1 and realization 2, respectively, when the control parameter k is equal to 0.85. The red dot in Figure 5(e) represents the stable equilibrium point of realization 1, and the initial condition around the equilibrium point converges to stable equilibrium point. The blue dot in Figure 5(f) represents the unstable equilibrium point of realization 2, and the initial condition around the unstable equilibrium point forms the periodic motion. In Figure 5(g), there is only one stable equilibrium point of realization 1, and all different initial states converge to the same steady state.

5. Conclusions

Nonlinear dynamical analysis was performed to study the buoyancy ventilation of a typical four-zone underground building. A new model with four zones that described the buoyancy ventilation of the underground buildings was proposed and validated by results from the previous studies. The new model contained four nonlinear ordinary differential equations. The criteria for the stability and existence of equilibrium points were derived mathematically in detail about three different scenarios. The criterion for scenario 1 (k was fixed and control α) is summarized in Tables 1 and 2, which correspond $k > 0$ and $k < 0$, respectively; the criterion for scenario 2 (α was fixed and control κ) is summarized in Table 3. Two stable equilibrium points existed in scenario 3 (one heat source at the bottom of the building and control α). Finally, the phase portraits and vector field diagrams obtained by applying the fourth-order Runge–Kutta method are given.

Nomenclature

$q_1 \sim q_4$:	Mass flow rate at zones 1~4 (kg/s)
$T_1 \sim T_4$:	Air temperature at zones 1~4 (K)
T_a:	Outdoor air temperature (K)
$S_1 \sim S_4$:	Coefficient of mass flow impedance at zones 1~4
$M_1 \sim M_4$:	Thermal mass at zones 1~4 (kg)
E_1:	Total heat gain at zone 1 (kW)
E_2:	Total heat gain at zone 2 (kW)
C_p:	Specific heat of air (kJ/(kg·K))
t:	Time (s)
ξ:	Mass ratio between zones 1 or 2 and zones 3 or 4
g:	Gravitational acceleration (m/s^2)
H_1:	Height of zone 3 (left tunnel) (m)
H_2:	Height of zone 4 (right tunnel) (m)
k:	Heat ratio between two zones E_2/E_1
$\Delta T_1 \sim \Delta T_4$:	Temperature difference between indoor and outdoor air at zones 1~4 (°C)
α:	Height ratio between two zones H_2/H_1
$\Delta T_{10} \sim \Delta T_{40}$:	Temperature difference between indoor and outdoor air at zones 1~4 in steady state (°C)
ρ_0:	Ambient air density (kg/m^3)
$J(Q)$:	Jacobian matrix of equilibrium point Q
λ:	Eigenvalue of coefficient matrix.

Data Availability

All data used to support the findings of this study are available from the corresponding author upon request.

Conflicts of Interest

The authors declare that they have no conflicts of interest.

Acknowledgments

References

[1] W. Yao, C. Wang, Y. Sun, C. Zhou, and H. Lin, "Synchronization of inertial memristive neural networks with time-varying delays via static or dynamic event-triggered control," *Neurocomputing*, vol. 404, pp. 367–380, 2020.

[2] W. Yao, C. Wang, J. Cao, Y. Sun, and C. Zhou, "Hybrid multisynchronization of coupled multistable memristive neural networks with time delays," *Neurocomputing*, vol. 363, pp. 281–294, 2019.

[3] C. Zhou, C. H. Wang, Y. C. Sun, and W. Yao, "Weighted sum synchronization of memristive coupled neural networks," *Neurocomputing*, vol. 403, pp. 225–232, 2020.

[4] C. Li, K. Qian, S. He, H. Li, and W. Feng, "Dynamics and optimization control of a robust chaotic map," *IEEE Access*, vol. 7, pp. 160072–160081, 2019.

[5] F. Yu, L. Liu, H. Shen et al., "Multistability analysis, coexisting multiple attractors and FPGA implementation of Yu-Wang four-wing chaotic system," *Mathematical Problems in Engineering*, vol. 2020, Article ID 7530976, 2020.

[6] F. Yu, L. Liu, B. Shen et al., "Dynamic analysis, circuit design and synchronization of a novel 6D memristive four-wing hyperchaotic system with multiple coexisting attractors," *Complexity*, vol. 2020, Article ID 5904607, 17 pages, 2020.

[7] Z. Wen, Z. Li, and X. Li, "Transient MMOs in memristive chaotic system via tiny perturbation," *Electronics Letters*, vol. 56, no. 2, pp. 78–80, 2020.

[8] Q. Zhao, C. Wang, and X. Zhang, "A universal emulator for memristor, memcapacitor, and meminductor and its chaotic circuit," *Chaos: An Interdisciplinary Journal of Nonlinear Science*, vol. 29, no. 1, p. 13141, 2019.

[9] L. Y. Wang, K. H. Sun, Y. X. Peng, and S. B. He, "Chaos and complexity in a fractional-order higher-dimensional multi-cavity chaotic map," *Chaos Solitons & Fractals*, vol. 131, Article ID 109488, 2020.

[10] X. Zhang, C. Wang, W. Yao, and H. Lin, "Chaotic system with bondorbital attractors," *Nonlinear Dynamics*, vol. 97, no. 4, pp. 2159–2174, 2019.

[11] Q. Deng and C. Wang, "Multi-scroll hidden attractors with two stable equilibrium points," *Chaos: An Interdisciplinary Journal of Nonlinear Science*, vol. 29, no. 9, p. 093112, 2019.

[12] Q. L. Deng, C. H. Wang, and L. M. Yang, "Four-wing hidden attractors with one stable equilibrium point," *International Journal of Bifurcation and Chaos*, vol. 30, no. 6, Article ID 2050086, 2020.

[13] M. J. Zhou and C. H. Wang, "A novel image encryption scheme based on conservative hyperchaotic system and closed-loop diffusion between blocks," *Signal Processing*, vol. 171, Article ID 107484, 2020.

[14] S. C. Wang, C. H. Wang, and C. Xu, "An image encryption algorithm based on a hidden attractor chaos system and the Knuth-Durstenfeld algorithm," *Optics and Lasers in Engineering*, vol. 128, Article ID 105995, 2020.

[15] C. Xu, J. R. Sun, and C. H. Wang, "An image encryption algorithm based on random walk and hyperchaotic systems," *International Journal of Bifurcation and Chaos*, vol. 30, no. 4, Article ID 2050060, 2020.

[16] K. Nitta, "Variety modes and chaos in smoke ventilation by ceiling chamber system," in *Proceedings of the 6th International IBPSA Conference*, Kyoto, Japan, 1999.

[17] G. R. Hunt and P. P. Linden, "The fluid mechanics of natural ventilation-displacement ventilation by buoyancy-driven flows assisted by wind," *Building and Environment*, vol. 34, no. 6, pp. 707–720, 1999.

[18] Y. Li, A. Delsante, Z. Chen et al., "Some examples of solution multiplicity in natural ventilation," *Building and Environment*, vol. 36, no. 7, pp. 851–858, 2001.

[19] J. Yuan and L. R. Glicksman, "Multiple steady states in combined buoyancy and wind driven natural ventilation: the conditions for multiple solutions and the critical point for

initial conditions," *Building and Environment*, vol. 43, no. 1, pp. 62–69, 2008.

[20] C. Gladstone and A. W. Woods, "On buoyancy-driven natural ventilation of a room with a heated floor," *Journal of Fluid Mechanics*, vol. 441, pp. 293–314, 2001.

[21] T. Chenvidyakarn and A. Woods, "Multiple steady states in stack ventilation," *Building and Environment*, vol. 40, no. 3, pp. 399–410, 2005.

[22] J. Gong and Y. Li, "Smoke flow bifurcation due to opposing buoyancy in two horizontally connected compartments," *Fire Safety Journal*, vol. 59, pp. 62–75, 2013.

[23] D. Yang, P. Li, H. Duan et al., "Multiple patterns of heat and mass flow induced by the competition of forced longitudinal ventilation and stack effect in sloping tunnels," *International Journal of Thermal Sciences*, vol. 138, pp. 35–46, 2019.

[24] P. Heiselberg, Y. Li, A. Andersen, M. Bjerre, and Z. Chen, "Experimental and CFD evidence of multiple solutions in a naturally ventilated building," *Indoor Air*, vol. 14, no. 1, pp. 43–54, 2004.

[25] B. Lishman and A. W. Woods, "On transitions in natural ventilation flow driven by changes in the wind," *Building and Environment*, vol. 44, no. 4, pp. 666–673, 2009.

[26] J. Yuan and L. R. Glicksman, "Transitions between the multiple steady states in a natural ventilation system with combined buoyancy and wind driven flows," *Building and Environment*, vol. 42, no. 10, pp. 3500–3516, 2007.

[27] E. Pulat and H. A. Ersan, "Numerical simulation of turbulent airflow in a ventilated room: inlet turbulence parameters and solution multiplicity," *Energy and Buildings*, vol. 93, pp. 227–235, 2015.

[28] F. Durrani, M. J. Cook, and J. J. McGuirk, "Evaluation of LES and RANS CFD modelling of multiple steady states in natural ventilation," *Building and Environment*, vol. 92, pp. 167–181, 2015.

[29] Z. D. Chen and Y. Li, "Buoyancy-driven displacement natural ventilation in a single-zone building with three-level openings," *Building and Environment*, vol. 37, no. 3, pp. 295–303, 2002.

[30] L. Yang, Y. Li, P. Xu, and G. Zhang, "Nonlinear dynamic aalysis of natural ventilation in a two-zone building: Part B-CFD simulations," *HVAC&R Research*, vol. 12, no. 2, pp. 257–278, 2006.

[31] L. Yang, P. Xu, and Y. Li, "Nonlinear dynamic analysis of natural ventilation in a two-zone building: part A-theoretical analysis," *HVAC&R Research*, vol. 12, no. 2, pp. 231–255, 2006.

[32] Y. Li, P. Xu, H. Qian, Q.-H. Deng, and J. Wu, "Flow bifurcation due to opposing buoyancy in two vertically connected open cavities," *International Journal of Heat and Mass Transfer*, vol. 49, no. 19-20, pp. 3298–3312, 2006.

[33] D. Yang, Y. Liu, C. Zhao, and S. Mao, "Multiple steady states of fire smoke transport in a multi-branch tunnel: theoretical and numerical studies," *Tunnelling and Underground Space Technology*, vol. 61, pp. 189–197, 2017.

[34] Y. Liu, Y. Xiao, G. Augenbroe et al., "The formation of multi-steady-states of buoyancy ventilation in underground building," *Tunnelling and Underground Space Technology*, vol. 82, pp. 613–626, 2018.

[35] Y. Liu, Y. Xiao, and J. L. Chen, "Nonlinear dynamic analysis of solution multiplicity of buoyancy ventilation in a typical underground structure," *Building and Environment*, vol. 171, Article ID 106674, 2020.

WILEY | Hindawi

Research Article

Introducing a Chaotic Component in the Control System of Soil Respiration

Peng An [iD],[1] Wen-Feng Wang [iD],[1,2,3] Xi Chen [iD],[3,4,5,6] Jing Qian,[3,7] and Yunzhu Pan [iD][2,8]

[1]*Laboratory of Pattern Analysis and Machine Intelligence, School of Electronic and Information Engineering, Ningbo University of Technology, Ningbo 315211, China*
[2]*Research Institute of Intelligent Engineering and Data Applications, School of Electronic and Electrical Engineering, Shanghai Institute of Technology, Shanghai 200235, China*
[3]*State Key Laboratory of Desert and Oasis Ecology, Xinjiang Institute of Ecology and Geography, Chinese Academy of Sciences, Urumqi 830011, China*
[4]*University of Chinese Academy of Sciences, Beijing 100049, China*
[5]*Sino-Belgian Joint Laboratory of Geo-Information, Urumqi 830011, China*
[6]*CAS Research Centre for Ecology and Environment of Central Asia, Urumqi 830011, China*
[7]*Center for Geo-Spatial Information, Shenzhen Institutes of Advanced Technology, Chinese Academy of Sciences, Shenzhen 518055, China*
[8]*School of Management, Cranfield University, Cranfield MK43 0AL, UK*

Correspondence should be addressed to Wen-Feng Wang; wangwenfeng@sit.edu.cn and Xi Chen; 373345553@qq.com

Chaos theory has been proved to be of great significance in a series of critical applications although, until now, its applications in analyzing soil respiration have not been addressed. This study aims to introduce a chaotic component in the control system of soil respiration and explain control complexity of this nonlinear chaotic system. This also presents a theoretical framework for better understanding chaotic components of soil respiration in arid land. A concept model of processes and mechanisms associated with subterranean CO_2 evolution are developed, and dynamics of the chaotic system is characterized as an extended Riccati equation. Controls of soil respiration and kinetics of the chaotic system are interpreted and as a first attempt, control complexity of this nonlinear chaotic system is tackled by introducing a period-regulator in partitioning components of soil respiration.

1. Introduction

Chaos is a kind of external, complex, and seemingly irregular motion in the deterministic system due to randomness [1]. The sensitivity of the chaotic system to the initial value makes the input changes of the chaotic system be reflected in the output rapidly, so the chaos theory provides a more realistic nonlinear modeling method [2]. Chaos theory has been proved to be of great significance in a series of critical applications [3–6]. The basic idea of chaos theory with complex nonlinear dynamics originated in the early 20th century, formed in the 1960s, and developed more in the 1970s–1980s [7–10]. Chaos is a complex nonlinear dynamic behavior. This theory reveals the unity of order and disorder, certainty, and randomness. It is regarded as the third most creative revolution in the field of science in the 20th century after relativity and quantum mechanics.

Because the chaos system can produce "unpredictable" pseudo-random orbits, many research studies focus on the related algorithms and performance analysis of constructing pseudo-random number generators utilizing chaos systems. For continuous chaotic systems, many chaotic pseudo-random sequences have been proved to have excellent statistical properties. However, until now, applications of chaos theory in analyzing soil respiration have not been addressed. It is necessary to introduce a chaotic component

in the control system of soil respiration and explain control complexity of this nonlinear chaotic system. In previous studies, we have found that soil respiration (R_s) estimate in arid regions should not have neglected the contribution of abiotic exchange [11]. Neglecting the contribution of inorganic component has resulted in overestimates of soil respiration in arid regions, which partly explains the truth of the well-known missing CO_2 sink [12]. The inorganic component of soil respiration (R_{io}) is therefore necessary to be taken into account for a more reliable estimate of soil respiration in arid regions [11, 12]. This study will further reanalyze the concept, kinetics, and data of R_{io} and show that it is a chaotic component of soil respiration in arid regions.

Objectives of this study are (1) to show that R_{io} is a chaotic component of soil respiration in arid land and present a theoretical framework for a better understanding of this chaotic component, (2) to interpret the chaotic system on controls of soil respiration and kinetics of the chaotic system, and (3) to reduce the control complexity of this nonlinear chaotic system by introducing a period regulator.

2. Theory and Kinetics

2.1. A Concept Model. We hypothesize that the underground CO_2 assignment in arid and semiarid regions has been regulated by a hidden loop in groundwater cycle. In brief, groundwater discharge and recharge have regulated the components of soil respiration. Based on this hypothesis, subsurface CO_2 transportation, dissolution, sequestration, and other reassignment processes in the soil-groundwater system are largely driven by precipitation, evaporation, irrigation, dew deposition, etc. These are hydrologic processes associated with the chaotic component R_{io} of soil respiration. Such processes regulate the storage and turnover rates of inorganic carbon and its dissolvable part in the profile of soils [11]. In arid regions with saline and sodic soils, apart from precipitation in the form of rain or snow, dew and fog also play a vital role in providing an essential source of water for soil [13]. CO_2 in soil can react with dew and then dissolve carbonate or even migrate into saline aquifer [14, 15].

Influenced by the hidden loop, soil respiration in arid regions is no longer a definite system. It becomes a nonlinear chaotic system. In order to describe the nonlinear chaotic system, the conceptual framework of known and unknown processes associated with the hidden loop in groundwater cycle, along with the possible mechanisms, is shown in Figure 1.

2.2. Kinetics of the Control System. The hypothesized hidden loop can explain particularity of CO_2 assignment in arid and semiarid regions. Differential, difference, and dynamic equations are used for modeling many problems arising in engineering and natural sciences [16, 17]. This suggests us to develop a differential equation to describe the hypothetical system kinetics. Since the absorbed CO_2 is hypothetically dissolved in saline aquifers, we characterized the dynamics of CO_2 concentration in the groundwater-soil system in

[18, 19] as a simple form of Riccati equation. Analytic solutions of the equation under some necessary and sufficient conditions were also presented.

However, there are still considerable uncertainties and difficulties in fully understanding the underlining mechanisms and critical factors driving such a hidden loop. One major challenge is how to characterize the structure of the soil-groundwater system [15]. It is natural to conjecture that the underlining groundwater cycling processes associated with subsurface CO_2 sequestration in different layers should be different. The whole story is shown in Figure 2.

3. Chaos and Control Complexity

3.1. Further Evidence for Being Chaotic. In previous publications, it was demonstrated that the variations of R_{io} originate from the physical forcing of abiotic factors such as soil salinity (EC), alkalinity (pH), temperature (T_s), and water content (WC$_s$) and their linear relationships with its daily mean intensity appear to be valid within a seasonal cycle as a whole. However, in diurnal cycles, taking into account the complicated and undetermined processes associated with the chaotic component R_{io}, the soil respiration system in arid land is a nonlinear chaotic system. Variability in the data of R_{io} presents further evidence for R_{io} being chaotic. Before the chaos theory was proposed, scientists had thought that there are only two kinds of phenomena—the phenomena which act strictly according to a rule and the phenomena which happen stochastically [20]. As seen in Figure 3, we construct a constant vector for the period control (CVPC) in variation of R_{io} (Figure 3(a)), but environmental controls of R_{io} are seen to interact (Figures 3(c)–3(f)). Practical variability of R_{io} looks stochastic (Figure 3(b)). CVPC for hourly variations of R_{io} in diurnal cycles is an exponent-sine coupled normalization transformation of time sequence (TSN), as follows:

$$\text{CVPC} = e^{\sin(\text{TSN})},$$

$$\text{TSN} = \frac{\pi(x - \min(x))}{12(\max(x) - \min(x))}, \quad x = [1, 2, \ldots, 24].$$
(1)

3.2. Control Complexity of the System. Since soil respiration in arid land is a nonlinear chaotic system, the resulted control complexity is naturally reconciled [21]. A well-known index to characterize the control complexity is temperature sensitivities (i.e., Q_{10}) of R_s. Analyses on data collected from previous studies revealed diel turbulence in Q_{10} values even if excluding the negative R_s data. On the basis of utilizing the basic and reanalyzed data collected from [21], we found that the variability of Q_{10} values is far from certain. All the Q_{10} values used in the analysis were calculated utilizing the simple model of R_s (the derivative of the exponential chemical reaction-temperature equation originally developed by Van't Hoff) [18, 19, 21], and for consistence, the negative values of R_s were not included in calculations of Q_{10}. Controls of T on Q_{10} at each
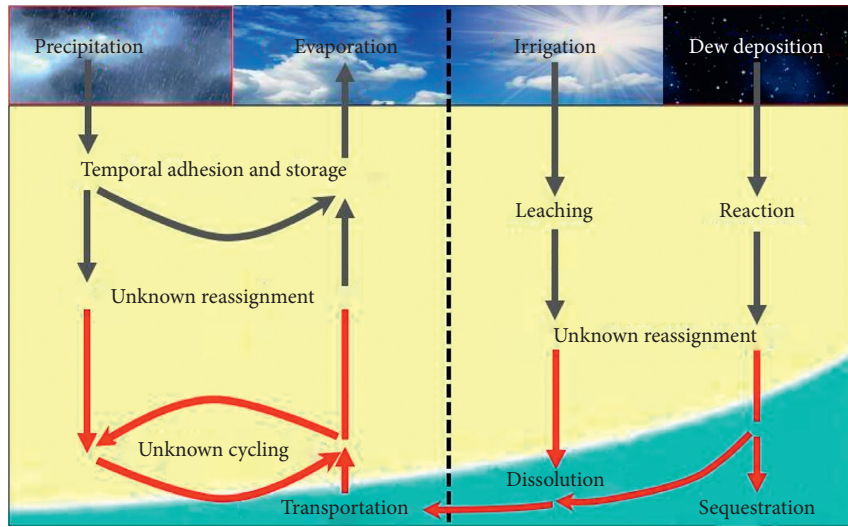
FIGURE 1: Story of the hidden loop in the nonlinear chaotic system, including known and unknown parts.
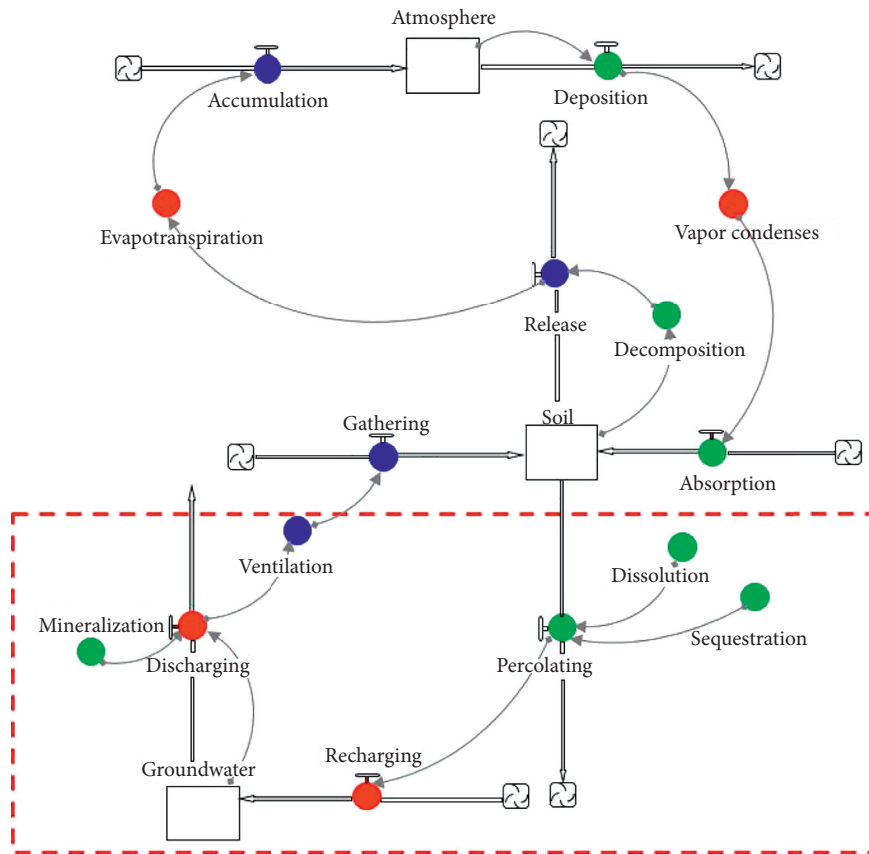
FIGURE 2: Hypothetical system kinetics of the hidden loop: (1) three carbon pools (the atmosphere, soil and groundwater) are connected through carbon cycles and water cycles, along with the underlining processes associated with CO_2 sinks (green solid circles) and sources (blue solid circles); (2) the inorganic CO_2 change beyond the red rectangle (if excluding influences of groundwater) are driven by evapotranspiration and vapor condenses, while the inorganic CO_2 assignment and ventilation within the red rectangle are largely driven by groundwater recharging/discharging.

site were, respectively, analyzed in linear regressions for a between-ecosystem comparison. Results from these analyses were further compared with the analyses of the variation of Q_{10} with T. Using Q_{10} values from both sites, the effects of WC_s on the Q_{10} of R_s to T_s and the Q_{10} of R_s to T_a were analyzed in quadratic regressions. In order to

(a)

(b)

(c)

(d)

(e)

(f)
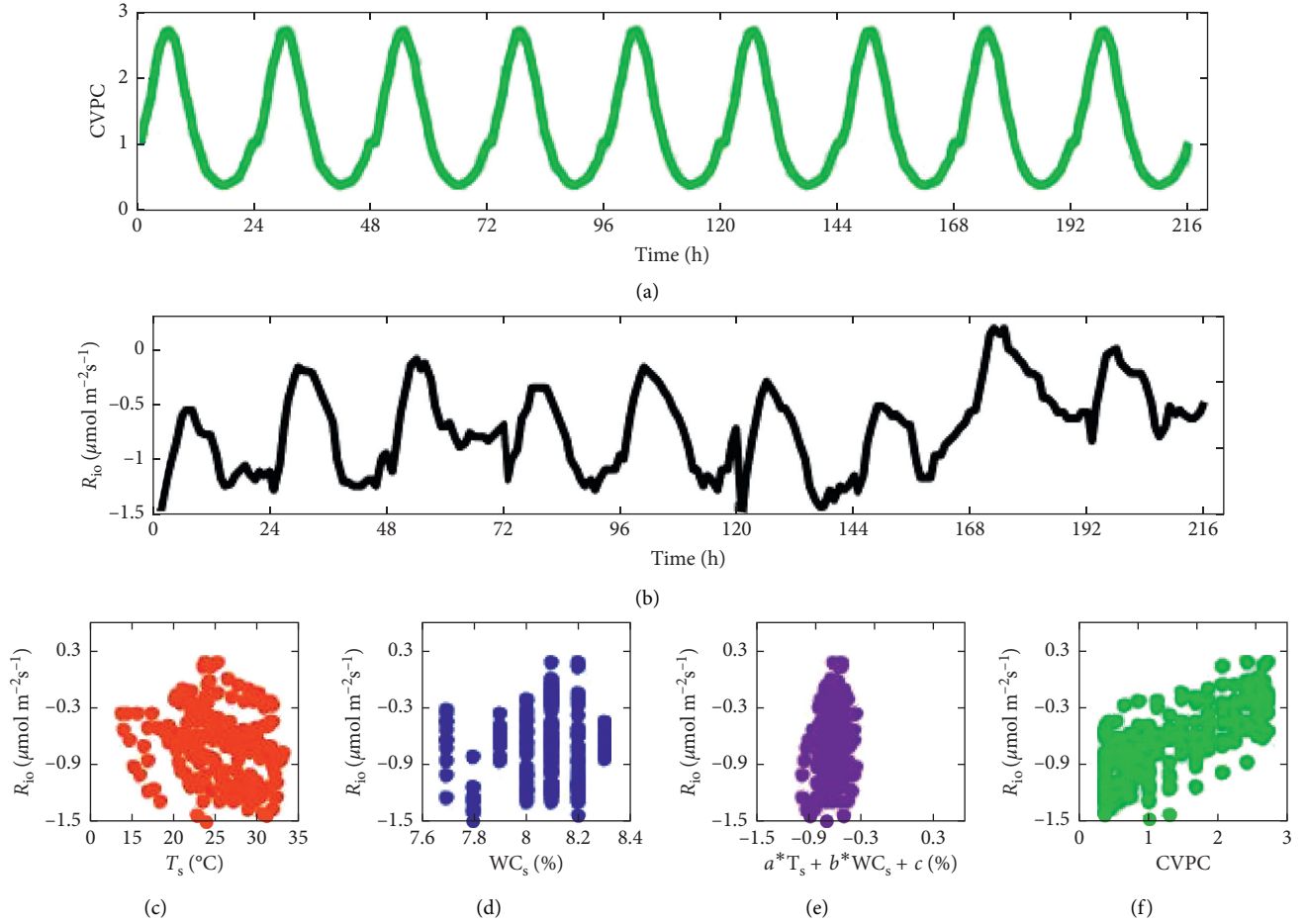
FIGURE 3: The period character of CVPC (a) almost coincides with the period character in the hourly scale variations of R_{io} (b). None of T_s (c), WC_s (d), and the optimal linear combination of T_s and WC_s (e) is better than CVPC (f) to describe the temporal pattern of R_{io} in diurnal cycles.

further test the role of WC_s in determining Q_{10}, four coupling models were employed to analyze coupling effects of T and WC_s on Q_{10}. The front two models were established under the hypothesis that the influences of WC_s and T on Q_{10} were mutually independent. The first model hypothesized that the influences of WC_s and T were linearly independent; the second model hypothesized that the influences of WC_s and T were exponentially independent. The latter two models were established under the hypothesis that the influences of WC_s and T on Q_{10} were not mutually independent. The third model hypothesized that Q_{10} was dominantly determined by WC_s and T linearly interacted on the responses of the Q_{10} to WC_s; the fourth model hypothesized that Q_{10} was dominantly determined by T and WC_s linearly interacted on the responses of Q_{10} to T. Descriptive statistics were used to calculate the R-squared values (R), root mean squared error (RMSE), and F-statistics vs. constant model and p values of the data from each set of reduplicates. The data analysis was processed using MATLAB (Mathworks, Natick, MA, USA), and the statistical analyses were synchronously conducted.

We further examined the variability of Q_{10} values, as seen in Figures 4 and 5.

4. Treating the Control Complexity

Taking into account negative R_s data in arid regions is strongly necessary to reduce uncertainties in the current global/regional carbon balance and in the predictions of future feedbacks in the coupled carbon-climate system ([15, 22–28]). Further modeling approach is advantageous to understand CO_2 footprints ([29–35]). For the convenience of statement, we describe the "doubly average" diurnal dynamics of R_{io} (being averaged among diverse soil sites and meanwhile averaged from different days) by the linear combination of TS, WCs, and CVPC. Let $\alpha1$, $\alpha2$, and $\alpha3$ be regression coefficients (termed as "parent parameters," invariable within each special soil site), respectively, and let ε be the residual; then, we have

$$R_{io} = \alpha_1 T_s + \alpha_2 WS_s + \alpha_3 CVPC + \varepsilon, \quad (2)$$

where CVPC for the hourly scale variations of R_{io} can be easily extended to daily or larger scales.

Utilizing the data in Figure 3 as inputs of equation (2) for a practical simulation, performance of treating the control complexity is shown in Figure 6. According to performance of the model on the third day (a1, b1), the
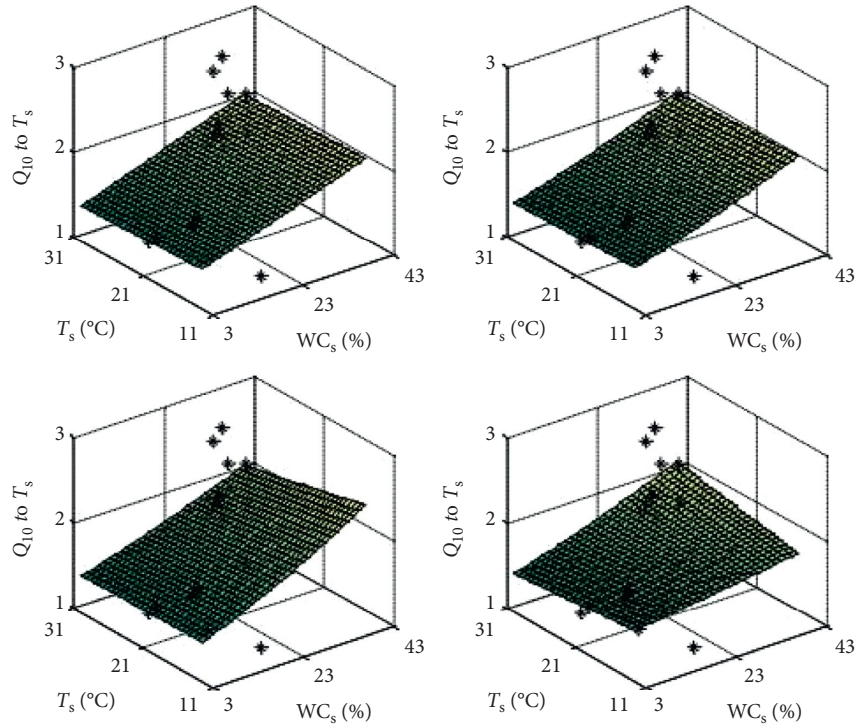
Figure 4: Diel turbulence in temperature sensitivities (Q_{10}) with soil temperature (T_s) and water content (WC_s).
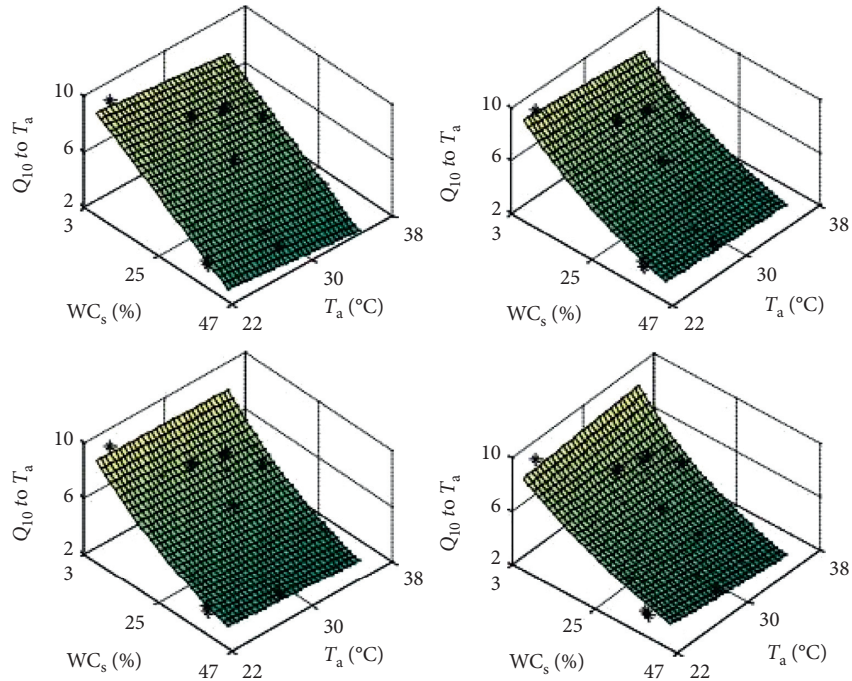
Figure 5: Diel turbulence in temperature sensitivities (Q_{10}) with air temperature (T_s) and water content (WC_s).

fifth day (a2, b2), the seventh day (a3, b3), and the eighth day (a4, b4) after 1 mm diurnal precipitation, the bias in the simulations by using equation (2) exists within a measuring period. However, this is according to performance of the model on the fifth day (c1, d1), the ninth day (c2, d2) after a 5-day continuous precipitation of

0.6~3.6 mm, and the first day after a precipitation of 1.7 mm (c3, d3). The model can even describe the variability of Rio on the days after a continuous precipitation and the day right after small-size rainfall. The model becomes invalid in the simulation on the first day after ~9.9 mm rainfall (c4, d4), when the intensity of Rio is
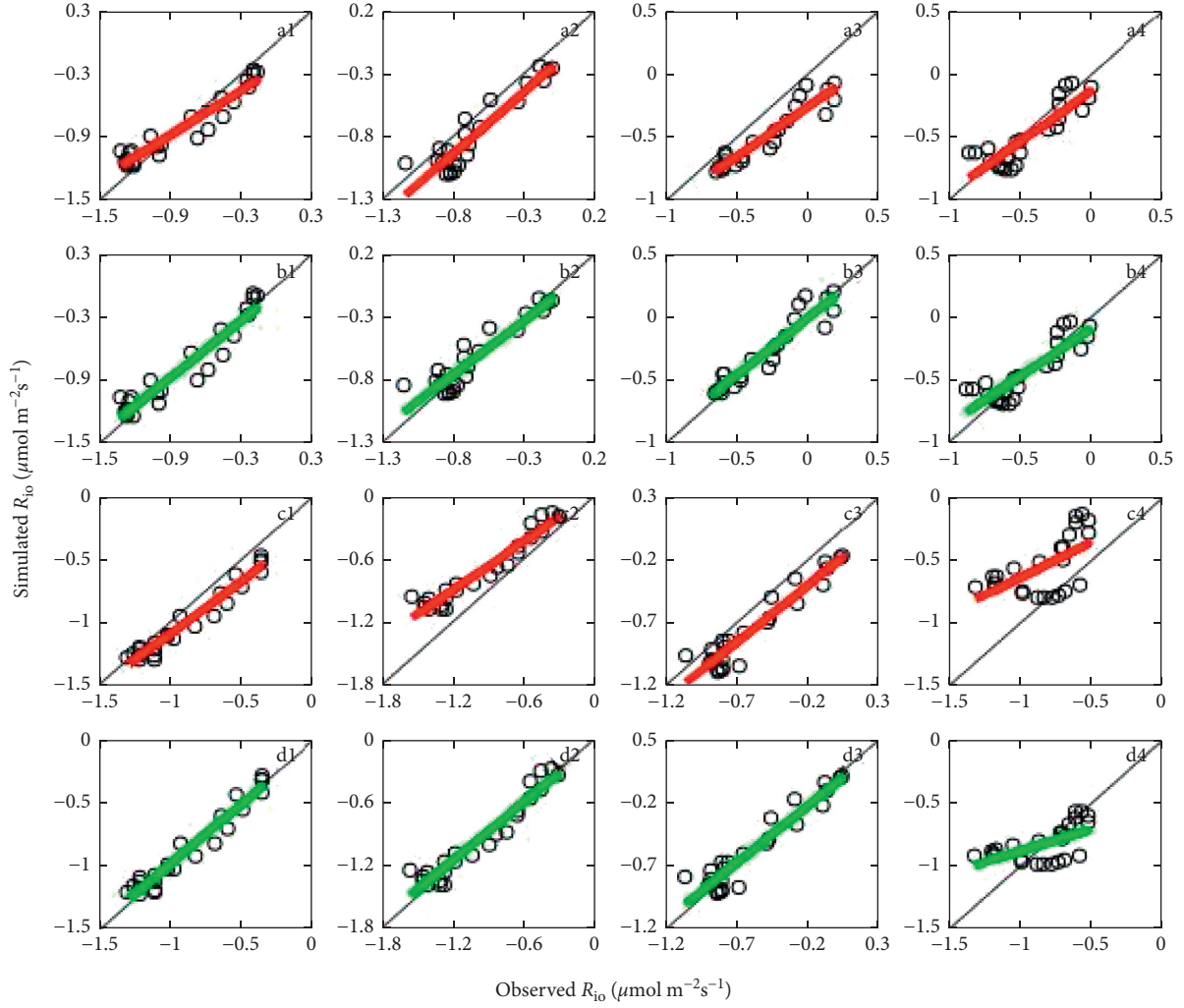
FIGURE 6: Treating the control complexity by the proposed model on subsequent days after rainfalls (a1–a4, c1–c4), which were modified in simulations by equation (2) (b1–b4, d1–d4).

changing too fast. Overall, the nonlinear chaotic system is simplified and can be further developed.

Due to potential overlap in environmental, temporal, and spatial components of ecological data, partitioning the variations among pure environmental controls, pure spatial controls, pure temporal controls, pure spatial component of environmental controls, pure temporal component of environmental controls, pure combined spatial and temporal component controls, combined temporal and spatial components of environmental controls, and unexplained component should be included in multivariate analysis of the chaotic system. The whole story of control complexity of this nonlinear chaotic system is therefore worthy of further investigation.

In reference [19], we have presented more details on the variations of the determining processes of R_{io} of soil respiration and characterize the dynamic of CO_2 concentration in the soil-groundwater system as an input-output balance equation, as follows:

$$C(nT + T) - C(nT) = \frac{(V_1 q + r^n) \cdot T - \int_{nT}^{nT+T} V_1 \cdot C(s) + r_n p_n ds}{V},$$

(3)

where $C(t)$ is CO_2 concentration in a considered gas room V_1 in the soil-groundwater system and q is the CO_2 concentration in the atmosphere. For the nth time interval $[nT, (n+1)T]$, r_n is the average ratio between the input and output of CO_2.

Suppose that the input of CO_2 into the soil-groundwater system was finally dissolved in the groundwater of volume V. Let $D(t)$ be the amount of DIC at t and the growth rate of DIC is r. As hypothesized in Section 2, the determining processes of R_{io} are driven by groundwater discharge (outflow) and recharge (inflow), with volume Q. Provide that outflow = inflow and assume that outflow after the inflow is uniformly mixed with the groundwater unit V. As seen in reference [18], the quality conversation law implies that

$$D(t + \Delta t) - D(t) = Qp\Delta t + \int_{t}^{t+\Delta t} rD(t) - Q\frac{D(t)}{V + Q}dt. \tag{4}$$

Finally, considering the restricting effect of current DIC, which is characterized as $R - \lambda D(t)$, equation (4) can be further improved as [18]

$$D(t + \Delta t) - D(t) = Qp\Delta t + \int_{t}^{t+\Delta t} r(R - \lambda D(t))D(t)$$
$$- Q\frac{D(t)}{V + Q}dt. \tag{5}$$

The next research priority is to analyze the characteristics of bifurcation and chaos in the inherent spatial and temporal variations of R_{io} by using Feigenbaum graphs [36] and further develop equations (2), (3), and (5). Based on this study, the natural increase of CO_2 is the third determining process of R_{io} besides the input and output of CO_2, which involves organic components of soil respiration. This process, along with the input and output of CO_2, determine the increase rate r of the difference between the subterranean and surficial CO_2 concentration and also determine the density of R_{io}.

5. Conclusion

For a better understanding of how soil CO_2 fluxes change with space and time, it is necessary to introduce R_{io} as a nonlinear chaotic component of soil respiration in arid land. Ecology is a study not how things but how things change with space and time, and hence, it is also necessary to interpret the control complexity of this chaotic component. In the assessment of the importance of organic and inorganic factors influencing R_{io}, inherent spatial and temporal variations in ecological data should be taken into account whenever possible. A next research priority is to analyze the characteristics of bifurcation and the chaos difference between the subterranean and surficial CO_2 concentration and further understand the whole story of the control complexity of R_{io}.

Data Availability

All the data utilized to support the theory and models of the present study are available from the corresponding authors upon request.

Conflicts of Interest

The authors declare that there are no conflicts of interest regarding the publication of this article.

Acknowledgments

References

[1] K. E. Kuert en and k J. W. Clar, "Chaos in neural systems," *Physics Letters*, vol. 114, pp. 413–418, 1986.

[2] Y. Xu, J. L. Mili, and J. Zhao, "A novel polynomial-chaos-based Kalman filter," *IEEE Signal Processing Letters*, vol. 26, no. 1, pp. 9–13, 2019.

[3] V. Avrutin, Z. T. Zhusubaliyev, D. Suissa et al., "Non-observable chaos in piecewise smooth systems," *Nonlinear Dynamics*, vol. 99, pp. 2031–2048, 2020.

[4] C. Wang, "Normal forms for partial neutral functional differential equations with applications to diffusive lossless transmission line," *International Journal of Bifurcation and Chaos*, vol. 30, no. 2, pp. 285–332, 2020.

[5] P. Del Hougne, M. F. Imani, and D. R. Smith, "Reconfigurable reflectionless coupling to a metasurface-tunable chaotic cavity," 2020, http://128.84.4.27/abs/2003.01766.

[6] C. B. Tabi, A. S. Etémé, and A. T. C. Mohamadou, "Unstable discrete modes in Hindmarsh-Rose neural networks under magnetic flow effect," *Chaos, Solitons & Fractals*, vol. 123, pp. 116–123, 2019.

[7] O. R. Kofané and S. Murugesh, "Rogue breather modes: topological sectors, and the "belt-trick," in a one-dimensional ferromagnetic spin chain," *Chaos, Solitons & Fractals*, vol. 122, pp. 262–269, 2019.

[8] N. Lüthen, S. Marelli, and B. Sudret, "Sparse polynomial chaos expansions: literature survey and benchmark," 2020, https://arxiv.org/abs/2002.01290.

[9] S. T. Kingni, K. Rajagopal, S. Iek et al., "Dynamical analysis, FPGA implementation and its application to chaos based random number generator of a fractal Josephson junction with unharmonic current-phase relation," *The European Physical Journal B*, vol. 93, p. 44, 2020.

[10] A. u. Rehman and X. Liao, "A novel robust dual diffusion/confusion encryption technique for color image based on chaos, DNA and SHA-2," *Multimedia Tools and Applications*, vol. 78, no. 2, pp. 2105–2133, 2019.

[11] X. Chen, G. Wang, and H. Ye, "Can soil respiration estimate neglect the contribution of abiotic exchange?" *Journal of Arid Land*, vol. 6, no. 2, pp. 129–135, 2014.

[12] W. Wang, X. Chen, L. Wang, H. Zhang, G. Yin, and Y. Zhang, "Approaching the truth of the missing carbon sink," *Polish Journal of Environmental Studies*, vol. 25, no. 4, pp. 1799–1802, 2016.

[13] I. Inglima, G. Alberti, T. Bertolini et al., "Precipitation pulses enhance respiration of Mediterranean ecosystems: the balance between organic and inorganic components of increased soil CO_2 efflux," *Global Change Biology*, vol. 15, no. 5, pp. 1289–1301, 2009.

[14] T. J. Kessler and C. F. Harvey, "The global flux of carbon dioxide into groundwater," *Geophysical Research Letters*, vol. 28, no. 2, pp. 279–282, 2001.

[15] P. Mielnick, W. A. Dugas, K. Mitchell, and K. Havstad, "Long-term measurements of CO_2 flux and evapotranspiration in a Chihuahuan desert grassland," *Journal of Arid Environments*, vol. 60, no. 3, pp. 423–436, 2005.

[16] A. M. A. El-Sayed and S. M. Salman, "Dynamic behavior and chaos control in a complex Riccati-type map," *Quaestiones Mathematicae*, vol. 39, no. 5, pp. 1–18, 2015.

[17] H. Jafari, H. Tajadodi, H. Nazari et al., "Numerical solution of non-linear Riccati differential equations with fractional order," *International Journal of Nonlinear Sciences & Numerical Simulation*, vol. 11, pp. 179–182, 2010.

[18] W. Wang, X. Chen, Y. Zhang et al., "Nanodeserts: a conjecture in nanotechnology to enhance quasi-photosynthetic CO_2 absorption," *International Journal of Polymer Science*, vol. 2016, Article ID 5027879, 10 pages, 2016.

[19] W. F. Wang, X. Chen, H. W. Zheng et al., "Intelligence in ecology: how internet of things expands insights into the missing CO_2 sink," *Scientific Programming*, vol. 2016, Article ID 4589723, 8 pages, 2016.

[20] J. Gleick and R. C. Hilborn, "Chaos, making a new science," *American Journal of Physics*, vol. 56, no. 11, pp. 1053-1054, 1988.

[21] W. F. Wang, X. Chen, X. L. Li et al., "Temperature dependence of soil respiration in arid region is reconciled," in *Proceedings of the ICCSIP 2018*, Beijing, China, November 2018.

[22] R. B. Myneni, J. Dong, C. J. Tucker et al., "A large carbon sink in the woody biomass of Northern forests," *Proceedings of the National Academy of Sciences*, vol. 98, no. 26, pp. 14784–14789, 2001.

[23] M. Reichstein, E. Falge, D. Baldocchi et al., "On the separation of net ecosystem exchange into assimilation and ecosystem respiration: review and improved algorithm," *Global Change Biology*, vol. 11, no. 9, pp. 1424–1439, 2005.

[24] D. S. Schimel, J. I. House, K. A. Hibbard et al., "Recent patterns and mechanisms of carbon exchange by terrestrial ecosystems," *Nature*, vol. 414, no. 6860, pp. 169–172, 2001.

[25] D. W. Schindler, "The mysterious missing sink," *Nature*, vol. 398, no. 6723, pp. 105–107, 1999.

[26] W. H. Schlesinger, "Carbon storage in the caliche of arid soils," *Soil Science*, vol. 133, no. 4, pp. 247–255, 1982.

[27] W. H. Schlesinger, "The formation of caliche in soils of the Mojave desert, California," *Geochimica et Cosmochimica Acta*, vol. 49, no. 1, pp. 57–66, 1985.

[28] W. H. Schlesinger, *Biogeochemistry: An Analysis of Global Change*, Academic Press, New York, NY, USA, 2nd edition, 1997.

[29] W. H. Schlesinger, "Carbon sequestration in soils: some cautions amidst optimism," *Agriculture, Ecosystems & Environment*, vol. 82, no. 1-3, pp. 121–127, 2000.

[30] P. C. Stoy, G. G. Katul, M. B. S. Siqueira et al., "An evaluation of models for partitioning eddy covariance-measured net ecosystem exchange into photosynthesis and respiration," *Agricultural and Forest Meteorology*, vol. 141, no. 1, pp. 2–18, 2006.

[31] E. T. Sundquist, "The global carbon dioxide budget," *Science*, vol. 259, no. 5097, pp. 934–941, 1993.

[32] P. P. Tans, I. Y. Fung, and T. Takahashi, "Observational contrains on the global atmospheric CO_2 budget," *Science*, vol. 247, no. 4949, pp. 1431–1438, 1990.

[33] B. R. Scanlon, K. E. Keese, A. L. Flint et al., "Global synthesis of groundwater recharge in semiarid and arid regions," *Hydrological Processes*, vol. 20, no. 15, pp. 3335–3370, 2006.

[34] A. Hyvärinen, P. O. Hoyer, M. Inki et al., "Topographic independent component analysis," *Neural Computation*, vol. 13, no. 7, pp. 1527–1558, 2001.

[35] C. Chenot, J. Bobin, J. Rapin et al., "Robust sparse blind source separation," *IEEE Signal Processing Letters*, vol. 22, no. 11, pp. 2172–2176, 2015.

[36] B. Luque, L. Lacasa, F. J. Ballesteros, and A. Robledo, "Feigenbaum graphs: a complex network perspective of chaos," *PLoS One*, vol. 6, no. 9, Article ID e22411, 2011.

Research Article

Multimodal Control by Variable-Structure Neural Network Modeling for Coagulant Dosing in Water Purification Process

Jun Zhang [ID] [1] and Da-Yong Luo [2]

[1]*School of Logistics and Transportation, Central South University of Forestry and Technology, Changsha 410000, China*
[2]*School of Information Science and Engineering, Central South University, Changsha 410075, China*

Correspondence should be addressed to Jun Zhang; linecon78@163.com

Stochastic neural network has the characteristics of good global convergence and fast gradient-based learning ability. It can be applied to multidimensional nonlinear systems, but its generalization ability is poor. In this paper, combined with rule base, through the PCA method, an improved multimodal variable-structure random-vector neural network algorithm (MM-P-VSRVNN) is proposed for coagulant dosing, which is a key production process in water purification process. Ensuring for qualified water, how to control coagulation dosage effectively, obtain valid production cost, and increase more profits is a focus in the water treatment plan. Different with the normal neural network mode, PCA is used to optimize hidden-layer nodes and update the neural network structure at every computation. This method rectifies coagulant dosage effectively while keeping valid coagulation performance. By the way, the MM-P-VSRVNN algorithm can decrease computation time and avoid overfitting learning ability. Finally, the method is proved feasible through the experiment and analyzed by the simulation result.

1. Introduction

In water purification process, one important point is coagulant dosing. The effect of coagulation is to make dosage mixed with colloidal particles and tiny suspended solids in raw water, subsided in live embodiment of the amorphous substance in the coagulation and sedimentation tank. Coagulant dosing is a complex, physical, and chemical process with time-varied, delay, and nonlinear characteristics. In addition, there are still many actual factors, such as pH value, turbidity, water flow rate, and coagulation dosage that affect coagulation performance. In many references about coagulant dosing, most water plants take two methods, namely, manual dosing and automatic dosing. Manual dosing mostly depends on workers' experience that is an obvious open-loop control method. It is difficult to save cost effectively. The second is automatic dosing; its control method is related with actual waterworks technology. There is still no uniform control method. Currently, PID control and feedforward control are commonly used, but some water plants still work in manual dosing. Take a water plant in Changsha as an example. Its coagulation effect takes about 90 minutes of delay, and the turbidity after coagulation, named turbidity before filtration, is generally about 5 NTU or less. And the most important thing is that the water plants are still in manual dosing that needs more workers to work by turns. The above being concerned, how to complete coagulant dosing automatically is a hot problem. At present, the automatic control of coagulant dosing mainly adopts a single-factor closed-loop method, which needs to change the method from traditional PID control to intelligent control for complex control objects [1, 2]. Researchers take some predictors to finish coagulant dosing with different manufacturing techniques. Some people try to find a mathematical model of coagulant dosing, as shown in [3–7]. In [3], based on the iterative feedback tuning (IFT), combined with Smith predictive control, a data-driven direct control method is proposed that need not understand the actual time-delay object model. It can initialize the controller and take online self-tuning. In [4], after studying coagulant

dosing process in water plants, a feedforward and feedback control method combined with the generalized predictive control (GPC) and PID is proposed for dosing. In [5], a two-stage control structure is designed for dosage target calculation and dynamic optimization of the coagulant dosing system. The model predictive control (MPC), a bounder control method, requires less information of the controlled object and proves its validity by simulation. In [6], this paper focuses on analyzing the structure and principle of coagulant dosing and uses predictive autodisturbance rejection control (PADRC) to design an online self-tuning dosing controller. In [7], a multimodal control strategy is proposed based on artificial intelligence, which simulates actual operation without any manual control and ensures the effect of coagulant dosing. Coagulant dosage mainly depends on the accuracy of the computation outcome of the system's mathematical mode. So, modeling accurately is the most difficult to realize the target here.

With the development of the artificial neural network (ANN), it provides another data-driven solution without any mathematical model for such a nonlinear system. Commonly used ANN also includes the radial basis function (RGF) neural network, backpropagation (BP) neural network, cerebella model control articulation (CMCA) neural network, and self-organizing neural network. Some people have applied these types of feedforward neural networks in coagulant dosing, as shown in [8–11]. In [8], a predictive control strategy is proposed for coagulant dosing in wastewater treatment process, an adaptive neural network model is established to analyze the relationship between dosage and detergency, and it is optimized by the gradient descent method. In [9], a RBF neural network predictor with a feedforward compensation is proposed. For a single-input and single-output system, a nonlinear autoregressive moving average model is built up and predicted for coagulant dosing. In [10] after analyzing the characters of raw water and finding out related factors of coagulant dosing, a feedforward controller is designed combined with the CMAC neural network and fuzzy algorithm, and offline modeling is finished in order to realize online optimization and predict coagulant dosage. In [11], a neural network and an adaptive fuzzy model are established to simulate the coagulant dosing process. Finally, simulation is proved valid. Take the neural network model is feasible that has a lower request, self-learning ability, and generalization ability. This method can be applied to complex industry process without building an accurate mathematical model [12]. However, those mentioned gradient-learning algorithms have an obvious problem: overfitting ability and local optimum. So, it is little difficult to design a specific neural network structure which is invariant with lower flexibility.

For improving the neural network, currently, random-vector neural networks have been developed rapidly in recent years because of their learning speed and generalization ability better than traditional neural network algorithms [13, 14]. In many applications, random-vector neural networks are also used in nonlinear complex systems and verified effectively [15–18]. As we know, water purification itself is a nonlinear complex industrial process; for the dynamic mechanism of coagulant dosing is complex, the internal state is unclear. If we need to find the functional relationship between input and output factors about coagulant dosing, it is very hard to do well in setting up a mathematical model. In this paper, we select a water plant in Changsha as the target and analyze its coagulant dosing process and related factors. Considering the difficulty of building up the neural network model, we propose a variable-structure random-vector neural network (VS-RVNN) model for online learning for optimization of coagulant dosage.

2. Analysis and Modeling for Coagulation Dosing Process

2.1. Analysis for Coagulation Dosing Process.
The water purification process mainly includes drug administration, coagulation-sedimentation, filtration, and chlorine disinfection. Each subprocess is independent and related to each other. The coagulation process is composed of data sampler, controller, coagulation-sedimentation tank, and execution equipment. Taking a water plant in Changsha as an example, its process is shown in Figure 1.

When raw water passes through the water pump room, its turbidity and flow velocity are measured before the coagulation tank. In addition, after the coagulant and running water are mixed in an appropriate proportion, the mixture enters the coagulation tank by the dosing pump and performs coagulation reaction with raw water. The coagulant dosing will take effects after about 90 minutes, meaning a long-delay process. At the outlet of the tank, turbidity is measured one more time and judged whether its values reach set values or not. The key point is that necessary data are sampled by equipment, computed by the controller, and an optimum coagulant for dosing pump operation is obtained. Pump adjusts its speed and opening to optimize online coagulant dosage. As we know, coagulant dosing process is complicated, varied, and nonlinear, with long delay. It cannot find the direct relationship between input and output information. So, it is not easy to establish a correct mathematical model.

2.2. Modeling and Control for Coagulant Dosing Process.
There are three common modeling methods at current, namely, mechanism model, knowledge-based model, and data-driven model. Firstly, the mechanism model depends too much on the system internal mechanism. However, a system becomes more nonlinear and strong coupling than before; its interior mechanism is complicated and cannot be shown obviously and clearly by formula. Secondly, the knowledge-based model mostly relies on limited expert knowledge with poor adaptability. Lastly, the data-driven model need not know what system's inner state is; however, it still can predict and give a reasonable decision by a lot of data analyses and intelligent deduction. After analyzing the three methods, establishing a data-driven model has become one powerful method for a complex system in recent years. Neural network model (NNM) is one of them that can deal
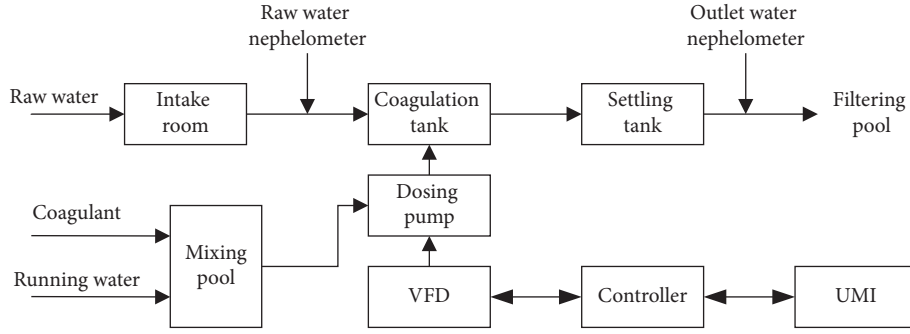
FIGURE 1: Schematic diagram of coagulation process.

with inaccurate and complicated information of the complex system [19–21]. In the paper, coagulant dosing process is just such a type without analyzing its mechanism, collecting insufficient and inaccurate expert knowledge. However, coagulant dosing process runs independently; its necessary parameters can be measured and monitored. Taking a water plant in Changsha as an example, water supply varies in different seasons and at different times of a day. Especially at rush hour, water supply must increase sharply. Then, co-agulant dosage will be predicted appropriately in advance. Furthermore, there are two main problems about the target water plant at current. One is that it still takes simple manual

dosing. The other problem is that system delay is a little long, and working condition is changeable. So, only one simple NNM cannot work useful with abrupt events. Through local investigation, we gather related data and get to a conclusion: turbidity, flow velocity, working pumps affect coagulation obviously. Other parameters such as pH and water tem-perature also affect coagulation slowly. How to control coagulant dosage is a concerned topic. It satisfies turbidity while decreasing production cost as much as possible. To sum up, aiming at the actual object, a nonlinear autore-gressive multimode (NARM) is set up as follows:

$$Y(t) = \begin{cases} f^1\left(x_1(t),\ldots,x_1(t-p_1),\ldots,x_k(t),\ldots,x_k(t-p_k),Y(t-1),\ldots,Y(t-q)\right), & \text{when modal} = 1, \\ \ldots \\ f^i\left(x_1(t),\ldots,x_1(t-p_1),\ldots,x_k(t),\ldots,x_k(t-p_k),Y(t-1),\ldots,Y(t-q)\right), & \text{when modal} = i, \end{cases} \tag{1}$$

where historical data are also concerned. A multimodal function is provided in formula (1). $x_i(t),\ldots,x_i(t-p_i)$ is the input data set, $Y(t)$ is the output, p_i, q is the lag step $(i = 1,\ldots,k)$, and $f^1(.),\ldots,f^i(.)$ are different respective nonlinear relations between input parameters and output parameters at different modes. Combining with NARM, for solving the above two problems concerned in this paper, we design a multimodal control scheme, as shown in Figure 2.

In the control scheme, rule base (RB) just contains a lot of dosing parameters and several modal decision rules. The most important focus is the variable-structure random-weight neural network (VS-RVNN). It can build up variable-structure NN which can optimize its model and online-compute the optimum dosage. RB will provide suitable operational parameters for the dosing pump. All data will be stored in a database after one computation is completed. According to the analysis for related factors of coagulant dosing in this part, RB will make a decision by systems' operating state, select the most suitable mode, and rectify existed rules. The neural network controller updates the target value and training data set, varies the computation model, calculates optimum dosage, and keeps continuous cycle operation. The whole control method mainly combines RB and VS-RVNN and designs a MM-P-VSRVNN algo-rithm. The design is figured out in Figures 3 and 4.

In Figure 3, about RB, we set multiple modes and design a mode switcher. Through the main influencing factors which have been defined, a series of decision rules are constructed and categorized into the designed mode. These rules are also the criterion of judgement for the switching mode. Furthermore, in each mode, there are some typical control rules about water pump control parameters. The selected control rule will be connected to the ANN controller as a guideline for further optimization.

In Figure 4, we design an initial NNM which has an initial value of hidden-layer nodes in the leftmost. When real-time data are sampled, NNM judges working mode once again and takes a new computation after retraining the neural network with the corresponding training data, and the hidden-layer nodes decrease from L to Ki by PCA (when mode $= i, i = 1,\ldots,n$), and the structure of the neural network is updated for real-time computation. This means NNM will have n-type structures after the PCA dimension.

Notation: here, NNM, proposed in Figure 4, has a variable structure. Because the number of hidden-layer nodes is always a key point for modeling, here, NNM is not fixed when we perform principal component analysis (PCA) for hidden-layer nodes. So, NNM has a variable structure at each computation. This method can effectively solve the
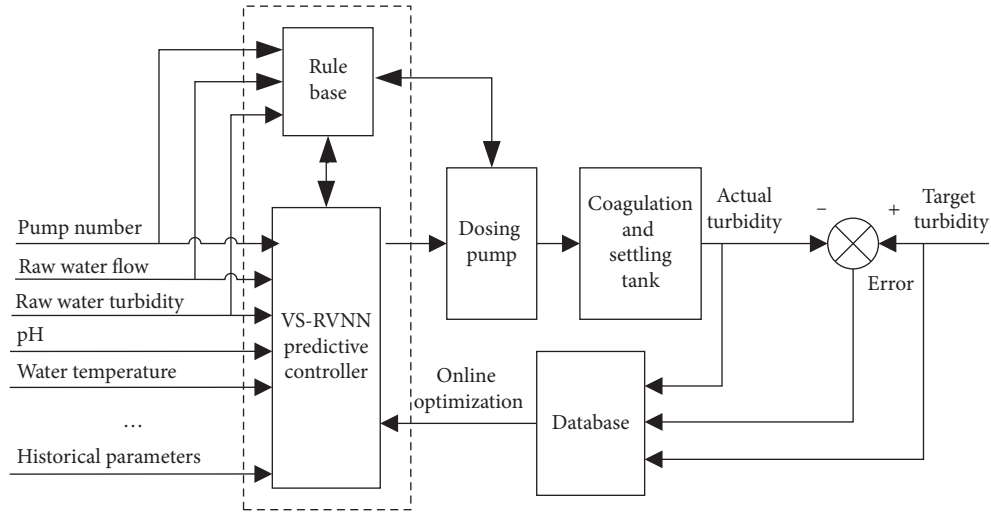
FIGURE 2: Multimodal control chart for coagulant dosing.
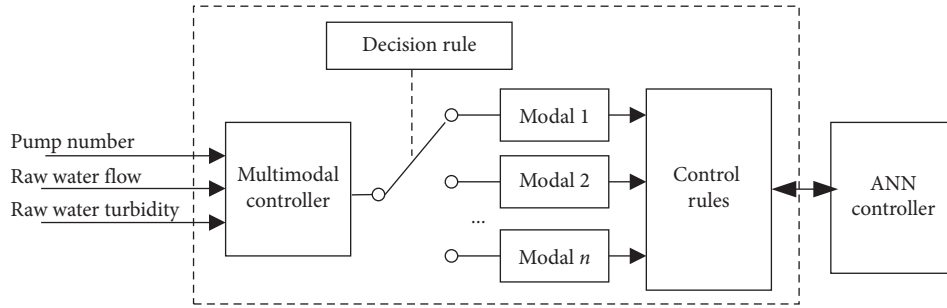
FIGURE 3: The diagram of rule base (RB).

problem of overfitting and robustness of neural networks and improve the computational speed and generalization ability.

3. MM-P-VSRVNN Algorithm

Combining with Section 2.2, the whole algorithm mainly includes two parts, namely, modal switching and dimensionality reduction by PCA. The prediction algorithm is executed by the MM-P-VSRVNN. It takes two stages: offline modeling and online optimization.

Here, the whole algorithm steps are as follows:

Before computation, we choose a multimodal data set for training samples: $Z = \{(x_i^k, y_i^k) \mid x_i^k \in R^M, y_i^k \in R^N,$ $i = 1, \ldots, M \mid$ when mode $= k\}$. And each mode has its independent data subset $\{Z_i \mid$ when mode $= i\}$ in it.

(i) Step 1: sample real-time data, and judge the working mode by RB. For example, if mode $= i$, it gives a decision for NNM and switches to the ith control strategy.

(ii) Step 2: build up a VS-RVNN with a random layer (L nodes) and an output layer (N nodes). The initial value of L is set to 60. The random layer can be constructed by the hidden layer and input layer.

(iii) Step 3: take the corresponding data subset of training samples for NNM. Then, the functional of the random layer is defined as $\{x_1, \ldots, x_N \mid \theta_1, \ldots, \theta_N\}$ when mode $= k$.

Then, the function of the random layer is defined as

$$g_j(x_i, \theta_j) = \varphi_j(\omega_j x_i + b_j), \quad 1 \le j \le L, \qquad (2)$$

where $\omega_j = (\omega_{j1}, \omega_{j2}, \ldots, \omega_{jn})$ is the input weight of the jth hidden-layer node, b_j is the threshold value of the jth hidden-layer node, $\theta_j = \omega_{\omega_j} \underline{j}$ is the random-weight vector of the hidden-layer nodes, and $x_i (i = 1, 2, \ldots, N)$ is the input to the network.

(iv) Step 4: set the training target, and start to train the NNM with the given data subset.

(v) Step 5: let $G_h = g_j(x_i, \theta_j)$. Repeat to run step 4 until training meets the given target. Otherwise, it restarts at step 2 and computes once again.

(vi) Step 6: construct a random-layer training matrix $G = [G_1, \ldots, G_H]^T$. Each column of G represents a random-layer output node, and each row represents a training sample output.

(vii) Step 7: perform weighted difference to training matrix G, and remove its nonlinear or multimodal
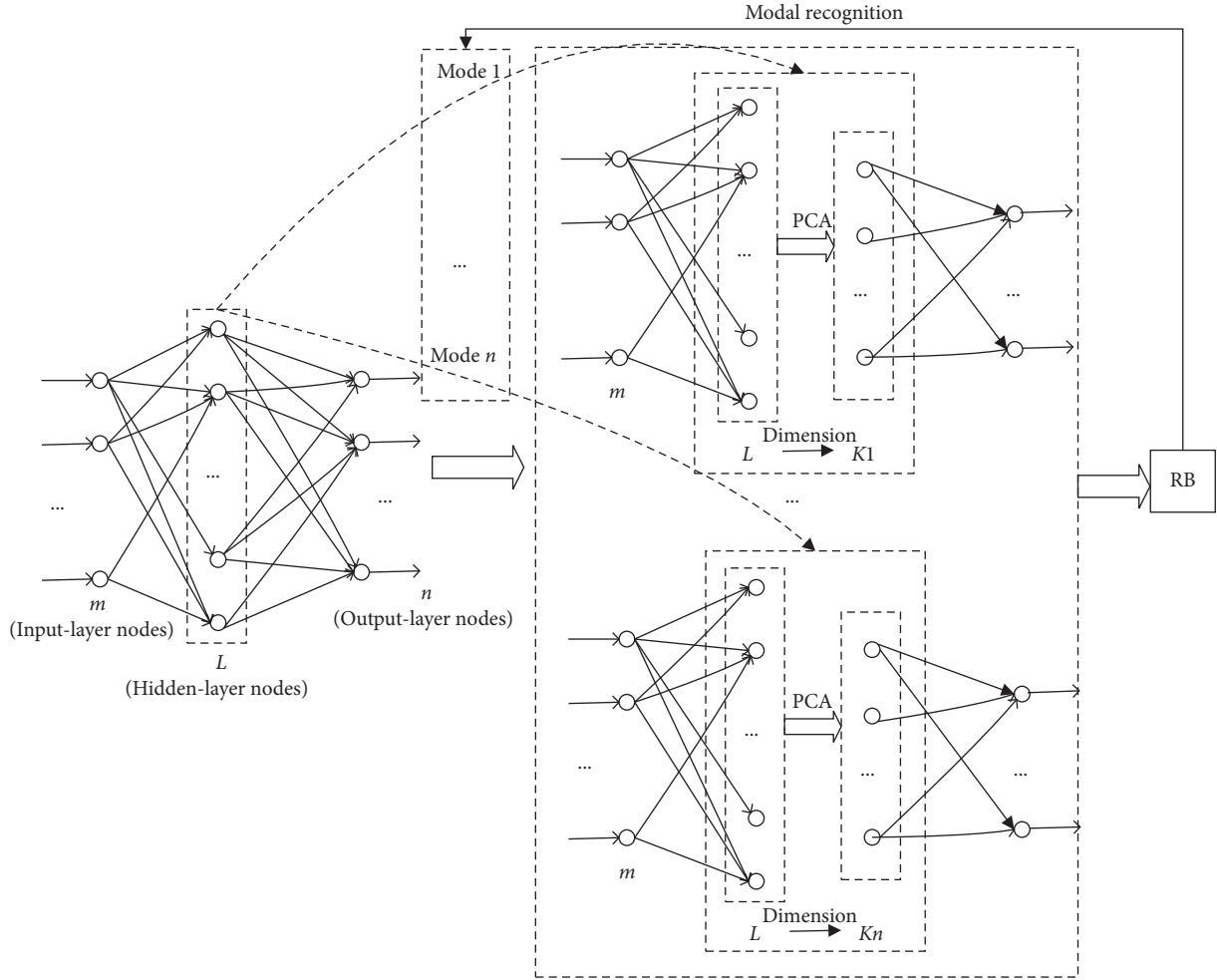
FIGURE 4: The diagram of a multimodal neural network.

characteristics. Next, continue to standardize G. Then, the standardized matrix is $\overline{G}$, and find its correlation coefficient matrix $\overline{S}$, which meets its mean value per column which is 0 and standard deviation which is 1:

$$\overline{S} = \begin{bmatrix} r_{11} & r_{12} & .. & r_{1l} \\ r_{21} & r_{22} & .. & r_{2l} \\ .. & .. & .. & .. \\ r_{l1} & r_{l2} & .. & r_{ll} \end{bmatrix}, \quad (i = 1, \ldots, l), \qquad (3)$$

where r_{ij} represents the correlation coefficient between variable i and variable j. After that, the eigenvalue decomposition of $\overline{S}$ is done, eigenvalues $\{\lambda_1, \ldots, \lambda_L\}$ and eigenvectors of $\overline{S}$ are computed, and these eigenvalues are sorted by size.

(viii) Step 8: calculate the contribution rate of each eigenvalue, and sort all eigenvalues to sum up the components' added contribution rate one by one and compute whether it is over 95 percent or not. If

it is, then count the d number of major components and construct a transfer matrix:

$$p = \begin{bmatrix} p_{11} & p_{12} & .. & p_{1L} \\ p_{21} & p_{22} & .. & p_{2L} \\ .. & .. & .. & .. \\ p_{k1} & p_{k2} & .. & p_{kL} \end{bmatrix} \quad \text{when mode} = i, \qquad (4)$$

which is based on its corresponding d eigenvectors, and the random-layer matrix $\overline{G}$ is met and satisfies the equality $\widehat{G} = GP$.

(ix) Step 9: input the latest collected samples into NNM, and calculate the function value of each output-layer node $f_l = \sum \beta_j g_j(x_i, \theta_j), 1 \le l \le N$. All necessary data are stored.

(x) Step 10: compare the predicted outcome with the dosage value in the RB, correct control parameters of pumps online, and finish dosing.

(xi) Step 11: update the training sample set.
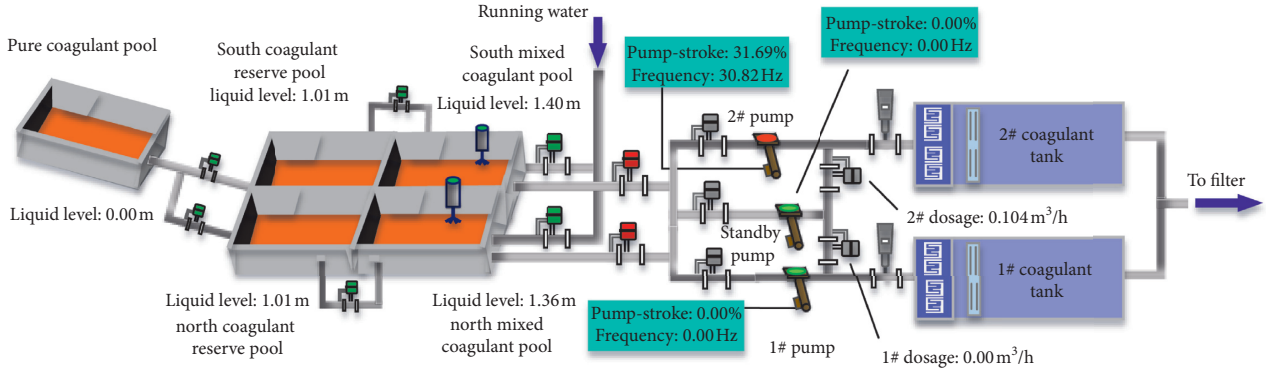
FIGURE 5: The diagram of the dosage system.

(xii) Step 12: wait for the next sampling, and repeat the work from steps 1 to 11.

Notation: compared with the traditional RVNN, RS-RVNN can perform mode switching and train the original neural network with the corresponding data set and system's control state. The output matrix of the hidden layer is obtained through multiple training times and can be reduced dimensionally by PCA. The neural network structure can be optimized under different modalities to ensure the system's continuous stability. Furthermore, the neural network controller implements dynamic optimization of the variable structure every time. Network training is performed during mode switching, and it enhances the flexibility of the controller.

4. Experiment Results and Discussion

In this paper, we analyze the actual water purification process of Changsha's water plant. This plant was built up as a two-phase project, which mainly has two storage tanks, alum tanks, coagulation tanks, and pump workshop for capacity expansion. And now, one of them is working. The water purification process with related parameters is shown timely and stored in the system database. Its coagulant dosing system is shown in Figure 5.

Through these data provided by applied instruments and electromechanical equipment, we choose the important factors related to coagulation efficiency: turbidity before filtration (NTU), turbidity of raw water (NTU), discharge of water (m^3/h), water temperature (°C), frequency (Hz), pH, pump stroke (percent), target turbidity (NTU), historical data of turbidity (NTU), water flow rate (m^3/h), and coagulant dosing (m^3/h). These are prepared for building up a NNM. Two of them, target turbidity (NTU) and prediction value of coagulant dosing (m^3/h), are output targets of the NNM. From parts 2 and 3, the number of hidden-layer nodes cannot be determined. In our NNM, we set an initial value (60) for hidden-layer nodes, which can be decreased by PCA. Then, the structure of the NNM is optimized, and the prediction for coagulant dosage is obtained. A new NNM is named P-VSRVNN.

TABLE 1: Dimension reduction for NNM by PCA (40 groups).

Data set (group)	Modal	Hidden-layer nodes after PCA
1	1	8
2	1	8
3	1	8
4	1	7
5	2	8
6	2	8
7	2	8
8	2	8
9	1	8
10	1	8
11	1	8
12	1	7
13	1	7
14	1	7
15	1	8
16	1	8
17	1	7
18	1	8
19	3	7
20	3	8
21	1	8
22	1	8
23	1	8
24	1	8
25	1	8
26	1	8
27	1	7
28	1	9
29	1	8
30	3	8
31	3	7
32	2	7
33	2	9
34	1	8
35	1	8
36	1	8
37	1	8
38	1	8
39	1	9
40	1	8

Coagulant dosing process contains 3 working modes. In this experiment, we select 1000 groups of data. Among them, 960-group data are divided into 3 subsets for training

TABLE 2: The first eight principal components' eigenvalue and variance contribution by PCA in one computation.

Principal components	Eigenvalue	Variance contribution (percent)	Accumulated variance contribution (percent)
1	20.1607660138651	33.6012766897752	33.6012766897752
2	14.1382412479112	23.5637354131853	57.1650121029605
3	9.55968664322995	15.9328110720499	73.0978231750104
4	5.33738215800062	8.89563693000104	81.9934601050114
5	4.28516886114769	7.14194810191281	89.1354082069243
6	1.83532313856500	3.05887189760834	92.1942801045326
7	1.24409369821930	2.62008336345786	94.2677696015648
8	0.895336966029005	1.49222827671501	95.7599978782798
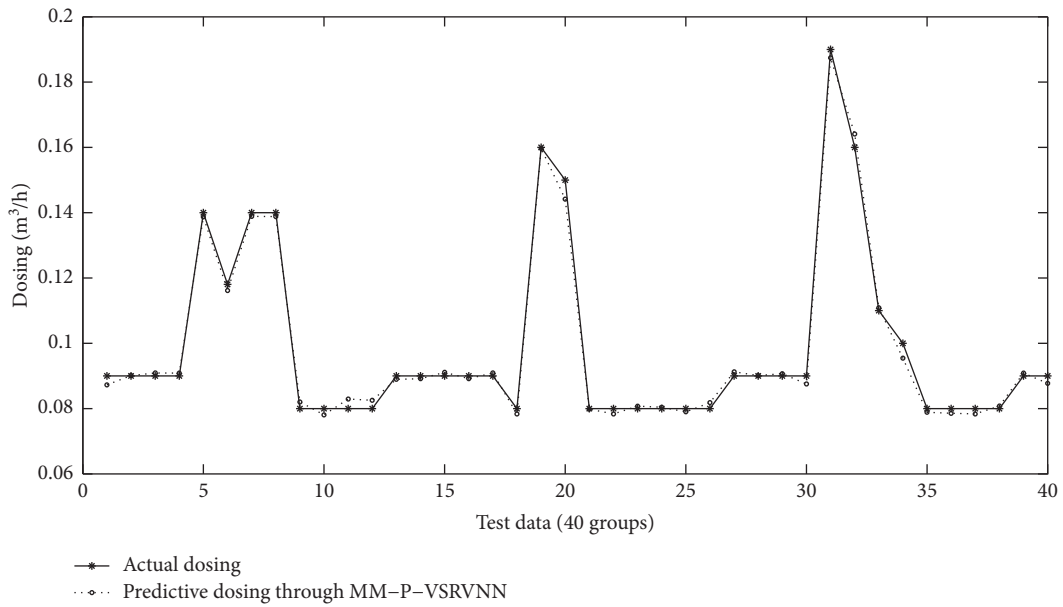
FIGURE 6: Prediction and actual value of coagulant dosage.
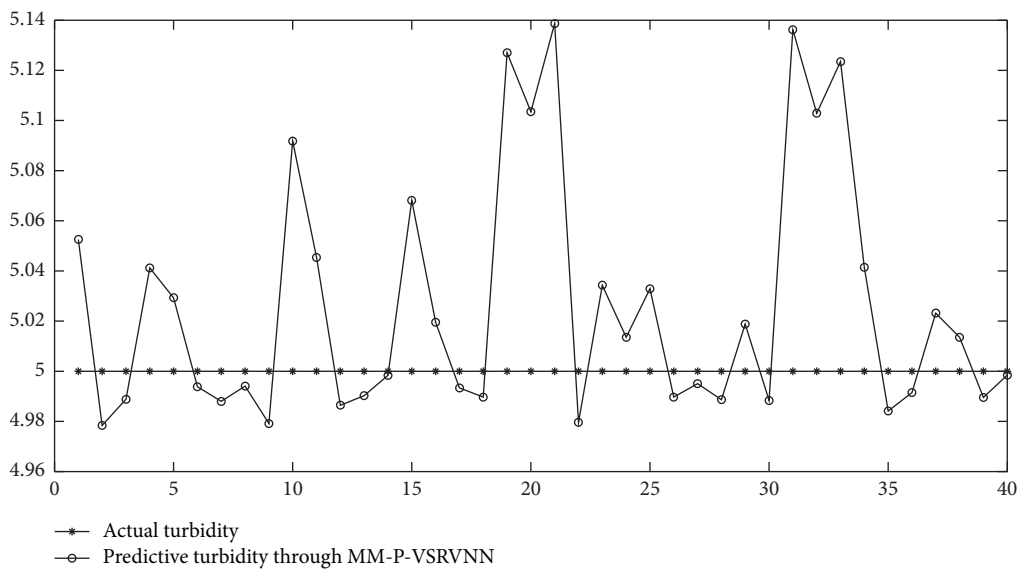
FIGURE 7: Prediction and actual value of turbidity before filtration.
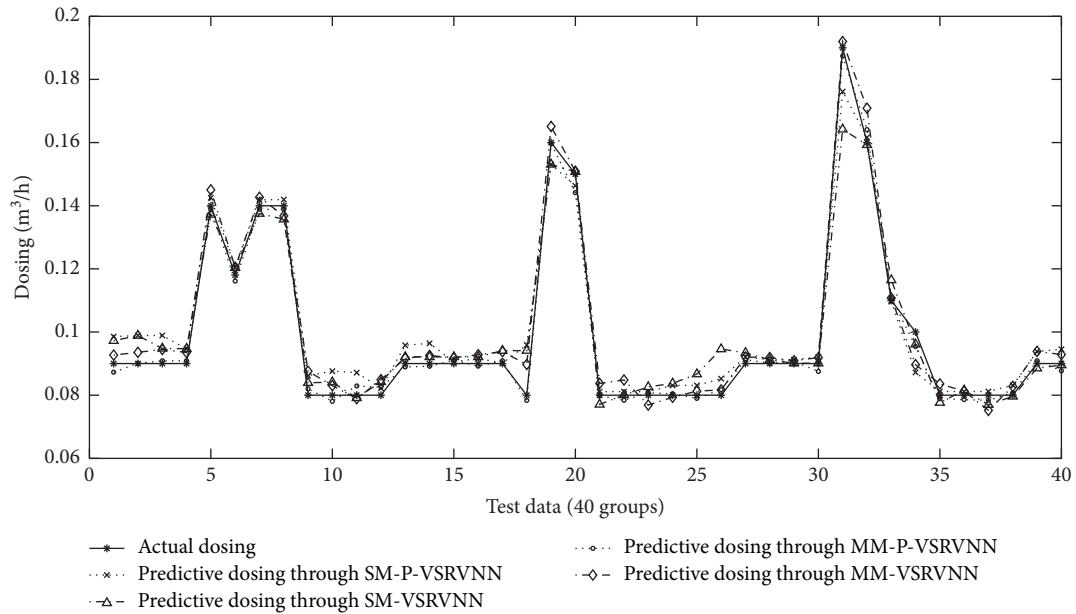
Figure 8: Prediction output for dosing with four different algorithms.
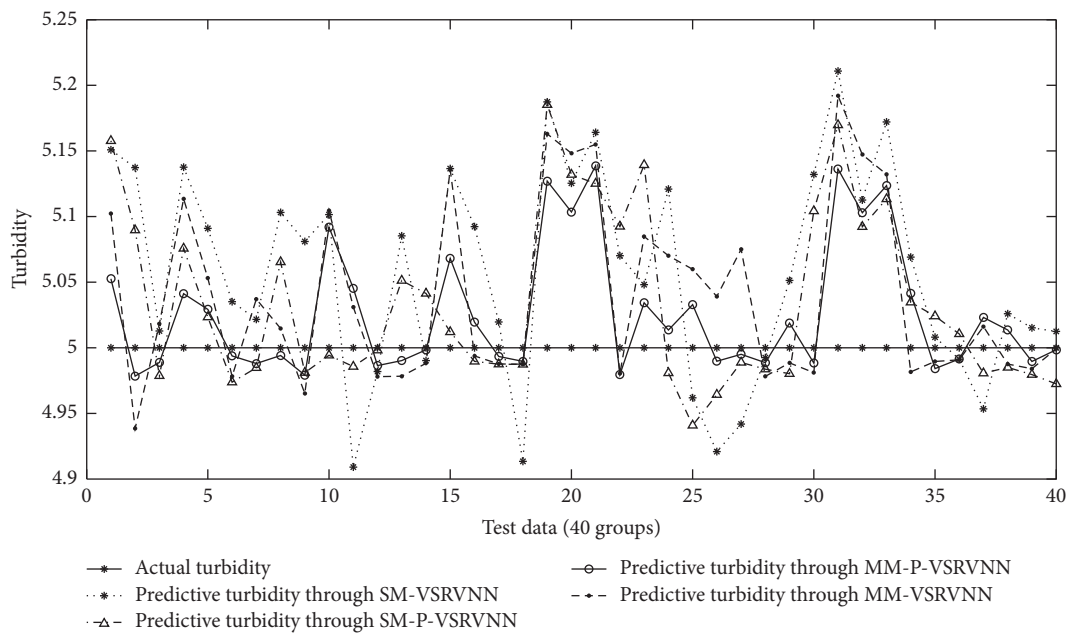
Figure 9: Prediction output for turbidity before filtration with four different algorithms.

different working modes. And each subset includes 320-group data. The remaining data are also divided into 3 types for testing. A new group of data is obtained by hourly sampling, which includes connected information working mode. We need to set up different NNMs for each different training set. The whole experiment includes such works as follows. The whole control model mentioned in the paper is called MM-P-VSRVNN.

(1) As NARM is described, building a valid optimized VSRVNN is a key work. It mainly computes node

contribution about 95 percent, retains the corresponding nodes, and avoids overfitting learning. VSRVNN is constructed offline with updated training set by PCA, which reduces 60 original hidden-layer nodes to k_i when it works in the ith mode. 40 groups of dimension reduction for the testing set are listed in Table 1.

Table 1 shows us that the structure of the VSRVNN is variable at different modes. Even at the same mode, optimized result may not be the same. The value of k is changed from 7 to 9, and 8 is the majority. Taking one computation as

TABLE 3: Statistics result comparison among four algorithms for predictive turbidity before filtration.

Predictive turbidity	MM-P-VSRVNN	MM-RVNN	SM-P-RVNN	SM-RVNN
Mean value (NTU)	5.026066	5.0387364	5.0339242	5.0571979
RMSE	0.0546	0.0735	0.0773	0.0968
MAE	0.1918	0.2303	0.2365	0.2817
SD	0.0480	0.0653	0.0670	0.0781

TABLE 4: Statistics result comparison among four algorithms for predictive dosage before filtration.

Predictive dosage	MM-P-VSRVNN	MM-RVNN	SM-P-RVNN	SM-RVNN
Mean value (m^3/h)	0.09853900	0.10123137	0.10128999	0.10019643
RMSE	0.0013	0.0016	0.0020	0.0063
MAE	0.0396	0.0587	0.0650	0.0645
SD	0.0251	0.0273	0.0282	0.0276

—◇— MM-P-VSRVNN (referenced value in list 3)
– * – MM-RVNN
······ SM-RVNN
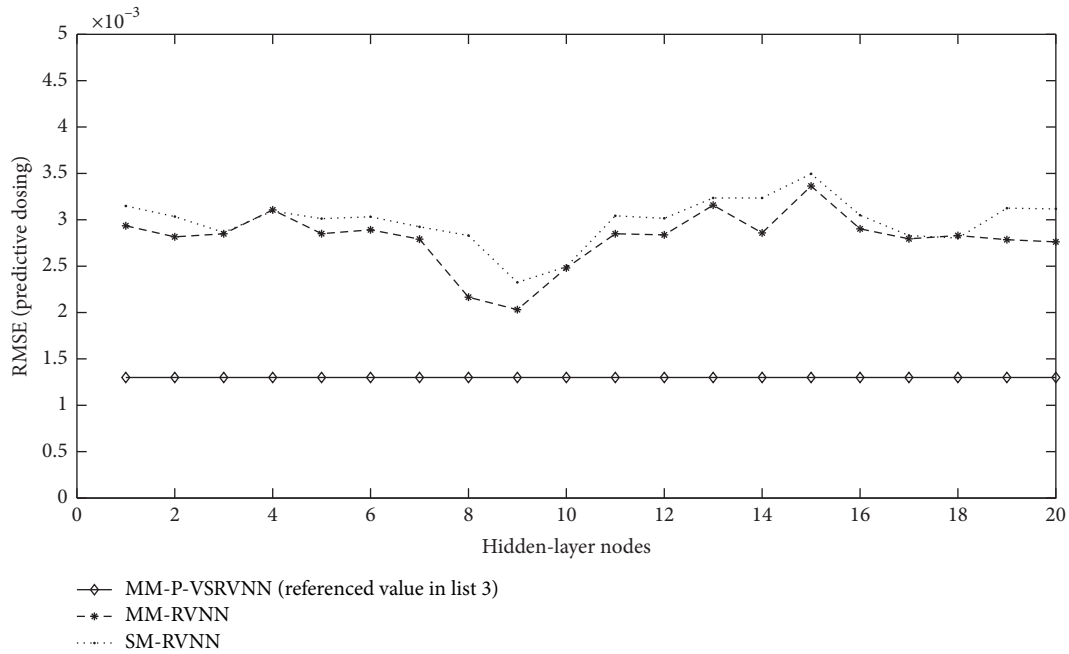
FIGURE 10: RMSE for predicted dosage by different algorithms when hidden-layer nodes varied from 1 to 20.

an example, the first eight principal components' analysis outcomes are shown in Table 2.

The first eight principal components' effects are added to more than 95 percent, which are displayed on the VSRVNN. Because its training set changes after one computation, the optimized result is also varied but still meets 95 percent node contribution. (2) For checking the validity of the VSRVNN, we program an algorithm named MM-P-VSRVNN. And contrasting its predicted results to actual values, the total 40 points are shown in Figures 6 and 7.

Two parameters are compared in separated figures. Real line labeled as "•" symbol is the actual dosage, and the other line labeled as "∘" is the predicted dosage. In this test, predicted dosage varies around the actual value and remains consistent with its tendency. Average predicted dosage is

reduced about 0.4165 percent in Figure 6; meanwhile, average predicted turbidity increases about 0.5 percent in Figure 7. The simulation result is acceptable for enterprise. To them, it already meets needs of water purification process, reduces total coagulant dosage and saves manufacturing cost to a certain extent. (3) A further test is to analyze the performance of the MM-P-VSRVNN in contrast with other three similar algorithms. Other similar algorithms are single-modal random-vector neural network (SM-RVNN), SM-RVNN after dimension reduction (SM-P-RVNN), and multimodal random-vector neural network (MM-RVNN). All predictive results are in contrast, visually, as shown in Figures 8 and 9.

On the contrary, all the algorithms are in contrast with their statistical parameters, separately named root mean
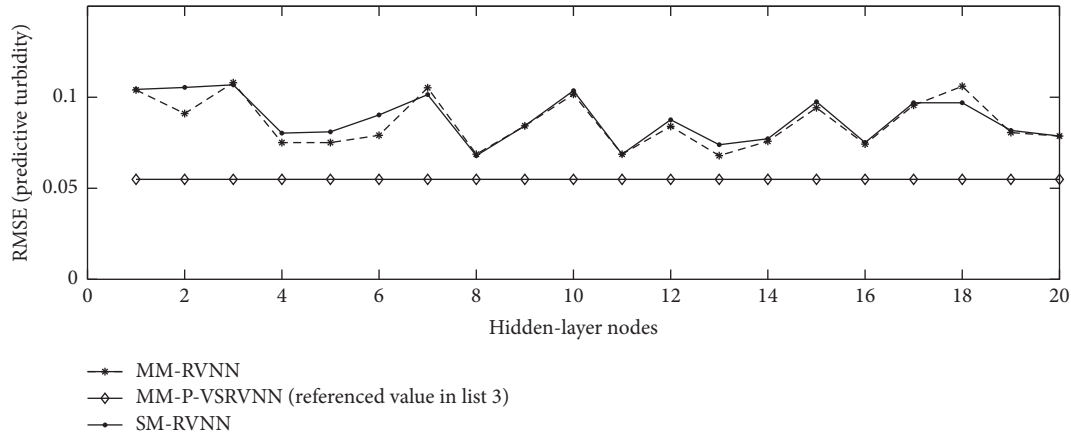
FIGURE 11: RMSE for predicted turbidity by different algorithms when hidden-layer nodes varied from 1 to 20.

square error (RMSE), mean absolute error (MAE), and standard deviation (SD). The statistical results are computed by different methods and shown in Tables 3 and 4.

These four aforementioned algorithms used the same data set and original mode. In Figure 6, the method provided in this paper has better result accuracy and tendency. It proves that, after quantitative computation, MM-P-VSRVNN can optimize the neural network mode and classify the operating mode that led to a better prediction.

(4) For improving the generalization ability of the MM-P-VSRVNN, NNM takes a new computation once a new group of data is measured. Then, NNM is optimized again because hidden-layer nodes vary. Now, for a further check, the next experiment changes the hidden-layer node number from 1 to 20 and computes RMSE for different algorithms. And these results are compared with those provided by the MM-P-VSRVNN in Figures 10 and 11.

In Figures 10 and 11, MM-P-VSRVNN provided in the paper has lower RMSE and better generalization ability, which can avoid the overfitting problem when the neural network is operating.

Notation: with all the experiments, as we know, the number of hidden-layer nodes takes a new update when a new computation occurs, computation mode is optimized, and the system provides a suitable result. By the way, this computation for RMSE is also operated until hidden-layer nodes increased to 300 one by one, but we found the operating time is too long, and the contrast result is indistinct. Therefore, considering the known information, we set the maximum number as 20.

5. Conclusion

This paper aims at coagulant dosing in water purification process for a water plant in Changsha. After analyzing the actual process and previous control modes, we put up a NNM and applied a new MM-P-VSRVNN algorithm for dosage prediction. This NNM is optimized by the MM-P-VSRVNN algorithm and gives an appropriate control result to perform a new dynamic dosing. At last, we also perform a series of experiments with the designed NNM and its algorithm to prove the practicability. The algorithm provides an improved method, and the coagulant dosing control realizes automatically.

Data Availability

All the data used to support the findings of this study are included within the article.

Conflicts of Interest

The authors declare no conflicts of interest.

Acknowledgments

References

[1] M. Ławryńczuk, "Explicit nonlinear predictive control of a distillation column based on neural models," *Chemical Engineering and Technology*, vol. 32, no. 10, pp. 1578–1587, 2009.

[2] J.-I. Park, N.-C. Jung, K.-C. Kwak, and M.-G. Chun, "Water quality prediction in a reservoir: linguistic model approach for interval prediction," *International Journal of Control, Automation and Systems*, vol. 8, no. 4, pp. 868–874, 2010.

[3] A. W. Xuefeng, "Data-driven direct control method for large lagging process of coagulation dosing in water plant," *Control Theory and Application*, vol. 28, no. 3, pp. 336–344, 2019.

[4] J. Zhang and D. Luo, "The Application of GPC control and PID control to coagulant dosing," *Information and Control*, vol. 41, no. 1, pp. 89–94, 2012.

[5] G. Chen and R. Ning, "Two-layered predictive control strategy of coagulant dosing systems," *Journal of Zhejiang University of Technology*, vol. 41, no. 4, pp. 436–441, 2013.

[6] D. Tang and X. Zhang, "Design of Predictive active disturbance rejection industry controller for coagulation dosing," *Control Engineering of China*, vol. 24, no. 10, pp. 2099–2108, 2017.

[7] R. Li, Q. Wu, and B. Liu, "Multimodal control of complex process with uncertainty for raw water purification of coagulant filing dosage," *Journal of Liaoning Technical University (Natural Science)*, vol. 35, no. 2, pp. 211–214, 2016.

[8] H. Mingzhi, Y. Ma, W. Jinquan, and W. Yan, "Simulation of a paper mill wastewater treatment using a fuzzy neural network," *Expert Systems with Applications*, vol. 36, no. 3, pp. 5064–5070, 2009.

[9] J. Wang, S. Liu, and W. Qi, "RBF network predictive control of coagulant dosage," *Journal of System Simulation*, vol. 21, no. 17, pp. 5540–5545, 2017.

[10] S. Xu, D. Liu, and B. Liu, "Application of fuzzy algorithm-based multiple CMAC neural networks in coagulant dosing system," *Computer Applications and Software*, vol. 33, no. 10, pp. 52–57, 2016.

[11] G.-D. Wu and S.-L. Lo, "Predicting real-time coagulant dosage in water treatment by artificial neural networks and adaptive network-based fuzzy inference system," *Engineering Applications of Artificial Intelligence*, vol. 21, no. 8, pp. 1189–1195, 2008.

[12] M. Yuan, P. Zhou, M. L. Li, R. F. Li, H. Wang, and T. Y. Chai, "Intelligent multivariable modeling of blast furnace molten-iron quality based on dynamic AGA-ANN and PCA," *Journal of Iron and Steel Research, International*, vol. 22, no. 60, pp. 487–495, 2015.

[13] P. Zhou, M. Yuan, H. Wang, Z. Wang, and T.-Y. Chai, "Multivariable dynamic modeling for molten iron quality using online sequential random vector functional-link networks with self-feedback connections," *Information Sciences*, vol. 325, pp. 237–255, 2015.

[14] P. Zhou, Y. Lv, H. Wang, and T. Chai, "Data-driven robust RVFLNs modeling of a blast furnace iron-making process using Cauchy distribution weighted M-estimation," *IEEE Transactions on Industrial Electronics*, vol. 64, no. 9, pp. 7141–7151, 2017.

[15] M. Zhang, X. Liu, and Z. Zhang, "A soft sensor for industrial melt index prediction based on evolutionary extreme learning machine," *Chinese Journal of Chemical Engineering*, vol. 24, no. 8, pp. 1013–1019, 2016.

[16] L. Zhang and D. Zhang, "Domain adaptation extreme learning machines for drift compensation in E-nose systems," *IEEE Transactions on Instrumentation and Measurement*, vol. 64, no. 7, pp. 1790–1801, 2015.

[17] H. Wang, P. Shi, H. Li, and Q. Zhou, "Adaptive neural tracking control for a class of nonlinear systems with dynamic uncertainties," *IEEE Transactions on Cybernetics*, vol. 47, no. 10, pp. 3075–3087, 2017.

[18] T. He, J. Lu, J. Ding, and C. Liu, "Prediction model of total carbon content of crude oil using ensemble random weights neural network optimized by particle swarm optimization," *Control Theory Application*, vol. 36, no. 2, pp. 192–199, 2019.

[19] M. He, J. Tang, X. Guo, and G. Yan, "Soft sensor for ball mill load using DAMRRWNN Model," *Acta Automatica Sinica*, vol. 45, no. 2, pp. 398–407, 2019.

[20] H. Li, "Network traffic prediction of the optimized BP neural network based on Glowworm Swarm Algorithm," *Systems Science & Control Engineering*, vol. 7, no. 2, pp. 64–70, 2019.

[21] M. S. Hasibuan, L. E. Nugroho, and P. I. Santosa, "Model detecting learning styles with artificial neural network," *Journal of Technology and Science Education*, vol. 9, no. 1, pp. 85–95, 2019.

Research Article

On the Security Analysis of a Hopfield Chaotic Neural Network-Based Image Encryption Algorithm

Yingchun Hu [ID]**, Simin Yu** [ID]**, and Zeqing Zhang**

School of Automation, Guangdong University of Technology, Guangzhou 510006, China

Correspondence should be addressed to Yingchun Hu; 1111704006@mail2.gdut.edu.cn

In this paper, the security analysis of a color image encryption algorithm based on Hopfield chaotic neural network is given. The original chaotic image encryption algorithm includes permutation encryption and diffusion encryption. The result of cryptanalysis shows that the chaotic sequences generated by this algorithm are independent of plaintext image, and there exist equivalent permutation key and equivalent diffusion key. Therefore, according to chosen-plaintext attack, the equivalent diffusion key and the equivalent permutation key can be obtained by choosing two special plaintext images and the corresponding ciphertext images, respectively, and the plaintext image is further recovered from the ciphertext image. Theoretical analysis and numerical simulation experiment results verify the effectiveness of the analytical method. Finally, some improved suggestions for the original encryption algorithm are proposed to promote the security.

1. Introduction

With the rapid development of network technology, the security and privacy protection problems of multimedia information have become a hot subject. In order to promote the security of information transmission, scholars have proposed a large amount of image encryption algorithms based on different mechanisms and theories, such as chaotic map [1–13], neural network [14], DNA [15–18], and so on. The security performance of the image encryption algorithms mainly depends on statistical test indicators, such as key space, histogram, key sensitivity analysis, information entropy, differential attack, and so on. However, statistical test indicator is an essential condition and not a sufficient condition for measuring security presented in [19]; moreover, some of them are proven to be insecure due to their inherent pitfalls [20–30]. Therefore, it is necessary to perform cryptanalysis in order to improve the security of the image encryption algorithms.

In recent years, many image encryption algorithms have been cryptanalyzed by the researchers. For example, in [20], the cryptanalysis of an image encryption cryptosystem based on binary bit planes extraction and multiple chaotic maps

(IEC-BPMC) proposed in [1] is given; it is pointed out that IEC-BPMC is insecure against chosen-plaintext attack. In [21], the security analysis of an image chaotic encryption algorithm based on Latin cubes and bit cubes presented in [2] is proposed; it is reported that the generation of Latin cubes is independent of plain image, while in the diffusion stage, when any one bit in the plain image changes, the corresponding number of bits in the cipher image follows the change with obvious regularity. According to chosen-plaintext attack, only a maximum of $2.5 \times \sqrt[3]{w \times h} + 6$ plaintext images are needed to crack the ciphertext images of size $w \times h$ resolution. In [22], according to chosen-ciphertext attack, the security analysis for a self-synchronization and closed-loop feedback-based chaotic stream cipher proposed in [3] is given; it has shown that, under the condition that only one unknown key needs to be deciphered while the remaining keys are all known, most secret keys can be deciphered accurately. In addition, the attack complexity of the proposed method is lower than that of the exhaustive attack. In [23], the security performance for an 8D self-synchronous and feedback-based chaotic stream cipher with low 8 bits of state variables for encryption proposed in [4] is analysed, according to known-plaintext

attack and divide-and-conquer attack, 49 secret keys can be obtained, and an improved chaotic stream cipher is proposed for improving the ability to resist divide-and-conquer attack and chosen-ciphertext attack. According to chosen-plaintext attack, in [24], the security analysis of an image encryption algorithm based on 3D bit matrix permutation presented in [5] is given and proposes some improved suggestions in order to enhance security performance. The cryptanalysis of the image encryption algorithm proposed in [7] is presented in [25]; it is reported that the equivalent secret keys can be obtained by utilizing chosen-plaintext attack and further recover the original plaintext image from the ciphertext image. In [26], the security analysis of an image encryption algorithm based on improved hyper-chaotic sequence presented in [8] is given; it is shown that only 1-pair known plaintext-ciphertext image can crack the original encryption algorithm by using known-plaintext attack. In [27], the cryptanalysis of an image encryption algorithm with one round diffusion structure proposed in [9] is reported to find that the original encryption algorithm has equivalent secret keys, so that it can be deciphered by known-plaintext and chosen-plaintext attack. In [28], it is pointed out that permutation-only encryption structure presented in [10] is insecure against known-plaintext attack and chosen-plaintext attack, respectively; for given image of size MN, the original encryption algorithm is cracked by only using $\lceil \log_L (MN) \rceil$ plaintext-ciphertext images. The image encryption algorithm based on DNA encoding and spatiotemporal chaos is proposed in [15]; nevertheless, it is broken in [29] by using chosen-plaintext attack and chosen-ciphertext attack with lower computation complexity and data complexity, respectively. In [30], the security analysis of an image encryption algorithm based on 2D Henon-Sine map and DNA proposed in [17] is given; it is found that cipher image can be cracked by utilizing chosen-plaintext attack without known keys, and its attack complexity is $O(18)$.

In 2019, a color image encryption algorithm based on Hopfield chaotic neural network (CIEA-HCNN) is given in [14]. CIEA-HCNN adopts permutation encryption-diffusion encryption structure; in the permutation encryption phase, firstly, the parameters of Arnold cat map are generated by chaotic sequence and then Arnold cat map is used to scramble the pixel positions of plaintext image. In the diffusion encryption stage, diffusion matrix is generated by utilizing Hopfield chaotic neural network, and then bitwise XOR operation is performed by using diffusion matrix on the scrambled image to obtain the ciphertext image. Some statistical test results are proposed in CIEA-HCNN, and it is claimed that the encryption algorithm has a higher security performance against various attacks. However, CIEA-HCNN has the following inherent defects from the view of cryptanalysis:

(1) The chaotic sequences generated by key-streams are independent of plaintext image; for given secret key parameters and the size of the plaintext image, the chaotic sequences remain unchanged regardless of the plaintext image.

(2) The diffusion encryption structure is too simple, there is no ciphertext feedback mechanism, and there exists equivalent diffusion key. According to chosen-plaintext attack, the equivalent diffusion key is broken by choosing one special plaintext image and its corresponding ciphertext image without known keys.

(3) The permutation encryption structure is a permutation-only encryption process. After deciphering the diffusion encryption structure, the original encryption algorithm becomes a permutation-only encryption structure; in [28], it is pointed out that permutation-only is insecure and cannot resist chosen-plaintext attack and known-plaintext attack. Moreover, parameters of Arnold cat map generated by chaotic sequence depend solely on the secret keys, and the position $(0, 0)$ is always mapped into itself in Arnold cat map.

According to the above shortcomings, one obtains that CIEA-HCNN is insecure, and it is vulnerable to chosen-plaintext attack or known-plaintext attack. An attacker can successfully crack the original encryption algorithm by using the equivalent diffusion key and the equivalent permutation key without knowing the secret keys.

The rest of the paper is organized as follows. Section 2 briefly introduces CIEA-HCNN under study. Section 3 analyses the security performance of CIEA-HCNN by using chosen-plaintext attack. Section 4 gives the numerical simulation experiments and the suggestions for improvement. Section 5 concludes the paper.

2. Chaotic Encryption Algorithm under Study

In this section, Hopfield chaotic neural network and Staged composite chaotic map proposed in [14] are first given, and then CIEA-HCNN is introduced in detail.

2.1. Hopfield Chaotic Neural Network. In 1982, American physicist Hopfield first proposed Hopfield chaotic neural network given in [31]. It is a fully connected neural network, mainly used providing model of simulation human memory. Simultaneously, Hopfield chaotic neural network is also a feedback neural network, and the output signal of each neuron in the network is usually fed back to itself by using other neurons. The iterative equation of Hopfield chaotic neural network is given by

$$x = -x_i + \sum_{i=1}^{3} w_{ij} v_i, \tag{1}$$

$$v_i = \tan h(x_i) = \frac{e^{x_i} - e^{-x_i}}{e^{x_i} + e^{-x_i}}, \tag{2}$$

$$w = \begin{bmatrix} 2 & -1 & 0 \\ 1.7 & 1.71 & 1.1 \\ -2.5 & -2.9 & 0.56 \end{bmatrix}, \tag{3}$$

where state variable $x_i \in [0,1]$, $i = 1,2,3$, $j = 1,2,3$, v denotes a hyperbolic tangent function, and w represents a weight matrix.

2.2. Staged Composite Chaotic Map.

Staged composite chaotic map is a novel phased chaotic map which combines Logistic map with Tent map, given by

$$
x_{n+1} = \begin{cases} 16\mu x_n (0.5 - \mu x_n), & (0 \le x_n < 0.25), \\ 16\mu (0.5 - x_n)(0.5 - \mu(0.5 - x_n)), & (0.25 \le x_n < 0.5), \\ 16\mu (x_n - 0.5)(0.5 - \mu(x_n - 0.5)), & (0.5 \le x_n < 0.75), \\ 16\mu (1 - x_n)(0.5 - \mu(1 - x_n)), & (0.75 \le x_n < 1), \end{cases}
\tag{4}
$$

where control parameter $\mu \in [0,2]$, state variable $x_n \in [0,1]$, $n = 0,1,2,\ldots$. The system is chaotic defined by equation (4) when $\mu \in (0.33, 2]$.

2.3. Description of CIEA-HCNN.

In [14], CIEA-HCNN consists of secret keys selection, chaotic sequences generation, permutation encryption, and diffusion encryption, as shown in Figure 1, where $x_1', x_2', \mu_1, \mu_2, m_0, m_r, m_g, m_b$ are secret key parameters, X, Y, Z, W are chaotic sequences generated by Staged composite chaotic map, α and β are parameters of Arnold cat map, T is a permutation matrix, H_1, H_2, H_3 are sequences generated by Hopfield chaotic neural network, D is a diffusion matrix, P is a color plaintext image, S is a temporary permutation encryption image of P, $S\prime$ is a permutation encryption image of P, C' is a diffusion encryption image of S', and C is a ciphertext image corresponding to the plaintext image P; the detailed encryption principles of CIEA-HCNN are presented as follows:

(1) Choose secret key parameters. CIEA-HCNN includes eight secret key parameters $x_1', x_2', \mu_1, \mu_2, m_0, m_r, m_g, m_b$, where x_1', x_2', μ_1, μ_2 are initial values and control parameters of Staged composite chaotic map and m_0, m_r, m_g, m_b are iterative numbers of Staged composite chaotic map.

(2) Generate chaotic sequences X, Y, Z, W. From equation (4), iterate Staged composite chaotic map m_0 times; one gets the chaotic sequence $X = \{x_1, x_2, \ldots, x_{m_0}\}$. Simultaneously, one obtains three chaotic sequences $Y = \{y_1, y_2, \ldots, y_{m_r}\}$, $Z = \{z_1, z_2, \ldots, z_{m_g}\}$, and $W = \{w_1, w_2, \ldots, w_{m_b}\}$. Actually, only four state variables $x_{m_0}, y_{m_r}, z_{m_g}, w_{m_b}$ are used in the following encryption process.

(3) Encrypt image by the chaotic encryption algorithm. The encryption object of CIEA-HCNN is a color plaintext image of size $M \times N \times 3$ denoted by $P = \{P(i,j,k)\}_{i=1,j=1,k=1}^{M,N,3}$, where $P \in \{0,1,\ldots,255\}$ [14], and hereinafter referred to as the plaintext image. The ciphertext image of P is represented by $C = \{C(i,j,k)\}_{i=1,j=1,k=1}^{M,N,3}$, where $C \in \{0,1,\ldots,255\}$. Besides, the plaintext image P has Red, Green, and Blue channels; for the sake of convenience of

expression, one simplifies the three channels to R, G, and B channels. The steps for CIEA-HCNN are shown as follows:

Step 1: Permutation Encryption. First, F transform x_{m_0} of the chaotic sequence X; one obtains control parameters α and β of Arnold cat map, given by

$$
\begin{cases} \alpha = \text{floor}\left(\text{mod}\left(x_{m_0} \times 2^{24}, N\right)\right), \\ \beta = \text{floor}\left(\text{mod}\left(\text{mod}\left(x_{m_0} \times 2^{48}, 2^{24}\right), N\right)\right), \end{cases}
\tag{5}
$$

where N is the width of the plaintext image P, mod represents a modular operation, and floor rounds a real number to the nearest integer.

In Figure 1, scramble R, G, B channels of P by utilizing Arnold cat map, respectively, and get the corresponding temporary permutation encryption image denoted by $S = \{S(i,j,k)\}_{i=1,j=1,k=1}^{M,N,3}$; the iterative equation of Arnold cat map is defined as

$$
\begin{pmatrix} x_{n+1} \\ y_{n+1} \end{pmatrix} = \begin{bmatrix} 1 & \alpha \\ \beta & \alpha\beta + 1 \end{bmatrix} \begin{pmatrix} x_{n+1} \\ y_{n+1} \end{pmatrix} \text{mod} N,
\tag{6}
$$

where (x_n, y_n) and (x_{n+1}, y_{n+1}) represent the before and after coordinate of permutation encryption through using Arnold cat map; moreover, the default number of Arnold cat map iterations is set as 1 [14]. According to Figure 1 and equation (6), one gets

$$
T = \begin{bmatrix} 1 & \alpha \\ \beta & \alpha\beta + 1 \end{bmatrix} = \begin{bmatrix} a & b \\ \delta & \varepsilon \end{bmatrix}.
\tag{7}
$$

Finally, scan R, G, B three channels of S in a raster order from left to right and up to down; one obtains the permutation encryption image $S\prime = \{S'(k,l)\}_{k=1,l=1}^{3,MN}$ with the size of $3 \times MN$, given by

$$
S\prime(k,l) = \begin{bmatrix} S'(1,1) & S'(1,2) & \cdots & S'(1,MN) \\ S'(2,1) & S'(2,2) & \cdots & S'(2,MN) \\ S'(3,1) & S'(3,2) & \cdots & S'(3,MN) \end{bmatrix}.
\tag{8}
$$

Step 2: Diffusion Encryption. First, set the chaotic sequences y_{m_r}, z_{m_g}, and w_{m_b} as the initial values of Hopfield chaotic neural network, substitute them into equations (1)-(2), iterate MN times, and get three sequences defined by $H_1(l)_{l=1}^{MN}, H_2(l)_{l=1}^{MN}, H_3(l)_{l=1}^{MN}$. Let $H = \{H(k,l)\}_{k=1,l=1}^{3,MN}$ be equal to $\{H_1(l)_{l=1}^{MN}, H_2(l)_{l=1}^{MN}, H_3(l)_{l=1}^{MN}\}$, such that

$$
H(k,l) = \begin{bmatrix} H(1,1) & H(1,2) & \cdots & H(1,MN) \\ H(2,1) & H(2,2) & \cdots & H(2,MN) \\ H(3,1) & H(3,2) & \cdots & H(3,MN) \end{bmatrix}.
\tag{9}
$$
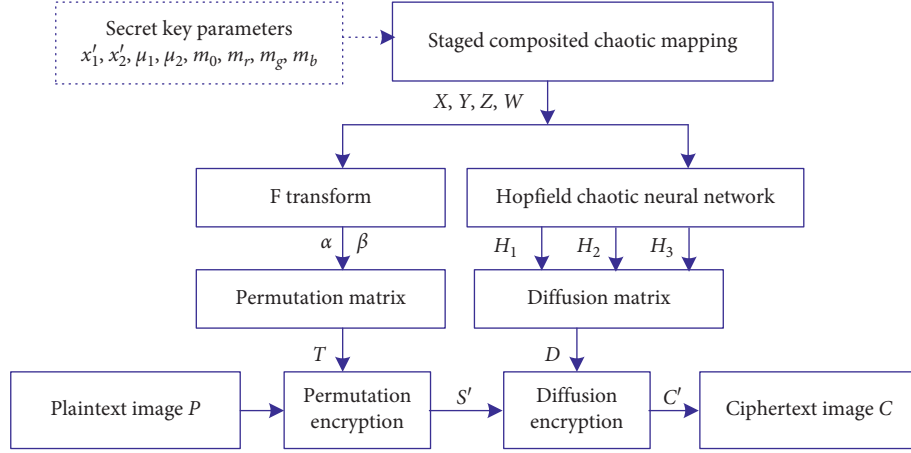
FIGURE 1: Block diagram of CIEA-HCNN.

Then, $H(k,l)$ is quantified to obtain the diffusion matrix $D = \{D(k,l)\}_{k=1,l=1}^{3,MN}$ given by

$$D(k,l) = \mathrm{mod}(\mathrm{round}((abs(H(k,l)) \\ -\mathrm{floor}(H(k,l))) \times 10^{14}), 256), \tag{10}$$

where round denotes a round-off function and abs is an absolute value function.

In Figure 1, perform bitwise XOR operation on the permutation encryption image $S\prime$ by utilizing diffusion matrix D, and then get the temporary ciphertext image $C\prime = \{C'(k,l)\}_{k=1,l=1}^{3,MN}$ defined as

$$C'(k,l) = D(k,l) \oplus S'(k,l), \tag{11}$$

where notation $\oplus$ denotes a bitwise XOR operation. Finally, convert the temporary ciphertext image C' into the ciphertext image C.

(4) Decrypt image by using chaotic decryption algorithm. Decryption is the inverse process of encryption. First, convert the ciphertext image C into the temporary ciphertext image $C\prime$, then perform bitwise XOR operation by using $C\prime$ and the diffusion matrix D, and get the permutation encryption image $S\prime$. Second, transform $S\prime$ into the temporary permutation encryption image S. Finally, implement anti-scramble encryption for S by means of Arnold cat map, and further recover the plaintext image P from the encrypted image C.

3. Cryptanalysis

3.1. Preliminary Analysis of CIEA-HCNN. According to Kerckhoff's assumptions [32], one gets that the cryptosystem is open and its security depends solely on the secret keys rather than the cryptosystem itself; that is, the attacker knows everything about the cryptosystem except for the

secret keys. If the cryptosystem cannot resist various attacks, it is insecure. There are generally four common attack types for cryptanalysis given in Table 1 from the hardest to the easiest types. In Table 1, ciphertext-only attack is the hardest type, and chosen-ciphertext attack is the easiest type. The adversary reveals secret keys or the equivalent keys to break the cryptosystem by using the four common attack types listed in Table 1.

According to Figure 1, one obtains that CIEA-HCNN adopts permutation encryption-diffusion encryption structure. First, the diffusion encryption structure of CIEA-HCNN is too simple, and the diffusion matrix D is independent of plaintext image or ciphertext image. Therefore, one gets that CIEA-HCNN has the equivalent diffusion key. According to chosen-plaintext attack, the equivalent diffusion key can be broken by just selecting one pure plaintext image and the corresponding ciphertext image.

After cracking the equivalent diffusion key, CIEA-HCNN is simplified to a permutation-only encryption algorithm. In [28], it is pointed out that permutation-only encryption algorithm is insecure. For given secret key parameters and the size of the plaintext image, the generated chaotic sequences remain unchanged which are unrelated to the plaintext image and the corresponding ciphertext image; therefore, the values of α and β in Arnold cat map are fixed, and further the permutation matrix T also remains unchanged. Indeed, the permutation matrix T is the equivalent permutation key of CIEA-HCNN. An attacker can break the permutation-only encryption algorithm by using the permutation matrix T. In addition, the position $(0,0)$ is always mapped into itself in Arnold cat map.

According to the above analysis, one gets that the security performance of CIEA-HCNN depends only on the diffusion matrix D and the permutation matrix T; indeed, it means that the equivalent diffusion key and the equivalent permutation key exist in CIEA-HCNN. The adversary can reveal the equivalent keys by using chosen-plaintext attack and further successfully break the original encryption algorithm. Therefore, the problem of cracking secret key parameters $x_1', x_2', \mu_1, \mu_2, m_0, m_r, m_g, m_b$ in the original encryption algorithm can be solved by chosen-plaintext attack

TABLE 1: Four common attack types for cryptanalysis.

Attack types	Available resource
Ciphertext-only attack	The attacker only knows the ciphertext
Known-plaintext attack	The attacker knows any given plaintext and also knows the corresponding ciphertext
Chosen-plaintext attack	The attacker can obtain access to the encryption machinery, choose the plaintext that would be useful for deciphering, and also know the corresponding ciphertext
Chosen-ciphertext attack	The attacker can obtain access to the decryption machinery, choose the ciphertext that would be useful for deciphering, and also know the corresponding plaintext

and transforming it into solving the equivalent diffusion key and the equivalent permutation key. Moreover, according to Figure 1, one obtains the simplified block diagram of CIEA-HCNN, as shown in Figure 2. In Figure 2, ET denotes the equivalent permutation key, and ED represents the equivalent diffusion key.
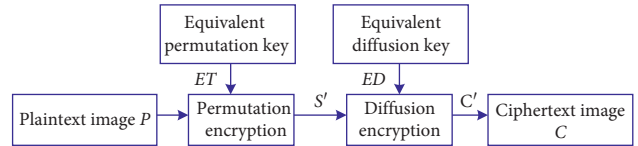
FIGURE 2: Simplified block diagram of CIEA-HCNN.

3.2. Cracking CIEA-HCNN by Using Chosen-Plaintext Attack.
The basic method of cracking the permutation encryption and the diffusion encryption structure shown in Figure 2 is that, according to chosen-plaintext attack, one adopts divide-and-conquer strategy to separate the permutation encryption from the diffusion encryption through choosing the plaintext that would be useful for breaking, on this basis, and further deciphering the equivalent permutation key ET and the equivalent diffusion key ED, respectively. The detailed procedures of cracking the equivalent permutation key ET and the equivalent diffusion key ED are presented as follows.

3.2.1. Deciphering the Equivalent Diffusion Key ED.
According to chosen-plaintext attack, choose a full zero image denoted by $P_1 = \{P_1(i, j, k)\}_{i=1, j=1, k=1}^{M,N,3}$, and get the corresponding ciphertext image defined as $C_1 = \{C_1(i, j, k)\}_{i=1, j=1, k=1}^{M,N,3}$. Next, using the obtained P_1 and C_1 as known conditions, one further gets the corresponding equivalent diffusion key ED.

The specific approaches for cracking the equivalent diffusion key ED are given as follows.

Step 1. Choose a full zero plaintext image as P_1, according to chosen-plaintext attack, and get its corresponding ciphertext image as C_1. From Figure 1, one obtains the temporary ciphertext image $C_1' = \{C_1'(k, l)\}_{k=1, l=1}^{3,MN}$ corresponding to C_1.

Step 2. According to equation (11) and Figure 2, one has

$$C_1'(k, l) = S_1'(k, l) \oplus ED(k, l). \tag{12}$$

Since all pixels of P_1 are zero, after performing the permutation encryption operation for P_1, $\{S_1(i, j, k)\}_{i=1, j=1, k=1}^{M,N,3} = \{S_1'(k, l)\}_{k=1, l=1}^{3,MN} = 0$ holds.

Step 3. From equations (11)-(12) with $\{S_1'(k, l)\}_{k=1, l=1}^{3,MN} = 0$, one obtains the equivalent diffusion key ED defined as

$$ED(k, l) = C_1'(k, l). \tag{13}$$

3.2.2. Deciphering the Equivalent Permutation Key ET.
After breaking the equivalent diffusion key ED, the original permutation encryption-diffusion encryption structure is simplified to permutation-only encryption structure. Besides, since the original image chaotic encryption algorithm adopts the same permutation matrix to the three channels of the plaintext image, the work of deciphering the equivalent permutation key ET sets the R channel of the plaintext image as an example as follows. First, choose a plaintext image defined as $P_2 = \{P_2(i, j, k)\}_{i=1, j=1, k=1}^{M,N,3}$, and suppose the pixels of coordinates (i_1, j_1) and (i_2, j_2) in R channel are $P_2(i_1, j_1, 1) = \zeta \neq 0$ and $P_2(i_2, j_2, 1) = \lambda \neq 0$, respectively. Moreover, $(i_1, j_1) \neq (1, 1)$, $(i_2, j_2) \neq (1, 1)$ and $\zeta \neq \lambda$, others are full zero, and let all pixels of G channel and B channel be full zero. One obtains the corresponding ciphertext image described by $C_2 = \{C_2(i, j, k)\}_{i=1, j=1, k=1}^{M,N,3}$. Then using the obtained P_2 and C_2 as known conditions, one further gets the corresponding equivalent permutation key ET. Note that the equivalent permutation key ET is not affected by the number of Arnold cat map iterations.

The specific steps for cracking the equivalent permutation key ET are presented as follows.

Step 1. According to chosen-plaintext attack, choose one plaintext image as P_2, and get its ciphertext image defined as C_2. Then, the temporary ciphertext image as $C_2' = \{C_2'(k, l)\}_{k=1, l=1}^{3,MN}$ is obtained by using the ciphertext image C_2.

Step 2. Substitute $\{C_2'(k,l)\}_{k=1,l=1}^{3,MN}$ and $\{ED(k,l)\}_{k=1,l=1}^{3,MN}$ with equation (11); the permutation encryption image denoted as $S_2' = \{S_2'(k,l)\}_{k=1,l=1}^{3,MN}$ is described by

$$S_2'(k,l) = ED(k,l) \oplus C_2'(k,l). \tag{14}$$

Step 3. Convert the permutation encryption image S_2' of size $3 \times MN$ into the temporary permutation encryption image $S_2 = \{S_2(i,j,k)\}_{i=1,j=1,k=1}^{M,N,3}$ of size $M \times N \times 3$, and then compare $S_2(:,:,1)$ with $P_2(:,:,1)$ one by one; one gets

$$\begin{cases} P_2(i_1,j_1,1) = S_2(m_1,n_1,1) = \zeta, \\ P_2(i_2,j_2,1) = S_2(m_2,n_2,1) = \lambda. \end{cases} \tag{15}$$

According to equations (6)-(7), one obtains

$$\begin{bmatrix} m_1 - 1 \\ n_1 - 1 \end{bmatrix} = ET \begin{bmatrix} i_1 - 1 \\ j_1 - 1 \end{bmatrix} \bmod N = \begin{bmatrix} a & b \\ \delta & \varepsilon \end{bmatrix} \begin{bmatrix} i_1 - 1 \\ j_1 - 1 \end{bmatrix} \bmod N, \tag{16}$$

$$\begin{bmatrix} m_2 - 1 \\ n_2 - 1 \end{bmatrix} = ET \begin{bmatrix} i_2 - 1 \\ j_2 - 1 \end{bmatrix} \bmod N = \begin{bmatrix} a & b \\ \delta & \varepsilon \end{bmatrix} \begin{bmatrix} i_2 - 1 \\ j_2 - 1 \end{bmatrix} \bmod N. \tag{17}$$

From equations (16)-(17), one sees that (i_1, j_1), (i_2, j_2), (m_1, n_1), and (m_2, n_2) are given, and only the equivalent permutation key ET is unknown; therefore, one can solve the equation by combining equations (16)-(17), defined as

$$\begin{cases} a = \left[\dfrac{(m_1 - 1) - b \times (j_1 - 1)}{(i_1 - 1)} \right] \bmod N, \\[3mm] b = \left[\dfrac{(m_2 - 1) \times (i_1 - 1) - (m_1 - 1) \times (i_2 - 1)}{(j_2 - 1) \times (i_1 - 1) - (j_1 - 1) \times (i_2 - 1)} \right] \bmod N, \\[3mm] \delta = \left[\dfrac{(n_1 - 1) - \varepsilon \times (j_1 - 1)}{(i_1 - 1)} \right] \bmod N, \\[3mm] \varepsilon = \left[\dfrac{(n_2 - 1) \times (i_1 - 1) - (n_1 - 1) \times (i_2 - 1)}{(j_2 - 1) \times (i_1 - 1) - (j_1 - 1) \times (i_2 - 1)} \right] \bmod N. \end{cases} \tag{18}$$

According to equation (18), one obtains the equivalent permutation key ET by adopting one special plaintext image and the corresponding ciphertext image.

For the sake of understanding the above analysis, take the plaintext image $P_3 = \{P_3(i,j,k)\}_{i=1,j=1,k=1}^{4,4,3}$ of size $4 \times 4 \times 3$ as an example, given by

$$P_3(:,:,1) = \begin{bmatrix} 0 & 0 & 0 & 0 \\ 0 & 1 & 2 & 0 \\ 0 & 0 & 0 & 0 \\ 0 & 0 & 0 & 0 \end{bmatrix},$$

$$P_3(:,:,2) = \begin{bmatrix} 0 & 0 & 0 & 0 \\ 0 & 0 & 0 & 0 \\ 0 & 0 & 0 & 0 \\ 0 & 0 & 0 & 0 \end{bmatrix}, \tag{19}$$

$$P_3(:,:,3) = \begin{bmatrix} 0 & 0 & 0 & 0 \\ 0 & 0 & 0 & 0 \\ 0 & 0 & 0 & 0 \\ 0 & 0 & 0 & 0 \end{bmatrix}.$$

After performing the permutation-only encryption on P_3, one gets the temporary permutation encryption image denoted by $S_3 = \{S_3(i,j,k)\}_{i=1,j=1,k=1}^{4,4,3}$, such that

$$S_3(:,:,1) = \begin{bmatrix} 0 & 0 & 0 & 0 \\ 0 & 2 & 0 & 0 \\ 0 & 0 & 0 & 0 \\ 0 & 0 & 1 & 0 \end{bmatrix},$$

$$S_3(:,:,2) = \begin{bmatrix} 0 & 0 & 0 & 0 \\ 0 & 0 & 0 & 0 \\ 0 & 0 & 0 & 0 \\ 0 & 0 & 0 & 0 \end{bmatrix}, \tag{20}$$

$$S_3(:,:,3) = \begin{bmatrix} 0 & 0 & 0 & 0 \\ 0 & 0 & 0 & 0 \\ 0 & 0 & 0 & 0 \\ 0 & 0 & 0 & 0 \end{bmatrix}.$$

According to equations (19)-(20), one has

$$\begin{cases} (i_1, j_1) = (2, 2), \\ (i_2, j_2) = (2, 3), \\ (m_1, n_1) = (4, 3), \\ (m_2, n_2) = (2, 2). \end{cases} \tag{21}$$

Then substituting equation (21) into equation (18), according to $N = 4$, one obtains $a = 1, b = 2, \delta = 3, \varepsilon = 3$ and further gets the equivalent permutation key ET, defined as

$$ET = \begin{bmatrix} 1 & 2 \\ 3 & 3 \end{bmatrix} \bmod 4. \tag{22}$$

3.2.3. Recover the Plaintext Image by Using the Equivalent Diffusion Key ED and the Equivalent Permutation Key ET. First, convert the ciphertext image C into the temporary ciphertext image $C\prime$. According to equation (11) and the equivalent diffusion key ED, the permutation encryption image denoted by $S\prime$ can be obtained from the temporary ciphertext image $C\prime$. Second, convert the permutation encryption image $S\prime$ into the temporary permutation encryption image denoted by S. Finally, recover the plaintext image defined by P from the ciphertext image C by utilizing the equivalent permutation key ET.

According to the above security analysis, the process of cracking CIEA-HCNN by adopting chosen-plaintext attack is described in Algorithm 1.

4. The Numerical Simulation Experiments for Breaking CIEA-HCNN

In the numerical simulation experiments, color images Lena, Baboon, and Pepper are taken as three examples, where the size of the image is 512×512. The secret keys are set as $x_1' = 0.6$, $x_2' = 0.7$, $\mu_1 = 1.46$, $\mu_2 = 1.5$, $m_0 = 1740$, $m_r = 150$, $m_g = 160$, and $m_b = 180$. The numerical simulation experiments are operated under MATLAB R2017a running on desktop computer with Intel (R) Core (TM) i7-7700 CPU 3.6 GHz, 16 G memory RAM, and 1 TB hard drive; the operation system is Microsoft Windows 7.

4.1. The Experiments for Breaking CIEA-HCNN by Using Chosen-Plaintext Attack. First, according to the analysis in Section 3.2.1, choose a full zero plaintext image of size 512×512 denoted by P_1 and get the corresponding ciphertext image C_1, as shown in Figures 3(a) and 3(b). Based on equation (12), P_1 and C_1, one obtains the equivalent diffusion key ED given by

$$ED = \begin{bmatrix} 14 & 22 & 235 & 32 & 251... & 8 & 204 & 43 & 90 & 27 \\ 113 & 92 & 79 & 61 & 173... & 179 & 198 & 197 & 13 & 26 \\ 221 & 55 & 122 & 95 & 18... & 41 & 72 & 103 & 88 & 166 \end{bmatrix}_{3 \times 262144}. \tag{23}$$

Second, according to Section 3.2.1, construct a color image of size 512×512 defined by P_2, let the pixels of the coordinates $(2, 2)$ and $(2, 3)$ be 1 and 2 in the R channel of the plaintext image P_2, other pixels are set as 0, and all pixels of the G and B channels are defined as 0, as shown in Figure 4(a). According to chosen-plaintext attack, one can get the corresponding ciphertext image of P_2 denoted by C_2, as shown in Figure 4(b). Recover the permutation encryption image represented by S_2' from the ciphertext image C_2 by using the equivalent diffusion key ED, and then convert the permutation encryption image into the temporary permutation encryption image S_2, as shown in Figure 4(c). Based on equation (15), and comparing P_2 with S_2, one gets

$$\begin{cases} P_2(2, 2, 1) = S_2(m_1, n_1, 1) = 1, \\ P_2(2, 3, 1) = S_2(m_2, n_2, 1) = 2. \end{cases} \tag{24}$$

According to equations (16)-(18), one obtains the equivalent permutation key ET defined as

$$ET = \begin{bmatrix} 1 & 162 \\ 275 & 7 \end{bmatrix} \mod (512). \tag{25}$$

Finally, according to Section 3.2.3, the plaintext images of Lena, Baboon, and Pepper with the size of 512×512 are recovered by using the equivalent diffusion key ED and the equivalent permutation key ET; moreover, in order to verify that the recovered plaintext image is equal to the original plaintext image, performing the bitwise XOR operation on them, one gets a full zero image. The breaking results on CIEA-HCNN with RGB color Lena, Baboon, and Pepper are shown in Figure 5.

4.2. Attack Complexity Analysis. The attack complexity consists of time complexity and data complexity. On the aspect of time complexity, according to chosen-plaintext attack, the cracking time of CIEA-HCNN is 11.164 seconds for the color image with the size of 512×512, and the encryption time is 5.813 seconds. Moreover, on the aspect of data complexity, given the same size of color image, the data complexity of breaking CIEA-HCNN is $O(1)$. Therefore, the experimental results verify that the attack method is both effective and efficient, meanwhile having lower attack complexity.

4.3. Suggestions for Improvement. According to the security defects of CIEA-HCNN, the suggestions for improvement are given as follows:

(1) In the permutation encryption structure, one can construct the combination of parameters of Arnold cat map and the characters of plaintext image such as all pixels sum and average and hash value of the plaintext information. One adopts multiple-round permutation encryption based on the encryption efficiency. Simultaneously, one suggests that using different permutation matrix performs the scrambling operation on the three R, G, B channels of the color image, respectively. Moreover, after the permutation encryption, exchange the pixel of coordinate $(0, 0)$ to the other random pixel to improve the security of the original permutation encryption.

(2) In the diffusion encryption structure, one could add some nonlinear diffusion encryption structure and ciphertext feedback mechanism to enhance the combination of plaintext, keys, and ciphertext and further promote the security of the original encryption algorithm.

(3) One suggests that multiple-round encryption algorithm is proposed to improve the security based on the higher efficiency.

Input: P_1, P_2, C
Output: Recover the plaintext image P from the given ciphertext image C
(1) $C_1 = Encryption(P_1)$
(2) According to equation (11), $ED = C_1$
(3) $C_2 = Encryption(P_2)$
(4) According to equation (11) and ED, $S_2' = bitxor(C_2, ED)$
(5) $S_2 \leftarrow S_2'$
(6) for $i = 1$ to M do
(7)   for $j = 1$ to N do
(8)   for $k = 1$ to 1 do
(9) $[m_1, n_1] = find(S_2(:, :, 1) == 1)$
(10) $[m_2, n_2] = find(S_2(:, :, 1) == 2)$
(11)   end for
(12)   end for
(13) end for
(14) $b = \mod((m_2 - m_1), N); a = \mod((m_1 - 1 - b), N)$
(15) $\varepsilon = \mod((n_2 - n_1), N); \delta = \mod((n_1 - 1 - \varepsilon), N)$
(16) $ET = [a \ b; \ \delta \ \varepsilon]$
(17) $S' = bitxor(C\prime, ED); S \leftarrow S'$
(18) $P = (ET)^{-1}(S)$
(19) return P

ALGORITHM 1: Cracking CIEA-HCNN by using chosen-plaintext attack.

(a)   (b)
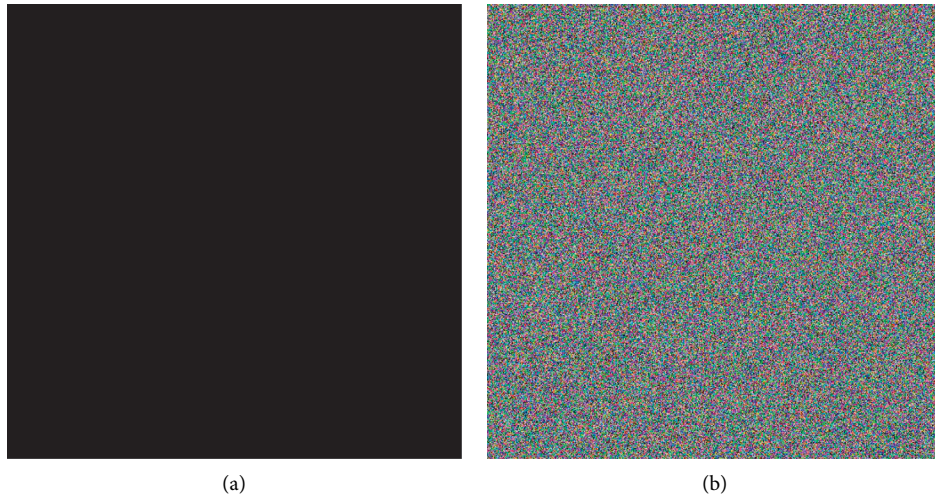
FIGURE 3: Zero plaintext image P_1 and its corresponding ciphertext image C_1. (a) Zero plaintext image P_1. (b) Its corresponding ciphertext image C_1.

(a)   (b)   (c)
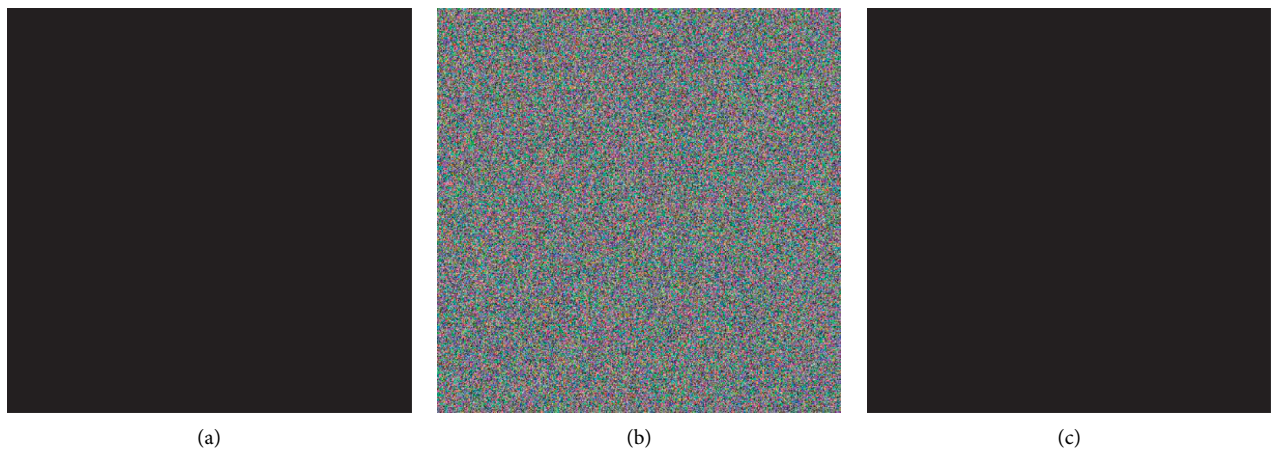
FIGURE 4: Plaintext image P_2, the corresponding ciphertext image C_2, and the temporary permutation encryption image S_2. (a) Plaintext image P_2. (b) The corresponding ciphertext image C_2. (c) The temporary permutation encryption image S_2.
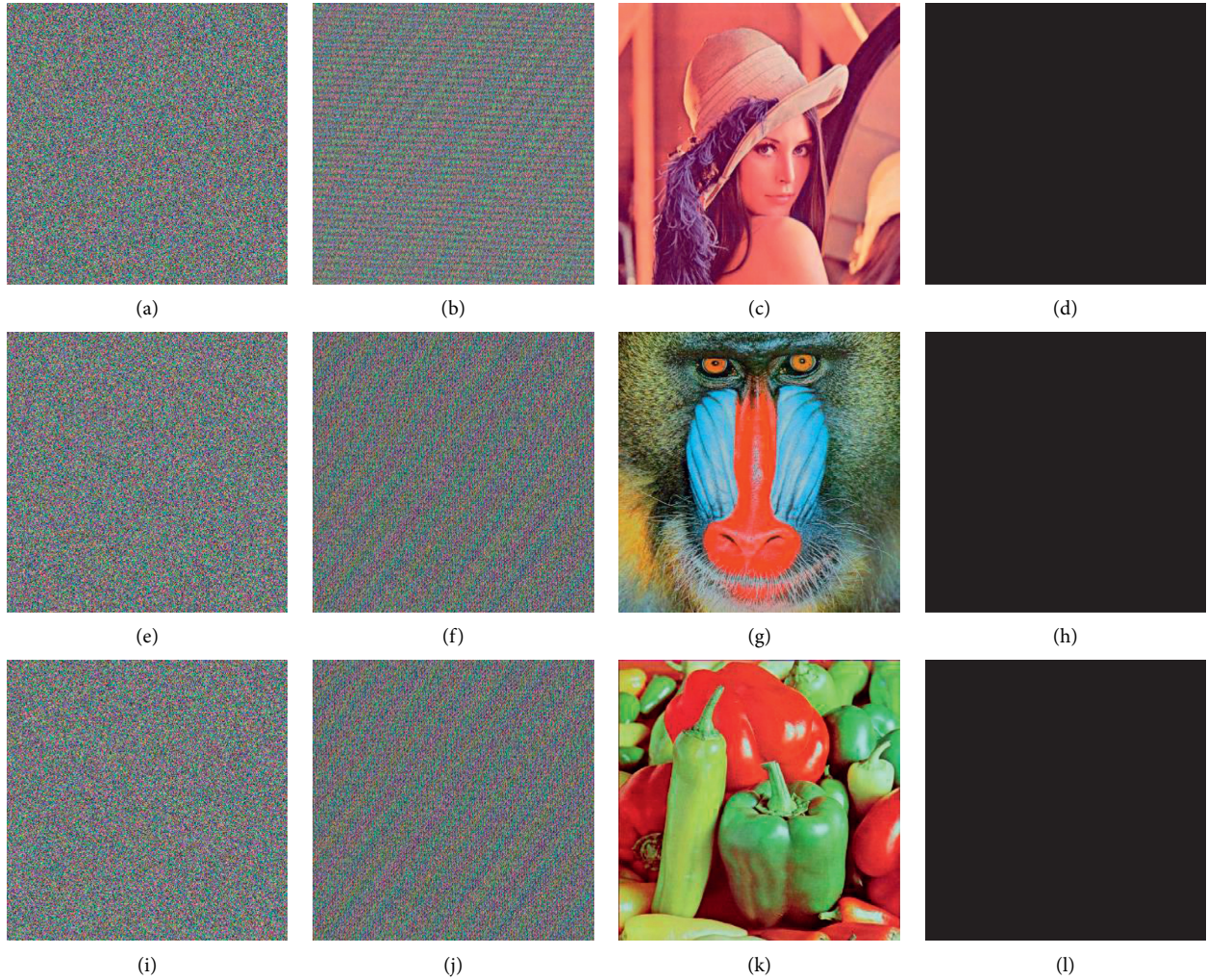
FIGURE 5: The breaking results on CIEA-HCNN with RGB color Lena, Baboon, and Pepper. (a) Lena ciphertext image. (b) Recovered permutation image of Lena. (c) Recovered plaintext image of Lena. (d) Difference image of Lena. (e) Baboon ciphertext image. (f) Recovered permutation image of Baboon. (g) Recovered plaintext image of Baboon. (h) Difference image of Baboon. (i) Pepper ciphertext image. (j) Recovered permutation image of Pepper. (k) Recovered plaintext image of Pepper. (l) Difference image of Pepper.

5. Conclusions

In this paper, the security analysis of a color image encryption algorithm based on Hopfield chaotic neural network called CIEA-HCNN is given. CIEA-HCNN adopts permutation encryption-diffusion encryption structure; from the view of cryptanalysis, it has the equivalent keys due to the inherent defects. Therefore, one can obtain the equivalent permutation key and the equivalent diffusion key by utilizing the chosen-plaintext attack and further crack CIEA-HCNN. Theoretical analysis and numerical simulation experiment results verify the effectiveness of the deciphering method; as for the color image of size $M \times N$, the data complexity is $O(1)$. Finally, some suggestions are proposed to improve the security of chaotic encryption algorithm. The reported results may help the designers of chaotic cryptography realize the importance of the essential structure of a color image encryption algorithm based on Hopfield chaotic neural network.

Data Availability

The data and code used to support the findings of this study are available from the corresponding author upon request.

Conflicts of Interest

The authors declare that there are no conflicts of interest regarding the publication of this paper.

Acknowledgments

References

[1] A. Shafique and J. Shahid, "Novel image encryption crypto-system based on binary bit planes extraction and multiple chaotic maps," *The European Physical Journal Plus*, vol. 133, no. 8, pp. 1–16, 2018.

[2] M. Xu and Z. Tian, "A novel image cipher based on 3D bit matrix and Latin cubes," *Information Sciences*, vol. 478, no. 4, pp. 1–14, 2019.

[3] Q. Gan, S. Yu, C. Li, J. Lü, Z. Lin, and P. Chen, "Design and ARM-embedded implementation of a chaotic map-based multicast scheme for multiuser speech wireless communication," *International Journal of Circuit Theory and Applications*, vol. 45, no. 11, pp. 1849–1872, 2017.

[4] Z. Lin, S. Yu, J. Lu, S. Cai, and G. Chen, "Design and ARM-embedded implementation of a chaotic map-based real-time secure video communication system," *IEEE Transactions on Circuits and Systems for Video Technology*, vol. 25, no. 7, pp. 1203–1216, 2015.

[5] W. Zhang, H. Yu, Y.-l. Zhao, and Z.-l. Zhu, "Image encryption based on three-dimensional bit matrix permutation," *Signal Processing*, vol. 118, no. 1, pp. 36–50, 2016.

[6] X. Li, Z. Xie, J. Wu, and T. Li, "Image encryption based on dynamic filtering and bit cuboid operations," *Complexity*, vol. 2019, Article ID 7485621, 16 pages, 2019.

[7] Z. Hua, Y. Zhou, C.-M. Pun, and C. L. P. Chen, "2D sine logistic modulation map for image encryption," *Information Sciences*, vol. 297, pp. 80–94, 2015.

[8] C. Zhu, "A novel image encryption scheme based on improved hyperchaotic sequences," *Optics Communications*, vol. 285, no. 1, pp. 29–37, 2012.

[9] B. Norouzi, S. Mirzakuchaki, S. M. Seyedzadeh, and M. R. Mosavi, "A simple, sensitive and secure image encryption algorithm based on hyper-chaotic system with only one round diffusion process," *Multimedia Tools and Applications*, vol. 71, no. 3, pp. 1469–1497, 2014.

[10] C. Fu, B.-b. Lin, Y.-s. Miao, X. Liu, and J.-j. Chen, "A novel chaos-based bit-level permutation scheme for digital image encryption," *Optics Communications*, vol. 284, no. 23, pp. 5415–5423, 2011.

[11] M. Zhou and C. Wang, "A novel image encryption scheme based on conservative hyperchaotic system and closed-loop diffusion between blocks," *Signal Processing*, vol. 171, p. 107484, 2020.

[12] G. Cheng, C. Wang, and H. Chen, "A novel color image encryption algorithm based on hyperchaotic system and permutation-diffusion architecture," *International Journal of Bifurcation and Chaos*, vol. 29, no. 9, p. 1950115, 2019.

[13] C. Xu, J. Sun, and C. Wang, "An image encryption algorithm based on random walk and hyperchaotic systems," *International Journal of Bifurcation and Chaos*, vol. 30, no. 4, p. 2050060, 2020.

[14] X.-Y. Wang and Z.-M. Li, "A color image encryption algorithm based on Hopfield chaotic neural network," *Optics and Lasers in Engineering*, vol. 115, no. 4, pp. 107–118, 2019.

[15] C. Song and Y. Qiao, "A novel image encryption algorithm based on DNA encoding and spatiotemporal chaos," *Entropy*, vol. 17, no. 10, pp. 6954–6968, 2015.

[16] X.-Y. Wang, Y.-Q. Zhang, and X.-M. Bao, "A novel chaotic image encryption scheme using DNA sequence operations," *Optics and Lasers in Engineering*, vol. 73, no. 5, pp. 53–61, 2015.

[17] J. Wu, X. Liao, and B. Yang, "Image encryption using 2D Hénon-Sine map and DNA approach," *Signal Processing*, vol. 153, no. 12, pp. 11–23, 2018.

[18] S. Wang, C. Wang, and C. Xu, "An image encryption algorithm based on a hidden attractor chaos system and the Knuth-Durstenfeld algorithm," *Optics and Lasers in Engineering*, vol. 128, p. 105995, 2020.

[19] F. Özkaynak, "Brief review on application of nonlinear dynamics in image encryption," *Nonlinear Dynamics*, vol. 92, no. 2, pp. 305–313, 2018.

[20] H. Wen and S. Yu, "Cryptanalysis of an image encryption cryptosystem based on binary bit planes extraction and multiple chaotic maps," *The European Physical Journal Plus*, vol. 134, no. 7, pp. 1–16, 2019.

[21] Z. Zhang and S. Yu, "On the security of a Latin-bit cube-based image chaotic encryption algorithm," *Entropy*, vol. 21, no. 9, p. 888, 2019.

[22] Z. Lin, G. Wang, X. Wang, S. Yu, and J. Lü, "Security performance analysis of a chaotic stream cipher," *Nonlinear Dynamics*, vol. 94, no. 2, pp. 1003–1017, 2018.

[23] Z. Lin, S. Yu, and X. Feng, "Cryptanalysis of a chaotic stream cipher and its improved scheme," *International Journal of Bifurcation and Chaos*, vol. 28, no. 7, Article ID 1850086, 2018.

[24] J. Wu, X. Liao, and B. Yang, "Cryptanalysis and enhancements of image encryption based on three-dimensional bit matrix permutation," *Signal Processing*, vol. 142, no. 1, pp. 292–300, 2018.

[25] W. Feng, Y. He, H. Li, and C. Li, "Cryptanalysis and improvement of the image encryption scheme based on 2D logistic-adjusted-sine map," *IEEE Access*, vol. 7, no. 1, pp. 12584–12597, 2019.

[26] C. Li, Y. Liu, T. Xie, and M. Z. Q. Chen, "Breaking a novel image encryption scheme based on improved hyperchaotic sequences," *Nonlinear Dynamics*, vol. 73, no. 3, pp. 2083–2089, 2013.

[27] L. Y. Zhang, Y. Liu, F. Pareschi et al., "On the security of a class of diffusion mechanisms for image encryption," *IEEE Transactions on Cybernetics*, vol. 48, no. 4, pp. 1163–1175, 2018.

[28] C. Li and K.-T. Lo, "Optimal quantitative cryptanalysis of permutation-only multimedia ciphers against plaintext attacks," *Signal Processing*, vol. 91, no. 4, pp. 949–954, 2011.

[29] H. Wen, S. Yu, and J. Lü, "Breaking an image encryption algorithm based on DNA encoding and spatiotemporal chaos," *Entropy*, vol. 21, no. 3, pp. 1–18, 2019.

[30] M. Li, M. Xu, J. Luo, and H. Fan, "Cryptanalysis of an image encryption using 2D henon-sine map and DNA approach," *IEEE Access*, vol. 7, no. 5, pp. 63336–63345, 2019.

[31] J. J. Hopfield, "Neural networks and physical systems with emergent collective computational abilities," *Proceedings of the National Academy of Sciences*, vol. 79, no. 8, pp. 2554–2558, 1982.

[32] D. R. Stinson, "Cryptography theory and practice," *Computers & Mathematics with Applications*, CRC Press, Boca Raton, FL, USA, 1995.

Research Article

A Novel Voltage-Controlled Tri-Valued Memristor and Its Application in Chaotic System

Xiaoyuan Wang [ID], Xue Zhang, and Meng Gao [ID]

School of Electronics and Information, Hangzhou Dianzi University, Hangzhou 310018, China

Correspondence should be addressed to Xiaoyuan Wang; youyuan-0213@163.com and Meng Gao; gaomengso@qq.com

Memristor is a kind of passive nonlinear element, which is widely used in nonlinear systems, especially chaotic systems, because of its nanometer size, nonvolatile property, and good nonlinear characteristics. Compared with general chaotic systems, chaotic systems based on memristors have richer dynamic characteristics. However, the current research mainly focuses on the binary and continuous chaotic systems based on memristors, and studies on the tri-valued and multi-valued memristor chaotic systems are relative scarce. For this reason, a mathematical model of tri-valued memristor is proposed, and the circuit characteristics of the model are studied. Furthermore, based on this model, a new chaotic system is designed and analyzed. This innovation enriches the types of chaotic systems and lays the foundation for the application of tri-valued and multi-valued memristors in nonlinear systems.

1. Introduction

In 1971, Chua postulated the concept of memristor according to the mathematical relationship between charge q and flux φ $(d\varphi = M\, dq)$ and called it the fourth basic circuit element [1]. In 2008, the Hewlett-Packard Lab realized a practical memristor device, which set off an upsurge of research studies on memristor models and their applications [2]. Memristors are widely used in microelectronics, neural network, nonvolatile storage, application and simulation of spontaneous behavior, hard switching, and dynamic storage [3–5]. One of the most typical applications of memristor is to construct a chaotic system. Compared with the general chaotic systems, chaotic oscillators constructed with memristors have more complex and special dynamic characteristics, wider range of parameters, and are extremely sensitive to the initial values. Especially, when appropriate parameters of the memristive chaotic system are given, hidden attractors and coexisting attractors will be behaved [6–8]. In recent years, chaotic oscillators based on memristors are widely used in confidential communication, file encryption, and artificial intelligence [9–11].

At present, the research on memristive chaotic systems mainly focuses on the binary and continuous memristors. In 2015, Ma introduced memristor into a four-wing chaotic system and finally obtained line equilibriums by adding a cross product term [12]. Kengne introduced a novel memristor-based oscillator, which was obtained from Shinriki's circuit by substituting the nonlinear positive conductance with a first-order memristive diode bridge [13]. In 2016, Wu used a memristor to replace the resistor in a parallel RC network and designed a simpler memristor-based Venturi oscillator [14]. By leading memristors into a multiwing chaotic system, Zhou obtained the multiwing hyperchaotic attractor and verified its dynamic characteristics by numerical simulation [15]. In 2017, Wang built a multiscroll chaotic system based on a multisegment memristor [16]. Hu designed two image encryption algorithms based on the chaotic sequences generated by a three-dimensional chaotic circuit based on memristor [17]. In 2018, Fonzin replaced the diode in the original TCMNL (Tamasevicius et al. (1997) oscillator) circuit with a memristor and implemented the hardware of the circuit [18]. In 2019, Min built a hyperchaotic system based on the memristor, which

has symmetric coexisting attractors and exhibits complex system characteristics. The correctness of the system was verified by hardware circuit experiments [19]. In 2020, Wang proposed a new hyperchaotic circuit by introducing memristor feedback into a simple Lorenz-like chaotic system. By further analyses, infinite equilibrium points, multiple stability, and symmetric coexisting attractors are found [20].

Nevertheless, compared with the continuous and binary memristors, tri-valued and multi-valued memristors have advantages of carrying more information. Constructing a chaotic system based on tri-valued memristors will generate new attractors, expand chaotic types, and broaden ideas for chaotic systems design. Consequently, it is of great significance and application value to propose a tri-valued memristor model and use the model to devise a chaotic system with good performance.

This paper is organized as follows. A specific mathematical model of a voltage-controlled tri-valued memristor is proposed and studied in Section 2. In Section 3, on the basis of the Lü system, a chaotic system with the proposed voltage-controlled tri-valued memristor is constructed. And, the basic characteristics of the system are analyzed in detail, including dissipative analysis, equilibrium point and stability analyses, and influences of system parameters and initial values on dynamic characteristics, etc. Conclusions are drawn in Section 4.

2. Voltage-Controlled Tri-Valued Memristor and its Characteristic Analysis

2.1. Mathematical Model of a Voltage-Controlled Tri-Valued Memristor. Different from binary and continuous memristors, this paper presents a mathematical model of a voltage-controlled tri-valued memristor, whose $q - \varphi$ relationship is given as follows:

$$q = -1.5 + 2.5\varphi + 4|\varphi + 1| - 2.5|\varphi - 1|. \tag{1}$$

According to the mathematical definition of memristors and the derivative of equation (1), the relationship between the memconductance and flux of the tri-valued memristor is given by

$$\frac{dq}{d\varphi} = G(\varphi) = [2.5 + 4\text{sgn}(\varphi + 1) - 2.5\text{sgn}(\varphi - 1)]$$

$$= \begin{cases} 1, & \varphi < -1, \\ 9, & -1 \leq \varphi \leq 1, \\ 4, & \varphi > 1, \end{cases} \tag{2}$$

where $G(\varphi)$ denotes memconductance, $\text{sgn}(x)$ represents the symbolic function; when $x > 0$, $\text{sgn}(x) = 1$ and when $x \leq 0$, $\text{sgn}(x) = -1$. The equation (2) shows that the magnitude of the flux φ affects the resistance state of the tri-valued memristor, which means that when the flux φ takes different values, the memristor is in three different memconductances. The flux-charge relationship described by

equation (1) and the flux- memconductance relationship described by equation (2) are shown in Figure 1.

Figure 1(a) indicates that the $q - \varphi$ relationship of the proposed memristor is described by a three-segment linear curve that passes through the origin, and each slope of the curve corresponds to the instantaneous conductance value of the memristor. Figure 1(b) intuitively depicts the effect of flux φ on the memconductance of the proposed memristor.

2.2. Circuit Characteristics of the Voltage-Controlled Tri-Valued Memristor. To study the circuit characteristics of the voltage-controlled tri-valued memristor, a sinusoidal signal $v(t) = v_0 \sin(2\pi f t)$ is applied to this model. According to the mathematical definition of the flux φ, the expression of $\varphi(t)$ can be shown as

$$\varphi(t) - \varphi(0) = \int_0^t v(\tau)d\tau = \int_0^t v_0 \sin(2\pi f \tau)d\tau$$

$$= -\frac{v_0}{2\pi f}\cos(2\pi f t) + \frac{v_0}{2\pi f}. \tag{3}$$

From equation (3), the $\varphi(t)$ can be written as

$$\varphi(t) = \varphi(0) - \frac{v_0}{2\pi f}\cos(2\pi f t) + \frac{v_0}{2\pi f}. \tag{4}$$

It can be seen from equation (4) that the magnitude of the flux φ is not only related to the initial value $\varphi(0)$ but also to the amplitude v_0 and the frequency f of the input voltage, and the change interval of $\varphi(t)$ can be obtained as $[\varphi(0), \varphi(0) + (v_0/\pi f)]$. Then, combined with equation (2), we can conclude the specific relationship between $\varphi(t)$ and the resistance state of the tri-valued memristor in Table 1, which manifests the initial value $\varphi(0)$, the amplitude v_0, and the frequency f of the input voltage are the main factors affecting the change of the resistance state of the proposed memristor. In Section 2.2.1, the influence of these three factors on the characteristics of the tri-valued memristor will be studied in detail.

2.2.1. Influence of Different $\varphi(0)$ Values on the Characteristics of Voltage-Controlled Tri-Valued Memristor. Table 1 indicates that, when the input amplitude v_0 and frequency f are fixed, the initial flux $\varphi(0)$ affects the resistance state of the tri-valued memristor. Let $v_0 = 2\,\text{V}$ and $f = 0.159\,\text{Hz}$, then $\varphi(t)$ belongs to the $[\varphi(0), \varphi(0) + 4]$ so when $\varphi(0)$ takes different values, the resistance states and hysteresis curves of the tri-valued memristor are different as shown in Figure 2, and these three curves correspond to Case3, Case5, and Case6 in Table 1. These results indicate that, when $\varphi(0)$ increases gradually, the tri-valued memristor changes from a tri-valued state to a binary state and finally to a single state.

2.2.2. Influence of Different v_0 Values on the Characteristics of Voltage-Controlled Tri-Valued Memristor. Let $\varphi(0) = -1.5$, $f = 0.159\,\text{Hz}$, then we can obtain the range of $\varphi(t)$ as $[-1.5,$
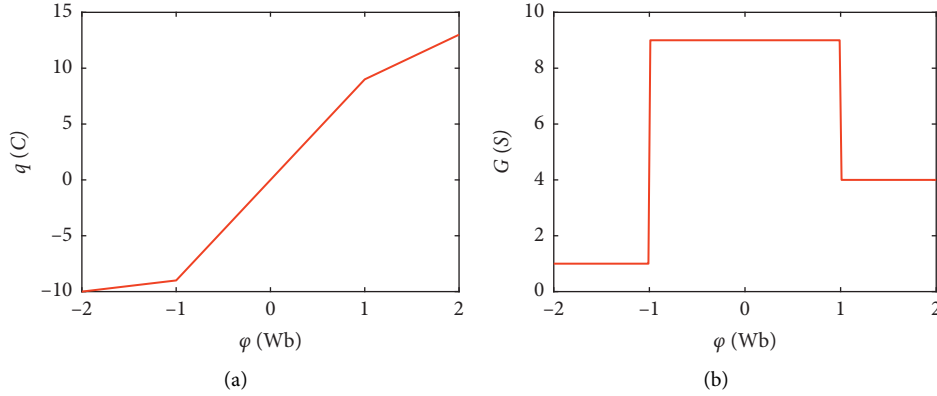
FIGURE 1: Characteristic curves of voltage-controlled tri-valued memristor model: (a) $\varphi - q$ curve; (b) $\varphi - G$ curve.

TABLE 1: Relationship between the number of resistance states of tri valued memristors and $\varphi(t)$.

Cases	Value range of $\varphi(t)$	Number of resistance states
Case1	$\varphi(0) < -1, \varphi(0) + v_0/\pi f < -1$	1
Case2	$\varphi(0) < -1, -1 < \varphi(0) + v_0/\pi f < 1$	2
Case3	$\varphi(0) < -1, \varphi(0) + v_0/\pi f > 1$	3
Case4	$-1 < \varphi(0) < 1, -1 < \varphi(0) + v_0/\pi f < 1$	1
Case5	$-1 < \varphi(0) < 1, \varphi(0) + v_0/\pi f > 1$	2
Case6	$\varphi(0) > 1, \varphi(0) + v_0/\pi f > 1$	1
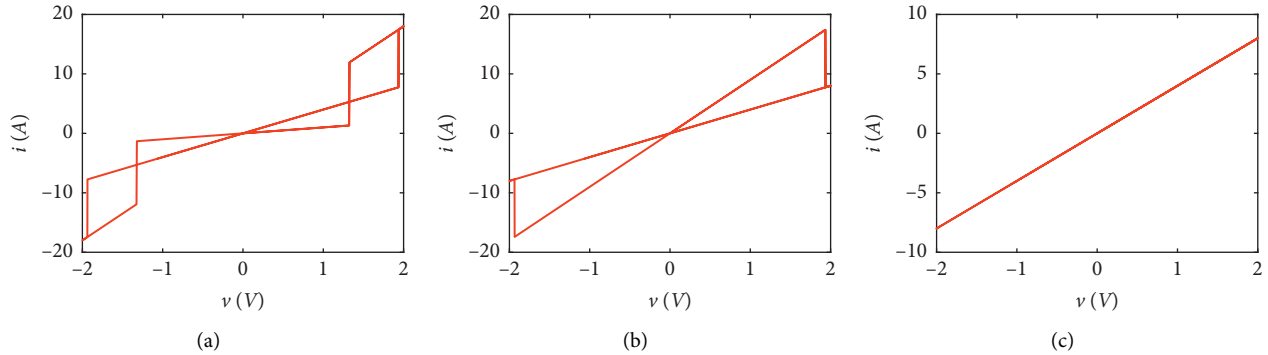
FIGURE 2: v-i curve of tri-valued memristor at different initial values: (a) $\varphi(0) = -1.5$ (Case3), (b) $\varphi(0) = -0.5$ (Case5), and (c) $\varphi(0) = 1.5$ (Case6).

$2v_0 - 1.5$]. Then, adjusting the input voltage amplitude v_0 to 0.2 V, 1.2 V, and 3 V, which corresponds to Case1, Case2, and Case3 in Table 1 respectively, we can finally obtain the v-i hysteresis curves with different shapes as shown in Figure 3.

The experimental results in Figure 3 illustrate that, when $\varphi(0)$ and f are definite, as the increase of v_0, the tri-valued memristor changes from single state to binary state and from binary state to tri-valued, the area of hysteresis curve also increases accordingly.

2.2.3. Influence of Different f Values on the Characteristics of Voltage-Controlled Tri-Valued Memristor. Let $\varphi(0) = -1.5$, $v_0 = 2$ V, then the range of $\varphi(t)$ is $[-1.5, 0.637/f - 1.5]$. When

the input voltage frequency f is adjusted to 0.1 Hz, 1 Hz, and 1.5 Hz (corresponding to Case3, Case2, and Case1 in Table 1, respectively), hysteresis curves at different input frequencies can be obtained, as shown in Figure 4, which shows that, when the frequency of the input signal increases, the tri-valued memristor changes from tri-valued memristor state to binary memristor state and finally to single memristor state, which is consistent with the theoretical derivation in Table 1.

2.2.4. Influence of Different Input Signals on the Characteristics of Tri-Valued Memristor. The above three influencing factors are all discussed under the condition of sinusoidal signal as the input. In this section, the circuit characteristics under different kinds of input signals are
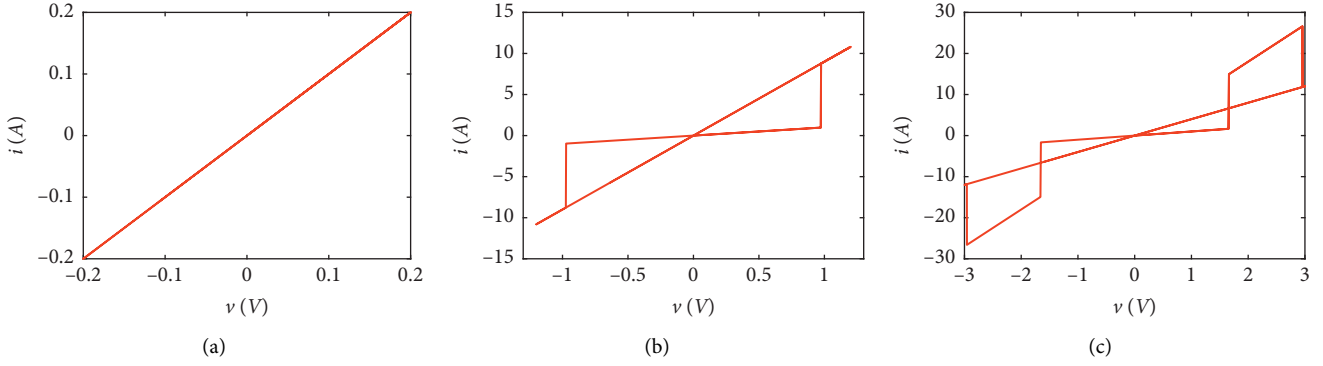
FIGURE 3: v-i curve of the tri-valued memristor at different amplitudes: (a) $v_0 = 0.2\,\text{V}$, (b) $v_0 = 1.2\,\text{V}$, and (c) $v_0 = 3\,\text{V}$.
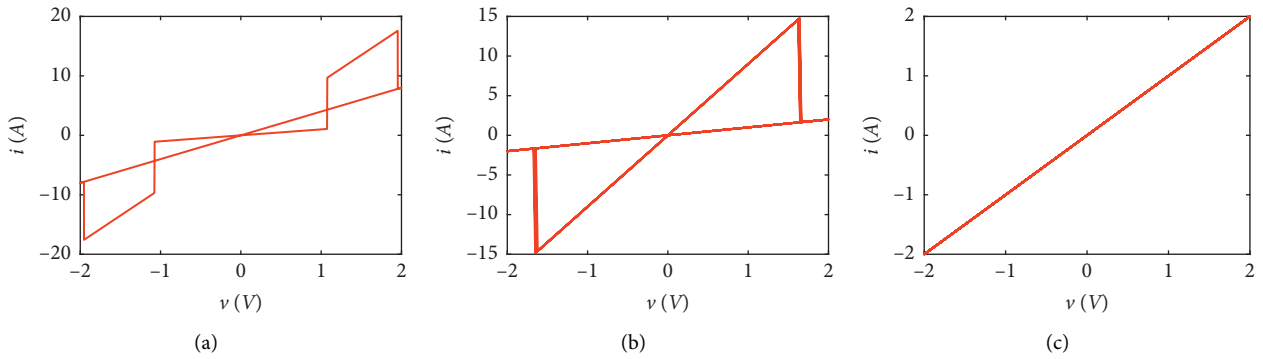
FIGURE 4: v-i curve of the tri-valued memristor at different frequencies: (a) $f = 0.1\,\text{Hz}$, (b) $f = 1\,\text{Hz}$, and (c) $f = 1.5\,\text{Hz}$.

studied. By applying sine, square, and triangular waves with amplitude of 4 V and frequency of 0.159 Hz to the tri-valued memristor model, respectively, and let $\varphi(0) = -1.5$, the hysteresis curves of the three input signals can be obtained, respectively, as shown in Figure 5.

From the above simulation results, it can be concluded that when the periodic signal of any zero DC component acts on the tri-valued memristor, its input and output responses can be represented as a hysteresis curve across the origin in the v-i plane, and all of these curves have three value characteristics.

3. Chaotic System Based on a Voltage-Controlled Tri-Valued Memristor

In 2001, Professor Lü proposed the famous Lü system [21], which can realize the conversion between Lorenz system [22] and Chen system [23]. In this paper, by adding a voltage-controlled tri-valued memristor model to the Lü system, a chaotic system based on a tri-valued memristor is generated as follows:

$$\begin{cases} \dot{x} = a(y - x), \\ \dot{y} = cy - xz, \\ \dot{z} = xy - bz - dG(w), \\ \dot{w} = z, \end{cases} \tag{5}$$

where a, b, c, and d are system parameters, all of them are real constants, and $G(w)$ represents the memconductance of the voltage-controlled tri-valued memristor shown in equation (2); here, the variable w is selected as a dimensionless mathematical representation of the flux φ. When the parameters are set as $a = 40$, $b = 5$, $c = 24.4$, and $d = 50$ and initial value $[x_0, y_0, z_0, w_0] = [0.01, 0.01, 0.01, 0.01]$, the phase diagrams of the system are as shown in Figure 6. The corresponding Lyapunov exponent values are calculated as $LE_1 = 4.2486$, $LE_2 = 0.0025$, $LE_3 = -0.004$, and $LE_4 = -24.8471$ by the Jacobi method. Figure 7 shows the Poincare mappings obtained when the cross planes are selected as $x = -10$ and $z = 50$, which are dense points with hierarchical structures. All the above results indicate that the system can be working as a chaotic oscillator under appropriate parameters and initial values.

3.1. Dissipative Analysis.
From the perspective of the dissipation of the chaotic system, to generate chaotic attractors, it is necessary for the system to be dissipative. So, we calculate the dissipativity of the system as follows:

$$\nabla V = \frac{\partial \dot{x}}{\partial x} + \frac{\partial \dot{y}}{\partial y} + \frac{\partial \dot{z}}{\partial z} + \frac{\partial \dot{w}}{\partial w} = -a + c - b. \tag{6}$$

Setting $a = 40$, $b = 5$, $c = 24.4$, and $d = 50$, we can get $\nabla V = -20.6 < 0$, implying that all trajectories are ultimately
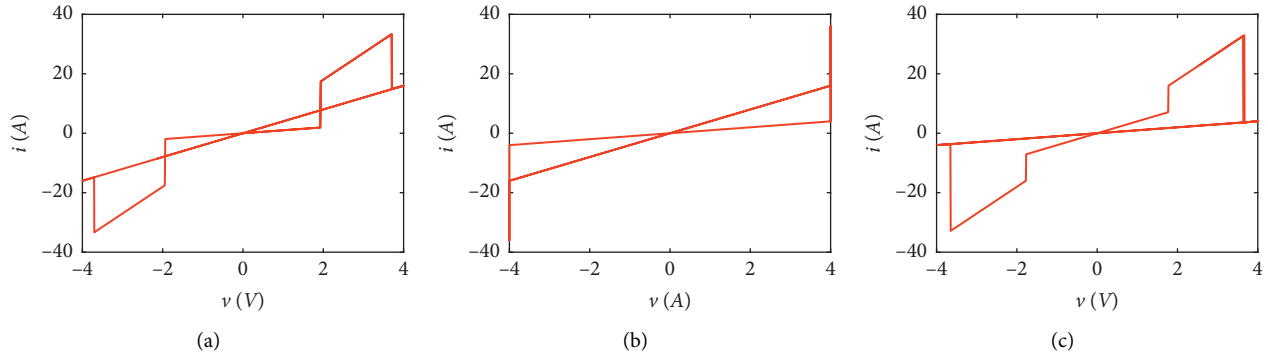
FIGURE 5: v-i curve of tri-valued memristor at different input signals: (a) sine wave, (b) square wave, and (c) triangular wave.
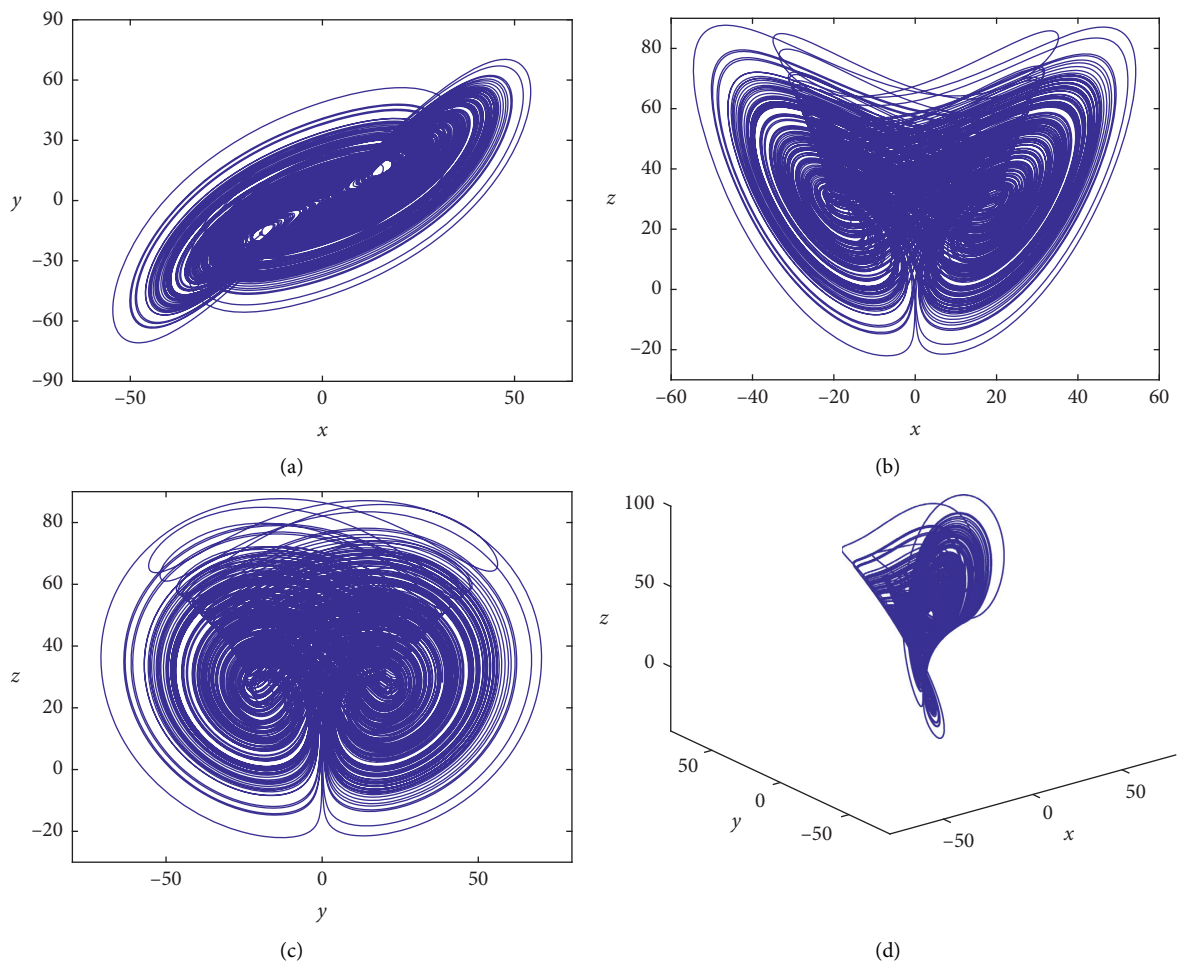
FIGURE 6: Phase diagrams of the system based on the tri-valued memristor: (a) x-y, (b) x-z, (c) y-z, and (d) x-y-z.

confined to a specific subset of zero volume and the system satisfies the conditions for chaos.

3.2. Equilibrium Point and Stability Analysis. Let $\dot{x} = \dot{y} = \dot{z} = \dot{w} = 0$ in equation (5), because all the system parameters a, b, c, and d are not nonzero, so we can obtain

$x = 0$, $y = 0$, $z = 0$, and $G(w) = 0$. But, as we know from the mathematical definition of the tri-valued memristor in equations (1) and (2), $G(w)$ is not equal to zero, so we can draw the conclusion that the chaotic system based on the novel tri-valued memristor has no equilibrium point, and the attractors generated by the system are hidden attractors.

(a)

(b)
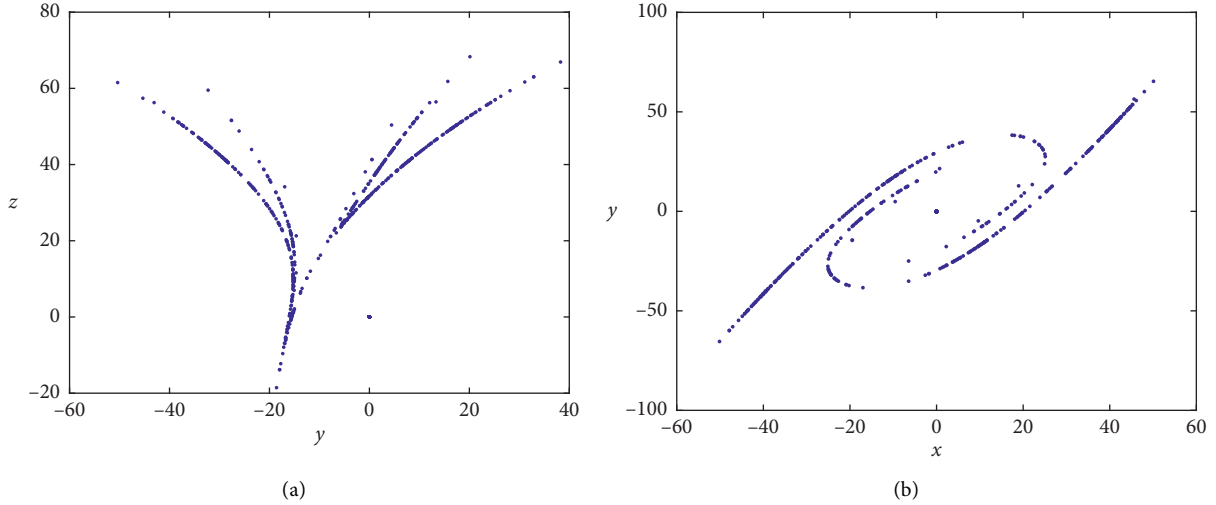
FIGURE 7: Poincare sections of the system: (a) $x = -10$ and (b) $z = 50$.
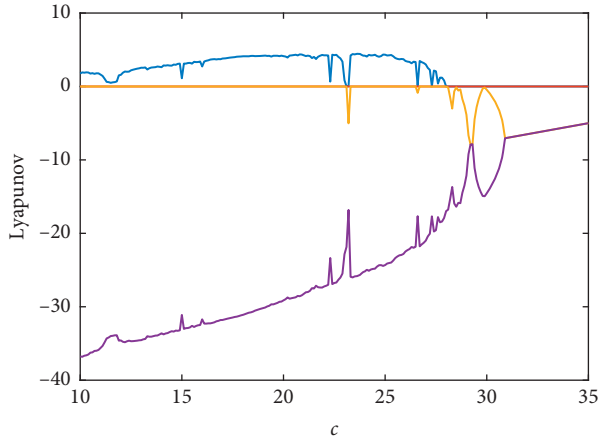
FIGURE 8: Lyapunov exponent spectrum corresponding to c.
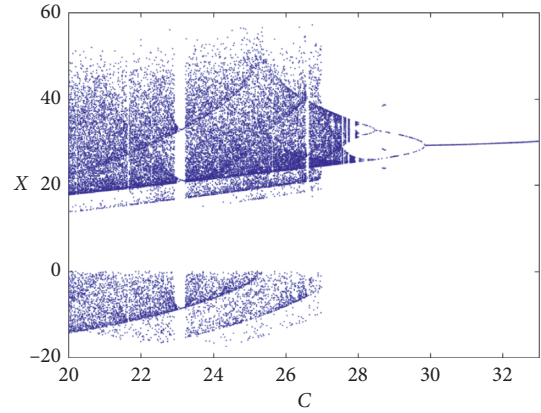
FIGURE 9: Bifurcation diagram corresponding to c.

3.3. Influence of System Parameters and Initial Values on Dynamic Characteristics

3.3.1. Influence of Parameter c on System Dynamics.
Given $[x_0, y_0, z_0, w_0] = [0.01, 0.01, 0.01, 0.01]$, $a = 40$, $b = 5$, and $d = 50$, the Lyapunov exponent spectrum and the bifurcation diagram of the system with respect to the parameter c can be obtained as shown in Figures 8 and 9. Table 2 presents the states of the system when the parameter c is in different intervals. And, Figure 10 shows the attractor phase diagrams of the system on the x-z plane when c takes different values.

3.3.2. Influence of the Initial Value on the System.
Chaos is extremely sensitive to initial values, and different initial values will eventually produce different trajectories. It is necessary to estimate the impact of initial conditions on system (5) for fixed sets of parameter values. The sensitivity of the sequences can be analyzed by measuring the correlation of the two sequences, which is defined by

TABLE 2: Under different system parameters c, the system is in different states.

Range of system parameter c	System state
[28.9, 29.2] [31, 33]	Period-1 state
[28.1, 28.5]	Period-2 state
[24, 27.5]	Chaotic state

$$Co = \frac{E[(X_t - \mu_X)(Y_t - \mu_Y)]}{\sigma_X \sigma_Y}, \tag{7}$$

where X_t and Y_t are two sequences generated by the system (5) with slight changes in its initial value, μ and σ are the mean value and standard deviation, and $E[\cdot]$ is the expectation function [24]. The closer the correlation value is to 0, the higher the sensitivity of the system is, and the greater the influence of the initial value on the system is.

In this paper, we slightly change each variable in the initial value $[x_0, y_0, z_0, w_0]$ with a 10^{-8} difference. Concretely taking the x_0 case as an example, let $x_0' = x_0 + 10^{-8}$, then we can obtain a different sequence pair (X_1, X_2) under initial values $[x_0, y_0, z_0, w_0] = [0.01, 0.01, 0.01, 0.01]$ and
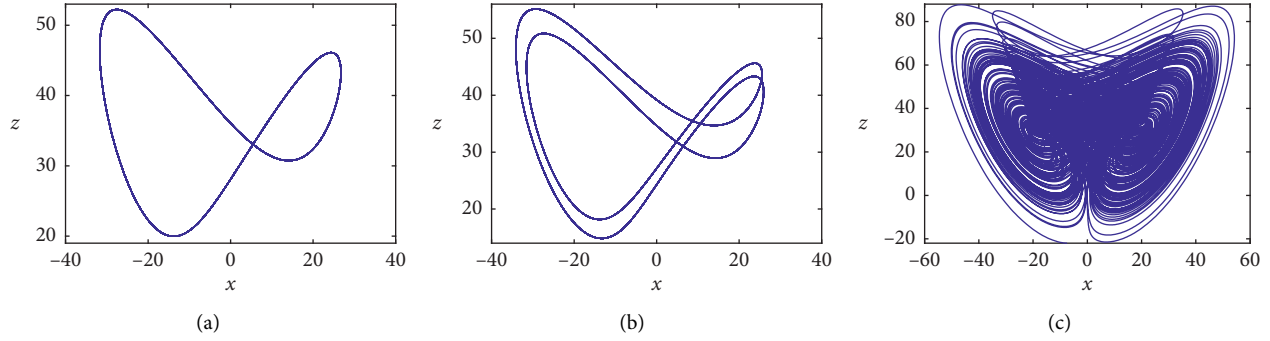
FIGURE 10: Influence of parameter c on the attractors of the x-z plane: (a) $c = 29$, period-1, (b) $c = 28.1$, period-2, and (c) $c = 24.4$, chaotic state.

TABLE 3: Correlation values of different sequences under tiny different initial values.

Initial values	Correlation of X_1, X_2	Correlation of Y_1, Y_2	Correlation of Z_1, Z_2
$x_0 - x_0'$ case	−0.0743	−0.0220	−0.0348
$y_0 - y_0'$ case	0.0084	−0.0002	−0.0799
$z_0 - z_0'$ case	0.0909	0.0475	0.0731
$w_0 - w_0'$ case	0.1278	0.1042	−0.1441
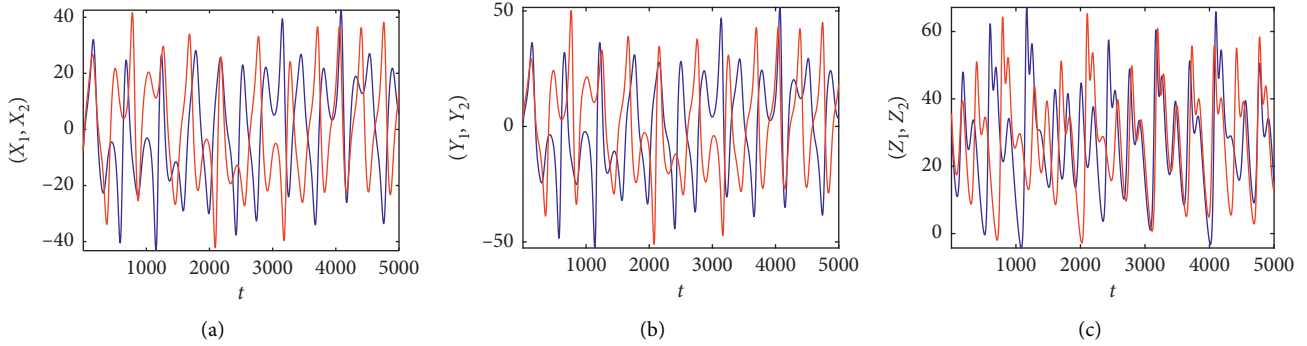
FIGURE 11: The timing diagrams of different sequence pairs of under $[x_0, y_0, z_0, w_0]$ and $[x_0', y_0, z_0, w_0]$: (a) (X_1, X_2), (b) (Y_1, Y_2), and (c) (Z_1, Z_2).

$[x_0', y_0, z_0, w_0] = [0.01 + 10^{-8}, 0.01, 0.01, 0.01]$. In the same way, we can get the other sequence pairs (Y_1, Y_2), (Z_1, Z_2), and (W_1, W_2) generated by applying a tiny change to y_0, z_0, and w_0 in the initial value. Table 3 shows the correlation results in each case. As can be seen, the correlation values of each sequence pair are extremely close to 0. To further illustrate the system's sensitivity to initial states, the timing diagrams of the sequence pairs (X_1, X_2), (Y_1, Y_2), and (Z_1, Z_2) under $x_0 - x_0'$ case are shown in Figure 11 as an example, which intuitively demonstrate the differences between the two output sequences generated by the system under tiny different initial conditions. So, we can conclude the system is extremely sensitive to the initial values.

4. Conclusion

In this paper, a voltage-controlled tri-valued memristor is proposed for the first time. To demonstrate its unique characteristics, the circuit characteristics, parameters properties, and influence factors on its properties have been studied in detail. And, then a novel chaotic system is successfully built based on the Lü system; by introducing the tri-valued memristor to the system, the maximum Lyapunov exponent has been improved. In addition, some conventional analyses like the influences of parameters and initial values on the system are considered. This study shows that the tri-valued memristor is suitable for building chaotic systems, which will enrich the types of nonlinear system, widen the application of tri-valued memristor, and lay a foundation for the subsequent application of tri-valued and multi-valued memristors.

Data Availability

The data used to support the findings of this study are available from the corresponding author upon request.

Conflicts of Interest

The authors declare that they have no conflicts of interest.

References

[1] L. O. Chua, "Memristor-the missing circuit element," *IEEE Transactions on Circuit Theory*, vol. 18, no. 5, pp. 507–519, 1971.

[2] D. B. Strukov, G. S. Snider, D. R. Stewart, and R. S. Williams, "The missing memristor found," *Nature*, vol. 453, no. 7191, pp. 80–83, 2008.

[3] K. D. Xu, Y. H. Zhang, L. Wang et al., "Two memristor SPICE models and their application in microwave devices," *IEEE Transactions on Nanotechnology*, vol. 13, no. 3, pp. 607–616, 2014.

[4] S. P. Adhikari, H. Kim, R. K. Budhathoki, C. Yang, and L. O. Chua, "A circuit-based learning architecture for multilayer neural networks with memristor bridge synapses," *IEEE Transactions on Circuits and Systems I Regular Papers*, vol. 62, no. 1, pp. 215–223, 2015.

[5] L. Guckert and E. E. Swartzlander, "Optimized memristor-based multipliers," *IEEE Transactions on Circuits and Systems I Regular Papers*, vol. 64, no. 2, pp. 373–385, 2017.

[6] M. Itoh and L. O. Chua, "Memristor oscillators," *International Journal of Bifurcation and Chaos*, vol. 18, no. 11, pp. 3183–3206, 2008.

[7] B. Muthuswamy, "Implementing memristor based chaotic circuits," *International Journal of Bifurcation and Chaos*, vol. 20, no. 5, pp. 1335–1350, 2010.

[8] K. Rajagopal, A. Akgul, V. T. Pham et al., "Multistability and coexisting attractors in a new circulant chaotic system," *International Journal of Bifurcation & Chaos*, vol. 29, no. 13, Article ID 1950174, 2019.

[9] Q. Liu, P.-Y. Li, M.-C. Zhang, and Y.-X. Sui, "Image encryption algorithm based on chaos system having Markov portion," *Journal of Electronics and Information Technology*, vol. 36, no. 6, pp. 1271–1277, 2014.

[10] A. Z. Tirkel, G. A. Rankin, R. M. Van Schyndel, W. J. Ho, N. R. Mee, and C. F. Osborne, "Electronic water mark," in *Proceedings of the DICTA Digital Image Computing, Technology and Applications*, vol. 93, pp. 666–673, Macquarie University, Sydney, Australia, pp. 666–673, December 1993.

[11] L. Wang and Y. Shen, "Design of controller on synchronization of memristor-based neural networks with time-varying delays," *Neurocomputing*, vol. 147, pp. 372–379, 2015.

[12] J. Ma, Z. Q. Chen, Z. L. Wang, and Q. Zhang, "A four-wing hyper-chaotic attractor generated from a 4-D memristive system with a line equilibrium," *Nonlinear Dynamics*, vol. 81, no. 3, pp. 1275–1288, 2015.

[13] J. Kengne, T. Z. Njitacke, V. K. Tamba, and A. N. Negou, "Periodicity, chaos, and multiple attractors in a memristor-based Shinriki's circuit," *Chaos: An Interdisciplinary Journal of Nonlinear*, vol. 25, no. 10, Article ID 103126, 2015.

[14] H. G. Wu, B. C. Bao, Z. Liu, Q. Xu, and P. Jiang, "Chaotic and periodic bursting phenomena in a memristive Wien-bridge oscillator," *Nonlinear Dynamics*, vol. 83, no. 1-2, pp. 893–903, 2016.

[15] L. Zhou, C. H. Wang, and L. L. Zhou, "Generating hyper-chaotic multiwing attractor in a 4D memristive circuit," *Nonlinear Dynamics*, vol. 85, no. 4, pp. 2653–2663, 2016.

[16] C. H. Wang, X. M. Liu, and H. Xia, "Multi-piecewise quadratic nonlinearity memristor and its 2N-scroll and 2N + 1-scroll chaotic attractors system," *Chaos*, vol. 27, no. 3, Article ID 033114, 2017.

[17] Q. Q. Hu, Y. B. Yu, L. F. Men, F. Lei, and H. Zhang, "Memristor-based chaotic circuit design on image En/decryption," in *Proceedings of the 2016 31st Youth Academic Conference of Chinese Association of Automation (YAC)*, pp. 56–60, Wuhan, China, November 2016.

[18] T. F. Fonzin, K. Srinivasan, J. Kengne, and F. B. Pelap, "Coexisting bifurcations in a memristive hyperchaotic oscillator," *Aeu International Journal of Electronics and Communications*, vol. 90, pp. 110–122, 2018.

[19] X. Min, X. Wang, P. Zhou, S. Yu, and H. H.-C. Lu, "An optimized memristor-based hyperchaotic system with controlled hidden attractors," *IEEE Access*, vol. 7, pp. 124641–124646, 2019.

[20] X. Wang, X. Min, P. Zhou, and D. S. Yu, "Hyperchaotic circuit based on memristor feedback with multistability and symmetries," *Complexity*, vol. 2020, Article ID 2620375, 10 pages, 2020.

[21] J. H. Lü and G. R. Chen, "A new chaotic attractor coined," *International Journal of Bifurcation and Chaos*, vol. 12, no. 3, pp. 659–661, 2002.

[22] E. N. Lorenz, "Deterministic nonperiodic flow," *Journal of the Atmospheric Sciences*, vol. 20, no. 2, pp. 130–141, 1963.

[23] G. R. Chen and T. Ueta, "Yet another chaotic attractor," *International Journal of Bifurcation and Chaos*, vol. 9, no. 7, pp. 1465-1466, 1999.

[24] G. Y. Hua and Y. C. Zhou, "Dynamic parameter-control chaotic system," *IEEE Transactions on Cybernetics*, vol. 46, no. 12, pp. 3330–3341, 2016.

WILEY | Hindawi

Research Article

Initial Value Determination of Chua System with Hidden Attractors and Its DSP Implementation

Xianming Wu [ID],[1] **Weijie Tan** [ID],[2] **and Huihai Wang** [ID][3]

[1]*School of Mechanical & Electrical Engineering, Guizhou Normal University, Guiyang 550025, China*
[2]*State Key Laboratory of Public Big Data, Guizhou University, Guiyang 550025, China*
[3]*School of Physics and Electronics, Central South University, Changsha 410083, China*

Correspondence should be addressed to Huihai Wang; wanghuihai_csu@csu.edu.cn

In this paper, a method for determining the initial value of the hidden attractors in the Chua system is studied. The initial value of the hidden attractors can be calculated quickly and accurately by the proposed method, and the hidden attractors can be found by numerical simulation. Then, the initial values of the hidden attractors are set accurately by digital signal processor (DSP), so as to the circuit realization of the chaotic system with hidden attractors is performed. The results show that the numerical simulation results of Matlab are consistent with the experimental results of DSP.

1. Introduction

In the last three decades, chaos has been widely used in neural networks [1–5], electronic circuits [6], image processing [7–10], random number generators [11], system synchronization [12–14], and secure communication [15–18] because of its characteristics of aperiodic, continuous broadband, noise-like, and unpredictable for a long time. Since Lorenz puts forward the first chaotic system in the study of atmospheric motion [19], the research and exploration of the chaotic system composed of ordinary differential equations have attracted researchers' great attention, and many new chaotic systems with complex dynamic attractors, such as multiscroll attractors [20] and coexistence attractors [21–23] have been constantly produced.

Because the domain of attraction of the hidden attractor does not intersect with any small neighbourhood of the equilibrium point, there is no general method to predict the existence of the hidden attractor, so it is of great theoretical and practical significance to study the hidden attractor in the field of machinery and so on [24, 25]. In 2011, Leonov et al. proposed a locating algorithm for hidden attractors [26] and used the algorithm to find hidden attractors of the Chua

system. Since then, the research on hidden attractors has attracted extensive interest of scholars. In 2012, Leonov et al. used the algorithm to find the hidden attractor in the Chua system with hyperbolic tangent function as nonlinear function [27]. In 2014, Zhao et al. used the algorithm to find the hidden attractor in a generalized autonomous Pol-Duffing system [28]. In the same year, Li et al. found the twin hidden attractors in the Chua system [29]. In 2017, Zhao et al. found the hidden attractor in a modified Chua system [30]. In the same year, Kuznetsov et al. also found coexistence limit cycle and symmetric hidden attractors in the Chua system [31]. Stankevich et al. analysed the scenario of the birth of the hidden attractor from its attractor basin in the Chua system [32]. These attractors are different from the classical Lorenz attractors, Chua attractors, and Chen attractors. They are not near the equilibrium point and cannot be calculated by traditional methods. Leonov et al. proposed an algorithm to determine the initial value of the hidden attractors and found the hidden attractors.

In 2016, Bao et al. designed the chaotic circuit of the chaotic system and found the hidden attractor of the system by PSIM simulation [33]. In [34], a three-dimensional autonomous chaotic circuit is designed, and the hidden attractor of the system is found by PSpice simulation. In

[35], a 5-D memristor chaotic circuit is designed. The hidden multiscroll attractors and hidden multiwing attractors are found by PSpice simulation. In [36], a 5D extreme multi-stable chaotic circuit is designed, and the hidden attractor of the system is found by PSpice simulation. In [37], a four-dimensional chaotic circuit is designed, and the coexistence hidden attractor of the system is found by PSpice simulation. In [38], a new chaotic circuit is designed by introducing the cosh function into the system in [37], and the coexistence hidden attractor of the system is found by PSpice simulation. In [39], by introducing a memristor to improve Fitz-hugh–Nagumo circuit, a new memristor chaotic circuit is designed, and the hidden attractor is found by PSIM simulation. However, the hidden attractor is studied by circuit simulation software, but the initial state of the experimental circuit is random, so the initial value of the hidden attractor cannot be set accurately.

In this paper, we study the method to determine the initial value of the hidden attractors in the Chua system. Its initial value of the hidden attractors can be set accurately by DSP, and the circuit realization of the chaotic system with hidden attractors is performed. The results show that the numerical simulation results of Matlab are consistent with the experimental results of DSP.

The rest of this work is organized as follows. Section 2 describes initial value determining algorithm for the Chua system with hidden attractors. Section 3 calculates initial values of hidden attractors and finds its hidden attractors. The Chua system with hidden attractors is implemented by DSP in Section 4. Finally, we conclude in Section 5.

2. Initial Value Determining Algorithm for Hidden Attractors

According to the initial value determining algorithm for the chaotic system with hidden attractors in [26], the Chua system with hidden attractors is

$$
\begin{cases}
\dfrac{dx}{dt} = a(y - x) - af(x), \\[2mm]
\dfrac{dy}{dt} = x - y + z, \\[2mm]
\dfrac{dz}{dt} = -by - cz,
\end{cases}
\tag{1}
$$

where $f(x) = mx + 0.5(n - m)(|x + 1| - |x - 1|)$, x, y, and z are system variables, and a, b, c, m, and n are system constants.

Now, system (1) is rewritten as lure system:

$$
\frac{dx}{dt} = Px + q\psi(r^*x) \quad , x \in R^3,
\tag{2}
$$

where $P = \begin{pmatrix} -a(1+m) & a & 0 \\ 1 & -1 & 1 \\ 0 & -b & -c \end{pmatrix}$, $q = \begin{pmatrix} -a \\ 0 \\ 0 \end{pmatrix}$, $r = \begin{pmatrix} 1 \\ 0 \\ 0 \end{pmatrix}$,

and $\psi(\sigma) = 0.5(n - m)(|\sigma + 1| - |\sigma - 1|)$.

Let k be the coefficient of harmonic linearization, and ε be an infinitesimal number, and equation (2) can be re-written as

$$
\frac{dx}{dt} = P_0 x + q\varepsilon\delta(r^*x),
\tag{3}
$$

where $P_0 = \begin{pmatrix} -a(1+m+k) & a & 0 \\ 1 & -1 & 1 \\ 0 & -b & -c \end{pmatrix}$, $\lambda_{1,2}^{P_0} = \pm i\omega_0$,

$\lambda_3^{P_0} = -d < 0$, and $\delta(\sigma) = \psi(\sigma) - k\sigma$.

Using nonsingular linear transformation $x = Sy$, equation (3) can be transformed as

$$
\frac{dy}{dt} = Hx + e\varepsilon\phi(u^*y),
\tag{4}
$$

where $H = \begin{pmatrix} 0 & -\omega_0 & 0 \\ \omega_0 & 0 & 0 \\ 0 & 0 & -d \end{pmatrix}$, $e = \begin{pmatrix} e_1 \\ e_2 \\ 1 \end{pmatrix}$, and $u = \begin{pmatrix} 1 \\ 0 \\ -h \end{pmatrix}$.

The transfer function of equation (4) can be expressed as

$$
W_H(p) = \frac{-e_1 p + e_2\omega_0}{p^2 + \omega_0^2} + \frac{h}{p + d}.
\tag{5}
$$

The transfer functions of system (3) can be expressed as

$$
W_{P_0}(p) = r^*(P_0 - pI)^{-1}q,
\tag{6}
$$

where p is complex variables, ω_0 is the initial frequency, which can be calculated by $\mathrm{Im}WH(\omega_0)F0$, and k is the harmonic linearization coefficient, which can be calculated by $k = -(\mathrm{Re}W_H i\omega_0)^{-1}$. From the equivalence of the transfer functions of systems (3) and (4), it can be concluded:

$$
\begin{cases}
k = \left(\dfrac{-a(m + mc + c) + (\omega_0^2 - b - c)}{a(1 + c)} \right), \\[4mm]
d = \left(\dfrac{\omega_0^2 - b + 1 + a + c + c^2}{(1 + c)} \right), \\[4mm]
h = \dfrac{a(c + b - (1 + c)d + d^2)}{(\omega_0^2 + d^2)}, \\[4mm]
e_1 = \dfrac{a(c + b - (1 + c)d - \omega_0^2)}{(\omega_0^2 + d^2)}, \\[4mm]
e_2 = \dfrac{a((1 + c - d)\omega_0^2 + d(c + b))}{(\omega_0(\omega_0^2 + d^2))}.
\end{cases}
\tag{7}
$$

System (3) is transformed by nonsingular linear transformation, and it can be concluded:

$$
\begin{cases}
H = S^{-1}P_0 S, \\
e = S^{-1}q, \\
u^* = r^* S.
\end{cases}
\tag{8}
$$

Let $S = \begin{pmatrix} s_{11} & s_{12} & s_{13} \\ s_{21} & s_{22} & s_{23} \\ s_{31} & s_{32} & s_{33} \end{pmatrix}$. We can obtain $s_{11} = 1$, $s_{12} = 0$, $s_{13} = -h$, $s_{21} = m + k + 1$, $s_{22} = -(\omega_0/a)$, $s_{23} = -(h(a(m + k + 1) - d))/a$, $s_{31} = (a(m + k) - \omega_0^2)/a$, $s_{32} = -(a(c + b)(m + k) + ab - c\omega_0^2)/a\omega_0$, and $s_{33} = h((a(m + k)(d - 1) + d(1 + a - d))/a)$.

For the infinitesimal number ε, the initial value of (4) is

$$y(0) = \begin{pmatrix} y_1(0) \\ y_2(0) \\ y_3(0) \end{pmatrix} = \begin{pmatrix} g_0 \\ 0 \\ 0 \end{pmatrix}. \tag{9}$$

From equation (9), the relationship between the initial values of equations (3) and (4) can be obtained:

$$x(0) = Sy(0) = S\begin{pmatrix} x_1(0) \\ x_2(0) \\ x_3(0) \end{pmatrix} = \begin{pmatrix} g_0 s_{11} \\ g_0 s_{21} \\ g_0 s_{31} \end{pmatrix}. \tag{10}$$

In this way, the initial value of system (1) is

$$x(0) = g_0,$$
$$y(0) = -g_0(m + k + 1), \tag{11}$$
$$z(0) = g_0 \frac{a(m+k) - \omega_0^2}{a},$$

where the description function of a_0 can be calculated as

$$\Phi(g) = \int_0^{2\pi/\omega_0} [\delta_1((\cos\omega_0 t)g, (\sin\omega_0 t)g, 0)\cos\omega_0 t \\ + \delta_2((\cos\omega_0 t)g, (\sin\omega_0 t)g, 0)\sin\omega_0 t]dt, \tag{12}$$

and the description function satisfies $\Phi(g_0) = 0$ and $b_1(d\Phi(g)/dg)|_{g=g_0} \neq 0$.

3. Numerical Simulation

According to the algorithm in [26], the initial values are $x_0 = [5.9, 0.3720, -8.4291]$ and $x_{00} = [-5.9, -0.3720, 8.4291]$. Based on the calculated initial value, the phase diagram is shown in Figure 1, and the attractor basin is shown in Figure 2.

From Figure 1, it can be seen that the hidden attractor can be found according to the initial value calculated by the algorithm in [26]. From Figure 2, the blue centre region is stable equilibrium, the red region is period-1 limit cycle, and the cyan region is divergent.

4. DSP Implementation of Chua System with Hidden Attractors

The realization of the chaotic system by hardware circuit is the most common method to verify the design of new chaotic system, including analog circuit and digital circuit. Analog circuit mainly adopts discrete components [13] and integrates circuit (IC) [40–42] design method, while digital circuit mainly adopts FPGA [43] and DSP [44–46]. It is difficult to design and debug chaotic circuit with discrete components, and the circuit is bulky. When using IC to design the chaotic oscillator, the chip area is greatly reduced, but the design of IC requires high chip technology, and the number of wings or scrolls of the attractor is difficult to control. Because the analog circuit cannot accurately set the initial state of the system and cannot reach the calculated initial value of the hidden attractors. FPGA and DSP have

high-speed data processing capability and can realize various processing algorithms through software programming [47, 48], which can conveniently realize the nonlinear characteristics of the chaotic system with hidden attractors.

4.1. Implementation of the Chaotic System. In this part, the chaotic system with hidden attractors is implemented on DSP platform. The block diagram of the working principle is shown in Figure 3. In the experiments, the Texas Instrument DSP device TMS320F28335 is employed. It is a 32 bit DSP running at 150 MHz with floating point operations. Such a high-speed clock rate is considered to be sufficient. In order to observe the phase diagrams of the attractor on the oscilloscope, the digital chaotic sequences generated on DSP are converted into analog signals. DAC8552, a 16 bit digital-to-analog converter with dual channels, is adopted. It connects DSP through SPI (serial peripheral interface).

The flowchart of the programming is shown in Figure 4. In the program, in order to reduce the effect of finite computing precision in digital circuits, all data types are defined as long double. After initializing DSP, we set the initial conditions, including initial values of state variables, and the system parameters. Iterative computation is started according to the initial values $[x_0, y_0, z_0]$. To keep the iteration not being affected by data processing, it is necessary to push the results of each iteration into the stack. Data processing includes two steps. Firstly, an appropriate positive number is added to all data to make sure all data is greater than zero. Secondly, all data is rescaled and truncated to make the output adapting the 16 bit digital-to-analog converter.

4.2. Runge–Kutta4 (RK4) Algorithm. According to the required iterative equation in Figure 4, we use the RK4 algorithm to realize the iterative equation of the Chua system with hidden attractors. RK4 is a derivative of Runge–Kutta basic model, which is used to solve ordinary differential equations with high accuracy, and mostly has proved itself superior to other solutions. RK4 algorithm is expressed as

$$\begin{cases} y_{i+1} = y_i + \frac{h}{6}(k_1 + 2k_2 + 2k_3 + k_4), \\ k_1 = f(x_i, y_i), \\ k_2 = f\left(x_i + \frac{h}{2}, y_i + \frac{h}{2}k_1\right), \\ k_3 = f\left(x_i + \frac{h}{2}, y_i + \frac{h}{2}k_2\right), \\ k_4 = f(x_i + h, y_i + hk_3). \end{cases} \tag{13}$$

According to the values of h, x_i, and y_i and calculating the values of k_1, k_2, k_3, and k_4, we can attain the value of y_{i+1}. Three equations of system (1) are substituted into equation (13), and the three state variables (x, y, z) of system (1) are solved, respectively:

(a)

(b)

(c)

(d)
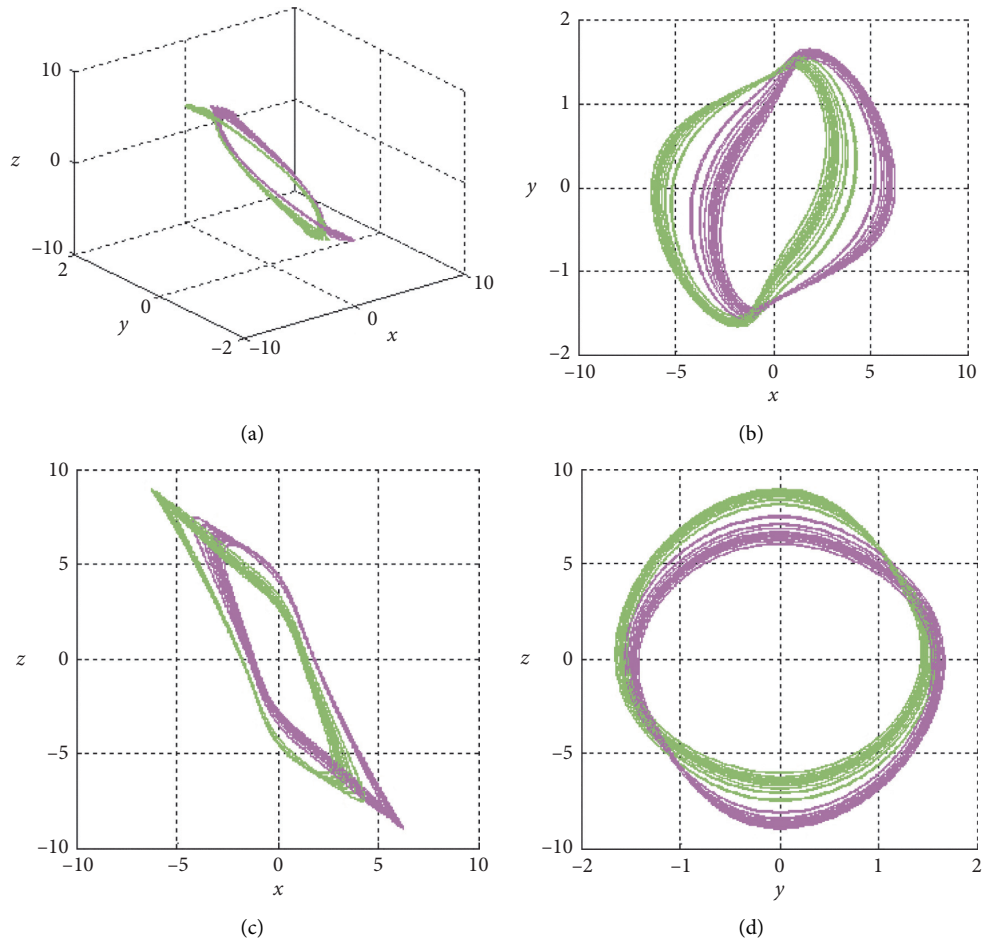
FIGURE 1: Phase diagrams of system (1); initial values: (5.9 0.3720 −8.4291) (magenta) and (−5.9 −0.3720 8.4291) (green).

(a)

(b)
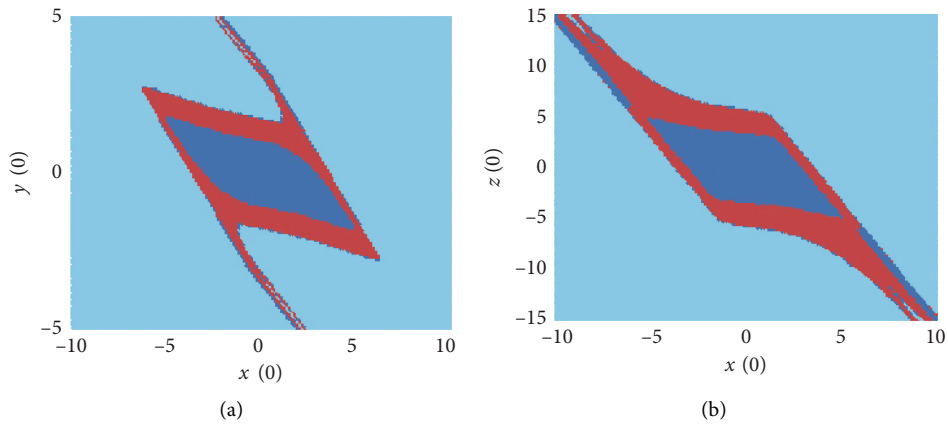
FIGURE 2: Continued.

(c)
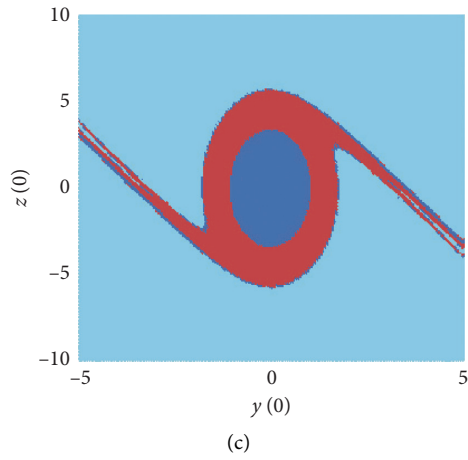
FIGURE 2: Attractor basin of system (1): (a) initial value x-y plane; (b) initial value x-z plane; (c) initial value y-z plane.
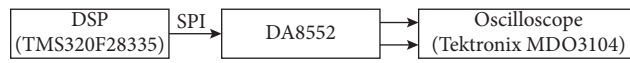
FIGURE 3: Working principle for implementing the Chua system with hidden attractors on DSP.
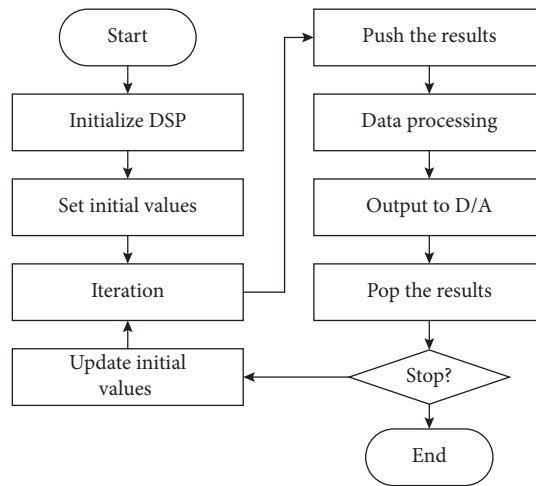
FIGURE 4: Flowchart for DSP implementation of the Chua system with hidden attractors.
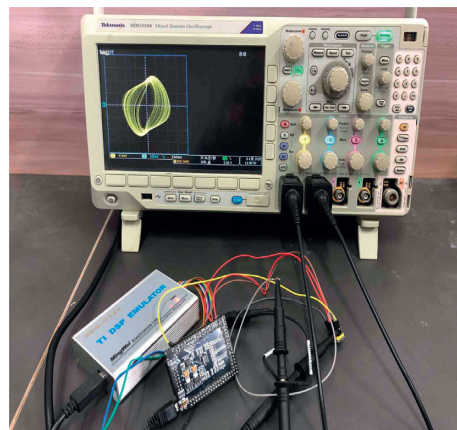
FIGURE 5: Hardware part of DSP implementation.

(a)

(b)

(c)
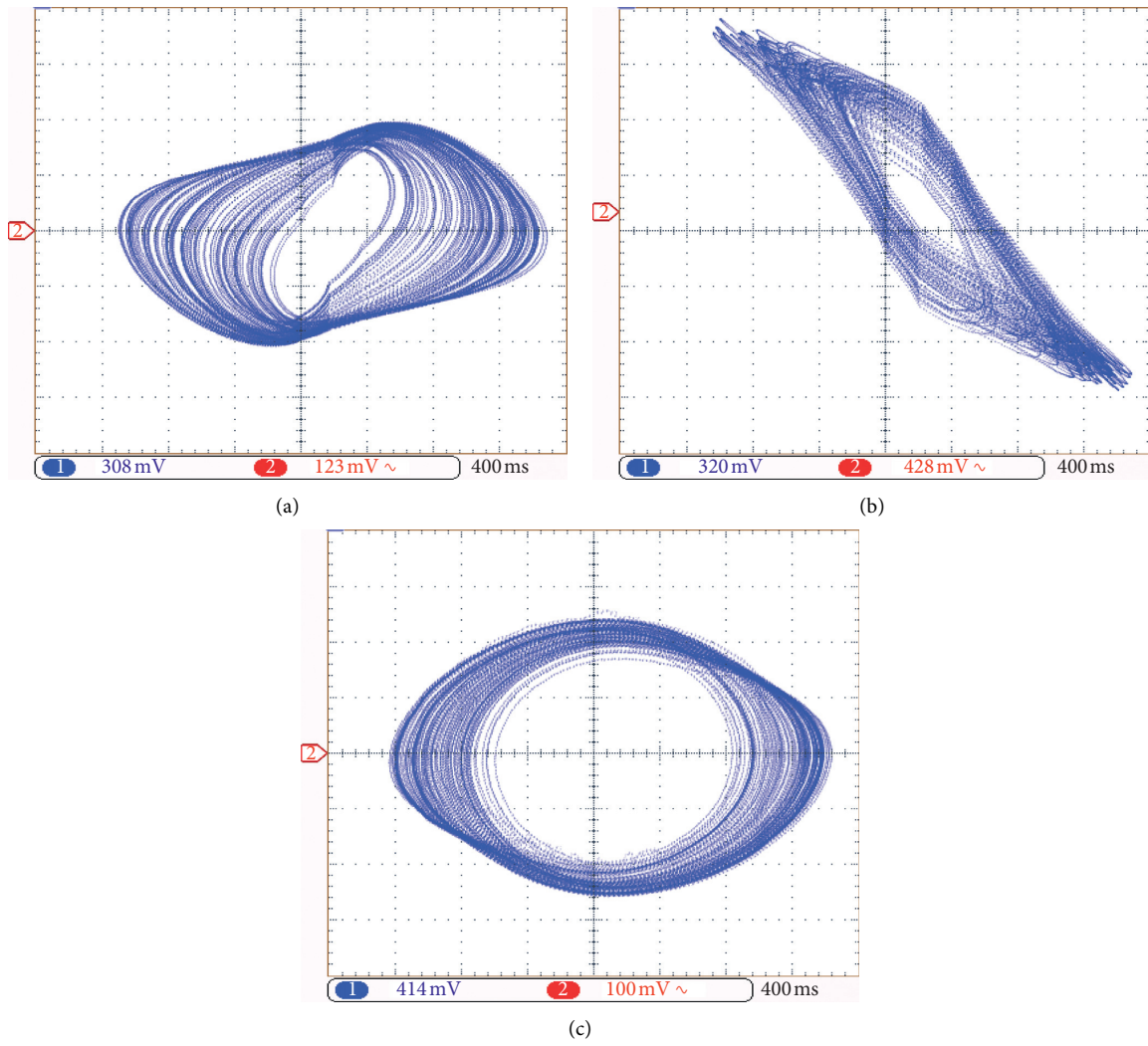
Figure 6: Hidden attractors by DSP implementation for $a = 8.4562$; $b = 12.0732$; $c = 0.0052$; $m = -1.1468$; $n = -0.1768$: (a) x-y plane; (b) x-z plane; (c) y-z plane.

(a)

(b)
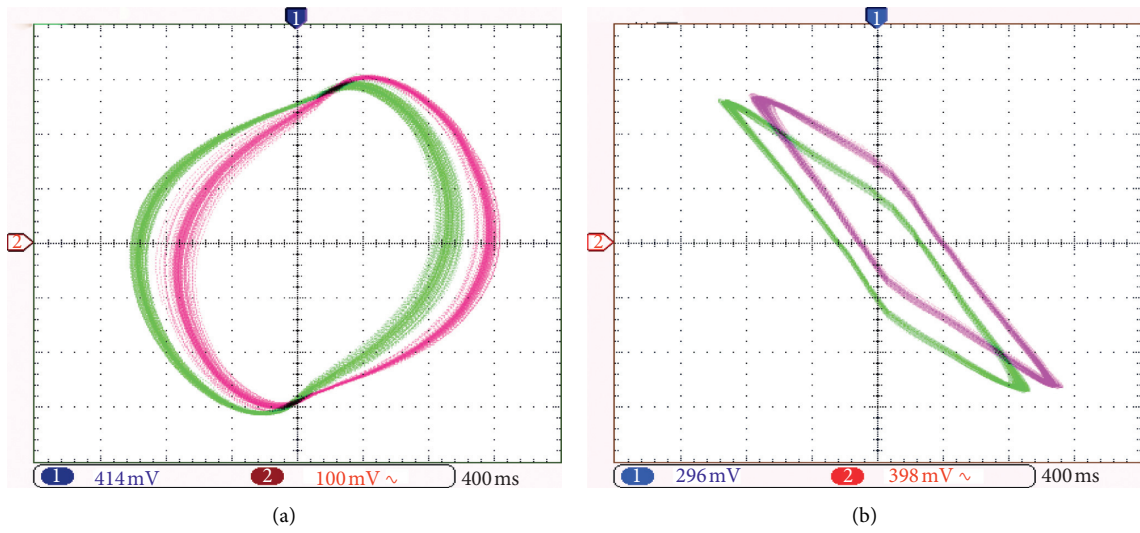
Figure 7: Continued.

(c)
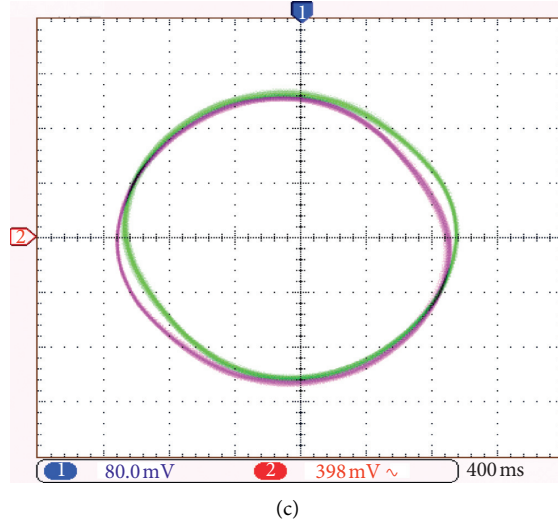
Figure 7: Hidden attractors by DSP implementation; initial values: (5.9 0.3720–8.4291) (magenta) and (−5.9 −0.3720 8.4291) (green): (a) x-y plane; (b) x-z plane; (c) y-z plane.

$$
\begin{cases}
K_{x1} = a - x_i - mx_i - 0.5\big((n-m)\big(|x_i+1|-|x_i-1|\big) + y_i\big), \\
K_{y1} = x_i - y_i + z_i, \\
K_{z1} = -by_i - cz_i, \\
K_{x2} = a\big(-\big(x_i + mx_i + 0.5(n-m)\big(|x_i+1|-|x_i-1|\big) + 0.5hK_{x1}\big) + \big(y_i + 0.5hK_{y1}\big)\big), \\
K_{y2} = \big(x_i + 0.5hK_{x1}\big) - \big(y_i + 0.5hK_{y1}\big) + \big(z_i + 0.5hK_{z1}\big), \\
K_{z2} = -b\big(y_i + 0.5hK_{y1}\big) - c\big(z_i + 0.5hK_{z1}\big), \\
K_{x3} = a\big(-\big(x_i + mx_i + 0.5(n-m)\big(|x_i+1|-|x_i-1|\big) + 0.5hK_{x2}\big) + \big(y_i + 0.5hK_{y2}\big)\big), \\
K_{y3} = \big(x_i + 0.5hK_{x2}\big) - \big(y_i + 0.5hK_{y2}\big) + \big(z_i + 0.5hK_{z2}\big), \\
K_{z3} = -b\big(y_i + 0.5hK_{y2}\big) - c\big(z_i + 0.5hK_{z2}\big), \\
K_{x4} = a\big(-\big(x_i + mx_i + 0.5(n-m)\big(|x_i+1|-|x_i-1|\big) + 0.5hK_{x3}\big) + \big(y_i + 0.5hK_{y3}\big)\big), \\
K_{y4} = \big(x_i + 0.5hK_{x3}\big) - \big(y_i + 0.5hK_{y3}\big) + \big(z_i + 0.5hK_{z3}\big), \\
K_{z4} = -b\big(y_i + 0.5hK_{y3}\big) - c\big(z_i + 0.5hK_{z3}\big), \\
x_{i+1} = x_i + \dfrac{h(k11 + 2k12 + 2k13 + k14)}{6}, \\
y_{i+1} = y_i + \dfrac{h(k21 + 2k22 + 2k23 + k24)}{6}, \\
z_{i+1} = z_i + \dfrac{h(k31 + 2k32 + 2k33 + k34)}{6}.
\end{cases}
\tag{14}
$$

4.3. Circuit Implementation Using DSP. We set $h = 0.001$, initial values $x_0 = [5.9 \; 0.3720 - 8.4291]$ and $x_{00} = [5.9 \; 0.3720 \; 8.4291]$, when $a = 8.4562$, $b = 12.0732$, $c = 0.0052$, $m = -1.1468$, and $n = -0.1768$. The system is realized by the DSP platform. Figure 5 shows the hardware part of DSP. Phase diagrams of the system are captured randomly by the oscilloscope, as shown in Figure 6. When $a = 8.4$, $b = 12.1$, $c = 0.005$, $m = -1.1$, and $n = 0.1$, its phase diagrams is shown in Figure 7. It indicates that the Chua system with hidden attractors is realized successfully on the DSP platform.

From Figures 5–7, it is observed that the DSP circuit can generate two hidden attractors.

5. Conclusions

In this paper, we calculate the initial values of the Chua system with hidden attractors, find its hidden attractors, and obtain its phase diagram and attractor basin. Since the analog circuit cannot accurately set its initial state and cannot achieve the calculated initial value of the hidden attractor, this paper uses DSP to realize the chaos system with hidden attractors. The results show that the numerical simulation is consistent with the experimental results of DSP, which provides a practical method for the circuit implementation of the chaotic system with hidden attractors. In the next work, we will study the hidden attractor applied to secure communication.

Data Availability

The data used to support the findings of this study are included within the article.

Conflicts of Interest

The authors declare that they have no conflicts of interest.

Authors' Contributions

The work presented in this paper was a collaboration of all authors. Xianming WU contributed the idea and wrote the paper. Weijie Tan and Huihai Wang did the simulation analysis and reviewed the paper.

Acknowledgments

References

[1] Z. T. Njitacke, S. D. Isaac, J. Kengne, A. N. Negou, and G. D. Leutcho, "Extremely rich dynamics from hyperchaotic hopfield neural network: hysteretic dynamics, parallel bifurcation branches, coexistence of multiple stable states and its analog circuit implementation," *The European Physical Journal Special Topics*, vol. 229, no. 6-7, pp. 1133–1154, 2020.

[2] F. Yu, L. Liu, L. Xiao, K. Li, and S. Cai, "A robust and fixed-time zeroing neural dynamics for computing time-variant nonlinear equation using a novel nonlinear activation function," *Neurocomputing*, vol. 350, pp. 108–116, 2019.

[3] F. Wang, L. Zhang, S. Zhou, and Y. Huang, "Neural network-based finite-time control of quantized stochastic nonlinear systems," *Neurocomputing*, vol. 362, pp. 195–202, 2019.

[4] J. Jin, L. Zhao, M. Li, F. Yu, and Z. Xi, "Improved zeroing neural networks for finite time solving nonlinear equations," *Neural Computing and Applications*, vol. 32, no. 9, pp. 4151–4160, 2020.

[5] H. Lin and C. Wang, "Influences of electromagnetic radiation distribution on chaotic dynamics of a neural network," *Applied Mathematics and Computation*, vol. 369, Article ID 124840, 2020.

[6] Y. M. Tan and C. H. Wang, "A simple locally active memristor and its application in HR neurons," *Chaos*, vol. 30, no. 5, Article ID 53118, 2020.

[7] L. M. Zhang, K. H. Sun, and W. H. Liu, "A novel color image encryption scheme using fractional-order hyperchaotic system and DNA sequence operations," *Chinese Physics B*, vol. 26, Article ID 100504, 2017.

[8] G. Cheng, C. Wang, and H. Chen, "A novel color image encryption algorithm based on hyperchaotic system and permutation-diffusion architecture," *International Journal of Bifurcation and Chaos*, vol. 29, no. 9, Article ID 1950115, 2019.

[9] M. Zhou and C. Wang, "A novel image encryption scheme based on conservative hyperchaotic system and closed-loop diffusion between blocks," *Signal Processing*, vol. 171, Article ID 107484, 2020.

[10] Z. Hua, Y. Zhou, and B. Bao, "Two-dimensional sine chaotification system with hardware implementation," *IEEE Transactions on Industrial Informatics*, vol. 16, no. 2, pp. 887–897, 2020.

[11] F. Yu, L. Liu, and S. Qian, "Chaos-based application of a novel multistable 5D memristive hyperchaotic system with coexisting multiple attractors," *Complexity*, vol. 2020, Article ID 8034196, 19 pages, 2020.

[12] L. Zhou, F. Tan, F. Yu, and W. Liu, "Cluster synchronization of two-layer nonlinearly coupled multiplex networks with multi-links and time-delays," *Neurocomputing*, vol. 359, no. 24, pp. 264–275, 2019.

[13] F. Yu, S. Qian, and X. Chen, "A new 4D four-wing memristive hyperchaotic system: dynamical analysis, electronic circuit design, shape synchronization and secure communication," *International Journal of Bifurcation and Chaos*, 2020.

[14] L. Zhou, F. Tan, and F. Yu, "A robust synchronization-based chaotic secure communication scheme with double-layered and multiple hybrid networks," *IEEE Systems Journal*, vol. 14, no. 2, pp. 2508–2519, 2020.

[15] Z. Hua, Y. Zhang, and Y. Zhou, "Two-dimensional modular chaotification system for improving chaos complexity," *IEEE Transactions on Signal Processing*, vol. 68, pp. 1937–1949, 2020.

[16] Z. Hua and Y. Zhou, "Exponential chaotic model for generating robust chaos," *IEEE Transactions on Systems, Man, and Cybernetics: Systems*, vol. 99, pp. 1–12, 2019.

[17] F. Yu, Z. Zhang, and L. Liu, "Secure communication scheme based on a new 5D multistable four-wing memristive hyperchaotic system with disturbance inputs," *Complexity*, vol. 2020, Article ID 5859273, 16 pages, 2020.

[18] F. Kuang, S. Zhang, Z. Jin, and W. Xu, "A novel SVM by combining kernel principal component analysis and improved chaotic particle swarm optimization for intrusion detection," *Soft Computing*, vol. 19, no. 5, pp. 1187–1199, 2015.

[19] E. N. Lorenz, "Deterministic nonperiodic flow," *Journal of the Atmospheric Sciences*, vol. 20, no. 2, pp. 130–141, 1963.

[20] Q. Deng and C. Wang, "Multi-scroll hidden attractors with two stable equilibrium points," *Chaos*, vol. 29, no. 9, Article ID 93112, 2019.

[21] G. D. Leutcho, J. Kengne, and R. Kengne, "Remerging Feigenbaum trees, and multiple coexisting bifurcations in a novel hybrid diode-based hyperjerk circuit with offset boosting," *International Journal of Dynamics and Control*, vol. 7, no. 1, pp. 61–82, 2019.

[22] G. D. Leutcho and J. Kengne, "A unique chaotic snap system with a smoothly adjustable symmetry and nonlinearity: chaos, offset-boosting, antimonotonicity, and coexisting multiple attractors," *Chaos, Solitons & Fractals*, vol. 113, pp. 275–293, 2018.

[23] G. D. Leutcho, J. Kengne, and T. FonzinFozin, "Multistability control of space magnetization in hyperjerk oscillator: a case study," *Journal of Computational and Nonlinear Dynamics*, vol. 15, no. 5, Article ID ID051004, 2020.

[24] L. Cui, M. Lu, and Q. Ou, "Analysis and circuit implementation of fractional order multi-wing hidden attractors," *Chaos, Solitons & Fractals*, vol. 138, Article ID 109894, 2020.

[25] H. Lin, C. Wang, and Y. Tan, "Hidden extreme multistability with hyperchaos and transient chaos in a Hopfield neural network affected by electromagnetic radiation," *Nonlinear Dynamics*, vol. 99, no. 3, pp. 2369–2386, 2020.

[26] G. A. Leonov, N. V. Kuznetsov, and V. I. Vagaitsev, "Localization of hidden Chua's attractors," *Physics Letters A*, vol. 375, no. 23, pp. 2230–2233, 2011.

[27] G. A. Leonov, N. V. Kuznetsov, and V. I. Vagaitsev, "Hidden attractor in smooth Chua systems," *Physica D: Nonlinear Phenomena*, vol. 241, no. 18, pp. 1482–1486, 2012.

[28] H. T. Zhao, Y. P. Lin, and Y. X. Dai, "Hidden attractors and dynamics of a general autonomous van der Pol–Duffing oscillator," *International Journal of Bifurcation and Chaos*, vol. 24, no. 6, Article ID 1450080, 2014.

[29] Q. D. Li, H. Z. Zeng, and X. S. Yang, "On hidden twin attractors and bifurcation in the Chua's circuit," *Nonlinear Dynamics*, vol. 77, no. 1-2, pp. 255–266, 2014.

[30] H. Zhao, Y. Lin, and Y. Dai, "Hopf bifurcation and hidden attractor of a modified Chua's equation," *Nonlinear Dynamics*, vol. 90, no. 3, pp. 2013–2021, 2017.

[31] N. V. Kuznetsov, O. A. Kuznetsova, G. A. Leonov, T. N. Mokaev, and N. V. Stankevich, "Hidden attractors localization in Chua circuit via the describing function method," *IFAC-PapersOnLine*, vol. 50, no. 1, pp. 2651–2656, 2017.

[32] N. V. Stankevich, N. V. Kuznetsov, and G. A. Leonov, "Scenario of the birth of hidden attractors in the Chua circuit," *International Journal of Bifurcation and Chaos*, vol. 27, no. 12, Article ID 1730038, 2017.

[33] B.-C. Bao, M. Chen, Q. Xu, and P. Jiang, "Hidden attractors in a practical Chua's circuit based on a modified Chua's diode," *Electronics Letters*, vol. 52, no. 1, pp. 23–25, 2016.

[34] S. T. Kingni, S. Jafari, V.-T. Pham, and P. Woafo, "Constructing and analyzing of a unique three-dimensional chaotic autonomous system exhibiting three families of hidden attractors," *Mathematics and Computers in Simulation*, vol. 132, pp. 172–182, 2017.

[35] X. Y. Hu, C. X. Liu, and L. Liu, "Multi-scroll hidden attractors and multi-wing hidden attractors in a 5-dimensional memristive system," *Chinese Physics B*, vol. 26, no. 11, Article ID 110502, 2017.

[36] S. Jafari, A. Ahmadi, A. J. M. Khalaf, H. R. Abdolmohammadi, V.-T. Pham, and F. E. Alsaadi, "A new hidden chaotic attractor with extreme multi-stability," *AEU-International Journal of Electronics and Communications*, vol. 89, pp. 131–135, 2018.

[37] J. P. Singh and B. K. Roy, "Multistability and hidden chaotic attractors in a new simple 4-D chaotic system with chaotic 2-torus behaviour," *International Journal of Dynamics and Control*, vol. 6, no. 2, pp. 529–538, 2018.

[38] V. R. F. Signing and J. Kengne, "Coexistence of hidden attractors, 2-torus and 3-torus in a new simple 4-D chaotic system with hyperbolic cosine nonlinearity," *International Journal of Dynamics and Control*, vol. 6, no. 4, pp. 1421–1428, 2018.

[39] H. Bao, W. Liu, and M. Chen, "Hidden extreme multistability and dimensionality reduction analysis for an improved non-autonomous memristive FitzHugh-Nagumo circuit," *Nonlinear Dynamics*, vol. 96, no. 3, pp. 1879–1894, 2019.

[40] J. Jin, "Programmable multi-direction fully integrated chaotic oscillator," *Microelectronics Journal*, vol. 75, pp. 27–34, 2018.

[41] J. Jin and L. Zhao, "Low voltage low power fully integrated chaos generator," *Journal of Circuits, Systems and Computers*, vol. 27, no. 10, Article ID 1850155, 2018.

[42] J. Jin and L. Cui, "Fully integrated memristor and its application on the scroll-controllable hyperchaotic system," *Complexity*, vol. 2019, Article ID 4106398, 8 pages, 2019.

[43] F. Yu, H. Shen, and L. Liu, "CCII and FPGA realization: a multistable modified four-order autonomous Chua's chaotic system with coexisting multiple attractors," *Complexity*, vol. 2020, Article ID 5212601, 17 pages, 2020.

[44] Y. Xiao, K. Sun, and S. He, "Constructing chaotic map with multi-cavity," *The European Physical Journal Plus*, vol. 135, no. 1, p. 21, 2020.

[45] H. H. Wang, K. H. Sun, and S. B. He, "Dynamic analysis and implementation of a digital signal processor of a fractional-order Lorenz-Stenflo system based on the adomian decomposition method," *Physica Scripta*, vol. 90, no. 1, Article ID 15206, 2014.

[46] W. Ai, K. Sun, and Y. Fu, "Design of multiwing-multiscroll grid compound chaotic system and its circuit implementation," *International Journal of Modern Physics C*, vol. 29, no. 6, Article ID 1850049, 2018.

[47] J.-L. Zhang, W.-Z. Wang, X.-W. Wang, and Z.-H. Xia, "Enhancing security of FPGA-based embedded systems with combinational logic binding," *Journal of Computer Science and Technology*, vol. 32, no. 2, pp. 329–339, 2017.

[48] V. Guglielmi, P. Pinel, D. Fournier-Prunaret, and A.-K. Taha, "Chaos-based cryptosystem on DSP," *Chaos, Solitons & Fractals*, vol. 42, no. 4, pp. 2135–2144, 2009.

Research Article

Bipartite Consensus of Heterogeneous Multiagent Systems with Diverse Input Delays

Hongtao Ye [ID],[1,2,3] Zhongqiu Chen,[1] Wenguang Luo,[3] Jiayan Wen,[3] and Kene Li[1]

[1]*School of Electrical and Information Engineering, Guangxi University of Science and Technology, Liuzhou 545036, China*
[2]*Guangxi Key Laboratory of Automatic Detecting Technology and Instruments, Guilin University of Electronic Technology, Guilin 541004, China*
[3]*Guangxi Key Laboratory of Automobile Components and Vehicle Technology, Guangxi University of Science and Technology, Liuzhou 545036, China*

Correspondence should be addressed to Hongtao Ye; yehongtao@126.com

This paper investigates the bipartite consensus problem of heterogeneous multiagent systems with diverse input delays. Based on the systems composed of first-order and second-order agents, the novel control protocols are designed. Using frequency-domain analysis and matrix theory, the corresponding upper bounds of the allowable delays are obtained under the undirected topology and directed topology, respectively. Finally, simulation examples are given to verify the theoretical analysis.

1. Introduction

Multiagent systems and its cooperative control [1] are widely used in many practical systems such as unmanned aerial vehicles (UAV) [2], monitoring and security [3], sensor network [4], and delay system [5–11].

It is noteworthy that most of the problems about the consensus of multiagent systems are focused on cooperative network. In fact, cooperative and competitive relationships exist extensively in both natural and engineered network systems, such as opinion dynamics in social networks [12] and biological systems [13]. The bipartite consensus was firstly proposed in [14], which defined a signed graph the edges with positive and negative weights to describe the cooperative and competitive relations between agents. Bipartite consensus can be used for formation control [15], obstacle avoidance of wheeled robots [16], and nano-quadcopters formation [17].

There are many factors that affect the stability of agents. The time delay problem is one of the important problems that affect the consensus of a multiagent system. The bipartite consensus problem of second-order multiagent systems with fixed time delays was studied in [18]. Based on

the second-order multiagent systems, Tian et al. [19] discussed the bipartite consensus problem of the system under different disturbances. The bipartite consensus with arbitrary finite communication delay was discussed in [20]. Most of the above work use undirected graphs as communication networks. Compared with undirected graphs [21], directed graphs [22–25] are more versatile and cost effective when the edge weights can be arbitrary between two agents.

This paper pays attention to bipartite consensus of heterogeneous MAS [26–28] with diverse input delays. As far as we know, there are few studies on this aspect, which is the motivation of this work. The theoretical analysis and simulation are presented under undirected topology and directed topology. The upper bounds of the allowable delays are given.

The rest of this article is structured as follows. Section 2 introduces some concepts and basic lemmas of graph theory. In Section 3, the bipartite consensus analysis of heterogeneous multiagent systems with multiple input delays under undirected and directed topologies is presented. In Section 4, two numerical examples are given to illustrate the validity of theoretical analysis. Finally, Section 5 draws some conclusions.

2. Preliminaries and Problem Formulation

2.1. Preliminaries. In this section, the concepts and lemmas of some preliminary diagrams are introduced. We consider a heterogeneous multiagent system with n agents. The connection between agents is represented by an undirected graph or directed graph $G = (V, \varepsilon, A)$, where $V = \{\zeta_1, \zeta_2, \ldots, \zeta_n\}$ represents the set of nodes, $\varepsilon \subseteq V \times V$ represents the set of edges, and $A = [a_{ij}] \in R^{n \times n}$ represents the adjacency matrix of G. As the multiagent system of cooperation and competition is studied in this paper, the value can be either positive or negative. Here, we choose $a_{ii} \neq 0$ for all $i \in \{1, 2, \ldots, n\}$. If $a_{ij} \neq 0$, nodes ζ_j and ζ_i have information exchange; then, node ζ_j is said to be the neighbor of node ζ_i. The set of neighbors of node ζ_i is denoted by $N_i = \{\zeta_j \mid (\zeta_j, \zeta_i) \in \varepsilon\}$. Graph G is strongly connected if there is a path between any two nodes in graph G. The Laplacian matrix of G is defined as $L_s = C - A$, where $C = \text{diag}\{\sum_{j=1}^n |a_{1j}|, \sum_{j=1}^n |a_{2j}|, \ldots, \sum_{j=1}^n |a_{nj}|\}$. Therefore, the elements of Laplacian matrix L_s are

$$L_s = \begin{cases} \sum_{\zeta_i \in N_i} |a_{ij}|, & j = i, \\ -a_{ij}, & j \neq i. \end{cases} \tag{1}$$

Assumption 1 (see [29]). $\sum_{j \in N_i} |a_{ij}| = 0, \forall i \in N_i$, and $\sum_{j \in N_l} |a_{ij}| = 0, \forall i \in N_l$.

Lemma 1 (see [30]). *For Assumption 1, Laplace's matrix L_s has at least two roots of zero. Give the time-delay system*

$$\dot{y}(t) = \sum_{i=1}^N A_i y(t - \tau_i), \tag{2}$$

where $y(t) \in R^n$, $A_i \in R^{n \times n}$, $\tau_i \in R$, and N is a positive integer.

Taking the Laplace transform, we can get the characteristic equation:

$$\det\left(sI - \sum_{i=1}^N A_i y(t - \tau_i)\right) = 0. \tag{3}$$

Lemma 2 (see [30]). *According to the characteristic equation of Lemma 1, if it has only two zero roots and the rest of its roots are on the left half-plane of the complex plane, then it has $\lim_{t \to \infty} y(t) = \alpha + \beta t$, where $\alpha \in R^n$ and $\beta \in R^n$ are constant vectors.*

Lemma 3 (see [31]). *Let $h(\lambda) = \arctan(\delta\mu(\lambda)/\mu(\lambda))$, where $\delta > 0$. When $\lambda > 0$, $\mu(\lambda) > 0$ increases monotonically; then, $h(\lambda)$ decreases monotonically.*

Lemma 4 (see [31]). *$y/(1 + y^2) < \arctan(y)$ holds for $y > 0$.*

Lemma 5 (see [30]). *If $m > 0$, then the inequality $y/(1 + y^2) < \arctan(y) + m$ holds for $y > 0$. If $-(\pi/2) < m < 0$, then there exists $y_0 > 0$, such that the inequality $y/(1 + y^2) < \arctan(y) + m$ holds for $y > y_0$.*

Lemma 6 (see [32]). *If and only if the connected graph G has a globally accessible node, Laplace's matrix L_s has a simple root 0. The corresponding right eigenvector is $1_n = [1, \ldots, 1]^T$, that is, $L1_\mathbf{n} = 0$.*

2.2. Problem Formulation. In this section, we will consider a heterogeneous multiagent system composed of agents, where m agents are second-order agents and $n - m$ agents are first-order agents. The information transmission of each agent in the heterogeneous system is represented by G, and each agent represents a node.

Suppose the input delay of each agent in the system is not consistent. The dynamics of each second-order agent is given as follows:

$$\begin{cases} \dot{x}_i(t) = v_i(t), \\ \dot{v}_i(t) = u_i(t - T_i) \quad i = 1, 2, \ldots, m, \end{cases} \tag{4}$$

where $x_i, v_i, u_i \in R$ represent the position, velocity, and control input of the second-order agent i, respectively. $T_i > 0$ represents the input delay. The dynamics of each first-order agent is given as follows:

$$\dot{x}_l = u_l(t - T_l) \quad l = m + 1, m + 2, \ldots, n, \tag{5}$$

where $x_l, u_l \in R$ represent the position and control input of the first-order agent l, respectively. $T_l > 0$ represents the input delay.

The bipartite consensus means all agents converge to a value which is the same for all in modulus but not in sign through distributed protocols. Similar to [33], the bipartite consensus protocols for the second-order agents are given by

$$u_i = k_1 \sum_{j \in N_i \cup N_l} |a_{ij}| (\text{sgn}(a_{ij})x_j - x_i)$$
$$+ k_2 \sum_{j \in N_i \cup N_l} |a_{ij}| (\text{sgn}(a_{ij})v_j - v_i) \quad i = 1, 2, \ldots, m, \tag{6}$$

where $k_1, k_2 > 0$.

Based on the dynamic neighbor estimation rule in [31, 34–36], an estimated speed is added to the first-order agent. The bipartite consensus protocols are given by

$$\dot{u}_l = v_l + k_2 \sum_{j \in N_i \cup N_l} |a_{lj}| (\text{sgn}(a_{lj})x_j - x_l)$$
$$\dot{v}_l = k_1 \sum_{j \in N_i \cup N_l} |a_{lj}| (\text{sgn}(a_{lj})x_j - x_l) \quad l = m + 1, m + 2, \ldots, n, \tag{7}$$

where $k_1, k_2 > 0$.

The main purpose of this paper is to study the bipartite consensus protocol for heterogeneous multiagents with diverse input delays under the undirected topology and directed topology, respectively.

3. Main Results

3.1. Bipartite Consensus under Undirected Topology. We will consider the bipartite consensus of heterogeneous multiagent systems with diverse input delays under undirected

topology in this section. This paper uses neighborhood estimation rules to estimate the speed of first-order agents. Using the dynamic change of the position of the agent around the first-order agents, the estimated velocity is substituted for its actual velocity. Based on the heterogeneous system with both cooperative and competitive relations, the second-order agent control protocol is designed as follows:

$$\dot{x}_i(t) = v_i(t),$$

$$\dot{v}_i(t) = k_1 \sum_{j \in N_i \cup N_l} |a_{ij}| \left(\text{sgn}(a_{ij}) x_j(t - \tau_i) - x_i(t - \tau_i) \right)$$

$$+ k_2 \sum_{j \in N_i \cup N_l} |a_{ij}| \left(\text{sgn}(a_{ij}) v_j(t - \tau_i) - v_i(t - \tau_i) \right),$$

$$i = 1, 2, \ldots, m,$$

(8)

and the first-order agent control protocol is designed as follows:

$$\dot{x}_l(t) = v_l(t - \tau_l) + k_2 \sum_{j \in N_i \cup N_l} |a_{lj}| \left(\text{sgn}(a_{lj}) x_j(t - \tau_l) - x_l(t - \tau_l) \right),$$

$$\dot{v}_l(t) = k_1 \sum_{j \in N_i \cup N_l} |a_{lj}| \left(\text{sgn}(a_{lj}) x_j(t) - x_l(t) \right),$$

$$l = m + 1, m + 2, \ldots, n,$$

(9)

where $\text{sgn}(\cdot)$ is the sign function, $k_1 > 0$ and $k_2 > 0$ are the control gains, N_i and N_l represent the neighborhood of the agent i and l, and τ_i and τ_l represent the input delay of the agent i and l.

Lemma 7. *For the heterogeneous multiagent systems (8) and (9), if and only if the Laplacian matrix L_s has at least one zero eigenvalue, the real parts of the rest of eigenvalues are positive, and satisfy the condition of inequality (10), and the systems can achieve bipartite consensus.*

$$\frac{\lambda_i \sqrt{k_1^2 + \omega_{ci}^2 k_2^2}}{\omega_{ci}^2} < 1,$$

(10)

where λ_i is the eigenvalue of L_s and ω_{ci} satisfies $\omega_{ci} = \arctan(\omega_{ci} k_2 / k_1)$.

Proof. Take the Laplace transform on (8) and (9); then, we can obtain

$$sX_i(s) = V_i(s),$$

$$sV_i(s) = k_1 \sum_{j \in N_i \cup N_l} |a_{ij}| \left(\text{sgn}(a_{ij}) X_j(s) - X_i(s) \right) e^{-\tau_i s}$$

$$+ k_2 \sum_{j \in N_i \cup N_l} |a_{ij}| \left(\text{sgn}(a_{ij}) V_j(s) - V_i(s) \right) e^{-\tau_i s},$$

$$i = 1, 2, \cdots, m,$$

(11)

$$sX_l(s) = V_l(s) e^{-\tau_l s} + k_2 \sum_{j \in N_i \cup N_l} |a_{lj}| \left(\text{sgn}(a_{lj}) X_j(s) - X_l(s) \right) e^{-\tau_l s},$$

$$sV_l(s) = k_1 \sum_{j \in N_i \cup N_l} |a_{lj}| \left(\text{sgn}(a_{lj}) X_j(s) - X_l(s) \right),$$

$$l = m + 1, m + 2, \ldots, n.$$

(12)

From (11) and (12), we can obtain

$$s^2 X(s) = -(k_1 + k_2 s) X(s) L_s e^{-\tau s},$$

(13)

where $\mathbf{X}(s) = [X_1(s), X_2(s), \ldots, X_n(s)]^T$ is the Laplace transform of $\mathbf{x}(t) = [x_1(t), x_2(t), \ldots, x_n(t)]^T$. Thus, the characteristic equation of (8) and (9) is given by

$$\det\left(s^2 I + (k_1 + k_2 s) L_s e^{-\tau s} \right) = 0.$$

(14)

Because the topology is undirected connected, 0 is a simple root of matrix L_s, and the rest of the roots are positive. Hence, $\text{rank}(L_s) = n - 1$. Let $\lambda_i, i = 1, 2, \ldots, n$ be the eigenvalue of L_s. Assume $\lambda_1 = 0, \lambda_i > 0, i = 2, 3, \ldots, n$, then (14) is equal to

$$s^2 \prod_{i=2,\ldots,n} \left(s^2 + \lambda_i (k_1 + k_2 s) e^{-\tau s} \right) = 0.$$

(15)

So, the equation has two roots of zero. Analyze the rest of the roots of the equation. For

$$s^2 + \lambda_i (k_1 + k_2 s) e^{-\tau s} = 0, \quad i = 2, 3, \ldots, n,$$

(16)

let $f(s) = 1 + g_i(j\omega) = 0$. Equation (16) can be written as $1 + \lambda_i (k_1 + k_2 s) e^{-\tau s} / s^2 = 0$, where $g_i(j\omega) = \lambda_i (k_1 + k_2 s) e^{-\tau s} / s^2$. Based on the Nyquist criterion, if and only if the curve $g_i(j\omega)$ does not include the point $(-1, j0)$, the characteristic root of equation (16) is located on the left half-plane of the complex plane. Then,

$$g_i(j\omega) = \frac{\lambda_i \sqrt{k_1^2 + \omega^2 k_2^2}}{\omega^2} e^{-j(\omega\tau + \pi - \arctan(\omega k_2 / k_1))}.$$

(17)

Then,

$$|g_i(j\omega)| = \frac{|\lambda_i| \sqrt{k_1^2 + \omega_{ci}^2 k_2^2}}{\omega_{ci}^2},$$

$$\arg(g_i(j\omega)) = -\omega\tau + \arctan(\omega k_2 / k_1),$$

(18)

where $\arg(\cdot)$ represents the phase. We know that when $\omega \in (0, +\infty)$, $|g_i(j\omega)|$ is monotonically decreasing. When curve $g_i(j\omega)$ crosses the real axis for the first time, ω_{ci} satisfies $-\omega\tau + \arctan(\omega k_2 / k_1) = 0$. Therefore,

$$|g_i(j\omega)| = \frac{|\lambda_i| \sqrt{k_1^2 + \omega_{ci}^2 k_2^2}}{\omega_{ci}^2} < 1.$$

(19)

In other words, (10) is true. Therefore, except for the two zero roots, all the characteristic roots of (14) are located in the left half-plane. Based on Lemma 2, it is true that $\lim_{t \to \infty} x(t) = \alpha + \beta t$, where $\alpha = [\alpha_1, \alpha_2, \ldots, \alpha_n]^T \in R^n$ and $\beta = [\beta_1, \beta_2, \cdots, \beta_n]^T \in R^n$ are constant vectors. From the

control protocols (8) and (9), it is true that $\lim_{t\to\infty} v(t) = \beta$, where $\mathbf{v}(t) = [v_1(t), v_2(t), \ldots, v_n(t)]^T$. For (8),

$$k_1 \sum_{j\in N_i \cup N_l} |a_{ij}|(\alpha_j - \alpha_i) + (k_1(t-\tau) + k_2)$$

$$\sum_{j\in N_i \cup N_l} |a_{ij}|(\beta_j - \beta_i) = 0, \quad i = 1, 2, \ldots, m. \quad (20)$$

And (20) is also true for any t, and we have

$$\sum_{j\in N_i \cup N_l} |a_{ij}|(\alpha_j - \alpha_i) = 0, \quad i = 1, 2, \ldots, m. \quad (21)$$

$$\sum_{j\in N_i \cup N_l} |a_{ij}|(\beta_j - \beta_i) = 0, \quad i = 1, 2, \ldots, m. \quad (22)$$

For (9),

$$\sum_{j\in N_i \cup N_l} |a_{lj}|(\alpha_j - \alpha_l) + t \sum_{j\in N_i \cup N_l} |a_{lj}|(\beta_j - \beta_l) = 0,$$

$$l = m+1, m+2, \ldots, n. \quad (23)$$

And (23) is also true for any t, and we have

$$\sum_{j\in N_i \cup N_l} |a_{lj}|(\alpha_j - \alpha_l) = 0, \quad l = m+1, m+2, \ldots, n, \quad (24)$$

$$\sum_{j\in N_i \cup N_l} |a_{lj}|(\beta_j - \beta_l) = 0, \quad l = m+1, m+2, \ldots, n. \quad (25)$$

From (21) and (24), it is true that $L\alpha = 0$. From (22) and (25), it is true that $L\beta = 0$. Because $\text{rank}(L) = n - 1$ and $L[1, \ldots, 1]^T = 0$. According to Lemma 6, we have $\alpha = a[1, \ldots, 1]^T$, $\beta = b[1, \ldots, 1]^T$. □

Theorem 1. *For the heterogeneous multiagent systems (8) and (9) under undirected communication topology, the systems can achieve bipartite consensus if the largest input delay satisfies $\tau_{\max} < \tau^*$, where $\tau^* = \arctan$* $(k_2/k_1 \sqrt{(\lambda_{\max}^2 k_2^2 + \sqrt{\lambda_{\max}^4 k_2^4 + 4\lambda_{\max}^2 k_1^2}/2)})/$

$\sqrt{(\lambda_{\max}^2 k_2^2 + \sqrt{\lambda_{\max}^4 k_2^4 + 4\lambda_{\max}^2 k_1^2}/2)}$, *and $\lambda_{\max}$ is the maximum eigenvalue of L_s.*

Proof. For Lemma 7, we can get $\omega_{ci}\tau = \arctan(\omega_{ci}k_2/k_1)$. Namely,

$$\tau = \frac{\arctan(\omega_{ci}k_2/k_1)}{\omega_{ci}}. \quad (26)$$

Taking the derivative of τ with respect to ω_{ci} for equation (24), we can obtain

$$\frac{d\tau}{d\omega_{ci}} = \frac{1}{\omega_{ci}^2}\left(\frac{\eta\omega_{ci}}{1+(\eta\omega_{ci})^2} - \arctan(\eta\omega_{ci})\right), \quad (27)$$

where $\eta = k_2/k_1$. According to Lemma 4, τ decreases as ω_{ci} increases.

Then,

$$\omega_{ci} > \sqrt{\frac{\lambda_i^2 k_2^2 + \sqrt{\lambda_i^4 k_2^4 + \lambda_i^2 k_1^2}}{2}}. \quad (28)$$

From (26), (28), and Lemma 3, we can obtain

$$\tau^* < \frac{\arctan\left((k_2/k_1)\sqrt{\left(\lambda_{\max}^2 k_2^2 + \sqrt{\lambda_{\max}^4 k_2^4 + 4\lambda_{\max}^2 k_1^2}\right)/2}\right)}{\sqrt{\left(\lambda_{\max}^2 k_2^2 + \sqrt{\lambda_{\max}^4 k_2^4 + 4\lambda_{\max}^2 k_1^2}\right)/2}}, \quad (29)$$

where $\lambda_{\max}$ is the maximum eigenvalue of L_s. □

3.2. Bipartite Consensus under Directed Topology.

We will study the bipartite consensus of heterogeneous multiagent systems with diverse input delays under directed topology in this section. The control protocols are designed as follows:

$$\dot{x}_i(t) = v_i(t),$$

$$\dot{v}_i(t) = k_1 \sum_{j\in N_i} |a_{ij}|\left(\text{sgn}(a_{ij})x_j(t-\tau_i) - x_i(t-\tau_i)\right) + k_1 \sum_{j\in N_l} |a_{ij}|\text{sgn}(a_{ij})x_j(t-\tau_i)$$

$$+ k_2 \sum_{j\in N_i} |a_{ij}|\left(\text{sgn}(a_{ij})v_j(t-\tau_i) - v_i(t-\tau_i)\right) + k_2 \sum_{j\in N_l} |a_{ij}|\text{sgn}(a_{ij})v_j(t-\tau_i), \quad i = 1, 2, \ldots, m, \quad (30)$$

$$\dot{x}_l(t) = v_l(t-\tau_l) + k_2 \sum_{j\in N_l} |a_{lj}|\left(\text{sgn}(a_{lj})x_j(t-\tau_l) - x_l(t-\tau_l)\right)$$

$$+ k_2 \sum_{j\in N_i} |a_{lj}|\text{sgn}(a_{lj})x_j(t-\tau_l), \quad (31)$$

$$\dot{v}_l(t) = k_1 \sum_{j\in N_l} |a_{lj}|\left(\text{sgn}(a_{lj})x_j(t) - x_l(t)\right) + k_1 \sum_{j\in N_i} |a_{lj}|\text{sgn}(a_{lj})x_j(t), \quad l = m+1, m+2, \ldots, n,$$

where $k_1 > 0, k_2 > 0$ are the control gains, N_i and N_l represent the neighborhood of the agent i and l, and τ_i and τ_l represent the input delay of the agent i and l.

Lemma 8. *For the heterogeneous multiagent systems (30) and (31), if and only if the Laplacian matrix L_s has at least two zero eigenvalues, the real parts of the rest of eigenvalues*

are positive, and satisfy the condition of inequality (32), and the systems can achieve bipartite consensus:

$$\frac{\lambda_i \sqrt{k_1^2 + \omega_{ci}^2 k_2^2}}{\omega_{ci}^2} < 1, \tag{32}$$

where λ_i is the eigenvalue of L_s, and ω_{ci} satisfies

$$\omega_{ci}\tau = \arctan\left(\frac{\omega_{ci}k_2}{k_1}\right) + \arctan\left(\frac{\mathrm{Im}(\lambda_i)}{\mathrm{Re}(\lambda_i)}\right). \tag{33}$$

Proof. The Laplace transform of (30) and (31):

$$sX_i(s) = V_i(s),$$
$$sV_i(s) = k_1 \sum_{j\in N_i} |a_{ij}|\left(\mathrm{sgn}(a_{ij})X_j(s) - X_i(s)\right)e^{-\tau_i s} + k_1 \sum_{j\in N_l} |a_{ij}|\left(\mathrm{sgn}(a_{ij})X_j(s)\right)e^{-\tau_i s}$$
$$+ k_2 \sum_{j\in N_i} |a_{ij}|\left(\mathrm{sgn}(a_{ij})V_j(s) - V_i(s)\right)e^{-\tau_i s} + k_2 \sum_{j\in N_l} |a_{ij}|\left(\mathrm{sgn}(a_{ij})X_j(s)\right)e^{-\tau_i s}, \quad i = 1, 2, \ldots, m, \tag{34}$$

$$sX_l(s) = V(s)e^{-\tau_l s} + k_2 \sum_{j\in N_l} |a_{lj}|\left(\mathrm{sgn}(a_{lj})X_j(s) - X_l(s)\right)e^{-\tau_l s}$$
$$+ k_2 \sum_{j\in N_l} |a_{lj}|\mathrm{sgn}(a_{lj})X_j(s)e^{-\tau_l s}, \tag{35}$$
$$sV_l(s) = k_1 \sum_{j\in N_l} |a_{lj}|\left(\mathrm{sgn}(a_{lj})X_j(s) - X_l(s)\right) + k_1 \sum_{j\in N_i} |a_{lj}|\mathrm{sgn}(a_{lj})V_j(s), \quad l = m+1, m+2, \ldots, n.$$

From Assumption 1, (34), and (35),

$$s^2 X(s) = -(k_1 + k_2 s)X(s)L_s e^{-\tau s}. \tag{36}$$

Then, the characteristic root of systems (31) and (32) is

$$\det\left(s^2 I + (k_1 + k_2 s)L_s e^{-\tau s}\right) = 0. \tag{37}$$

Let $\lambda_i, i = 1, 2, \ldots, n$ be the eigenvalue of L_s. Assume $\lambda_1 = \lambda_2 = 0$, $\lambda_i > 0$, $i = 3, 4, \ldots, n$; then, (37) is equal to

$$s^4 \prod_{i=3,\ldots,n} \left(s^2 + \lambda_i(k_1 + k_2 s)e^{-\tau s}\right) = 0. \tag{38}$$

Obviously, we know that the equation has four zero roots, and then we can analyze the rest of the characteristic roots of the equation. For

$$s^2 + \lambda_i(k_1 + k_2 s)e^{-\tau s} = 0, i = 3, 4, \ldots, n, \tag{39}$$

let $h(s) = 1 + g_i(j\omega) = 0$. Therefore, equation (39) can be written as $1 + \lambda_i(k_1 + k_2 s)e^{-\tau s}/s^2 = 0$, where $g_i(j\omega) = \lambda_i(k_1 + k_2 s)e^{-\tau s}/s^2$. Based on Nyquist's criterion, if and only if curve $g_i(j\omega)$ does not include point $(-1, j0)$, the characteristic root of equation (39) is located on the left half-plane of the complex plane. Then,

$$g_i(j\omega) = \frac{|\lambda_i|\sqrt{k_1^2 + \omega_{ci}^2 k_2^2}}{\omega_{ci}^2}$$
$$\cdot e^{-j\left(\omega\tau + \pi - \arctan(\omega k_2/k_1) - \arctan(\mathrm{Im}(\lambda_i)/\mathrm{Re}(\lambda_i))\right)}. \tag{40}$$

Therefore,

$$|g_i(j\omega)| = \frac{|\lambda_i|\sqrt{k_1^2 + \omega_{ci}^2 k_2^2}}{\omega_{ci}^2},$$
$$\arg(g_i(j\omega)) = -\omega\tau + \arctan\left(\frac{\omega k_2}{k_1}\right) + \arctan\left(\frac{\mathrm{Im}(\lambda_i)}{\mathrm{Re}(\lambda_i)}\right), \tag{41}$$

where $\arg(\cdot)$ represents the phase. And it can be seen that $|g_i(j\omega)|$ monotonically decreases for $\omega \in (0, +\infty)$. When curve $|g_i(j\omega)|$ crosses the real axis for the first time, ω_{ci} satisfies
$-\omega\tau + \arctan(\omega k_2/k_1) + \arctan(\mathrm{Im}(\lambda_i)/\mathrm{Re}(\lambda_i)) = 0$.

In addition, if the characteristic root of (37) falls on the left half-plane, there is

$$|g_i(j\omega)| = \frac{|\lambda_i|\sqrt{k_1^2 + \omega_{ci}^2 k_2^2}}{\omega_{ci}^2} < 1. \tag{42}$$

In other words,

$$\frac{|\lambda_i|\sqrt{k_1^2 + \omega_{ci}^2 k_2^2}}{\omega_{ci}^2} < 1. \tag{43}$$

Therefore, except for the four zero roots, all the characteristic roots of (37) are located in the left half-plane. According to Lemma 6 and Theorem 1, we can get $\alpha = a[1, \ldots, 1]^T$ and $\beta = b[1, \ldots, 1]^T$. □

Theorem 2. *For the heterogeneous multiagent systems (30) and (31) under directed communication topology, the systems can achieve bipartite consensus if the largest input delay satisfies $\tau_{\max} < \tau^* = \min(\tau_a, \tau_b)$, where $\tau_a = \arctan(k_2/k_1 \sqrt{|\lambda|_{\max}^2 k_2^2 + \sqrt{|\lambda|_{\max}^4 k_2^4 + 4|\lambda|_{\max}^2 k_1^2}/2}) + \theta_{\max}/\sqrt{|\lambda|_{\max}^2 k_2^2 + \sqrt{|\lambda|_{\max}^4 k_2^4 + 4|\lambda|_{\max}^2 k_1^2}/2}$.*

$\theta_{\max} = \arctan(\mathrm{Im}(\lambda_i)/\mathrm{Re}(\lambda_i))$, $|\lambda|_{\max}$ is the maximum modulus of λ_i, $\tau_b = \arctan(\widetilde{\omega}_{\max}k_2/k_1) - \theta_{\max}/\widetilde{\omega}_{\max}$, $\widetilde{\omega}_{\max} = \max_{3\le i\le n}\{\widetilde{\omega}_{ci}\}$, $\widetilde{\omega}_{ci}$ is the root of equation, $1/\omega_{ci}(\eta\omega_{ci}/1 + (\eta\omega_{ci})^2) - \arctan(\eta\omega_{ci}) - \arctan(\mathrm{Im}(\lambda_i)/\mathrm{Re}(\lambda_i)) = 0$, and $\eta = k_2/k_1$.
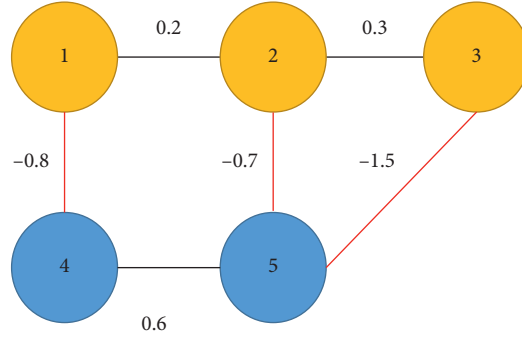
FIGURE 1: Undirected topology of a multiagent system.

(a)

(b)
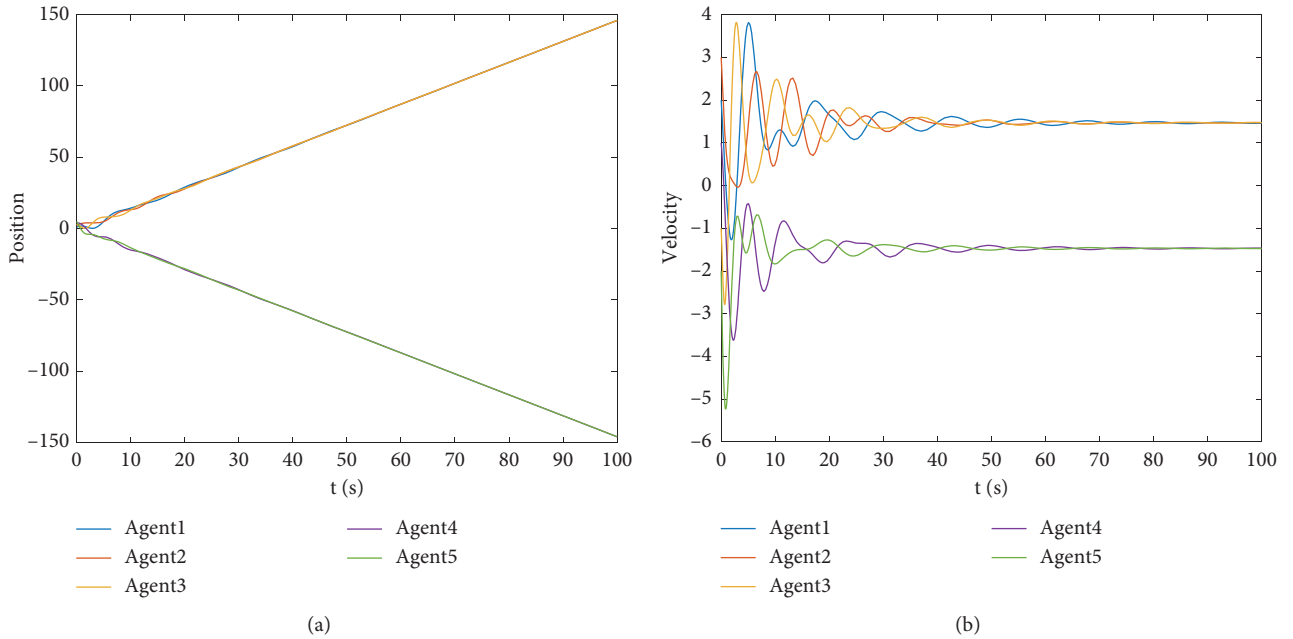
FIGURE 2: $\tau_1 = 0.5, \tau_2 = 0.4, \tau_3 = 0.3, \tau_4 = 0.2,$ and $\tau_5 = 0.1$. (a) Position trajectories of all agents. (b) Velocity trajectories of all agents.

Proof. From (33), we can obtain

$$\tau = \frac{\arctan\left(\omega_{ci} k_2 / k_1\right) + \arctan\left(\operatorname{Im}\left(\lambda_i\right) / \operatorname{Re}\left(\lambda_i\right)\right)}{\omega_{ci}}. \quad (44)$$

Taking the derivative of τ with respect to ω_{ci} for equation (44), we can obtain

$d\tau / d\omega_{ci} = (1/\omega_{ci}^2)(\eta\omega_{ci} / 1 + (\eta\omega_{ci})^2 - \arctan(\eta\omega_{ci}) - \arctan(\operatorname{Im}(\lambda_i) / \operatorname{Re}(\lambda_i)))$, where $\eta = k_2 / k_1$.

According to Lemma 5, if $m = \arctan(\operatorname{Im}(\lambda_i) / \operatorname{Re}(\lambda_i)) > 0$, then $\omega_{ci} > 0$ and $d\tau / d\omega_{ci} < 0$. According to (32), we can obtain $\omega_{ci} > \sqrt{|\lambda_i|^2 k_2^2 + \sqrt{|\lambda_i|^4 k_2^4 + |\lambda_i|^2 k_1^2} / 2}$.

Then, using Lemma 8, we have. $\tau = \arctan\left(k_2 / k_1 \sqrt{|\lambda_i|^2 k_2^2 + \sqrt{|\lambda_i|^4 k_2^4 + 4|\lambda_i|^2 k_1^2} / 2}\right) + \arctan(\operatorname{Im}(\lambda_i) / \operatorname{Re}(\lambda_i)) / \sqrt{|\lambda_i|^2 k_2^2 + \sqrt{|\lambda_i|^4 k_2^4 + 4|\lambda_i|^2 k_1^2} / 2}$.

According to Lemma 5, if $-\pi / 2 < m = \arctan(\operatorname{Im}(\lambda_i) / \operatorname{Re}(\lambda_i)) < 0$, then there exists $\widetilde{\omega}_{ci} > 0$, when $\omega_{ci} > \widetilde{\omega}_{ci}$ and $d\tau / d\omega_{ci} < 0$. $\widetilde{\omega}_{ci}$ is the root of

$$\frac{1}{\omega_{ci}}\left(\eta\omega_{ci} / 1 + (\eta\omega_{ci})^2\right) - \arctan(\eta\omega_{ci}) - \arctan(\operatorname{Im}(\lambda_i) / \operatorname{Re}(\lambda_i)) = 0, \quad (45)$$

where $\eta = k_2 / k_1$.

Similarly, using Lemma 8, we have $\tau = \arctan(\omega_{ci} k_2 / k_1) + \arctan(\operatorname{Im}(\lambda_i) / \operatorname{Re}(\lambda_i)) / \omega_{ci}$.

In conclusion, according to Lemma 3, the maximum allowable upper bound of the system is $\tau^* = \min(\tau_a, \tau_b)$, where

$$\tau_a = \frac{\arctan\left((k_2 / k_1)\sqrt{|\lambda|_{\max}^2 k_2^2 + \sqrt{|\lambda|_{\max}^4 k_2^4 + 4|\lambda|_{\max}^2 k_1^2} / 2}\right) + \theta_{\max}}{\sqrt{|\lambda|_{\max}^2 k_2^2 + \sqrt{|\lambda|_{\max}^4 k_2^4 + 4|\lambda|_{\max}^2 k_1^2} / 2}},$$

$$\tau_b = \frac{\arctan(\widetilde{\omega}_{\max} k_2 / k_1) - \theta_{\max}}{\widetilde{\omega}_{\max}},$$

$$(46)$$
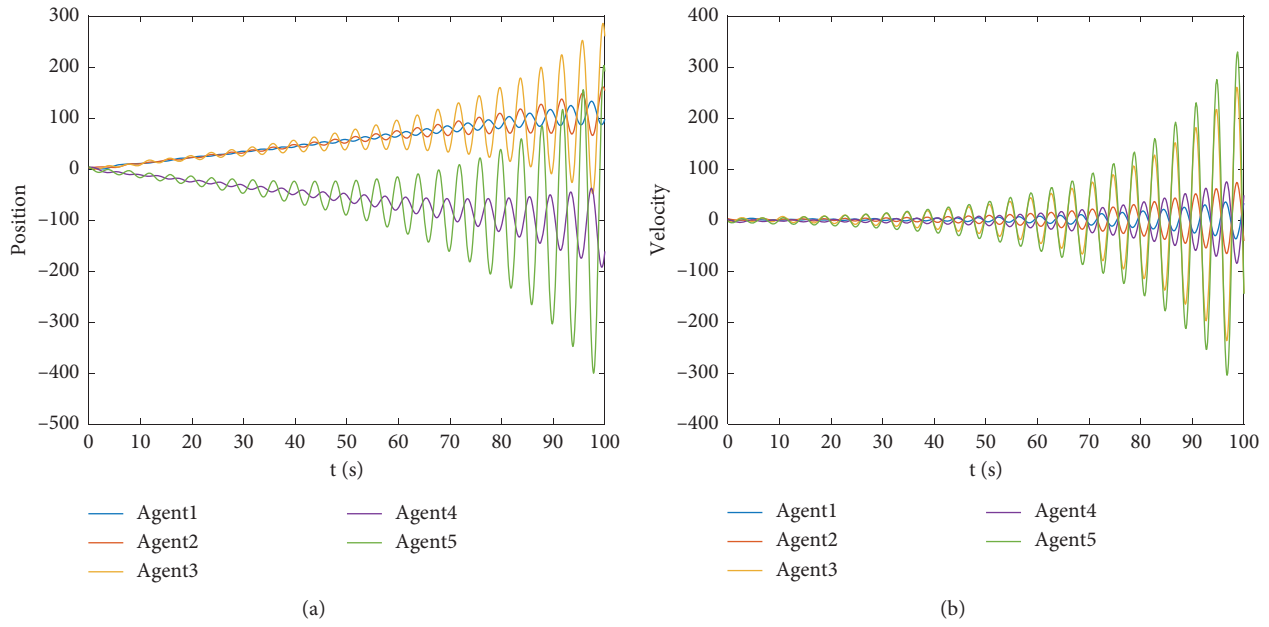
FIGURE 3: $\tau_1 = 0.4$, $\tau_2 = 0.3$, $\tau_3 = 0.4$, $\tau_4 = 0.3$, and $\tau_5 = 0.6$. (a) Position trajectories of all agents. (b) Velocity trajectories of all agents.
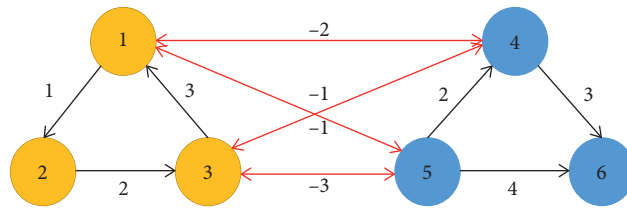
FIGURE 4: Directional topology of a multiagent system.
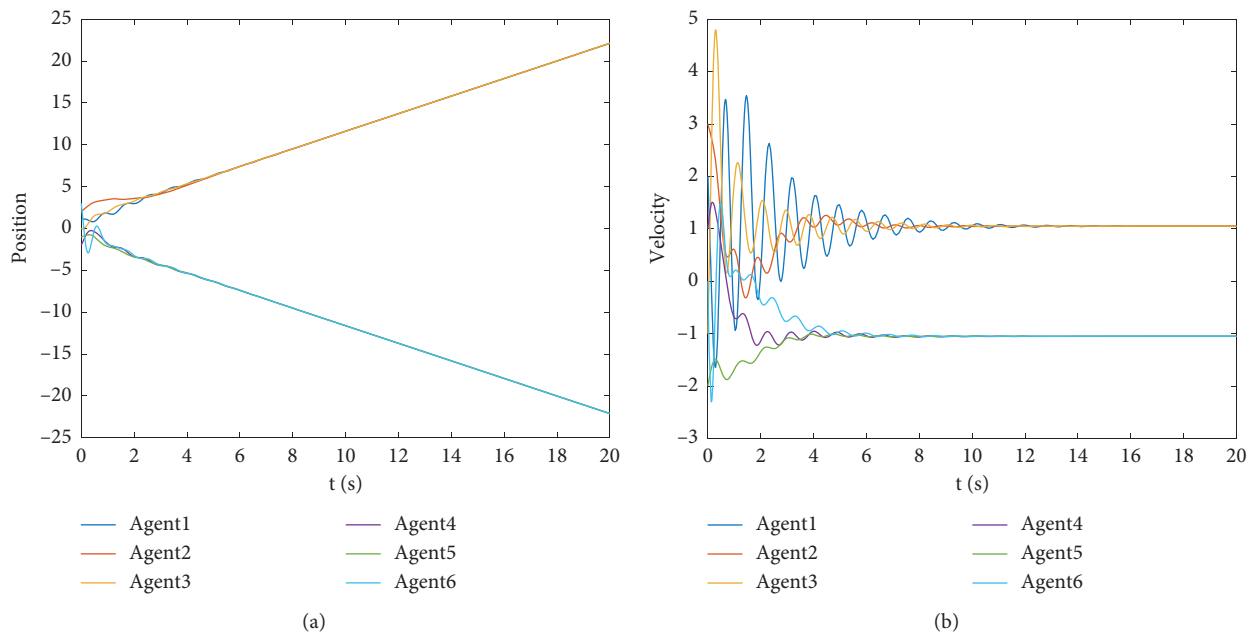
FIGURE 5: $\tau_1 = 0.17$, $\tau_2 = 0.16$, $\tau_3 = 0.15$, $\tau_4 = 0.14$, $\tau_5 = 0.13$, and $\tau_6 = 0.12$. (a) Position trajectories of all agents. (b) Velocity trajectories of all agents.

(a)

(b)
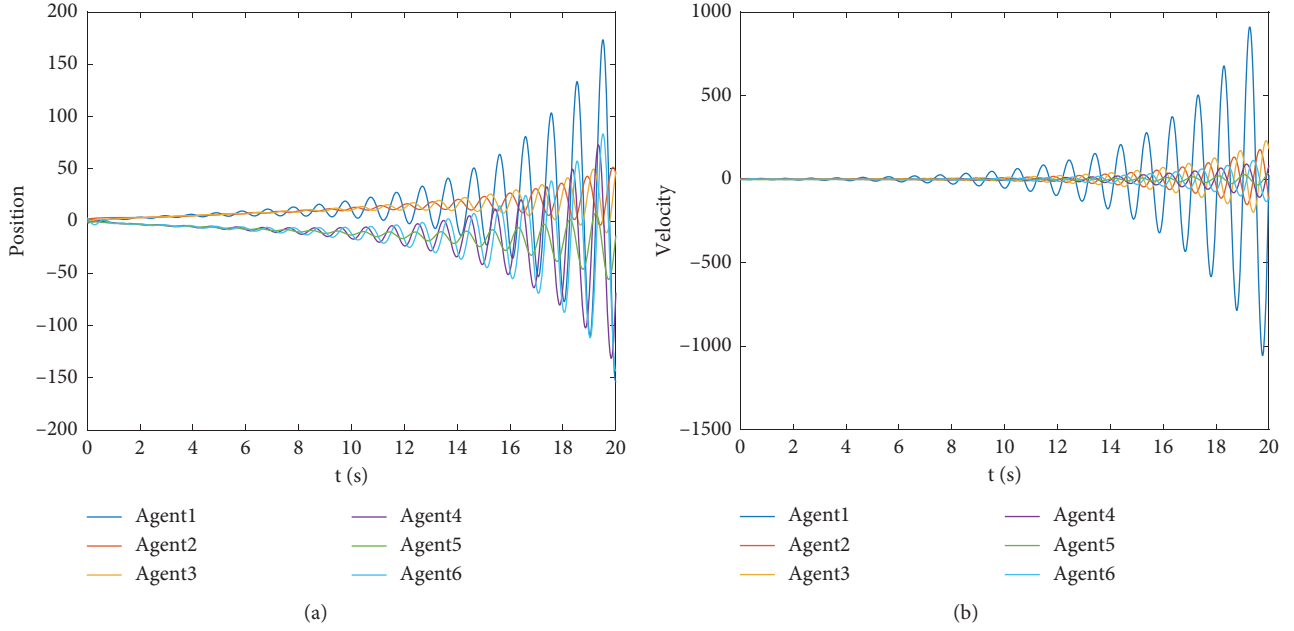
FIGURE 6: $\tau_1 = 0.22, \tau_2 = 0.14, \tau_3 = 0.15, \tau_4 = 0.16, \tau_5 = 0.15,$ and $\tau_6 = 0.14$. (a) Position trajectories of all agents. (b) Velocity trajectories of all agents.

$\theta_{\max} = \arctan(\operatorname{Im}(\lambda_i)/\operatorname{Re}(\lambda_i)), \widetilde{\omega}_{\max} = \max_{3 \leq i \leq n}\{\widetilde{\omega}_{ci}\}, \widetilde{\omega}_{ci}$ is the root of equation $1/\omega_{ci}(\eta\omega_{ci}/1 + (\eta\omega_{ci})^2) - \arctan(\eta\omega_{ci}) - \arctan(\operatorname{Im}(\lambda_i)/\operatorname{Re}(\lambda_i)) = 0$, and $\eta = k_2/k_1$. □

4. Numerical Examples and Simulations

Example 1. We will test and verify the results obtained by a multiagent system with five agents in this section. The initial conditions are randomly set and the topology is shown in Figure 1. The maximum eigenvalue of L_s is $\lambda_{\max} = 4.0445$. $k_1 = 0.45$ and $k_2 = 0.3$. According to Theorem 1, we obtain $\tau^* < 0.5057$. Let $\tau_1 = 0.5, \tau_2 = 0.4, \tau_3 = 0.3, \tau_4 = 0.2,$ and $\tau_5 = 0.1$. It is clear that bipartite consensus can be achieved when the input delays are below the upper bound of the allowable delay (see Figure 2). Let $\tau_1 = 0.4, \tau_2 = 0.3, \tau_3 = 0.4, \tau_4 = 0.3,$ and $\tau_5 = 0.6$. The bipartite consensus cannot be achieved when one of input delays exceeds the upper bound of the allowable delay (see Figure 3).

Example 2. We will test and verify the results obtained by a multiagent system with six agents in this section. The initial conditions are randomly set and the topology is shown in Figure 4. The maximum eigenvalue of L_s is $\lambda_{\max} = 7.9101 + 1.3498i$. Let $k_1 = 1$ and $k_2 = 1$. According to Theorem 2, we obtain $\tau^* < 0.2$. When $\tau_1 = 0.17, \tau_2 = 0.16, \tau_3 = 0.15, \tau_4 = 0.14, \tau_5 = 0.13,$ and $\tau_6 = 0.12$, bipartite consensus can be achieved (see Figure 5). When $\tau_1 = 0.22, \tau_2 = 0.14, \tau_3 = 0.15, \tau_4 = 0.16, \tau_5 = 0.15,$ and $\tau_6 = 0.14$, bipartite consensus cannot be achieved (see Figure 6).

5. Conclusions

Different from the previous work, we consider bipartite consensus of heterogeneous multiagent systems with diverse input delays. Based on the matrix theory and the frequency domain theory, the maximum input delay for the systems to achieve bipartite consensus is obtained. The future work will extend the existing work to time-varying input delays.

Data Availability

No data were used to support this study.

Conflicts of Interest

The authors declare that there are no conflicts of interest regarding the publication of this paper.

Acknowledgments

References

[1] R. Olfati-Saber and R. M. Murray, "Consensus problems in networks of agents with switching topology and time-delays," *IEEE Transactions on Automatic Control*, vol. 49, no. 9, pp. 1520–1533, 2004.

[2] X. Dong, B. Yu, Z. Shi, and Y. Zhong, "Time-varying formation control for unmanned aerial vehicles: theories and applications," *IEEE Transactions on Control Systems Technology*, vol. 23, no. 1, pp. 340–348, 2015.

[3] S.-L. Du, X.-M. Sun, M. Cao, and W. Wang, "Pursuing an evader through cooperative relaying in multi-agent surveillance networks," *Automatica*, vol. 83, pp. 155–161, 2017.

[4] C. Song, L. Liu, G. Feng, and S. Xu, "Coverage control for heterogeneous mobile sensor networks on a circle," *Automatica*, vol. 63, pp. 349–358, 2016.

[5] Z.-X. Li and H.-B. Ji, "Robust delay-dependent H∞ consensus control for multi-agent systems with input delays," *Acta Automatica Sinica*, vol. 40, no. 11, pp. 2556–2562, 2014.

[6] T. Qi, L. Qiu, and J. Chen, "MAS consensus and delay limits under delayed output feedback," *IEEE Transactions on Automatic Control*, vol. 62, no. 9, pp. 4660–4666, 2017.

[7] X. Xu, L. Liu, and G. Feng, "Consensus of discrete-time linear multiagent systems with communication, input and output delays," *IEEE Transactions on Automatic Control*, vol. 63, no. 2, pp. 492–497, 2018.

[8] Y.-H. Lan, B. Wu, Y.-X. Shi, and Y.-P. Luo, "Iterative learning based consensus control for distributed parameter multiagent systems with time-delay," *Neurocomputing*, vol. 357, pp. 77–85, 2019.

[9] J. Liu, Y. Zhang, C. Sun, and Y. Yu, "Fixed-time consensus of multi-agent systems with input delay and uncertain disturbances via event-triggered control," *Information Sciences*, vol. 480, pp. 261–272, 2019.

[10] F. Ye, W. Zhang, and L. Ou, "H2 consensus control of time-delayed multi-agent systems: a frequency-domain method," *ISA Transactions*, vol. 66, pp. 437–447, 2017.

[11] F. Ye, B. Sun, L. Ou, and W. Zhang, "Disturbance observer-based control for consensus tracking of multi-agent systems with input delays from a frequency domain perspective," *Systems & Control Letters*, vol. 114, pp. 66–75, 2018.

[12] A. S. Morteza, "Networks, crowds and markets: reasoning about a highly connected world," *Journal of the Royal Statistical Society*, vol. 175, no. 4, p. 1073, 2012.

[13] C. Parisien, C. H. Anderson, and C. Eliasmith, "Solving the problem of negative synaptic weights in cortical models," *Neural Computation*, vol. 20, no. 6, pp. 1473–1494, 2008.

[14] C. Altafini, "Consensus problems on networks with antagonistic interactions," *IEEE Transactions on Automatic Control*, vol. 58, no. 4, pp. 935–946, 2013.

[15] J. P. Hu, Z. H. Xiao, Y. L. Zhou, and J. Y. Yu, "Formation control over antagonistic networks," in *Proceedings of the 32nd Chinese Control Conference*, pp. 6879–6884, Xi'an, China, 2013.

[16] J. Qin, W. Fu, W. X. Zheng, and H. Gao, "On the bipartite consensus for generic linear multiagent systems with input saturation," *IEEE Transactions on Cybernetics*, vol. 47, no. 8, pp. 1948–1958, 2017.

[17] X. Gong, J. J. R. Liu, Y. M. Wang, and Y. K. Cui, "Distributed finite-time bipartite consensus of multi-agent systems on directed graphs: theory and experiment in nano-quadcopters formation," *Journal of the Franklin Institute*, In press, 2020.

[18] P. L. Li, Y. Liu, Y. D. Zhao, and J. Yang, "Consensus control for second-order multi-agent with time-delay on antagonistic networks," in *Proceedings of the 35th Chinese Control Conference*, pp. 8066–8071, Chengdu, China, 2016.

[19] H. Tian, C. L. Liu, and G. Y. Liu, "Bipartite consensus problem of second-order Multi-agent systems with disturbances," in *15th International Conference on Control, Automation, Robotics and Vision*, Singapore, Singapore, November 2018.

[20] X. Guo, J. Lu, A. Alsaedi, and F. E. Alsaadi, "Bipartite consensus for multi-agent systems with antagonistic interactions and communication delays," *Physica A: Statistical Mechanics and Its Applications*, vol. 495, pp. 488–497, 2018.

[21] H. Wu, K. Gao, and B. R. An, "A class of second-order consensus protocol in multi-agent systems with multiple input delays," *Journal of Systems Science and Complexity*, vol. 32, no. 5, pp. 1–10, 2019.

[22] J. Ling, J. Liang, and M. Du, "Bipartite consensus problems on Second-order signed networks with heterogeneous topologies," *IEEE Access*, vol. 8, pp. 39420–39427, 2020.

[23] B. Sourav and P. Suraijt, "Lag-bipartite consensus of linear multi-agent systems under saturating input over signed graph," *IET Control Theory & Applications*, vol. 13, no. 3, pp. 434–443, 2019.

[24] J. Liu, H. Li, and J. Luo, "Bipartite consensus in Networked Euler-Lagrange systems with uncertain parameters under a Cooperation-Competition network topology," *IEEE Control Systems Letters*, vol. 3, no. 3, pp. 494–498, 2019.

[25] H. Zhang, Y. Cai, Y. Wang, and H. Su, "Adaptive bipartite event-triggered output consensus of heterogeneous linear multiagent systems under fixed and switching topologies," *IEEE Transactions on Neural Networks and Learning Systems*, pp. 1–15, 2020.

[26] Y. L. Cai, H. G. Zhang, Y. Liu, and Q. He, "Distributed bipartite finite-time event-triggered output consensus for heterogeneous linear multi-agent systems under directed signed communication topology," *Applied Mathematics and Computation*, vol. 378, pp. 1–18, 2020.

[27] E. Li, Q. Ma, and G. Zhou, "Bipartite output consensus for heterogeneous linear multi-agent systems with fully distributed protocol," *Journal of the Franklin Institute*, vol. 356, no. 5, pp. 2870–2884, 2019.

[28] Q. Ma, G. Zhou, and E. Li, "Adaptive bipartite output consensus of heterogeneous linear multi-agent systems with antagonistic interactions," *Neurocomputing*, vol. 373, pp. 50–55, 2020.

[29] J. Yu and L. Wang, "Group consensus of multi-agent systems with directed information exchange," *International Journal of Systems Science*, vol. 43, no. 2, pp. 334–348, 2012.

[30] G. G. Wen, Y. G. Yu, Z. X. Peng, and W. Hu, "Dynamical group consensus of heterogeneous multi-agent systems with input time delays," *Neurocomputing*, vol. 175, pp. 278–286, 2015.

[31] C. L. Liu and F. Liu, "Dynamical consensus seeking of heterogeneous multi-agent systems under input delays," *International Journal of Communication Systems*, vol. 26, pp. 1243–1258, 2012.

[32] L. Lin, B. Francis, and M. Maggiore, "Necessary and sufficient graphical conditions for formation control of unicycles," *IEEE Transactions on Automatic Control*, vol. 50, no. 1, pp. 121–127, 2005.

[33] W. Ren and E. Atkins, "Distributed multi-vehicle coordinated control via local information exchange," *International Journal of Robust & Nonlinear Control*, vol. 17, no. 10-11, pp. 1002–1033, 2007.

[34] L. H. Ji, X. H. Yu, and C. J. Li, "Group consensus for heterogeneous multi-agent systems in the competition networks

with input time delay," *IEEE Transactions on Systems, Man, and Cybernetics: Systems*, pp. 1–9, 2018.

[35] H. Ye, M.-M. Li, W.-G. Luo, and Y.-X. Qin, "Finite-Time consensus of heterogeneous multi-agent systems without velocity measurements and with disturbances via integral sliding mode control," *IEEE Access*, vol. 6, pp. 62255–62260, 2018.

[36] Y. J. Hong, J. P. Hu, and L. Gao, "Tracking control for multi-agent consensus with an active leader and variable topology," *Automatica*, vol. 42, no. 7, pp. 1177–1182, 2006.

WILEY | Hindawi

Research Article

Projection Synchronization of a Class of Complex Chaotic Systems with Both Uncertainty and Disturbance

Hongsheng Sha,[1] Guijuan Wang [ID],[2] Tao Hao,[3] and Zuoxun Wang [ID][1]

[1]*School of Electrical Engineering and Automation, Qilu University of Technology, Shandong Academy of Sciences, Jinan 250353, China*
[2]*School of Electrical Engineering and Automation, Shandong Jianzhu University, Jinan 250101, China*
[3]*School of Electrical Engineering and Automation, Shandong Labor Vocational and Technical College, Jinan 250353, China*

Correspondence should be addressed to Zuoxun Wang; wangzuoxun@126.com

This paper mainly investigates the projection synchronization of complex chaotic systems with both uncertainty and disturbance. Using the linear feedback method and the uncertainty and disturbance estimation- (UDE-) based control method, the projection synchronization of such systems is realized by two steps. In the first step, a linear feedback controller is designed to control the nominal complex chaotic systems to achieve projection synchronization. An UDE-based controller is proposed to estimate the whole of uncertainty and disturbance in the second step. Finally, numerical simulations verify the feasibility and effectiveness of the control method.

1. Introduction

The chaotic synchronization phenomenon that caused a great sensation in academia was firstly proposed by Pecora and Carroll in early 1990 [1]. They achieved chaotic synchronization of two identical systems with different initial conditions in electronic experiments. Until now, many types of chaotic synchronization have been discovered, such as complete synchronization, phase synchronization, lag synchronization, antisynchronization, and projection synchronization, and many other important results have been obtained (see references [2–8]). Especially, projective synchronization has received much attention due to its faster communication and proportionality between the dynamical systems. In case of projective synchronization, the master and the slave system can be synchronized up to a scaling factor and the scaling factor is a constant transformation between the driving and the response variables that can further increase the security of secure communication and the transmission speed of communication. It has potential application prospects in the field of chaotic secure communication.

Many control methods about chaotic projection synchronization have been reported [9–29]. However, most controllers are complicated in structure and difficult in design. Due to the complexity of structure, many control methods are not suitable for projective synchronization control of complex chaotic systems. Among these, the linear feedback controller, because of its simple structure, easy design, and good control effect, was used to realize the projection synchronization of given complex chaotic system. Moreover, in the simulation experiment, it is also proved that the linear feedback controller has a good experimental effect.

We note that most of the literature on solving the control problems of chaotic systems with external perturbations is generally complex and difficult to implement. Moreover, when designing the controller, the method to deal with the external disturbance is just simply to cancel the disturbance term from the formula of the controller, and it is not rigorous in nonlinear system control theory. In fact, in the field of nonlinear system control, the UDE-based controller can deal with many structured and unstructured robust control problems and has been applied to the engineering field in

some literatures [30–32]. In the simulation experiment, we have noticed that the UDE control method, which is composed of filters with appropriate bandwidth, has an ideal processing effect on the external disturbance of the system which is finally used by us.

The main contribution of this paper is to design a physical controller, which is simple in form, to realize the projection synchronization of a complex chaotic system. A linear feedback UDE-based control method is proposed by combining the linear feedback controller and the UED-based controller in two steps. A linear feedback control controller is designed for the nominal complex chaotic system in the first step. In the second step, an UDE-based controller is proposed to estimate the whole of uncertainty and disturbance. In the end, two complex chaotic systems with numerical simulations are used to verify the validity and effectiveness of the proposed theoretical results.

2. Preliminary

Consider the following controlled chaotic system:

$$\dot{X} = F(X) + B^*U^*, \tag{1}$$

where $X \in R^n$ is the state, $F(X) = (F_1(X), \cdots, F_n(X))^T$ is a continuous vector function, $B^* \in R^{n \times l}$, and $U^* = (U_1^*, \cdots, U_l^*)^T$ is the controller to be designed, $l \geq 1$.

Let system (1) be the master system; then, the slave system is given as follows:

$$\dot{Y} = F(Y), \tag{2}$$

where $Y \in R^n$ is the state and $F(Y) = (F_1(Y), \cdots, F_n(Y))^T$ is a continuous vector function.

Let $e = X - \alpha Y$, where $\alpha = \text{Diag}(\alpha_1, \cdots, \alpha_n)$, and the error system is shown as follows:

$$\dot{e} = F(X) - \alpha F(X) + B^*U^*, \tag{3}$$

where $e \in R^n$ is the state vector.

Definition 1. Consider the controlled error system (3). If $\lim_{t \to \infty} \|e(t)\| = 0$, then the master system (1) and the slave system (2) are called to achieve projection synchronization.

According to the results in [17], a lemma is introduced as follows.

Remark 1. The projection synchronization of system (1) is achieved if and only it is divided into the following two subsystems:

$$\dot{W}_m = A(Z)W_m, \tag{4}$$

$$\dot{Z} = H(Z, W_m), \tag{5}$$

where $W_m \in R^s$, $Z \in R^{n-s}$, $s \geq 1$, $A(Z) \in R^{s \times s}$ is a matrix with constants and variable Z, and $H(Z, W_m)$ is nonlinear continuous function.

An algorithm was also proposed in [17], by which we can solve the solutions of the projection synchronization and choose the variables W_m and Z.

2.1. Linear Feedback Control-Like Method for Chaos Projection Synchronization.
Note that the subsystem $\dot{W}_m = A(Z)W_m$ is a linear system with respect to variable W_m if the variable Z is considered a constant. Thus, the linear feedback control method is very suitable to be adopted to solve the projective synchronization problem of a given nominal complex chaotic system (i.e., there is no both uncertainty and disturbance). We briefly introduce the linear control method next.

Lemma 1. *Consider the following controlled system:*

$$\dot{W}_m = A(Z)W_m + B_1U, \tag{6}$$

where W_m, Z, $A(Z)$ are given in equations (4) and (5) and $B_1 \in R^{s \times r}$; then, the linear feedback controller is designed as follows:

$$U = K(Z)W_m, \tag{7}$$

where $K(Z)$ satisfies the matrix $(A(Z) + B_1K(Z))$ which is Hurwitz no matter what Z is.

2.2. UDE-Based Control Method.
It is well known that model uncertainty and external disturbance are inevitable in actual control problem, and the UDE-based control method [32] is an effective tool to deal with that problem.

Consider the following system:

$$\dot{x} = f(x) + u_d + bu, \tag{8}$$

where $x \in R^n$ is the state, $u_d = \Delta f(x) + d(t)$ is the whole of model uncertainty and external disturbance, $b \in R^{n \times k}$ is a constant matrix, $k \geq 1$, and $u \in R^k$ is the controller to be designed.

The stable linear reference model is given as

$$\dot{x}_m = A_mx_m + B_mC, \tag{9}$$

where $x_m \in R^n$ is the reference state, $A_m \in R^{n \times n}$ is the Hurwitz matrix, $B_m \in R^{n \times k}$, and $C \in R^{k \times 1}$ is a piecewise continuous and uniformly bounded command to the system.

Lemma 2 (see [32]). *Consider system (8). If the designed filter $g_f(t)$ satisfies the following condition:*

$$\tilde{u}_d = \hat{u}_d - u_d \longrightarrow 0, \tag{10}$$

where $\hat{u}_d = (\dot{x} - f(x) - bu) * g_f(t)$, then the UDE-based controller u is designed as

$$u = b^+\left\{-f(x) + \ell^{-1}\left[\frac{1}{1 - G_f(s)}\right] * (A_mx + B_mC - Ke)\right\}$$

$$- b^+\left\{\ell^{-1}\left[\frac{sG_f(s)}{1 - G_f(s)}\right] * x(t)\right\}, \tag{11}$$

where ℓ^{-1} denotes the inverse Laplace transform operator, $b^+ = (b^Tb)^{-1}b^T$, $*$ is the convolution operator, and $G_f(s) = \ell[g_f(t)]$.

Remark 2. According to the existing result in [32], the following two filters are often used. One is the first-order low-pass filter:

$$G_f(s) = \frac{1}{\tau s + 1}. \tag{12}$$

The other is the secondary filter:

$$G_f(s) = \frac{as + c - w_0^2}{s^2 + as + c}, \tag{13}$$

where $w_0 = 4\pi$, $a = 10w_0$, and $c = 100w_0$.

3. Main Results

In this section, the UDE-based linear feedback control method is proposed in two steps. In the first step, the linear feedback control method is proposed for the nominal system. The UDE-based control method is given in the second step.

3.1. Linear Feedback Control Method for Projection Synchronization. Consider the following nominal system:

$$\dot{X} = F(X) + BU, \tag{14}$$

where $X \in R^n$ is the state vector, $F(X) = (F_1(X), \cdots, F_n(X))^T$ is a continuous function, $B \in R^{n \times r}, r \geq 1$, $U = (U_1, \cdots, U_r)^T$ is the linear feedback controller to be designed, and $(F(X), B)$ is assumed to be controllable.

If the projection synchronization of system (14) exists, then it can be divided into the following two subsystems:

$$\dot{W}_m = A(Z)W_m + B_1U, \tag{15}$$

$$\dot{Z} = H(Z, W_m), \tag{16}$$

where W_m, Z, $A(Z)$, $H(Z, W_m)$ are given in equations (4) and (5), respectively, $B_1 \in R^{s \times r}$ is given in equation (6), and $(A(Z), B_1)$ is also controllable.

The corresponding slave system is presented as follows:

$$\dot{W}_s = A(Z)W_s, \tag{17}$$

where $H(Z, W_m)$ is given in equation (15), $W_m \in R^r$, $Z \in R^{n-r}$, and $A(Z)$ is a constant matrix.

Let $e = W_m - \beta W_S$ be the error state, where the scalar $|\beta| \neq 0, 1$, and the error system is obtained as follows:

$$\dot{e} = A(Z)e + B_1U. \tag{18}$$

Theorem 1 Consider error system (18). *If $(A(Z), B_1)$ is controllable no matter what Z is, then the linear feedback controller U is designed as follows:*

$$U = K(Z)e, \tag{19}$$

where $K(Z)$ satisfies the matrix $(A(Z) + B_1K(Z))$ which is Hurwitz no matter what Z is; then, error system (18) is globally asymptotically stable. That is, the master system (15)

and the slave system (17) achieve the projection synchronization.

Proof. Since the matrix $(A(Z) + B_1K(Z))$ is Hurwitz no matter what Z is, error system (18) is globally asymptotically stable; therefore, the master system (15) and the slave system (17) achieve the projection synchronization. □

3.2. UDE-Based Control Method for Projection Synchronization. In this section, the UDE controller is proposed to cancel the uncertainty and disturbance of the complex chaotic system.

Consider the following controlled master system:

$$\dot{W}_m = A(Z)W_m + B_1V + U_d, \tag{20}$$

where W_m, Z, $A(Z)$, $H(Z, W_m)$ are given in equations (4) and (5), respectively, $B_1 \in R^{s \times r}$ is given in equation (6), $(A(Z), B_1)$ is controllable, $U_d = \Delta A(Z) + D(t)$, $\Delta A(Z)$ represents the uncertainty and $D(t)$ represents the disturbance, and V is the controller to be designed, in which

$$V = U + u_{ude}. \tag{21}$$

The corresponding salve system is

$$\dot{W}_s = A(Z)W_s. \tag{22}$$

Let $e = W_m - \beta W_s$ be the error state vector, where $|\beta| \neq 0, 1$; then, the corresponding error system is shown as follows:

$$\dot{e} = A(Z)e + u_d + B_1V. \tag{23}$$

The controller V is designed in two steps:

Step one: according to Theorem 1, the linear feedback controller U is designed for the nominal system.

Step two: the controller u_{ude} is proposed according to the following theorem.

Theorem 2 Consider error system (23). *If the designed filter $g_f(t)$ satisfies the following condition:*

$$\tilde{u}_d = \hat{u}_d - u_d \longrightarrow 0, \tag{24}$$

where $\hat{u}_d = (\dot{e} - A(Z, e) - B_1u_{ude}) * g_f(t)$, then the UDE-based controller u is designed as

$$u_{ude} = B_1^+ \left\{ \ell^{-1}\left[\frac{G_f}{1 - G_f(s)}\right] * A(Z, e) - \ell^{-1}\left[\frac{sG_f(s)}{1 - G_f(s)}\right] * e(t) \right\}, \tag{25}$$

where $A(Z, e) = (A(Z) + B_1K(Z))e$, $B_1^+ = (B_1^TB)^{-1}B_1^T$, ℓ^{-1} is the inverse Laplace transform, $*$ is the convolution sign, and $G_f(s) = \ell[g_f(t)]$.

Proof. Substituting V in (21) into system (23) results in

$$\dot{e} = A(Z)e + u_d + B_1V = (A(Z) + B_1K(Z))e + Bu_{ude} - u_d. \tag{26}$$

According to condition (24), it leads to
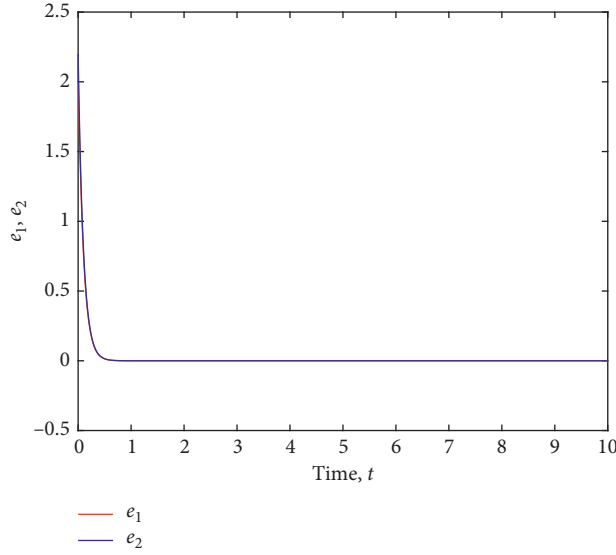
FIGURE 1: e_1, e_2 are asymptotically stable.
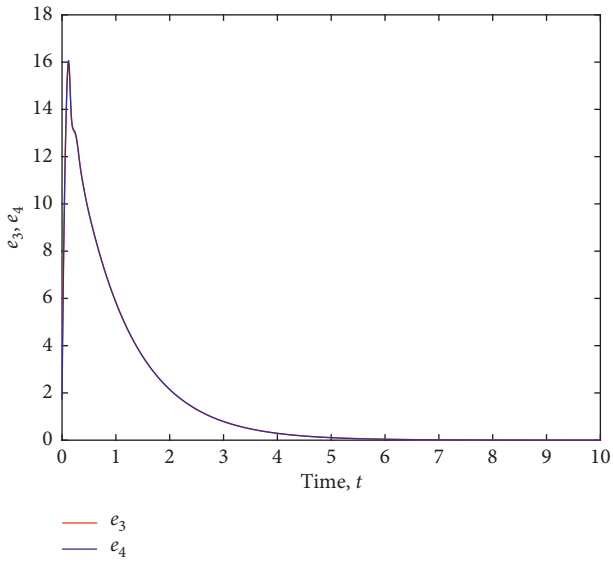
FIGURE 2: e_3, e_4 are asymptotically stable.

$$B_1 u_{ude} = -\hat{u}_d. \tag{27}$$

Thus,

$$\dot{e} = A(z) + BV + u_d = A(Z, e) + \tilde{u}_d \tag{28}$$

is globally asymptotically stable, which completes the proof.   □

4. Illustrative Example with Numerical Simulation

In this section, one example with numerical simulations is used to demonstrate the effectiveness and validity of the proposed results.

Consider the following complex Lorenz system:

$$\dot{x}_1 = 10(x_1 - x_2),$$

$$\dot{x}_2 = 110x_1 - x_1 x_3 - x_2, \tag{29}$$

$$\dot{x}_3 = -2x_3 + \frac{1}{2}(\overline{x}_1 x_2 + x_1 \overline{x}_2),$$

where $x_1 = x_1^r + j x_1^i$, $x_2 = x_2^r + j x_2^i$ are complex variables, x_3 is a real variable, $j^2 = -1$ represents imaginary unit, and $\overline{x}_1$ and $\overline{x}_2$ are complex conjugate variables of x_1, x_2, respectively.

Separating the real and imaginary parts of complex variables x_1, x_2 in system (29), i.e., setting $X_1 = x_1^r$, $X_2 = x_1^i$, $X_3 = x_2^r$, $X_4 = x_2^i$, and $X_5 = x_3$ representing x_5, a new real-variable system is shown as follows:

$$\dot{X}_1 = 10(X_3 - X_1),$$
$$\dot{X}_2 = 10(X_4 - X_2),$$
$$\dot{X}_3 = 110X_1 - X_1 X_5 - X_3, \tag{30}$$
$$\dot{X}_4 = 110X_2 - X_2 X_5 - X_4,$$
$$\dot{X}_5 = -2X_5 + X_1 X_3 + X_2 X_4.$$

4.1. The Existence of Projection Synchronization of the Complex Lorenz System. According to the results in [17], for system (30), the results are obtained as follows:

$$F_1(\alpha X) - \alpha_1 F_1(\alpha X) = 10(\alpha_3 - \alpha_1)X_3 \equiv 0,$$
$$F_2(\alpha X) - \alpha_2 F_2(\alpha X) = 10(\alpha_4 - \alpha_2)X_4 \equiv 0,$$
$$F_3(\alpha X) - \alpha_3 F_3(\alpha X) = (\alpha_1 - \alpha_1 \alpha_5)X_1 - (\alpha_3 - \alpha_1 \alpha_5)X_3 \equiv 0,$$
$$F_4(\alpha X) - \alpha_4 F_4(\alpha X) = (\alpha_2 - \alpha_2 \alpha_5)X_2 - (\alpha_4 - \alpha_2 \alpha_5)X_4 \equiv 0,$$
$$F_5(\alpha X) - \alpha_5 F_5(\alpha X) = (\alpha_5 - \alpha_1 \alpha_3)X_5 - (\alpha_1 \alpha_3 - \alpha_2 \alpha_4)X_1 X_3 \equiv 0.$$
$$\tag{31}$$

It results in
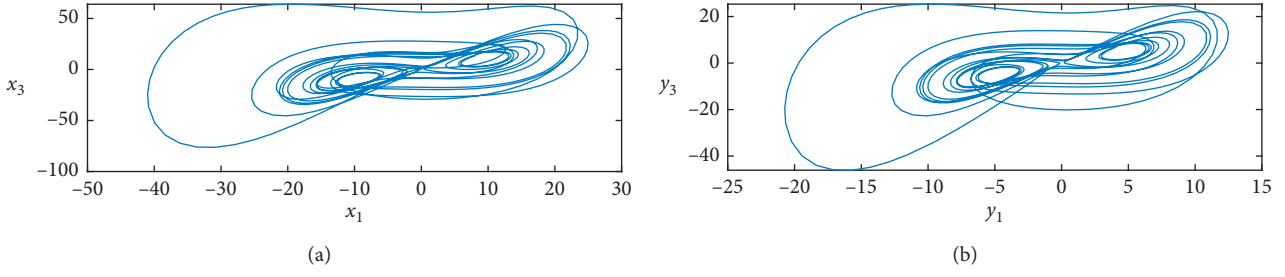
FIGURE 3: The phase portrait of master subsystem and the slave subsystem.
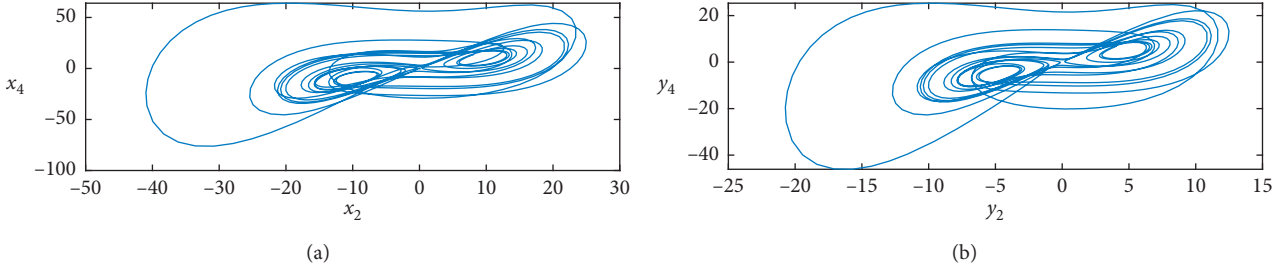
FIGURE 4: The phase portrait of master subsystem and the slave subsystem.
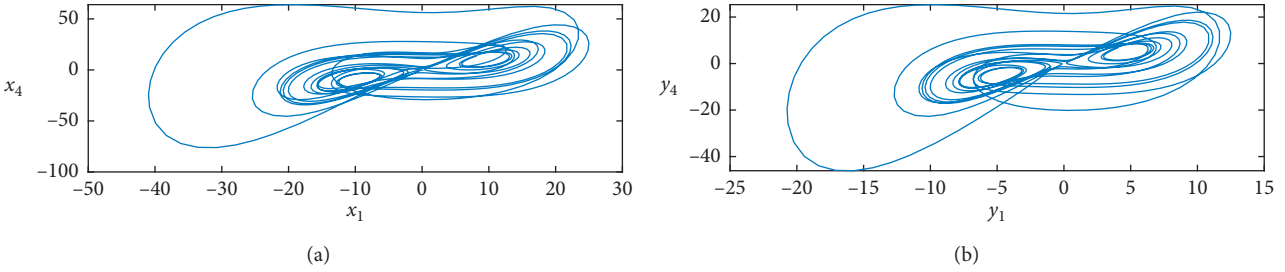
FIGURE 5: The phase portrait of master subsystem and the slave subsystem.

$$\alpha_1 = \alpha_3, \tag{32}$$

$$\alpha_2 = \alpha_4, \tag{33}$$

$$\begin{aligned}\alpha_1 &= \alpha_1\alpha_5,\\ \alpha_3 &= \alpha_1\alpha_5,\end{aligned} \tag{34}$$

$$\begin{aligned}\alpha_2 &= \alpha_2\alpha_5,\\ \alpha_4 &= \alpha_2\alpha_5,\end{aligned} \tag{35}$$

$$\begin{aligned}\alpha_5 &= \alpha_1\alpha_3,\\ \alpha_1\alpha_3 &= \alpha_2\alpha_4.\end{aligned} \tag{36}$$

It is easy to obtain that $\alpha = \mathrm{Diag}\,(\beta, \beta, \beta, \beta, 1)$ is the one solution of equations (32)–(35), where $|\beta| \neq 1$ is a nonzero scalar.

Thus, the master system (30) is divided into the following two subsystems:

$$\dot{W}_m = A(Z)W_m, \tag{37}$$

$$\dot{Z} = H(Z, W_m), \tag{38}$$

where

$$W_m = \begin{pmatrix} X_1 \\ \vdots \\ X_4 \end{pmatrix},$$

$$Z = X_5, \tag{39}$$

$$A(Z) = \begin{pmatrix} -10 & 0 & 10 & 0 \\ 0 & -10 & 0 & 10 \\ 110 - Z & 0 & -1 & 0 \\ 0 & 110 - Z & 0 & -1 \end{pmatrix},$$

$$H(Z, W_m) = -2Z + W_{m1}W_{m3} + W_{m2}W_{m4}. \tag{40}$$
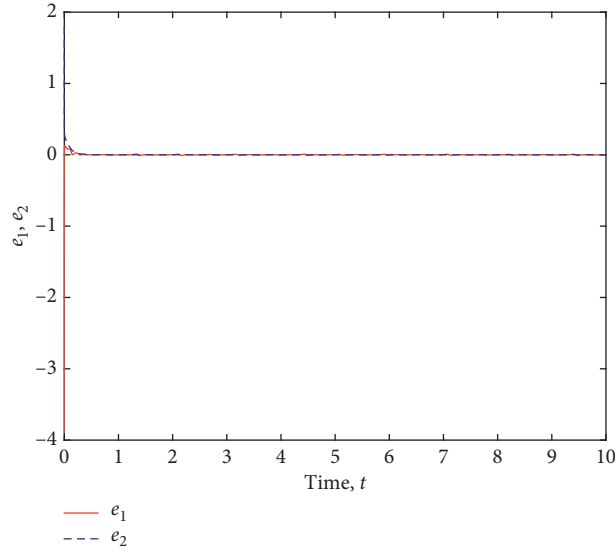
FIGURE 6: e_1, e_2 are asymptotically stable.
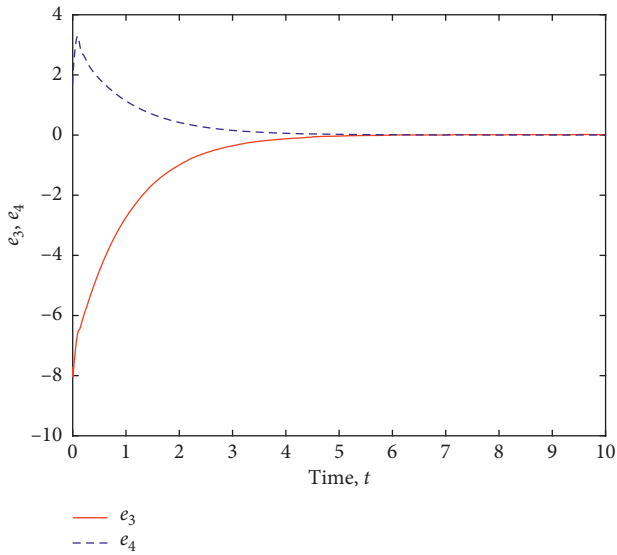
FIGURE 7: e_3, e_4 are asymptotically stable.

FIGURE 8: The phase portrait of master subsystem and the slave subsystem.

4.2. The UDE-Based Linear Feedback Controller Design.
The UDE-based linear feedback controller is designed by the following two steps.

Step one:

$$\dot{W}_m = A(Z)W_m + B_1U. \tag{41}$$

W_m, Z, $A(Z)$ are given in equations (38) and (39), respectively, and

$$B_1 = \begin{pmatrix} 1 & 0 \\ 0 & 1 \\ 0 & 0 \\ 0 & 0 \end{pmatrix}. \tag{42}$$

Then, the corresponding slave system is given as follows:

$$\dot{W}_s = A(Z)W_s. \tag{43}$$

$A(Z)$, Z are given in equations (38) and (39), respectively.

Let $e = W_m - \beta W_s$, where $\beta = 2$, and the uncontrolled error system is given as follows:

$$\begin{aligned}
\dot{e}_1 &= 10(e_3 - e_1), \\
\dot{e}_2 &= 10(e_4 - e_2), \\
\dot{e}_3 &= (110 - X_5)e_1 - e_3, \\
\dot{e}_4 &= (110 - X_5)e_2 - e_4.
\end{aligned} \tag{44}$$
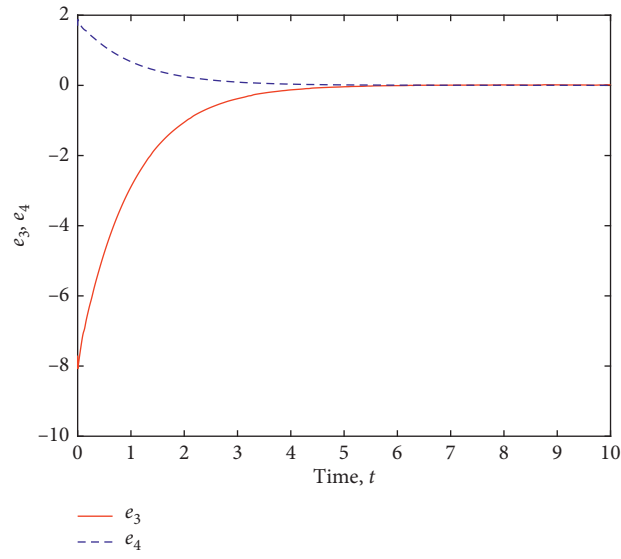
Figure 9: The phase portrait of master subsystem and the slave subsystem.

(a)

(b)
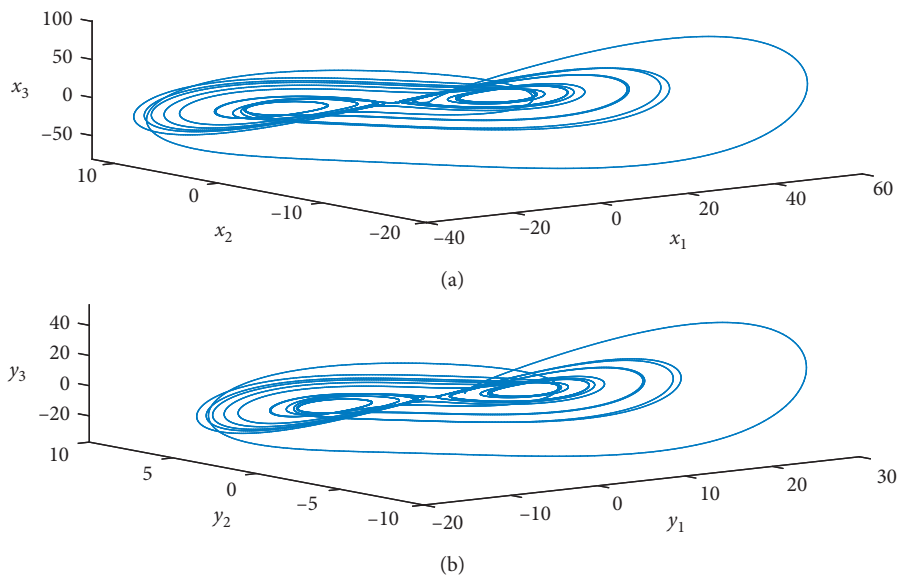
Figure 10: The phase portrait of master subsystem and the slave subsystem.

(a)
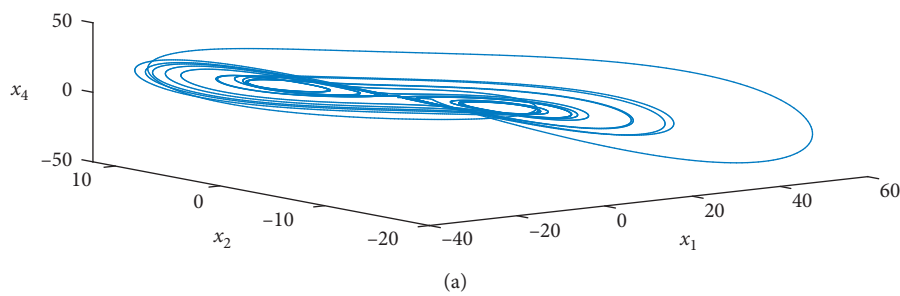
Figure 11: Continued.

(b)
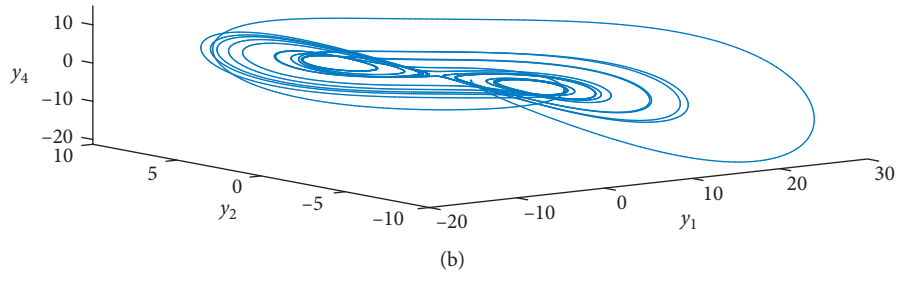
FIGURE 11: The phase portrait of master subsystem and the slave subsystem.

(a)

(b)
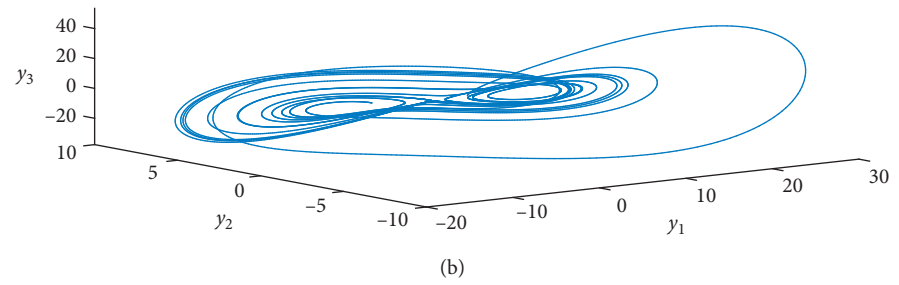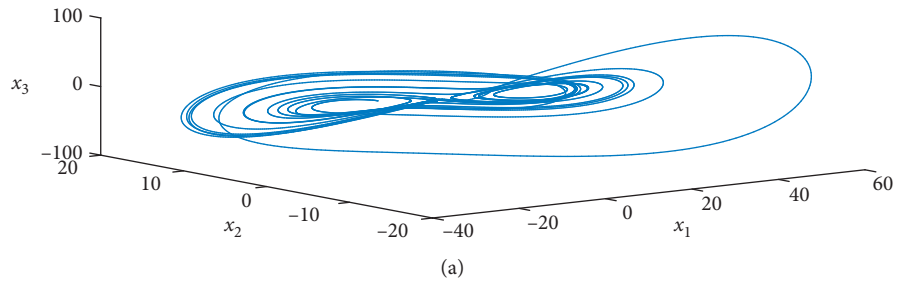
FIGURE 12: $\widehat{u}_{d1}$ tends to u_{d1}.

(a)

(b)
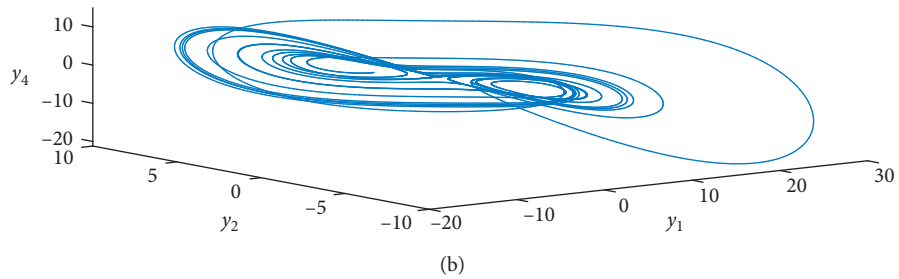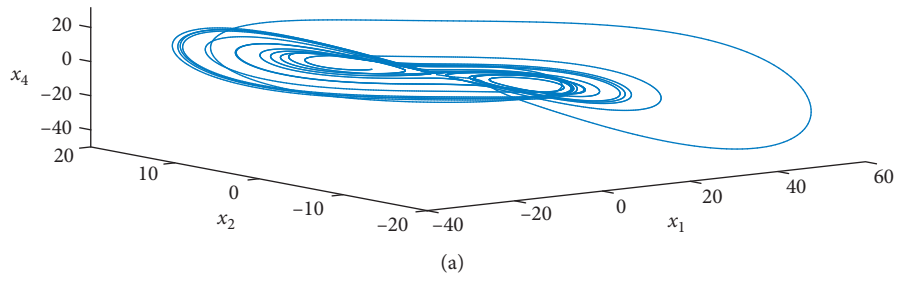
FIGURE 13: $\widehat{u}_{d2}$ tends to u_{d2}.
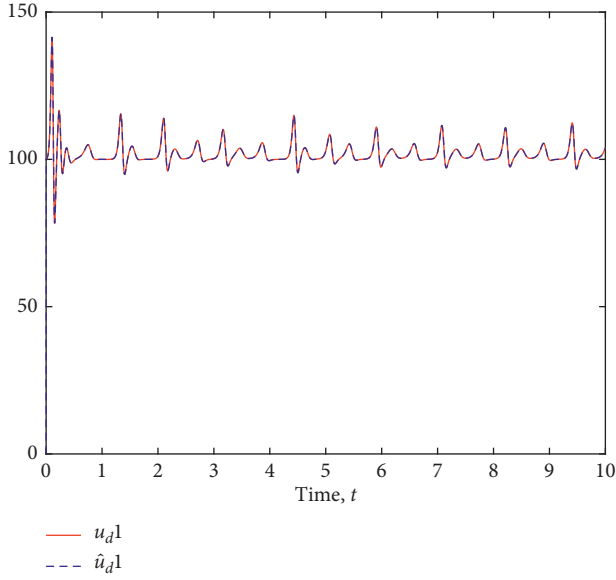
FIGURE 14: e_1, e_2 are asymptotically stable.

FIGURE 15: e_3, e_4 are asymptotically stable.

Note that if $e_1 = 0$ and $e_2 = 0$, the following system:

$$\begin{aligned} \dot{e}_3 &= -e_3, \\ \dot{e}_4 &= -e_4, \end{aligned} \tag{45}$$

is globally asymptotically stable.

Thus, $(A(Z), B_1)$ is controllable. According to Theorem 1, the linear feedback controller U is obtained as follows:

$$U = K(Z)e = \begin{pmatrix} -10e_3 \\ -10e_4 \end{pmatrix}. \tag{46}$$

Numerical simulation is given, and the initial values of the master-slave systems of given complex Lorenz system are chosen as follows: $X_1(0) = 0.1$, $X_2(0) = 0.2$, $X_3(0) = 0.3$, $X_4(0) = -0.3$, $X_5(0) = 1.1$, $Y_1(0) = -1$, $Y_2(0) = -1$, $Y_3(0) = -1$, $Y_4(0) = -1$.

From Figures 1 and 2, we observed that under linear feedback control, the error system between the master system and slave system is globally asymptotically stable. Through the observation of Figures 3–5, it is found that the master system and slave system achieve the projection synchronization. That is, the controlled master system and slave system have the same phase portrait, but the axis is different.

Step two: consider the following master system with both model uncertainty and external disturbance:

$$\dot{W}_m = A(Z)W_m + B_1 V + U_d, \tag{47}$$

where $A(Z)$ is given in equation (39), $H(Z, W_m)$ is presented in equation (40), B_1 is given in equation (42), and U_d is the whole of model uncertainty and external disturbance.

The salve system is

$$\dot{W}_s = A(Z)W_s, \tag{48}$$

where $A(Z)$ is given in equation (39).

Let $e = W_m - \beta W_s$; then, the error system is shown as follows:

$$\dot{e} = A(Z)e + U_d + B_1 V, \tag{49}$$

where

$$V = U + u_{ude}, \tag{50}$$

where U is given in equation (46).

According to Theorem 2, the UDE-based controller u_{ude} is designed as follows:

$$u_{ude} = \begin{pmatrix} u_{ude1} \\ u_{ude2} \end{pmatrix} = \begin{pmatrix} \ell^{-1}\left\{ \left[\dfrac{G_f}{1 - G_f(s)} \right] * (-10e_1) - \left[\dfrac{sG_f(s)}{1 - G_f(s)} \right] * e_1 \right\} \\ \ell^{-1}\left\{ \left[\dfrac{G_f}{1 - G_f(s)} \right] * (-10e_2) - \left[\dfrac{sG_f(s)}{1 - G_f(s)} \right] * e_2 \right\} \end{pmatrix}, \tag{51}$$
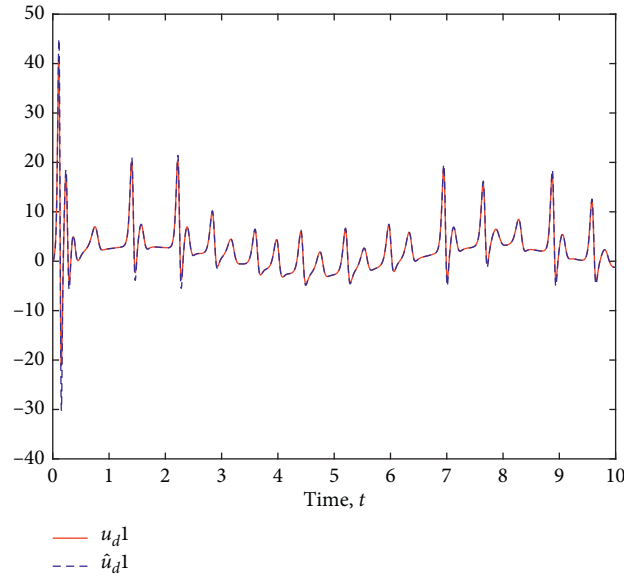
FIGURE 16: $\widehat{u}_{d1}$ tends to u_{d1}.
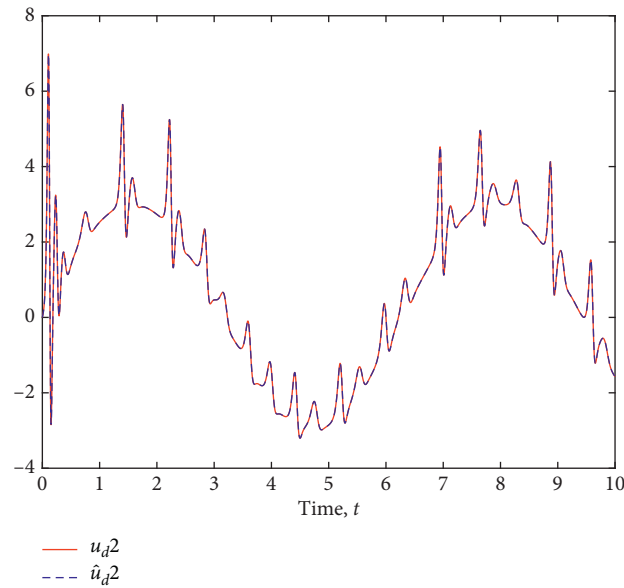
FIGURE 17: $\widehat{u}_{d2}$ tends to u_{d2}.

where ℓ^{-1} is the inverse Laplace transform, $*$ is the convolution sign, $G_f(s) = \ell[g_f(t)]$, and the design of the filter $g_f(t)$ is given in Lemma 2.

Numerical simulation results are given with the following conditions: $X_1(0) = 0.1, X_2(0) = 0.2, X_3(0) = 0.3, X_4(0) = -0.3, X_5(0) = 1.1, \quad Y_1(0) = -1, Y_2(0) = -1, \quad Y_3(0) = -1, Y_4(0) = -1, \beta = 2$.

Case 1:

$$U_d = \begin{pmatrix} 0.1X_1X_2 + 100 \\ 0.2X_3X_4 + 400 \end{pmatrix}. \tag{52}$$

Case 2:

$$U_d = \begin{pmatrix} 0.1X_1X_2 + 0.1\sin(t) \\ 0.2X_3X_4 + 0.3\sin(t) \end{pmatrix}. \tag{53}$$

It can be seen from Figures 6–9 that the error system is asymptotically stable. Through the observation of Figures 10–13, it is found that the master system and slave system achieve the projection synchronization. That is, the controlled master system and slave system have the same phase portrait, but the axis is different. Figure 14 shows that $\widehat{u}_{d1}$ tends to u_{d1}, and Figure 15 shows that $\widehat{u}_{d2}$ tends to u_{d2}. Similarly, we found that $\widehat{u}_{d1}$ tends to u_{d1} and $\widehat{u}_{d2}$ tends to u_{d2} from Figures 16 and 17.

5. Conclusion

In conclusion, the projective synchronization of a class of complex chaotic systems with both uncertainty and disturbance has been solved. First, the linear feedback control method is proposed for the nominal system (without uncertainty and disturbance), and projection synchronization of such system has been realized. Then, the UDE-based linear feedback control method is presented by two steps, by which the projection synchronization of the complex chaotic systems with both uncertainty and disturbance has been completed. Finally, an experimental simulation example has been used to verify the feasibility and effectiveness of the obtained results.

Data Availability

No data were used to support this study.

Conflicts of Interest

The authors declare that they have no conflicts of interest.

Acknowledgments

References

[1] L. M. Pecora and T. L. Carroll, "Synchronization in chaotic systems," *Physical Review Letter*, vol. 64, no. 8–19, pp. 821–824, 1990.

[2] P. Y. Li, J. Du, S. L. Li, Y. Zheng, and B. Jia, "The synchronization of *N* cascade-coupled chaotic systems," *Complexity*, vol. 2019, Article ID 2709820, 10 pages, 2019.

[3] L. M. Zou, Y. Peng, Y. M. Feng, and Z. Tu, "Stabilization and synchronization of memristive chaotic circuits by impulsive control," *Complexity*, vol. 2017, Article ID 5186714, 10 pages, 2017.

[4] L. Ren and R. Guo, "A necessary and sufficient condition of anti-synchronization for chaotic systems and its applications," *Mathematical Problems in Engineering*, vol. 2015, Article ID 434651, 7 pages, 2015.

[5] C. Wang, R. Chu, and J. Ma, "Controlling a chaotic resonator by means of dynamic track control," *Complexity*, vol. 21, no. 1, pp. 370–378, 2015.

[6] B. Li, X. B. Zhou, and Y. Wang, "Combination synchronization of three different fractional-order delayed chaotic systems," *Complexity*, vol. 2019, Article ID 5184032, 9 pages, 2019.

[7] L. Ren, R. Guo, and U. E. Vincent, "Coexistence of synchronization and anti-synchronization in chaotic systems," *Archives of Control Sciences*, vol. 26, no. 1, pp. 69–79, 2016.

[8] R.-W. Guo, "Simultaneous synchronizaiton and anti-synchronization of two identical new 4D chaotic systems," *Chinese Physics Letters*, vol. 28, no. 4, pp. 040205–040209, 2011.

[9] J. H. Prez-Cruz, P. A. Tamayo-Meza, and M. Figueroa, "Exponential synchronization of chaotic Xian system using linear feedback control," *Complexity*, vol. 2019, Article ID 4706491, 10 pages, 2019.

[10] X. B. Yang, Y. G. He, and C. L. Li, "Dynamics feature and synchronization of a robust fractional-order chaotic system," *Complexity*, vol. 2018, Article ID 8797314, 12 pages, 2018.

[11] L. Moysis, E. Petavratzis, M. Marwan, C. Volos, H. Nistazakis, and S. Ahmad, "Analysis, synchronization, and robotic application of a modified hyperjerk chaotic system," *Complexity*, vol. 2020, Article ID 2826850, 15 pages, 2020.

[12] R. Xu and F. Zhang, "ε-Nash mean-field games for general linear-quadratic systems with applications," *Automatica*, vol. 114, pp. 1–6, 2020.

[13] X. Yi, R. Guo, and Y. Qi, "Stabilization of chaotic systems with both uncertainty and disturbance by the UDE-based control method," *IEEE Access*, vol. 8, no. 1, pp. 62471–62477, 2020.

[14] S. Banerjee, S. J. Theesar, and J. Kurths, "Generalized variable projective synchronization of time delayed systems," *Chaos*, vol. 23, Article ID 01311801, 2013.

[15] M. Chen, S.-Y. Shao, P. Shi, and Y. Shi, "Disturbance-observer-based robust synchronization control for a class of fractional-order chaotic systems," *IEEE Transactions on Circuits and Systems II: Express Briefs*, vol. 64, no. 4, pp. 417–421, 2017.

[16] G. Al-mahbashi, M. S. M. Noorani, and S. A. Bakar, "Projective lag synchronization in drive-response dynamical networks with delay coupling via hybrid feedback control," *Nonlinear Dynamics*, vol. 82, no. 3, pp. 1569–1579, 2015.

[17] R. Guo, "Projective synchronization of a class of chaotic systems by dynamic feedback control method," *Nonlinear Dynamics*, vol. 90, no. 1, pp. 53–64, 2017.

[18] E. E. Mahmoud, "Dynamics and synchronization of new hyperchaotic complex Lorenz system," *Mathematical and Computer Modelling*, vol. 55, no. 7-8, pp. 1951–1962, 2012.

[19] G. M. Mahmoud and M. E. Ahmed, "Modified projective synchronization and control of complex Chen and Lü systems," *Journal of Vibration and Control*, vol. 17, no. 8, pp. 1184–1194, 2011.

[20] G. M. Mahmoud, M. E. Ahmed, and E. E. Mahmoud, "Analysis of hyperchaotic complex Lorenz systems," *International Journal of Modern Physics C*, vol. 19, no. 10, pp. 1477–1494, 2008.

[21] G. M. Mahmoud, M. A. Al-Kashif, and S. A. Aly, "Basic properties and chaotic synchronization of complex Lorenz system," *International Journal of Modern Physics C*, vol. 18, no. 2, pp. 253–265, 2007.

[22] E. E. Mahmoud and F. S. Abood, "A new nonlinear chaotic complex model and its complex antilag synchronization," *Complexity*, vol. 2017, Article ID 3848953, 13 pages, 2017.

[23] W. S. Sayed, M. M. R. Henein, S. K. Abd-El-Hafiz, and A. G. Radwan, "Generalized dynamic switched synchronization between combinations of fractional-order chaotic systems," *Complexity*, vol. 2017, Article ID 9189120, 17 pages, 2017.

[24] D. B. Huang, "Simple adaptive-feedback controller for identical chaos synchronization," *Physical Review E*, vol. 71, no. 3, Article ID 037203, 2005.

[25] D. B. Huang, "Adaptive-feedback control algorithm," *Physical Review E*, vol. 73, no. 6, Article ID 066204, 2006.

[26] B. B. Ren and J. G. Dai, "UDE-based robust boundary control for an unstable parabolic PDE with unknown input disturbance," *Automatica*, vol. 93, pp. 363–368, 2018.

[27] Q. C. Zhong, V. Kadirkam, and A. Kuperman, "UDE-based controller equipped with a multi-band-stop filter to improve the voltage quality of inverters," *IEEE Transactions on Industrial Electronics*, vol. 64, no. 9, pp. 7433–7443, 2017.

[28] A. Kuperman and Q.-C. Zhong, "UDE-based linear robust control for a class of nonlinear systems with application to

wing rock motion stabilization," *Nonlinear Dynamics*, vol. 81, no. 1-2, pp. 789–799, 2015.

[29] D. Ghosh and S. Banerjee, "Projective synchronization of time-varying delayed neural network with adaptive scaling factors," *Chaos, Solitons & Fractals*, vol. 53, pp. 1–9, 2013.

[30] B. Ren, Q.-C. Zhong, and J. Dai, "Asymptotic reference tracking and disturbance rejection of UDE-based robust control," *IEEE Transactions on Industrial Electronics*, vol. 64, no. 4, pp. 3166–3176, 2017.

[31] B. Ren, Q.-C. Zhong, and J. Chen, "Robust control for a class of nonaffine nonlinear systems based on the uncertainty and disturbance estimator," *IEEE Transactions on Industrial Electronics*, vol. 62, no. 9, pp. 5881–5888, 2015.

[32] Q.-C. Zhong and D. Rees, "Control of uncertain nonlinear system using an uncertainty and disturbance estimator," *Journal of Dynamic Systems, Measurement, and Control*, vol. 126, no. 4, pp. 905–910, 2004.

WILEY | Hindawi

Research Article

Distributed Adaptive Sliding Mode Control for Vehicle Platoon with Uncertain Driving Resistance and Actuator Saturation

Jia-cheng Song and **Yong-feng Ju**

School of Electronic and Control Engineering, Chang'an University, Xi'an 710064, China

Correspondence should be addressed to Jia-cheng Song; songjiacehng@hotmail.com and Yong-feng Ju; yfju@chd.edu.cn

Vehicle platoon has been demonstrated to be a promising driving pattern for its prominent advantages in enhancing traffic safety, improving highway capacity, and increasing fuel economy as well as reducing carbon emissions. However, the uncertain driving resistance and saturated actuator output decay the control performance and may even lead to the instability of a vehicle platoon. Therefore, a distributed adaptive sliding mode control algorithm for vehicle platoon with uncertain driving resistance and actuator saturation is proposed in this paper. First of all, sliding mode control technique, together with the coupled sliding surface (CSS) method, is adopted to design the vehicle platoon control algorithm and an adaptive updating law is proposed to estimate the unknown driving resistance coefficients. Then, for the problem of actuator saturation, an antiwindup compensation-based approach is utilized to attenuate the integral windup of the adaptive platoon control laws in the case of actuator saturation. In addition, considering the chattering problem inherent in sliding mode control, a sigmoid-like function $\text{sgn}(\cdot)$ is deployed to weaken the influence of chattering, which is expected to enhance the driving comfortableness. Both theoretical analysis and numerical simulation verify the feasibility and effectiveness of the proposed vehicle platoon algorithm.

1. Introduction

In recent years, the automated highway system (AHS) has gained considerable attentions from governments, automobile manufactures, and academia because of the increasing traffic congestion problem in large cities [1–3]. As an effective measure to relieve congestions, platoon control [4, 5], which requires vehicles to move in a string with predefined intervehicle distance and with the same velocity, has demonstrated its unique advantage in enhancing traffic safety, improving highway capacity, increasing fuel economy, and reducing carbon emissions [6–8].

During the past few years, many achievements have been developed for vehicle platoon control, such as backstepping approach [9], information consensus approach [10, 11], adaptive sliding mode approach [12], etc. However, most of the above works treat the vehicle platoon control problem in a simplified fashion without considering the driving resistance inherent in the vehicle dynamics. As a matter of fact, driving resistance, which includes rolling resistance, air resistance, and grade resistance [13], has significant influence on vehicle platoon such as degrading the controller performance and leading to the instability of a vehicle string [14]. In addition, driving resistance is virtually influenced by many factors such as vehicle mass, motorcycle type, and road and weather conditions [15, 16], some of which may even vary with the driving conditions [17]. Therefore, it is a great challenge in obtaining the driving resistance parameters in an accurate way.

For the problem of unknown driving resistance in vehicle dynamics, Altmannshofer and Endisch [18] proposed a robust parameter estimation algorithm for identifying the vehicle driving resistance. Tannoury et al. [16] designed a nonlinear observer for the estimation of tire radius and

rolling resistance to compensate for the unknown parameters. Guo et al. [14] deployed a quadratic function to represent the unknown and time-varying coefficients of driving resistance. However, as for the unknown driving resistance in vehicle platoon control, existing literatures mainly treat it as time-varying external disturbance without explicitly obtaining its true value [12]. In [9], the uncertain driving resistance in vehicle dynamics is modeled as an unknown time-varying disturbance and an adaptive method is adopted to estimate this value. Similarly, the uncertain driving resistance is described as a bounded disturbance and also estimated by adaptive approach in [14]. In [13], the vehicle resistance, which is relevant to vehicle mass, weather conditions, deadweight, motorcycle type, etc., is analyzed and the vehicle platoon model is established.

On the other hand, the mechanical constraints, especially the actuator saturation [19], are important concern in vehicle dynamics. The actuator saturation of vehicle, whether it is the servo motor for an electric vehicle or engine for a gasoline vehicle, has been proved to be the source of performance degradation in vehicle driving procedure [20], which therefore deserves further investigation in vehicle platoon control. However, to the best of our knowledge, literatures that specifically address this issue seem very few. As a ubiquitous phenomenon in mechanical systems, actuator saturation, which is usually referred to as input saturation, has been intensively investigated in various control domains. In [20], by explicitly considering the actuator saturation, a novel robust adaptive control law is proposed to ensure the stability of the closed-loop system for high-speed train. In [21], the Nussbaum function is introduced to compensate for the nonlinear term arising from input saturation. In [22], a saturated adaptive robust control strategy, by adding an anti-windup block, is designed for vehicle active suspension systems, which is beneficial for the stability and performance preservation in the presence of saturation. In [23], an adaptive coordinated control algorithm of multiple high-speed trains with input saturation is proposed, where an antiwindup compensation block is used to optimize the control algorithm such that it is more resilient to input saturation. In [24], a smooth function $\tanh(\cdot)$ is introduced to handle the "actuator saturation" problem in vehicle platoon such that the control input can always be below the maximum inputs. Therefore, the above work provides fruitful inspirations for the actuator saturation problem of vehicle platoon.

In this paper, we are trying to investigate the vehicle-platoon problem with uncertain driving resistance and actuator saturation via adaptive sliding mode control approach. Firstly, coupled sliding surface (CSS) is deployed to link interconnected vehicles and an adaptive control method is adopted to identify and estimate the variations of resistance coefficients. After that, a distributed adaptive sliding mode control algorithm for vehicle platoon with uncertain driving resistance is proposed. Then, an antiwindup compensation based approach is utilized to attenuate the integral windup of the adaptive platoon control laws in case of actuator saturation. Moreover, the chattering phenomena inherent in sliding mode control are relieved by using a sigmoid-like function. Finally, various numerical simulations are performed to demonstrate the feasibility and effectiveness of the proposed control algorithm.

The rest of this paper is organized as follows. In Section 2, the vehicle dynamic model and the problems considered in this paper are described. In Section 3, the adaptive sliding mode controller is designed to realize the vehicle platoon in the presence of uncertain driving resistance and actuator saturation. Simulations are performed in Section 4 to demonstrate the feasibility and effectiveness of our algorithm. Concluding remarks are given in Section 5.

2. Vehicle Dynamics and Problem Formulation

Assume a vehicle platoon, which consists of a string of autonomous vehicles, includes a leader vehicle and n followers. As is shown in Figure 1, each follower regulates its motion according to the received information (e.g., position, velocity, and acceleration) from its front and back vehicles via wireless communication technique.

2.1. Vehicle Dynamics. Consider a vehicle platoon moving in a string with the following longitudinal dynamics:

$$
\begin{cases}
\dot{r}_i(t) = v_i(t), \\
M_i \dot{v}_i(t) = F_i(t) - f_i, \\
i = 1, 2, \ldots, n,
\end{cases}
\tag{1}
$$

where M_i is the mass of the ith vehicle, $r_i(t)$ and $v_i(t)$ denote the ith vehicle's position and velocity, respectively, and $F_i(t)$, which is taken as the control input, represents the traction or braking force of the ith vehicle. In addition, f_i denotes its driving resistance.

Generally, f_i is influenced by the rolling resistance f_r, air resistance f_w, and grade resistance f_g, etc. [25], which can be described as

$$
f_i = f_r + f_w + f_g.
\tag{2}
$$

The explicit form of f_r, f_w, and f_g can be written as follows:

(i) Rolling resistance f_r:

$$
f_r = Wk,
\tag{3}
$$

where W is the normal load and k is the rolling resistance coefficient following such experience values as

$$
k = 0.0076 + 0.000056v,
\tag{4}
$$

where v is the velocity of vehicle.

(ii) Air resistance f_w:

$$
f_w = \frac{1}{2} C_D A \rho v^2,
\tag{5}
$$

where C_D is the coefficient of air resistance, A is windward area of vehicle, and ρ is the air density.
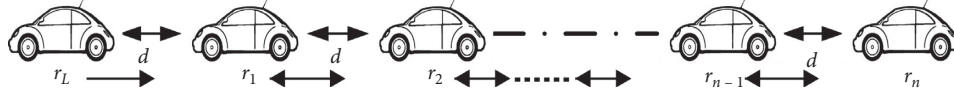
FIGURE 1: Topological structure of vehicle platoon.

(iii) Grade resistance f_g:

If the vehicle is running on the hill, the component of gravity along the slope is defined as the grade resistance

$$f_g = G \sin \alpha, \tag{6}$$

where G and α are, respectively, the gravity and road-grade.

As k, C_D, and ρ are uncertain values and heterogeneous with respect to different vehicles, therefore, f_i is time-varying in different driving speed and road conditions. To facilitate the research, we write f_i as

$$f_i = A(t) + B(t)v_i + C(t)v_i^2, \tag{7}$$

where $A(t), B(t), C(t)$, describing the uncertainty of driving resistance, are unknown and time-varying values.

In order to simplify the protocol design and stability analysis, we rewrite (1) as

$$\begin{cases} \dot{r}_i(t) = v_i(t), \\ \dot{v}_i(t) = F_i(t) - a_i(t) - b_i(t)v_i(t) - c_i(t)v_i(t)^2, \end{cases} \tag{8}$$

where $u_i(t) := (F_i(t)/M_i)$ denotes the acceleration or deceleration of vehicle i (it is designed as the control input in this paper) and $a_i(t) := (A_i(t)/M_i)$, $b_i(t) := (B_i(t)/M_i)$, $c_i(t) := (C_i(t)/M_i)$ are the vehicle driving resistance coefficients by considering the influence of vehicle mass M_i.

2.2. Problem Formulation. Generally speaking, the main purpose of vehicle platoon is to enhance the highway capacity and relieve traffic congestion by maintaining the desired safety distance between two consecutive vehicles and reaching the velocity consensus among vehicles [4].

In particular, the time-varying driving resistance will inevitably influence the vehicle dynamics and decay the vehicle platoon performance. Therefore, one needs to specifically design the distributed control input $u_i(t)$ for a single vehicle such that the vehicle platoon is achieved under the disturbance of time-varying driving resistance.

In addition, due to the physical and mechanical limitations of actuators, the control input $u_i(t)$ for vehicles will be under some constraints. The control input $u_i(t)$ with saturation is given in the following form:

$$u_i(t) = \text{sat}(u_{\min}, u_i(t), u_{\max})$$

$$= \begin{cases} u_{\min}, & \text{if } u_i(t) < u_{\min}, \\ u_i(t), & \text{if } u_{\min} \le u_i(t) \le u_{\max}, \\ u_{\max}, & \text{if } u_i(t) > u_{\max}, \end{cases} \tag{9}$$

where $u_{\min}$ and $u_{\max}$ are known constants, which represent the bounds of the control force.

Based on above description, the main control objective of this paper can be concluded as follows:

(1) The vehicle platoon is achieved such that the follower's velocity can converge to the velocity of the leader and each vehicle can maintain a safe intervehicle distance to avoid collision with each other

(2) The unknown time-varying coefficients $a_i(t)$, $b_i(t)$, and $c_i(t)$ can be estimated such that the vehicle platoon is achieved by handling the parameter uncertainties via an adaptive control approach

(3) When the control input exceeds the maximum output of the vehicle actuator (servo motor for an electric vehicle or engine for a gasoline vehicle), the proposed algorithm can regulate the actuator output autonomously such that the actuator life as well as the vehicle platoon performance is guaranteed

3. Distributed Adaptive Sliding Mode Control Algorithm for Vehicle Platoon

Firstly, the position tracking error for the ith vehicle is defined as

$$e_i = (r_{i-1} - r_i) - d, \tag{10}$$

where $d > 0$ is a constant value, representing the required distance between two consecutive vehicles.

We also denote the velocity error by

$$\tilde{v}_i = v_{i-1} - v_i. \tag{11}$$

Here, the following assumptions are made for facilitating the control protocol design and theoretical analysis.

Assumption 1. $a_i(t)$, $b_i(t)$, and $c_i(t)$ are bounded variables; i.e., $a_i(t) \le a_i^+$, $b_i(t) \le b_i^+$, and $c_i(t) \le c_i^+$.

3.1. Vehicle Platoon Control Algorithm with Uncertain Driving Resistance. We first consider the case of vehicle platoon with uncertain driving resistance. For the dynamics of vehicles with error e_i, the control objective is to make e_i converge to zero and to guarantee string stability.

Hence, sliding mode control technique is employed to develop the vehicle platoon controller; we choose each sliding surface as

$$n_i = \dot{e}_i + \alpha_i e_i, \tag{12}$$

where $\alpha_i > 0$ is a positive constant.

The solution of (12) is

$$e_i(t) = \frac{n_i}{\alpha_i} + \exp(-\alpha_i t)e_i(0) - \frac{n_i}{\alpha_i}\exp(-\alpha_i(t-t_0)). \quad (13)$$

From (13), one can see that when $t \longrightarrow \infty$, $e_i \longrightarrow (n_i/\alpha_i)$. As α_i is a positive constant, $e_i \Leftrightarrow n_i$. Furthermore, combined with (12), we have $\dot{e}_i \longrightarrow 0$ when $n_i \longrightarrow 0$.

Taking the time derivative of (12), one obtains

$$\dot{n}_i = \ddot{e}_i + \alpha_i \dot{e}_i = (\ddot{r}_{i-1} - \ddot{r}_i) + \alpha_i \dot{e}_i. \quad (14)$$

It is worth noting that (14) only describes the characteristic of a single vehicle. In order to describe the stability of the whole platoon, we adopt the coupled sliding surface (CSS) [7] of the ith vehicle for the control of the whole platoon system

$$N_i = \beta_i n_i - n_{i+1}, \quad (15)$$

where $\beta_i > 0 \, (i = 1, 2, \ldots, n)$ is a weighting factor.

Since n_{i+1} does not exist for the last vehicle (i.e., $i = n$), we set $n_{i+1} = 0$. Then, we have $\mathbf{N}_1 := [n_1, n_2, \ldots, n_n]^T$ and $\mathbf{N}_2 := [N_1, N_2, \ldots, N_n]^T$; the relationship between $\mathbf{N}_1$ and $\mathbf{N}_2$ can be described as

$$\mathbf{N}_2 = \mathbf{B}\mathbf{N}_1, \quad (16)$$

where

$$\mathbf{B} = \begin{bmatrix} \beta_1 & -1 & 0 & \cdots & 0 \\ 0 & \beta_2 & -1 & \cdots & 0 \\ \vdots & \vdots & \vdots & \ddots & \vdots \\ 0 & 0 & 0 & \cdots & -1 \\ 0 & 0 & 0 & \cdots & \beta_n \end{bmatrix}, \quad (17)$$

with $\beta_i > 0 \, (i = 1, 2, \ldots, n)$ being the parameters to be designed.

In order to illustrate the same convergence of $\mathbf{N}_1$ and $\mathbf{N}_2$, the following lemma is given.

Lemma 1 (see [7]). *Equivalence of the convergence of the CSS and each sliding surface toward zero: $\mathbf{N}_2$ becomes zero if and only if $\mathbf{N}_1$ becomes zero at the same time.*

Therefore, the problem of making n_i and e_i converge to zero is converted into making N_i converge to zero. The time derivative of N_i in (15) can be written as

$$\begin{aligned} \dot{N}_i &= \beta_i \dot{n}_i - \dot{n}_{i+1} \\ &= \beta_i(\ddot{r}_{i-1} - \ddot{r}_i + \alpha_i \dot{e}_i) - (\ddot{r}_i - \ddot{r}_{i+1} + \alpha_{i+1} \dot{e}_{i+1}) \quad (18) \\ &= -(\beta_i + 1)(u_i - a_i - b_i v_i - c_i v_i^2) + D_i, \end{aligned}$$

where $D_i = \beta_i \ddot{r}_{i-1} + \ddot{r}_{i+1} + \alpha_i \beta_i \dot{e}_i - \alpha_{i+1} \dot{e}_{i+1}$.

Accordingly, the novel adaptive platoon control law for the ith vehicle is designed as

$$u_i = \frac{k_1}{\beta_i + 1}N_i + \frac{1}{\beta_i + 1}D_i + \text{sgn}(N_i)(\hat{a}_i^+ + \hat{b}_i^+ v_i + \hat{c}_i^+ v_i^2), \quad (19)$$

where k_1 is a positive parameter that needs to be designed and $\hat{a}_i^+$, $\hat{b}_i^+$, and $\hat{c}_i^+$ are the estimated values of unknown constant coefficients a_i^+, b_i^+, and c_i^+.

The adaptive estimation law for unknown coefficients is determined by

$$\begin{cases} \dot{\hat{a}}_i^+ = \lambda_1(\beta_i + 1)N_i, \\ \dot{\hat{b}}_i^+ = \lambda_2(\beta_i + 1)N_i|v_i|, \\ \dot{\hat{c}}_i^+ = \lambda_3(\beta_i + 1)N_i v_i^2, \end{cases} \quad (20)$$

where $\lambda_1, \lambda_2, \lambda_3 > 0$ are positive constants.

Particularly, when $i = n$, we know $N_n = \beta_n n_n$ from the definition of (15); the time derivative of N_n can be described as

$$\begin{aligned} \dot{N}_n &= \beta_n \dot{n}_n \\ &= \beta_n(\ddot{r}_{n-1} - \ddot{r}_n + \alpha_n \dot{e}_n) \quad (21) \\ &= -\beta_n(u_n - a_n - b_n v_n - c_n v_n^2) + D_n, \end{aligned}$$

where $D_n = \beta_n(\ddot{r}_{n-1} + \alpha_n \dot{e}_n)$ for $i = n$.

The adaptive platoon control law for the nth vehicle is therefore formulated as

$$u_n = \frac{k_2}{\beta_n}N_n + \frac{1}{\beta_n}D_n + \text{sgn}(N_n)(\hat{a}_n^+ + \hat{b}_n^+ v_n + \hat{c}_n^+ v_n^2), \quad (22)$$

where k_2 is a positive parameter that needs to be designed.

Thus, the coefficients adaptation law can be designed as

$$\begin{cases} \dot{\hat{a}}_n^+ = \lambda_1 \beta_n N_n, \\ \dot{\hat{b}}_n^+ = \lambda_2 \beta_n N_n|v_n|, \\ \dot{\hat{c}}_n^+ = \lambda_3 \beta_n N_n v_n^2. \end{cases} \quad (23)$$

Then, the following theorem, which guarantees the stability of each vehicle and string stability of the whole vehicle platoon, can be obtained.

Theorem 1. *Consider a vehicle platoon described by (8), the proposed control algorithm of vehicle platoons (19) and (22) and the adaptive control law of coefficients (20) and (23) can ensure that the sliding surfaces N_i and n_i and the distance error e_i converge to zero.*

Proof. First, we define the estimation error of coefficients $\tilde{a}_i^+$, $\tilde{b}_i^+$, and $\tilde{c}_i^+$ as

$$\begin{cases} \tilde{a}_i^+ = \hat{a}_i^+ - a_i^+, \\ \tilde{b}_i^+ = \hat{b}_i^+ - b_i^+, \\ \tilde{c}_i^+ = \hat{c}_i^+ - c_i^+. \end{cases} \quad (24)$$

Choose the following Lyapunov function candidates:

$$V = \sum_{i=1}^{n} V_i, \quad (25)$$

where

$$V_i = \frac{1}{2}N_i^2 + \frac{1}{2\lambda_1}\tilde{a}_i^+ 2 + \frac{1}{2\lambda_2}\tilde{b}_i^+ 2 + \frac{1}{2\lambda_3}\tilde{c}_i^+ 2. \quad (26)$$

Then, the time derivative of V_i can be calculated as

$$\dot{V}_i = N_i \dot{N}_i + \frac{1}{\lambda_1} \tilde{a}_i^+ \dot{\tilde{a}}_i^+ + \frac{1}{\lambda_2} \tilde{b}_i^+ \dot{\tilde{b}}_i^+ + \frac{1}{\lambda_3} \tilde{c}_i^+ \dot{\tilde{c}}_i^+. \tag{27}$$

Because a_i^+, b_i^+, and c_i^+ are constants, we know $\dot{\tilde{a}}_i^+ = \dot{\hat{a}}_i^+$, $\dot{\tilde{b}}_i^+ = \dot{\hat{b}}_i^+$, and $\dot{\tilde{c}}_i^+ = \dot{\hat{c}}_i^+$ according to (24). Combining (18) and (20) with (27) yields

$$\dot{V}_i = -k_1 N_i^2 - (\beta_i + 1) N_i \left[(\hat{a}_i^+ - a_i) + (\hat{b}_i^+ - b_i) v_i + (\hat{c}_i^+ - c_i) v_i^2 \right]$$
$$+ (\beta_i + 1) N_i \left(\tilde{a}_i^+ + \tilde{b}_i^+ v_i + \tilde{c}_i^+ v_i^2 \right). \tag{28}$$

According to Young's inequality [14], we have

$$\begin{cases} a_i \leq a_i^+, \\ b_i v_i \leq b_i^+ |v_i|, \\ c_i v_i^2 \leq c_i^+ v_i^2. \end{cases} \tag{29}$$

Substituting (29) into (28) gives

$$\dot{V}_i \leq -k_1 N_i^2 - (\beta_i + 1) N_i \left[(\hat{a}_i^+ - a_i^+) + (\hat{b}_i^+ - b_i^+) v_i + (\hat{c}_i^+ - c_i^+) v_i^2 \right]$$
$$+ (\beta_i + 1) N_i \left(\tilde{a}_i^+ + \tilde{b}_i^+ v_i + \tilde{c}_i^+ v_i^2 \right)$$
$$\leq -k_1 N_i^2. \tag{30}$$

Thus,

$$\dot{V} \leq -k_1 \sum_{i=1}^{n} N_i^2 \leq 0. \tag{31}$$

From (30) and (31), we know that $\dot{V}_i$ and $\dot{V}$ are negative semidefinite; therefore, V_i and V are not monotonic increasing and boundedness. In addition, we can also obtain that N_i is boundedness and $\dot{N}_i$ is boundedness.

Taking the derivative of (30) and (31), we have $\ddot{V}_i \leq -(k_1/2) N_i \dot{N}_i$, $\ddot{V} \leq (k_1/2) \sum_{i=1}^{n} N_i \dot{N}_i$. As $\ddot{V}_i$ and $\ddot{V}$ are

boundedness, $\dot{V}_i$ and $\dot{V}$ are uniformly continuous. According to the Barbalat lemma, we know that $\lim_{t \to \infty} \dot{V}_i = 0$ and $\lim_{t \to \infty} \dot{V} = 0$. Since k_1 is positive, $\lim_{t \to \infty} N_i = 0$ for all i. This implies that $\mathbf{N}_2$, $\mathbf{N}_1$, and e_i in Lemma 1 converge to zero. □

Remark 1. Cconstrued sliding surface (12) facilitates the control design and stability analysis. Open-loop dynamics (12) contains e_i and $\dot{e}_i$; the closed-loop dynamics $\dot{n}_i$ will contain system dynamics (8) and the control input u_i. Inspired by the adaptive technique, the control inputs (19) and (22) and the adaptive laws (19) and (23) can be designed by choosing the suitable Lyapunov function.

Remark 2. The main objective of the designed controller is to make N_i, $\tilde{a}_i^+$, $\tilde{b}_i^+$, and $\tilde{c}_i^+$ converge to zero; thus the Lyapunov function V_i is chosen as (26). The principle of controller design is to make $\dot{V}_i \leq 0$.

3.2. Vehicle Platoon Control Algorithm with Uncertain Driving Resistance and Actuator Saturation. In practice, the actuator saturation of vehicles has proved to be a source of performance degradation [26]. To handle this problem, an antiwindup compensation block is used to modify the control input such that it is more resilient to actuator saturation. An antiwindup compensator is used to generate a signal $\phi_i(t)$ for each vehicle as the output of a differential equation:

$$\begin{cases} \dot{\phi}_i(t) = -\chi_i \phi_i(t) + (\beta_i + 1)(u_{i0}(t) - u_i(t)), \\ \dot{\phi}_n(t) = -\chi_n \phi_n(t) + \beta_n (u_{n0}(t) - u_n(t)). \end{cases} \tag{32}$$

Let $\delta_i(t) = N_i(t) - \phi_i(t)$. We have the following error dynamic system:

$$\begin{cases} \dot{\delta}_i(t) = -(\beta_i + 1)(u_i(t) - a_i - b_i v_i - c_i v_i^2) - (\beta_i + 1)(u_{i0}(t) - u_i(t)) + D_i + \chi_i \phi_i(t), \\ \dot{\delta}_n(t) = -\beta_n (u_n(t) - a_n - b_n v_n - c_n v_n^2) - \beta_n (u_{n0}(t) - u_n(t)) + D_n + \chi_n \phi_n(t). \end{cases} \tag{33}$$

By considering explicitly the actuator saturation of vehicles, the modified adaptive control input $u_i(t)$ for each vehicle can be written as

$$u_i(t) = \mathrm{sat}(u_{\min}, u_{i0}(t), u_{\max}), \tag{34}$$

$$u_{i0}(t) = \frac{k_1}{\beta_i + 1} \delta_i + \frac{1}{\beta_i + 1} D_i - \frac{1}{\beta_i + 1} \chi_i \phi_i(t)$$
$$+ \mathrm{sgn}(\delta_i) (\hat{a}_i^+ + \hat{b}_i^+ v_i + \hat{c}_i^+ v_i^2). \tag{35}$$

The adaptive estimation laws for unknown coefficients are determined by

$$\begin{cases} \dot{\hat{a}}_i^+ = \lambda_1 (\beta_i + 1) \delta_i, \\ \dot{\hat{b}}_i^+ = \lambda_2 (\beta_i + 1) \delta_i |v_i|, \\ \dot{\hat{c}}_i^+ = \lambda_3 (\beta_i + 1) \delta_i v_i^2. \end{cases} \tag{36}$$

The adaptive platoon control law of the nth vehicle is therefore formulated as

$$u_{n0}(t) = \frac{k_n}{\beta_n} \delta_n + \frac{1}{\beta_n} D_n - \frac{1}{\beta_n} \chi_n \phi_n(t) + \mathrm{sgn}(\delta_n) (\hat{a}_n^+ + \hat{b}_n^+ v_n + \hat{c}_n^+ v_n^2). \tag{37}$$

The coefficients adaptation law is designed as

$$\begin{cases} \dot{\hat{a}}_n^+ = \lambda_1 \beta_n \delta_n, \\ \dot{\hat{b}}_n^+ = \lambda_2 \beta_n \delta_n |v_n|, \\ \dot{\hat{c}}_n^+ = \lambda_3 \beta_n \delta_n v_n^2. \end{cases} \tag{38}$$

The signal $\phi_i(t)$ is used for attenuating the integral windup of the adaptive coordinated control laws in case of actuator saturation. When actuator saturation happens, there will be a rise of error $\phi_i(t)$, and meanwhile the signal N_i will also increase, which in turn ensures that no sudden rise will happen to the newly defined tracking error $\delta_i(t)$. When the actuator saturation stops, the term $u_{i0}(t) - u_i(t) = 0$, and the signal $\phi_i(t)$ will converge to zero.

In addition, for the signal $\phi_i(t)$, we have the following theorem.

Theorem 2. *For the signal $\phi_i(t)$, there exists a positive ϖ_i such that, for any $t > 0$, it holds that*

$$|\phi_i(t)| \leq \left| \frac{(u_{i0}(t) - u_i(t))(\beta_i + 1)}{\chi_i} \right| + \varpi_i. \tag{39}$$

Proof. From (32), we can obtain that

$$\phi_i(t) = \phi_i(0)e^{-\chi_i t} + \frac{(u_{i0}(t) - u_i(t))(\beta_i + 1)}{\chi_i} e^{-\chi_i t} \int_0^t e^{-\chi_i \varpi} d\varpi$$

$$= \phi_i(0)e^{-\chi_i t} + \frac{(u_{i0}(t) - u_i(t))(\beta_i + 1)}{\chi_i} \left(1 - e^{-\chi_i t} \right), \tag{40}$$

which implies that $|\phi_i(t)| \leq |(u_{i0}(t) - u_i(t))(\beta_i + 1)/\chi_i|$ as $t \longrightarrow \infty$. Thus, there exists a positive scaler ϖ_i, such that, for any $t > 0$, it holds that $|\phi_i(t)| \leq |(u_{i0}(t) - u_i(t))(\beta_i + 1)/\chi_i|$; i.e., $\phi_i(t)$ is bounded.

The following theorem will provide our result on the vehicle platoon with actuator saturation. □

Theorem 3. *Consider a vehicle platoon described by (8), the proposed control algorithm of vehicle platoon (35) and (37) and the adaptive control law of coefficients (36) and (38) can ensure the desired distances between two consecutive vehicles. Then, we have the following results:*

(1) *When the saturation does not occur, i.e., $u_i - u_{i0} = 0$, all the results in Theorems 1 and 2 will hold automatically.*

(2) *When the saturation occurs, i.e., $u_i - u_{i0} \neq 0$, the modified $\delta_i(t)$ will converge to zero, and N_i will also converge to zero by adjusting variable χ_i in Theorem 2. This implies that $\mathbf{N}_2$, $\mathbf{N}_1$, and e_i in Lemma 1 converge to zero.*

Proof. For the case that the actuator is not saturated, $u_i - u_{i0} = 0$, the results in Theorem 1 hold automatically.

When saturation occurs, for the error dynamic (33) of the vehicles movement with control input (35) and (37), construct the following Lyapunov-like function candidate:

$$V = \sum_{i=1}^n V_i, \tag{41}$$

where

$$V_i = \frac{1}{2}\delta_i^2 + \frac{1}{2\lambda_1}\tilde{a}_i^+ 2 + \frac{1}{2\lambda_2}\tilde{b}_i^+ 2 + \frac{1}{2\lambda_3}\tilde{c}_i^+ 2. \tag{42}$$

Then, the time derivative of V_i can be calculated as

$$\dot{V}_i = \delta_i \dot{\delta}_i + \frac{1}{\lambda_1}\tilde{a}_i^+ \dot{\tilde{a}}_i^+ + \frac{1}{\lambda_2}\tilde{b}_i^+ \dot{\tilde{b}}_i^+ + \frac{1}{\lambda_3}\tilde{c}_i^+ \dot{\tilde{c}}_i^+. \tag{43}$$

Because a_i^+, b_i^+, and c_i^+ are constants, we know that $\dot{\tilde{a}}_i^+ = \dot{\hat{a}}_i^+$, $\dot{\tilde{b}}_i^+ = \dot{\hat{b}}_i^+$, and $\dot{\tilde{c}}_i^+ = \dot{\hat{c}}_i^+$ according to (24). Therefore,

$$\dot{V}_i \leq -k_1\delta_i^2 - (\beta_i + 1)\delta_i \left[(\hat{a}_i^+ - a_i^+) + (\hat{b}_i^+ - b_i^+)v_i + (\hat{c}_i^+ - c_i^+)v_i^2 \right]$$

$$+ (\beta_i + 1)\delta_i (\tilde{a}_i^+ + \tilde{b}_i^+ v_i + \tilde{c}_i^+ v_i^2)$$

$$\leq -k_1\delta_i^2. \tag{44}$$

Thus,

$$\dot{V} \leq -k_1 \sum_{i=1}^n \delta_i^2 \leq 0. \tag{45}$$

Using the same analysis method as in Theorem 1, it can be shown that δ_i will converge to zero eventually. From Theorem 2, we know that variable χ_i can be adjusted, and $\phi_i(t)$ can also be adjusted to an arbitrarily small value. Therefore, we have $N_i \approx \delta_i$. Combining Theorem 2 and equations (12) and (15), we know that n_i and e_i will converge to zero eventually. □

3.3. Reduction of Chattering. It is well known that the sliding mode control has inherently the phenomena of chattering, which is detrimental for the system performance [27]. In this paper, a sigmoid-like function $(\delta_i/(|\delta_i + \varsigma|))$ is used to replace the $\text{sgn}(\cdot)$ function, where ς is a small positive constant.

Then, the control input $u_i(t)$ of the ith vehicle can be rewritten as

$$u_i(t) = \text{sat}(u_{\min}, u_{i0}(t), u_{\max}), \tag{46}$$

where $u_{i0}(t)$ is the calculated control input. It is determined by

$$u_{i0}(t) = \frac{k_1}{\beta_i + 1}\delta_i + \frac{1}{\beta_i + 1}D_i - \frac{1}{\beta_i + 1}\chi_i\phi_i(t) + \frac{\delta_i}{|\delta_i| + \varsigma}\left(\widehat{a}_i^+ + \widehat{b}_i^+ v_i + \widehat{c}_i^+ v_i^2\right).$$
(47)

The adaptive estimation law of ith vehicle for unknown coefficients is determined by

$$\begin{cases} \dot{\widehat{a}}_i^+ = \dfrac{\lambda_1(\beta_i + 1)\delta_i^2}{|\delta_i| + \varsigma}, \\[3mm] \dot{\widehat{b}}_i^+ = \dfrac{\lambda_2(\beta_i + 1)\delta_i^2|v_i|}{|\delta_i| + \varsigma}, \\[3mm] \dot{\widehat{c}}_i^+ = \dfrac{\lambda_3(\beta_i + 1)\delta_i^2 v_i^2}{|\delta_i| + \varsigma}. \end{cases}$$
(48)

Similar to the previous case, $u_{n0}(t)$ of the nth vehicle can be described as

$$u_{i0}(t) = \frac{k_1}{\beta_n}\delta_n + \frac{1}{\beta_n}D_n - \frac{1}{\beta_n}\chi_n\phi_n(t) + \frac{\delta_n}{|\delta_n| + \varsigma}\left(\widehat{a}_n^+ + \widehat{b}_n^+ v_n + \widehat{c}_n^+ v_n^2\right).$$
(49)

The adaptive estimation law of the nth vehicle for unknown coefficients is determined by

$$\begin{cases} \dot{\widehat{a}}_n^+ = \dfrac{\lambda_1\beta_n\delta_n^2}{|\delta_n| + \varsigma}, \\[3mm] \dot{\widehat{b}}_n^+ = \dfrac{\lambda_2\beta_n\delta_n^2|v_n|}{|\delta_n| + \varsigma}, \\[3mm] \dot{\widehat{c}}_n^+ = \dfrac{\lambda_3\beta_n\delta_n^2 v_n^2}{|\delta_n| + \varsigma}. \end{cases}$$
(50)

4. Numerical Simulations

To verify the feasibility and effectiveness of the proposed platoon control algorithm, numerical simulations are performed with 8 vehicles (1 leader and 7 followers).

4.1. Simulation Setup. Without loss of generality, we suppose the vehicle platoon drives in various driving conditions, such as acceleration, cruising, and braking. In addition, we also consider the influence of time-varying driving resistance as a disturbance on the vehicle velocity in the form of sine wave.

Therefore, the desired velocity of the leading vehicle is specifically designed as

$$\begin{cases} v_L(t) = 20\sin\left(\dfrac{\pi}{200}t\right), & \text{if } t < 100, \\[3mm] v_L(t) = 20, & \text{if } 100 \le t < 150, \\[3mm] v_L(t) = 20 + 3\sin\left(\dfrac{\pi}{10}t\right), & \text{if } 150 \le t < 170, \\[3mm] v_L(t) = 20, & \text{if } 170 \le t < 230, \\[3mm] v_L(t) = 20 + 3\sin\left(\dfrac{\pi}{10}t\right), & \text{if } 230 \le t < 250, \\[3mm] v_L(t) = 20, & \text{if } 250 \le t < 320, \\[3mm] v_L(t) = 20 + 3\sin\left(\dfrac{\pi}{10}t\right), & \text{if } 320 \le t < 340, \\[3mm] v_L(t) = 20, & \text{if } 340 \le t < 400, \\[3mm] v_L(t) = 20\sin\left(\dfrac{\pi}{200}t\right), & \text{if } 400 \le t < 500, \\[3mm] v_L(t) = 0, & \text{if } 500 \le t < 520. \end{cases}$$
(51)

Inspired by our previous work on adaptive control for vehicle platoon [24], the variation of driving resistance coefficients a_i, b_i, c_i is assumed to be determined by $a_i = a1(1 + \sin(t))$, $b_i = b1(1 + \cos(3t))$, $c_i = c1(1 + \cos(4t))$, respectively. It should be pointed out that a_i, b_i, c_i are time-varying and bounded, so they can model the uncertainty and external noise of the vehicle. The other parameters such as $a1$, $b1$, $c1$, initial states of vehicles, and control parameters are listed in Tables 1 and 2.

4.2. Simulation Results. To better illustrate the effectiveness of the proposed vehicle platoon control algorithm, three simulation cases are performed.

Case 1. Platoon with uncertain driving resistance.

In this case, we only consider the influence of uncertain driving resistance for vehicle platoon, where (19), (20), (22), and (23) are applied to the vehicle.

Figure 2(a) shows the vehicle velocities and velocity errors (between followers and leader) in the simulation, from which one can clearly see that the velocity of followers will approach the leader's velocity and the velocity errors will decline to an extremely small value around zero. Figure 2(b) gives the position curves of all vehicles in the platoon, from which we can see that vehicles will not collide during the whole driving cycle. Figure 2(c) also demonstrates that all vehicles will keep a given distance (about 10 m) under the proposed platoon

TABLE 1: Initial states of each vehicle and initial estimated values of driving resistance coefficients.

Vehicle	Leader	V1	V2	V3	V4	V5	V6	V7
$v(0)$	0	0	0	0	0	0	0	0
$\dot{v}(0)$	0	0	0	0	0	0	0	0
$r(0)$	68	63	46	38	30	21	8	0
$\hat{a}^+(0)$	0	0.8	0.9	0.85	0.85	0.8	0.85	0.8
$\hat{b}^+(0)$	0	0.004	0.004	0.0045	0.004	0.0045	0.004	0.0045
$\hat{c}^+(0)$	0	0.00016	0.00016	0.00016	0.00016	0.00016	0.00016	0.00016
$a1$	0	0.3	0.4	0.4	0.4	0.5	0.4	0.5
$b1$	0	0.004	0.003	0.005	0.004	0.005	0.004	0.005
$c1$	0	0.00018	0.00016	0.00014	0.00017	0.00015	0.00017	0.00015

TABLE 2: Control parameters of vehicles.

d	α_i	β_i	λ_i	k_1	k_2	$u_{\min}$	$u_{\max}$
10	100	5	10^{-10}	0.5	0.5	−2	2
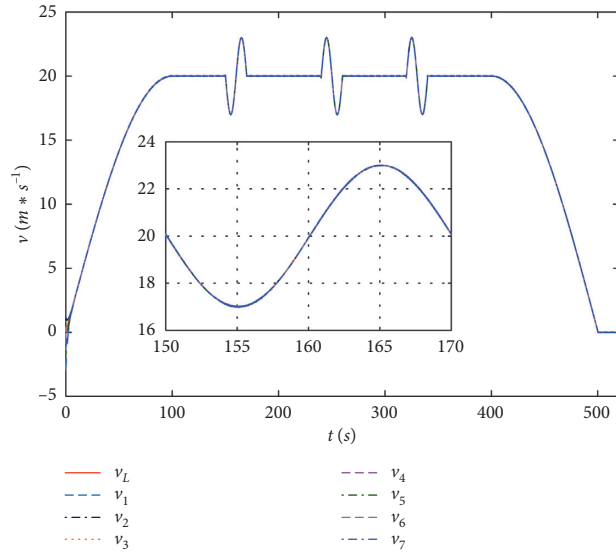
(a)
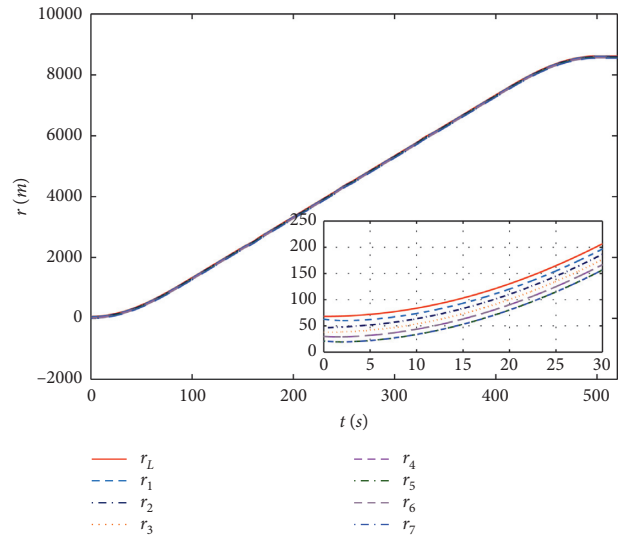
(b)
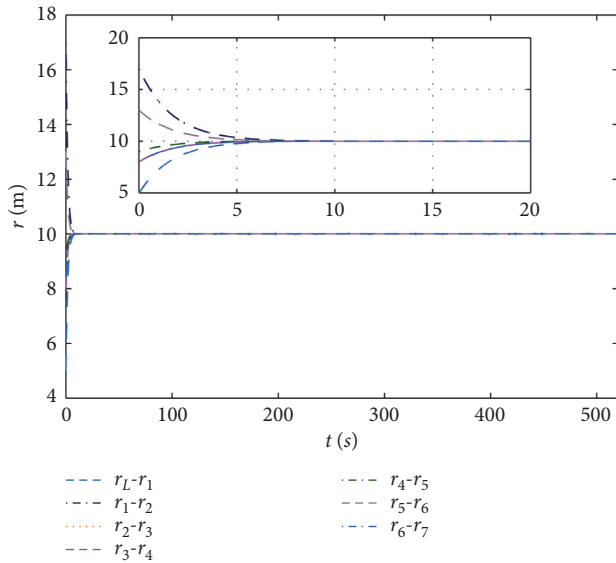
(c)
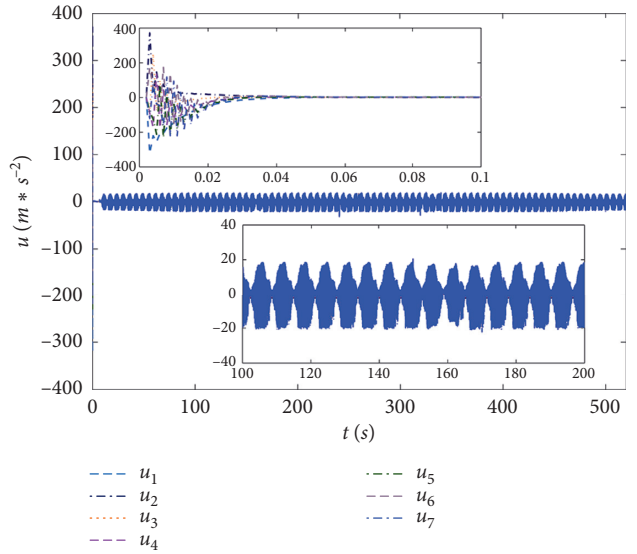
(d)

FIGURE 2: The simulation results of each vehicle with uncertain driving resistance: (a) the velocity curves; (b) the position curves; (c) the distances curves between two neighbor vehicles; (d) the control input curves.

(a)

(b)

(c)

(d)
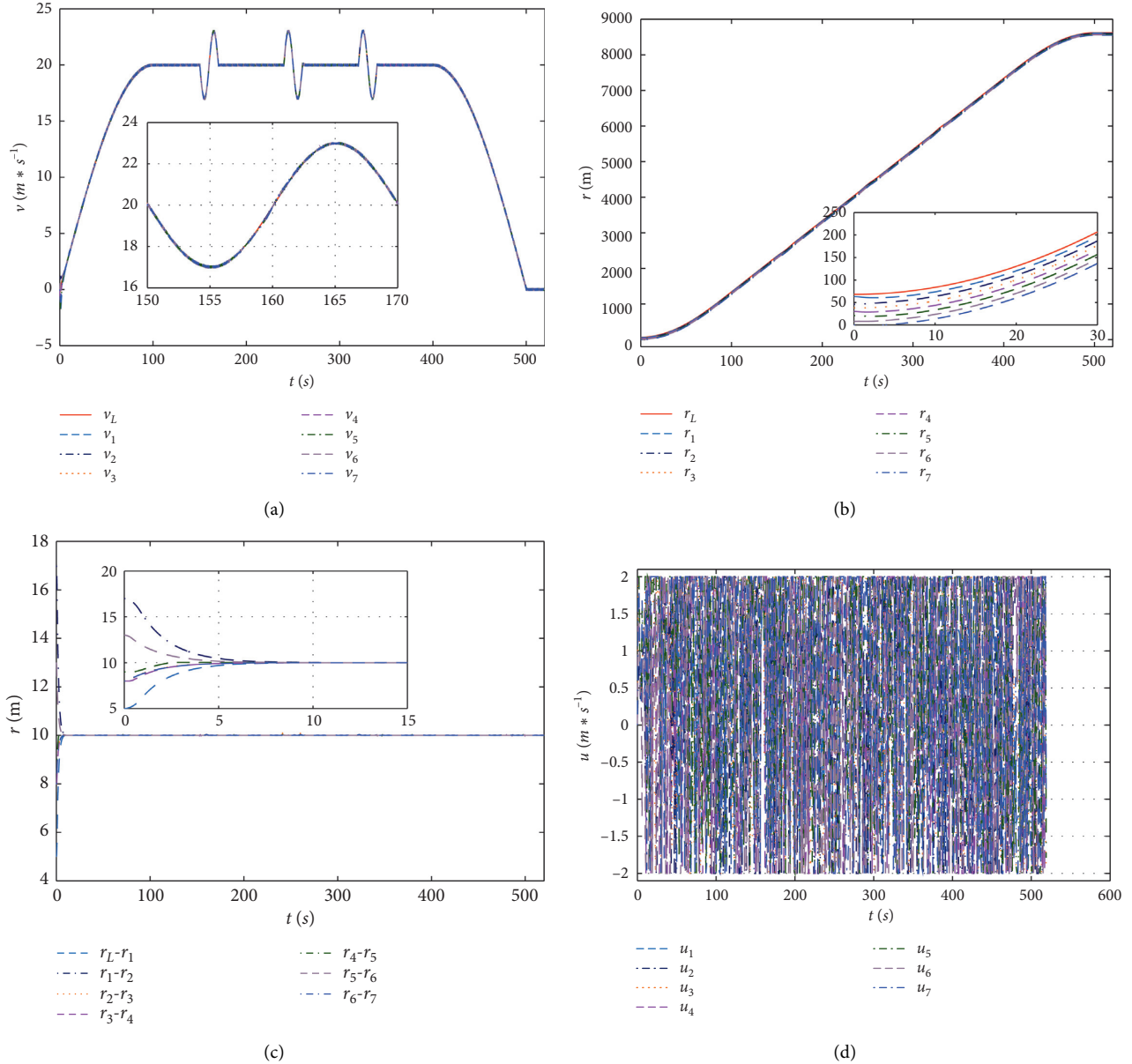
FIGURE 3: The simulation results of each vehicle with uncertain driving resistance and actuator saturation: (a) the velocity curves; (b) the position curves; (c) the distances curves between two neighbor vehicles; (d) the control input curves.

algorithms (19) and (22). Figure 2(d) shows the control input (acceleration or deceleration) of all followers, from which we can see that the control input decreases sharply from 400 m/s² to 20 m/s² within about 0.03 s. Then, the control input will converge to a relatively steady state (around 20 m/s² and −20 m/s²). However, such control input is infeasible in practical applications, as it exceeds the maximum output of vehicle actuator and causes the phenomena of actuator saturation. Therefore, we will consider the problem of actuator saturation in Case 2.

Case 2. Platoon with actuator saturation.

In this case, the control laws (34), (35), and (37) and coefficients adaptive laws (36) and (38) are applied to the vehicle platoon. We set the initial values of signal ϕ_i as $\phi_i = 0$

and $\dot{\phi}_i = 0$ for $i = 1, 2, \ldots, n$. The parameter of χ_i is chosen as $\chi_i = 100$ for $i = 1, 2, \ldots, n$.

Figure 3(a) shows the vehicle velocities and velocity errors (between followers and leader) by considering the influence of actuator saturation in the simulation. Compared with Figure 2(a), the control algorithms (34), (35), and (37) can also guarantee the performance of vehicle velocities and velocity errors. From Figures 3(b) and 3(c), we can also see that the proposed algorithms (34), (35), and (37) can maintain a desired intervehicle distance with their neighbors to ensure driving safety. Figure 3(d) gives the control input of all followers; it is obvious that the input (acceleration or deceleration) can be limited to 2 m/s by adopting the proposed control algorithms (34), (35), and (37), which satisfies the maximum output of vehicle actuators.

(a)

(b)

(c)

(d)
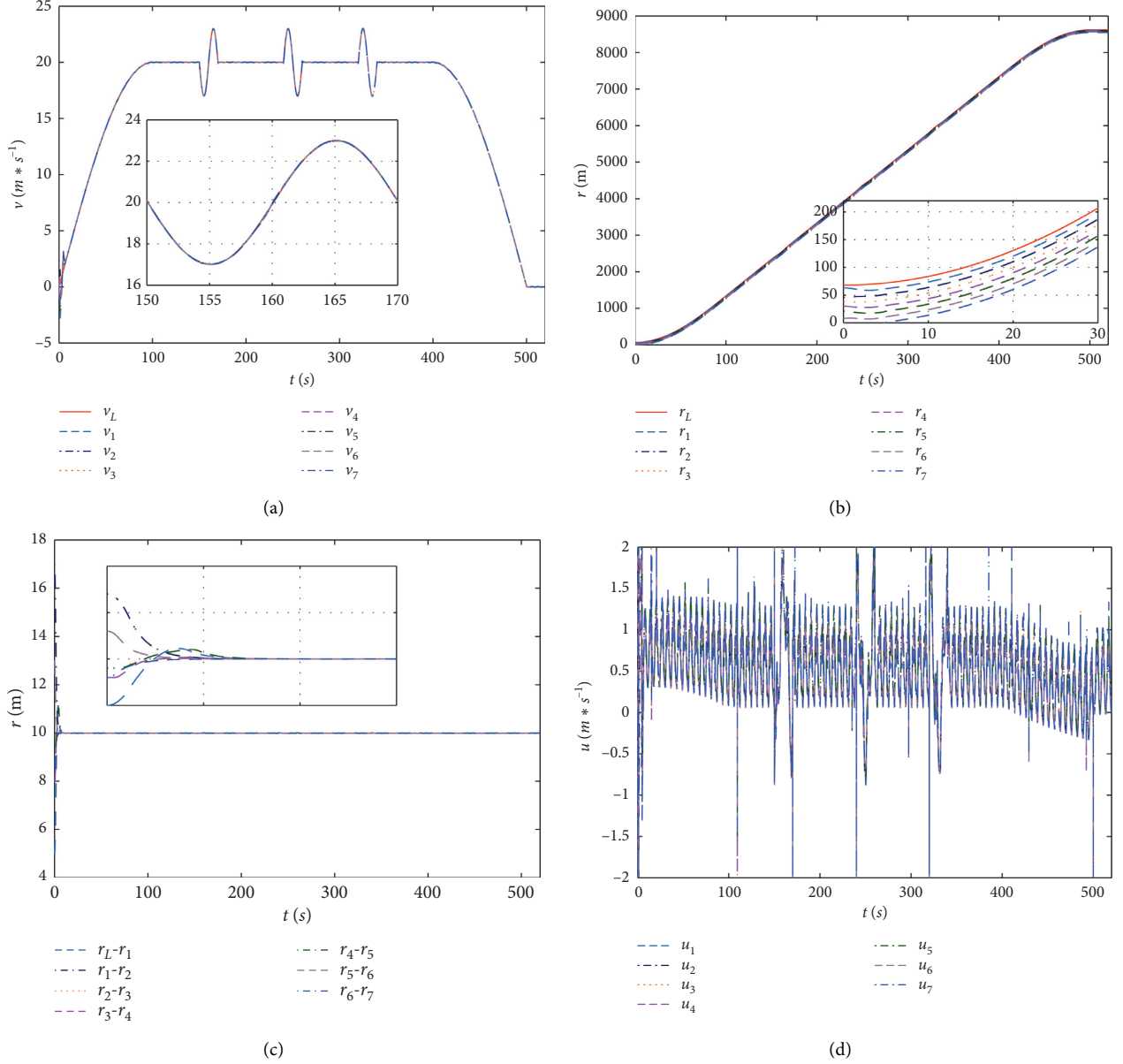
Figure 4: The simulation results of each vehicle with uncertain driving resistance, actuator saturation, and reduced chattering: (a) the velocity curves; (b) the position curves; (c) the distances curves between two neighbor vehicles; (d) the control input curves.

However, it triggers the chattering phenomenon, which may deteriorate the vehicle actuator and lead to the driving uncomfortableness for passengers.

To avoid chattering in practical implementation, the modified control algorithms (47) and (49) are proposed and simulations are performed in Case 3.

Case 3. Platoon with reduced chattering

In this case, the control laws (47) and (49) and coefficients adaptive laws (48) and (50) are applied to the vehicle platoon. The sigmoid-like function $(\delta_i/(|\delta_i + \varsigma|))$ is used to replace the $\text{sgn}(\cdot)$, where

$$\varsigma = 1 * 10^{-5}. \tag{52}$$

Figure 4(a) shows the vehicle velocities and velocity errors (between followers and leader). Compared with Figure 3(a), the amendment control algorithms (47) and (49) have not greatly influenced the performance of vehicle velocities and velocity errors. From Figures 4(b) and 4(c), one can see that the proposed amendment algorithms (47) and (49) can also maintain a desired intervehicle distance with their neighbors, which ensures the driving safety of vehicle platoon. Figure 4(d) illustrates the control input of all followers; it is obvious that influence of chatting is significantly

weakened compared with Figure 3(d). Therefore, better vehicle platoon performance can be obtained and the driving comfortableness can be enhanced.

*Remark 3.* In Case 1, we only consider the influence of uncertain driving resistance for vehicle platoon, where (19), (20), (22), and (23) are applied to the vehicle. However, it exceeds the maximum output of vehicle actuator and causes the phenomena of actuator saturation. Therefore, we consider the problem of actuator saturation in Case 2. And the control laws (34), (35), and (37) and coefficients adaptive laws (36) and (38) are applied to the vehicle platoon. However, it triggers the chattering phenomenon in simulation, which may deteriorate the vehicle actuator and lead to the driving uncomfortableness for passengers. To avoid chattering in practical implementation, the modified control algorithm (47), (49) is proposed and simulations are performed in Case 3. Finally, better vehicle platoon performance is obtained and the driving comfortableness is enhanced.

5. Conclusions

In this paper, we discuss the distributed adaptive control problem for vehicle platoon with uncertain driving resistance and actuator saturation. Coupled sliding surface (CSS) is deployed to link interconnected vehicles and an adaptive control method is adopted to estimate the variations of resistance coefficients. An antiwindup compensation based approach is utilized to attenuate the integral windup of the adaptive platoon control laws in case of actuator saturation. Theoretical results are verified via numerical simulations, which demonstrate that the proposed control algorithm can make every vehicle keep the desired distance with the preceding vehicle and all followers' velocity will gradually converge to the velocity of the leader even in the presence of uncertain driving resistance coefficients and actuator saturation.

Data Availability

The data used to support the findings of this paper are included within the article and are available from the corresponding author upon request.

Disclosure

Part of the content of this paper has been accepted for a podium presentation at the 36th Chinese Control Conference (CCC).

Conflicts of Interest

The authors declare that they have no conflicts of interest.

Acknowledgments

References

[1] E. Ahmed and H. Gharavi, "Cooperative vehicular networking: a survey," *IEEE Transactions on Intelligent Transportation Systems*, vol. 19, no. 3, pp. 996–1014, 2018.

[2] M. Taiebat, A. L. Brown, H. R. Safford, S. Qu, and M. Xu, "A review on energy, environmental, and sustainability implications of connected and automated vehicles," *Environmental Science & Technology*, vol. 52, no. 20, pp. 11449–11465, 2018.

[3] S. E. Shladover, "PATH at 20-history and major milestones," *IEEE Transactions on Intelligent Transportation Systems*, vol. 8, no. 4, pp. 584–592, 2007.

[4] E. Coelingh and S. Solyom, "All aboard the robotic road train," *IEEE Spectrum*, vol. 49, no. 11, pp. 34–39, 2012.

[5] Z. Wang, Y. Bian, S. E. Shladover, G. Wu, S. E. Li, and M. J. Barth, "A survey on cooperative longitudinal motion control of multiple connected and automated vehicles," *IEEE Intelligent Transportation Systems Magazine*, vol. 12, no. 1, pp. 4–24, 2020.

[6] M. di Bernardo, P. Falcone, A. Salvi, and S. Santini, "Design, analysis, and experimental validation of a distributed protocol for platooning in the presence of time-varying heterogeneous delays," *IEEE Transactions on Control Systems Technology*, vol. 24, no. 2, pp. 413–427, 2016.

[7] M. di Bernardo, S. A. Salvi, and S. Santini, "Distributed consensus strategy for platooning of vehicles in the presence of time-varying heterogeneous communication delays," *IEEE Transactions on Intelligent Transportation Systems*, vol. 16, no. 1, pp. 102–112, 2015.

[8] S. Santini, A. S. A. Salvi, M. SegataPescape, and R. Lo Cigno, "A consensus-based approach for platooning with intervehicular communications and its validation in realistic scenarios," *IEEE Transactions on Vehicular Technology*, vol. 66, no. 3, pp. 1985–1999, 2017.

[9] J.-W. Kwon and D. Chwa, "Adaptive bidirectional platoon control using a coupled sliding mode control method," *IEEE Transactions on Intelligent Transportation Systems*, vol. 15, no. 5, pp. 2040–2048, 2014.

[10] Y. Li, K. Li, T. Zheng, X. Hu, H. Feng, and Y. Li, "Evaluating the performance of vehicular platoon control under different network topologies of initial states," *Physica A: Statistical Mechanics and Its Applications*, vol. 450, pp. 359–368, 2016.

[11] P. Yang, M. Y. Tang, and X. Zhu, "Consensus based control algorithm for nonlinear vehicle platoons in the presence of time delay," *International Journal of Control, Automation and Systems*, vol. 17, no. 3, pp. 752–764, 2019.

[12] D. Swaroop, S. B. Hedrick, and S. B. Choi, "Direct adaptive longitudinal control of vehicle platoons," *IEEE Transactions on Vehicular Technology*, vol. 50, no. 1, pp. 150–161, 2001.

[13] M. Yan, J. Song, P. Yang, and Y. Tang, "Distributed adaptive sliding mode control for vehicle platoon with uncertain driving resistance," in *Proceedings of the 36th Chinese Control Conference (CCC) 2017*, pp. 9396–9400, IEEE, Dalian, China, July 2017.

[14] X. Guo, F. J. Wang, and R. S. H. Teo, "Distributed adaptive integrated-sliding-mode controller synthesis for string stability of vehicle platoons," *IEEE Transactions on Intelligent Transportation Systems*, vol. 17, no. 9, pp. 2419–2429, 2016.

[15] V. Filaretov, A. Zhirabok, A. Zuev, and A. Procenko, "The development of system of accommodation to faults of navigation sensors of underwater vehicles with resistance to

disturbance," in *Proceedings of the 14th International Conference on Control, Automation and Systems (ICCAS), 2014*, pp. 1548–1553, IEEE, Seoul, Republic of Korea, October 2014.

[16] C. E. Tannoury, S. Moussaoui, F. Plestan, N. Romani, and G. Pita-Gil, "Synthesis and application of nonlinear observers for the estimation of tire effective radius and rolling resistance of an automotive vehicle," *IEEE Transactions on Control Systems Technology*, vol. 21, no. 6, pp. 2408–2416, 2013.

[17] G. Shi-Gen, D. Hai-Rong, N. Bin et al., "Cooperative adaptive bidirectional control of a train platoon for efficient utility and string stability," *Chinese Physics B*, vol. 24, no. 9, Article ID 090506, 2015.

[18] S. Altmannshofer and C. Endisch, "Robust vehicle mass and driving resistance estimation," in *Proceedings of the American Control Conference (ACC), 2016*, pp. 6869–6874, IEEE, Boston, MA, USA, July 2016.

[19] M. Chen, S. S. Ge, and B. Ren, "Adaptive tracking control of uncertain MIMO nonlinear systems with input constraints," *Automatica*, vol. 47, no. 3, pp. 452–465, 2011.

[20] S. Gao, H. Dong, Y. Chen, B. Ning, G. Chen, and X. Yang, "Approximation-based robust adaptive automatic train control: an approach for actuator saturation," *IEEE Transactions on Intelligent Transportation Systems*, vol. 14, no. 4, pp. 1733–1742, 2013.

[21] Y. Li, S. Tong, and T. Li, "Adaptive fuzzy output-feedback control for output constrained nonlinear systems in the presence of input saturation," *Fuzzy Sets and Systems*, vol. 248, pp. 138–155, 2014.

[22] W. Sun, Z. Zhao, and H. Gao, "Saturated adaptive robust control for active suspension systems," *IEEE Transactions on Industrial Electronics*, vol. 60, no. 9, pp. 3889–3896, 2013.

[23] S. Li, L. Yang, and Z. Gao, "Adaptive coordinated control of multiple high-speed trains with input saturation," *Nonlinear Dynamics*, vol. 4, no. 83, pp. 2157–2169, 2016.

[24] M. Yan, Y. Tang, P. Yang, and L. Zuo, "Consensus based platoon algorithm for velocity-measurement-absent vehicles with actuator saturation," *Journal of Advanced Transportation*, vol. 2017, Article ID 8023018, 8 pages, 2017.

[25] R. Rajamani, *Vehicle Dynamics and Control*, Springer Science & Business Media, Berlin, Germany, 2011.

[26] Y. Cao, D. Stuart, W. Ren, and Z. Meng, "Distributed containment control for multiple autonomous vehicles with double-integrator dynamics: algorithms and experiments," *IEEE Transactions on Control Systems Technology*, vol. 19, no. 4, pp. 929–938, 2011.

[27] H. Nijmeijer and A. Van Der Schaft, *Nonlinear Dynamical Control Systems*, Springer, Berlin, Germany, 2013.

WILEY | Hindawi

Research Article

Signal Denoising Method Based on Improved Wavelet Threshold Function for Microchip Electrophoresis C⁴D Equipment

Yaonan Tong (iD)**, Jingui Li, Yaohui Xu, and Lichen Cao**

School of Information Science and Engineering, Hunan Institute of Science and Technology, Yueyang, Hunan 414006, China

Correspondence should be addressed to Yaonan Tong; tongyaon@hnist.edu.cn

A signal denoising method using improved wavelet threshold function is presented for microchip electrophoresis based on capacitively coupled contactless conductivity detection (ME-C⁴D) device. The evaluation results of denoising effect for the ME-C⁴D simulation signal show that using Daubechies 5 (db5) wavelet at a decomposition level 4 can produce the best performance. Furthermore, the denoising effect is compared with, as well as proved to be superior to, the existing techniques, such as Savitzky–Golay, Fast Fourier Transform, and soft threshold method. This method has been successfully applied to the self-developed ME-C⁴D equipment. After executing this method, the noise is cleanly removed, and the signal peak shape and peak area are well maintained.

1. Introduction

Microfluidic technology, especially microchip electrophoresis based on capacitively coupled contactless conductivity detection (ME-C⁴D) [1–3], has become a very important and promising branch of miniaturized total chemical analysis systems (μ-TAS) [4–6]. Because of its advantages of little samples and reagents consumption, fast analysis speed, high separation efficiency, and convenient miniaturization, microfluidic technology has been widely used in different fields, such as biomedicine [7, 8], food inspection [9], environmental monitoring [10], clinical application [11], and so on.

The ME-C⁴D device analyzes the ion composition in solution by detecting the change of electrical conductivity based on the coupling capacitance between the electrode and insulation layer of the chip [12–15]. Therefore, it can effectively avoid some troubles of electrochemical contact detect method, such as electrode scaling, electrolysis bubble, electric field interference, and so on [13–16]. But the ME-C⁴D device has poor anti-electromagnetic interference ability and low sensitivity [17–19]. The inherent noise of the system and the structure of the microfluidic chip will cause the ME-C⁴D signal to be disturbed, thus affecting the

analysis of the detection results and reducing its accuracy. Therefore, finding an appropriate method for signal denoising is an extremely important processing step before analysis and diagnosis.

The traditional signal denoising methods mainly include Fourier transform and curve fitting method. The Fourier transform is simple and easy to implement, but it is difficult to solve the noise filtering of nonstationary signals. The curve fitting method has high accuracy, but there are difficulties in selecting fitting points. The wavelet transform (WT), that developed rapidly from the 1980s, can fully highlight the characteristics of some aspects of problem, which has been widely used in capillary electrophoresis (CE) signal denoising [20, 21]. Furthermore, the wavelet threshold denoising developed from WT has better performance [22]. The denoising effect of this method mainly depends on the selection of threshold function. Some traditional threshold functions such as hard threshold and soft threshold are widely used for signal denoising due to the simple structure and good efficiency. For example, Liu uses hard threshold function to denoise microchip CE signal sampled from a home-built laser-induced fluorescence detection system [19]. Zhang et al. improve the soft threshold function to enhance the electrochemiluminescence CE signal denoising

effect [22]. The above WT methods can achieve excellent denoising effect, but paid less attention to the maintenance of wave peak area, which is a very important feature for analyzing the ME-C⁴D signal, and can reflect the content of the ion component to be detected [23]. Therefore, they are not very suitable for the ME-C⁴D signal.

The objective of this work is to develop an effective denoising method with minimal impact on the signal peak shape and area for improving the performance of the ME-C⁴D device. We have improved the wavelet threshold function according to the ME-C⁴D signal characteristics. Evaluation of denoising effect for the ME-C⁴D simulation signal has been done by selecting various wavelets and different decomposition levels, and it was found that db5 wavelet at level 4 is the optimal solution. Furthermore, the proposed method has been successfully applied to the self-developed ME-C⁴D equipment for signal denoising.

2. Materials and Methods

2.1. Chemicals. Potassium chloride, sodium chloride, lithium chloride sample solution, and MES-His buffer solution were of analytical grade, purchased from Sinopharm Chemical Reagent Co., Ltd. All chemicals were degassed ultrasonically for 5 minutes before being used and filtered with a $0.22 \, \mu m$ pore water microfiltration membrane.

2.2. Apparatus. A self-developed ME-C⁴D equipment used in the experiment described is shown in Figure 1. The microchip (cross-shaped structure; the chip separation channel length is 50 mm, 50 μm in width, and 25 μm in depth) was placed on the testing table of the detector. Under a given high-voltage electric field, the directional migration of the microchannel solution will occur. When the ions flow through the detector at the end of the channel, the induced current signal will be converted to a voltage signal and finally displayed on the computer after a series of processing steps. Among them, the control of voltage, sample injection time, and signal waveform can be controlled by the computer. The monitoring software on the PC terminal was self-developed.

2.3. Noise Sources. The analysis channel in the microfluidic chip is micron level, and the noncontact conductance detection is completed based on capacitive coupling principle. Therefore, the detected ME-C⁴D signal is very weak and will be disturbed by a lot of noise. In order to eliminate noise effectively, it is necessary to analyze the cause of noise and take corresponding measures to deal with it according to different noise sources.

According to the ME-C⁴D signal detection principle and experimental results, the interference and noise of the solution electrical conductivity signal mainly come from two sources. One is the inherent noise of the system, such as the external noise signal from the detection circuit caused by the action of electricity, magnetism, etc., which can be directly filtered through the hardware in the microfluidic chip detection device. The other is high-frequency noise, which is caused by the fast acquisition rate, microchip, detect circuits,
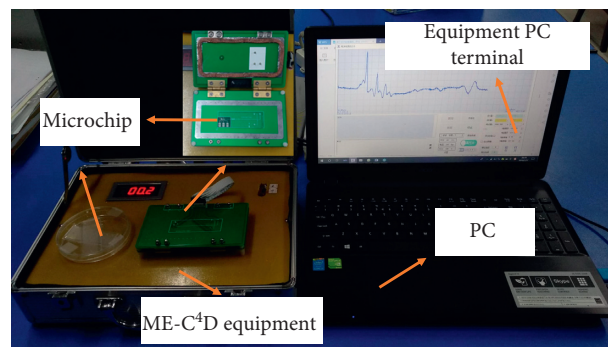
FIGURE 1: Self-developed ME-C⁴D equipment.

environmental disturbances, and so on [24]. It is difficult to filter by optimizing the hardware design of the ME-C⁴D equipment. The threshold method based on wavelet transform has a good denoising performance. Therefore, this paper studies the appropriate denoising method based on wavelet transform.

2.4. Wavelet Thresholding Denoising Theory. It is assumed that the ME-C⁴D signal with noise which is collected by microchip electrophoresis analysis device can be expressed as

$$f(i) = s(i) + n(i), \quad i = 0, 1, 2, \ldots, N-1, \quad (1)$$

where $f(i)$ is the ME-C⁴D signal with noise, $s(i)$ is a pure ME-C⁴D signal, and the noise signal is represented by $n(i)$. Because it is very difficult to recover $s(i)$ directly from the noisy signal $f(i)$, the useful signal and noise can be separated by processing the corresponding wavelet decomposition coefficients according to the different characteristics of it's in the wavelet transform. In practical applications, the useful signals are usually in the low frequency band, while the noise signals are usually in the high-frequency band. According to this characteristic, we can firstly decompose the signal by wavelet transform. As an example, three-level decomposition is shown in Figure 2. The noise-containing signal is decomposed into a low-frequency coefficient (CA1) and a high-frequency coefficient (CD1). CA1 can be further decomposed to form a new low-frequency coefficient (CA2) and a new high-frequency coefficient (CD2). With the increase of the decomposition level, the wavelet coefficient amplitude of the useful signal is basically unchanged, while the amplitude of wavelet coefficient of noise is rapidly attenuated to zero [25]. Therefore, the wavelet coefficients after decomposition can be processed by selecting appropriate threshold function, and then the signal can be reconstructed to achieve the effect of denoising.

2.5. Denoising by Improved Threshold Function. The wavelet coefficients of the ME-C⁴D signal have strong correlation at different decomposition levels, while the wavelet coefficients of the noise are weak or irrelevant [26], which is suitable for the denoising range of wavelet transform. The ME-C⁴D
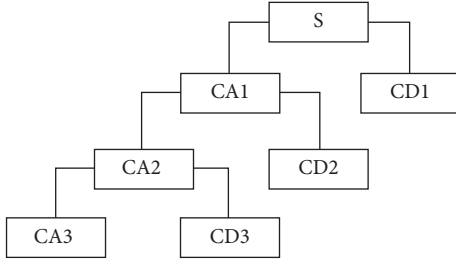
FIGURE 2: Signal three-level wavelet decomposition diagram.

FIGURE 3: Soft threshold function graph.

signal denoising procedure by wavelet transform is as follows:

(1) A suitable wavelet basis function similar to the original ME-C^{4}D signal is selected and the number of decomposition layers is determined. The J layer wavelet decomposition of the noise ME-C^{4}D signal is carried out by using Mallet algorithm, and the high-frequency coefficient components and low-frequency coefficient components of different decomposition scales are obtained.

(2) Select the threshold and use a threshold function to quantify the high-frequency wavelet coefficients from layer 1 to layer J.

(3) The low-frequency coefficients of layer J and the high-frequency coefficients of layer 1 to layer J processed by threshold function are inversely transformed to obtain the denoised ME-C^{4}D signal.

The denoising effect mainly depends on the selection threshold and the design of threshold function in step (2). In this work, the classical fixed threshold is adopted, and its expression is

$$\lambda = \sigma\sqrt{2\lg N}, \qquad (2)$$

where λ is the threshold, N is the length of the ME-C^{4}D signal, and σ represents the standard deviation of the noise signal. σ is used to measure the strength of the noise signal, and $\sigma = \mathrm{median}(w_{jk})/0.6745$, where $\mathrm{median}(\cdot)$ means the return median function.

There are two classical types of threshold functions for wavelet denoising, that is, hard and soft threshold. The soft threshold function is more representative. It can be defined as

$$\widehat{w}_{jk} = \begin{cases} w_{jk} - \lambda, & w_{jk} \geq \lambda, \\ 0, & |w_{jk}| < \lambda, \\ w_{jk} + \lambda, & w_{jk} \leq -\lambda, \end{cases} \qquad (3)$$

where w_{jk} is the wavelet coefficient of the original signal after wavelet transform, $\widehat{w}_{jk}$ is the estimated wavelet coefficient after quantification, and λ is the threshold. The soft threshold function graph is depicted in Figure 3.

It can be seen from Figure 3 that the soft threshold function has a good continuity, which overcomes the shortcomings of discontinuity in the hard threshold
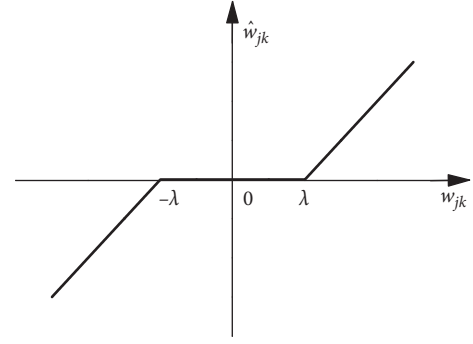
function and solves the problem that some oscillations will occur in the reconstructed signal. However, there is a constant deviation between original and estimated value of the wavelet coefficient. It is bound to make the reconstructed signal produce distortion and reduce the accuracy. In addition, the wavelet denoising principle illustrates that the smaller wavelet coefficients are also composed of useful signals and noises [27]. However, according to equation (3), if the wavelet coefficients with absolute values smaller than the threshold are set to zero, some useful signal information will be lost and thus the signal-to-noise ratio (SNR) will be reduced.

In order to overcome the above defects of soft threshold function and improve the denoising effect, a new threshold function should meet the following requirements:

(1) The function is continuous at the threshold points.

(2) The constant deviation between the original and quantized wavelet coefficients is reduced as much as possible. However, if the deviation is reduced to zero, it will become a hard threshold function, which cannot achieve the improvement effect [25].

(3) Retain some useful signal information in smaller wavelet coefficients to reduce signal distortion.

Based on the three above requirements, this paper introduces nonlinear function and variable parameters and proposes an improved threshold function:

$$\widehat{w}_{jk} = \begin{cases} w_{jk} + \mathrm{sign}(w_{jk}) \cdot (-\lambda + a\lambda^3), & |w_{jk}| \geq \lambda, \\ aw_{jk}^3, & |w_{jk}| < \lambda, \end{cases} \qquad (4)$$

where a is a variable parameter less than $1/\lambda^2$. The improved threshold function has continuity and overcome the defect of constant deviation of soft threshold function. By multiplying a with the smaller wavelet coefficient w_{jk}, the removal ratio of noise signal can be controlled by adjusting the value of a. By this mean, the useful signal information in the small wavelet coefficients can be retained flexibly, so the denoised signal is closer to the original one. These properties of this improved threshold function and the corresponding proof are presented as follows:

(1) Continuity analysis is

$$\lim_{w_{jk} \longrightarrow -\lambda^{-}} \widehat{w}_{jk} = \lim_{w_{jk} \longrightarrow -\lambda^{+}} \widehat{w}_{jk} = -a\lambda^{3}, \qquad (5)$$

$$\lim_{w_{jk} \longrightarrow \lambda^{-}} \widehat{w}_{jk} = \lim_{w_{jk} \longrightarrow \lambda^{+}} \widehat{w}_{jk} = a\lambda^{3}. \qquad (6)$$

The threshold function is continuous at threshold λ and $-\lambda$. Therefore, the threshold function is continuous over the whole real number field.

(2) Progressive analysis is

$$\lim_{w_{jk} \longrightarrow +\infty} \frac{\widehat{w}_{jk}}{w_{jk}} = \lim_{w_{jk} \longrightarrow +\infty} \left(1 + \frac{a\lambda^{3} - \lambda}{w_{jk}}\right) = 1, \qquad (7)$$

$$\lim_{w_{jk} \longrightarrow -\infty} \frac{\widehat{w}_{jk}}{w_{jk}} = \lim_{w_{jk} \longrightarrow -\infty} \left(1 + \frac{\lambda - a\lambda^{3}}{w_{jk}}\right) = 1. \qquad (8)$$

When $w_{jk} \longrightarrow \infty$, $\widehat{w}_{jk}$ takes $\widehat{w}_{jk} = w_{jk}$ as the asymptote and approaches w_{jk} infinitely, so as to reduce the deviation between the original and the threshold quantized wavelet coefficients as much as possible.

The comparison between hard, soft, and improved function is shown in Figure 4. When a is 0, the improved threshold function is equivalent to the traditional soft threshold function, and when $a \longrightarrow 1/\lambda^{2}$, the estimated value $\widehat{w}_{jk}$ is closer to the original wavelet coefficient w_{jk}. The parameters can be adjusted freely to denoising different signals. Therefore, the improved threshold function was significantly better than the soft threshold function at adaptive ability and flexibility.

3. Results and Discussion

3.1. Denoising of the ME-C^{4}D Simulation Signal. The ME-C^{4}D signal has some peaks, generally represented as Gaussian peaks, reflecting the characteristic spectral lines of a particular substance. When analyzing the substance composition, the obtained peaks' spectra are compared with the characteristic spectral line of some substances. Then, the detected peaks' spectra can indicate which components are contained in the mixture [28].

Due to the lack of standard testing equipment, the simulation means are often used in the research of μ-TAS signal denoising [22, 29]. When the effectiveness is verified by simulation, the method is applied to the self-developed instrument. Based on the simulation model to capillary electrophoresis signal [29], and according to the characteristics of actual ME-C^{4}D signal, a mathematical model of simulation signal was established as follows:

$$I = \frac{A_1}{\sqrt{2\pi}\sigma_1} e^{-\left((t-t_1)^2/2\sigma_1^2\right)} + \frac{A_2}{\sqrt{2\pi}\sigma_2} e^{-\left((t-t_2)^2/2\sigma_2^2\right)}$$
$$\qquad (9)$$
$$+ \frac{A_R}{\sqrt{2\pi}\sigma_R} e^{-\left((t-t_R)^2/2\sigma_R^2\right)} + I_0,$$

--- Hard threshold function
— Improved threshold function
·-·- Soft threshold function
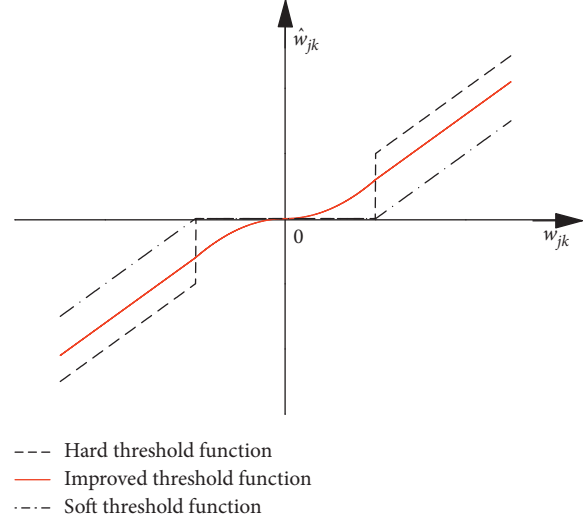
FIGURE 4: Improved threshold function graph.

where I is the simulation ME-C^{4}D signal, A_R is the area of the peak, t_R represents the central peak position, σ_R represents the half peak width, and I_0 is used to adjust the position of the baseline.

As the Gaussian white noise is close to the noise in the actual ME-C^{4}D signal, a certain proportion of Gaussian white noise was added to an ideal signal. The mathematical model can be expressed as follows:

$$f = I + \beta \cdot \text{noise}, \qquad (10)$$

where noise is Gaussian white noise signal, and β is the proportional coefficient. The ideal and noisy signals are simulated and shown in Figure 5.

3.1.1. Evaluation of Denoising Effect. In order to intuitively compare the denoising effect of different methods on ME-C^{4}D simulation signals, the following two evaluation indexes were introduced:

(1) Signal-to-noise ratio (SNR) is

$$\text{SNR} = 10\log \frac{\sum_{i=1}^{N} f^2(i)}{\sum_{i=1}^{N} \left[f(i) - \widehat{f}(i)\right]^2} \text{ (dB)}. \qquad (11)$$

(2) Root mean square error (RMSE) is

$$\text{RMSE} = \sqrt{\frac{1}{n} \sum_{i=1}^{N} \left[f(i) - \widehat{f}(i)\right]^2}, \qquad (12)$$

where $f(i)$ is the original signal, $\widehat{f}(i)$ is the reconstructed signal after denoising, n is the sampling points, and N is the signal length. The above two equations indicate that the larger SNR is, the smaller RMSE is, and the better signal denoising effect is.
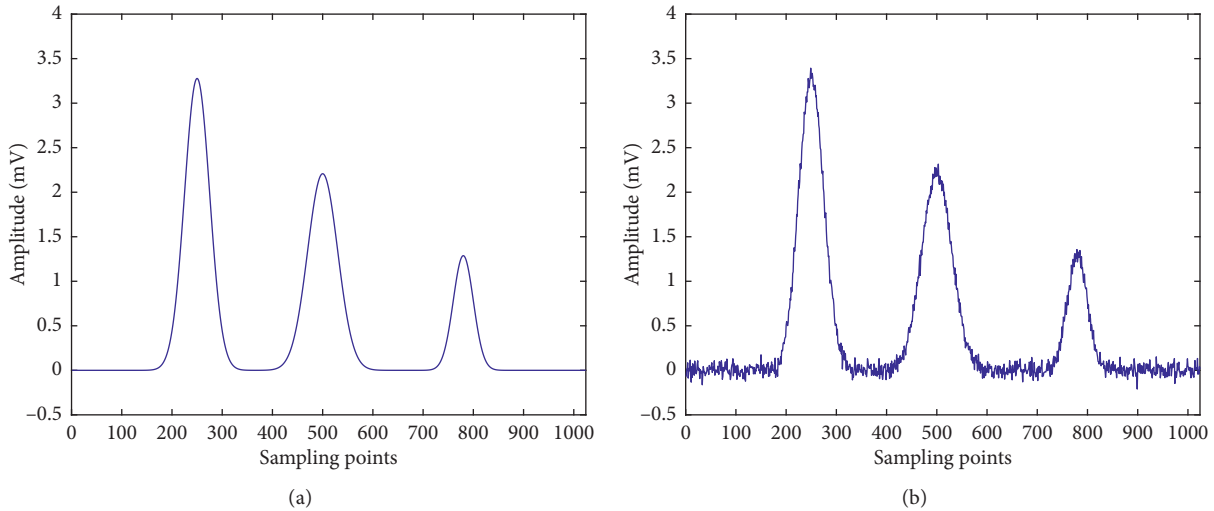
FIGURE 5: Simulation ME-C^{4}D signal and its noisy signal. (a) Simulation ideal signal. (b) Simulation noisy signal.

3.1.2. Selection of Wavelet Basis and Decomposition Level.

Using different wavelet basis functions to denoise the same type of signal will produce different effects. Generally, wavelet bases should have the following characteristics: linear phase, short support, higher vanishing distance, etc. [30]. However, few wavelet bases can have these characteristics at the same time. In this paper, several common wavelet bases were selected for denoising experiments. The comparative analysis of common wavelet bases characteristics is shown in Table 1.

In order to select the optimal wavelet basis and obtain the best denoising effect, three different wavelet bases of db1~db9, sym1~sym9, and coif1~coif5 were evaluated in this paper, and the improved threshold function was used to denoise the signal containing noise. The SNR and RMSE curves of the denoised signals are shown in Figure 6.

After denoising with db5 wavelet basis, the SNR is the largest, and the RMSE is the smallest, so the denoising effect is the best (Figure 6). Therefore, db5 wavelet basis was used in the following experiments.

In the process of signal denoising by wavelet transform, the selection of appropriate decomposition layers is also very important problem. On the one hand, the larger the number of decomposition layers, the greater the difference between noise and signal performance, and the easier it is to separate. On the other hand, too many layers will make the reconstructed signal more distorted, which will affect the denoising effect to a certain extent. Therefore, it is necessary to deal with this contradiction strictly when selecting the level of decomposition for getting better denoising effect.

On the premise of selecting db5 wavelet basis, the denoising effect of simulated ME-C^{4}D signal under different decomposition layers is depicted in Figure 7. It shows that the 4-layer decomposition can get a good signal denoising effect.

3.1.3. Comparison with Other Denoising Methods.

In order to verify the denoising effect of the proposed method,

different methods were used to carry out the simulation experiment for the ME-C^{4}D signal with different SNR Gaussian white noise. The SNR and RMSE comparison data for the denoise signal are shown in Table 2.

The denoising method presented in this paper has the highest SNR and the lowest RMSE; the denoising effect was significantly better than other methods (Table 2, shown in boldface).

Figure 8 shows the denoising results by the Savitzky–Golay, Fast Fourier Transform, soft threshold method, and the proposed method, respectively. By analyzing the waveform after denoising, it can be seen that the Savitzky–Golay and Fast Fourier Transform were used to denoise the signal, the noise is still apparent (Figures 8(a) and 8(b)). The ME-C^{4}D signal after denoising by the soft threshold method the signal baseline is smooth, but part of the characteristic signal information is lost (Figure 8(c)). After denoising with the proposed method, the noise is basically removed, the baseline is smooth, the characteristic signal is well retained, and the reconstructed signal after denoising is closer to the original signal (Figure 8(d)). Therefore, the proposed method has more advantages over the above methods for ME-C^{4}D signal denoising.

3.2. Application.

After theoretical analysis and simulation verification, the proposed method was applied to denoising for the actual signal, which was detected by self-developed ME-C4D and delivered to PC terminal.

The buffer solution of 10 mM MES-His (pH 6.15) and the target sample solution of 0.1 mM were introduced to the corresponding position of the microchip and then placed on the detection table of the self-developed equipment. Set the excitation signal source parameter $f = 200$ kHz, Vpp = 60 V, high voltage injection 1 s; the collected ME-C^{4}D signals are shown in Figure 9.

The transverse axis is the number of sampling points; every 10 sampling points represent the time of 1 s. The longitudinal coordinate represents the amplitude, and the

TABLE 1: Common wavelet bases characteristics.

Basis	db$N$	sym$N$	coif$N$
Symmetry	Approximate symmetry	Approximate symmetry	Approximate symmetry
Orthogonality	Have	Have	Have
Compact support	Have	Have	Have
Support length	$2N-1$	$2N-1$	$6N-1$
Filter length	$2N$	$2N$	$6N$
Vanishing moments	N	N	$2N$

(a)   (b)
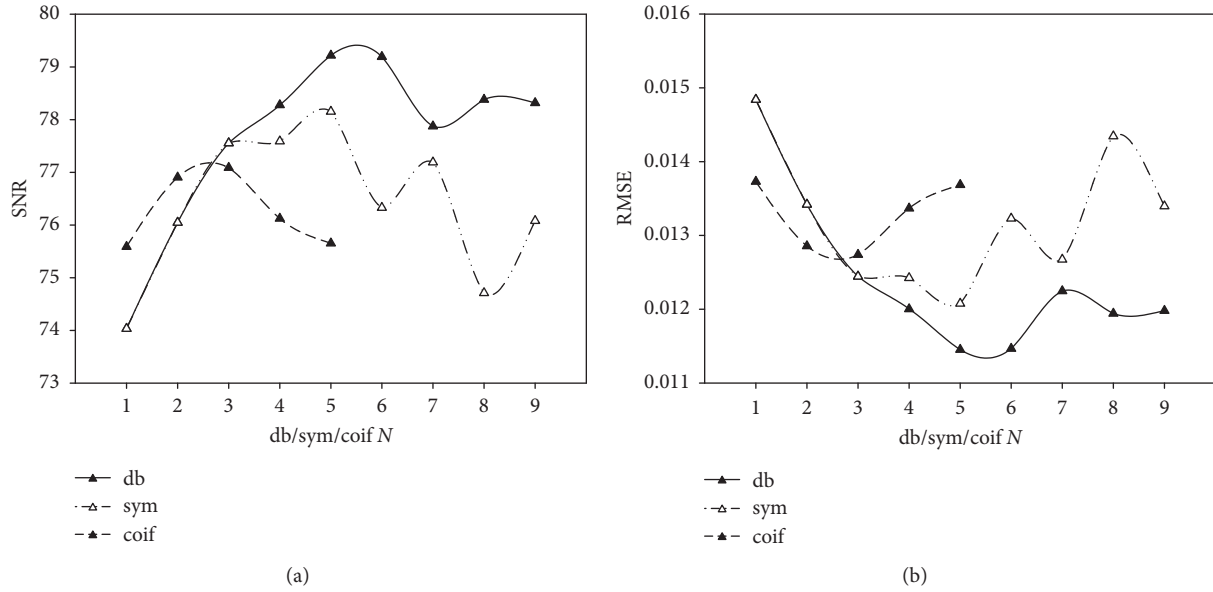
FIGURE 6: SNR and RMSE after denoising with different wavelet bases. (a) SNR after denoising with different wavelet bases. (b) RMSE after denoising with different wavelet bases.
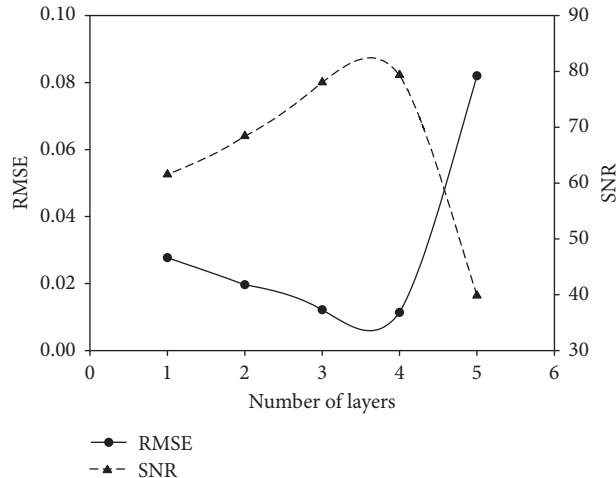
FIGURE 7: SNR and RMSE after denoising at different decomposition levels.

three wave peaks represent K^+, Na^+, Li^+. It is clear that the ME-C^{4}D signal is interfered by a certain degree of noise.

Since the above signal is acquired from the device and the noise is not artificially added, we cannot obtain the original ideal noise-free signal; thus, the evaluation indexes SNR and RMSE cannot be used to quantitatively analyze the denoising effect [31]. For the actual collected ME-C^{4}D signal, what is really valuable is the peak, especially the peak area or peak height, which reflects the component content of the substance to be measured. Therefore, the peak area or peak height can be used as the evaluation index for denoising effect. Because the peak area can be obtained by multiplying

TABLE 2: Comparison results of simulation signal denoising with different methods.

Parameter	Savitzky–Golay	Fast Fourier transform	Soft threshold method	Proposed method	SNR of noisy signal (dB)
SNR	54.6092	59.2802	65.1503	**71.4715**	
RMSE	0.0392	0.0310	0.0231	**0.0169**	21
SNR	64.0419	70.9654	74.6367	**78.6393**	
RMSE	0.0245	0.0173	0.0144	**0.0118**	25
SNR	72.1866	76.0289	80.9725	**85.7153**	
RMSE	0.0163	0.0134	0.0105	**0.0083**	29
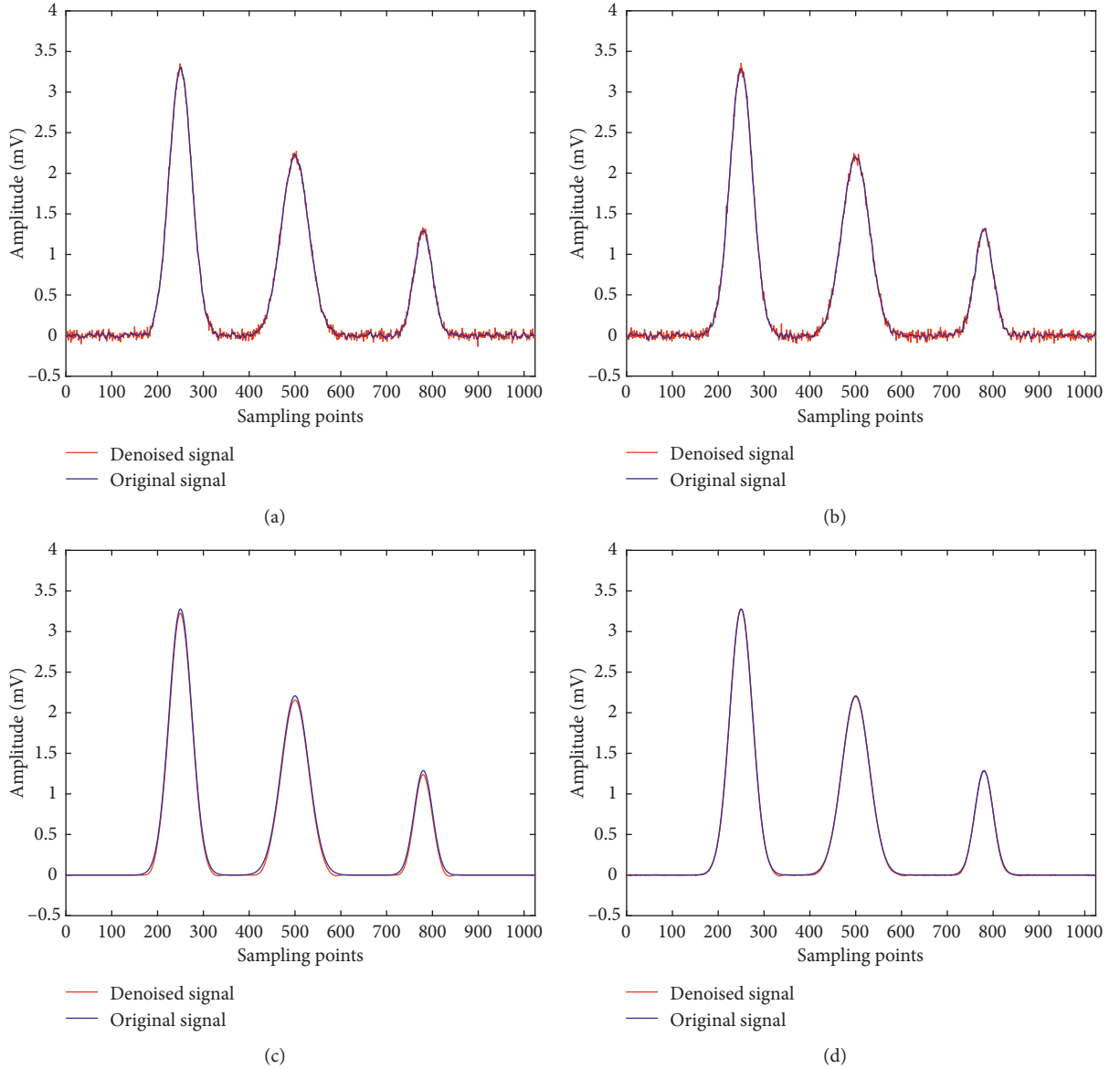
FIGURE 8: The results of simulation signal denoising of 29 dB by different methods. (a) Savitzky–Golay. (b) Fast Fourier Transform. (c) Soft threshold method. (d) The proposed method.

the peak height and the half width, the peak area distortion is used only as the evaluation index to quantitatively analyze the denoising processing effect of the ME-C^{4}D signal. The lower the peak area error is, the lower the distortion is, and the better the denoising effect is.

$$\Delta A = \left| \frac{(A_d - A_o)}{A_d} \right| \times 100, \qquad (13)$$

where A is the peak area of ME-C^{4}D signal; subscripts d and o represent before and after signal processing, respectively.
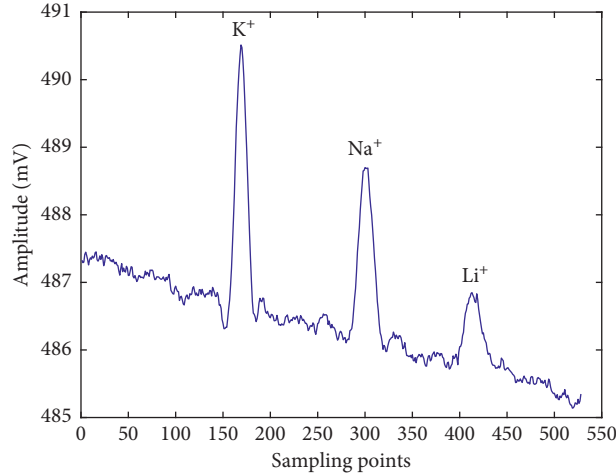
FIGURE 9: Detection signal with concentrations of 0.1 mM.
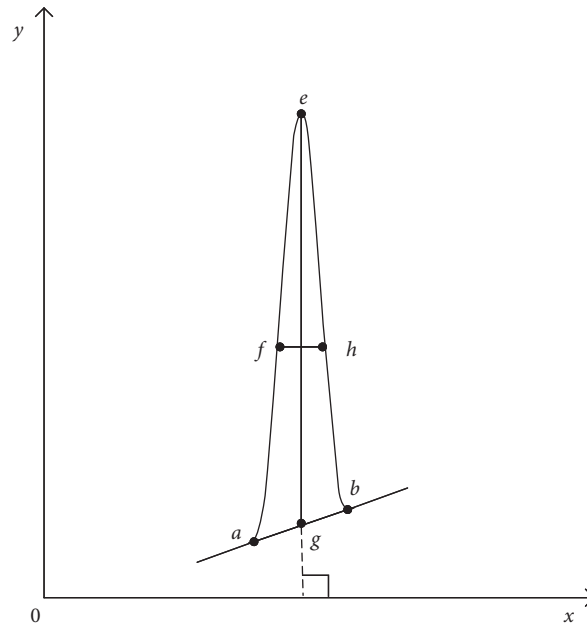
FIGURE 10: Schematic diagram of peak area calculation method.

Generally speaking, the peak area distortion degree kept within 5% belongs to the normal range.

For peaks with symmetrical shape and no baseline drift, the peak height is the vertical distance from the peak top to the baseline at the bottom of the peak, and the half peak width is the width at 1/2 the peak height. However, when the peak shape is asymmetrical and there is a baseline drift, the calculation of peak area by the above method will produce a large error. Therefore, this paper uses the following method to calculate the peak area.

The schematic diagram for calculating the peak area is shown in Figure 10. Firstly, the baseline AB is determined by the first derivative method. A threshold value is set, when the first derivative is greater than the threshold, it is determined as the starting point of the peak. When the first derivative changes from positive to negative, it is judged as the apex of the peak. After the apex is

determined, if the absolute value of the first derivative value of the signal is less than the threshold, it is defined as the end point of the peak. Then, a line perpendicular to the x-axis is drawn from the apex E of the peak. This line intersects the baseline AB at point G, and the length of EG is the peak height (h_{EG}). Finally, a line parallel to the x-axis and through the midpoint of the EG is drawn. This line intersects the wave peak at two points, F and H, and the length of FH is half width of the peak (σ_{FH}). So, the peak area can be calculated as

$$A = h_{EG} \times \sigma_{FH}. \tag{14}$$

The improved threshold function denoising method is adopted to denoise the signal in Figure 9, and the results are shown in Figure 11(d). In order to fully verify the effectiveness of the improved threshold function method for denoising the ME-C^{4}D signal, the denoising results of
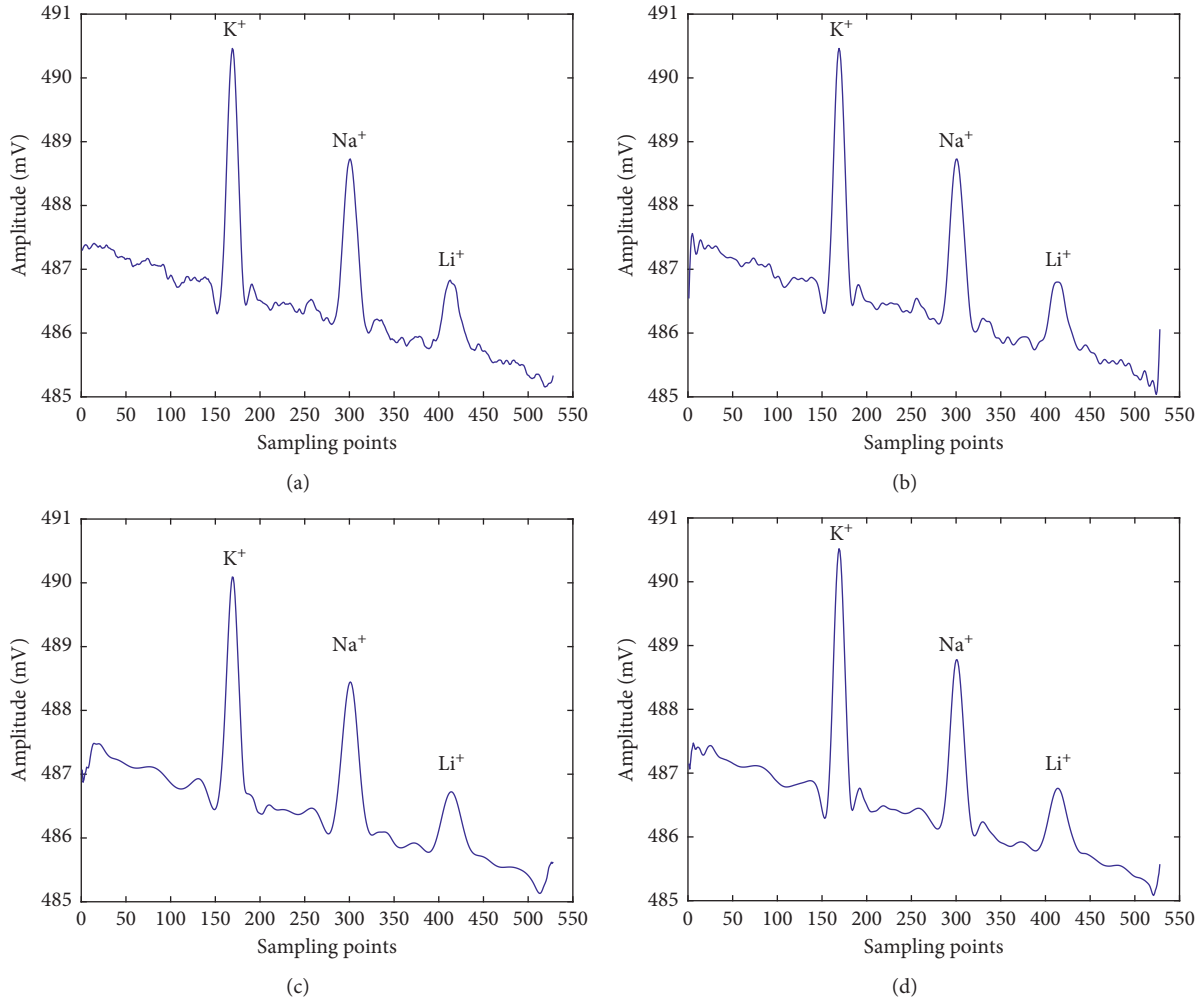
Figure 11: Effect of different methods on signal denoising with concentration of 0.1 mM. (a) Savitzky–Golay. (b) Fast Fourier transform. (c) Soft threshold method. (d) Proposed method.

Savitzky–Golay method, Fast Fourier Transform method, and traditional soft threshold method are used for comparative analysis. The denoising effect is shown in Figures 11(a)–11(c). The peak area distortion degrees after denoising of each method are calculated according to (13) and (14), as shown in Table 3.

It can be seen from the data in Table 3 that after Savitzky–Golay and Fast Fourier Transform are used to denoise the ME-C^{4}D signal, the peak area distortion of the third peak of the signal is greater than 5%, and Figures 11(a) and 11(b) are showing that there is still some noise left in the reconstructed signal after denoising, which has a certain impact on the accuracy of the ME-C^{4}D signal analysis. When using soft threshold function to denoise, the baseline is smooth and the noise is basically removed, but the area distortion of the first peak and the third peak are 10.9102% and 12.5462%, respectively, which greatly affects the determination of the content of the measured substance. Obviously, the new proposed method can remove the noise well, the denoised signal is smooth, and the peak areas of the three peaks remain basically unchanged. All these above suggest that the

Table 3: Peak area distortion after denoising by different methods.

Denoising method	Peak area distortion		
	First peak (%)	Second peak (%)	Third peak (%)
Savitzky–Golay	0.2532	0.7758	7.4411
Fast Fourier transform	0.3032	0.4154	6.2670
Soft threshold method	10.9106	3.6005	12.5462
Proposed method	**1.4160**	**0.8991**	**3.9441**

improved threshold function method in this paper is effective and superior to the existing methods.

4. Concluding Remarks

In this work, a method of ME-C^{4}D signal denoising based on an improved threshold function of wavelet transform is proposed. The simulation experiment results suggest that the proposed method in this paper is superior to Savitzky–Golay,

Fast Fourier Transform, and soft threshold method. The study on the denoising of the actual detection signals of samples with concentrations of 0.1 mM proves that the proposed method has excellent denoising effect and powerful peak area preservation ability. Therefore, this method has important practical value for signal denoising of ME-C^{4}D. Furthermore, the improved threshold function method has some limitations, such as the value of the variable parameter a is manually selected by our experience. It is expected that an algorithm will be designed in the future to realize parameter optimization.

Abbreviation

ME-C^{4}D: Microchip electrophoresis based on capacitively coupled contactless conductivity detection.

Data Availability

The data used to support the findings of this study are available from the corresponding author upon request.

Conflicts of Interest

The authors declare that they have no conflicts of interest regarding the publication of this paper.

Acknowledgments

References

[1] K. A. Mahabadi, I. Rodriguez, C. Y. Lim et al., "Capacitively coupled contactless conductivity detection with dual top-–bottom cell configuration for microchip electrophoresis," *Electrophoresis*, vol. 31, no. 6, pp. 1063–1070, 2010.

[2] K. C. A. Rezende, R. C. Moreira, L. P. L. Logrado et al., "Authenticity screening of seized whiskey samples using electrophoresis microchips coupled with contactless conductivity detection," *Electrophoresis*, vol. 37, no. 21, pp. 2891–2895, 2016.

[3] F. Q. Nie, M. Macka, and B. Paull, "Micro-flow injection analysis system: on-chip sample preconcentration, injection and delivery using coupled monolithic electroosmotic pumps," *Lab on A Chip*, vol. 7, no. 11, 2007.

[4] A. Manz, N. Graber, and H. M. Widmer, "Miniaturized total chemical analysis systems: a novel concept for chemical sensing," *Sensors and Actuators B (Chemical)*, vol. 1, no. 1–6, pp. 244–248, 1990.

[5] T. Vilkner, D. Janasek, and A. Manz, "Micro total analysis systems. Recent developments," *Analytical Chemistry*, vol. 76, no. 12, pp. 3373–3386, 2004.

[6] G. F. Christopher and S. L. Anna, "Topical review: microfluidic methods for generating continuous droplet streams," *Journal of Physics D Applied Physics*, vol. 40, no. 19, pp. 3373–3386, 2007.

[7] D. Liu, H. Zhang, F. Fontana, J. T. Hirvonen, and H. A. Santos, "Current developments and applications of microfluidic technology toward clinical translation of nanomedicines," *Advanced Drug Delivery Reviews*, vol. 128, pp. 54–83, 2018.

[8] H. Kimura, Y. Sakai, and T. Fujii, "Organ/body-on-a-chip based on microfluidic technology for drug discovery," *Drug Metabolism and Pharmacokinetics*, vol. 33, no. 1, pp. 43–48, 2017.

[9] H. Yu, G. Z. Cai, L. Y. Zheng et al., "A microfluidic signal-off biosensor for rapid and sensitive detection of Salmonella using magnetic separation and enzymatic catalysis," *Food Control*, vol. 103, pp. 186–193, 2019.

[10] G. Chen, Y. Lin, and J. Wang, "Microchip capillary electrophoresis with electrochemical detection for monitoring environmental pollutants," *Current Analytical Chemistry*, vol. 2, no. 1, pp. 43–50, 2006.

[11] L. Mou, R. H. Dong, B. F. Hu et al., "Hierarchically structured microchip for point-of-care immunoassays with dynamic detection ranges," *Lab on a Chip*, vol. 19, 2019.

[12] R. M. Guijt, E. Baltussen, G. van der Steen et al., "Capillary electrophoresis with on-chip four-electrode capacitively coupled conductivity detection for application in bioanalysis," *Electrophoresis*, vol. 22, no. 12, pp. 2537–2541, 2001.

[13] K. Pavel and P. C. Hauser, "Capacitively coupled contactless conductivity detection for microseparation techniques-recent developments," *Electrophoresis*, vol. 32, no. 1, pp. 30–42, 2011.

[14] W. K. T. Coltro, R. S. Lima, T. P. Segato et al., "Capacitively coupled contactless conductivity detection on microfluidic systems-ten years of development," *Analytical Methods*, vol. 4, no. 1, 2012.

[15] Z. Huang, M. Yang, H. You, and Y. Xie, "Concurrent determination and separation of inorganic cations and anions in microchip electrophoresis with precisely controlled high-voltage," *Electrophoresis*, vol. 39, no. 14, pp. 1802–1807, 2018.

[16] K. Pavel and P. C. Hauser, "A review of the recent achievements in capacitively coupled contactless conductivity detection," *Analytica Chimica Acta*, vol. 607, no. 1, pp. 15–29, 2008.

[17] F. Georg, H. Anna, S. Walter et al., "End-to-end differential contactless conductivity sensor for microchip capillary electrophoresis," *Analytical Chemistry*, vol. 82, no. 8, pp. 3270–3275, 2010.

[18] W. Cao, X. Chen, X. Yang, and E. Wang, "Discrete wavelets transform for signal denoising in capillary electrophoresis with electrochemiluminescence detection," *Electrophoresis*, vol. 24, no. 18, pp. 3124–3130, 2003.

[19] B.-F. Liu, Y. Sera, N. Matsubara, K. Otsuka, and S. Terabe, "Signal denoising and baseline correction by discrete wavelet transform for microchip capillary electrophoresis," *Electrophoresis*, vol. 24, no. 18, pp. 3260–3265, 2003.

[20] Y. N. Tong, Y. G. He, H. M. Li et al., "Method for wavelet transformation using switched-current circuit with approximation optimization in frequency domain," *Journal of Electronic Measurement and Instrument*, vol. 28, no. 3, pp. 262–271, 2014.

[21] C. Gao, M. Shen, X. Liu, L. Wang, and M. Chu, "End-point static control of basic oxygen furnace (BOF) steelmaking based on wavelet transform weighted twin support vector regression," *Complexity*, vol. 2019, Article ID 7408725, 16 pages, 2019.

[22] H. F. Zhang, X. W. Liu, X. H. Shao et al., "The study of the improved wavelet thresholding with translation invariant de-

noising on capillary electrophoresis signal," in *Proceedings of the 2009 4th IEEE International Conference on Nano/Micro Engineered and Molecular Systems*, Shenzhen, China, 2009.

[23] X. Y. Chen and J. Y. Mo, "Application of lifting-scheme based wavelet transform to the chemical signals," *Journal of Instrumental Analysis*, vol. 23, no. 1, pp. 5–8, 2004.

[24] C. Chen, W. Teng, and J. H. Hahn, "Nanoband electrode for high-performance in-channel amperometric detection in dual-channel microchip capillary electrophoresis," *Electrophoresis*, vol. 32, no. 8, pp. 838–843, 2011.

[25] J. Y. Chen, Y. W. Zhan, H. Y. Cao et al., "Wavelet denoising based on continuous differentiable threshold function and scale threshold," *Journal of Electronic Measurement and Instrument*, vol. 32, no. 10, pp. 169–176, 2018.

[26] G. W. Chen, X. B. Liu, D. Wang et al., "Denoising of MEMS gyroscope based on improved wavelet transform," *Journal of Electronics & Information Technology*, vol. 41, no. 5, pp. 1025–1031, 2019.

[27] J. W. Zhang, Y. Feng, and W. Li, "Research on wavelet denoising method based on an improved threshold function," *Electronic Design Engineering*, vol. 25, no. 9, pp. 137–140, 2017.

[28] W. Wu, "Research and implementation of capillary electrophoresis signal acquisition and storage system based on uTAS," Master thesis, Shanghai University, Shanghai, China, 2006.

[29] W. P. Yan, C. C. Xu, and J. H. Li, "The use of discrete wavelets for signal denoising in microchip capillary electrophoresis," in *Proceedings of the 2006 6th World Congress on Intelligent Control and Automation*, vol. 7, pp. 5254–5258, Dalian, China, 2006.

[30] H. Xing and Y. Yan, "Detection of low-flying target under the sea clutter background based on volterra filter," *Complexity*, vol. 2018, Article ID 1513591, 12 pages, 2018.

[31] H. Y. Li, Y. L. Zhou, F. Tian et al., "Wavelet-based vibration signal denoising algorithm with a new adaptive threshold function," *Chinese Journal of Scientific Instrument*, vol. 36, no. 10, pp. 2200–2206, 2015.

WILEY | Hindawi

Research Article

A Multiscroll Chaotic Attractors with Arrangement of Saddle-Shapes and Its Field Programmable Gate Array (FPGA) Implementation

Faqiang Wang [ID] **and Yufang Xiao** [ID]

State Key Laboratory of Electrical Insulation and Power Equipment, School of Electrical Engineering, Xi'an Jiaotong University, Xi'an 710049, China

Correspondence should be addressed to Faqiang Wang; faqwang@xjtu.edu.cn

Based on the step function and signum function, a chaotic system which can generate multiscroll chaotic attractors with arrangement of saddle-shapes is proposed and the stability of its equilibrium points is analyzed. The under mechanism for the generation of multiscroll chaotic attractors and the reason for the arrangement of saddle shapes and being symmetric about y-axis are presented, and the rule for controlling the number of scroll chaotic attractors with saddle shapes is designed. Based on the core chips including Altera Cyclone IV EP4CE10F17C8 Field Programmable Gate Array and Digital to Analog Converter chip AD9767, the peripheral circuit and the Verilog Hardware Description Language program for realization of the proposed multiscroll chaotic system is constructed and some experimental results are presented for confirmation. The research result shows that the occupation of multipliers and Phase-Locked Loops in Field Programmable Gate Array is zero.

1. Introduction

Since the advent of the Lorenz chaotic system in 1976, the proposal, analysis, control, and synchronization of chaotic systems and their applications and the corresponding educational research have become a hot topic [1–22]. In particular, the multiscroll chaotic system has more complex dynamics than the single-scroll or two-scroll chaotic system so that it has been caused widespread concern and in-depth research. Therefore, designing the chaotic system which can generate multiple chaotic attractors is still significant. It can not only provide the good candidate for chaos application but also enrich the content of nonlinear circuit. So far, according to the shape of chaotic attractors in the phase plane, the types of multiple chaotic attractors mainly include multiscroll chaotic attractors [1–7, 16–18], multifolded torus chaotic attractors [8, 9], multiwing chaotic attractors [10–14, 19], and multi-star chaotic attractors [15]. For example, based on Chua's circuit and using a sinusoidal

function, a chaotic system which is capable of generating multiscroll chaotic attractors was proposed and verified by using the hardware circuit with the universal trigonometric converter AD639 in [1]. Ozoguz et al. designed the chaotic system which can generate multiscroll chaotic attractors by using the inverse tangent function and designed the corresponding hardware experimental circuit with nonlinear transconductance [2]. Yu designed a chaotic system that can generate chaotic attractors of multiple vortexes by using a triangular wave function [3]. Lu and Chen summarized the methods of generating chaotic systems with multiple vortex-coil chaotic attractors and the applications of such systems [4]. Yu et al. designed a chaotic system that can generate multifolded torus chaotic attractors with multiple piecewise functions and gave the system parameter design rules when generating multifolded torus chaotic attractors [8]. In the case of multiwing chaotic attractors, Luo et al. designed a multiwing chaotic system by using signum functions and the corresponding hardware circuit experiment [10]. Zhang and

Yu [11] designed a class of fractional-order multiwing chaotic system. A chaotic system which has capable of generating multiscroll, multiring, multistar, and multiflower chaotic attractors is proposed [15]. The above research results greatly enrich the content of nonlinear circuits and present a foundation for the application of multichaotic attractors.

In addition, with the rise of digital chaotic secure communication, chaotic systems are widely realized by Digital Signal Processor [23, 24], Field Programmable Gate Array [25–27], Advanced RISC Machine [28, 29], Arduino [30, 31], and other digital chips. For example, He et al. implemented a fractional-order Lorenz hyperchaotic system by using Digital Signal Processor [23]. Tlelo-Cuautle et al. implemented a multiscroll chaotic generator by designing Verilog Hardware Description Language program in Field Programmable Gate Array [27]. Lin et al. applied Advanced RISC Machine to design chaotic maps and realize their real-time secret video communication [29]. Pano-Azucena et al. implemented multidimensional multiscroll chaotic systems and realized chaotic secure communication in Arduino [30]. The above research results lay a solid foundation for digital chaotic secure communication. However, as indicated in references [32, 33], compared with Digital Signal Processor, Advanced RISC Machine, and Arduino, it has more advantageous to implement the chaotic system by using Field Programmable Gate Array since it has high flexibility and high computational efficiency. Hence, Field Programmable Gate Array attracts people's attention to implement nonlinear dynamics of systems, especially chaotic or hyperchaotic systems, including chaotic cellular neural network system [34], image chaotic communication [35], secure color image encryption algorithm based on chaotic signals [36], fractional order chaotic system [37], and a wireless hyperchaotic communication system [38].

In this paper, based on the step function and the signum function, a multiscroll chaotic system which is capable of generating multiscroll chaotic attractors with arrangement of saddle shape in the phase plane is proposed. The under mechanism of the occurrence of multiscroll chaotic attractors and the reason for the arrangement of saddle shapes are analyzed. Based on the Altera Cyclone IV EP4CE10F17C8 Field Programmable Gate Array and Digital to Analog Converter chip AD9767, the peripheral circuit and Verilog Hardware Description Language program are designed to realize the multiscroll chaotic system for confirmation.

2. Mathematical Model of Multiscroll Chaotic System

The mathematical model of the proposed multiscroll chaotic system is as follows:

$$\begin{cases} \dot{x} = 128(y - x), \\ \dot{y} = \text{sign}(x)(16 - 128z + f(z)), \\ \dot{z} = -dz + 16|8x - f(x) + f(-x)|, \end{cases} \tag{1}$$

where

$$f(x) = \sum_{j=1}^{m} \varepsilon(x - b_j),$$

$$f(z) = \sum_{l=1}^{n} a_l \varepsilon(z - c_l), \tag{2}$$

$$\varepsilon(x - b_j) = \begin{cases} 1, & x \ge b_j, \\ 0, & x < b_j, \end{cases} \tag{3}$$

$$\varepsilon(z - c_l) = \begin{cases} 1, & z \ge c_l, \\ 0, & z < c_l, \end{cases} \tag{4}$$

$$\text{sign}(x) = \begin{cases} 1, & x > 0, \\ 0, & x = 0, \\ -1, & x < 0. \end{cases} \tag{5}$$

where x, y, and z are system variables; a_l, b_j, c_l, d, m, and n are system parameters, b_j, c_l, and d are positive numbers, and $b_{j+1} > b_j$ and $c_{l+1} > c_l$. Note that (3) and (4) are the definitions of step functions and (5) is the definition of signum function.

When $m = 1$, $n = 1$, $a_1 = 16$, $b_1 = 0.125$, $d = 64$, and $c_1 = 0.2$ are selected and the initial value being $(x_0, y_0, z_0) = (0.25, 0.125, 0.25)$, the numerical simulation results from Matlab software are presented in Figures 1(a) and 1(b). Figure 1(a) is the phase diagram of the system in the y-z plane, and Figure 1(b) is the Poincaré map on $x = y$ plane. In addition, due to the fact that the classical method for the LEs computation were designed for smooth systems only [39], here the improved and effective method was proposed by Danca in 2015 [40], which can be used to calculate the Lyapunov exponents of discontinuous system, is applied to obtain the Lyapunov exponents of the proposed system and the results are $LE_1 = 9.1141$, $LE_2 = 0$, and $LE_3 = -51.1867$. Therefore, the system is a chaotic system. At the same time, it can be seen from Figure 1(a) that the system has six-scroll chaotic attractors. Among them, four-scroll chaotic attractors are arranged in a row, and the other two are in obliquely above. Obviously, the arrangement of these six-scroll chaotic attractors seems a saddle shape and symmetric about y-axis.

3. Equilibrium Point and Its Stability Analysis

Considering the case of $m = 1$ and $n = 1$, equation (1) can be written as follows:

$$\begin{cases} \dot{x} = 128(y - x), \\ \dot{y} = \text{sign}(x)(16 - 128z + a_1\varepsilon(z - c_1)), \\ \dot{z} = -dz + 16|8x - \varepsilon(x - b_1) + \varepsilon(-x - b_1)|. \end{cases} \tag{6}$$

Let the left derivative term of equation (6) be zero, and the equilibrium point of system (6) can be obtained as follows:

$$\begin{cases} y - x = 0, \\ \text{sign}(x)(16 - 128z + a_1\varepsilon(z - c_1)) = 0, \\ -dz + 16|8x - \varepsilon(x - b_1) + \varepsilon(-x - b_1)| = 0. \end{cases} \tag{7}$$

Note that, for the third formula in equation 7, when d is positive, z must satisfy $z \ge 0$ to make the system have equilibrium points.
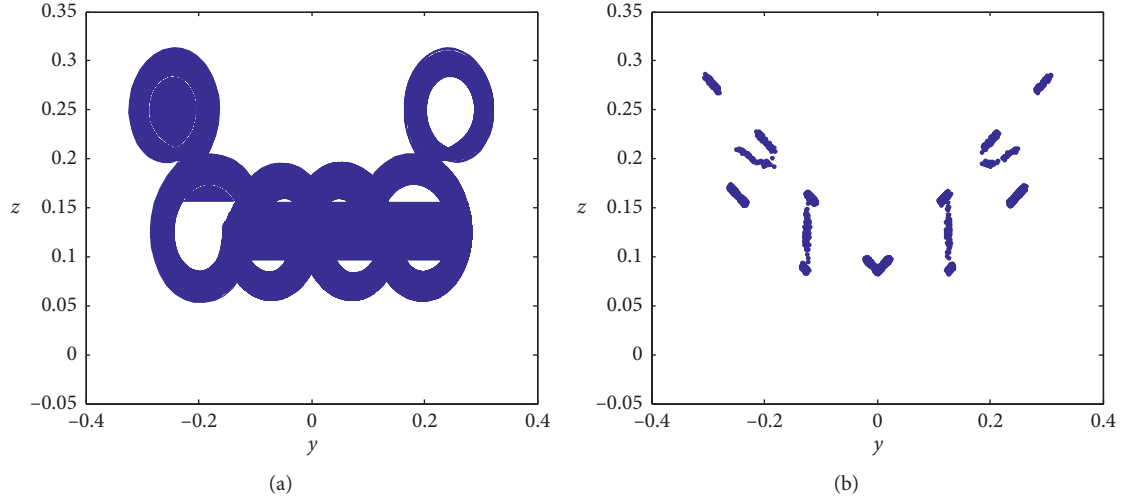
FIGURE 1: Numerical simulation results under $m = 1$ and $n = 1$. (a) y-z phase diagram shows six-scroll chaotic attractors; (b) Poincaré map on $x = y$ plane shows its chaotic operation.

Let (X, Y, Z) be the equilibrium point of system (6), and according to the second formula in equation (7), we can obtain $X = 0$ or

$$Z = \begin{cases} 0.125 + \dfrac{a_1}{128}, & \text{when } z \geq c_1, \\ \\ 0.125, & \text{when } z < c_1. \end{cases} \tag{8}$$

If $X = 0$, then $(X, Y, Z) = (0, 0, 0)$.

If X is not equal to zero, the equilibrium point of system (6) is

$$(X, Y, Z) = \begin{cases} \left(\dfrac{\pm 0.0625\, dZ + 1}{8}, \dfrac{\pm 0.0625\, dZ + 1}{8}, Z \right), \\ \\ \text{when } x \geq b_1, \\ \\ \left(\dfrac{\pm 0.0625\, dZ}{8}, \dfrac{\pm 0.0625\, dZ}{8}, Z \right), \\ \\ \text{when } -b_1 < x < b_1, \ x \neq 0, \\ \\ \left(\dfrac{\pm 0.0625\, dZ - 1}{8}, \dfrac{\pm 0.0625\, dZ - 1}{8}, Z \right), \\ \\ \text{when } x \leq -b_1. \end{cases} \tag{9}$$

Therefore, the system may have 13 equilibrium points.

However, when selecting $a_1 = 16$, $b_1 = 0.125$, $d = 64$, and $c_1 = 0.2$ and substituting them into equation (9), it is found that system (6) only has the following seven equilibrium points:

$$(X, Y, Z) = \begin{cases} S_1 = (0.25, 0.25, 0.25), \\ S_2 = (0.1875, 0.1875, 0.125), \\ S_3 = (0.0625, 0.0625, 0.125), \\ S_4 = (-0.0625, -0.0625, 0.125), \\ S_5 = (-0.1875, -0.1875, 0.125), \\ S_6 = (-0.25, -0.25, 0.25), \\ S_7 = (0, 0, 0). \end{cases} \tag{10}$$

The stability of system (6) under the above equilibrium points can be determined by calculating the eigenvalue of its Jacobian matrix at the corresponding equilibrium points. The Jacobian matrix is

$$\text{Jac} = \begin{bmatrix} -128 & 128 & 0 \\ 2\delta(x)(16 - 128z + a_1\varepsilon(z - c_1)) & 0 & sign(x)(-128 + a_1\delta(z - c_1)) \\ g(x) & 0 & -d \end{bmatrix}, \tag{11}$$

where $\delta(x)$ is the impulse function, when $x = 0$, $\delta(x) = \inf$ (inf is positive infinity) and when $x \neq 0$, $\delta(x) = 0$. Besides,

$$g(x) = 16 sign\left(8x - \varepsilon(x - b_1) + \varepsilon(-x - b_1)\right)\left(8 - \delta(x - b_1)\right. \\ \left. - \delta(-x - b_1)\right).$$

(12)

After substituting $S_7 = (0, 0, 0)$ and the above parameters into equation (11), we can obtain

$$\text{Jac7} = \begin{bmatrix} -128 & 128 & 0 \\ \inf & 0 & 0 \\ 0 & 0 & -64 \end{bmatrix}.$$

(13)

Obviously, there is a positive infinity element in the matrix Jac7, and its eigenvalues cannot be calculated. However, the characteristic equation of the matrix can be derived, and its result is

$$(\lambda + 64)\left(\lambda^2 + 128\lambda - 128\inf\right) = 0.$$

(14)

Therefore, its eigenvalues are $\lambda_1 = -64$, $\lambda_2 = -64 + (4096 + 128\inf)^{0.5}$, and $\lambda_3 = -64 - (4096 + 128\inf)^{0.5}$. $S_7 = (0, 0, 0)$ is unstable so that the system trajectory will be exponentially away from this equilibrium point.

Additionally, the eigenvalues at the other six equilibrium points S_1–S_6 are $\lambda_1 = -202.644$, $\lambda_2 = 5.322 + 101.59i$, and $\lambda_3 = 5.322 - 101.59i$. Therefore, these six equilibrium points are all index -2 saddle-focus equilibrium points. In other means, around these six equilibrium points, the system trajectory spirals from one equilibrium point to another, and finally the six scroll chaotic attractors are formed. Thus, the step function and the signum function are all indispensable for generating multiscroll chaotic attractors.

In particular, among these six equilibrium points, in the y-z plane, there are four equilibrium points (S_2, S_3, S_4, and S_5) whose Z values are all equal to 0.125 so that these four equilibrium points are arranged in a row. The Z values of the other two equilibrium points (S_1 and S_6) are equal to 0.25. Combined with the Y values of the two equilibrium points, it can be seen that these two equilibrium points are located obliquely above the equilibrium points S_2 and S_5, respectively. Therefore, the arrangement of these six-scroll chaotic attractor eventually presents a saddle shape and be symmetric about y-axis.

4. The under Mechanism for Generation of Multiscroll Chaotic Attractors

From the above numerical simulation from Matlab software and theoretical analysis, it can be seen that when $m = 1$ and $n = 1$ are selected, the system will generate six-scroll chaotic attractors. If the appropriate values are selected for m, n, and other parameters, the number of scrolls for chaotic attractors should be $C_1 m + C_2 n + C_3$, where C_1, C_2, and C_3 are parameters.

Assume that $a_1 = 16$, $b_1 = 0.125$, $d = 64$, and $c_1 = 0.2$ are unchanged. When $n = 1$, $m = 2$, and $b_2 = 0.25$, the numerical simulation results of the system are shown in Figure 2(a). Obviously, the system has eight-scroll chaotic attractors.

When $m = 1$, $n = 2$, $a_2 = 32$, and $c_2 = 0.3$, the numerical simulation results of the system are shown in Figure 2(b). Obviously, the system still has eight-scroll chaotic attractors, but its arrangement is different from that of Figure 2(a).

When $m = 2$, $b_2 = 0.25$, $n = 2$, $a_2 = 32$, and $c_2 = 0.3$, the numerical simulation results of the system are shown in Figure 2(c). Obviously, the system now has ten-scroll chaotic attractors.

According to the above numerical simulation results, the following formula can be obtained:

$$\begin{cases} 2C_1 + C_2 + C_3 = 8, \\ C_1 + 2C_2 + C_3 = 8, \\ 2C_1 + 2C_2 + C_3 = 10. \end{cases}$$

(15)

Therefore, one can obtain that $C_1 = 2$, $C_2 = 2$, and $C_3 = 2$ so that this chaotic system can generate $2m + 2n + 2$ scroll chaotic attractors, where m can control the saddle in the saddle shape. The larger m is, the wider the saddle is; n can control the saddle bridge in the saddle shape; the larger the n is, the higher the saddle bridge is.

5. FPGA Implementation of Saddle-Shaped Multiscroll Chaotic System

The Altera Cyclone IV EP4CE10F17C8 Field Programmable Gate Array is used. In addition, in order to observe the output waveform and compare it with the numerical simulation results, the Digital to Analog Converter chip AD9767 (14-bit) is used to convert the Field Programmable Gate Array calculation result into analog output and connect it to the oscilloscope GDS 3254 for observation.

When designing the program, by considering the chaotic region of the proposed multiscroll chaotic system, the resolution, and the Digital to Analog Converter chip AD9767 (14-bit), the fixed-point data format 32Q26 is used, in which the highest 1 bit is the sign bit, the next highest 5 bits are the integer bits, and the remaining 26 bits are the decimal places.

To calculate equation (1), first discretize equation (1) as follows:

$$\begin{cases} x_{k+1} = x_k + \Delta t \times 128(y_k - x_k), \\ y_{k+1} = y_k + \Delta t \times \left(sign(x_k)(16 - 128z_k + f(z_k))\right), \\ z_{k+1} = z_k + \Delta t \times \left(-dz_k + 16|8x_k - f(x_k) + f(-x_k)|\right), \end{cases}$$

(16)

where Δt is a discrete step and is equal to 1/512.

$$f(x_k) = \sum_{j=1}^{m} \varepsilon\left(x_k - b_j\right), \\ f(z_k) = \sum_{l=1}^{n} a_l \varepsilon\left(z_k - c_l\right).$$

(17)

Assuming that $V_k = (x_k, y_k, z_k, w_k)^T$, equation (16) can be expressed as follows:

$$V_{k+1} = V_k + \Delta t \times G(V_k).$$

(18)

Here, the second-order Runge–Kutta algorithm with two calculation steps is used for calculation. The first step is to update the data in half-step calculations:

(a)

(b)

(c)
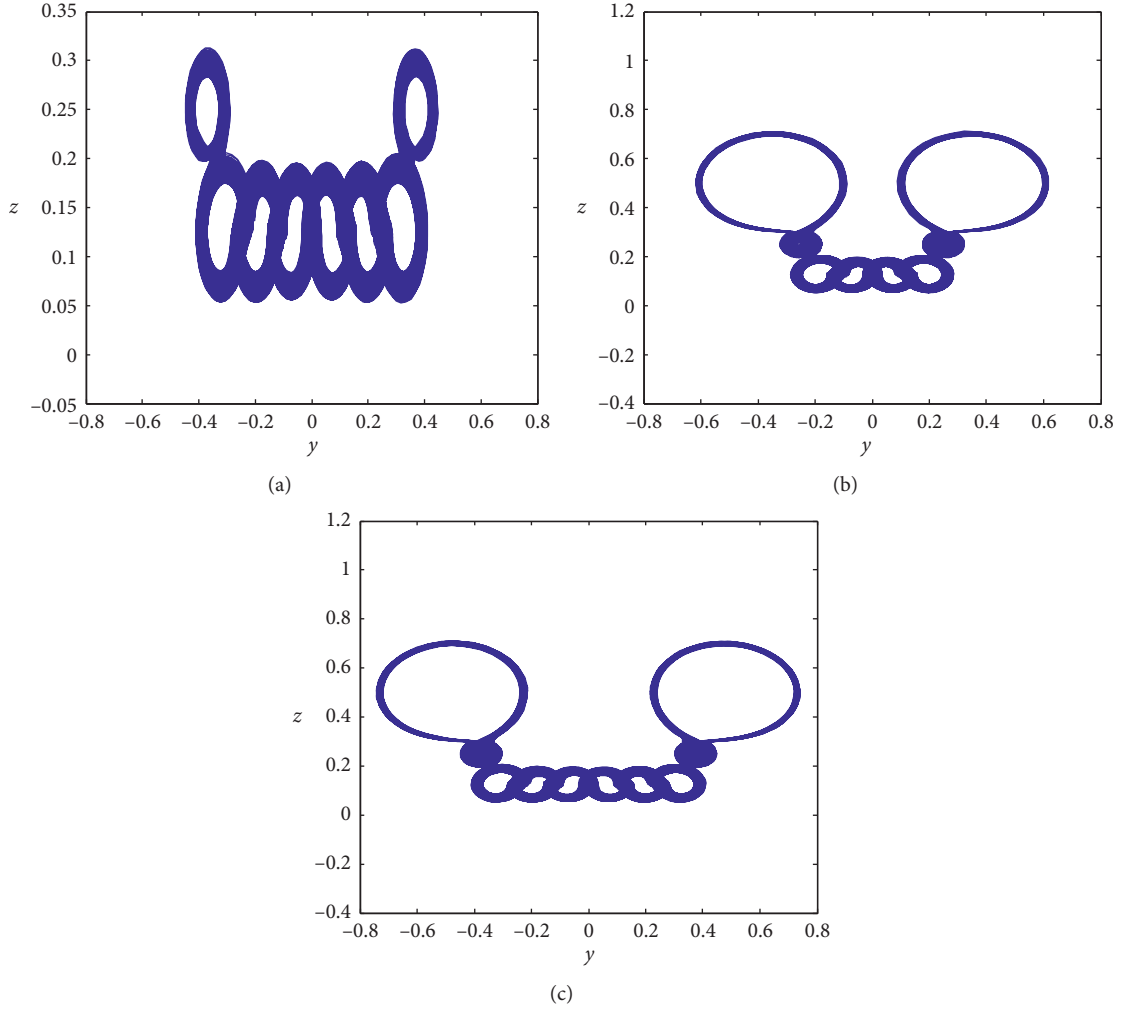
FIGURE 2: Numerical simulation results of saddle-shaped multiscroll chaotic attractors: (a) eight-scroll chaotic attractors for $m = 2$ and $n = 1$; (b) eight-scroll chaotic attractors for $m = 1$ and $n = 2$; (c) ten-scroll chaotic attractors for $m = 2$ and $n = 2$.

$$V_{k+0.5} = V_k + \frac{\Delta t}{2} \times G(V_k). \qquad (19)$$

The second step is to calculate the update data with $V_{k+0.5}$ and obtain V_{k+1}:

$$V_{k+1} = V_k + \Delta t \times G(V_{k+0.5}). \qquad (20)$$

After successfully designed by Verilog Hardware Description Language, the program is burned into the Field Programmable Gate Array through Universal Serial Bus Blaster, then the program will be converted into a hardware list, and the corresponding digital circuit will be formed in the Field Programmable Gate Array to realize the operation. The Register Transfer Level Viewer in the Quartus II is shown in Figure 3. Note that the "clock" and "rst1" in Figure 3 are the clock and reset signals of the Field Programmable Gate Array, respectively, "clock1," "clock2," "wreset1," and "wreset2" are the clock and reset signals of the Digital to Analog Converter chip, respectively, "ouput_en" is the output enable terminal and is active high, "x [13..0]," "y [13..0]," and "z [13..0]" are the digital outputs of x, y, and z at
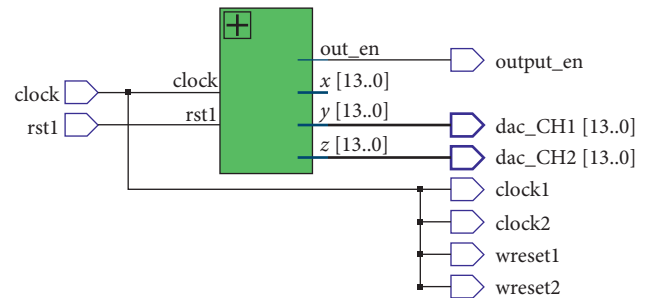
FIGURE 3: Register transfer level viewer when field programmable gate array implements the multiscroll chaotic system.

the time of each step, "dac_CH1 [13..0]" and "dac_CH2 [13..0]" output "y [13..0]" and "z [13..0]" to the Digital to Analog Converter chip AD9767 for digital-to-analog conversion, respectively.

The experimental results are shown in Figure 4. Figure 4(a) shows the experimental results of the y-z phase diagram under $m = 1$ and $n = 1$, and Figure 4(b) shows the experimental results of the y-z phase diagram under $m = 2$

(a)

(b)

(c)

(d)
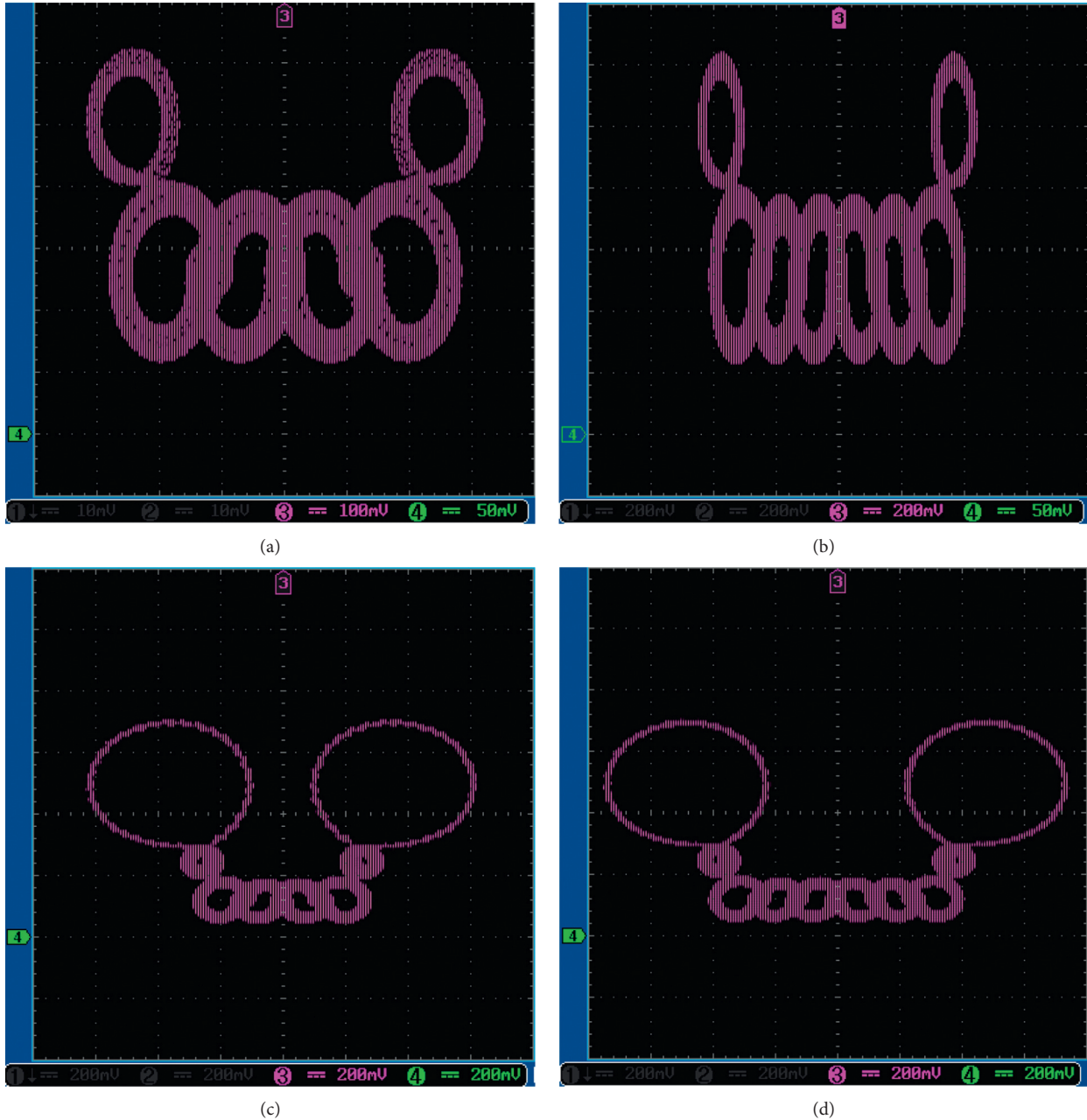
FIGURE 4: Experimental results of multiscroll chaotic systems: (a) six-scroll chaotic attractors for $m = 1$ and $n = 1$; (b) eight-scroll chaotic attractors for $m = 2$ and $n = 1$; (c) eight-scroll chaotic attractors for $m = 1$ and $n = 2$; (d) ten-scroll chaotic attractors for $m = 2$ and $n = 2$.

and $n = 1$, Figure 4(c) shows the experimental results of the y-z phase diagram under $m = 1$ and $n = 2$, and Figure 4(d) shows the experimental results of the y-z phase diagram under $m = 2$ and $n = 2$. Comparing Figure 4 with the corresponding graphs in Figures 1 and 2, the results of these two sides are consistent, which indicates the feasibility and effectiveness of using FPGA to realize the multiscroll chaotic system which is capable of generating saddle-shaped multiscroll chaotic attractors.

Also, in the Quartus II interface, the resources occupied by these multiscroll chaotic systems that can generate saddle-shaped multiscroll chaotic attractors when using the Altera Cyclone IV EP4CE10F17C8 Field Programmable Gate Array design program are 20% of the logic cells, 19% of pins, and 24% of memory bits. Particularly, due to the fact that the proposed multiscroll chaotic system is a piecewise linear system, and the coefficients are equal to 2^N where N is the nature number so that the multiplication in the system can be realized by shift bit in Verilog HDL program which leads to 0% of multipliers being used. Additionally, the clock signal for the Field Programmable Gate Array equals the clock1 and clock2 signals for the Digital to Analog Converter chip so that it is no need to use Phase-Locked Loops in Verilog HDL program which leads to 0% of PLLs being used.

6. Conclusion

Theoretical analysis, numerical simulation, and Field Programmable Gate Array experiments show that the reason for the proposed multiscroll chaotic system, which can produce saddle-shapes $2m + 2n + 2$ scroll chaotic attractors, is that the system has $2m + 2n + 2$ index -2 saddle-focus equilibrium points and the arrangement of the index -2 saddle-focus equilibrium points in y-z plane is saddle shaped. Moreover, by selecting m and n, the number of scrolls of chaotic attractors and their arrangement shape can be controlled. In addition, the Verilog Hardware Description Language program that implements this multiscroll chaotic system is designed with the core device Altera Cyclone IV EP4CE10F17C8 Field Programmable Gate Array and Digital to Analog Converter chip AD9767, and the results from the Quartus II show that the multiplier and Phase-Locked Loops occupying the Field Programmable Gate Array's resources are both zero. Therefore, compared with other multiscroll chaotic systems that must be implemented by multipliers or Phase-Locked Loops in Field Programmable Gate Array, the proposed multiscroll chaotic system occupies less Field Programmable Gate Array resources.

Data Availability

The data used to support the findings of this study are available from the corresponding author upon request.

Conflicts of Interest

The authors declare that there are no conflicts of interest regarding the publication of this paper.

Acknowledgments

References

[1] W. K. S. Tang, G. Q. Zhong, G. Chen, and K. F. Man, "Generation of n-scroll attractors via sine function," *IEEE Transactions on Circuits and Systems I: Fundamental Theory and Applications*, vol. 48, no. 11, pp. 1369–1372, 2001.

[2] S. Özoğuz, A. S. Elwakil, and K. N. Salama, "n-scroll chaos generator using nonlinear transconductor," *Electronics Letters*, vol. 38, no. 14, pp. 685-686, 2002.

[3] S.-M. Yu, "Circuit implementation for generating three-dimensional multi-scroll chaotic attractors via triangular wave series," *Acta Physica Sinica*, vol. 54, no. 4, pp. 1500–1509, 2005.

[4] J. H. Lü and G. R. Chen, "Generating multiscroll chaotic attractors: theories, methods and applications," *International Journal of Bifurcation and Chaos*, vol. 16, no. 4, pp. 775–858, 2006.

[5] F.-Q. Wang and C.-X. Liu, "A new multi-scroll chaotic system," *Chinese Physics*, vol. 15, no. 12, pp. 2878–2882, 2006.

[6] X.-X. Ai, K.-H. Sun, S.-B. He, and H.-H. Wang, "Design and application of multi-scroll chaotic attractors based on simplified Lorenz system," *Acta Physica Sinica*, vol. 63, no. 12, pp. 106–116, 2014.

[7] G.-T. Zhang and F.-Q. Wang, "A novel multi-scroll chaotic generator: analysis, simulation, and implementation," *Chinese Physics B*, vol. 27, no. 1, Article ID 018201, 2018.

[8] S. M. Yu, Q. H. Lin, and S. S. Qiu, "A family of multiple-folded torus chaotic attractors," *Acta Physica Sinica*, vol. 53, no. 7, pp. 2084–2088, 2004.

[9] F.-Q. Wang and C.-X. Liu, "Simulation of a family of multi-folded torus and multi-scroll chaotic attractors," *Acta Physica Sinica*, vol. 56, no. 4, pp. 1983–1987, 2007.

[10] X. W. Luo, C. H. Wang, and Z. Wan, "Grid multi-wing butterfly chaotic attractors generated from a new 3-D quadratic autonomous system," *Nonlinear Analysis-Modelling and Control*, vol. 19, no. 2, pp. 272–285, 2014.

[11] C. X. Zhang and S. M. Yu, "Generation of multi-wing chaotic attractor in fractional order system," *Chaos, Solitons and Fractals*, vol. 44, no. 10, pp. 845–850, 2011.

[12] M. W. Luo, X. H. Luo, and H. Q. Li, "A family of four-dimensional multi-wing chaotic system and its circuit implementation," *Acta Physica Sinica*, vol. 62, no. 2, pp. 153–158, 2013.

[13] C. X. Zhang and S. M. Yu, "On constructing complex grid multi-wing hyperchaotic system: theoretical design and circuit implementation," *International Journal of Circuit Theory and Applications*, vol. 41, no. 3, pp. 221–237, 2013.

[14] G. S. Hu, "Scheme for doubling the number of wings in hyperchaotic attractors," *Acta Physica Sinica*, vol. 58, pp. 8139–8145, 2009.

[15] F. Q. Wang, R. M. Wang, H. H. C. Iu, C. X. Liu, and T. Fernando, "A novel multi-shape chaotic attractor and its FPGA implementation," *IEEE Transactions on Circuits and Systems II: Express Briefs*, vol. 66, no. 12, pp. 2062–2066, 2019.

[16] X. Zhang and C. H. Wang, "A novel multi-attractor period multi-scroll chaotic integrated circuit based on CMOS wide adjustable CCCII," *IEEE Access*, vol. 7, pp. 16336–16350, 2019.

[17] X. Zhang and C. H. Wang, "Multiscroll hyperchaotic system with hidden attractors and its circuit implementation," *International Journal of Bifurcation and Chaos*, vol. 29, no. 9, Article ID 1950117, 2019.

[18] Q. L. Deng and C. H. Wang, "Multi-scroll hidden attractors with two stable equilibrium points," *Chaos: An Interdisciplinary Journal of Nonlinear Science*, vol. 29, no. 9, Article ID 093112, 2019.

[19] L. Zhou, C. H. Wang, and L. L. Zhou, "A novel no-equilibrium hyperchaotic multi-wing system via introducing memristor," *International Journal of Circuit Theory and Applications*, vol. 46, no. 1, pp. 84–98, 2018.

[20] J.-M. Ginoux, H. Ruskeepää, M. Perc et al., "Is type 1 diabetes a chaotic phenomenon?" *Chaos, Solitons and Fractals*, vol. 111, pp. 198–205, 2018.

[21] P. H. O. Silva, L. G. Nardo, S. A. M. Martins, E. G. Nepomuceno, and M. Perc, "Graphical interface as a teaching aid for nonlinear dynamical systems," *European Journal of Physics*, vol. 39, no. 6, Article ID 065105, 2018.

[22] M. Perc, "Visualizing the attraction of strange attractors," *European Journal of Physics*, vol. 26, no. 4, pp. 579–587, 2005.

[23] S. B. He, K. H. Sun, and H. H. Wang, "Complexity analysis and DSP implementation of the fractional-order Lorenz hyperchaotic system," *Entropy*, vol. 17, no. 12, pp. 8299–8311, 2015.

[24] S. Penaud, J. Guittard, P. Bouysse, and R. Quere, "DSP implementation of self-synchronised chaotic encoder decoder," *Electronics Letters*, vol. 36, no. 4, p. 365, 2000.

[25] M. S. Azzaz, C. Tanougast, S. Sadoudi, R. Fellah, and A. Dandache, "A new auto-switched chaotic system and its

FPGA implementation," *Communications in Nonlinear Science and Numerical Simulation*, vol. 18, no. 7, pp. 1792–1804, 2013.

[26] I. Koyuncu, A. T. Ozcerit, and I. Pehlivan, "Implementation of FPGA-based real time novel chaotic oscillator," *Nonlinear Dynamics*, vol. 77, no. 1-2, pp. 49–59, 2014.

[27] E. Tlelo-Cuautle, A. D. J. Quintas-Valles, L. G. D. L. Fraga, and J. D. J. Rangel-Magdaleno, "VHDL descriptions for the FPGA implementation of PWL-function-based multi-scroll chaotic oscillators," *PLoS One*, vol. 11, no. 12, Article ID 0168300, 2016.

[28] X. Y. Zhang, S. M. Yu, P. Chen, J. H. Lü, J. B. He, and Z. S. Lin, "Design and ARM-embedded implementation of a chaotic secure communication scheme based on H.264 selective encryption," *Nonlinear Dynamics*, vol. 89, no. 3, pp. 1949–1965, 2017.

[29] Z. S. Lin, S. M. Yu, J. H. Lü, S. T. Cai, and G. R. Chen, "Design and ARM-embedded implementation of a chaotic map-based real-time secure video communication system," *IEEE Transactions on Circuits and Systems for Video Technology*, vol. 25, no. 7, pp. 1203–1216, 2015.

[30] A. D. Pano-Azucena, J. D. J. Rangel-Magdaleno, E. Tlelo-Cuautle, and A. D. J. Quintas-Valles, "Arduino-based chaotic secure communication system using multi-directional multi-scroll chaotic oscillators," *Nonlinear Dynamics*, vol. 87, no. 4, pp. 2203–2217, 2017.

[31] C. E. Castañeda, D. López-Mancilla, R. Chiu et al., "Discrete-time neural synchronization between an Arduino micro-controller and a compact development system using multi-scroll chaotic signals," *Chaos, Solitons and Fractals*, vol. 119, pp. 269–275, 2019.

[32] M. Alcin, I. Pehlivan, and I. Koyuncu, "Hardware design and implementation of a novel ANN-based chaotic generator in FPGA," *Optik*, vol. 127, no. 13, pp. 5500–5505, 2016.

[33] E. Won, "A hardware implementation of artificial neural networks using field programmable gate arrays," *Nuclear Instruments and Methods in Physics Research Section A: Accelerators, Spectrometers, Detectors and Associated Equipment*, vol. 581, no. 3, pp. 816–820, 2007.

[34] Z. P. Chen, P. F. Cai, and E. Z. Dong, "A chaotic cellular neural network system research and implementation based on FPGA," *Advanced Materials Research*, vol. 605–607, pp. 1734–1737, 2013.

[35] Y. Luo, S. Yu, and J. Liu, "Design and implementation of image chaotic communication via FPGA embedded ethernet transmission," in *Proceeding of the International Workshop on Chaos-Fractals Theories and Applications*, pp. 148–152, Shenyang, China, November 2009.

[36] C.-H. Yang and S.-J. Huang, "Secure color image encryption algorithm based on chaotic signals and its FPGA realization," *International Journal of Circuit Theory and Applications*, vol. 46, no. 12, pp. 2444–2461, 2018.

[37] E. Z. Dong, M. F. Yuan, F. F. Han, J. G. Tong, and S. Z. Du, "Topological horseshoe analysis and FPGA implementation of a classical fractional order chaotic system," *IEEE Access*, vol. 7, pp. 129095–129103, 2019.

[38] S. Said, C. Tanougast, M. S. Azzaz, and A. Dandache, "Design and FPGA implementation of a wireless hyperchaotic communication system for secure real-time image transmission," *EURASIP Journal of Image Video Processing*, vol. 2013, no. 1, pp. 1–18, 2013.

[39] A. Wolf, J. B. Swift, H. L. Swinney, and J. A. Vastano, "Determining lyapounov exponents from a time series," *Physica D: Nonlinear Phenomena*, vol. 16, no. 3, pp. 285–317, 1985.

[40] M. F. Danca, "Lyapunov exponents of a class of piecewise continuous systems of fractional order," *Nonlinear Dynamics*, vol. 81, no. 1-2, pp. 227–237, 2015.

WILEY | Hindawi

Research Article
Analysis of the Financial Chaotic Model with the Fractional Derivative Operator

Mamadou Diouf[1] and Ndolane Sene [iD][2]

[1]*Centre de Recherche Economique Appliqué (CREA)/Laboratoire d'Analyse de Recherche et d'Etude du Développement (LARED), UCAD/FASEG, Dakar, Senegal*
[2]*Laboratoire Lmdan, Département de Mathématiques de la Décision, Université Cheikh Anta Diop de Dakar, Faculté des Sciences Economiques et Gestion, BP 5683 Dakar Fann, Senegal*

Correspondence should be addressed to Ndolane Sene; ndolanesene@yahoo.fr

Numerical discretization for the fractional differential equations is applied to the chaotic financial model described by the Caputo derivative. The graphical representations to support the numerical discretization are presented. We profit by analyzing the impact generated by the variations of the saving rate, the per investment cost, and the elasticity of demands in the dynamics of the solutions obtained with our numerical scheme. Notably, we use bifurcation diagrams to quantify the impact of the saving rate, the per investment cost, and the elasticity of demands, as well as the Lyapunov exponent to characterize the existence of chaos for the chosen value of the fractional order. The chaos observed depends strongly on these previously mentioned parameters. We finish by proposing a suitable control to synchronize the drive system and the response fractional financial model, using Lyapunov direct methods. The stability analysis of the equilibrium points of the chaotic financial model has been presented.

1. Introduction

The debate related to the savings and saving rate, the investment and the investment rate, and demands and the elasticity of demands continues to aliment the literature reviews and researches in economics, finance, and mathematics. We make discussions related to these parameters in the economy and finance before going further. In macroeconomic literature, the determinants of the savings are not the same as those of investments. Savings depend mainly on income and wealth, while investment depends on profitability and risky [1]. However, although savings and investment result from two independent decisions, they are necessarily the same in a closed economy [2, 3]. Savings are not necessarily used for domestic investment. They can be invested in the exterior of a country. In the case of capital mobility, the savings of each country will go to the part of the world which offers the highest rate of return [4]. Hence, an increase in national savings will mainly affect a large current account surplus or simply reduce the deficit rather than an increase in domestic investment and economic growth. In classical macroeconomics, the growth of production depends first on investment, which in turn depends on the savings rate. In this case, the interaction between demand and supplying funds determines the level of investment. Note that the investment demand is a negative function according to the real interest rate. The savings are a positive function according to the interest rate. As a result, a shift to the right of the investment demand function will generate an increase in investment rates and an increase in the equilibrium of investment and savings. The investigations between the investment and the savings are reported in many papers; in Turgot [5] and in Benston and Smith [6], savings are considered as automatically devoted to the financing of investment.

Following the literature, the savings can be considered as a source of instability for demand. The Keynesian and Neo-Keynesian and their macroeconomic models,

contrary to the neoclassical ones, attribute a passive role to savings. According to Keynesian and Neo-Keynesian, economic growth is explained by the investments. For them, the savings stop economic growth because it generates a demand deficit. Thus the investment is privileged to reduce the demand deficit and induce economic growth and more savings. In [7], Keynes emphasizes the links between the amount of investment and the volume of employment. In [8], Domar considers the growth model, where he explains that maintaining full employment requires growth in investment. All Keynesian and Neo-Keynesian theoretical models highlight the impact of savings in the process of economic growth and, in particular, the link it maintains with investment and demand. The investigations were related to the empirical developments on the savings and investment rate. In these directions, Feldstein and Stock in [9] prove empirically the holders of capital prefer to keep savings in their country to protect themselves against currency risk and political risk. Thus, the national savings stay in their country, and the domestic investment increases. Obsefeld in [10] stipulates in a base empirical study that, for a large open economy like that of the United States, domestic savings and investment could go together, even if the international capital market worked perfectly. However, it is not justified to consider a strong correlation between savings and investment, implying low capital mobility as announced by Feldstein and Stock in [9]. For more empirical investigations, see Tobin in [11], Dramani et Laye in [12], Esso et Keho in [13], Dries and Pepermans [14], and so forth. At last, the elasticity of demand measures the reaction of buyers to the changes in market conditions. It permits analyzing the variation in the demand with greater precision [15]. Thus, the elasticity of demand is a concept that measures the degree of sensitivity of demand to price (price elasticity) or income ("income elasticity") variations. Among the determinants of demand, we can cite price, income, product quality, and tastes, or preferences.

We note in the literature many discussions related to the concepts of savings, saving rate, investment, investment rate, investment of demand, and the elasticity of demand, permitting opening the door for new applications. In this paper, we focus on these concepts in the context of the financial model taking into account all these concepts. We mainly focus on the chaotic financial model in the context of fractional calculus. We propose a new numerical scheme and depict the solutions according to this numerical scheme and analyze as well the impact of the saving rate, the per investment cost, and the elasticity of demands. There exist investigations related to the fractional financial models. In [16], Shahiri et al. propose the stability and the synchronization of the fractional financial chaotic model. In [17], Xin and Li introduce a new fractional for order financial chaotic model, propose the numerical schemes using Adam's Bashford method, and illustrate their results with graphical representations. In [18], Chen et al. present the financial 3D chaotic model and introduce the financial 4D chaotic model and propose feedback control to stabilize the

chaotic model. In [19], Gao and Ma present the Hopf bifurcation of the chaotic financial model with time delay. In [20], Kumar and Kumar present a new financial chaotic model and also propose the stability analysis of the introduced model using the Lyapunov direct method. In [21], Xu and He investigate the synchronization of the fractional 3D financial model using an active control method. In [22], Wang et al. propose the fractional financial chaotic model with a different order of the fractional derivative. For many other investigations on chaotic systems, refer to [23–25].

Our motivation and novelty are to propose a new numerical scheme based on the solution of the fractional differential equations. Our numerical schemes will open new doors in numerical methods in fractional calculus and in finance, where the mathematical models are preferred to analyze the behavior of the financial markets. This new paper contributes to the applications of fractional derivatives in finance and economics. Note that there exist many applications of fractional derivatives [26–29] in physics [27, 30, 31], science and engineering [27, 32], mathematical modeling [27, 33], and others fields [26, 34–36]. The context of the fractional derivative is considered in our paper because the memory effect of the dynamical systems is taken into account, which is important for economics and financial models.

In Part 2, we recall the fractional tools. In Part 3, we present the fractional financial chaotic model. In Part 4, we give the qualitative properties like the existence and the uniqueness of the solution of the proposed model. In Part 5, we introduce our new numerical discretization. In Part 6, we give numerical simulations and interpretations. In Part 7, we propose synchronization investigations. In Part 8, we finish with concluding remarks.

2. Basic Fractional Calculus Operators

We recall the tools related to the fractional calculus. We address in this section the fractional Caputo derivative, the fractional Riemann-Liouville derivative, and their associated integral. We give the following definitions.

Definition 1 (see [27, 29]). Consider the function $x: [0, +\infty[\longrightarrow \mathbb{R};$ the fractional derivative in sense of Riemann-Liouville, of order α, is represented by the relationship

$$D^{\alpha} x(t) = \frac{1}{\Gamma(1-\alpha)} \frac{\mathrm{d}}{\mathrm{d}t} \int_0^t x(s)(t-s)^{-\alpha} \mathrm{d}s, \qquad (1)$$

with the relation

$$\frac{\mathrm{d}x(t)}{\mathrm{d}t} = \lim_{h \longrightarrow 0} \frac{x(t+h) - x(t)}{h}, \qquad (2)$$

where $t > 0$ and the order $\alpha \in (0, 1)$ and $\Gamma(\ldots)$ is the gamma Euler function.

Definition 2 (see [27, 29]). Consider the function $x: [0, +\infty[\longrightarrow \mathbb{R};$ the fractional derivative in sense of Caputo, of order α, is represented by the relationship

$$D_c^\alpha x(t) = \frac{1}{\Gamma(1-\alpha)} \int_0^t \frac{dx}{ds}(t-s)^{-\alpha}ds, \qquad (3)$$

with the relation

$$\frac{dx(t)}{dt} = \lim_{h \to 0} \frac{x(t+h) - x(t)}{h}, \qquad (4)$$

where $t > 0$ and the order $\alpha \in (0,1)$ and $\Gamma(\ldots)$ is the gamma Euler function.

Definition 3 (see [27, 29]). The Riemann-Liouville fractional integral is represented as the following form for the function $x: [0, +\infty[\longrightarrow \mathbb{R}$:

$$(I^\alpha x)(t) = \frac{1}{\Gamma(\alpha)} \int_0^t (t-s)^{\alpha-1}x(s)ds, \qquad (5)$$

where the function $\Gamma(\ldots)$ represents the Gamma Euler function with the order $\alpha > 0$.

3. Fractional Financial Chaotic Model

In this section, we present the chaotic model used in finance and economy in the context of fractional time order derivative. The chaotic financial model considered in our works can be represented with the integer-order derivative as the following form:

$$\partial_t x = z + yx - ax, \qquad (6)$$

$$\partial_t y = 1 - by - x^2, \qquad (7)$$

$$\partial_t z = -x - cz, \qquad (8)$$

with the initial conditions defined by the following equations:

$$\begin{aligned} x(0) &= x_0, \\ y(0) &= y_0, \\ z(0) &= z_0, \end{aligned} \qquad (9)$$

where the variable x represents the interest rate, y denotes the investment demand, and the variable z denotes the price exponent. The parameter a means the saving rate; the parameter b represents the per investment cost; the parameter c indicates the elasticity of demands. The generalization of the dynamical system described by equations (6)–(8) can be done using the fractional-order derivative due to the memory effect. In other words, the deterministic of the dynamical systems is, in general, well modeled by the fractional-order derivative. Therefore, in this paper, we consider the fractional-order derivative to model the chaotic financial model. The chaotic model is known to be very sensitive to the initial condition; this point will be focused more on an understanding of the financial market. In other words, to understand more precisely the evolutions of the interest rate, the investment demand, and the price exponent, the following equations represent the fractional financial chaotic model considered in this paper:

$$D_c^\alpha x = z + yx - ax, \qquad (10)$$

$$D_c^\alpha y = 1 - by - x^2, \qquad (11)$$

$$D_c^\alpha z = -x - cz. \qquad (12)$$

We make the following assumptions related to the initial conditions:

$$\begin{aligned} x(0) &= x_0, \\ y(0) &= y_0, \\ z(0) &= z_0. \end{aligned} \qquad (13)$$

4. Qualitative Properties of the Fractional Model

In this section, we prove that the fractional financial chaotic model represented by equations (10)–(12) has unique solution. We consider the following function:

$$\phi(t, x) = z + yx - ax. \qquad (14)$$

The Lipschitz continuous condition and the Lipchitz constant are provided in the following reasoning. We assume that x, y, and z are all bounded. We have

$$\begin{aligned} \|\phi(t, x_1) - \phi(t, x_2)\| &= \|z + yx_1 - ax_1 - z - yx_2 + ax_2\| \\ &\leq \|y\|\|x_1 - x_2\| + a\|x_1 - x_2\| \\ &\leq [a + \epsilon]\|x_1 - x_2\|, \end{aligned} \qquad (15)$$

where, according to the assumptions, we have $\|y\| \leq \epsilon$.

Using the function ϕ, we construct a Picard's operator using the fractional integral; we have the following equation:

$$\Delta x = x(0) + I^\alpha \phi(t, x). \qquad (16)$$

We prove that the operator Δ is bounded. We adopt the following reasoning. We apply the Euclidean norm; that is,

$$\begin{aligned} \|\Delta x - x(0)\| &= \|I^\alpha \phi(t, x)\| \\ &\leq \|\phi\| I^\alpha(1) \\ &\leq \left[\frac{T^\alpha}{\Gamma(\alpha+1)}\right]\|\phi\|. \end{aligned} \qquad (17)$$

Equation (15) proves ϕ is Lipschitz continuous, which implies, in particular, that the function ϕ is bounded; that is, $\|\phi\| \leq \epsilon_1$. By substituting in equation (17), we obtain equation defined by

$$\|\Delta x - x(0)\| \leq \left[\frac{T^\alpha}{\Gamma(\alpha+1)}\right]\epsilon_1. \qquad (18)$$

We now provided a condition under which the operator Δ is a contraction. We adopt the following procedure to provide this condition:

$$\begin{aligned}
\|\Delta x_1 - \Delta x_2\| &= \|I^\alpha[\phi(t, x_1) - \phi(t, x_2)]\| \\
&\leq I^\alpha \|\phi(t, x_1) - \phi(t, x_2)\| \\
&\leq \|\phi(t, x_1) - \phi(t, x_2)\| I^\alpha(1) \\
&\leq \left[\frac{T^\alpha}{\Gamma(\alpha+1)}\right][a+\epsilon]\|x_1 - x_2\|.
\end{aligned} \tag{19}$$

That is, Picard's operator is a contraction when the relation is defined by

$$\frac{T^\alpha}{\Gamma(\alpha+1)} \leq \frac{1}{a+\epsilon}, \tag{20}$$

which in turn implies that, under Banach fixed theorem, the solution of the fractional differential equation described by equation (10) exists and is unique. The uniqueness of the solution can be established using the following reasoning. We suppose two different solutions x_1 and x_2 for the fractional differential equation defined by equation (10). We suppose the following relationship is held:

$$x_1(t) = x_1(0) + I^\alpha \phi(t, x_1), \tag{21}$$

$$x_2(t) = x_2(0) + I^\alpha \phi(t, x_1). \tag{22}$$

The difference between equations (21) and (22) yields

$$x_1(t) - x_2(t) = I^\alpha[\phi(t, x_1) - \phi(t, x_2)]. \tag{23}$$

Applying the norm to equation (23), we get the following relationships:

$$\begin{aligned}
\|x_1 - x_2\| &= \|I^\alpha[\phi(t, x_1) - \phi(t, x_2)]\| \\
&\leq I^\alpha \|\phi(t, x_1) - \phi(t, x_2)\| \\
&\leq \|\phi(t, x_1) - \phi(t, x_2)\| I^\alpha(1) \\
&\leq \left[\frac{T^\alpha}{\Gamma(\alpha+1)}\right][a+\epsilon]\|x_1 - x_2\|.
\end{aligned} \tag{24}$$

From them, we have the following equation:

$$\|x_1 - x_2\|\left[1 - \left[\frac{T^\alpha}{\Gamma(\alpha+1)}\right][a+\epsilon]\right] \leq 0. \tag{25}$$

That implies $\|x_1 - x_2\| \leq 0$. Furthermore, we know by definition of the Euclidean norm $\|x_1 - x_2\| \geq 0$. Thus, we conclude that the following equation is held; that is,

$$x_1 = x_2. \tag{26}$$

The solution of equation (10) is unique. We conclude that the first equation of the financial chaotic model has a solution and this solution is unique.

In the second step, we consider the following function in our procedure:

$$\varphi(t, y) = 1 - by - x^2. \tag{27}$$

We adopt the previous procedure by providing the Lipschitz continuous condition and the Lipschitz constant for the function φ. We assume that x, y, and z are bounded. We have the following relation:

$$\begin{aligned}
\|\varphi(t, y_1) - \varphi(t, y_2)\| &= \|1 - by_1 - x^2 - 1 + by_2 + x^2\| \\
&\leq b\|y_1 - y_2\|.
\end{aligned} \tag{28}$$

Using the function φ, we construct a Picard's operator using the fractional integral; we have the following equation:

$$\Omega y = y(0) + I^\alpha \varphi(t, y). \tag{29}$$

We prove the operator Ω is bounded. We adopt the following reasoning. We apply the Euclidean norm; that is,

$$\begin{aligned}
\|\Omega y - y(0)\| &= \|I^\alpha \varphi(t, y)\| \\
&\leq \|\varphi\| I^\alpha(1) \\
&\leq \left[\frac{T^\alpha}{\Gamma(\alpha+1)}\right]\|\varphi\|.
\end{aligned} \tag{30}$$

Equation (28) proves φ is Lipchitz continuous, which implies, in particular, that the function φ is bounded, that is, $\|\varphi\| \leq \epsilon_2$. Replacing into equation (30), we obtain the equation defined by

$$\|\Omega y - y(0)\| \leq \left[\frac{T^\alpha}{\Gamma(\alpha+1)}\right]\epsilon_2. \tag{31}$$

We now provided a condition under which the operator Ω is a contraction. We adopt the following procedure to provide this condition:

$$\begin{aligned}
\|\Omega y_1 - \Omega y_2\| &= \|I^\alpha[\varphi(t, y_1) - \varphi(t, y_2)]\| \\
&\leq I^\alpha \|\varphi(t, y_1) - \varphi(t, y_2)\| \\
&\leq \|\varphi(t, y_1) - \varphi(t, y_2)\| I^\alpha(1) \\
&\leq \left[\frac{T^\alpha}{\Gamma(\alpha+1)}\right]b\|y_1 - y_2\|.
\end{aligned} \tag{32}$$

That is, Picard's operator Ω is a contraction when the relation defined by

$$\frac{T^\alpha}{\Gamma(\alpha+1)} \leq \frac{1}{b}, \tag{33}$$

is held, which in turn implies that, under Banach fixed theorem, the solution of the fractional differential equation described by equation (11) exists and is unique. The uniqueness of the solution can be established using the following reasoning. We suppose different solutions y_1 and y_2 for the fractional differential equation defined by equation (11). That is, the following relationships are held:

$$y_1(t) = y_1(0) + I^\alpha \varphi(t, y_1), \tag{34}$$

$$y_2(t) = y_2(0) + I^\alpha \varphi(t, y_1). \tag{35}$$

The difference between equations (34) and (35) yields

$$y_1(t) - y_2(t) = I^\alpha[\varphi(t, y_1) - \varphi(t, y_2)]. \tag{36}$$

Applying the norm to equation (36), we get the following relationships:

$$\begin{aligned} \|y_1 - y_2\| &= \|I^\alpha[\varphi(t, y_1) - \varphi(t, y_2)]\| \\ &\leq I^\alpha\|\varphi(t, y_1) - \varphi(t, y_2)\| \\ &\leq \|\varphi(t, y_1) - \varphi(t, y_2)\|I^\alpha(1) \\ &\leq \left[\frac{T^\alpha}{\Gamma(\alpha + 1)}\right]b\|y_1 - y_2\|. \end{aligned} \tag{37}$$

From them, we have the following equation:

$$\|y_1 - y_2\|\left[1 - \left[\frac{T^\alpha}{\Gamma(\alpha + 1)}\right]b\right] \leq 0. \tag{38}$$

That implies $\|y_1 - y_2\| \leq 0$. Furthermore, we know by the definition of the Euclidean norm $\|y_1 - y_2\| \geq 0$. Thus, we obtain the following equation:

$$y_1 = y_2. \tag{39}$$

Then the solution of equation (11) is unique. We conclude that the second equation of the financial chaotic model has one solution.

In the third step, we consider the following function in our reasoning:

$$\psi(t, y) = -x - cz. \tag{40}$$

We adopt the same reasoning as in the first and the second steps. We assume that x, y, and z are bounded. We have the following relation:

$$\begin{aligned} \|\psi(t, z_1) - \psi(t, z_2)\| &= \|-x - cz_1 + x + cz_2\| \\ &\leq c\|z_1 - z_2\|. \end{aligned} \tag{41}$$

Using the function ψ, we construct a Picard's operator using the fractional integral; we have the following equation:

$$\Lambda z = z(0) + I^\alpha\psi(t, z). \tag{42}$$

We prove the operator Λ is bounded. We adopt the following reasoning. We apply the Euclidean norm; that is,

$$\begin{aligned} \|\Lambda z - z(0)\| &= \|I^\alpha\psi(t, z)\| \\ &\leq \|\psi\|I^\alpha(1) \\ &\leq \left[\frac{T^\alpha}{\Gamma(\alpha + 1)}\right]\|\psi\|. \end{aligned} \tag{43}$$

Equation (41) proves ψ is Lipschitz continuous, which implies, in particular, that the function ψ is bounded, that is, $\|\psi\| \leq \epsilon_3$. Replacing into equation (43), we obtain the equation defined by

$$\|\Lambda z - z(0)\| \leq \left[\frac{T^\alpha}{\Gamma(\alpha + 1)}\right]\epsilon_3. \tag{44}$$

We now provide a condition under which the operator Λ is a contraction. We adopt the following procedure to provide this condition:

$$\begin{aligned} \|\Lambda z_1 - \Lambda z_2\| &= \|I^\alpha[\psi(t, z_1) - \varphi(t, y_2)]\| \\ &\leq I^\alpha\|\psi(t, z_1) - \psi(t, y_2)\| \\ &\leq \|\psi(t, z_1) - \psi(t, y_2)\|I^\alpha(1) \\ &\leq \left[\frac{T^\alpha}{\Gamma(\alpha + 1)}\right]c\|z_1 - z_2\|. \end{aligned} \tag{45}$$

That is, Picard's operator Λ is a contraction when the relation defined by

$$\frac{T^\alpha}{\Gamma(\alpha + 1)} \leq \frac{1}{c}, \tag{46}$$

is held, which in turn implies that, under Banach fixed theorem, the solution of the fractional differential equation described by equation (12) exists and is unique. The uniqueness of the solution can be established using the following reasoning. We suppose different solutions z_1 and z_2 for the fractional differential equation defined by equation (12). That is, the following relationships are held:

$$z_1(t) = z_1(0) + I^\alpha\psi(t, z_1), \tag{47}$$

$$z_2(t) = z_2(0) + I^\alpha\psi(t, z_1). \tag{48}$$

The difference between equations (47) and (48) yields

$$z_1(t) - z_2(t) = I^\alpha[\psi(t, z_1) - \psi(t, z_2)]. \tag{49}$$

Applying the norm to equation (49), we get the following relationships:

$$\begin{aligned} \|z_1 - z_2\| &= \|I^\alpha[\psi(t, z_1) - \psi(t, z_2)]\| \\ &\leq I^\alpha\|\psi(t, z_1) - \psi(t, z_2)\| \\ &\leq \|\psi(t, z_1) - \psi(t, z_2)\|I^\alpha(1) \\ &\leq \left[\frac{T^\alpha}{\Gamma(\alpha + 1)}\right]c\|z_1 - z_2\|. \end{aligned} \tag{50}$$

From them, we have the following equation:

$$\|z_1 - z_2\|\left[1 - \left[\frac{T^\alpha}{\Gamma(\alpha + 1)}\right]c\right] \leq 0. \tag{51}$$

That implies $\|z_1 - z_2\| \leq 0$. Furthermore, we know by the definition of the Euclidean norm $\|z_1 - z_2\| \geq 0$. Thus, we conclude the following equation:

$$z_1 = z_2. \tag{52}$$

That is, the solution of the fractional differential equation (12) is unique. We conclude that the third equation of the financial chaotic model has one solution.

5. Discretization Procedures for the Financial Chaotic Model

In this section, we propose the numerical discretization of the chaotic financial equation with implicit numerical discretization in the context of fractional calculus. The method exposed in this section uses Picard's operator previously defined in this paper. The following relationships give the solutions of the equations of the fractional financial chaotic model (10)–(13) using the Riemann-Liouville integral:

$$x(t) = x(0) + I^\alpha \phi(t, x), \qquad (53)$$

$$y(t) = y(0) + I^\alpha \varphi(t, y), \qquad (54)$$

$$z(t) = z(0) + I^\alpha \psi(t, z). \qquad (55)$$

The standard discretization at (t_n) in the context of the Caputo derivative is described in the following procedure. In the first step, equations (53)–(55) are written in the following form:

$$\begin{aligned} x(t_n) &= x(0) + I^\alpha \phi(t_n, x), \\ y(t_n) &= y(0) + I^\alpha \varphi(t_n, y), \\ z(t_n) &= z(0) + I^\alpha \psi(t_n, z). \end{aligned} \qquad (56)$$

The explicit representations when we translate the Riemann-Liouville integral are given by the following forms:

$$x(t_n) = x(0) + \frac{1}{\Gamma(\alpha)} \sum_{j=0}^{n} \int_{t_j}^{t_{j+1}} (t_n - s)^{\alpha-1} \phi(s, x(s)), \qquad (57)$$

$$y(t_n) = y(0) + \frac{1}{\Gamma(\alpha)} \sum_{j=0}^{n-1} \int_{t_j}^{t_{j+1}} (t_n - s)^{\alpha-1} \varphi(s, tyn(s)), \qquad (58)$$

$$z(t_n) = z(0) + \frac{1}{\Gamma(\alpha)} \sum_{j=0}^{n-1} \int_{t_j}^{t_{j+1}} (t_n - s)^{\alpha-1} \psi(s, z(s)). \qquad (59)$$

We consider the grid $t_n = t_0 + nh$, where h represents a constant step size. Using implicit discretizations of the integral parts of the above equations (57) and (58), we arrive at the following discretizations:

$$\begin{aligned} x(t_n) &= x(0) + h^\alpha \left[\overline{b}_n^{(\alpha)} \varphi(0) + \sum_{j=0}^{n} b_{n-j}^{(\alpha)} \phi(t_j, x_j) \right], \\ y(t_n) &= y(0) + h^\alpha \left[\overline{b}_n^{(\alpha)} \varphi(0) + \sum_{j=0}^{n} b_{n-j}^{(\alpha)} \varphi(t_j, y_j) \right], \\ z(t_n) &= z(0) + h^\alpha \left[\overline{b}_n^{(\alpha)} \varphi(0) + \sum_{j=0}^{n} b_{n-j}^{(\alpha)} \psi(t_j, z_j) \right], \end{aligned} \qquad (60)$$

where the discretization parameters reported in the literature are given by

$$\overline{b}_n^{(\alpha)} = \frac{(n-1)^\alpha - n^\alpha(n-\alpha-1)}{\Gamma(2+\alpha)}, \qquad (61)$$

and, for $n = 1, 2, \ldots$,

$$\begin{aligned} b_0^{(\alpha)} &= \frac{1}{\Gamma(2+\alpha)}, \\ b_n^{(\alpha)} &= \frac{(n-1)^{\alpha+1} - 2n^{\alpha+1} + (n+1)^{\alpha+1}}{\Gamma(2+\alpha)}. \end{aligned} \qquad (62)$$

Let $x(t_n)$, $y(t_n)$, and $z(t_n)$ be the numerical approximations and let x_n, y_n, and z_n be the exact solutions. Then residual functions as reported in the literature of fractional calculus for the implicit numerical discretization are given by the functions

$$\begin{aligned} |x(t_n) - x_n| &= \mathcal{O}\left(h^{\min\{\alpha+1, 2\}}\right), \\ |y(t_n) - y_n| &= \mathcal{O}\left(h^{\min\{\alpha+1, 2\}}\right), \\ |z(t_n) - z_n| &= \mathcal{O}\left(h^{\min\{\alpha+1, 2\}}\right). \end{aligned} \qquad (63)$$

From them, the convergence of the implicit discretization of equations (10)–(12) is obtained when h converges to 0. The stability of the numerical discretizations reported in this paper is ensured by the Lipschitz continuous condition of the functions ϕ, φ, and ψ. The numerical discretizations of the functions ϕ, φ, and ψ are represented by the equations

$$\begin{aligned} \phi(t_j, x_j) &= z^j + y^j x^j - ax^j, \\ \varphi(t_j, y_j) &= 1 - by^j - (x^j)^2, \\ \psi(t_j, z_j) &= -x^j - cz^j. \end{aligned} \qquad (64)$$

6. Numerical Simulations and Discussions

In this section, we simulate the new discretization proposed in the previous section. We fix the following initial conditions: $x(0) = 1$, $y(0) = 2$, and $z(0) = 0.9$. In the first simulation in Figure 1, we consider $a = 0.9$, $b = 0.2$, $c = 1.5$, and the order $\alpha = 0.95$. We represent the behavior of the fractional chaotic model in three dimensions. The considered step size is given by $h = 0.01$ and $T = 1000[s]$.

In Figure 2, we observe the behavior of the solution of the financial chaotic model with respect to the directions x and z.

In Figure 3, we observe the behavior of the solution of the financial chaotic model with respect to the directions x and y.

We analyze the impact of the saving amount a. We represent the dynamics of the fractional financial chaotic model in the following figures with the different values of the saving rate $a = 0.1$ seen in Figures 4–6 and $a = 0.2$ seen in Figures 7–9. We notice we have chaotic behaviors when a increases and is approximatively between 0.2 and 1. But we note high chaotic behaviors when the saving amount is less than approximatively 0.1. The value of the interest rate can explain the high chaotic behaviors. Note that the savings rate measures, for example, the amount of income of households, businesses, and government savings. To be more precise, the savings rate indicates a nation's health as it shows trends in savings, which lead to investments. The recessions and

FIGURE 1: Dynamic behavior of fractional financial chaotic model with $\alpha = 0.95$.

FIGURE 4: Dynamic behavior of fractional financial chaotic model with $\alpha = 0.95$.
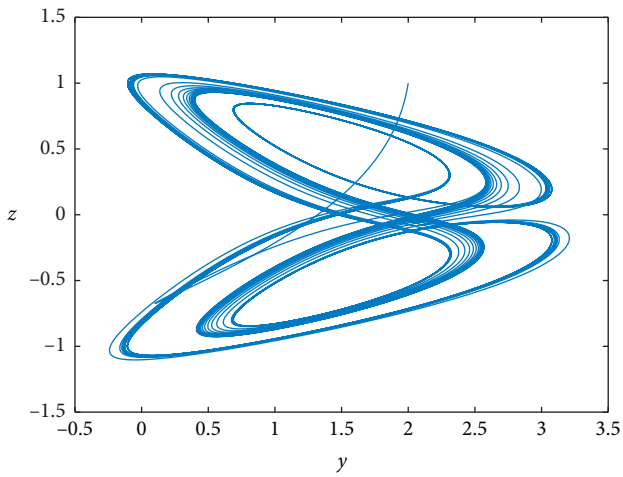
FIGURE 2: Dynamic behavior of fractional financial chaotic model with $\alpha = 0.95$.
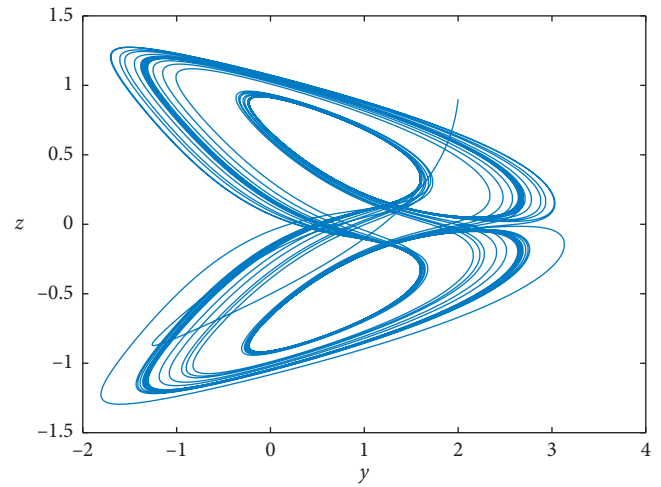
FIGURE 5: Dynamic behavior of fractional financial chaotic model with $\alpha = 0.95$.
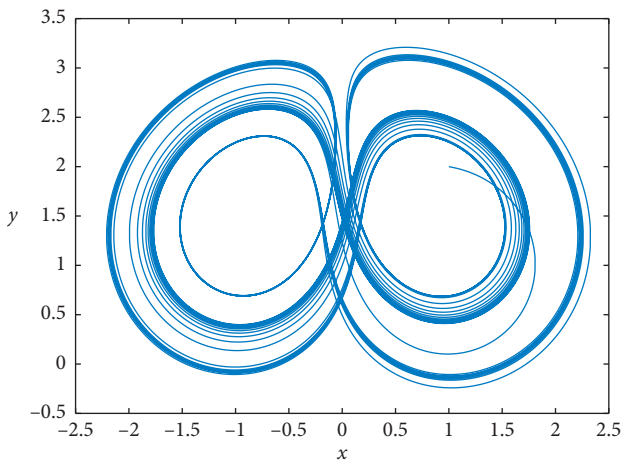
FIGURE 3: Dynamic behavior of fractional financial chaotic model with $\alpha = 0.95$.
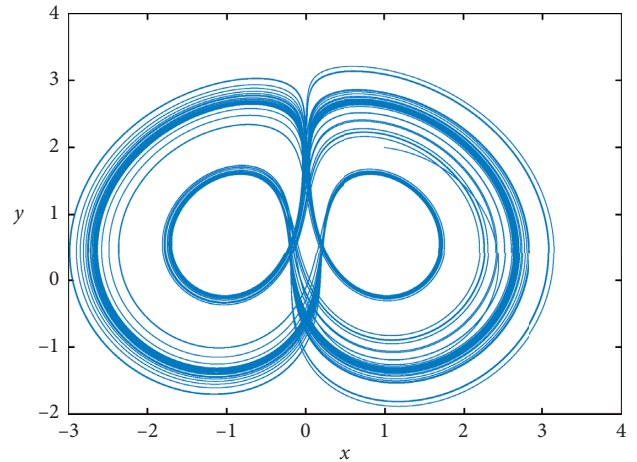
FIGURE 6: Dynamic behavior of fractional financial chaotic model with $\alpha = 0.95$.
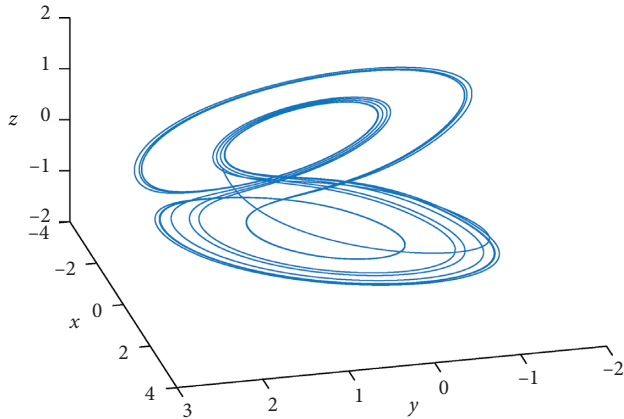
FIGURE 7: Dynamic behavior of fractional financial chaotic model with $\alpha = 0.95$.
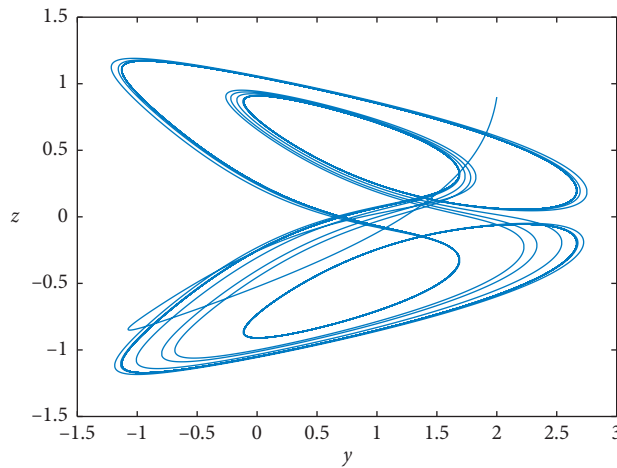
FIGURE 8: Dynamic behavior of fractional financial chaotic model with $\alpha = 0.95$.
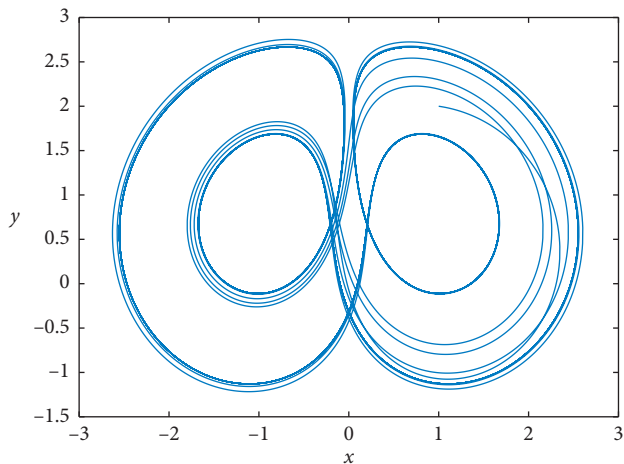
FIGURE 9: Dynamic behavior of fractional financial chaotic model with $\alpha = 0.95$.

economic shocks impact the saving rate, and in these conditions, we note periods of high economic uncertainty. Thus, people defer current spending to prepare for an uncertain economic future. In our context, when the saving amount is less than approximatively 0.1, we are in periods of recessions, and the chaotic behavior is high. The future of economic growth becomes difficult to predict. Changes in market interest can also influence the saving rate and thus influence the high chaotic dynamic when the saving amount is less than approximatively 0.1.

We analyze the impact of the per investment cost b. We depict, for more understanding in the following Figures 10–15, the behaviors of the dynamics of the fractional financial chaotic model with $b = 0.25$ in Figure 10 and $b = 0.4$ in Figure 13. We note the chaotic dynamic is conserved between approximatively 0.2 and 0.3, but when the per investment cost exceeds 0.4, the chaotic behavior is displayed. All investments carry costs, real costs, and not merely the opportunity costs of an investor choosing to forego one asset in favor of another. There exist different types of investment costs; thus, different investments carry different types of costs: expensive ratio, marketing costs, and others. More chaotic behaviors are observed in $(0, 0.3)$ because in practice when the cost in the investment is not high, it is better for the investors. A high investment cost rate does not generate profit for the investors.

We finish by analyzing the impact of the elasticity of demands c. We represent in Figures 16–21 the behavior of the dynamics of the fractional financial chaotic model with $c = 1$ in Figure 16 and $c = 2$ in Figure 19. We note the chaotic dynamic is conserved between approximately 0 and 2. Still, when the elasticity of demands exceeds 2, the chaotic behaviors are displayed, and the solutions of the financial model become stable and describe cycle. Note that elasticity is the degree to which the desire for something changes as its price rises. When $c = 0$, we are in case of perfectly inelastic demand, and $c = 1$ corresponds to unitary elasticity demand, while $c < 1$ corresponds to relatively inelastic demand. We remark for high elasticity with $c < 2$; the chaotic behaviors are very high too. Thus the predictions are complicated to be done. But when the elasticity of demands exceeds 2, then the chaotic behaviors are displayed, and the behaviors can be predicted easily in this case. This phenomenon is not currently in the financial market and is not reasonable in practice.

7. Synchronization of Fractional Chaotic Financial Model

In this section, we study the synchronization of the fractional financial model. The objective of synchronization consists of making two chaotic financial models oscillate in the same way. To arrive at our end, we consider two models: the driving system and the response system. All of them are constructed using the fractional financial chaotic model described by equations (10)–(12). Our objective will be to synchronize the driving and the response model using a controller. Therefore a nonlinear fractional system that gives signals between the driving system and the response system
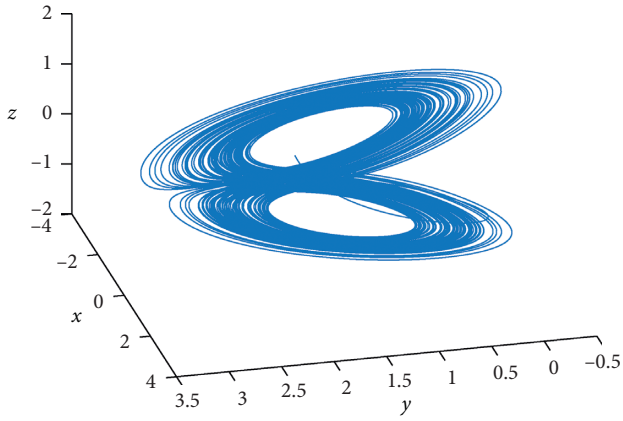
FIGURE 10: Dynamic behavior of fractional financial chaotic model with $\alpha = 0.95$.

FIGURE 11: Dynamic behavior of fractional financial chaotic model with $\alpha = 0.95$.

FIGURE 12: Dynamic behavior of fractional financial chaotic model with $\alpha = 0.95$.
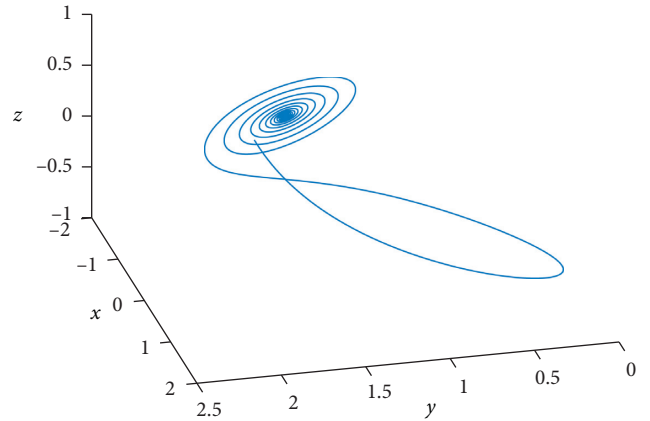
FIGURE 13: Dynamic behavior of fractional financial chaotic model with $\alpha = 0.95$.
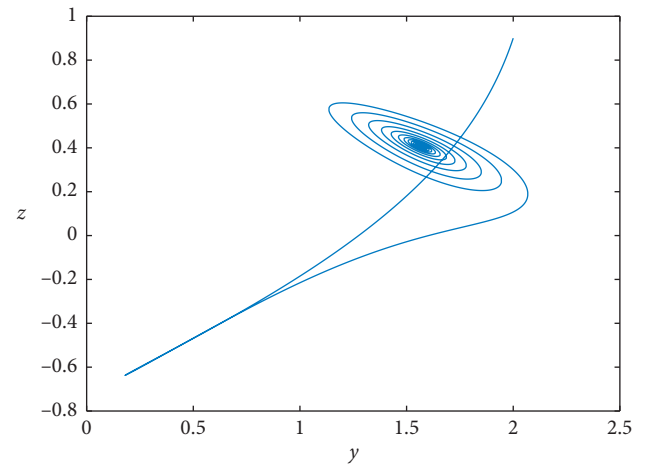
FIGURE 14: Dynamic behavior of fractional financial chaotic model with $\alpha = 0.95$.
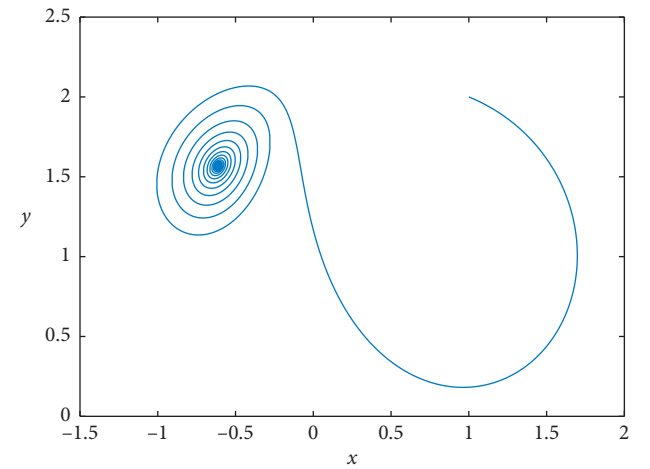
FIGURE 15: Dynamic behavior of fractional financial chaotic model with $\alpha = 0.95$.
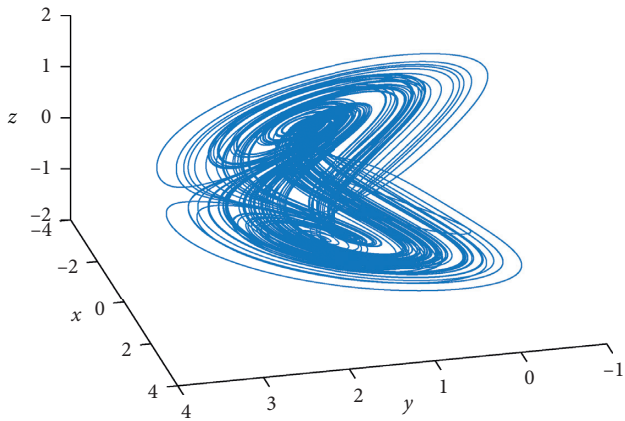
FIGURE 16: Dynamic behavior of fractional financial chaotic model with $\alpha = 0.95$.

FIGURE 17: Dynamic behavior of fractional financial chaotic model with $\alpha = 0.95$.

FIGURE 18: Dynamic behavior of fractional financial chaotic model with $\alpha = 0.95$.

FIGURE 19: Dynamic behavior of fractional financial chaotic model with $\alpha = 0.95$.
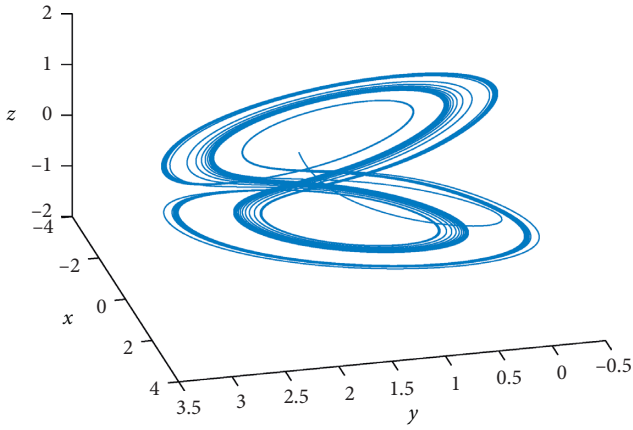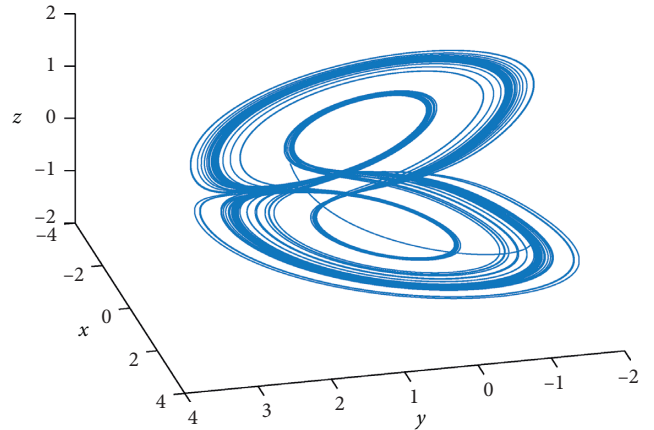

FIGURE 20: Dynamic behavior of fractional financial chaotic model with $\alpha = 0.95$.
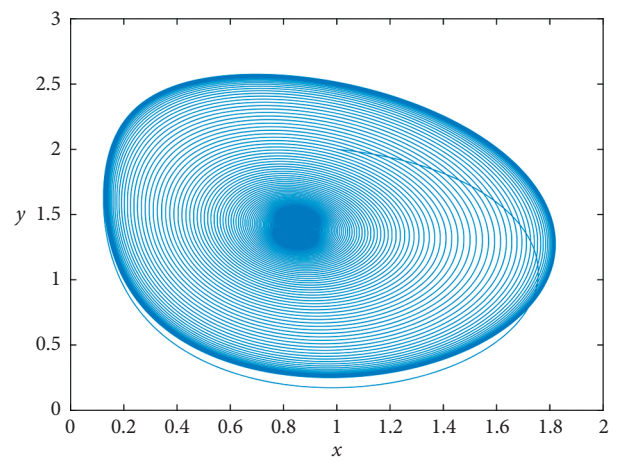
FIGURE 21: Dynamic behavior of fractional financial chaotic model with $\alpha = 0.95$.
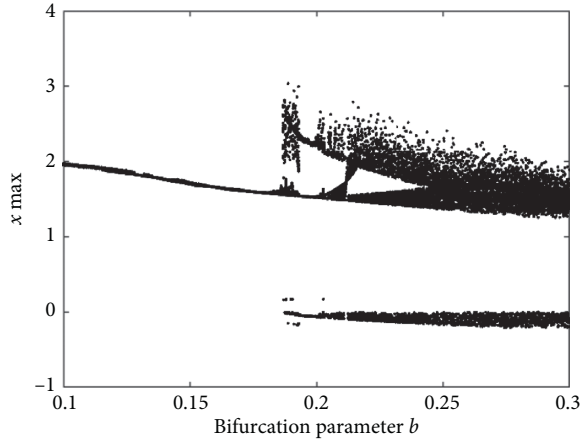
FIGURE 22: Bifurcation diagram with the variation of the parameter b.
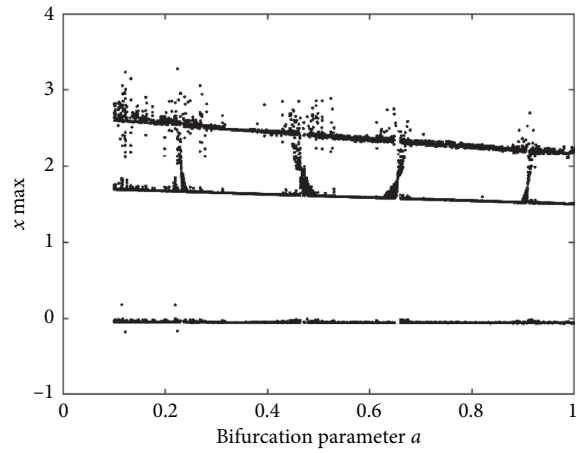
FIGURE 23: Bifurcation diagram with the variation of the parameter a.
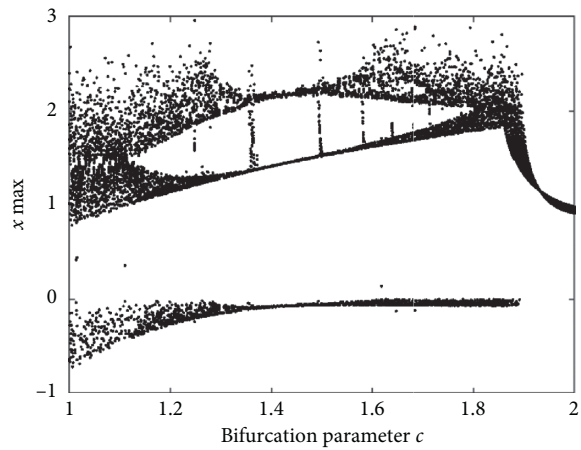
FIGURE 24: Bifurcation diagram with the variation of the parameter c.

should be designed. Consider the driving fractional chaotic financial model provided by

$$
\begin{aligned}
D_c^\alpha x_1 &= x_3 + x_2 x_1 - a x_1, \\
D_c^\alpha x_2 &= 1 - b x_2 - x_1^2, \\
D_c^\alpha x_3 &= -x_1 - c x_3.
\end{aligned}
\tag{65}
$$

Consider the response fractional chaotic financial model given by

$$
\begin{aligned}
D_c^\alpha y_1 &= y_3 + y_2 y_1 - a y_1 + u_1, \\
D_c^\alpha y_2 &= 1 - b y_2 - y_1^2 + u_2, \\
D_c^\alpha y_3 &= -y_1 - c y_3 + u_3,
\end{aligned}
\tag{66}
$$

where the control $u = (u_1, u_2, u_3)$. We define the synchronization error described by the following forms:

$$
\begin{aligned}
e_1 &= y_1 - x_1, \\
e_2 &= y_2 - x_2, \\
e_3 &= y_3 - x_3.
\end{aligned}
\tag{67}
$$

In this section, we provide a condition under which the control u exists such that $\lim_{t \longrightarrow +\infty} \|e\| = \lim_{t \longrightarrow +\infty} \|y - x\| = 0$, where $e = (e_1, e_2, e_3)$, $x = (x_1, x_2, x_3)$, and $y = (y_1, y_2, y_3)$. We use the Lyapunov direct method to prove this statement. The following equation represents the fractional synchronization error system:

$$
D_c^\alpha e_1 = e_3 - a e_1 + x_1 e_1 + y_2 e_1 + u_1, \tag{68}
$$

$$
D_c^\alpha e_1 = e_3 - a e_1 + x_1 e_1 + y_2 e_1 + u_1, \tag{69}
$$

$$
D_c^\alpha e_3 = -e_1 - c e_3 + u_3. \tag{70}
$$

We suppose the control design u given by $u = (-x_1 e_1 - y_2 e_1, e_1 x_1 + e_1 y_1, 0)$ and we choose the Lyapunov function defined by

$$
V(e_1, e_2, e_3) = e_1^2 + e_2^2 + e_3^2. \tag{71}
$$

The main idea is to utilize the stability condition applied to quadratic function given the relationship $D^\alpha e^T e \le e^T D^\alpha e$ [35, 37]. The Caputo derivative along the trajectories of equations (68)–(70) is given by the following calculations:

$$
\begin{aligned}
D_t^\kappa V &\le e_1 D_c^{\alpha, \rho} e_1 + e_2 D_c^\alpha e_2 + e_3 D_c^\alpha e_3 \\
&\le e_1 [e_3 - a e_1] + e_2 [-b e_2] + e_3 [-e_1 - c e_3] \\
&\le -a e_1^2 - b e_2^2 - c e_3^2 \\
&\le -[a + b + c] \|e\|^2.
\end{aligned}
\tag{72}
$$

Thus, under the supposed control, the trivial equilibrium of fractional synchronization error system is globally asymptotically stable, which in turn implies $\lim_{t \longrightarrow +\infty} \|e\| = \lim_{t \longrightarrow +\infty} \|y - x\| = 0$. Finally, the signal feedback control u synchronizes the financial chaotic system (10)–(12).

8. Stability Analysis, Bifurcation Diagram, and Lyapunov Exponent

In this section, we analyze the dynamic behaviors of the fractional financial chaotic model, the stability analysis, the bifurcation diagram, and the Lyapunov exponent, explicitly. The stability analysis of the equilibrium points studies the asymptotic behavior of the solutions around the equilibrium point. The bifurcation concept will help us to quantify the sensitivity of the fractional financial model when one of the parameters of the model varies into a specific interval. At last, the Lyapunov exponent characterizes the existence of chaotic behavior. Note that when the Lyapunov exponent is large and positive, then we detect the presence of high chaos. In more simple terms, the Lyapunov exponent represents the average exponential ratio of the convergence between adjacent orbits of the nonlinear systems in the phase space.

In this section, we begin the investigations with the local stability analysis in the context of the fractional-order derivative. The classical method used to study the local stability with the Jacobian matrix is not the same as the method used in fractional context. In fractional context, we use the Matignon criterion [38]. The equilibrium point x^* for the fractional differential equation $D_t^\alpha x = Ax$ is said to be locally stable if only the following relationship is held [38]:

$$|\arg(\lambda(A))| > \frac{\alpha\pi}{2}. \tag{73}$$

The procedure in the local stability in the fractional context is presented in [39]. The method consists of calculating the Jacobian matrix in the context of integer-order derivative, calculating the characteristic polynomial with the standard method, and calculating the eigenvalues with the algebraic method, and we finish by testing all eigenvalues satisfying Matignon criterion (equation (73)) including the fractional order. First of all, the equilibrium points of the fractional financial equations (10)–(12) are obtained after solving the equations

$$0 = z + yx - ax,$$
$$0 = 1 - by - x^2, \tag{74}$$
$$0 = -x - cz,$$

and we obtain the following equilibrium points after calculations:

$$E_0 = \left(0, \frac{1}{b}, 0\right),$$

$$E_1 = \left(\sqrt{\frac{-b+c-abc}{c}}, \frac{ac+1}{c}, -\sqrt{\frac{-b+c-abc}{c^3}}\right), \tag{75}$$

$$E_2 = \left(-\sqrt{\frac{-b+c-abc}{c}}, \frac{ac+1}{c}, \sqrt{\frac{-b+c-abc}{c^3}}\right).$$

For simplification, we directly take the values of the parameters used in the fractional financial chaotic model in Section 6. We continue by considering the following values

$a = 0.9, b = 0.2$, and $c = 1.5$; thus $E_0 = (0, 5, 0)$. The Jacobian matrix at the point E_0 is given by

$$J = \begin{pmatrix} 4.1 & 0 & 1 \\ 0 & -0.2 & 0 \\ -1 & 0 & -1.5 \end{pmatrix}. \tag{76}$$

The characteristic polynomial of the Jacobian matrix is represented after calculation in the following form:

$$P(\lambda) = -\lambda^3 + 2.4\lambda^2 + 5.67\lambda + 1.03. \tag{77}$$

The eigenvalues of the Jacobian matrix are given by $\lambda_1 = -1.3$, $\lambda_2 = -0.2$, and $\lambda_3 = 3.9$. We remark that $|\arg(\lambda_1)| = \pi/ > \alpha\pi/2$, $|\arg(\lambda_2)| = \pi > \alpha\pi/2$, and $|\arg(\lambda_3)| = 0 < \alpha\pi/2$. Thus, using the Matignon criterion in equation (73), we conclude that the equilibrium point E_0 is unstable.

We continue with the second equilibrium point $E_1 = (0.8, 1.6, -0.6)$. The Jacobian matrix at the point E_1 is given by

$$J = \begin{pmatrix} 0.7 & 0.8 & 1 \\ -1.6 & -0.2 & 0 \\ -1 & 0 & -1.5 \end{pmatrix}. \tag{78}$$

The characteristic polynomial of the Jacobian matrix is represented after calculation in the following form:

$$P(\lambda) = -\lambda^3 - \lambda^2 - 1.39\lambda - 1.91. \tag{79}$$

The eigenvalues of the Jacobian matrix are given by $\lambda_1 = -1.1860$, $\lambda_2 = 0.0929 - 1.2657i$, and $\lambda_3 = 0.0929 + 1.2657i$. We remark that $\arg(\lambda_1) = \pi/ > \alpha\pi/2$, $\arg(\lambda_2) = 274\pi/180 > \alpha\pi/2$, and $\arg(\lambda_3) = 86\pi/180 > \alpha\pi/2$ when $\alpha < 0.96$. Thus, using the Matignon criterion in equation (73), we conclude that the equilibrium point E_1 is locally stable if the order satisfies $\alpha < 0.96$. The condition $\alpha < 0.96$ justifies our choice related to $\alpha = 0.95$. We finish by the equilibrium point $E_2 = (-0.8, 1.6, 0.6)$. The Jacobian matrix at the point E_2 is given by

$$J = \begin{pmatrix} 0.7 & -0.8 & 1 \\ 1.6 & -0.2 & 0 \\ -1 & 0 & -1.5 \end{pmatrix}. \tag{80}$$

After checking, we remark that the rest of the calculations do not change. Thus the characteristic polynomial of the Jacobian matrix is given in the following form:

$$P(\lambda) = -\lambda^3 - \lambda^2 - 1.39\lambda - 1.91. \tag{81}$$

The eigenvalues of the Jacobian matrix are given by $\lambda_1 = -1.1860$, $\lambda_2 = 0.0929 - 1.2657i$, and $\lambda_3 = 0.0929 + 1.2657i$. We remark that $|\arg(\lambda_1)| = \pi/ > \alpha\pi/2$, $|\arg(\lambda_2)| = 274\pi/180 > \alpha\pi/2.$, and $|\arg(\lambda_3)| = 86\pi/180 > \alpha\pi/2$ when $\alpha < 0.96$. Thus, using the Matignon criterion in equation (73), we conclude that the equilibrium point E_2 is locally stable if the order satisfies $\alpha < 0.96$. The condition $\alpha < 0.96$ justifies our choice related to $\alpha = 0.95$ also.

To confirm the investigation in Section 6, we discuss the impact of the parameters using the bifurcation diagrams.

In the first case, we suppose the saving amount $a = 0.9$, the elasticity of demands $c = 1.5$, and all other conditions in Section 6 are maintained. Still, we consider the per investment cost varies into the interval $b \in [0.1, 0.3]$. The bifurcation diagram due to the variation of the per investment cost can be observed in Figure 22. That confirms as well the explanations in Section 6.

We continue with the bifurcation diagram obtained with the variation of the saving amount a. We fix the elasticity of demands $c = 1.5$ and the per investment cost $b = 0.2$; we consider the saving amount varies into the interval $a \in [0.1, 1]$. The bifurcation diagram due to the variation of the saving amount can be observed in Figure 23. That confirms as well the explanations in Section 6.

We finish with the bifurcation diagram obtained with the variation of the elasticity of demands. We fix the saving amount $a = 0.9$ and the per investment cost $c = 0.2$; we consider the elasticity of demands varies into the interval $c \in [1, 2]$. The bifurcation diagram due to the variation of the elasticity of demands can be observed in Figure 24. That confirms as well the explanations in Section 6.

In conclusion, we note very complex bifurcation generated by the variation of the parameters of the fractional financial chaotic system. In finance and economics, the complex bifurcation means we are in the context of recessions; in other words, we notice a significant decline in economic activities, and we particularly notice the increase in unemployment. The recession represents an economic situation during which the economy contracts. During this phase, all economic indicators are slowing down. This period is generally accompanied by a fall in salary and a fall in household purchasing power, thus causing a sharp drop in household consumption. In general, the predictions are very complicated to be made as can be observed with the diagram bifurcation in Figure 24.

At last, we finish with the Lyapunov exponent, whose role is to detect the existence of chaos. We give a brief investigation because the investigations related to the Lyapunov exponent for the fractional financial chaotic model can be found in [40]. We remind that, for the fractional-order $\alpha = 0.95$ and with $a = 0.9$, $b = 0.2$, and $c = 1.5$, the maximum Lyapunov exponent at $t = 110$ is given by $LE_{max} = 0.0420$; the algorithm for getting the Lyapunov exponent in the context of fractional-order derivative can be found in [41]. Note that the numerical method used in [41] should be replaced by our numerical schemes proposed in this paper. We observe that the Lyapunov exponent given by $LE_{max} = 0.0420$ is positive, which proves the existence of chaos as described in Section 6. We conclude that our investigations in Section 6 are confirmed by the maximal value of the Lyapunov exponent. The existence of chaos at $\alpha = 0.95$ can also justify our choice related to the value of the fractional derivative.

9. Conclusion

A numerical method for the financial chaotic model has been discussed in the context of the fractional calculus. The impact of the saving amount, the per investment cost, and the elasticity of demands in the behaviors of the solution of the fractional financial chaotic model has been analyzed as well. The economical interpretations have been proposed for more understanding of the importance of these present investigations. For more understanding of the chaotic behavior of the chaotic financial model, the stability analysis of the equilibrium points, the bifurcation theory to analyze the impact of the parameters of the financial model carefully, and the Lyapunov exponent to detect the existence of the chaos have been discussed in this paper. For future work, it will be very interesting to study what will happen when the quadratic function x^2 is replaced by quadric function x^4 and what will be the maximal value of the Lyapunov exponent when chaos is detected. This problem is stated in the literature, but many questions are not solved. This paper supports the applications of fractional calculus in economics and finance. Future investigations can be developed in these directions.

Data Availability

No data were used to support this study.

Conflicts of Interest

The authors declare that they have no conflicts of interest.

References

[1] A. Chouchane-Verdier, "Une analyse empirique de l'impact de la libéralisation financière en Afrique subsaharienne sur la période 1983–1996," *Revue Tiers Monde*, vol. 179, no. 3, pp. 617–641, 2004.

[2] R. M. Solow, "A contribution to the theory of economic growth," *The Quarterly Journal of Economics*, vol. 70, no. 1, pp. 65–94, 1956.

[3] T. W. Swan, "Economic growth and capital accumulation," *Economic Record*, vol. 32, no. 2, pp. 334–361, 1956.

[4] R. E. Lucas, "On the mechanics of economic development," *Journal of Monetary Economics*, 1989.

[5] Turgot, "Paragon of the continental enlightenment," *The Journal of Law and Economics*, vol. 19, no. 3, pp. 607–619, 1976.

[6] G. J. Benston and C. W. Smith, "A transactions cost approach to the theory of financial intermediation," *The Journal of Finance*, vol. 31, no. 2, pp. 215–231, 1976.

[7] J. M. Keynes, "The general theory of employment, interest and money," *The Collected Writings*, vol. 7, pp. 1971–1979, Cambridge university Press, Cambridge, UK, 1964.

[8] E. D. Domar, "Expansion and employment," *The American Economic Review*, vol. 37, no. 1, pp. 34–55, 1947.

[9] M. Feldstein and J. H. Stock, "The use of a monetary aggregate to target nominal GDP," in *Monetary Policy*, pp. 7–69, The University of Chicago Press, Chicago, IL, USA, 1994.

[10] M. Obstfeld, *How Integrated Are World Capital Markets? Some New Tests (No. W2075)*, National Bureau of Economic Research, Cambridge, MA, USA, 1986.

[11] R. Tobin, "The psychological significance of pubertal change," in *Girls at Puberty*, pp. 127–154, Springer, Boston, MA, USA, 1983.

[12] L. Dramani and O. Laye, *Les Déterminants de L'investissement Privé au Sénégal: Une Approche VAR strucurel, Republique du Senegal*, Ministere de l'Economie et des Finances, 2008.

[13] J. L. Esso and Y. Keho, "The savings-investment relationship: cointegration and causality évidence from UEMOA countries," *International Journal of Economics and Finance*, vol. 2, no. 1, pp. 174–181, 2010.

[14] N. Dries and R. Pepermans, "How to identify leadership potential: development and testing of a consensus model," *Human Resource Management*, vol. 51, no. 3, pp. 361–385, 2012.

[15] A. Marshall, *Principles of Economics*, Mcmillan, London, UK, 8th edition, 1890.

[16] M. T. Shahiri, A. N. Ranjbar, R. Ghaderi, S. H. Hosseinnia, and S. Momani, "Control and synchronization of chaotic fractional-order coullet system via," *Active Controller* no. 2, 2012, https://arxiv.org/abs/1206.2415.

[17] B. Xin and Y. Li, "0-1 test for chaos in a fractional order financial system with investment incentive," *Abstract and Applied Analysis*, vol. 2013, p. 10, 2013.

[18] C. Chen, T. Fan, and B. Wang, "Inverse optimal control of hyperchaotic finance system," *World Journal of Modelling and Simulation*, vol. 10, no. 2, pp. 83–91, 2014.

[19] Q. Gao and J. Ma, "Chaos and Hopf bifurcation of a finance system," *Nonlinear Dynamics*, vol. 58, no. 1-2, pp. 209–216, 2009.

[20] D. Kumar and S. Kumar, "Construction of four dimensional chaotic finance model and its applications," *International Journal of Pure and Applied Mathematics*, vol. 118, no. 22, pp. 1171–1187, 2018.

[21] Y. Xu and Z. He, "Synchronization of variable order fractional financial system via active control method," *Central European Journal Physics*, vol. 11, no. 6, 2013.

[22] Z. Wang, X. Huang, and G. Shi, "Analysis of nonlinear dynamics and chaos in a fractional order financial system with time delay," *Computers & Mathematics with Applications*, vol. 62, no. 3, pp. 1531–1539, 2011.

[23] W. Shaojie, H. Shaobo, A. Yousefpour, H. Jahanshahi, R. Repnik, and M. Perc, "Chaos and complexity in a fractional-order financial system with time delays," *Chaos, Solitons Fractals*, vol. 131, Article ID 109521, 2020.

[24] A. Akgul, C. Arslan, and B. Aricioglu, "Design of an Interface for random number Generators based on Integer and fractional order chaotic systems," *Chaos, Theory and Applications*, vol. 1, no. 1, pp. 1–18, 2019.

[25] K. Rajagopal, A. Akgul, S. Jafari, A. Karthikeyan, U. Cavusoglu, and S. Kacar, "An exponential jerk system, its fractional-order form with dynamical analysis and engineering application," *Soft Computing*, vol. 24, no. 10, pp. 7469–7479, 2020.

[26] J. Fahd, T. Abdeljawad, and D. Baleanu, "On the generalized fractional derivatives and their Caputo modification," *The Journal of Nonlinear Sciences and Applications*, vol. 10, no. 5, pp. 2607–2619, 2017.

[27] A. A. Kilbas, H. M. Srivastava, and J. J. Trujillo, *Theory and Applications of Fractional Differential Equations*, p. 204, North-Holland Mathematics Studies, Elsevier, Amsterdam, Netherlands, 2006.

[28] T. Mekkaoui, Z. Hammouch, D. Kumar, and J. Singh, "A new approximation scheme for solving ordinary differential equation with gomez-atangana-caputo fractional derivative," *Methods of Mathematical Modelling*, p. 51, CRC Press, Boca Raton, FL, USA, 2019.

[29] I. Podlubny, *Fractional Differential Equations, Mathematics in Science and Engineering*, p. 198, Academic Press, New York, NY, USA, 1999.

[30] N. Sene, "Integral balance methods for Stokes' first equation described by the left generalized fractional derivative," *Physics*, vol. 1, no. 1, pp. 154–166, 2019.

[31] N. Sene, "Second-grade fluid model with Caputo-Liouville generalized fractional derivative," *Chaos, Solitons & Fractals*, vol. 133, p. 109631, 2020.

[32] N. Sene and A. N. Fall, "Homotopy perturbation ρ-laplace transform method and its application to the fractional diffusion equation and the fractional diffusion-reaction equation," *Fractal and Fractional*, vol. 3, no. 2, p. 14, 2019.

[33] N. Sene and A. Atangana, "Integral-balance methods for the fractional diffusion equation described by the caputo-generalized fractional derivative," *Methods of Mathematical Modelling*, p. 83, CRC Press, Boca Raton, FL, USA, 2019.

[34] N. Sene, "Stability analysis of the generalized fractional differential equations with and without exogenous inputs," *Journal of Nonlinear Sciences and Applications*, vol. 12, no. 9, pp. 562–572, 2019.

[35] N. Sene, "Global asymptotic stability of the fractional differential equations," *Journal of Nonlinear Sciences and Applications*, vol. 13, pp. 171–175, 2020.

[36] M. Yavuz, "Characterizations of two different fractional operators without singular kernel," *Mathematical Modelling of Natural Phenomena*, vol. 14, no. 3, p. 302, 2019.

[37] N. Sene, "Stability analysis of electrical RLC circuit described by the Caputo-Liouville generalized fractional derivative," *Alexandria Engineering Journal*, 2020.

[38] D. Matignon, "Stability results on fractional differential equations to control processing," in *Proceedings of the Computational Engineering in Syatems and Application Multiconference; IMACS*, vol. 2, pp. 963–968, Lille, France, 1996.

[39] E. Ahmed, A. M. A. El-Sayed, and H. A. A. El-Saka, "On some Routh-Hurwitz conditions for fractional order differential equations and their applications in Lorenz, Rössler, Chua and Chen systems," *Physics Letters A*, vol. 358, no. 1, pp. 1–4, 2006.

[40] W.-C. Chen, "Nonlinear dynamics and chaos in a fractional-order financial system," *Chaos, Solitons & Fractals*, vol. 36, no. 5, pp. 1305–1314, 2008.

[41] M.-F. Danca and N. Kuznetsov, "Matlab code for Lyapunov exponents of fractional-order systems," *International Journal of Bifurcation and Chaos*, vol. 28, no. 5, Article ID 1850067, 2018.

WILEY | Hindawi

Research Article

Generation of Tunable Microwave Frequency Comb Utilizing a Semiconductor Laser Subject to Optical Injection from an SFP Module Modulated by an Arbitrary Periodic Signal

Qingchun Zhao [ID]**, Maohai Zhai, Wenbo Shi, and Bin Wu**

School of Computer and Communication Engineering, Northeastern University at Qinhuangdao, Qinhuangdao, Hebei 066004, China

Correspondence should be addressed to Qingchun Zhao; zhaoqingchun2000@163.com

In this paper, a microwave frequency comb (MFC) is generated from a semiconductor laser subject to optical injection from a commercial small form-factor pluggable (SFP) optical module which is modulated by an arbitrary periodic signal. A sinusoidal signal or square wave signal is employed as the arbitrary periodic signal instead of the electric pulse signal adopted in the former references. When the frequency of the modulated signal is 1 GHz, the MFC with a maximal bandwidth of 15 GHz can be obtained. In addition, taking a sinusoidal signal as an example, the influence of the injection optical power to the slave laser and the modulation frequency of the optical module on the generation of the MFC is analyzed in detail. Finally, the results of MFC generated with a square wave signal injection are presented. The experimental results of this paper provide an important reference for the practical applications of MFC.

1. Introduction

With the external disturbances such as external optical injection, optical feedback, or opto-electric feedback, a semiconductor laser can produce some nonlinear dynamic phenomena, including period one oscillation [1, 2], period-doubling oscillation, quasiperiod oscillation, and chaos [3–8]. In addition, a semiconductor laser can also generate microwave frequency comb (MFC) under the external optical injection. MFC is widely used in frequency measurement, radar detection, frequency conversion, radio-over-fiber (RoF) transmission system, and other fields due to the advantages of multiple continuous microwave signals, flexible and adjustable comb line spacing, wide frequency range, and high comb spacing precision [2, 9–11]. Therefore, generation of stable and high-quality MFC has become a research hotspot.

Some methods of generating MFC have been reported up to now. The MFC signal with a bandwidth of 3 GHz was generated by using the subharmonic frequency locked state generated by the opto-electric feedback of semiconductor laser [12]. But the comb spacing of the frequency comb was not strictly equal. Moreover, the noise of noncomb component was obvious. By injecting the regular optical pulse generated by opto-electric feedback of semiconductor laser into the other semiconductor lasers, the MFC signal was generated with an amplitude of ±5 dB and bandwidth of 20 GHz [13, 14]. However, the signal was unstable, and the comb line spacing was small. By adopting the nonlinear effect of STM tunnel junction, the generation of the MFC signal with up to 200 harmonics was realized. The central frequency of the highest harmonic is 14.85 GHz. Yet there are some disadvantages such as difficult to tune the comb spacing and large phase noise [15–17]. In addition, the numerical simulations and experiments have been presented for the generation of tunable MFC signal by semiconductor laser subject to optical injection, in which the master laser is modulated by a periodic electric pulse signal [18–20].

In this paper, a tunable MFC signal is obtained by using an external optical injection semiconductor laser. The master laser is a commercial SFP optical module modulated by a periodic electronic signal not just a periodic electric pulse signal used in [20]. The modulation signal in this experiment is the sinusoidal signal produced by a RF signal generator or the square wave signal produced by a bit-error-rate tester (BERT). As the master laser, in order to reduce the cost and the complexity of the setup, we use a commercial optical module which is cheap, simple, and easy to be modulated.

2. Experimental Setup

The experimental setup of the tunable MFC produced by a semiconductor laser subject to the optical injection from a SFP optical module modulated by a sinusoidal signal is presented in Figure 1. The master laser is a 2.5 Gb/s small form-factor pluggable (SFP, Finisar) optical module, yet the slave laser is a distributed feedback (DFB) semiconductor laser without a build-in optical isolator. The optical power and central wavelength of the slave laser are controlled by the current source circuit and the temperature control circuit, respectively. The SFP module generates an optical signal that changes with the modulation of a sinusoidal signal from a RF signal generator (SG, IFR 2042, 5.4 GHz). After being amplified by erbium-doped fiber amplifier (EDFA), the light enters the variable optical attenuator (VOA) to adjust the injected optical power. A polarization controller (PC) is adopted to adjust the polarization state. Then, the light enters the slave laser through the optical circulator (OC) to generate a new optical signal utilizing nonlinear interaction. A 50 : 50 optical coupler is adopted to divide light into two beams. One beam enters a photodetector (PD, Picometrix, PT-40D/AC) with a bandwidth of 40 GHz to convert the optical signal into electrical signal. The output electrical signal is gathered by the electrical spectrum analyzer (ESA, Rohde & Schwarz, FSEK20, 40 GHz). The other beam enters the optical spectrum analyzer (OSA, Anritsu, MS9710C) to analyze the optical spectrum.

The frequency range of the sinusoidal signal generated from the signal generator is changed from 0.5 GHz to 5.4 GHz in this experiment. The SFP is an optical module that meets the dense wavelength division multiplexing (DWDM) wavelength requirements. The actual output wavelength is 1549.76 nm. In order to adjust the injected optical power for a large range, the EDFA is necessary. The output power of the SFP is small, but the power can be amplified to 11.3 dBm by EDFA working under the automatic power control (APC). The VOA is employed to adjust the optical power injecting into the slave laser with an initial attenuation coefficient of 11 dB. The bias voltage of the photodetector with a transimpedance amplifier is +4 V, yet the voltage for the transimpedance amplifier is +3.3 V. For this experiment, the optimal MFC signal is obtained by adjusting the frequency of the sinusoidal signal from the signal generator, the PC, and the VOA.
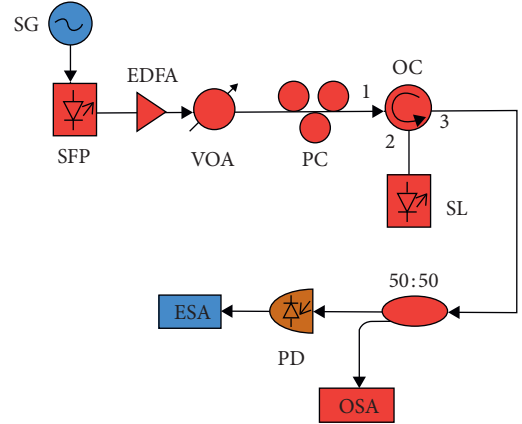
Figure 1: Experimental setup. SFP: small form-factor pluggable; EDFA: erbium-doped fiber amplifier; VOA: variable optical attenuator; PC: polarization controller; OC: optical circulator; SL: slave laser; PD: photodetector; ESA: electrical spectrum analyzer; OSA: optical spectrum analyzer; SG: signal generator.

3. Effect of the Injection Optical Power on MFC

The initial frequency of the signal generator is 1 GHz with an amplitude of +0.7 V. The attenuation coefficient of the VOA is between 11 dB and 25 dB with an attenuation step of 1 dB. When the attenuator coefficient is 11 dB, the obtained MFC is shown in Figure 2(a). The comb line spacing of the MFC is equal to the frequency of the modulation signal, which is 1 GHz. The bandwidth of MFC can be determined by the electrical spectrum analyzer as follows. Firstly, the function of electrical spectrum analyzer to find the peak value is used to directly locate the component with the highest power for the frequency comb. The frequency of the component is 3 GHz, and the power is −27.95 dBm, which is the third comb line of the MFC. In this paper, the bandwidth for the MFC is defined as 10 dB [20], that is, the maximum power value minus 10 dBm. Then, the MFC component within this range is the bandwidth. Accordingly, an isoline with a power of −27.95 dBm is drawn to determine the upper bound. Secondly, an isoline with the power of −37.95 dBm is drawn to determine the lower bound. It can be seen from Figure 2(a) that there are 15 comb line components between the two power contour lines. Therefore, the bandwidth of the MFC is 15 GHz. The peak power difference for each comb line is small. Hence, the MFC signal quality is good. Although there is a frequency component greater than 15 GHz, the signal power is lower than −37.95 dBm, which is not considered in the bandwidth.

The MFC signal is shown in Figure 2(b) when the attenuation coefficient of the VOA is set to 20 dB. The frequency of the modulation signal is 1 GHz; hence, the frequency of the generated MFC signal is an integral multiple of 1 GHz, that is, from 1 GHz and 2 GHz to 11 GHz. Except these frequencies, noise appears. It can be seen that there is a lot of noise at the bottom of some frequency comb lines. The frequency comb with the high frequency part is almost submerged by noise. The signal quality is not as good, as shown in Figure 2(a), but the MFC with a wide spectrum

(a)

(b)

(c)

(d)
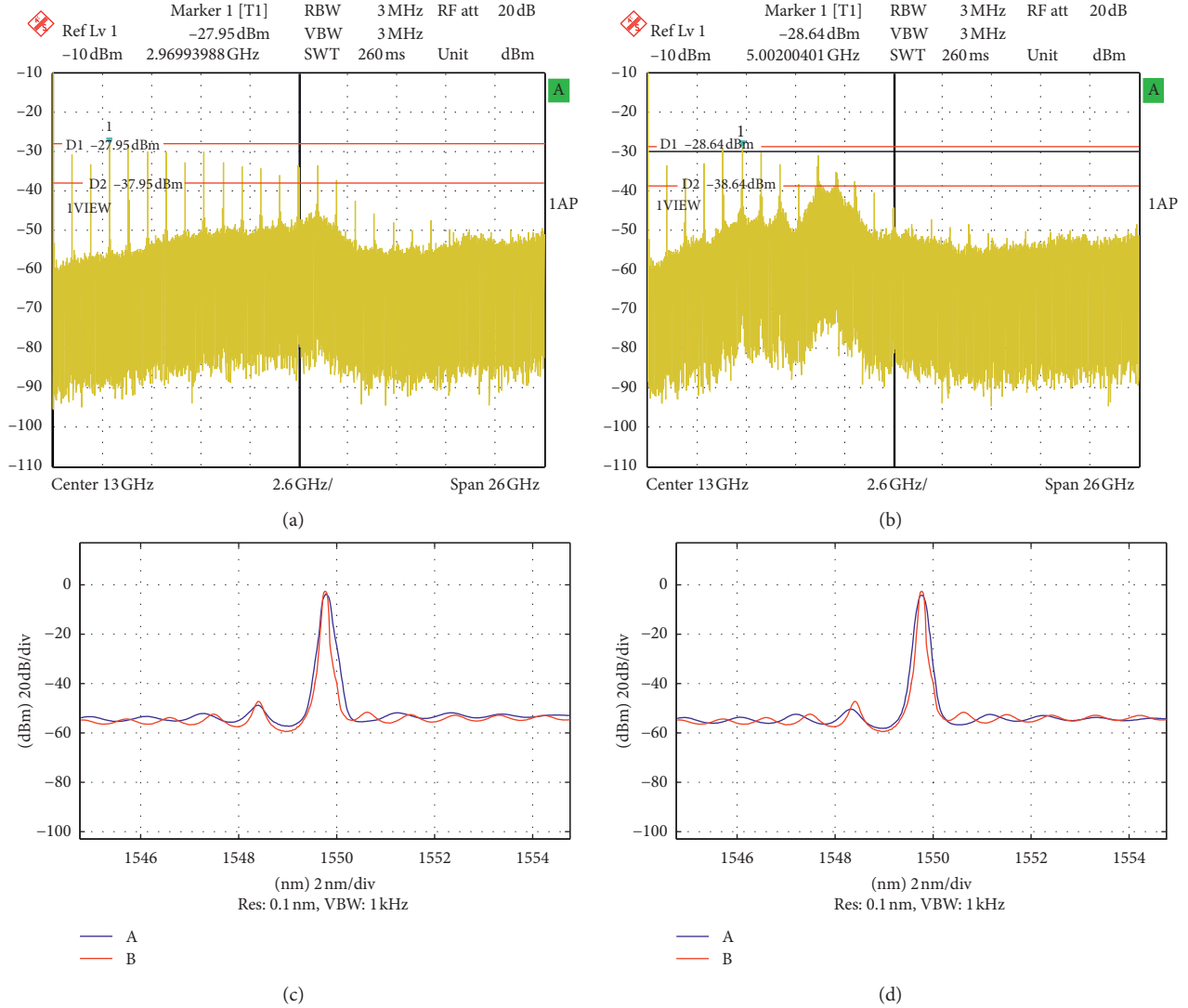
FIGURE 2: Electrical spectrum of the MFC when the modulation signal frequency is 1 GHz and the attenuator coefficient of VOA is 11 dB (a) and 20 dB (b). The optical spectrum when the attenuator coefficient of VOA is 11 dB (c) and 20 dB (d) For (c) and (d), curve A denotes the optical spectrum of the optical signal generated from SL with the injection from SFP module. Curve B denotes the optical spectrum of the SFP module.

can still be obtained. According to the above method of bandwidth determination, it can be concluded that the bandwidth of the MFC is 11 GHz for this case.

For this experiment, we also measured the optical spectrum of the optical signal generated from SL after optical injection. Figure 2(c) is the optical spectrum when the attenuation coefficient of the VOA is 11 dB. Curve A is the optical spectra of the optical signal generated from SL after optical injection, while curve B denotes the optical spectra of the SFP module. It can be seen that the central wavelength of the optical signal generated from SL after optical is equal to that of the SFP module. That is to say, when the central wavelength of the master laser and the slave laser is equal, the MFC can be obtained. Figure 2(d) is the optical spectrum of the VOA when the attenuation coefficient is 20 dB. It can be seen that the optical spectrum hardly changes with the increasing attenuation coefficient.

The injection optical power from the SFP module decreases gradually by adjusting the attenuation of VOA. The bandwidth of the MFC changes with the attenuation coefficient, as shown in Figure 3. When the attenuation coefficient is from 11 dB to 13 dB or from 24 dB to 25 dB, the bandwidth of the MFC does not change. When the attenuation coefficient is from 14 dB to 24 dB, the MFC bandwidth presents a general decreasing trend with the increasing attenuation coefficient. Therefore, the bandwidth of the MFC generated in this experiment generally decreases with the decrease in the output power of the SFP module, but the overall fluctuation is not big.

4. Effect of Modulation Frequency on MFC

During this section, the attenuation coefficient of VOA is maintained at 11 dB. Figure 4(a) shows the generated MFC
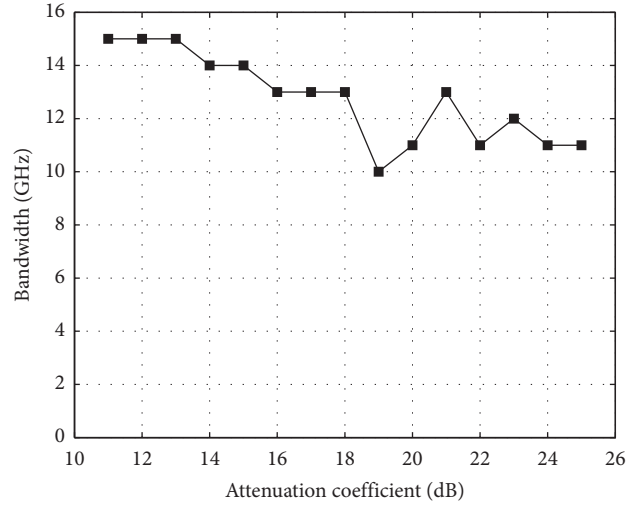
Figure 3: Influence of the output optical power of the SFP optical module on the MFC. The *X*-axis is represented by the attenuation coefficient of the VOA.

(a)

(b)
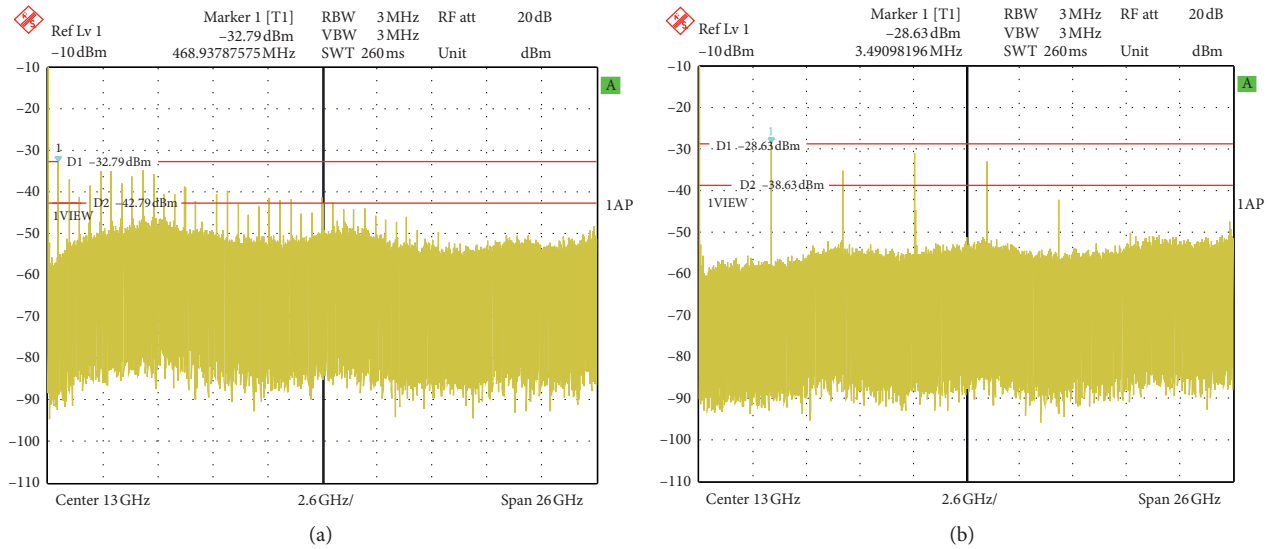
Figure 4: Generated MFC when the modulation frequency is 0.5 GHz (a) and 3.5 GHz (b).

when the modulation frequency from the signal generator is 0.5 GHz. It can be seen that the comb line spacing of the MFC is equal to the frequency of the modulation signal, i.e., 0.5 GHz. Compared with the result of 1 GHz modulation frequency in Figure 2(a), when the modulation frequency is 0.5 GHz, the power of the low-frequency base part increases, so the quality of the obtained MFC decreases. The bandwidth for the MFC shown in Figure 4(a) is 7 GHz. The obtained MFC is shown in Figure 4(b) when the output frequency of the signal generator is 3.5 GHz. The comb line spacing is 3.5 GHz, which equals to the sinusoidal signal modulation frequency. However, the frequency comb of the high frequency part disappears. As shown in Figure 4(b), the MFC whose overall base is flat is better than the result presented in Figure 4(a). The bandwidth for the MFC shown in Figure 4(b) is 14 GHz.

The relationship between the bandwidth of the MFC and the modulation frequency is displayed in Figure 5. With the

increasing modulation frequency, the bandwidth of MFC is generally increasing. When the modulation frequency is between 1 GHz and 2 GHz, the bandwidth decreases slightly. The quality of the MFC is not very good. Generally speaking, when the range of the modulation frequency is from 2.5 GHz to 5 GHz, the bandwidth begins to increase. Moreover, not only the noise is relatively small and the comb line is clean but also the power distribution of each comb line is relatively uniform.

5. MFC Generated with Square Wave Signal Modulation

In order to illustrate that a MFC signal can be generated from a semiconductor laser subject to optical injection from a SFP module modulated by arbitrary periodic signal, a square wave signal is employed as the modulated signal.
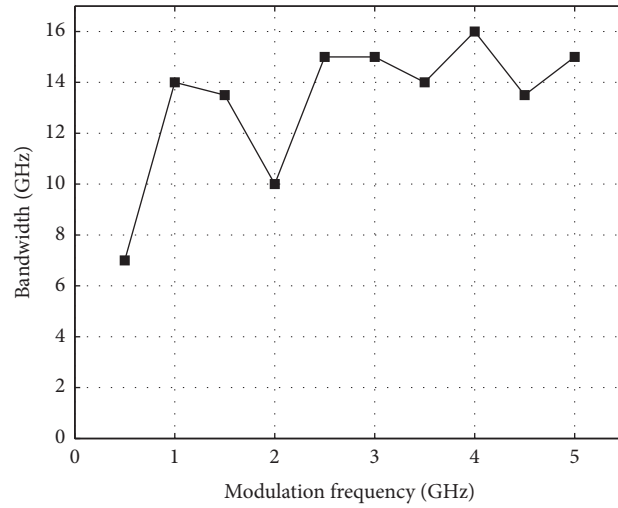
FIGURE 5: Effect of modulation frequency on MFC.

(a)
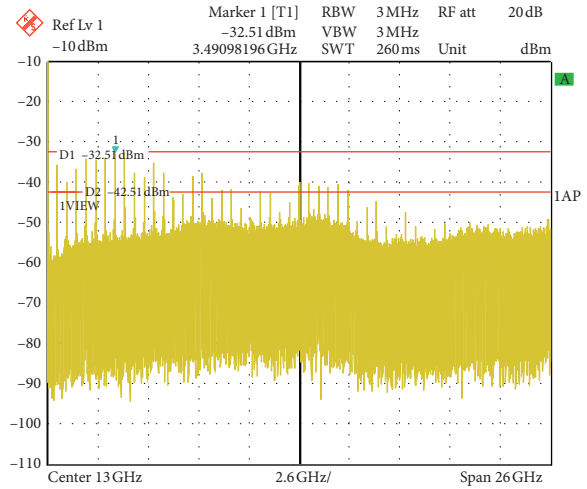
(b)
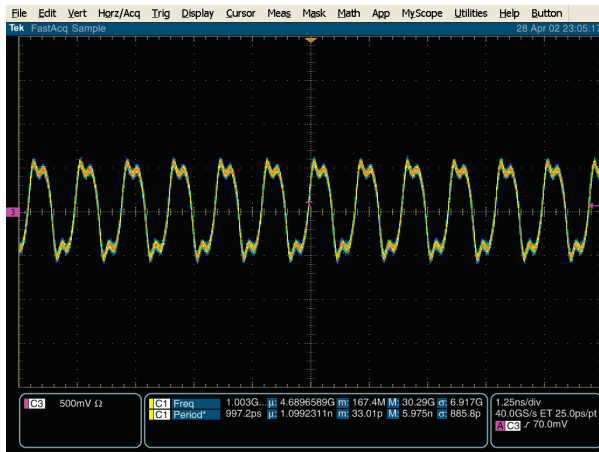
(c)
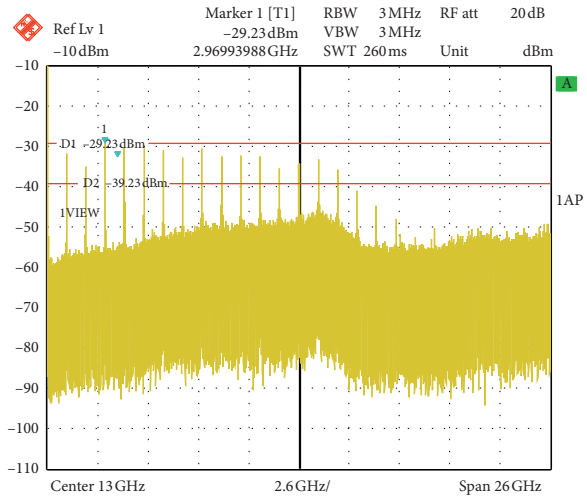
(d)

FIGURE 6: Results of the MFC generated by the square wave signal modulation. (a) and (c) are the 0.5 GHz and 1 GHz square wave signals, respectively. (b) and (d) are the generated MFC with the modulation of 0.5 GHz and 1 GHz square wave signals, respectively.

During this experiment, a bit-error-rate tester (BERT, Anritsu, MP1632A, 3.2 Gb/s) is utilized to generate a square wave signal. By the way, a bit-error-rate tester is generally arranged to generate the pseudorandom bit sequence. The specific setting is to utilize the pattern setting function in the pattern editor menu of the BERT. The data output from the pulse pattern generator (PPG) of the BERT is the square wave signal when the running mode is selected as programmable pattern (PRGM) and set the pattern type as periodic 0 and 1. The time-domain waveform is displayed on a real-time digital oscilloscope (OSC, Tektronix, TDS7404B, 4 GHz, 20 GS/s).

The square wave signal generated by the BERT is employed to modulate the SFP module. Figure 6(a) presents the square wave signal with the output frequency of 0.5 GHz. Figure 6(b) displays the corresponding MFC signal generated by slave laser with the optical injection from SFP module with the modulation of the square wave signal. For this case, the bandwidth of MFC signal is 6 GHz. Comparing the MFC obtained this time with that obtained from the sinusoidal signal with the modulation frequency of 0.5 GHz, the bandwidth is 6 GHz and 7 GHz, respectively. Not only the difference of the bandwidth is not big but also the main characteristics of the base noise distribution, comb line, and comb line power distribution of the MFC are similar.

When the frequency of the square wave signal is 1 GHz, the results of the oscilloscope and the electronic spectra are shown in Figures 6(c) and 6(d), respectively. The comb line spacing of the MFC signal increases from 0.5 GHz to 1 GHz when the square wave signal is 1 GHz. The number of the comb lines decreases, and the power of comb lines component within the bandwidth increases. Hence, the MFC signal quality generally improves. When the frequency of modulation signal is 1 GHz, the bandwidth of the MFC signal obtained with the square wave signal and the sinusoidal signal is 15 GHz and 14 GHz, respectively. The results of the two MFC signals on the electronic spectrum analyzer are approximately the same. This is a strong proof of the argument put forward in this paper; that is, the MFC can be generated from a semiconductor laser with optical injection from a modulated SFP module by arbitrary periodic signal.

Other waveforms, such as triangle-wave signal or periodic pulse signal, can also be adopted as the modulated signal, which can be generated by arbitrary waveform generator (AWG) with high bandwidth. At present, we have no such high-bandwidth AWG in our laboratory. In future, we will conduct some experiments to generate MFC with the modulation signal produced by AWG.

6. Conclusions

In this paper, a sinusoidal signal or square wave signal is employed as a periodic signal to modulate the SFP module in order to realize the generation of the microwave frequency comb signal from the semiconductor laser with the injection from the SFP module. The proposed setup can generate stable microwave frequency comb signal in the range of 6 GHz–16 GHz. The results of this paper provide a useful reference for the practical application of the microwave frequency comb signal.

Data Availability

The data used to support the findings of this study are available from the corresponding author upon request.

Conflicts of Interest

The authors declare that there are no conflicts of interest regarding the publication of this paper.

Acknowledgments

References

[1] S. Ji, Y. Hong, P. S. Spencer, J. Benedikt, and I. Davies, "Broad tunable photonic microwave generation based on period-one dynamics of optical injection vertical-cavity surface-emitting lasers," *Optics Express*, vol. 25, no. 17, pp. 19863–19871, 2017.

[2] C. Cui and S.-C. Chan, "Performance analysis on using period-one oscillation of optically injected semiconductor lasers for radio-over-fiber uplinks," *IEEE Journal of Quantum Electronics*, vol. 48, no. 4, pp. 490–499, 2012.

[3] T. B. Simpson, J. M. Liu, K. F. Huang, and K. Tai, "Nonlinear dynamics induced by external optical injection in semiconductor lasers," *Quantum and Semiclassical Optics: Journal of the European Optical Society Part B*, vol. 9, no. 5, pp. 765–784, 1997.

[4] F.-Y. Lin, S.-Y. Tu, C.-C. Huang, and S.-M. Chang, "Nonlinear dynamics of semiconductor lasers under repetitive optical pulse injection," *IEEE Journal of Selected Topics in Quantum Electronics*, vol. 15, no. 3, pp. 604–611, 2009.

[5] Y.-S. Juan and F.-Y. Lin, "Photonic generation of broadly tunable microwave signals utilizing a dual-beam optically injected semiconductor laser," *IEEE Photonics Journal*, vol. 3, no. 4, pp. 644–650, 2011.

[6] J.-W. Wu, Q. Qiu, X.-P. Zhang, and Y. H. Won, "Simultaneous generation of microwave, millimeter-wave, and terahertz photonic signal based on two-color semiconductor laser subject to single-beam optical injection," *IEEE Journal of Selected Topics in Quantum Electronics*, vol. 23, no. 4, pp. 1–8, 2017.

[7] J.-P. Zhuang, X.-Z. Li, S.-S. Li, and S.-C. Chan, "Frequency-modulated microwave generation with feedback stabilization using an optically injected semiconductor laser," *Optics Letters*, vol. 41, no. 24, pp. 5764–5767, 2016.

[8] K.-H. Lo, S.-K. Hwang, and S. Donati, "Optical feedback stabilization of photonic microwave generation using period-one nonlinear dynamics of semiconductor lasers," *Optics Express*, vol. 22, no. 15, pp. 18648–18661, 2014.

[9] Y.-H. Hung and S.-K. Hwang, "Photonic microwave stabilization for period-one nonlinear dynamics of semiconductor lasers using optical modulation sideband injection locking," *Optics Express*, vol. 23, no. 5, pp. 6520–6532, 2015.

[10] S.-K. Hwang, C.-Y. Lin, and D.-H. Liang, "All-optical frequency conversion using nonlinear dynamics of semiconductor lasers subject to external optical injection," in

Proceeding of the Semiconductor Lasers and Laser Dynamics III, vol. 6997, Strasbourg, France, May 2008.

[11] Y. Matsui, R. Schatz, T. Pham et al., "55 GHz bandwidth distributed reflector laser," *Journal of Lightwave Technology*, vol. 35, no. 3, pp. 397–403, 2017.

[12] S.-C. Chan, G.-Q. Xia, and J.-M. Liu, "Optical generation of a precise microwave frequency comb by harmonic frequency locking," *Optics Letters*, vol. 32, no. 13, pp. 1917–1919, 2007.

[13] Y.-S. Juan and F.-Y. Lin, "Microwave-frequency-comb generation utilizing a semiconductor laser subject to optical pulse injection from an optoelectronic feedback laser," *Optics Letters*, vol. 34, no. 11, pp. 1636–1638, 2009.

[14] Y.-S. Juan and F.-Y. Lin, "Ultra broadband microwave frequency combs generated by an optical pulse-injected semiconductor laser," *Optics Express*, vol. 17, no. 21, pp. 18596–18605, 2009.

[15] M. J. Hagmann, A. Efimov, A. J. Taylor, and D. A. Yarotski, "Microwave frequency-comb generation in a tunneling junction by intermode mixing of ultrafast laser pulses," *Applied Physics Letters*, vol. 99, no. 1, Article ID 011112, 2011.

[16] M. J. Hagmann, A. J. Taylor, and D. A. Yarotski, "Observation of 200th harmonic with fractional linewidth of 10−10 in a microwave frequency comb generated in a tunneling junction," *Applied Physics Letters*, vol. 101, no. 24, Article ID 241102, 2012.

[17] M. J. Hagmann, F. S. Stenger, and D. A. Yarotski, "Linewidth of the harmonics in a microwave frequency comb generated by focusing a mode-locked ultrafast laser on a tunneling junction," *Journal of Applied Physics*, vol. 114, no. 22, Article ID 223107, 2013.

[18] L. Fan, G.-Q. Xia, X. Tang et al., "Tunable ultra-broadband microwave frequency combs generation based on a current modulated semiconductor laser under optical injection," *IEEE Access*, vol. 5, pp. 17764–17771, 2017.

[19] X.-Q. Xu, L. Fan, G.-Q. Xia, and Z.-M. Wu, "Numerical investigation on ultra-broadband tunable microwave frequency comb generation using a semiconductor laser under regular pulse injection," *IEEE Access*, vol. 6, pp. 55284–55290, 2018.

[20] L. Fan, G.-Q. Xia, T. Deng et al., "Generation of tunable and ultra-broadband microwave frequency combs based on a semiconductor laser subject to pulse injection from a current modulated laser," *IEEE Photonics Journal*, vol. 10, no. 6, pp. 1–10, 2018.

WILEY | Hindawi

Research Article
Higher-Order Multifractal Detrended Partial Cross-Correlation Analysis for the Correlation Estimator

Keqiang Dong [ID] **and Xiaojie Gao**

College of Science, Civil Aviation University of China, Tianjin 300300, China

Correspondence should be addressed to Keqiang Dong; hongzhangdong@163.com

In this paper, we develop a new method to measure the nonlinear interactions between nonstationary time series based on the detrended cross-correlation coefficient analysis. We describe how a nonlinear interaction may be obtained by eliminating the influence of other variables on two simultaneous time series. By applying two artificially generated signals, we show that the new method is working reliably for determining the cross-correlation behavior of two signals. We also illustrate the application of this method in finance and aeroengine systems. These analyses suggest that the proposed measure, derived from the detrended cross-correlation coefficient analysis, may be used to remove the influence of other variables on the cross-correlation between two simultaneous time series.

1. Introduction

There are numerous real-world systems where the output signals are nonstationary and exhibit complex self-correlation or cross-correlation over a broad range of time scales. The output signals can be characterized by power-law correlations. One method, which has proved to be quite useful to detect the degree of interrelation between two stationary variables, is Pearson's correlation coefficient [1]:

$$r = \frac{\langle (X - \langle X \rangle) \cdot (Y - \langle Y \rangle) \rangle}{\sigma_X \cdot \sigma_Y}, \tag{1}$$

where $\langle X \rangle$ is the arithmetic average of X and σ_X is its standard deviation and likewise for Y. Proposition of Pearson's correlation coefficient (PCC) has achieved great success in multivariate analysis, such as the principal component analysis [2], random matrix theory [3], and singular value decomposition [4].

Nevertheless, in real-world systems, nonlinear and nonstationary characteristics are present. Therefore, PCC may not be suitable to describe the interrelation between two variables that are nonlinear and nonstationary. For dealing with the drawbacks of PCC, the detrended cross-correlation

analysis (DCCA) method and the DCCA coefficient are proposed by Stanley and Podobnik [5, 6]. The advantage of the DCCA method is that it allows the detection of cross-correlations between noisy signals with embedded polynomial trends, which can mask the true cross-correlations in the fluctuations of signals. The DCCA method is widely applied to measure the cross-correlations in different fields, such as social sciences [7], biology [8], climatology [9], geophysics [10, 11], transportation [12, 13], seismic signals [11, 14], economics [15–20], and aeroengine dynamics [21–24].

Recently, multifractal analysis is one of the major interests for researchers from interdisciplinary domains to uncover the scaling properties and understand the hidden information. Among these researchers, many of them applied the multifractal analysis to meteorology [25–27], electroencephalography [28], and economics [29–31]. Later, as some researchers thought of extending the research of multifractal analysis to the detrended cross-correlations between time series, the multifractal detrended cross-correlation analysis (MFDXA) was proposed [32–34].

The cross-correlation between two variables may be influenced by other variables. Hence, we have to be alert to

the possibilities of spurious correlation while investigating the cross-correlation. Then, the methods of partial correlation and partial correlation coefficient are therefore proposed to measure the degree of association between two random variables [35, 36]. The linear effect may be removed using the partial correlation coefficient (partial CC):

$$r_{XY,\xi} = \frac{\langle (X' - \langle X' \rangle) \cdot (Y' - \langle Y' \rangle) \rangle}{\sigma_{X'} \cdot \sigma_{Y'}} = \frac{r_{XY} - r_{X\xi} \cdot r_{Y\xi}}{\sqrt{\left(1 - r_{X\xi}^2\right) \cdot \left(1 - r_{Y\xi}^2\right)}}, \tag{2}$$

where $X' = X - L_X(\xi)$ and $L_X(\xi) = c_0 + c_1\xi$ to minimize the mean $E(X - L_X(\xi))^2$ and likewise for Y'. If n additional variables are to be accounted for, say $\xi_1, \xi_2, \ldots, \xi_n$, the nth-order partial CC can be computed by [36]

$$r_{XY.12\cdots n} = \frac{r_{XY.12\cdots n-1} - r_{Xn.12\cdots n-1}r_{Yn.12\cdots n-1}}{\sqrt{\left(1 - r_{Xn.12\cdots n-1}^2\right)\left(1 - r_{Yn.12\cdots n-1}^2\right)}}. \tag{3}$$

Lately, the detrended partial cross-correlation analysis and multifractal detrended partial cross-correlation analysis (MFDPXA) which can measure cross-correlations between nonlinear time series influenced by common external forces is proposed [37, 38].

In order to remove the spurious correlation and improve the estimation performance for quantifying the intrinsic interactions between two nonstationary time series, this paper proposes the method of nth-order multifractal detrended partial cross-correlation analysis by incorporating the partial correlation coefficient with the multifractal detrended cross-correlation analysis.

The rest of the paper is organized as follows. In the next section, we introduce the multifractal DCCA coefficient method and propose the method of nth-order multifractal detrended partial cross-correlation analysis. In Section 3, we show the data results for the randomly generated dataset and stock and engine dataset by the proposed methods. Finally, we draw some conclusions in Section 4.

2. Methodologies

2.1. Multifractal Detrended Partial Cross-Correlation Analysis. For the sake of clarity, we begin with a summary of the multifractal DCCA coefficient algorithm. For two series $\{r_i(t)\}$ and $\{r_j(t)\}$ with equal length N, where $t = 1, 2, \ldots, N$, the computational procedure of the multifractal DCCA coefficient is as follows:

Step 1: construct the profile of each series by eliminating the mean value:

$$R_i(t) = \sum_{k=1}^{t} (r_i(k) - \langle r_i \rangle),$$

$$R_j(t) = \sum_{k=1}^{t} (r_j(k) - \langle r_j \rangle), \tag{4}$$

$$t = 1, 2, \ldots, N,$$

where $\langle r_i \rangle$ and $\langle r_j \rangle$ are the average values of $\{r_i(t)\}$ and $\{r_j(t)\}$, respectively.

Step 2: divide the profiles $\{R_i(k)\}$ and $\{R_j(k)\}$ into $N_s = \text{int}(N/s)$ nonoverlapping units of equal length s. Considering that N is usually not a multiple of the time scale s, we repeat the same procedure by starting from the opposite end of the sequence in order to take the whole series into account. Thus, we obtain $2N_s$ segments of equal length s. In this paper, we follow the previous literature practice and set $10 \leq s \leq N/4$.

Step 3: for each segment $v (v = 1, 2, \ldots, N_s, N_s + 1, \ldots, 2N_s)$, the local trends $\{\widetilde{R}_i^v(k)\}$ and $\{\widetilde{R}_j^v(k)\}$ are estimated on the basis of a least-squares fit of the sequences $\{R_i(k)\}$ and $\{R_j(k)\}$, respectively. The corresponding detrended covariance for $v = 1, 2, \ldots, N_s$ is

$$f_{\text{DCCA}}^2(s, v) = \frac{1}{s} \sum_{t=1}^{s} \left(R_i^{(v-1)s+t}(t) - \widetilde{R}_i^v(t)\right)\left(R_j^{(v-1)s+t}(t) - \widetilde{R}_j^v(t)\right), \tag{5}$$

and for $v = N_s + 1, N_s + 2, \ldots, 2N_s$ is

$$f_{\text{DCCA}}^2(s, v) = \frac{1}{s} \sum_{t=1}^{s} \left(R_i^{N-(v-N_s)s+t}(t) - \widetilde{R}_i^v(t)\right)$$
$$\cdot \left(R_j^{N-(v-N_s)s+t}(t) - \widetilde{R}_j^v(t)\right), \tag{6}$$

where $\{\widetilde{R}_i^v(k)\}$ and $\{\widetilde{R}_j^v(k)\}$ are the fitting polynomials in the segment v.

Step 4: calculate the average of multifractal detrended covariance fluctuation function $F_{\text{DCCA}}^q(s, v)$ over all segments:

$$F_{\text{DCCA}}^q(s, v) = \left\{\frac{1}{2N_s} \sum_{v=1}^{2N_s} \left[f_{\text{DCCA}}^2(s, v)\right]^{q/2}\right\}^{1/q}. \tag{7}$$

Generally, q can take any real value, except zero. For $q = 0$, the equation becomes

$$F_0(s) = \exp\left(\frac{1}{2N_s} \sum_{m=1}^{N_s} \ln F(s, m)\right). \tag{8}$$

For $q = 2$, $F_{\text{DCCA}}^q(s, v)$ is equal to the detrended cross-correlation fluctuation function $F_{\text{DCCA}}^2(s)$.

Step 5: estimate the multifractal DCCA coefficient:

$$\rho_{ij}^q(s) = \frac{F_{\text{DCCA}}^q(s)}{F_{\text{DFA}\{r_i(t)\}}^q(s) F_{\text{DFA}\{r_j(t)\}}^q(s)}. \tag{9}$$

For $q = 2$, the standard DCCA coefficient $\rho_{ij}(s)$ is retrieved.

Step 6: compute the multifractal detrended partial cross-correlation coefficient between X and Y by eliminating the influence of the controlling variable ξ_1 on X and Y analogous to the generalization of the correlation coefficient to partial correlation coefficient:

$$\rho_{XY,1}^q = \frac{\rho_{XY}^q - \rho_{X1}^q \rho_{Y1}^q}{\sqrt{\left(1 - \left(\rho_{X1}^q\right)^2\right)\left(1 - \left(\rho_{Y1}^q\right)^2\right)}}, \quad (10)$$

named the first-order multifractal detrended partial cross-correlation coefficient (first-order MFDPCC coefficient), where X, Y are random variables, ξ_1 is the controlling variable, and $\rho_{XY}^q, \rho_{X1}^q, \rho_{Y1}^q$ represent the mean of MFDCCA coefficients for X and Y, X and ξ_1, and Y and ξ_1, respectively.

For $q = 2$, the first-order detrended partial cross-correlation coefficient (first-order DPCC coefficient) is retrieved.

2.2. The nth-Order Multifractal Detrended Partial Cross-Correlation Analysis and n-Controlling-Variables Detrended Partial Cross-Correlation Coefficient.

Considering the cross-correlation between X and Y affected by more than one variable in complex systems, we define the second-order multifractal detrended partial cross-correlation coefficient (second-order MFDPCC coefficient) by using the partial correlation method [36]:

$$\rho_{XY,12}^q = \frac{\rho_{XY,1}^q - \rho_{X2,1}^q \rho_{Y2,1}^q}{\sqrt{\left(1 - \left(\rho_{X1}^q\right)^2\right)\left(1 - \left(\rho_{Y2,1}^q\right)^2\right)}}, \quad (11)$$

where X, Y are random variables, controlling variables ξ_1, ξ_2 are not related to each other, and $\rho_{XY.1}, \rho_{X2.1}$, and $\rho_{Y2.1}$ are first-order MFDPCC coefficients.

Generally, the nth-order multifractal detrended partial cross-correlation coefficient (nth-order MFDPCC coefficient) is as follows:

$$\rho_{XY,12\cdots n}^q = \frac{\rho_{XY,12\cdots n-1}^q - \rho_{Xn,12\cdots n-1}^q \rho_{Yn,12\cdots n-1}^q}{\sqrt{\left(1 - \left(\rho_{Xn,12\cdots n-1}^q\right)^2\right)\left(1 - \left(\rho_{Yn,12\cdots n-1}^q\right)^2\right)}}, \quad (12)$$

where $\rho_{XY.12\cdots n-1}^q$, $\rho_{Xn.12\cdots n-1}^q$, and $\rho_{Yn.12\cdots n-1}^q$ are $(n-1)$ th-order MFDPCC coefficients and controlling variables $\xi_1, \xi_2, \ldots, \xi_n$ are not related to each other. For $q = 2$, the nth-order detrended partial cross-correlation coefficient (nth-order DPCC coefficient) is retrieved.

In general, the nth-order partial cross-correlation is necessary when these controlling variables $\xi_1, \xi_2, \ldots, \xi_n$ are not related to each other. Nevertheless, in real-world systems, the variables $\xi_1, \xi_2, \ldots, \xi_n$ generated by large number of interacting units are cross-correlated. Therefore, we define the n-controlling-variables multifractal detrended partial cross-correlation coefficient (n-variables MFDPCC) by equation (12) for related controlling variables $\xi_1, \xi_2, \ldots, \xi_n$. Note that when the controlling variables $\xi_1, \xi_2, \ldots, \xi_n$ are not related to each other, the n-variables MFDPCC is equivalent to the nth-order MFDPCC.

3. Data and Analysis

3.1. Two-Component ARFIMA Process.

In order to test the robustness of the proposed n-controlling-variables MFDPCC coefficient method, power-law cross-correlated time series $\{u_i\}$ and $\{v_i\}$ are generated by using the two-component ARFIMA stochastic process in this section [18, 39, 40]. In this model, the series is defined by

$$\begin{cases} u_i = [WU_i + (1 - W)V_i] + \varepsilon_i, \\ v_i = [WV_i + (1 - W)U_i] + \widetilde{\varepsilon}_i, \\ U_i = \sum_{j=1}^{\infty} a_j(\rho_1)u_{i-j}, \\ V_i = \sum_{j=1}^{\infty} a_j(\rho_2)v_{i-j}, \end{cases} \quad (13)$$

where $a_j(\rho) = \Gamma(j - \rho)/\Gamma(-\rho)\Gamma(i + j)$ $(0 < \rho < 0.5)$ is weight, W is a free parameter to control the coupling strength between $\{u_i\}$ and $\{v_i\}$ $(0.5 \leq W \leq 1)$, and ε_i and $\widetilde{\varepsilon}_i$ are independent and identically distributed (i.i.d.) Gaussian variables with $\langle \varepsilon_i \rangle = \langle \widetilde{\varepsilon}_i \rangle = 0$ and $\langle \varepsilon_i^2 \rangle = \langle \widetilde{\varepsilon}_i^2 \rangle = 1$ [18, 39]. For different values of W, the different coupling strength between the variables $\{u_i\}$ and $\{v_i\}$ is $1 - W$. In this section, the two-component ARFIMA series $\{u_i\}$ and $\{v_i\}$ with parameter $\rho_1 = \rho_2 = 0.3$ and $W = 0.5$, denoted by X and Y, are employed to detect the interactions between two time series. Then, the effect of white noise sequence ξ_1 on the cross-correlation of the two series X and Y is tested to investigate the validity of the n-controlling-variables MFDPCC coefficient analysis mentioned in this paper. For this purpose, we study the difference between the mean of the MFDCCA coefficient and the n-controlling-variables MFDPCC coefficient for any parameter q by using the influence degree function $I(n, q)$. The influence degree function is defined as

$$I(n, q) = \left| \rho_{XY,12\cdots n}^q - \rho_{XY}^q \right|. \quad (14)$$

We calculate the influence degree function $I(n, q)$ of the synthetical signals using the proposed first-order MFDPCC coefficient and present the influence degree function $I(1, q)$ vs. parameter q in Figure 1. The results of the influence degree values of different q are just about nil, which indicates that there is hardly any effect of white noise sequence on cross-correlation of the two series X and Y.

3.2. Stock Market.

To further exemplify the potential utility of the n-controlling-variables MFDPCC coefficient method for analyzing real-world data, we study daily closing prices of fifteen stock markets including the São Paulo Index (IBOV), the Dow Jones Index (DJI), the NASDAQ Index (IXIC), the Standard & Poor 500 Composite Stock Price Index (SPX),
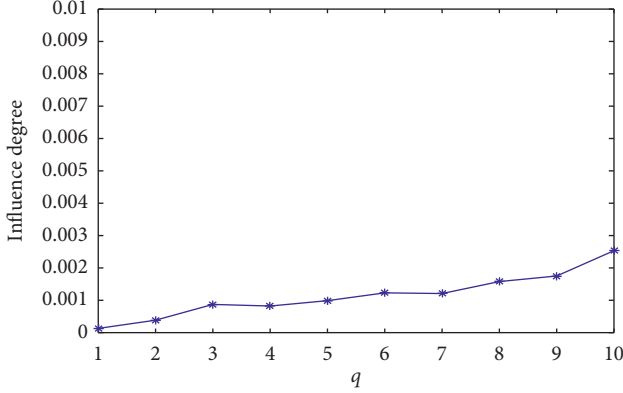
FIGURE 1: The effect of white noise sequence ξ_1 on cross-correlation of the two series X and Y.

FIGURE 2: The mean of DCCA coefficients between the stock series.

FIGURE 3: The influence degree of the first-order detrended partial cross-correlation in stock market and the influence degree of the first-order multifractal detrended partial cross-correlation coefficient in stock market (inset).

the FTSE Global Equity Index Series (FISE), the French CAC 40 (FCHI), German DAX Index (GDAXI), Nikkei 255 Index (N255), Korea Composite Index (KS11), Hang Seng Index (HSI), Australian Standard & Poor's 200 (AS51), Mumbai Index (SENSEX), Russian Index (RTS), Shanghai Composite Index (SSEC), and Shenzhen Composite Index (SZI). Datasets are from January 04, 1993, to January 03, 2019.

Figure 2 shows the mean of DCCA coefficients for the stock series. The mean of DCCA coefficient between DJI and SPX is 0.97, which performs relevantly different from other DCCA coefficients. It indicates the close cross-correlation between the American stock markets. The next largest DCCA coefficient $\rho = 0.92$ is obtained by SSEC and SZI, which indicates the close cross-correlation in Chinese mainland stock markets.

The mean of DCCA coefficients between SZI and stock markets in developed countries (GDAXI, N225, KS11, and AS51) is less than 0.3. It shows that SZI has a weak relationship with stock markets in developed countries. The mean of DCCA coefficients between SZI and HSI is in an intermediate state, which indicates the existence of cross-correlation in Chinese stock markets.

Next, we analyze the effect of the other thirteen stock markets on cross-correlation characteristics between SSEC and SZI, by applying the influence degree of first-order DPCC coefficient. For the effect on cross-correlation characteristics between the SSEC and SZI, the largest influence degree $I = 0.05$ is obtained by HSI, which shows the information exchange between the Chinese stock market, as seen in Figure 3. The next largest $I = 0.04$ is acquired by SENSEX, which indicates the association between the stock markets in developing countries (Indian and Chinese stock markets). The I values of other stock time series are less than 0.1, which indicates little information exchange between the Chinese mainland stock market and other stock markets. The influence degree values of 13 stock markets for first-order MFDPCC coefficient with $q = 1, 2, \ldots, 10$ are also demonstrated in the upper left of Figure 3.

During the analysis, we observe the effect of HSI on cross-correlation characteristics between SSEC and SZI from influence degree function $I(1, q)$ that decreases as the scale q increases. And this infers the change of multifractal cross-correlation.
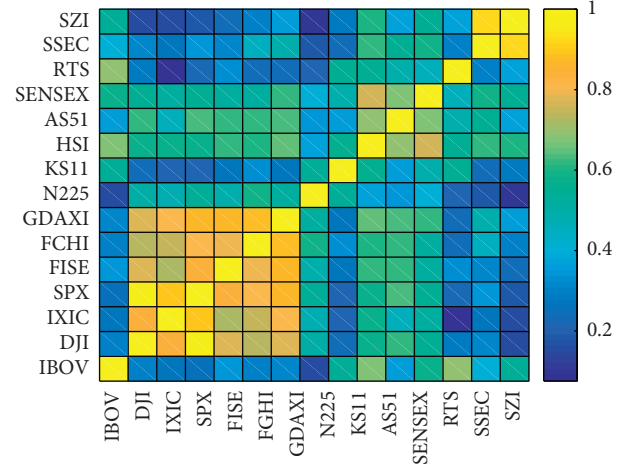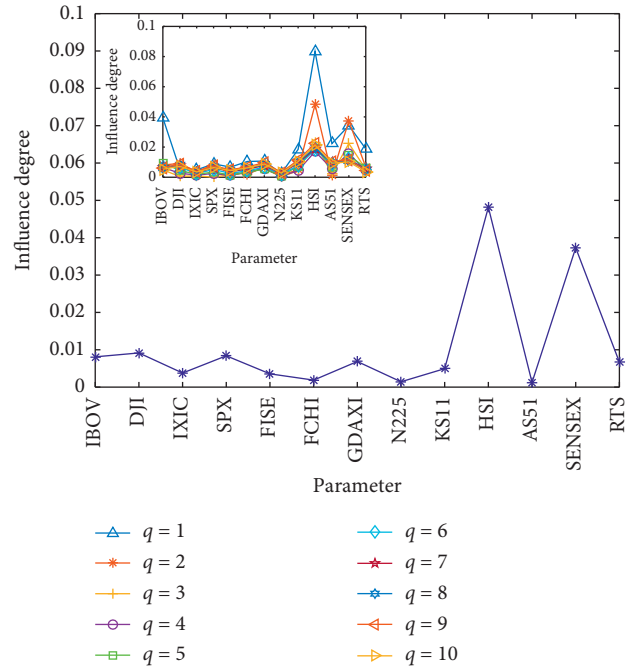
In order to capture the change of multifractal cross-correlation between two nonstationary time series influenced by common external forces, multifractal detrended partial cross-correlation analysis (MFDPXA) is employed [38]. We also investigate the multifractal behavior between the bivariate time series through MFDPXA method for comparison. The result shows that both the corresponding spectra $f_{xy}(\alpha)$ and $f_{xy,z}(\alpha)$ are wide, but the latter is narrower than the former, which is presented in Figure 4.

Here, we perform cross-correlation analysis using MFDPXA method and give the multifractal spectrum for SZI and SSEC time series in which HSI shows significant
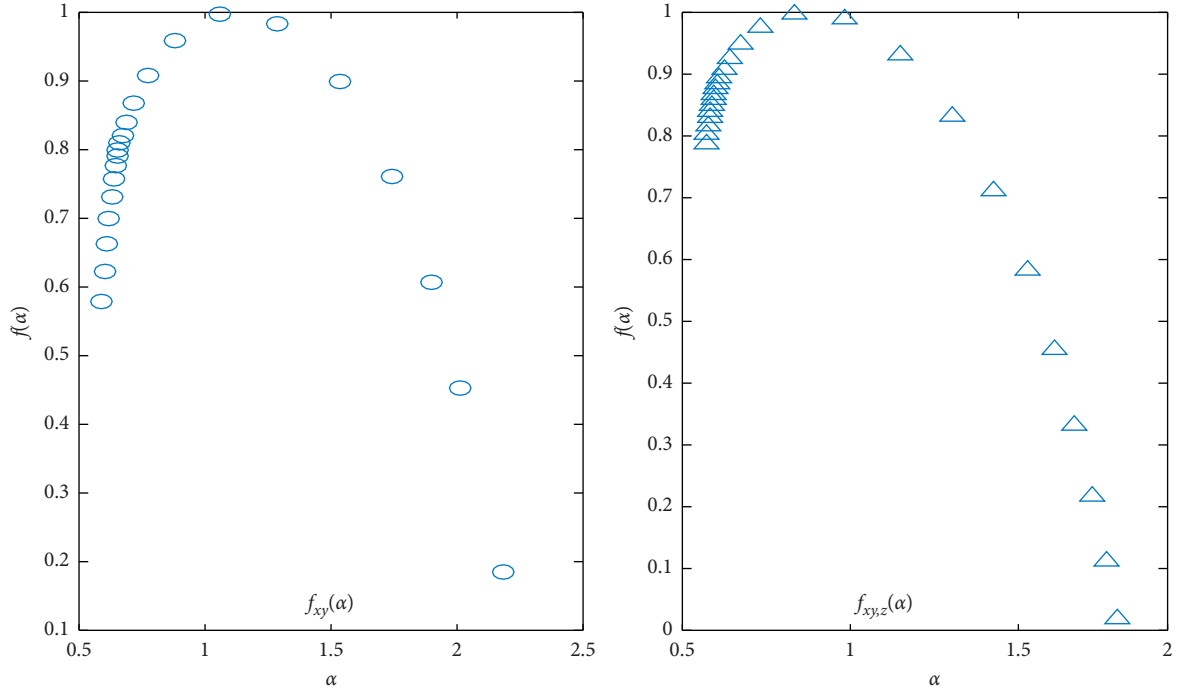
FIGURE 4: The multifractal spectra $f_{xy}(\alpha)$ of bivariate time series obtained through MFDXA method and $f_{xy,z}(\alpha)$ of bivariate time series obtained through MFDPXA, where x, y, and z denote the SSEC, SZI, and HSI.

influence on multifractal spectrum, as seen in Figure 4. We compare the obtained influence degrees with the aforementioned method and infer that the HSI has significant influence on SZI and SSEC time series. These similar results imply that the partial cross-correlation method is quite efficient in eliminating external common influence factor.

Applied to scalar variables, the first-order MFDPCC will detect the intrinsic interactions by removing the correlations of controlling variables. When variables are time series, this application is equivalent to removal of zero delay correlations, whereas delayed correlations are not considered [36, 37, 40, 41]. Therefore, we investigate the delayed effect of variable ξ_1 on the correlation between variables X and Y. Because the two variables X and Y in question may themselves be correlated at nonzero delays, we write the multifractal detrended partial cross-correlation between X and Y, given ξ_1, as a function of two time delays:

$$\rho^q_{XY(\tau_1),1(\tau_2)} = \frac{\rho^q_{XY(\tau_1)} - \rho^q_{X1(\tau_2)}\rho^q_{Y(\tau_1)1(\tau_2)}}{\sqrt{\left(1 - \left(\rho^q_{X1(\tau_2)}\right)^2\right)\left(1 - \left(\rho^q_{Y(\tau_1)1(\tau_2)}\right)^2\right)}},$$

(15)

where τ_1 is the delay between variables X and Y and τ_2 is the delay between variables X and ξ_1.

In this section, we estimate the delayed effect of HSI on the correlation between SSEC and SZI by using the time delay influence degree $I(q, \tau_1, \tau_2) = |\rho^q_{XY(\tau_1),1(\tau_2)} - \rho^q_{XY}|$. Figure 5 shows the time delay influence degree for $q = 2$. The effect of τ_1 on influence degree is weaker than that of τ_2 on influence degree.

We now analyze the 2-controlling-variables effect of the other thirteen stock markets on cross-correlation characteristics between SSEC and SZI, by giving a set of two controlling variables. In Figure 6, we illustrate the comparative relation of the influence degree of 2-controlling-variables DPCC coefficients for 13×13 elements by the matrix diagram.

We note that the structure of the matrix is symmetrical and that element at the intersection of row i and column j represents the influence of controlling variables ξ_i, ξ_j on the cross-correlation of SSEC and SZI, where the 2-controlling-variables ξ_i, ξ_j ($i, j = 1, 2, \ldots, 13$) are the stock time series from IBOV, DJI, IXIC, SPX, FISE, FCHI, GDAXI, N255, KS11, HSI, AS51, SENSEX, and RTS. Therefore, we analyze the top left corner of the matrix. It can be seen that the largest element is the intersection of row 2 and column 10, i.e., SENSEX and HSI, which indicates the association between the Indian and Chinese stock markets. This is consistent with our result of first-order MFDPCC coefficient method.

Concerning the influence degree $I(2, q)$ of the 2-controlling-variables MFDPCC, we demonstrate 5 cases (HSI and SENSEX, HSI and RTS, SENSEX and KS11, FCHI and N255, and IXIC and FISE) for $q = 1, 2, \ldots, 10$ in Figure 7. The largest influence degree is the case SENSEX and HSI, which is consistent with the 2-controlling-variables DPCC method.

3.3. Aeroengine Time Series. Previous research studies show that the aeroengine gas path parameters such as low-pressure rotor speed ($N1$), high-pressure rotor speed ($N2$),
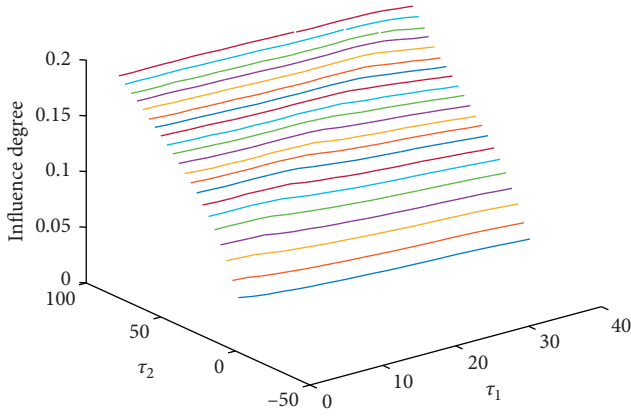
FIGURE 5: The time delay influence degree for delay τ_1 between SSEC and SZI and delay τ_2 between SSEC and HSI.
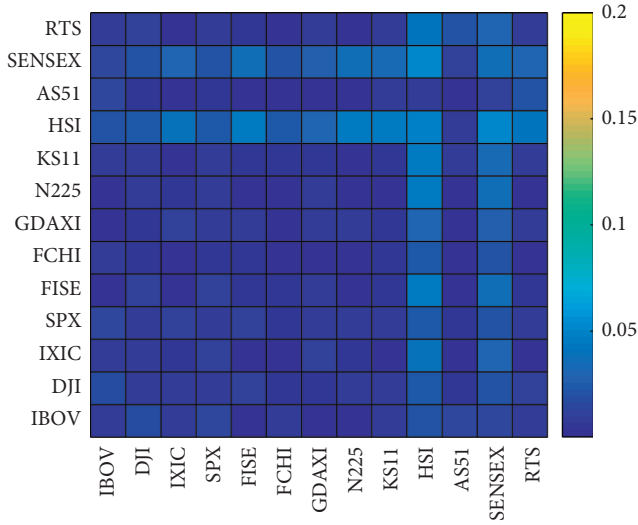
FIGURE 6: The influence degree of the 2-controlling-variables detrended partial cross-correlation.

FIGURE 7: The influence degree of the 2-controlling-variables multifractal detrended partial cross-correlation.
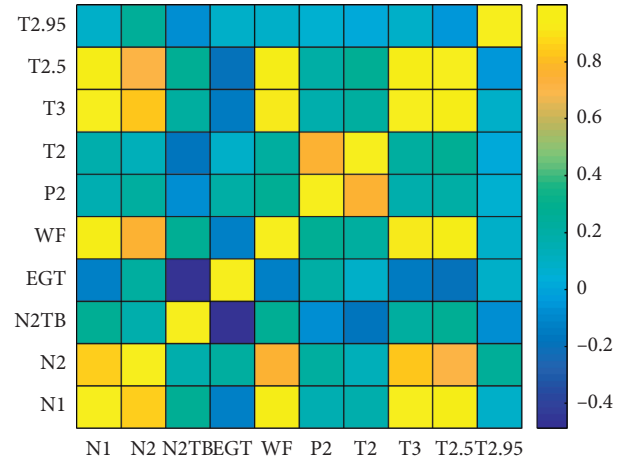
FIGURE 8: The mean of standard DCCA coefficients for the time series of aeroengine system gas path parameters.

and fuel flow (WF) play an important role in understanding the aeroengine system [21, 42]. The mean of DCCA coefficients for the aeroengine time series is shown in Figure 8, where the average DCCA coefficient between $N1$ and $N2$ is 0.85, which shows the close cross-correlation between $N1$ and $N2$.

We here investigate the partial correlation between $N1$ and $N2$ given a set of eight controlling variables, including WF, exhaust gas temperature (EGT), $N2$ tracked vibration channel B (N2TB), inlet air pressure (P2), outlet temperature of high-pressure compressor (T3), outlet temperature of low-pressure compressor (T2.5), and other temperatures (T2 and T2.95).

In Figure 9, we plot the influence degree of first-order DPCC coefficient, investigating the effect of the other eight controlling variables on cross-correlation characteristics between $N1$ and $N2$. The largest influence degree $I = 0.51$, obtained by T3, shows the information exchange between the outlet temperature of high-pressure compressor and the rotor speed system. The next largest $I = 0.22$ is acquired by

WF, which indicates the association between the fuel flow system and rotor speed system.

The result of the influence degree $I(1, q)$ for eight aeroengine parameters applying by first-order MFDPCC coefficient with $q = 1, 2, \ldots, 10$ is also demonstrated in the upper left of Figure 9. The effect of T3 on cross-correlation characteristics, observed from influence degree function $I(1, q)$, decreases as the scale q increases. It indicates that the multifractal cross-correlation differs across values of q.

Further, we apply the MFDPXA method on aforementioned $N1$ and $N2$ time series considering the T3 as common influencing factor. It is observed from Figure 10 that the corresponding spectra $f_{xy}(\alpha)$ and $f_{xy,z}(\alpha)$ are wide which shows the strength of multifractal behavior in analyzed time series. We observe that the width of singularity spectrum $f_{xy,z}(\alpha)$ is narrower, and this implies the strength
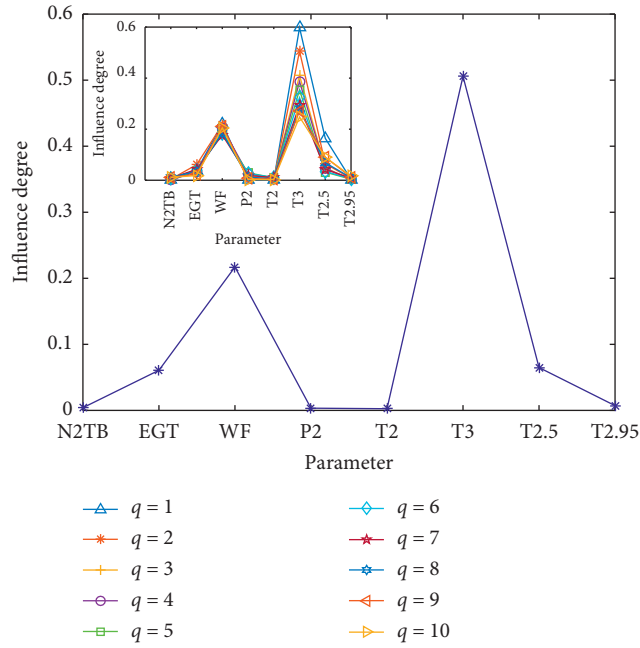
FIGURE 9: The influence degree of the first-order detrended partial cross-correlation in aeroengine system and the influence degree of the first-order multifractal detrended partial cross-correlation coefficient in aeroengine system (the upper left figure).
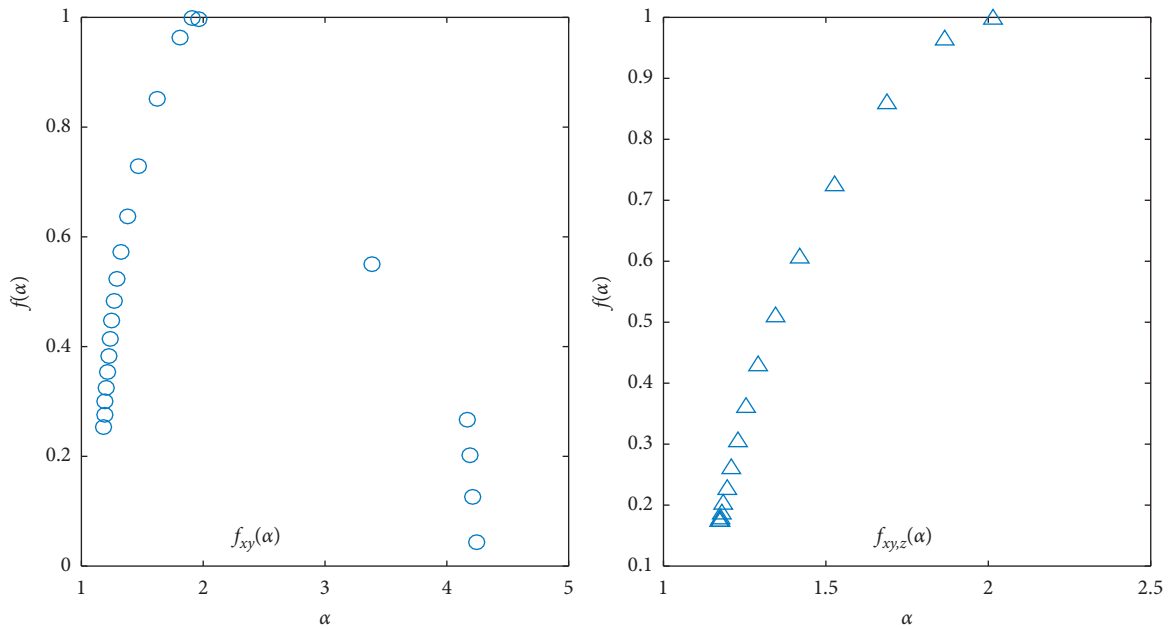
FIGURE 10: The multifractal spectrum $f_{xy}(\alpha)$ of bivariate time series obtained through MFDXA method and $f_{xy,z}(\alpha)$ of bivariate time series obtained through MFDPXA, where x, y, and z denote $N1$, $N2$, and T3.

of multifractal nature is weak in analyzed bivariate time series.

Here, we estimate the delayed effect of T3 on the correlation between N1 and N2 by using the time delay influence degree $I(q, \tau_1, \tau_2)$. Figure 11 shows the time delay influence degree for $q = 2$. It is obvious that the time delay influence degree gradually increases and then declines as a single-peak curve when τ_2 remains constant. As τ_2 increases,

the peak value of time delay influence degree shifts rightward.

The next observation concerns the influence degree of 2-controlling-variables DPCC coefficient in the aeroengine system. We now analyze the influence of two controlling parameters on the cross-correlation between $N1$ and $N2$. In Figure 12, we illustrate the comparative relation of the influence degree of 2-controlling-variables DPCC
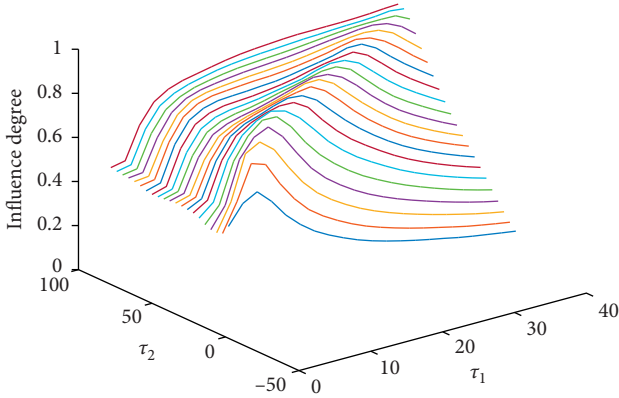
FIGURE 11: The time delay influence degree for delay τ_1 between $N1$ and $N2$ and delay τ_2 between $N1$ and $T3$.
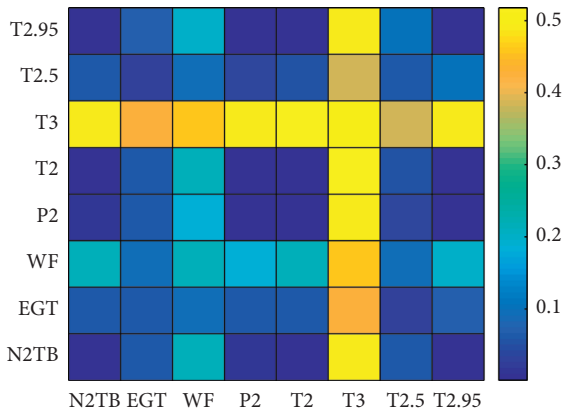
FIGURE 12: The influence degree of the 2-controlling-variables detrended partial cross-correlation for aeroengine system.
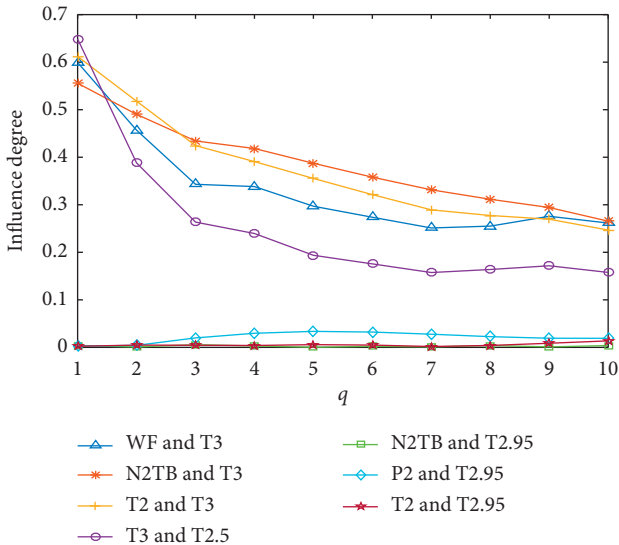
FIGURE 13: The influence degree of the 2-controlling-variables multifractal detrended partial cross-correlation for the aeroengine system.

coefficient for aeroengine system. It can be seen that the larger elements in the symmetrical matrix are located at row 3 or column 6, which denote T3 has a greater impact on the correlation between $N1$ and $N2$.

Concerning the influence degree $I(2, q)$ of the 2-controlling-variables MFDPCC, we demonstrate 7 cases (T3 and WF, T3 and N2TB, T3 and T2, T3 and T2.5, T2.95 and N2TB, T2.95 and P2, and T2.95 and T2) for $q = 1, 2, \ldots, 10$ in Figure 13. Larger influence degrees exist in the cases with the presence of T3 (T3 and WF, T3 and N2TB, T3 and T2, and T3 and T2.5), which is consistent with the 2-controlling-variables DPCC method, as seen in Figure 12.

For the aeroengine, the parameters $N1$ and $N2$ are chosen to indicate the engine thrust which depends on the throttle lever angle. Hence, the cross-correlation between them is strong. The temperature and pressure parameters are linked with many factors, including the compressor power, combustion efficiency, throttle lever angle, etc. Therefore, the dynamic interaction of these three groups makes the aeroengine function. These results estimate the influence of temperature and pressure parameters on the cross-correlation between $N1$ and $N2$.

4. Conclusion

In this paper, we propose the nth-order multifractal detrended partial cross-correlation analysis method and the n-controlling-variables multifractal detrended partial cross-correlation analysis method for understanding the interactions between two nonstationary time series. For comparing these new methods with classical measures, we introduce the influence degree function. We then apply the n-controlling-variables multifractal detrended partial cross-correlation analysis of stock markets and aeroengine performance parameters and measure the influence degree function of the partial cross-correlation in a dynamic system.

To understand the numerous real-world systems where the output signals exhibit complex cross-correlation, both cross-correlation and partial correlation are subjects of investigation. The information of n-variables MFDPCC helps people to research information exchange in complex systems. This paper gives two examples, stock markets and aeroengine systems. For stock time series, our results indicate that, concerning closing index values, there is little information exchange between the Chinese stock markets and the American-European stock markets, whereas the SSEC, SZI, and HSI, by first-order MFDPCC method and 2-controlling-variables MFDPCC, show frequent and abundant information exchange in Chinese stock markets. For aeroengine performance parameters, our results show that there is some information exchange between the engine rotor system and the aeroengine parameters, such as the outlet temperature of the high-pressure compressor and the fuel flow.

We believe that the MFDPCC method can be used to detect the intrinsic interactions among multiple dynamical systems, and therefore it can be widely applied to many research fields such as the aeroengine health monitoring systems and the investment portfolio where the covariance is employed to explore the interaction of assets income.

The multifractal detrended partial cross-correlation analysis is used to delete the possible indirect correlation, but it may also delete valuable information. This problem

required further investigation, both experimental and theoretical. Hence, the results of this paper should be considered as preliminary results on the multifractal detrended partial cross-correlation analysis. Therefore, we hope that this study will be extended to analyze the filtered information.

Data Availability

The stock market data used to support the findings of this study are available from the corresponding author upon request. The aeroengine data used to support the findings of this study have not been made available because of commercial secrets.

Conflicts of Interest

The authors declare that they have no conflicts of interest.

Acknowledgments

References

[1] K. Pearson, "Note on regression and inheritance in the case of two parents," *Proceedings of the Royal Society*, vol. 58, pp. 240–242, 1895.

[2] K. Pearson, "On lines and planes of closest fit to systems of points in space," *The London, Edinburgh, and Dublin Philosophical Magazine and Journal of Science*, vol. 2, no. 11, pp. 559–572, 1901.

[3] E. P. Wigner, "Characteristic vectors of bordered matrices with infinite dimensions," *The Annals of Mathematics*, vol. 62, no. 3, pp. 548–564, 1955.

[4] G. Golub and W. Kahan, "Calculating the singular values and pseudo-inverse of a matrix," *Journal of the Society for Industrial and Applied Mathematics Series B Numerical Analysis*, vol. 2, no. 2, pp. 205–224, 1965.

[5] B. Podobnik and H. E. Stanley, "Detrended cross-correlation analysis: a new method for analyzing two nonstationary time series," *Physical Review Letters*, vol. 100, Article ID 084102, 2008.

[6] G. F. Zebende, "DCCA cross-correlation coefficient: quantifying level of cross-correlation," *Physica A: Statistical Mechanics and Its Applications*, vol. 390, no. 4, pp. 614–618, 2011.

[7] A. Machado Filho, M. F. da Silva, and G. F. Zebende, "Autocorrelation and cross-correlation in time series of homicide and attempted homicide," *Physica A: Statistical Mechanics and Its Applications*, vol. 400, pp. 12–19, 2014.

[8] C. Xue, P. Shang, and W. Jing, "Multifractal detrended cross-correlation analysis of BVP model time series," *Nonlinear Dynamics*, vol. 69, no. 1-2, pp. 263–273, 2012.

[9] R. T. Vassoler and G. F. Zebende, "DCCA cross-correlation coefficient apply in time series of air temperature and air relative humidity," *Physica A: Statistical Mechanics and Its Applications*, vol. 391, no. 7, pp. 2438–2443, 2012.

[10] S. Shadkhoo and G. R. Jafari, "Multifractal detrended cross-correlation analysis of temporal and spatial seismic data," *The European Physical Journal B*, vol. 72, no. 4, pp. 679–683, 2009.

[11] E. B. S. Marinho, A. M. Y. R. Sousa, and R. F. S. Andrade, "Using detrended cross-correlation analysis in geophysical data," *Physica A: Statistical Mechanics and Its Applications*, vol. 392, no. 9, pp. 2195–2201, 2013.

[12] K. Dong, P. Shang, and A. Lin, "Chaotic SVD method for minimizing the effect of seasonal trends in detrended cross-correlation analysis," *DCDIS Series B: Applications & Algorithms*, vol. 18, pp. 261–277, 2011.

[13] X. Zhao, P. Shang, A. Lin, and G. Chen, "Multifractal Fourier detrended cross-correlation analysis of traffic signals," *Physica A: Statistical Mechanics and Its Applications*, vol. 390, no. 21-22, pp. 3670–3678, 2011.

[14] R. A. Ribeiro, M. V. M. Mata, L. S. Lucena, U. L. Fulco, and G. Corso, "Spatial analysis of oil reservoirs using detrended fluctuation analysis of geophysical data," *Nonlinear Processes in Geophysics*, vol. 21, no. 5, pp. 1043–1049, 2014.

[15] Q. Fan and D. Li, "Multifractal cross-correlation analysis in electricity spot market," *Physica A: Statistical Mechanics and Its Applications*, vol. 429, pp. 17–27, 2015.

[16] X. Zhao, P. Shang, and W. Shi, "Multifractal cross-correlation spectra analysis on Chinese stock markets," *Physica A: Statistical Mechanics and Its Applications*, vol. 402, pp. 84–92, 2014.

[17] B. Podobnik, D. Horvatic, A. M. Petersen, and H. E. Stanley, "Cross-correlations between volume change and price change," *Proceedings of the National Academy of Sciences*, vol. 106, no. 52, pp. 22079–22084, 2009.

[18] B. Podobnik, Z. Q. Jiang, W. X. Zhou, and H. E. Stanley, "Statistical tests for power-law cross-correlated processes," *Physical Review E*, vol. 84, p. 66118, 2011.

[19] I. Gvozdanovic, B. Podobnik, D. Wang, and H. Eugene Stanley, "1/f behavior in cross-correlations between absolute returns in a US market," *Physica A*, vol. 391, pp. 2860–2866, 2012.

[20] X. Y. Qian, Y. M. Liu, Z. Q. Jiang, B. Podobnik, W. X. Zhou, and H. E. Stanley, "Detrended partial cross-correlation analysis of two time series influenced by common external forces," *Physical Review E*, vol. 91, Article ID 062816, 2015.

[21] K. Dong, Y. Gao, and C. Zhu, "Aero engine data correlation by means of detrended fluctuation analysis," *International Review of Aerospace Engineering*, vol. 5, pp. 251–255, 2012.

[22] K. Dong, J. Fan, and Y. Gao, "Cross-correlations and structures of aero-engine gas path system based on dcca coefficient and rooted tree," *Fluctuation and Noise Letters*, vol. 14, p. 1550014, 2015.

[23] K. Dong, Y. Gao, and L. Jing, "Correlation tests of the engine performance parameter by using the detrended cross-correlation coefficient," *Journal of the Korean Physical Society*, vol. 66, pp. 539–543, 2015.

[24] K. Dong, Y. Gao, and N. Wang, "EMD method for minimizing the effect of seasonal trends in detrended cross-correlation analysis," *Mathematical Problems in Engineering*, vol. 2013, Article ID 493893, 7 pages, 2013.

[25] P. Baranowski, J. Krzyszczak, C. Slawinski et al., "Multifractal analysis of meteorological time series to assess climate impacts," *Climate Research*, vol. 65, pp. 39–52, 2015.

[26] N. Kalamaras, K. Philippopoulos, D. Deligiorgi, C. G. Tzanis, and G. Karvounis, "Multifractal scaling properties of daily air temperature time series," *Chaos, Solitons and Fractals*, vol. 98, pp. 38–43, 2017.

[27] J. Ei, J. Zhang, X. Liu, and F. Li, "Multi-fractal scaling comparison of the air temperature and the surface temperature over China," *Physica A*, vol. 462, pp. 783–792, 2016.

[28] S. Debdeep, R. Rinku, and M. Manjunatha, "Epilepsy and seizure characterisation by multifractal analysis of EEG subbands," *Biomedical Signal Processing*, vol. 41, pp. 264–270, 2018.

[29] S. Bayraci, "Testing for multi-fractality and efficiency in selected sovereign bond markets: a multi-fractal detrended moving average (MF-DMA) analysis," *International Journal of Computational Economics and Econometrics*, vol. 8, pp. 95–120, 2018.

[30] Z. Jiang, W. Xie, W. Zhou, and D. Sornette, "Multifractal analysis of financial markets: a review," *Reports on Progress in Physics*, vol. 82, no. 12, p. 125901, 2019.

[31] C. Yao, C. Liu, and W. Ju, "Multifractal analysis of the WTI crude oil market, US stock market and EPU," *Physica A*, vol. 550, p. 124096, 2020.

[32] W. Zhou, "Multifractal detrended cross-correlation analysis for two nonstationary signals," *Physical Review E*, vol. 77, Article ID 066211, 2008.

[33] C. Tzanis, I. Koutsogiannis, K. Philippopoulos, and N. Kalamaras, "Multifractal detrended cross-correlation analysis of global methane and temperature," *Remote Sensing*, vol. 12, p. 557, 2020.

[34] C. Zhang, Z. Ni, and L. Ni, "Multifractal detrended cross-correlation analysis between PM2.5 and meteorological factors," *Physica A*, vol. 438, pp. 114–123, 2015.

[35] K. Pearson, "On some novel properties of partial and multiple correlation coefficients in a universe of manifold characteristics," *Biometrika*, vol. 11, pp. 231–1238, 1916.

[36] S. Eran, D. Rotem, and A. Moshe, "Partial cross-correlation analysis resolves ambiguity in the encoding of multiple movement features," *Journal of Neurophysiology*, vol. 95, pp. 1966–1975, 2006.

[37] N. Zhang, A. Lin, and P. Yang, "Detrended moving average partial cross-correlation analysis on financial time series," *Physica A*, vol. 542, p. 122960, 2020.

[38] H. Sri Sai, M. Pal, and P. Manimaran, "Multifractal detrended partial cross-correlation analysis on Asian markets," *Physica A*, vol. 531, Article ID 121778, 2019.

[39] B. Podobnik, D. Horvatic, A. L. Ng, H. E. Stanley, and P. C. Ivanov, "Modeling long-range cross-correlations in two-component ARFIMA and FIARCH processes," *Physica A*, vol. 387, pp. 3954–3959, 2008.

[40] K. Dong, L. Long, H. Zhang, and X. Su, "The Lempel-Ziv measure based pedigree map to detect and evaluate correlation between aero-engine gas path system variables," *Physica A*, vol. 525, pp. 1080–1087, 2019.

[41] Y. Song, C. Kube, J. Zhang, and X. Li, "Higher-order spatial correlation coefficients of ultrasonic backscattering signals using partial cross-correlation analysis," *The Journal of the Acoustical Society of America*, vol. 147, pp. 757–768, 2020.

[42] K. Dong, H. Zhang, and Y. Gao, "Dynamical mechanism in aero-engine gas path system using minimum spanning tree and detrended cross-correlation analysis," *Physica A*, vol. 465, pp. 363–369, 2017.

Research Article

Stabilization of a Class of Complex Chaotic Systems by the Dynamic Feedback Control

Zhi Liu[1] and Rongwei Guo [iD][2]

[1]*School of Information Engineering, Key Laboratory of TCM Data Cloud Service in Universities of Shandong (Shandong Management University), Shandong Management University, Jinan 250357, China*
[2]*School of Mathematics and Statistics, Qilu University of Technology (Shandong Academy of Sciences), Jinan 250353, China*

Correspondence should be addressed to Rongwei Guo; rongwei_guo@163.com

The stabilization problem of the complex chaotic system is investigated in this paper. First, a systematic method is proposed, by which a given complex chaotic system can be transformed into its equivalent real chaotic system. Then, both simple and physical controller is designed for the corresponding real chaotic system by the dynamic feedback control method, thereby the controller for the original complex chaotic system is obtained. Especially, for some complex system, the controller is obtained by the linear feedback control method. Finally, two illustrative examples with numerical simulations are used to verify the validity and effectiveness of the theoretical results.

1. Introduction

It is well known that the first chaotic system was proposed by Lorenz in 1963. From then on, many works have been done about both theoretical results and applications, see Refs. [1–15] and the references therein. Complex chaotic system whose state variables belong to complex space is another important type of chaotic dynamical system, which has been widely investigated in both theorem and applications and has become a hot topic in recent years, for details see Refs. [16–24]. Especially, the encryption effect is better due to the fact that the complex chaotic system is composed of real and imaginary numbers. Since the dynamic behavior of the complex system is more complicated than that of the real chaotic system, the control problems of such system is very difficult. Many researchers usually adopted this strategy; they firstly transfer the complex chaotic system into its corresponding real chaotic system by separating the real parts and imaginary parts of the complex state variables and then they investigate the control method of the real chaotic system. Ultimately, the control problems of such complex system were realized.

However, on one hand, there is lack of a systematic method in the first step, i.e., for a specific complex chaotic system, a specific method is applied to transform it into its equivalent real chaotic system. How to find a systematic method by which the complex chaotic system can be transformed into its equivalent real chaotic system is not only important in theory but also significant in applications; thus, it stimulates our work in this paper.

On the other hand, most of the controllers designed in the aforementioned existing results are complicated; thereby, they are hard to be performed in real applications. As a matter of fact, how to design a both simple and physical controller to realize the control problems of the complex chaotic systems is also important both in theory and applications. Among the existing methods, the dynamic feedback control method and the linear feedback control method are widely applied, and thus these two methods are adopted by this study.

Motivated by the above conclusions, the stabilization problem of the complex chaotic system is studied by the dynamic feedback control method. The main contributions of this paper are given as follows:

(1) A systematic method is proposed, which can be used to transform a given complex chaotic system into its equivalent real chaotic system

(2) Both simple and physical controller is designed for the original complex chaotic system is obtained by the dynamic feedback control method and the linear feedback control method, respectively, and numerical simulations are performed to verify the above theoretical results

Before ending this section, we present some notations used in this paper. $\mathbb{R}^n$ is the n dimensional Euclidean space, $\mathbb{C}^n$ is the n dimensional complex space, I_n denotes the $n \times n$ identity matrix, $\mathcal{M}_{m \times n}$ denotes the set of $m \times n$ real matrices, $\otimes$ is the Kronecker product, and $\propto$ is the semitensor product (STP), i.e., let $M_{m \times n} \in \mathcal{M}_{m \times n}$, $N_{p \times q} \in \mathcal{N}_{p \times q}$, and $t = \mathrm{lcm}\{n, p\}$ be the least common multiple of n and p. The STP of M and N is defined as

$$M \propto N = (M \otimes I_{t/n})(N \otimes I_{t/p}) \in \mathcal{M}_{mt/n \times qt/p}, \quad (1)$$

where

$$M \otimes N = \begin{pmatrix} M_{11}N & M_{12}N & \cdots & M_{1n}N \\ \vdots & \vdots & \vdots & \vdots \\ M_{m1}N & M_{m2}N & \cdots & M_{mn}N \end{pmatrix} \in \mathcal{M}_{mp \times np}. \quad (2)$$

$\mathrm{Re}(\cdot)$ and $\mathrm{Im}(\cdot)$ represent the real part and the imaginary part of $(\cdot)$, respectively, and i is the imaginary unit, i.e., $i^2 = -1$.

2. Preliminary

Consider the following controlled chaotic system:

$$\dot{w} = G(w) + bv, \quad (3)$$

where $w \in \mathbb{R}^n$ is the state, $G(w) \in \mathbb{R}^n$ is continuous function with $G(0) = 0$, $b \in \mathbb{R}^{n \times r}$ is a constant matrix, and $v \in \mathbb{R}^r$ is the controller to be designed.

Lemma 1 (see [18]). *Consider system (3). If $(G(w), b)$ can be stabilized, then the designed controller v is of the following form:*

$$v = K(t)w, \quad (4)$$

where $K = k(t)b^T$, and the feedback gain $k(t)$ is updated by the following equation:

$$\dot{k}(t) = -\|w\|^2. \quad (5)$$

3. Problem Formulation

Consider the following controlled complex chaotic system:

$$\dot{p} = f(p) + bu, \quad (6)$$

where

$$p = \begin{pmatrix} z \\ x \end{pmatrix},$$

$$z = \begin{pmatrix} z_1 \\ z_2 \\ \vdots \\ z_m \end{pmatrix}, \quad (7)$$

$$x = \begin{pmatrix} x_{m+1} \\ x_{m+2} \\ \vdots \\ x_n \end{pmatrix},$$

$z \in \mathbb{C}^m$ and $x \in \mathbb{R}^{n-m}$ are the state, $m \geq 1$,

$$f(p) = f(x, z, \overline{z}) = \begin{pmatrix} M(x)z + H(i)x \\ N(z, \overline{z}, x) \end{pmatrix}, \quad (8)$$

where $\overline{z}$ is the conjugate of z, $M(x) \in \mathbb{R}^{m \times m}$, $H(i) \in \mathbb{C}^{m \times (n-m)}$ is a complex constant matrix, and $N(x, z, \overline{z}) \in \mathbb{R}^{n-m}$, $b \in \mathbb{R}^{n \times r}$, $u \in \mathbb{C}^r$ is the designed controller, i.e.,

$$H(i) = \begin{pmatrix} h_1(i) \\ h_2(i) \\ \vdots \\ h_m(i) \end{pmatrix}, \quad (9)$$

$$b = \begin{pmatrix} b_1 & 0 \\ 0 & b_2 \end{pmatrix},$$

where $h_j(i) \in \mathbb{C}^{n-m}$, $j = 1, \ldots, m$, $b_1 \in \mathbb{R}^{m \times s}$, $b_2 \in \mathbb{R}^{(n-m) \times (r-s)}$, $1 \leq s \leq r$,

$$u = \begin{pmatrix} u_z \\ u_x \end{pmatrix},$$

$$u_z = \begin{pmatrix} u_1 \\ u_2 \\ \vdots \\ u_k \end{pmatrix}, \quad (10)$$

$$u_x = \begin{pmatrix} u_{k+1} \\ u_{k+2} \\ \vdots \\ u_r \end{pmatrix},$$

that is, $u_z \in \mathbb{C}^k$, $u_x \in \mathbb{R}^{r-k}$, and $1 \leq k < r$.

Remark 1. The complex chaotic system of equation (6) is very common, which covers a lot of complex chaotic systems, such as complex Lorenz system and complex hyperchaotic Lorenz system.

The goal of this paper is to investigate the stabilization of system (6), i.e., how to design a controller u to guarantee

$$\lim_{t \to \infty} p(t) = 0. \tag{11}$$

4. Main Results

4.1. A Systematic Method which is Used to Transform a Complex System into its Equivalent Real System. In this section, a systematic method proposed, by which a complex system can be transformed into its equivalent real system.

Theorem 1. *Consider the complex chaotic system (6). Its equivalent real system is described as the following form:*

$$\dot{y} = F(y) + BU, \tag{12}$$

where $y \in \mathbb{R}^{m+n}$ is the state, $F(y) \in \mathbb{R}^{m+n}$ is continuous function with $F(0) = 0$, $B \in \mathbb{R}^{(m+n) \times (k+r)}$ is a constant matrix, and $U \in \mathbb{R}^{k+r}$ is the controller to be designed.

Proof. Let $z_j = y_{2j-1} + y_{2j} \times i$, $j = 1, \ldots, m$, and $y_{2m+l} = x_{m+l}$, $1 \le l \le n - m$; then, the equivalent real system (12) is obtained, i.e.,

$$y = \begin{pmatrix} y_z \\ y_x \end{pmatrix},$$

$$y_z = \begin{pmatrix} y_1 \\ y_2 \\ \vdots \\ y_{2m} \end{pmatrix},$$

$$y_x = \begin{pmatrix} y_{2m+1} \\ y_{2m+2} \\ \vdots \\ y_{m+n} \end{pmatrix},$$

$$F(y) = \begin{pmatrix} F_1(y) \\ F_2(y) \\ \vdots \\ F_{m+n}(y) \end{pmatrix},$$

$$\begin{pmatrix} F_1(y) \\ F_2(y) \\ \vdots \\ F_{2m}(y) \end{pmatrix} = M^*(x) \times y_z + H^* \times y_x,$$

$$M^*(x) = M(x) \otimes I_2,$$

$$H^* = \begin{pmatrix} \mathrm{Re}(h_1(i)) \\ \mathrm{Im}(h_1(i)) \\ \vdots \\ \mathrm{Re}(h_m(i)) \\ \mathrm{Im}(h_m(i)) \end{pmatrix},$$

$$B = \begin{pmatrix} B_1 & 0 \\ 0 & b_2 \end{pmatrix},$$

$$B_1 = b_1 \otimes I_2,$$

$$U = \begin{pmatrix} U_z \\ U_x \end{pmatrix}, \tag{13}$$

$$U_z = \begin{pmatrix} \mathrm{Re}(u_1) \\ \mathrm{Im}(u_1) \\ \vdots \\ \mathrm{Re}(u_k) \\ \mathrm{Im}(u_k) \end{pmatrix},$$

$$U_2 = u_x. \qquad \square$$

Remark 2. Since the complex chaotic system (6) is equivalent to the corresponding real system (12). Thus, the stabilization problem of system (12) is investigated and the controller U is designed. Moreover, the controller u of system (6) is obtained by

$$u = \begin{pmatrix} 1 & i \end{pmatrix} \propto U = \begin{pmatrix} U_1 + U_2 \times i \\ U_3 + U_4 \times i \\ \vdots \\ U_{2r-1} + U_{2r} \times i \end{pmatrix}. \tag{14}$$

Remark 3. For a given general controlled complex chaotic system of the following form:

$$\dot{z} = f(z) + bu, \tag{15}$$

where $z \in \mathbb{C}^n$ is the state, $f(z) \in \mathbb{C}^n$ is continuous function with $f(0) = 0$, and $b \in \mathbb{R}^{n \times r}$ and $u \in \mathbb{C}^r$ are the designed controller, $r \ge 1$.

By Theorem 1, its equivalent real system is obtained as follows:

$$\dot{y} = F(y) + BU, \tag{16}$$

where $y \in \mathbb{R}^{2n}$ is the state, $F(y) \in \mathbb{R}^{2n}$ is continuous function with $F(0) = 0$, $B \in \mathbb{R}^{2n \times 2r}$ is a constant matrix, and $U \in \mathbb{R}^{2r}$ is the controller to be designed, i.e.,

$$y = \begin{pmatrix} \mathrm{Re}(z_1) \\ \mathrm{Im}(z_1) \\ \vdots \\ \mathrm{Re}(z_n) \\ \mathrm{Im}(z_n) \end{pmatrix},$$

$$F(y) = \begin{pmatrix} \mathrm{Re}(f_1(z)) \\ \mathrm{Im}(f_1(z)) \\ \vdots \\ \mathrm{Re}(f_n(z)) \\ \mathrm{Im}(f_n(z)) \end{pmatrix}, \qquad (17)$$

$$B = b \otimes I_2,$$

$$U = \begin{pmatrix} \mathrm{Re}(u_1) \\ \mathrm{Im}(u_1) \\ \vdots \\ \mathrm{Re}(u_r) \\ \mathrm{Im}(u_r) \end{pmatrix}.$$

If the complex chaotic system in which there exist model uncertainty and external disturbance, we present the following result.

Corollary 1. *Consider the following complex chaotic system with both model uncertainty and external disturbance:*

$$\dot{p} = f(p) + u_d + bu, \qquad (18)$$

where p, $f(p)$, b, and u are given in equations (7)–(10), respectively,

$$u_d = \Delta f(p) + d(t) = \begin{pmatrix} u_{d1} \\ u_{d2} \\ \vdots \\ u_{dn} \end{pmatrix}, \qquad (19)$$

where $\Delta f(p) \in \mathbb{C}^n$ stands for the model uncertainty and $d(t) \in \mathbb{R}^n$ is the external disturbance. Its equivalent real system is described as the following form:

$$\dot{y} = F(y) + BU + U_D, \qquad (20)$$

where y, $F(y)$, B, and U are the same as those in Theorem 1, and

$$U_D = \begin{pmatrix} \mathrm{Re}(u_{d1}) \\ \mathrm{Im}(u_{d1}) \\ \vdots \\ \mathrm{Re}(u_{dn}) \\ \mathrm{Im}(u_{dn}) \end{pmatrix}. \qquad (21)$$

4.2. Stabilization of the Complex Chaotic System. In this section, the stabilization of the complex chaotic system is investigated by the dynamic feedback control method and the linear feedback control method, respectively, and the conclusions are presented.

Theorem 2. *Consider system (12). If $(F(y), B)$ can be stabilized, then the controller U is designed of the following form:*

$$U = K(t)y, \qquad (22)$$

where $K = k(t)B^T$, and $k(t)$ is updated by

$$\dot{k}(t) = -\|y\|^2. \qquad (23)$$

Remark 4. According to equation (14), the controller u for system (6) is obtained; thus, the stabilization of system (6) is realized.

If system (12) has some special structure, the stabilization problem of such system can be realized by the linear feedback control method, and the result is proposed.

Theorem 3. *Consider system (12) of the following form:*

$$y = \begin{pmatrix} Y \\ X \end{pmatrix},$$

$$F(y) = \begin{pmatrix} A(X)Y \\ G(X, Y) \end{pmatrix}, \qquad (24)$$

$$B = \begin{pmatrix} B_Y \\ 0 \end{pmatrix},$$

i.e.,

$$\dot{Y} = A(X)Y + B_Y U,$$
$$\dot{X} = G(X, Y), \qquad (25)$$

with

$$\dot{X} = G(X, 0), \qquad (26)$$

is globally asymptotically stable. If $(F(y), B)$ is controllable, then the designed controller U is of the following form:

$$U = K(X)Y, \qquad (27)$$

where $K(X)$ meets the matrix $B_Y K(X) + A(X)$ is Hurwitz whatever X is.

Proof. Since $(F(y), B)$ is controllable, thus $(A(X), B_Y)$ is also controllable whatever X is. According to the pole assignment theory, the controller U given in (27) is as requested, which completes the proof. □

5. Illustrative Examples with Numerical Simulations

In this section, we shall take two complex chaotic systems for example to show how to apply the obtained theoretical results, and then numerical simulations are performed to

verify the effectiveness and the validity of the aforementioned theoretical results.

Example 1. The controlled complex Lorenz chaotic system [25], which is presented as follows:

$$\dot{p} = f(p) + bu, \tag{28}$$

where

$$p = \begin{pmatrix} z \\ x \end{pmatrix},$$

$$z = \begin{pmatrix} z_1 \\ z_2 \end{pmatrix}, \tag{29}$$

$$x = x_3,$$

i.e., $m = 2$, $n = 3$, and

$$f(p) = f(x, z, \bar{z}) = \begin{pmatrix} M(x)z + H(i)x \\ N(x, z, \bar{z}) \end{pmatrix},$$

$$b = \begin{pmatrix} b_1 & 0 \\ 0 & b_2 \end{pmatrix} = b_1 = \begin{pmatrix} 0 \\ 1 \\ 0 \end{pmatrix},$$

$$\tag{30}$$

$$M(x) = \begin{pmatrix} -10 & 10 \\ 110 - x_3 & -1 \end{pmatrix},$$

$$H(i) = 0,$$

$$N(x, z, \hat{z}) = -2x_3 + \frac{1}{2(\bar{z}_1 z_2 + z_1 \bar{z}_2)}.$$

According to Theorem 1, the equivalent real system is obtained as follows:

$$\dot{y} = F(y) + BU, \tag{31}$$

where

$$y = \begin{pmatrix} y_z \\ y_x \end{pmatrix},$$

$$y_z = \begin{pmatrix} y_1 \\ y_2 \\ y_3 \\ y_4 \end{pmatrix},$$

$$y_x = y_5,$$

$$F(y) = \begin{pmatrix} F_1(y) \\ F_2(y) \\ \vdots \\ F_5(y) \end{pmatrix},$$

$$\begin{pmatrix} F_1(y) \\ F_2(y) \\ F_3(y) \\ F_4(y) \end{pmatrix} = M(x) \otimes I_2 \times y_z$$

$$= \begin{pmatrix} -10 & 0 & 10 & 0 \\ 0 & -10 & 0 & 10 \\ 110 - y_5 & 0 & -1 & 0 \\ 0 & 110 - y_5 & 0 & -1 \end{pmatrix} \begin{pmatrix} y_1 \\ y_2 \\ y_3 \\ y_4 \end{pmatrix},$$

$$B = B_1 = b_1 \otimes I_2 = \begin{pmatrix} 0 & 0 \\ 0 & 0 \\ 1 & 0 \\ 0 & 1 \\ 0 & 0 \\ 0 & 0 \end{pmatrix},$$

$$U = U_z = \begin{pmatrix} U_1 \\ U_2 \end{pmatrix},$$

$$\tag{32}$$

i.e.,

$$\dot{y}_1 = -10y_1 + 10y_3,$$

$$\dot{y}_2 = -10y_2 + 10y_4,$$

$$\dot{y}_3 = (110 - y_5)y_1 - y_3 + U_1, \tag{33}$$

$$\dot{y}_4 = (110 - y_5)y_2 - y_4 + U_2,$$

$$\dot{y}_5 = -2y_5 + y_1 y_3 + y_2 y_4.$$

Note that if $y_3 = y_4 = 0$, then the following subsystem

$$\dot{y}_1 = -10y_1,$$

$$\dot{y}_2 = -10y_2, \tag{34}$$

$$\dot{y}_5 = -2y_5,$$

is globally asymptotically stable; thus, $(F(y), B)$ can be stabilized.

According to Theorem 2, the controller U is designed as follows:

$$U = K(t)y = k(t) \begin{pmatrix} 0 & 0 & 1 & 0 & 0 \\ 0 & 0 & 0 & 1 & 0 \end{pmatrix} y = k(t) \begin{pmatrix} y_3 \\ y_4 \end{pmatrix} = \begin{pmatrix} k(t)y_3 \\ k(t)y_4 \end{pmatrix},$$

$$\tag{35}$$

where $K = k(t)B^T$ and $\dot{k}(t) = -\|y\|^2$. Thus,

$$u = (1 \quad i) \propto U = (1 \quad i) \propto \begin{pmatrix} k(t)y_3 \\ k(t)y_4 \end{pmatrix} = k(t)z_2. \tag{36}$$

Numerical simulation is carried out with the initial conditions: $y(0) = [-5, 3, -2, -6, 7]$, $k(0) = -1$. Figure 1 shows y_1, y_2, and y_3 are asymptotically stable, and Figure 2 shows y_4 and y_5 are asymptotically stable, which implies the $z(t)$ and $x(t)$ are stabilized. Figure 3 shows the feedback gain $k(t)$ approaches to constant.
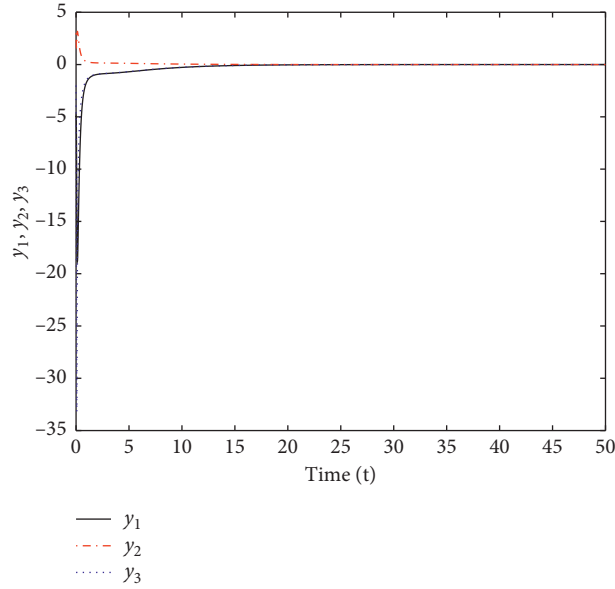
FIGURE 1: y_1, y_2, and y_3 are asymptotically stable.
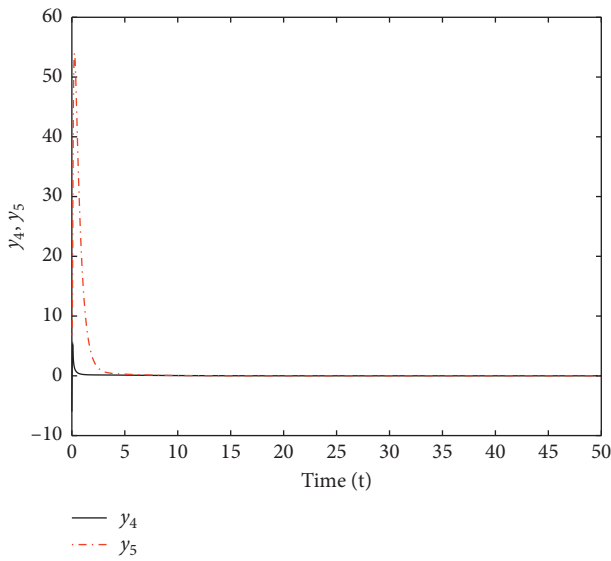
FIGURE 2: y_4 and y_5 are asymptotically stable.

FIGURE 3: $k(t)$ approaches to constant.

According to Theorem 3, the controller U is designed as follows:

$$U = K(X)Y = \begin{pmatrix} 0 & 0 & (X-110) & 0 \\ 0 & 0 & 0 & (X-110) \end{pmatrix} Y = \begin{pmatrix} (X-110)Y_1 \\ (X-110)Y_2 \end{pmatrix},$$

(37)

where

$$Y = \begin{pmatrix} Y_1 \\ Y_2 \\ Y_3 \\ Y_4 \end{pmatrix} = \begin{pmatrix} y_1 \\ y_2 \\ y_3 \\ y_4 \end{pmatrix},$$

(38)

$$X = y_5.$$

Thus,

$$u = (1 \ \ i) \propto U = (1 \ \ i) \propto \begin{pmatrix} (x_3 - 110)y_1 \\ (x_3 - 110)y_2 \end{pmatrix} = (x_3 - 110)z_1.$$

(39)

Numerical simulation is carried out with the initial conditions: $y(0) = [-5, 3, -2, -6, 7]$. Figure 4 shows y_1, y_2, and y_3 are asymptotically stable, and Figure 5 shows y_4 and y_5 are asymptotically stable, which implies the $z(t)$ and $x(t)$ are stabilized.

Example 2. The controlled complex hyperchaotic Lorenz system [26], which is presented as follows:

$$\dot{p} = f(p) + bu,$$

(40)

where
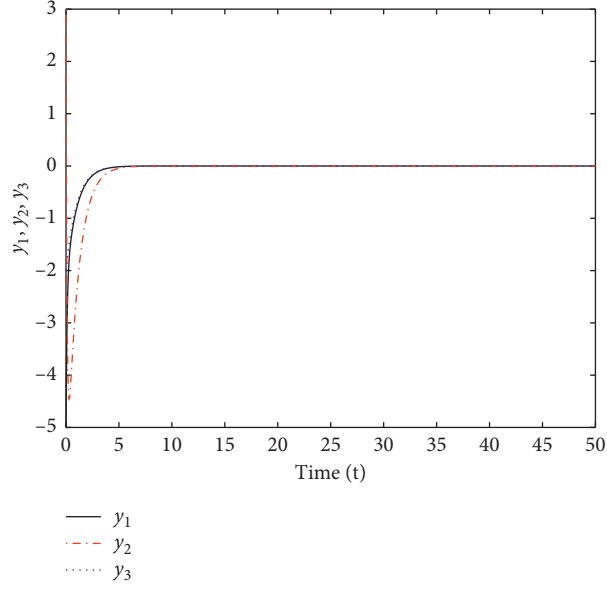
FIGURE 4: $y_1, y_2,$ and y_3 are asymptotically stable.
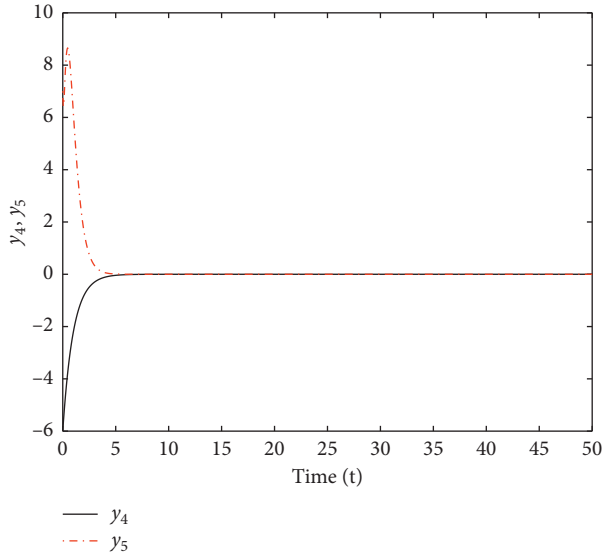
FIGURE 5: y_4 and y_5 are asymptotically stable.

$$p = \begin{pmatrix} z \\ x \end{pmatrix},$$

$$z = \begin{pmatrix} z_1 \\ z_2 \end{pmatrix}, \qquad (41)$$

$$x = \begin{pmatrix} x_3 \\ x_4 \end{pmatrix},$$

that is, $m = 2$, $n = 4$, and

$$f(p) = f(x, z, \overline{z}) = \begin{pmatrix} M(x)z + H(i)x \\ N(x, z, \overline{z}) \end{pmatrix},$$

$$b = \begin{pmatrix} b_1 & 0 \\ 0 & b_2 \end{pmatrix} = b_1 = \begin{pmatrix} 0 \\ 1 \\ 0 \\ 0 \end{pmatrix},$$

$$M(x) = \begin{pmatrix} -14 & 14 \\ 45 - x_3 & -1 \end{pmatrix}, \qquad (42)$$

$$H(i) = \begin{pmatrix} 0 & 1+i \\ 0 & 0 \end{pmatrix},$$

$$N(x, z, \overline{z}) = \begin{pmatrix} -5x_3 + \dfrac{1}{2(\overline{z}_1 z_2 + z_1 \overline{z}_2)} \\ -5.5x_4 + \dfrac{1}{2(\overline{z}_1 z_2 + z_1 \overline{z}_2)} \end{pmatrix}.$$

According to Theorem 1, the equivalent real system is obtained as follows:

$$\dot{y} = F(y) + BU, \qquad (43)$$

where
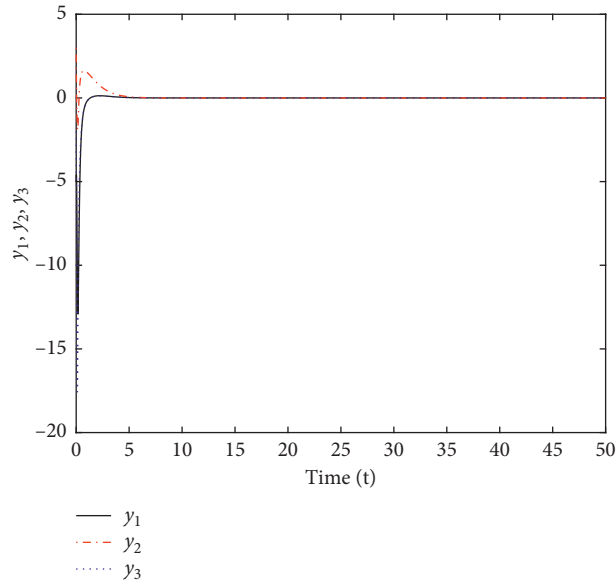
FIGURE 6: y_1, y_2, and y_3 are asymptotically stable.
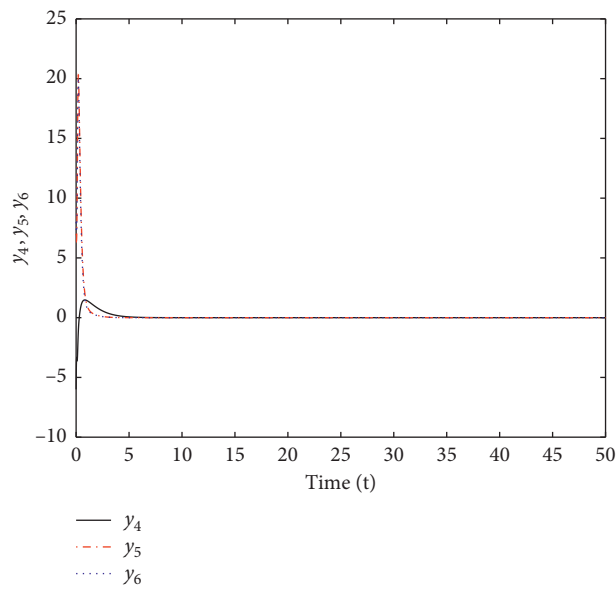
FIGURE 7: y_4, y_5, and y_6 are asymptotically stable.
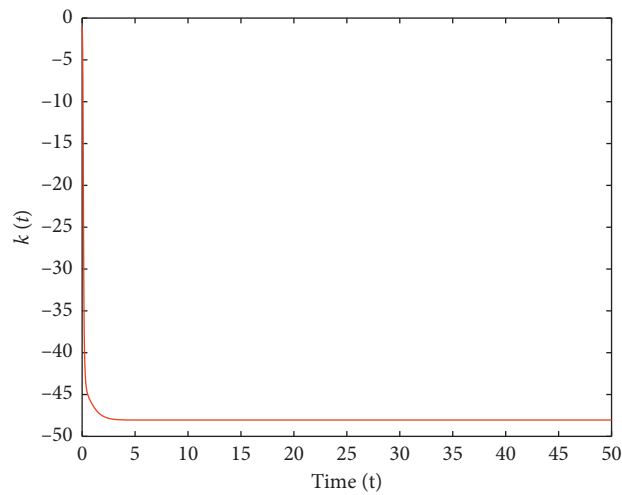
FIGURE 8: $k(t)$ tends to constant.

$$y = \begin{pmatrix} y_z \\ y_x \end{pmatrix},$$

$$y_z = \begin{pmatrix} y_1 \\ y_2 \\ y_3 \\ y_4 \end{pmatrix},$$

$$y_x = \begin{pmatrix} y_5 \\ y_6 \end{pmatrix},$$

$$F(y) = \begin{pmatrix} F_1(y) \\ F_2(y) \\ \vdots \\ F_6(y) \end{pmatrix},$$

$$H^* = \begin{pmatrix} 0 & 1 \\ 0 & 1 \\ 0 & 0 \\ 0 & 0 \end{pmatrix},$$

$$\begin{pmatrix} F_1(y) \\ F_2(y) \\ F_3(y) \\ F_4(y) \end{pmatrix} = M(x) \otimes I_2 \times y_z + H^* \times y_x$$

$$= \begin{pmatrix} -14 & 0 & 14 & 0 \\ 0 & -14 & 0 & 14 \\ 45 - y_5 & 0 & -1 & 0 \\ 0 & 45 - y_5 & 0 & -1 \end{pmatrix} \begin{pmatrix} y_1 \\ y_2 \\ y_3 \\ y_4 \end{pmatrix} + \begin{pmatrix} 0 & 1 \\ 0 & 1 \\ 0 & 0 \\ 0 & 0 \end{pmatrix} \begin{pmatrix} y_5 \\ y_6 \end{pmatrix}$$

$$= \begin{pmatrix} -14(y_1 - y_3) + y_5 \\ -14(y_2 - y_4) + y_6 \\ (45 - y_5)y_1 - y_3 \\ (45 - y_5)y_2 - y_4 \end{pmatrix}$$

$$B = B_1 = b_1 \otimes I_2 = \begin{pmatrix} 0 & 0 \\ 0 & 0 \\ 1 & 0 \\ 0 & 1 \\ 0 & 0 \\ 0 & 0 \end{pmatrix},$$

$$U = U_z = \begin{pmatrix} U_1 \\ U_2 \end{pmatrix},$$

$$(44)$$

i.e.,

$$\dot{y}_1 = -14(y_1 - y_3) + y_5,$$
$$\dot{y}_2 = -14(y_2 - y_4) + y_6,$$
$$\dot{y}_3 = (45 - y_5)y_1 - y_3 + U_1,$$
$$\dot{y}_4 = (45 - y_5)y_2 - y_4 + U_2, \qquad (45)$$
$$\dot{y}_5 = -5y_5 + y_1 y_3 + y_2 y_4,$$
$$\dot{y}_6 = -5.5y_6 + y_1 y_3 + y_2 y_4.$$

Notice that if $y_3 = y_4 = 0$, then the following system

$$\dot{y}_1 = -14y_1,$$
$$\dot{y}_2 = -14y_2,$$
$$\dot{y}_5 = -5y_5, \qquad (46)$$
$$\dot{y}_6 = -5.5y_6,$$

is globally asymptotically stable; thus, $(F(y), B)$ can be stabilized.

According to Theorem 2, the controller U is designed as follows:

$$U = K(t)y = k(t)\begin{pmatrix} 0 & 0 & 1 & 0 & 0 \\ 0 & 0 & 0 & 1 & 0 \end{pmatrix} y = k(t)\begin{pmatrix} y_3 \\ y_4 \end{pmatrix} = \begin{pmatrix} k(t)y_3 \\ k(t)y_4 \end{pmatrix}, \qquad (47)$$

where $K = k(t)B^T$ and $\dot{k}(t) = -\|y\|^2$.

Therefore,

$$u = \begin{pmatrix} 1 & i \end{pmatrix} \propto U = \begin{pmatrix} 1 & i \end{pmatrix} \propto \begin{pmatrix} k(t)y_3 \\ k(t)y_4 \end{pmatrix} = k(t)z_2. \qquad (48)$$

Numerical simulation is performed with the initial conditions: $y(0) = [-5, 3, -2, -6, 7, -8], k(0) = -1$. Figure 6 shows $y_1, y_2,$ and y_3 are asymptotically stable, and Figure 7 shows $y_4, y_5,$ and y_6 are asymptotically stable, which means that the $z(t)$ and $x(t)$ are stabilized. Figure 8 shows the feedback gain $k(t)$ tends to constant.

6. Conclusions

In conclusion, the stabilization problem of the complex chaotic system has been studied in this paper. First, a systematic method has been proposed, which is applied to transform the complex chaotic system into its equivalent real chaotic system. Then, both simple and physical controllers have been designed for the complex chaotic system by the dynamic feedback control method and the linear feedback control method, respectively. Finally, two illustrative examples with numerical simulations have been performed to verify the validity and effectiveness of the theoretical results.

Data Availability

No data were used in this paper.

Conflicts of Interest

The authors declare that there are no conflicts of interest regarding the publication of this paper.

Acknowledgments

References

[1] E. Ott, C. Grebogi, and J. A. Yorke, "Controlling chaos," *Physical Review Letters*, vol. 64, no. 11, pp. 1196–1199, 1990.

[2] H. Nijmeijer, "A dynamical control view on synchronization," *Physica D: Nonlinear Phenomena*, vol. 154, no. 3-4, pp. 219–228, 2001.

[3] R. Guo, "A simple adaptive controller for chaos and hyperchaos synchronization," *Physics Letters A*, vol. 372, no. 34, pp. 5593–5597, 2008.

[4] A. Yang, L. Li, Z. Wang, and R. Guo, "Tracking control of a class of chaotic systems," *Symmetry*, vol. 11, no. 4, p. 568, 2019.

[5] K. Su and C. Li, "Control chaos in fractional-order system via two kinds of intermittent schemes," *Optik*, vol. 126, no. 20, pp. 2671–2673, 2015.

[6] C. Li, K. Su, and J. Zhang, "Amplitude control and projective synchronization of a dynamical system with exponential nonlinearity," *Applied Mathematical Modelling*, vol. 39, no. 18, pp. 5392–5398, 2015.

[7] Z. Wang and R. Guo, "Hybrid synchronization problem of a class of chaotic systems by an universal control method," *Symmetry*, vol. 10, no. 11, p. 552, 2018.

[8] R. Xu and F. Zhang, "ϵ-nash mean-field games for general linear-quadratic systems with applications," *Automatica*, vol. 114, pp. 1–6, 2020.

[9] L. Ren, R. Guo, and U. E. Vincent, "Coexistence of synchronization and anti-synchronization in chaotic systems," *Archives of Control Sciences*, vol. 26, no. 1, pp. 69–79, 2016.

[10] C. Kong, H. Chen, and C. L Li, "Controlling chaotic spin-motion entanglement of ultracold atoms via spin-orbit coupling," *Chaos*, vol. 28, no. 2, Article ID 023115, 2018.

[11] C. Li and W. Hai, "Constructing multiwing attractors from a robust chaotic system with non-hyperbolic equilibrium points," *Automatika*, vol. 59, no. 2, pp. 184–193, 2018.

[12] C. Li, K. Qian, S. He, H. Li, and W. Feng, "Dynamics and optimization control of a robust chaotic map," *IEEE Access*, vol. 7, pp. 160072–160081, 2019.

[13] W. Yu, P. Guo, Q. Wang et al., "On a periodic capital injection and barrier dividend strategy in the compound poisson risk model," *Mathematics*, vol. 8, no. 4, p. 511, 2020.

[14] W. Yu, F. Wang, Y. Huang, and H. Liu, "Social optimal mean field control problem for population growth model," *Asian Journal of Control*, pp. 1–8, 2019.

[15] S. Hammam, M. Benrejeb, M. Feki, and P. Borne, "Feedback control design for Rössler and Chen chaotic systems anti-synchronization," *Physics Letters A*, vol. 374, pp. 2835–2840, 2010.

[16] X. Yi, R. Guo, and Y. Qi, "Stabilization of chaotic systems with both uncertainty and disturbance by the UDE-based control method," *IEEE Access*, vol. 8, no. 1, pp. 62471–62477, 2020.

[17] C. M Jiang, A. Zada, M. T. Senel, and T. X. Li, "Synchronization of bidirectional N-coupled fractional-order chaotic systems with ring connection based on antisymmetric structure," *Advances in Difference Equations*, vol. 456, p. 2019, 2019.

[18] R. Guo, "Projective synchronization of a class of chaotic systems by dynamic feedback control method," *Nonlinear Dynamics*, vol. 90, no. 1, pp. 53–64, 2017.

[19] H. Liu, Y. Zhang, A. Kadir, and Y. Xu, "Image encryption using complex hyper chaotic system by injecting impulse into parameters," *Applied Mathematics and Computation*, vol. 360, no. 1, pp. 83–93, 2019.

[20] F. Nian, X. Liu, and Y. Zhang, "Sliding mode synchronization of fractional-order complex chaotic system with parametric and external disturbances," *Chaos, Solitons & Fractals*, vol. 116, no. 11, pp. 22–28, 2018.

[21] J. Sun, W. Deng, G. Cui, and Y. Wang, "Real combination synchronization of three fractional-order complex-variable chaotic systems," *Optik*, vol. 127, no. 23, pp. 11460–11468, 2016.

[22] V. K. Yadav, R. Kumar, A. Y. T. Leung, and S. Das, "Dual phase and dual anti-phase synchronization of fractional order chaotic systems in real and complex variables with uncertainties," *Chinese Journal of Physics*, vol. 57, no. 2, pp. 282–308, 2019.

[23] J. Liu and S. Liu, "Complex modified function projective synchronization of complex chaotic systems with known and unknown complex parameters," *Applied Mathematical Modelling*, vol. 48, no. 8, pp. 440–450, 2017.

[24] S. Zheng, "Synchronization analysis of time delay complex-variable chaotic systems with discontinuous coupling," *Journal of the Franklin Institute*, vol. 353, no. 6, pp. 1460–1477, 2016.

[25] A. Rauh, L. Hannibal, and N. B. Abraham, "Global stability properties of the complex lorenz model," *Physica D: Nonlinear Phenomena*, vol. 99, no. 1, pp. 45–58, 1996.

[26] S. AL-Azzawi, "Study of dynamical properties and effective of a state u for hyperchaotic Pan systems," *AL-Rafidain Journal of Computer Sciences and Mathematics*, vol. 10, no. 3, pp. 89–99, 2013.

WILEY | Hindawi

Research Article

Line Spectrum Chaotification on QZS Systems with Time-Delay Control

Jing Zhang [ID], Tao Tang, and Wenhua Fang

School of Mechanical Engineering, Hunan Institute of Science and Technology, Yueyang 414006, China

Correspondence should be addressed to Jing Zhang; zhangjing819@hnu.edu.cn

Chaotification can be employed to weaken or eliminate the feature of line spectra of waterborne noise. The efficiency of this method lies on the use of small control. The analysis reveals that the critical control gain depends on the stiffness of vibration isolation systems. Thus, an isolation raft system based on quasi-zero-stiffness (QZS) property is proposed for line spectrum chaotification. A nonlinear time-delay controller is derived accordingly. Comparative analysis shows that the new approach allows much smaller control, and the intensity of line spectra is further reduced. Numerical simulations also indicate other advantages with the introduction of QZS system into chaotification.

1. Introduction

The spectra of the radiated waterborne noises of underwater vehicles are usually divided into two categories. One is continuous broadband spectra corresponding to noise induced by water current and bubble burst. The other is discrete narrowband line spectra mainly caused by propeller and machinery vibrations. Line spectra consist of closely spaced spectral lines that characterize the intensity of noise components. Line spectra of radiated noise from machinery vibration signify the features of operating underwater vehicles, such as the speed and distance of moving objects. Thus, line spectra have been generally utilized for identifying underwater vehicles and thus regarded as harmful signals for the vehicle safety.

Extensive efforts have been made to attenuate machinery vibrations for the reduction of noise spectra through vibration isolation techniques [1–3]. It has been known that the linear vibration isolation techniques can reduce the intensity of line spectra in a certain frequency bandwidth but cannot change the structure of line spectra of vibration noises due to the frequency fidelity. It means that a sinusoidal input of vibration source to an isolation system will simply turn out a sinusoidal output unable to eliminate the line spike at the frequency. To cope with the problem, an innovative idea [4] was proposed to change the spectra configuration by chaotification [4–7] rather than only rely on vibration attenuation. With a special mechanism, the response of the simple harmonic excitation from the vibration source to the base can present a chaotic state. The process can be called line spectrum chaotification, and the line spectrum structure without control and the line spectrum structure with control are shown in Figure 1. Chaotification is a new technique of making use of broadband nature of chaos to blur and change the feature of line spectra. The mechanism is that a nonlinear isolation system, installed in between the vibrating machine and supporting base, is designed with control which enables to convert a periodic excitation (narrowband input of machinery vibration) into a chaotic one (broadband output on a supporting base) to improve the concealment capability of underwater vehicles.

Lou et al. [4] first reported that a Duffing-type vibration isolator excited by harmonic forces might generate a broadband continuous spectrum at special parameter settings. Through a chaotification process, the intensity of line spectra transmitted to the base could be reduced. The feasibility of this approach was verified thoroughly in an experiment [5]. To enable chaotification for wider range of parameter settings, a parametric perturbation scheme [6] was proposed by using generalized chaos synchronization [8]. However, the
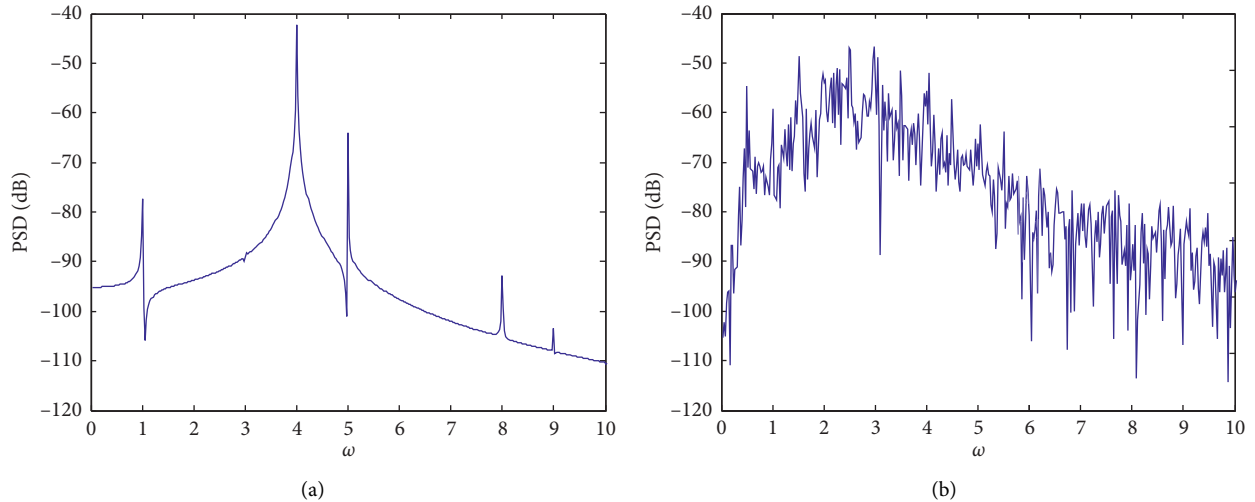
Figure 1: Comparison of line spectrum structure before (a) and after (b) chaotification.

persistence of chaotification may not be guaranteed since this scheme could deteriorate the system installation stability. This problem could be avoided by using a state perturbation approach [9]. Inspired by the work [8], chaotification [10] could be realized by employing the projective synchronization method [11], where a nonlinear vibration isolation system (VIS) is driven into a chaotic state by coupling a Duffing system. However, this approach requires large control energy and seems impractical for applications. We will elaborate later that control energy is very much concerned because not only there is a limitation of energy on board but also larger control energy may result in poor quality when reconstructing line spectra. A discrete impact method [12] based on Lyapunov exponents was proposed for chaotifying a Duffing type of VIS. This method also suffers the limitation for chaotification persistence and small controls.

It is known that the existence of time-delay feedback can extend a simple dynamic system into high dimensional one. This nature could make chaotification of a time-delay system readily applicable. In this regard, a new strategy by using time-delay feedback control was introduced for line spectrum chaotification [13–18]. Stability analysis [14] of a double-layer vibration isolation floating raft system (VIFRS) with a linear time-delay feedback control was carried out, and a set of critical criteria for stability switches are derived. These criteria provide a theoretical guidance for the setting of the system parameters and control parameters to achieve chaotification. Strictly speaking, these criteria are not necessary conditions but chaotification of VIFRS seems more likely with the criteria. For a better understanding, Li et al. [16] studied the dynamic behavior of the double-layer nonlinear isolation raft and revealed a variety of response solutions under time-delay control. Furthermore, chaotification of a two-dimensional VIFRS with dual time-delay feedback control was investigated [18]. A more sophisticated methodology originally developed from antichaos control [19, 20] could be employed for line spectrum reconstruction [17] of double-layer VIFRS. The significance of this work [17] is to provide a standard procedure for time-delay

controller design which promises the occurrence of chaotification in the sense of Li and Yoke criteria [19]. This method based on nonlinear time-delay control notably outperforms the linear time-delay approaches [14, 18], especially in the requirement of small control. Different from the previous ideas, Zhou et al. [15] proposed a chaotification method totally based on spectrum optimization. This method can realize chaotification of VIFRS without exactly knowing system parameter settings or operational conditions, which is effective, easy to use, and handy in real applications.

The existing research works mainly focus on the generation of chaotic response in the floating raft isolation systems. In the purpose of altering the line spectrum configuration and eliminating spectrum line spikes, abundant results from numerical simulations [13, 15, 17] indicate that small control energy can lead to a better quality of chaotification in terms of the line spectrum intensity and broadness of spectrum bandwidth. Pursuing small control for chaotification is one of the key issues in the line spectrum reconfiguration. In this paper, we will propose time-delay control on a quasi-zero-stiffness (QZS) raft system for the improvement of both chaotification and isolation efficiency. The QZS system is a kind of nonlinear VIS with the characteristics of high static and low dynamic stiffness [21–25]. In the following study, we will first elaborate what factors affect the control energy. Then, we will introduce a newly developed QZS system [26] for line spectra control. Based on the new system, we will derive the nonlinear time-delay controller for chaotification. Numerical simulation will show the advance of the approach. By combining time-delay scheme with the QZS system, we can significantly decrease the critical control gain and meanwhile can effectively change the line spectrum configuration.

2. Critical Control Gain

In this section, we will state the key factors that dominate the minimum required control gain for chaotification, which is

referred to as critical control gain. Firstly, we look into a single degree-of-freedom (DOF) VIS and then extend the discussion to a double-layer VIS. Consider a nonlinear isolation system with a time-delay control:

$$\dot{x} = \mathbf{f}(\mathbf{x}) + \mathbf{g}(\mathbf{x})K_t\varphi(\tau_d), \tag{1}$$

where $\mathbf{x}$ is a state vector, $\mathbf{f}(\mathbf{x})$ and $\mathbf{g}(\mathbf{x}) \in R^n$ are vector field, K_t is a control gain, and $\varphi(\tau_d)$ is a time-delay feedback control function. The form of $\varphi(\tau_d)$ is not restricted which may be either linear or nonlinear function.

As shown in Figure 2(a), the mass m is supported by a nonlinear spring with quadratic and cubic nonlinearity, a linear damper, and an actuator which is utilized to implement time-delay feedback control. The governing equation of the single DOF mass-spring system with time-delay feedback control can be written as

$$M\ddot{x} + C\dot{x} + K_1(x - \Delta x) + K_3(x - \Delta x)^3$$
$$= F_0\cos(\omega_0 t) + K_t\varphi(\tau_d), \tag{2}$$

where K_t is the feedback gain, $\varphi(\tau_d)$ is the time-delay feedback control function, C is the damping coefficient, K_1 and K_3 are the stiffness coefficients, F_0 and ω_0 are the amplitude and frequency of the harmonic excitation, respectively, and Δx denotes the static deformation of the spring subjected to the system static weight.

We define the following nondimensional parameters, and setting $X = x - \Delta x$,

$$\omega_n = \sqrt{\frac{K_1}{M}},$$
$$\xi = \frac{C}{2M\omega_n},$$
$$\eta = \frac{K_3}{M}, \tag{3}$$
$$f_0 = \frac{F_0}{M},$$
$$\omega_t = \sqrt{\frac{K_t}{M}},$$

the governing equation can be rewritten as

$$\ddot{X} + 2\xi\omega_n\dot{X} + \omega_n^2 X + \eta X^3 = f_0\cos\omega_0 t + \omega_t^2\varphi(\tau_d). \tag{4}$$

By defining $x_1 = X$ and $x_2 = \dot{X}$, the equation of motion without external excitation force can be written in the autonomous form:

$$\begin{cases} \dot{x}_1 = x_2, \\ \dot{x}_2 = -2\xi\omega_n x_2 - \omega_n^2 x_1 - \eta x_1^3 + \omega_t^2\varphi(\tau_d). \end{cases} \tag{5}$$

The system possess the equilibrium point $A(0,0)$. Giving a perturbed motion $(\Delta x_1, \Delta x_2)$ at the equilibrium point $A(0,0)$, it may yield two linearized time-delay differential equations:

$$\begin{cases} \Delta\dot{x}_1 = \Delta x_2, \\ \Delta\dot{x}_2 = -2\xi\omega_n\Delta x_2 - \omega_n^2\Delta x_1 + \omega_t^2\Delta x_1(t - \tau_d). \end{cases} \tag{6}$$

Note that the form of time-delay feedback control function $\varphi(\tau_d)$ may be arbitrary. If it is linear, the linearized part of $\varphi(\tau_d)$ is $\Delta x_1(t - \tau_d)$. If it is nonlinear, $\varphi(\tau_d)$ can be expressed in Taylor series of $\sum a_n\Delta x_1^n(t - \tau_d)$. Because of the vibration amplitude of a real VIS is often very small, the high order terms can be ignored and the dominant term is still $\Delta x_1(t - \tau_d)$. A very useful method for determining system stability is bifurcation analysis. According to the theorem proposed [27], the characteristic equation can be written as

$$P_1(\lambda) + P_2(\lambda)e^{-\lambda\tau} = 0, \tag{7}$$

where

$$P_1 = \lambda^2 + 2\xi\omega_n\lambda + \omega_n^2,$$
$$P_2 = -\omega_t^2. \tag{8}$$

When the real part of a certain eigenvalue changes from negative to zero or even to positive, the time-delay increased may cause the occurrence of Hopf bifurcation. That is to say, there exists a critical time-delay τ_{dc}, at which the system with time-delay feedback control will loose stability and then the following characteristic equation has a purely imaginary root [27]. Suppose that $\lambda = i\nu$ is the purely imaginary root of the characteristic equation:

$$R_1(\nu) + iQ_1(\nu) + [R_2(\nu) + iQ_2(\nu)][\cos(\nu\tau) - i\sin(\nu\tau)] = 0, \tag{9}$$

where

$$R_1(\nu) = -\nu^2 + \omega_n^2,$$
$$R_2(\nu) = -\omega_t^2,$$
$$Q_1(\nu) = 2\xi\omega_n\nu, \tag{10}$$
$$Q_2(\nu) = 0.$$

Separating the real and imaginary parts of the above-mentioned equation may give

$$R_1(\nu) + R_2(\nu)\cos(\nu\tau) + Q_2(\nu)\sin(\nu\tau) = 0,$$
$$Q_1(\nu) - R_2(\nu)\sin(\nu\tau) + Q_2(\nu)\cos(\nu\tau) = 0. \tag{11}$$

By squaring the above equations and then summing the results, we may obtain a quadratic equation after defining a new variable $\mu = \nu^2$:

$$\mu^2 + (4\xi^2 - 2)\omega_n^2\mu + (\omega_n^4 - \omega_t^4) = 0. \tag{12}$$

The roots of equation (12) can be obtained as

$$\mu_{1,2} = \frac{(2 - 4\xi^2)\omega_n^2 \pm \sqrt{16\xi^2(\xi^2 - 1)\omega_n^4 + 4\omega_t^4}}{2} = (1 - 2\xi^2)\omega_n^2 \pm \sqrt{\Delta}. \tag{13}$$

Due to the fact that $1 - 2\xi^2 > 0$ is always satisfied for engineering applications and if $\Delta \geq 0$ equation (12) has one positive root at least, then the critical time-delay τ_{dc} can also
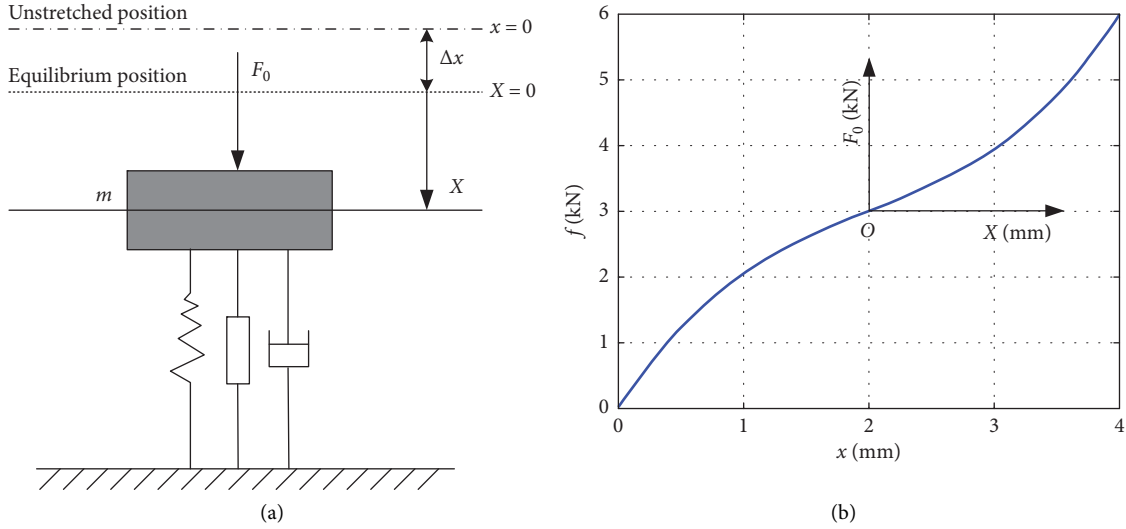
FIGURE 2: A single DOF nonlinear VIS: (a) system model and (b) load-displacement curve.

be acquired. So, the system goes into the state of chaos through Hopf bifurcation only when

$$K_{tc} \geq 2\xi\sqrt{\left(1 - \xi^2\right)}K_1, \qquad (14)$$

where ξ is the damping ratio. The relationship in equation (14) reveals that the critical control gain K_{tc} is only related to ξ and K_1 of the isolation system.

Figure 3 plots the variation of the critical control gain versus the equivalent linear stiffness for different damping ratios. Obviously, K_{tc} is linearly dependent on system stiffness K_1 and nonlinearly dependent on the damping ratio ξ. It delivers an important clue that the system can be much easily disturbed into the chaotic state when the system's stiffness and damping are small. This finding motivates us to look for small stiffness isolation system, which is beneficial not only for chaotification but also for vibration attenuation. We will show later that small control gain leads to small control energy and results in low intensity of chaotified line spectra.

The nonlinear VIFRS [14] can be regarded as a double DOF mass-spring system, as shown in Figure 4. M_1 and M_2 denote the isolated equipment and the floating raft, respectively. M_1 is supported by a linear damper and a nonlinear spring which possesses quadric and cubic nonlinearity. M_2 is supported by a linear damper and a linear spring which are connected with a fixed ground base. There
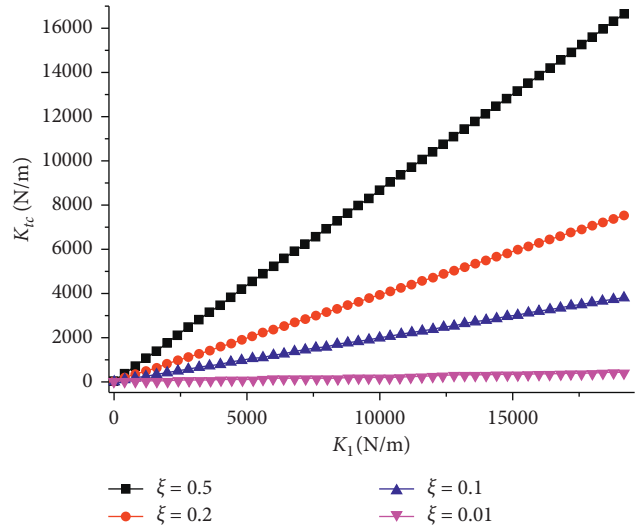
FIGURE 3: The critical control gain K_{tc} of a single DOF VIS with time-delay control for chaotification versus different equivalent linear stiffnesses K_1 and different damping ratios ξ.

is an actuator installed between M_1 and M_2, which is utilized to implement time-delay feedback control for chaotification.

The governing equations with time-delay feedback control are given by

$$
\begin{aligned}
M_1\ddot{x}_1 &= -C_1\left(\dot{x}_1 - \dot{x}_2\right) - \left(K_1 - 2U_1H + 3U_2H^2\right)\left(x_1 - x_2\right) + \left(U_1 - 3U_2H\right)\left(x_1 - x_2\right)^2 - U_2\left(x_1 - x_2\right)^3 + F_0\cos\omega_0 t + K_t\varphi(\tau_d), \\
M_2\ddot{x}_2 &= -C_2\dot{x}_2 - K_2 x_2 + C_1\left(\dot{x}_1 - \dot{x}_2\right) + \left(K_1 - 2U_1H + 3U_2H^2\right)\left(x_1 - x_2\right) - \left(U_1 - 3U_2H\right)\left(x_1 - x_2\right)^2 + U_2\left(x_1 - x_2\right)^3 - K_t\varphi(\tau_d),
\end{aligned}
\tag{15}
$$

where C_1 is the damping coefficient of the nonlinear vibration isolator; K_1, U_1, and U_2 are the linear, quadric, and cubic stiffness coefficients of the nonlinear vibration isolator, respectively. The equivalent linear stiffness at the static

equilibrium point is $K_0 = K_1 - 2U_1H + 3U_2H^2$, where $H = h_1 - h_2$, C_2 is the damping coefficient of the damper between the floating raft and fixed ground, K_2 is the stiffness coefficient of the linear spring, F_0 and ω_0 are the amplitude
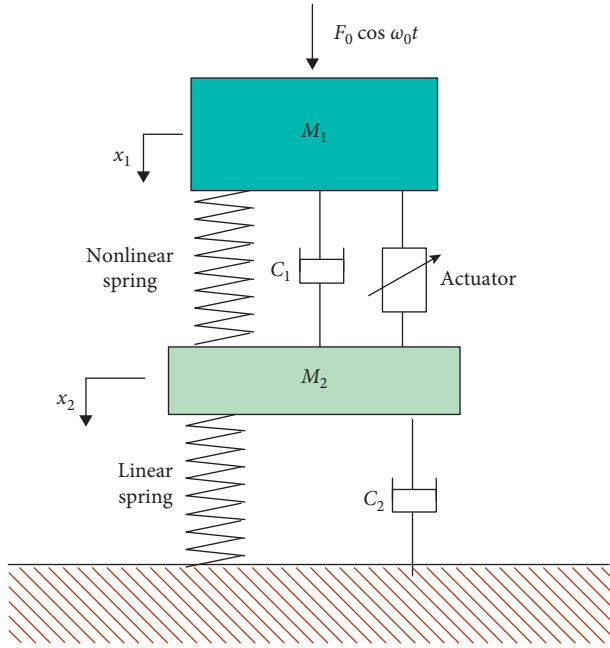
FIGURE 4: The structure diagram of a double DOF VIFRS.

and frequency of the harmonic excitation, respectively, K_t is the feedback control gain, and $\varphi(\tau_d)$ is the time-delay feedback control function.

For the double-layer VIS with time-delay control [14], the derivation of critical control gain is much complicated, and it can only be expressed in an implicit form. We are interested in the critical boundary for the control gain where chaotification can be implemented effectively. To find the critical condition for chaotification in the time-delay system (15), we firstly impose a linearization on the double-layer nonlinear VIFRS at an equilibrium point. Giving a perturbation to the system, it yields a set of linearized time-delay differential equations. By taking the Laplace transform, we can get the characteristic equation from which the eigenvalues are investigated for the stability switches on the parameter domain of time-delay settings and control gains.

Figure 5 illustrates the skeleton region for the stability switches on the parameter plane of the time-delay and control gain. The white region indicates the feasible area where we can apply chaotification, while the region marked in gray color denotes the infeasible area for chaotification. The critical boundaries consist of a number of solid curves. In Figure 5(a), there is a region bracketed by two dashed lines in vertical direction. As the time-delay increases to infinity $\tau \longrightarrow \infty$, these dashed lines define the boundary for chaotification. The corresponding value K_{tc} of the control gain is the required minimum control gain, regarded as the critical control gain. For the case where the system stiffness is set at $K_0 = 9600\,(\mathrm{N/m})$, as shown in Figure 5(a), the critical value of the control gain is $|K_{tc}| = 2112\,(\mathrm{N/m})$. When the system stiffness is decreased to $K_0 = 2400\,(\mathrm{N/m})$, as shown Figure 5(b), the skeleton structure is similar but the critical control gain becomes much smaller, as $|K_{tc}| = 1224\,(\mathrm{N/m})$. It reveals that when the system stiffness decreases the critical

control gain decreases as well, very similar to the case of the single DOF system.

To understand the relationship between the critical control gain and the system's settings, Figure 6 shows the effects of the variation of the equivalent linear stiffness and damping on the critical control gains. With the increase of the equivalent linear stiffness K_0, the critical control gain K_{tc} increases nonlinearly unlike the linear relationship of a single DOF VIS. The curve trend also shows the significant effect for the variation of the damping coefficients C_1 and C_2 on the critical control gain. It strongly implies that small control energy required for chaotification greatly depends on small stiffness K_0 and small damping of the system. Especially, when K_0 is small, K_{tc} drops quickly with the decrease of K_0.

We know that the feedback control gain K_t represents the level of control energy to be inputted. The increase of the control gain leads to the increase of vibration amplitude generally, and accordingly the intensity of the line spectra increases as well, surely harmful to the concealment capability of underwater vehicles. In order to explain this fact quantitatively, we define the intensity of line spectra as the root mean square values of the normal difference between the spectrum peak values with control and the spectrum value at excitation frequency without control. We can obtain the relationship between the intensity of the line spectra and the feedback control gain, as shown in Figure 7.

Figure 7 plots the intensity of the line spectra under the variation of feedback control gain K_t. Obviously, the intensity of the line spectra is linearly dependent on the K_t approximately. As the absolute value of control gain increases, the intensity of line spectra increases proportionally. This diagram indicates that the smaller control leads to the lower intensity of line spectra.

3. Controller for a QZS Vibration Isolation System

In this section, the QZS system [26] is introduced to a double-layer VIS for chaotification due to its favorable feature of quasi-zero-stiffness. Based on this system, the analytical function of time-delay feedback control is derived by using the methodology [17].

In the double-layer isolation system, as shown in Figure 8, we consider a QZS system placed on the upper layer and a linear isolation system placed on the bottom layer. It is known that the QZS system [26] has the characteristics of high static and low dynamic stiffness. At the equilibrium state, the QZS system theoretically has zero stiffness, which is a perfect model for chaotification in terms of small energy control.

The QZS isolation system uses the negative stiffness of magnetic springs to offset the positive stiffness at the equilibrium state yielding the property of zero stiffness, which offers high static stability but very low dynamic stiffness around the equilibrium state. The theoretical analysis and experimental results [26] show the excellent attenuation performance in terms of the force transmissibility in comparison with conventional vibration isolation

(a)

(b)
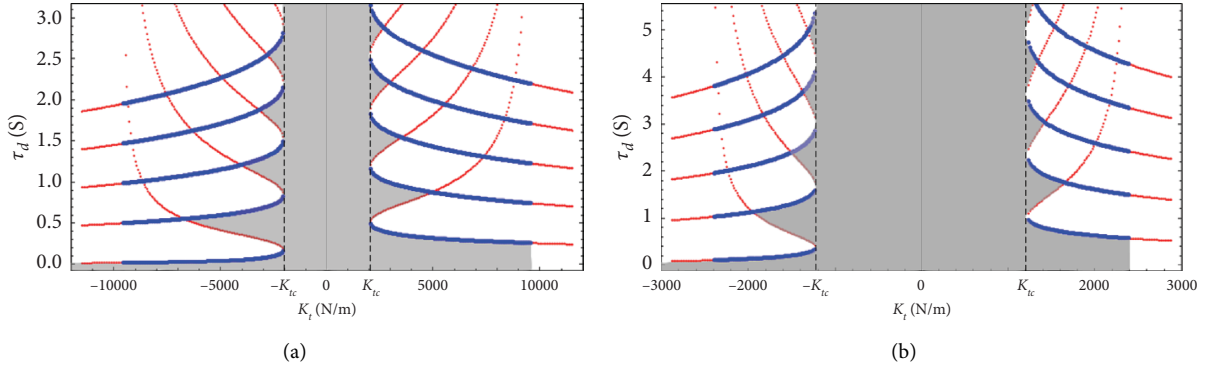
FIGURE 5: The skeleton for stability switches on the parameter plane of the time delay and control gain, indicating the feasible area (white) and infeasible area (gray) for chaotification when the system stiffness is (a) $K_0 = 9600\,(\text{N/m})$ and (b) $K_0 = 2400\,(\text{N/m})$.
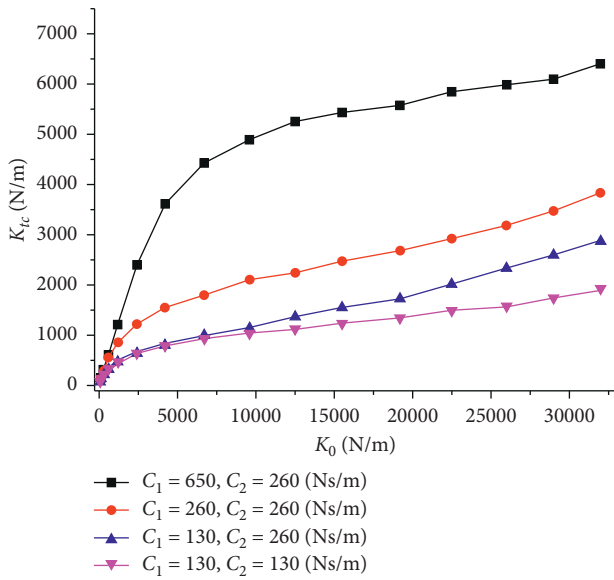
FIGURE 6: The critical control gain for chaotification versus different equivalent linear stiffnesses for different damping (C_1 and C_2 are the damping coefficients of the double-layer system, respectively).

technology. Note that this mechanical property provides a combination of two advantages. Number one, it can most effectively isolate vibration due to its inherent low natural frequency, especially outperform in the low-frequency band; number two, it allows us to use small control for chaotification.

The stiffness of the QZS system can be modeled by a unique cubic term of displacement [26], while there is no linear stiffness. The equations for the double-layer QZS system with time-delay control can be formulated as follows:

$$M_1\ddot{x}_1 = -C_1(\dot{x}_1 - \dot{x}_2) - K(x_1 - x_2)^3 + F_0\cos\omega_0 t + K_t\varphi(\tau_d),$$

$$M_2\ddot{x}_2 = -C_2\dot{x}_2 - K_2 x_2 + C_1(\dot{x}_1 - \dot{x}_2) + K(x_1 - x_2)^3 - K_t\varphi(\tau_d),$$

(16)

where C_1 and C_2 are the damping coefficient of the QZS isolator and the bottom isolator, respectively, K and K_2 are the stiffness coefficient of the QZS isolator and linear spring,
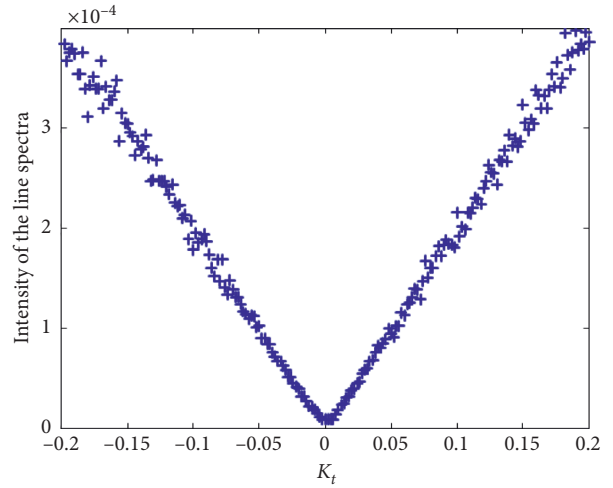
FIGURE 7: The intensity of the line spectra versus feedback control gain ($\sigma = 50, \tau = 20$).
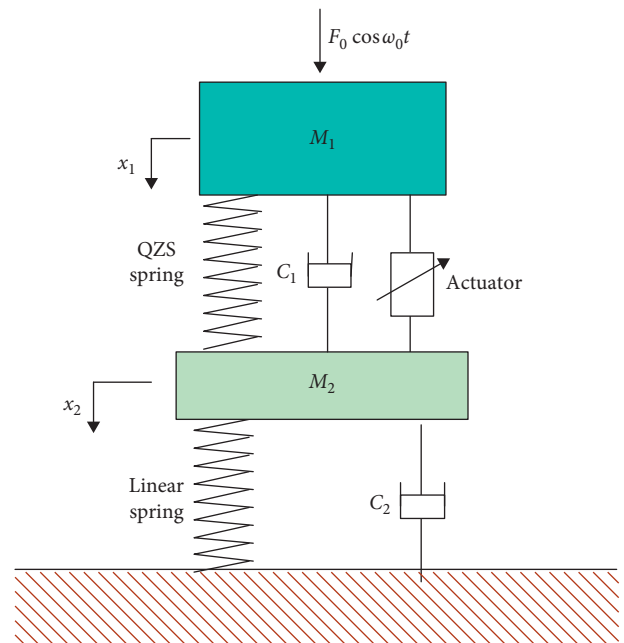
FIGURE 8: The structure diagram of a double-layer QZS system.

respectively, F_0 and ω_0 are the amplitude and frequency of the harmonic excitation, respectively, K_t is the feedback control gain, and $\varphi(\tau_d)$ is the time-delay feedback control function to be derived.

The governing equations (16) can be transformed to a standard form of the first-order governing equations, given by

$$\dot{x}_1 = y_1,$$

$$\dot{y}_1 = -\frac{C_1}{M_1}(y_1 - y_2) - \frac{K}{M_1}(x_1 - x_2)^3 + \frac{F_0}{M_1}\cos\omega_0 t + \frac{K_t}{M_1}\varphi(\tau_d),$$

$$\dot{x}_2 = y_2,$$

$$\dot{y}_2 = -\frac{C_2}{M_2}y_2 - \frac{K_2}{M_2}x_2 + \frac{C_1}{M_2}(y_1 - y_2) + \frac{K}{M_2}(x_1 - x_2)^3 - \frac{K_t}{M_2}\varphi(\tau_d).$$

(17)

We use vector $\mathbf{x} = \begin{bmatrix} x_1 & y_1 & x_2 & y_2 \end{bmatrix}^T$ to denote the system state, where x_1 and x_2 are the displacements and y_1 and y_2 are the velocities of M_1 and M_2, respectively. The controlled system (17) can be expressed in a general form of the single-input and single-output system given by

$$\dot{x} = \mathbf{f}(\mathbf{x}) + \mathbf{g}(\mathbf{x})\delta\mathbf{x}(t),$$
$$y = h(\mathbf{x}),$$

(18)

where $\delta\mathbf{x}(t) = K_t\varphi(\tau_d)$ is the input of the feedback control, $h(\mathbf{x})$ is the output function of the system, and

$$\mathbf{f}(\mathbf{x}) = \begin{bmatrix} y_1 \\ -\dfrac{C_1(y_1 - y_2)}{M_1} - \dfrac{K(x_1 - x_2)^3}{M_1} + \dfrac{F_0\cos\omega_0 t}{M_1} \\ y_2 \\ -\dfrac{C_2 y_2}{M_2} - \dfrac{K_2 x_2}{M_2} + \dfrac{C_1(y_1 - y_2)}{M_2} + \dfrac{K(x_1 - x_2)^3}{M_2} \end{bmatrix},$$

$$\mathbf{g}(\mathbf{x}) = \begin{bmatrix} 0 \\ \dfrac{1}{M_1} \\ 0 \\ -\dfrac{1}{M_2} \end{bmatrix}.$$

(19)

A nonlinear time-delay feedback controller for chaotification can be derived based on the differential geometry theory and the definition of Li and Yoke Chaos [19, 20]. It follows the procedure. Firstly, the above-mentioned nonlinear isolation system (18) is transformed into a standard linear system by a set of nonlinear transformation functions. The set of nonlinear transformation functions are defined by

$$\mathbf{z} = \Phi(\mathbf{x}) = \begin{bmatrix} \varphi_1(x_1, x_2, \cdots, x_n) \\ \varphi_2(x_1, x_2, \cdots, x_n) \\ \vdots \\ \varphi_n(x_1, x_2, \cdots, x_n) \end{bmatrix} = \begin{bmatrix} h(\mathbf{x}) \\ L_f h(\mathbf{x}) \\ \vdots \\ L_f^{n-1} h(\mathbf{x}) \end{bmatrix}, \quad (20)$$

where $\Phi(\mathbf{x})$ is a partial diffeomorphism and $L_f h(\mathbf{x}), \ldots, L_f^{n-1} h(\mathbf{x})$ are Lie derivatives. If the relative degree in a neighborhood of equilibrium point is exactly equal to the degree of the system, the nonlinear isolation system can be exactly transformed into a standard linear system as

$$\dot{z} = \mathbf{A}z + \mathbf{B}v, \quad (21)$$

where $\mathbf{z}$ is the state vector of the linear system, v is the control function, $\mathbf{A}$ is the state coefficient matrix, and $\mathbf{B}$ is the control coefficient matrix. A nonlinear time-delay controller for chaotification in this linearized system can be derived through the technique [19, 20].

Based on the lemma below, the output function of $h(\mathbf{x})$ can be obtained and the control function of $\delta\mathbf{x}(t)$ for chaotification can be designed accordingly. The Lemma from nonlinear control theory is listed as follows.

Lemma 1. *(see [28]) A nonlinear control system is feedback linearizable on a neighborhood D of an equilibrium point if and only if*

(1) $rank\begin{bmatrix} \mathbf{g}(\mathbf{x}) & ad_f\mathbf{g}(\mathbf{x}) & \cdots & ad_f^{n-1}\mathbf{g}(\mathbf{x}) \end{bmatrix} = n, \quad x \in D$

(2) $span\{\mathbf{g}(\mathbf{x}), ad_{\mathbf{f}}\mathbf{g}(\mathbf{x}), \cdots, ad_{\mathbf{f}}^{n-2}\mathbf{g}(\mathbf{x})\}$ is involutive on D

Then, a solution of output $y = h(\mathbf{x})$ from the following partial differential equations can be determined:

$$\frac{\partial h(\mathbf{x})}{\partial \mathbf{x}}\begin{bmatrix} \mathbf{g}(\mathbf{x}) & ad_f\mathbf{g}(\mathbf{x}) & \ldots & ad_f^{n-2}\mathbf{g}(\mathbf{x}) \end{bmatrix} = 0. \quad (22)$$

Point $A(0, 0, 0, 0)$ is an equilibrium point of system (17). Based on this, we can acquire an analytical time-delay control function with Lemma 1. According to the definition, we can obtain $ad_f\mathbf{g}(\mathbf{x})$, $ad_f^2\mathbf{g}(\mathbf{x})$, and $ad_f^3\mathbf{g}(\mathbf{x})$, respectively. Using the parameter $a = x_1 - x_2$, we have

$$ad_f \mathbf{g}(\mathbf{x}) = \frac{\partial \mathbf{g}}{\partial \mathbf{x}} \mathbf{f} - \frac{\partial \mathbf{f}}{\partial \mathbf{x}} \mathbf{g} = \begin{bmatrix} -\dfrac{1}{M_1} \\[2ex] \dfrac{C_1}{M_1^2} + \dfrac{C_1}{(M_1 M_2)} \\[2ex] \dfrac{1}{M_2} \\[2ex] -\dfrac{C_1}{(M_1 M_2)} - \dfrac{C_1}{M_2^2} - \dfrac{C_2}{M_2^2} \end{bmatrix}, \tag{23}$$

$$\mathrm{ad}_{\mathbf{f}}^2 \mathbf{g}(\mathbf{x}) = \frac{\partial (\mathrm{ad}_{\mathbf{f}} \mathbf{g}(\mathbf{x}))}{\partial \mathbf{x}} \mathbf{f} - \frac{\partial \mathbf{f}}{\partial \mathbf{x}} (\mathrm{ad}_{\mathbf{f}} \mathbf{g}(\mathbf{x}))$$

$$= \begin{bmatrix} -\dfrac{C_1 (M_1 + M_2)}{(M_1^2 M_2)} \\[2ex] \dfrac{\left[C_1 C_2 M_1^2 - 3 a^2 K M_1 M_2 (M_1 + M_2) + C_1^2 (M_1 + M_2)^2 \right]}{(M_1^3 M_2^2)} \\[2ex] \dfrac{\left[C_2 M_1 + C_1 (M_1 + M_2) \right]}{(M_1 M_2^2)} \\[2ex] \dfrac{\left[-C_1^2 (M_1 + M_2)^2 - C_1 C_2 M_1 (2M_1 + M_2) + M_1 \left(-C_2^2 M_1 + M_2 (K_2 M_1 + 3 a^2 K (M_1 + M_2)) \right) \right]}{(M_1^2 M_2^3)} \end{bmatrix}, \tag{24}$$

$$ad_f^3 \mathbf{g}(\mathbf{x}) = \frac{\partial \left(ad_f^2 \mathbf{g}(\mathbf{x}) \right)}{\partial \mathbf{x}} \mathbf{f} - \frac{\partial \mathbf{f}}{\partial \mathbf{x}} \left(ad_f^2 \mathbf{g}(\mathbf{x}) \right) = \begin{bmatrix} \Lambda_1 \\ \Lambda_2 \\ \Lambda_3 \\ \Lambda_4 \end{bmatrix}, \tag{25}$$

where

$$\Lambda_1 = -\frac{\left[C_1 C_2 M_1^2 - 3 a^2 K M_1 M_2 (M_1 + M_2) + C_1^2 (M_1 + M_2)^2 \right]}{(M_1^3 M_2^2)},$$

$$\Lambda_2 = \frac{\left[2 C_1^2 C_2 M_1^2 (M_1 + M_2) + C_1^3 (M_1 + M_2)^3 + C_1 M_1 \left(C_2^2 M_1^2 - M_2 (K_2 M_1^2 + 6 a^2 K (M_1 + M_2)^2) \right) - 3 a K M_1^2 M_2 (a C_2 M_1 + 2 M_2 (M_1 + M_2)(y_1 - y_2)) \right]}{(M_1^4 M_2^3)},$$

$$\Lambda_3 = \frac{\left[C_1^2 (M_1 + M_2)^2 + C_1 C_2 M_1 (2M_1 + M_2) + M_1 \left(C_2^2 M_1 - M_2 (K_2 M_1 + 3 a^2 K (M_1 + M_2)) \right) \right]}{(M_1^2 M_2^3)},$$

$$\Lambda_4 = \left[-C_1^3 (M_1 + M_2)^3 - C_1^2 C_2 M_1 \left(3 M_1^2 + 4 M_1 M_2 + M_1^2 \right) + C_1 M_1 \left(-C_2^2 M_1 (3 M_1 + M_2) + M_2 \left(6 a^2 K (M_1 + M_2)^2 + K_2 M_1 (2 M_1 + M_2) \right) \right) \right.$$
$$\left. + M_1^2 \left(-C_2^3 M_1 + C_2 M_2 (2 K_2 M_1 + 3 a^2 K (2 M_1 + M_2)) + 6 a K M_2^2 (M_1 + M_2)(y_1 - y_2) \right) \right] / (M_1^3 M_2^4). \tag{26}$$

After simplification of matrix transformation and inserting the particular values of the system parameters, we can determine the rank of matrix $\begin{bmatrix} \mathbf{g} & ad_{\mathbf{f}} \mathbf{g} & ad_{\mathbf{f}}^2 \mathbf{g} & ad_{\mathbf{f}}^3 \mathbf{g} \end{bmatrix}$.

Next, we will determine the rank of matrix $\begin{bmatrix} \mathbf{g} & ad_{\mathbf{f}} \mathbf{g} & ad_{\mathbf{f}}^2 \mathbf{g} & [ad_{\mathbf{f}} \mathbf{g}, ad_{\mathbf{f}}^2 \mathbf{g}] \end{bmatrix}$ in order to estimate the second condition of Lemma 1:

$$\left[\mathbf{g}, ad_f^2 \mathbf{g}\right] = \frac{\partial\left(ad_f^2 \mathbf{g}(\mathbf{x})\right)}{\partial \mathbf{x}} \mathbf{g} - \frac{\partial \mathbf{g}}{\partial \mathbf{x}}\left(ad_f^2 \mathbf{g}(\mathbf{x})\right) = \begin{bmatrix} 0 \\ 0 \\ 0 \\ 0 \end{bmatrix}, \tag{27}$$

$$\left[ad_\mathbf{f}\mathbf{g}, ad_\mathbf{f}^2\mathbf{g}\right] = \frac{\partial\left(ad_\mathbf{f}^2 \mathbf{g}(\mathbf{x})\right)}{\partial \mathbf{x}} ad_\mathbf{f}\mathbf{g} - \frac{\partial\left(ad_\mathbf{f}\mathbf{g}\right)}{\partial \mathbf{x}}\left(ad_\mathbf{f}^2 \mathbf{g}(\mathbf{x})\right) = \begin{bmatrix} 0 \\ \dfrac{6aK\left(M_1 + M_2\right)^2}{\left(M_1^3 M_2^2\right)} \\ 0 \\ -\dfrac{6aK\left(M_1 + M_2\right)^2}{\left(M_1^2 M_2^3\right)} \end{bmatrix}. \tag{28}$$

For system (16), we assign a set of parameters:

$$M_1 = 85\,\text{kg},$$
$$M_2 = 42.5\,\text{kg},$$
$$C_1 = C_2 = 260\,(\text{Ns/m}), \tag{29}$$
$$K = 2.80681 \times 10^7 \left(\text{N/m}^3\right),$$
$$K_2 = 3.84 \times 10^4\,(\text{N/m}),$$

and we can evaluate the relative degree:

$$\text{rank}\left[\mathbf{g}\ \ ad_\mathbf{f}\mathbf{g}\ \ ad_\mathbf{f}^2\mathbf{g}\ \ ad_\mathbf{f}^3\mathbf{g}\right] = 4. \tag{30}$$

Based on equations (23)–(25) and (28) and the parameter values, we can obtain

$$\text{rank}\left[\mathbf{g}\ \ ad_\mathbf{f}\mathbf{g}\ \ ad_\mathbf{f}^2\mathbf{g}\ \ \left[ad_\mathbf{f}\mathbf{g}, ad_\mathbf{f}^2\mathbf{g}\right]\right] = 3. \tag{31}$$

Thus, we conclude that the linear subspace $\Delta = \text{span}\left\{\mathbf{g}\ \ ad_f\mathbf{g}\ \ ad_f^2\mathbf{g}\right\}$ is also involutive on a neighborhood D of the equilibrium point $A(0, 0, 0, 0)$. The controlled system (18) has a relative degree of 4 at $A(0, 0, 0, 0)$.

From condition (22) in Lemma 1, we can derive the output function of $y = h(\mathbf{x})$ from the partial differential equations:

$$\frac{\partial h(\mathbf{x})}{\partial \mathbf{x}}\mathbf{g}(\mathbf{x}) = \frac{1}{M_1}\frac{\partial h(\mathbf{x})}{\partial y_1} - \frac{1}{M_2}\frac{\partial h(\mathbf{x})}{\partial y_2} = 0, \tag{32}$$

$$\frac{\partial h(\mathbf{x})}{\partial \mathbf{x}}ad_\mathbf{f}\mathbf{g}(\mathbf{x}) = -\frac{1}{M_1}\frac{\partial h(\mathbf{x})}{\partial x_1} + \left(\frac{C_1}{M_1^2} + \frac{C_1}{M_1 M_2}\right)\frac{\partial h(\mathbf{x})}{\partial y_1} + \frac{1}{M_2}\frac{\partial h(\mathbf{x})}{\partial x_2} - \left(\frac{C_1}{M_1 M_2} + \frac{C_1}{M_2^2} + \frac{C_2}{M_2^2}\right)\frac{\partial h(\mathbf{x})}{\partial y_2} = 0, \tag{33}$$

$$\frac{\partial h(\mathbf{x})}{\partial \mathbf{x}}ad_\mathbf{f}^2\mathbf{g}(\mathbf{x}) = -\left(\frac{C_1}{M_1^2} + \frac{C_1}{M_1 M_2}\right)\frac{\partial h(\mathbf{x})}{\partial x_1} + \left(\frac{C_1\left(C_2 M_1^2 + C_1\left(M_1 + M_2\right)^2\right)}{M_1^3 M_2^2}\right)\frac{\partial h(\mathbf{x})}{\partial y_1}$$
$$+ \left(\frac{C_1}{M_1 M_2} + \frac{C_1}{M_2^2} + \frac{C_2}{M_2^2}\right)\frac{\partial h(\mathbf{x})}{\partial x_2} + \left(\frac{-C_1^2\left(M_1 + M_2\right)^2 - C_1 C_2 M_1\left(2M_1 + M_2\right) + M_1^2\left(-C_2^2 + K_2 M_2\right)}{M_1^2 M_2^3}\right)\frac{\partial h(\mathbf{x})}{\partial y_2} = 0. \tag{34}$$

There are multiple solutions for the set of equations (32)–(34). One of the solutions for the abovementioned equations could be derived as

$$y = h(\mathbf{x}) = -\frac{K_2 M_1}{C_2 M_2}x_1 - \frac{K_2 M_2 - C_2^2}{C_2 M_2}x_2 + \frac{M_1}{M_2}y_1 + y_2. \tag{35}$$

According to Wang et al. [19, 20], if the map associated with $\delta\mathbf{x}(t)$ is a bounded chaotic map and the time-delay is sufficiently large, then the output $y(t)$ of the system equation with time-delay (17) could be chaotic. The solution of $y = h(\mathbf{x})$ is not unique and accordingly there are multiple solutions for $\delta\mathbf{x}(t)$. We may choose various bounded functional forms. Here, the sinusoidal form of

$\delta \mathbf{x}(t) = \widetilde{K}_t \sin(\sigma y(t - \tau_d))$ is utilized for the controller, and we have

$$\delta \mathbf{x}(t) = \widetilde{K}_t \sin \left[\sigma \left(-\frac{K_2 M_1}{C_2 M_2} x_1(t - \tau_d) - \frac{K_2 M_2 - C_2^2}{C_2 M_2} x_2(t - \tau_d) + \frac{M_1}{M_2} \dot{x}_1(t - \tau_d) + \dot{x}_2(t - \tau_d) \right) \right]. \tag{36}$$

By inserting the values of the system parameters, we obtain the control function:

$$\delta \mathbf{x}(t) = \widetilde{K}_t \sin [\sigma(-295.4 x_1(t - \tau_d) - 141.6 x_2(t - \tau_d) \\ + 2\dot{x}_1(t - \tau_d) + \dot{x}_2(t - \tau_d))], \tag{37}$$

where the control gain $\widetilde{K}_t$, the feedback frequency σ, and the time-delay τ_d are the control parameters for the nonlinear time-delay feedback controller (37).

4. Chaotification on the QZS Vibration Isolation System

We will illustrate the benefits by proposing the 2-DOF QZS isolation system for chaotification, in comparison with the case of nonlinear isolation system used in [17]. The discussion will be focused on the three aspects including the effective reduction of critical control gain, the suppression of line spectra, and how the feature of line spectra of the system would be weakened or even be eliminated by using the approach.

4.1. Effective Reduction of Critical Control Gain. We are interested in the actual reduction of the control gain when applying chaotification on the 2-DOF QZS VIS. By setting the control parameters at $\sigma = 50$ and $\tau_d = 20$ s, we will examine the persistence of chaotification across the variation of control gain $\widetilde{K}_t$, with particular concerns on the critical control gain for the onset of chaos. We will compare the difference between the nonlinear model in [14, 17] and the QZS model proposed in this paper under the same loading conditions.

Figure 9(a) shows the global bifurcation of the nonlinear model [17], and Figure 9(b) shows the global bifurcation of the QZS model (17). Line dots in the vicinity of the origin represent periodic motions, and the cloudy dots represent the onset of chaos. From Figure 9(a), we can see that chaotification occurs when $|\widetilde{K}_t| \geq 0.452$ N. For the corresponding QZS system (17), as shown in Figure 9(b), chaotification starts when $|\widetilde{K}_t| \geq 0.008$ N and maintains across the whole parametric domain. Note that there is a significant difference in the required control gain between the two systems; the minimum control for the QZS system is only about 1.77% of that, for the nonlinear system. It indicates that the QZS system outperforms the nonlinear system [17] in terms of using small control in chaotification.

Figure 9 also indicates that the small control gain gives rise to relatively low amplitude of system responses, which means small control for chaotification can lead to low intensity of line spectra as well. Apart from the benefit of using small control, the QZS system inherently enables to attenuate vibration in low-frequency bandwidth. Thus, the utilization of the QZS system allows for the synergistic benefits of both chaotification and vibration isolation and is greatly favorable and attractive to applications.

4.2. Suppression of Line Spectra. We may benefit from the introduction of the QZS system (17) into chaotification. A comparison between the system [17] and the QZS system (17) will be carried out to indicate the performance in the reduction of the intensity of line spectra.

We show a numerical example in Figure 10, where the power spectral density (PSD) of chaotified system responses is plotted for system [17] and the QZS system (17), respectively, under the same loading conditions and the external excitation. In general, the spike line of the power spectra induced by the external excitation is covered by the continuous power spectra of chaotified responses. Thus, there is no significant spike lines protruded from the base of power spectra. The profile of the power spectra also indicates the broadband nature of system responses, implying the effectiveness of chaotification for the both systems under control.

Figure 10(a) shows that the peak value for system [17] is about −71.68 dB, while Figure 10(b) shows that the peak value for the QZS system is about −81.47 dB. Obviously, in terms of line spectrum suppression, the QZS system outperforms system [17] by about 10 dB. For the interval from 0 to 20 in the frequency domain, we can see that the QZS system is more efficient in the reduction of the intensity of line spectra. This advantage lies on two factors. Number one, the control gain required for system [17] is much larger than that of the QZS system. Small control results in low intensity of line spectra. Number two, the QZS system has better attenuation ability, especially in the low-frequency bandwidth. This nature reduces the intensity of power spectra of the response.

4.3. Reconstruction of Line Spectra. In the course of numerical analysis of line spectrum reconstruction, we can observe that chaotification on the QZS vibration isolation system constantly persists across a large range of settings for the time-delay τ_d and the feedback frequency σ. The profile of power spectra could be altered by choosing different settings of the control parameter pair (τ_d, σ). We are interested in the results where the reconstructed pattern of power spectra is smooth and broadened without line spikes protruded from the base of the power spectra when applying time-delay control. The whole purpose of chaotification is to eliminate the signature of line spectra induced by vibration excitations. In this regard, optimal design [15] of the control parameter
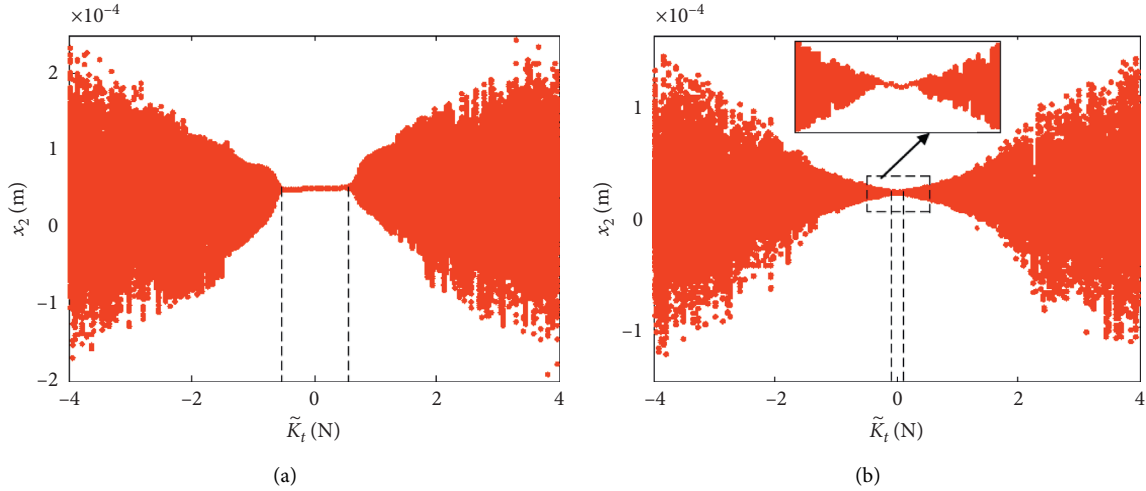
FIGURE 9: The system response versus feedback control gain $\widetilde{K}_t$; the cloudy dots represent chaotic motion and line dots denote periodic motion. (a) Response of nonlinear system [17] and (b) response of the QZS system (17).
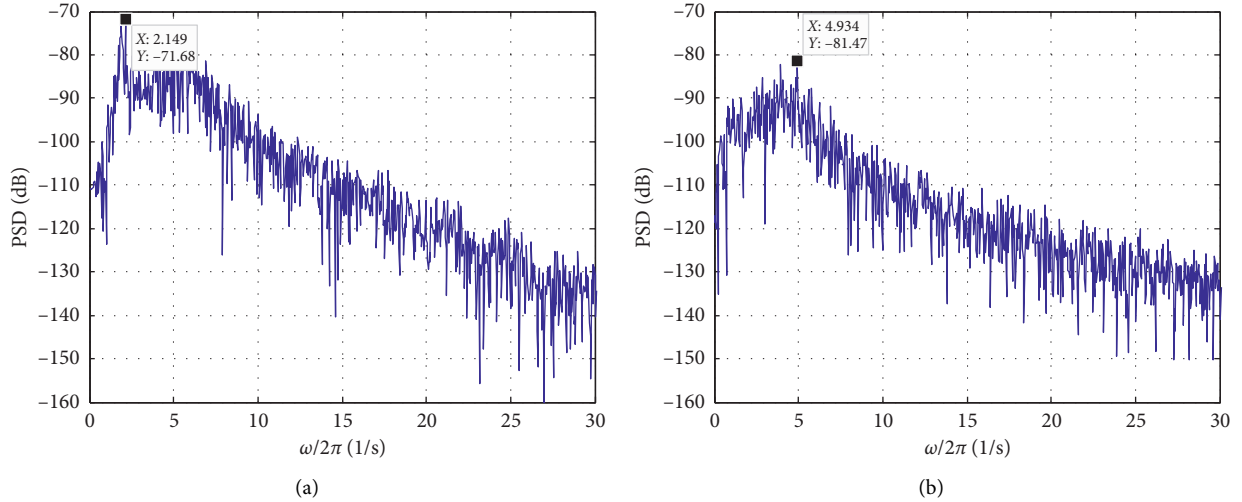
FIGURE 10: Power spectral densities of chaotified responses for (a) the nonlinear system [17] and (b) the QZS system, under the excitation at the frequency of $(\omega/2\pi) = 15.9155$.

pair (τ_d, σ) will be useful for obtaining a favorable configuration of line spectra.

In what follows, we will examine the effect of chaotification on the reconstruction of power spectra. There is a significant difference in the patterns of power spectra before and after the implementation of control. Since the formation of line spectra much depends on the excitation frequency, we consider three typical frequencies at the low frequency at 1.6711 which is smaller than the first natural frequency at 1.7311 of system (17), the intermediate frequency at 4.7746 which is in between the first and second natural frequency, and the high frequency at 22.2817 which is far away from the second natural frequency at 5.7234. We will see how the line spikes of power spectra induced by excitations, as shown in the 1st row of Figure 10, can be masked by chaotification at the three frequencies, as shown in the 2$^{\text{nd}}$ row of Figure 11.

Case 1. Chaotification at low-excitation frequency at $(\omega/2\pi) = 1.6711$.

Figure 11(a) illustrates the patterns of power spectra without control. There are two line spikes protruded from the base of power spectra, where the first peak represents a periodic motion at the excitation frequency and the second peak represents a subharmonic motion near the first resonance induced by the excitation. Surely, the system experiences periodic oscillations and the line feature of the power spectra is obvious. On the contrary, Figure 11(b) shows the reconstructed pattern of the power spectra after applying control, where the parameter pair of optimal control [15] is set at $(\tau_d, \sigma)_{\text{opt}} = (0.8266, 1.8026)$ and the control gain is $\widetilde{K}_{tc} = 50$ N. It can be observed that the new shape of the power spectra completely masks the second line spike but is unable to cover up the first spike. Based on extensive numerical tests, we found that it is relatively difficult to

(a)

(b)

(c)

(d)

(e)

(f)
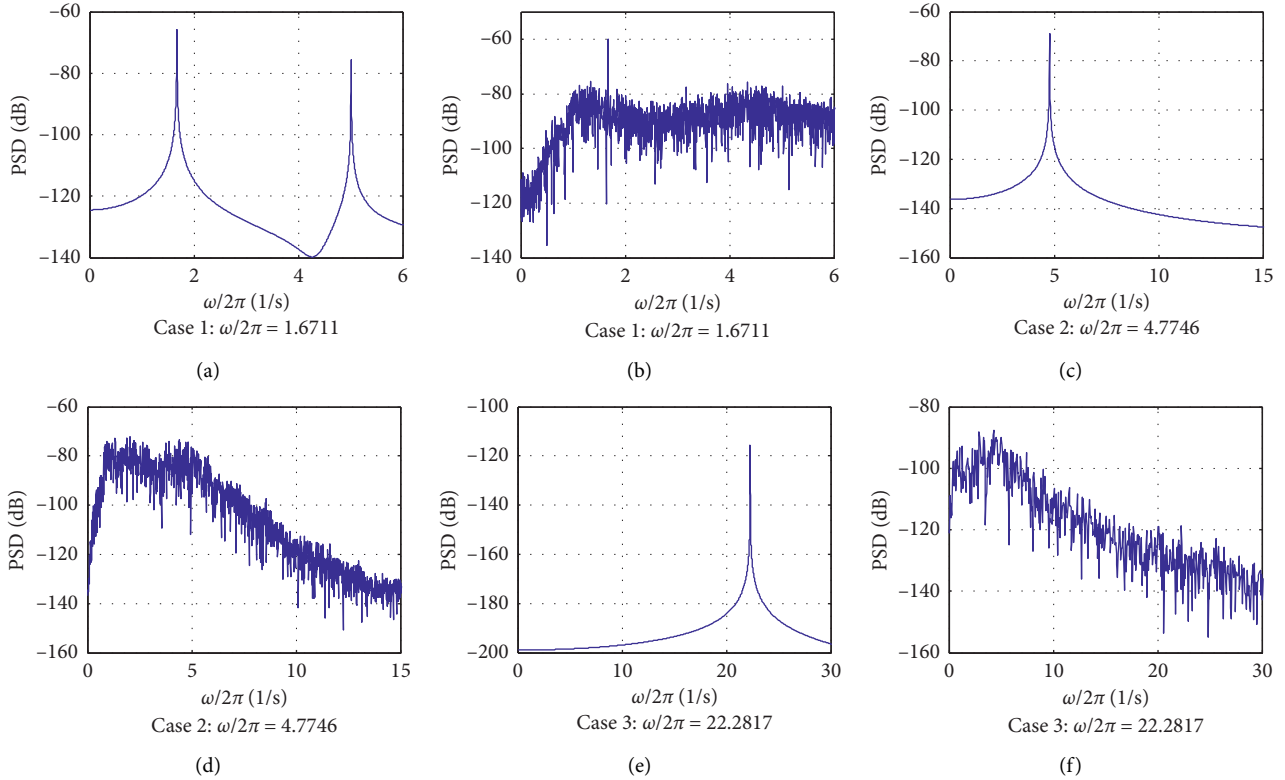
FIGURE 11: Profiles of power spectral densities of the QZS system response transmitted to the base without control (the 1st row) and with control (the 2nd row) at different excitation frequencies.

eliminate the line spikes in the low-frequency band in comparison with high-frequency band. Nevertheless, chaotification can weaken the signature of line spectra in general, and the feature of the second spike is completely eliminated.

Case 2. Chaotification at intermediate frequency at $(\omega/2\pi) = 4.7746$.

Similarly, Figure 11(c) shows the power spectra without control when applying an excitation at $(\omega/2\pi) = 4.7746$. The line spike protruded from the base indicates a periodic motion of the system at excitation frequency, and the intensity of the line spike is -68.98 dB. This line spectrum signifies the features of the machinery vibration of vehicles, for example, the operating speed according to the frequency of the line spike and the distance between the noise source and signal detector by the intensity of the line spectrum. To eliminate the features, we implement chaotification by setting the parameter pair of optimal control at $(\tau_d, \sigma)_{opt} = (0.2789, 1.1964)$, and the control gain $\widetilde{K}_{tc} = 45$ N. Figure 11(d) shows the reconstructed pattern of the power spectra of the system with the control. It is clear to be seen that the feature of the line spike is completely eliminated and replaced by the chaotic broadband spectra. Moreover, the intensity of the spectra around the excitation frequency is reduced to -79.03 dB. There is about 10 dB reduction. It means that, for certain frequency, the optimal chaotification not only covers the line spectra but also is possible to decrease its intensity.
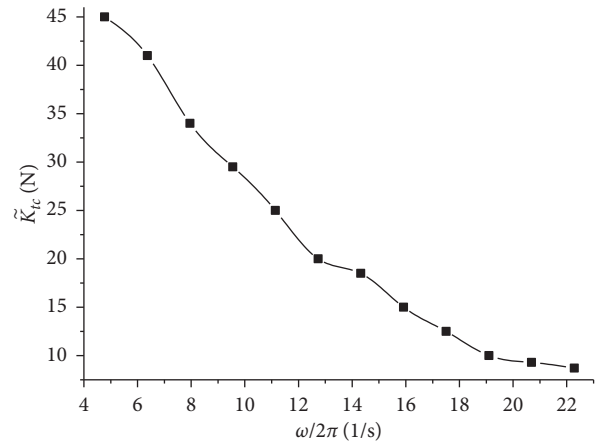
FIGURE 12: The required control gains for chaotification versus the excitation frequency.

Case 3. Chaotification at high frequency at $(\omega/2\pi) = 22.2817$.

Figure 11(e) shows the line spectrum without control when excited at $(\omega/2\pi) = 22.2817$, while Figure 11(f) shows the reformed pattern of the power spectra by applying the control at $(\tau_d, \sigma)_{opt} = (0.3970, 65.0355)$ and the control gain $\widetilde{K}_{tc} = 8.7$ N. The feature of the line spectrum at the excitation frequency is covered by the chaotic broadband spectra. However, the intensity of power spectra corresponding to the low-frequency bandwidth increases in this case.

Nevertheless, the power spectra after chaotification do not carry the information of the signal feature of the vibration source.

The required control gain for effective chaotification in general decreases as the external excitation frequency increases. This characteristic can be observed from Cases 1–3, where the control gain for chaotification reduces corresponding to the frequencies. Figure 12 plots the trend to describe the relationship between the required control gains and the excitation frequency for chaotification. In general, the higher excitation frequency, the less control energy required for chaotification. Meanwhile, the line spectra at high excitation frequency can be eliminated more easily.

5. Conclusion

The most valuable part of this paper is to propose a QZS system for chaotification that can be used to reduce the feature of line spectra induced by machinery vibration of underwater vehicles. This work combines the characteristic of small stiffness of the QZS system with the need of small control in chaotification, leading to the advantages of the reduction of the intensity of line spectra and the improvement of efficiency in the reconstruction of line spectra.

A standard procedure has been presented for the chaotification on a double-layer QZS system. We have shown the derivation of the nonlinear time-delay controller for such a system. Numerical simulations have illustrated the superior performance of the QZS system in terms of the required critical control gain and the suppression of line spectra in comparison with a nonlinear model previous studied in [17], especially outperformed in low-frequency band. In the reconstruction of line spectrum patterns, chaotification can effectively change a narrowband line spectrum induced by a harmonic excitation into a spectrum pattern with broad bandwidth. We have examined the performance of the new system in low-, intermediate-, and high-frequency bands divided according to the natural frequencies of the system. It showed that the feature of line spectra could be completely eliminated for the intermediate- and high-frequency bandwidth. It is relatively difficult to remove the line spikes in the low-frequency band, but the signal feature can be greatly weakened through a chaotification process.

Data Availability

Some or all data, models, or code that support the findings of this study are available from the corresponding author upon reasonable request.

Conflicts of Interest

The authors declare that they have no conflicts of interest.

Acknowledgments

References

[1] M. W. Hiller, M. D. Bryant, and J. Umegaki, "Attenuation and transformation of vibration through active control of magnetostrictive terfenol," *Journal of Sound and Vibration*, vol. 134, no. 3, pp. 507–519, 1989.

[2] M. D. Jenkins, P. A. Nelson, R. J. Pinnington, and S. J. Elliott, "Active isolation of periodic machinery vibrations," *Journal of Sound and Vibration*, vol. 166, no. 1, pp. 117–140, 1993.

[3] C. Spelta, F. Previdi, S. M. Savaresi, G. Fraternale, and N. Gaudiano, "Control of magnetorheological dampers for vibration reduction in a washing machine," *Mechatronics*, vol. 19, no. 3, pp. 410–421, 2009.

[4] J.-J. Lou, S.-J. Zhu, L. He, and X. Yu, "Application of chaos method to line spectra reduction," *Journal of Sound and Vibration*, vol. 286, no. 3, pp. 645–652, 2005.

[5] J.-J. Lou, S.-J. Zhu, L. He, and Q.-W. He, "Experimental chaos in nonlinear vibration isolation system," *Chaos, Solitons & Fractals*, vol. 40, no. 3, pp. 1367–1375, 2009.

[6] X. Yu, S. J. Zhu, and S. Y. Liu, "A new method for line spectra reduction similar to generalized synchronization of chaos," *Journal of Sound and Vibration*, vol. 306, no. 3–5, pp. 835–848, 2007.

[7] S. Y. Liu, X. Yu, and S. J. Zhu, "Study on the chaos anti-control technology in nonlinear vibration isolation system," *Journal of Sound and Vibration*, vol. 310, no. 4-5, pp. 855–864, 2008.

[8] N. F. Rulkov, M. M. Sushchik, L. S. Tsimring, and H. D. I. Abarbanel, "Generalized synchronization of chaos in directionally coupled chaotic systems," *Physical Review E*, vol. 51, no. 2, pp. 980–994, 1995.

[9] Y. Li, D. Xu, Y. Fu, and J. Zhou, "Chaotification and optimization design of a nonlinear vibration isolation system," *Journal of Vibration and Control*, vol. 18, no. 14, pp. 2129–2139, 2012.

[10] G. L. Wen, Y. Z. Lu, Z. Y. Zhang, C. S. Ma, H. F. Yin, and Z. Cui, "Line spectra reduction and vibration isolation via modified projective synchronization for acoustic stealth of submarines," *Journal of Sound and Vibration*, vol. 324, no. 3–5, pp. 954–961, 2009.

[11] D. L. Xu, "Control of projective synchronization in chaotic systems," *Physical Review E*, vol. 63, no. 2, Article ID 027201, 2001.

[12] Z. H. Zhang, S. J. Zhu, and S. Y. Liu, "A new method of chaotic anti-control for line spectra reduction of vibration isolation system," in *Proceedings of the ASME International Design Engineering Technical Conferences and Computers and Information in Engineering Conference*, vol. 3, pp. 31–36, The American Society of Mechanical Engineers, New York, NY, USA, August 2010.

[13] J. X. Zhou, D. L. Xu, and Y. L. Li, "Chaotifing duffing-type system with large parameter range based on optimal time-delay feedback control," in *Proceedings of 2010 International Workshop on Chaos-Fractal Theories and Applications*, pp. 121–126, Kunming, China, October 2010.

[14] Y. L. Li, D. L. Xu, Y. M. Fu, and J. X. Zhou, "Stability and chaotification of vibration isolation floating raft systems with time-delayed feedback control," *Chaos: An Interdisciplinary Journal of Nonlinear Science*, vol. 21, no. 3, Article ID 033115, 2011.

[15] J. Zhou, D. Xu, J. Zhang, and C. Liu, "Spectrum optimization-based chaotification using time-delay feedback control," *Chaos, Solitons & Fractals*, vol. 45, no. 6, pp. 815–824, 2012.

[16] Y. Li, D. Xu, Y. Fu, and J. Zhou, "Nonlinear dynamic analysis of 2-DOF nonlinear vibration isolation floating raft systems with feedback control," *Chaos, Solitons & Fractals*, vol. 45, no. 9-10, pp. 1092–1099, 2012.

[17] J. Zhang, D. Xu, J. Zhou, and Y. Li, "Chaotification of vibration isolation floating raft system via nonlinear time-delay feedback control," *Chaos, Solitons & Fractals*, vol. 45, no. 9-10, pp. 1255–1265, 2012.

[18] Y. Li, D. Xu, Y. Fu, and J. Zhou, "Chaotification of a nonlinear vibration isolation system by dual time-delayed feedback control," *International Journal of Bifurcation and Chaos*, vol. 23, no. 6, Article ID 1350096, 2013.

[19] X. F. Wang, G. Chen, and X. Yu, "Anticontrol of chaos in continuous-time systems via time-delay feedback," *Chaos: An Interdisciplinary Journal of Nonlinear Science*, vol. 10, no. 4, pp. 771–779, 2000.

[20] X. F. Wang, "Generating chaos in continuous-time systems via feedback control," in *Chaos Control: Theory and Applications*, G. R. Chen and X. Yu, Eds., vol. 292, pp. 179–204, Springer, Berlin, Germany, 2003.

[21] A. Carrella, M. J. Brennan, and T. P. Waters, "Static analysis of a passive vibration isolator with quasi-zero-stiffness characteristic," *Journal of Sound and Vibration*, vol. 301, no. 3–5, pp. 678–689, 2007.

[22] I. Kovacic, M. J. Brennan, and T. P. Waters, "A study of a nonlinear vibration isolator with a quasi-zero stiffness characteristic," *Journal of Sound and Vibration*, vol. 315, no. 3, pp. 700–711, 2008.

[23] A. Carrella, M. J. Brennan, I. Kovacic, and T. P. Waters, "On the force transmissibility of a vibration isolator with quasi-zero-stiffness," *Journal of Sound and Vibration*, vol. 322, no. 4-5, pp. 707–717, 2009.

[24] J. Zhou, L. Dou, K. Wang, D. Xu, and H. Ouyang, "A nonlinear resonator with inertial amplification for very low-frequency flexural wave attenuations in beams," *Nonlinear Dynamics*, vol. 96, no. 1, pp. 647–665, 2019.

[25] K. Wang, J. Zhou, C. Cai, D. Xu, and H. Ouyang, "Mathematical modeling and analysis of a meta-plate for very low-frequency band gap," *Applied Mathematical Modelling*, vol. 73, pp. 581–597, 2019.

[26] D. Xu, Q. Yu, J. Zhou, and S. R. Bishop, "Theoretical and experimental analyses of a nonlinear magnetic vibration isolator with quasi-zero-stiffness characteristic," *Journal of Sound and Vibration*, vol. 332, no. 14, pp. 3377–3389, 2013.

[27] J. Forde and P. Nelson, "Applications of Sturm sequences to bifurcation analysis of delay differential equation models," *Journal of Mathematical Analysis and Applications*, vol. 300, no. 2, pp. 273–284, 2004.

[28] A. Isidori, *Nonlinear Control Systems*, vol. 2, Springer, Berlin, Germany, 1999.

Research Article

The Solvability of Fractional Elliptic Equation with the Hardy Potential

Siyu Gao,[1] Shuibo Huang [ID],[1,2] Qiaoyu Tian [ID],[1] and Zhan-Ping Ma [ID][3]

[1]*School of Mathematics and Computer Science, Northwest Minzu University, Lanzhou, Gansu 730030, China*
[2]*Key Laboratory of Streaming Data Computing Technologies and Application, Northwest Minzu University, Lanzhou, Gansu 730030, China*
[3]*School of Mathematics and Information Science, Henan Polytechnic University, Jiaozuo, Henan 454003, China*

Correspondence should be addressed to Shuibo Huang; huangshuibo2008@163.com

In this paper, we study the existence and nonexistence of solutions to fractional elliptic equations with the Hardy potential
$$\begin{cases} (-\Delta)^s u - \lambda(u/|x|^{2s}) = u^{r-1} + \delta g(u), & \text{in } \Omega, \\ u(x) > 0, & \text{in } \Omega, \\ u(x) = 0, & \text{in } \mathbb{R}^N \setminus \Omega, \end{cases}$$
where $\Omega \subset \mathbb{R}^N$ is a bounded Lipschitz domain with $0 \in \Omega$, $(-\Delta)^s$ is a fractional Laplace operator, $s \in (0,1)$, $N > 2s$, δ is a positive number, $2 < r < r(\lambda, s) \equiv (N + 2s - 2\alpha_\lambda / N - 2s - 2\alpha_\lambda) + 1$, $\alpha_\lambda \in (0, ((N-2s)/2))$ is a parameter depending on λ, $0 < \lambda < \Lambda_{N,s}$, and $\Lambda_{N,s} = 2^{2s}(\Gamma^2((N+2s)/4))/(\Gamma^2((N-2s)/4))$ is the sharp constant of the Hardy–Sobolev inequality.

1. Introduction

In this paper, we consider the solvability of the following fractional elliptic problem:

$$\begin{cases} (-\Delta)^s u - \lambda \dfrac{u}{|x|^{2s}} = u^{r-1} + \delta g(u), & \text{in } \Omega, \\ u > 0, & \text{in } \Omega, \\ u = 0, & \text{in } \mathbb{R}^N \setminus \Omega, \end{cases} \tag{1}$$

where $\Omega \subset \mathbb{R}^N$ is a bounded Lipschitz domain with $0 \in \Omega$, $s \in (0,1)$, $N > 2s$, $2 < r < r(\lambda, s) \equiv ((N + 2s - 2\alpha_\lambda)/(N - 2s - 2\alpha_\lambda)) + 1$, $0 < \lambda < \Lambda_{N,s}$, and $\Lambda_{N,s} = 2^{2s}((\Gamma^2((N+2s)/4))/(\Gamma^2((N-2s)/4)))$ is the sharp constant of the Hardy–Sobolev inequality; the fractional Laplace operator $(-\Delta)^s$ is defined by

$$(-\Delta)^s u = C(N,s)\text{P.V.} \int_{\mathbb{R}^N} \frac{u(x) - u(y)}{|x - y|^{N+2s}} \, dy, \tag{2}$$

where P.V. stands for the Cauchy principal value and constant $C(N,s)$ is a constant.

Recently, much attention has been devoted to the study of fractional Laplacian equations. One of the reasons comes from the fact that the fractional Laplacian arises in various areas and different applications, such as phase transitions, finance, stratified materials, flame propagation, ultra-relativistic limits of quantum mechanics, and water waves. For more details, see [1–6] and references therein.

For fractional elliptic problems with the Hardy potential, Abdellaoui et al. [7] obtained the existence and summability of solutions to a class of nonlocal elliptic problem:

$$\begin{cases} (-\Delta)^s u - \lambda \dfrac{u}{|x|^{2s}} = f(x,u), & \text{in } \Omega, \\ u > 0, & \text{in } \Omega, \\ u = 0, & \text{in } \mathbb{R}^N \setminus \Omega, \end{cases} \tag{3}$$

with $f \in L^m(\Omega)$ and $0 < \lambda < \Lambda_{N,s}$. They mainly considered the summability of solutions to (3) with $f(x, u) = f(x)$ and the existence and regularity of solutions to (3) with $f(x, u) = h(x)/u^\sigma$. Mi et al. [8] obtained the combined influence of the Hardy potential and lower order terms on the existence and regularity of solutions to the problem:

$$
\begin{cases}
(-\Delta)^s u - \lambda \dfrac{u}{|x|^{2s}} + u^p = f(x), & \text{in } \Omega, \\[2mm]
u > 0, & \text{in } \Omega, \\[2mm]
u = 0, & \text{in } \mathbb{R}^N \setminus \Omega.
\end{cases}
\tag{4}
$$

Barrios et al. [9] discussed the existence and multiplicity of solutions to the following fractional elliptic equation:

$$
\begin{cases}
(-\Delta)^s u - \lambda \dfrac{u}{|x|^{2s}} = u^p + \mu u^q, & \text{in } \Omega, \\[2mm]
u > 0, & \text{in } \Omega, \\[2mm]
u = 0, & \text{in } \mathbb{R}^N \setminus \Omega,
\end{cases}
\tag{5}
$$

where $0 < \lambda < \Lambda_{N,s}$, $0 < q < 1$,

$$
1 < p < p(\lambda, s) = \frac{N + 2s - 2\alpha_\lambda}{N - 2s - 2\alpha_\lambda},
\tag{6}
$$

and $\alpha_\lambda \in (0, (N - 2s/2))$ is a parameter depending on λ. They shown that problem (5) has at least one solution if $1 < p < p(\lambda, s)$ and problem (5) has no solution if $p > p(\lambda, s)$.

Recently, Shang et al. [10] studied the existence and multiplicity of positive solutions to the following problem:

$$
(-\Delta)^s u - \mu \frac{u}{|x|^{2s}} = \lambda g(x) u^p + K(x) u^{2^*_s - 1}, \quad \text{in } \mathbb{R}^N,
\tag{7}
$$

where $s \in (0, 1)$, $N > 2s$, $0 < p < 2^*_s - 1$, and $0 < \mu < \Lambda_{N,s}$. Some other results of fractional elliptic equations with the Hardy potential, see [7, 9, 11–14] and references therein.

The local version of quasilinear problem related to problem (8) has been considered by Boccardo et al. [15]. They analyzed the existence of nontrivial solutions to the following problem:

$$
\begin{cases}
-\Delta_p u = |u|^{r-2} u + \lambda g(u), & \text{in } \Omega, \\
u > 0, & \text{in } \Omega, \\
u = 0, & \text{on } \partial\Omega,
\end{cases}
\tag{8}
$$

where $\Omega \subset \mathbb{R}^N$ is a smooth bounded domain, $1 < p < N$, $r > p$, $g: \Omega \times \mathbb{R} \longrightarrow \mathbb{R}$ is a Carathéodory function, and there exist constants $c_1 > 0$ and $q \in (1, p)$ such that $g(s) \le c_1 s^{q-1}$ for any $s > 0$.

Motivated by the above works, the aim of this paper is to study the existence of solutions to problem (1) by the method of subsuper solutions and taking into advantage the combined effect of concave and convex nonlinearity.

We make the following assumptions:

(F1)

$$
2 < r < r(\lambda, s) \equiv \frac{N + 2s - 2\alpha_\lambda}{N - 2s - 2\alpha_\lambda} + 1,
\tag{9}
$$

where $\alpha_\lambda \in (0, ((N - 2s)/2))$ is a parameter depending on λ.

(F2) $g: \Omega \times \mathbb{R} \longrightarrow \mathbb{R}$ is Carathéodory function, and there exist constants $c_1 > 0$ and $q \in (1, 2)$, such that, for any $\sigma > 0$,

$$
g(\sigma) \le c_1 \sigma^{q-1}.
\tag{10}
$$

(F3) The function

$$
u \longrightarrow u^{r-1} + \delta g(u) \text{ is nondecreasing.}
\tag{11}
$$

(F4) Define

$$
M_0 = \varliminf_{z \longrightarrow 0^+} \frac{g(z)}{z},
\tag{12}
$$

for all $\tau > 0$,

$$
M_1(\tau) = \inf_{0 \le z \le (\tau \lambda_1)^{1/(r-2)}} \frac{g(z)}{z},
\tag{13}
$$

where λ_1 is the first eigenvalue of $(-\Delta)^s$ in Ω.

Now, we state our main result.

Theorem 1. *Suppose* (F1) − (F4) *hold. Then, there exists a positive constant δ_0, such that, for all $\delta \in (\lambda_1/M_0, \delta_0]$, problem (1) has at least a nonnegative solution if $M_0 > (\lambda_1/\delta_0)$, where M_0 is defined by (12).*

Remark 1. In order to prove the above theorem, we study directly to the pseudodifferential operator, without the harmonic extension to an extra dimension by transforming the nonlocal problem into a local problem due to Caffarelli and Silvestre [16].

Remark 2. To establish the upper bound for r (see (9)), we consider a radial solution $w = A|x|^{((2s-N)/2)+\beta}$ with constant $A > 0$ to the problem:

$$
(-\Delta)^s w - \lambda \frac{w}{|x|^{2s}} = w^{r-1}.
\tag{14}
$$

We obtain

$$
\begin{aligned}
& A\gamma_\beta |x|^{-2s+((2s-N)/2)+\beta} - \lambda A |x|^{-2s+((2s-N)/2)+\beta} \\
& = A^{r-1} |x|^{(((2s-N)/2)+\beta)(r-1)},
\end{aligned}
\tag{15}
$$

where

$$\gamma_\beta := \frac{\pi^{2s}\Gamma((N+2s+2\beta)/4)\Gamma((N+2s-2\beta)/4)}{\Gamma((N-2s-2\beta)/4)\Gamma((N-2s+2\beta)/4)}. \quad (16)$$

In order to have homogeneity, we have

$$\frac{2s-N}{2}+\beta = \frac{-2s}{r-2}. \quad (17)$$

Thus, we deduce that $\gamma_\beta - \lambda = A^{r-2}$. Since $A > 0$, we conclude that $\gamma_\beta - \lambda > 0$. Note that the map γ: $[0, ((N-2s)/2)) \longmapsto (0, \Lambda_{N,s}]$ is decreasing about β, see [17, 18]. Hence, there is a unique element α_λ such that $\gamma_{\alpha_\lambda} = \lambda$. Thus, we have $\alpha_\lambda > \beta$, that is,

$$\alpha_\lambda > \frac{-2s}{r-2}+\frac{N-2s}{2}, \quad (18)$$

which implies that

$$r < \frac{N+2s-2\alpha_\lambda}{N-2s-2\alpha_\lambda}+1 := r(\lambda, s). \quad (19)$$

Therefore, we can construct a supersolution to problem (1) for $r < r(\lambda, s)$, just modifying the w found above. Thus, $r(\lambda, s)$ is the threshold for the existence to problem (1).

Now, we consider the nonexistence of solution to problem (1).

Theorem 2. *Suppose* $(F1) - (F4)$ *hold. Then, problem (1) has no solution in* H_0^s *if for some* $\tau > 1$, $M_1(\tau) > 0$, *and* $\delta > \lambda_1/M_1(\tau)$, *where* M_0 *and* M_1 *are defined by (12) and (13), respectively.*

The following two examples also appeared in [15].

Remark 3. An example of function $g(\sigma) \equiv \sigma^q$ with $0 < q < 1$, which satisfies conditions (10) and (11) for any $\delta \in (0, \delta_0]$, such that problem (1) has at least one positive solution. In this condition $M_0 = \infty$, by (52), we have $\eta^{r-q}c_1^{-1}C_1^{2-q}(C_1 - C_1^r) \geq \delta$. Define

$$\Phi(C_1) = \eta^{r-q}c_1^{-1}C_1^{2-q}(C_1 - C_1^r). \quad (20)$$

It is easy to see that

$$\frac{d}{dC_1}\Phi(C_1) = 0 \Longleftrightarrow C_1 = C_{1,0} := \left(\frac{3-q}{2-q+r}\right)^{1/(r-1)}. \quad (21)$$

We have to prove that δ is smaller than the minimum of $\Phi(C_1)$. Therefore, we have

$$\delta_0 = \Phi(C_{1,0}) = \eta^{r-q}c_1^{-1}\left(\frac{3-q}{2-q+r}\right)^{1/(r-1)}\left[\left(\frac{3-q}{2-q+r}\right)^{(2-q)/(r-1)}-\left(\frac{3-q}{2-q+r}\right)^{(1-q+r)/(r-1)}\right]. \quad (22)$$

Moreover, by (10) and (13), we have for any $\tau > 1$,

$$M_1(\tau)\delta_0 \leq M_1(1)\delta_0 \leq c_1\delta_0 \inf_{0 < z \leq \lambda_1^{1/(r-2)}}|z|^{q-2} \equiv c_1\delta_0\lambda_1^{(q-2)/(r-2)}. \quad (23)$$

Thus, for any $\tau > 1$, $M_1(\tau) \leq c_1\lambda_1^{(q-2)/(r-2)}$. Hence, problem (1) has no solution at least $\delta > c_1\lambda_1^{(r-q)/(r-2)}$. Therefore, the result of the above theorem is more general than [9].

Remark 4. We consider the function

$$g(\sigma) = \frac{\sigma|\sigma|^{\theta-1}}{1+\sigma|\sigma|^{\alpha-1}}, \quad (24)$$

for $0 < \alpha < \theta < 1$. We easily deduce that conditions (10) and (11) are fulfilled and $M_0 = \infty$. On the contrary,

$$M_1(\tau) = \inf_{0 \leq z \leq (\tau\lambda_1)^{1/(r-2)}}\frac{z^{\theta-1}}{1+z^\alpha}. \quad (25)$$

If $\alpha > \theta - 1$, the function $z^{\theta-1}/(1+z^\alpha)$ is monotone decreasing for $z \geq 0$. Then,

$$M_1(\tau) = \frac{(\tau\lambda_1)^{(\theta-1)/(r-2)}}{1+(\tau\lambda_1)^{\alpha/(r-2)}}. \quad (26)$$

Similarly, in this case, problem (1) has no solution provided

$$\delta > \lambda_1^{(r-\theta-1)/(r-2)}\left(1+\lambda_1^{\alpha/(r-2)}\right). \quad (27)$$

Remark 5. The function $\tau \longrightarrow M_1(\tau)$ is nonincreasing. Hence, if $\delta > \lambda_1/M_1(\tau_0)$, for some $\tau_0 > 1$, the results of Theorem 1 will be true for any $\tau > \tau_0$.

The paper is organized as follows. In Section 2, we present some definitions and preliminary tools, which will be used in the Proof of Theorems 1 and 2. The Proof of Theorems 1 and 2 are given in Section 3 and Section 4, respectively.

2. Preliminaries and Function Setting

In this section, we recall some known results for reader's convenience.

Denote the space

$$\mathcal{L}^s := \left\{u: \mathbb{R}^N \longrightarrow \mathbb{R} \text{ is measurable: } \int_{\mathbb{R}^N}\frac{|u(x)|}{(1+|x|^{N+2s})}dx < \infty\right\}, \quad (28)$$

equipped with the norm

$$\|u\|_{\mathcal{L}^s} := \int_{\mathbb{R}^N}\frac{|u(x)|}{(1+|x|^{N+2s})}dx. \quad (29)$$

Let Ω be an open subset of $\mathbb{R}^N$. Given $u \in \mathscr{L}^s$ and φ in the Schwartz class, the distribution $(-\Delta)^s u$ in $\mathscr{D}'(\Omega)$ is defined as

$$\langle (-\Delta)^s u, \varphi \rangle = \int_{\mathbb{R}^N} u(-\Delta)^s \varphi \, dx, \quad \text{for any } \varphi \in C_c^\infty(\Omega). \tag{30}$$

We give some useful facts for the fractional Sobolev space.

Definition 1. Let $s \in (0,1)$, and define the fractional Sobolev space:

$$H^s(\mathbb{R}^N) = \left\{ u \in L^2(\mathbb{R}^N) : |\xi|^s \hat{u} \in L^2(\mathbb{R}^N) \right\}. \tag{31}$$

We need to consider the space $X_0^s(\Omega)$, which is defined as

$$X_0^s(\Omega) = \left\{ u \in H^s(\mathbb{R}^N), u = 0 \text{ a.e. in } \mathbb{R}^N \backslash \Omega \right\}, \tag{32}$$

with the norm

$$\|u\|_{X_0^s(\Omega)} = \left(\int_Q \frac{|u(x) - u(y)|^2}{|x-y|^{N+2s}} \, dx \, dy \right)^{1/2}, \tag{33}$$

where $Q = \mathbb{R}^{2N} \backslash (\Omega^c \times \Omega^c)$. The pair $(X_0^s(\Omega), \|.\|_{X_0^s(\Omega)})$ yields a Hilibert space (see Lemma 7 in [19]).

We have to use the classical Sobolev theorem.

Theorem 3 (see [20], Theorem 6.5). *Let $s \in (0,1)$, then there exists a positive constant $S = S(N, s)$, such that, for any measurable and compactly supported function u: $\mathbb{R}^N \longrightarrow \mathbb{R}$, we have*

$$\|u\|_{L^{2_s^*}(\mathbb{R}^N)}^2 \leq S \int_{\mathbb{R}^N} \int_{\mathbb{R}^N} \frac{|u(x) - u(y)|^2}{|x-y|^{N+2s}} \, dx \, dy, \tag{34}$$

where 2_s^* is the so-called Sobolev critical exponent.

In this paper, we consider the existences of energy solution to problem (1) with the critical and subcritical cases.

Definition 2. We say that $u \in X_0^s(\Omega)$ is an energy solution to problem (1), if for any $\varphi \in X_0^s(\Omega)$,

$$\int_\Omega |u|^{r-2} u \varphi \, dx < \infty,$$

$$\int_\Omega \frac{u\varphi}{|x|^{2s}} \, dx < \infty,$$

$$\frac{C(N,s)}{2} \int_Q \frac{(u(x) - u(y))(\varphi(x) - \varphi(y))}{|x-y|^{N+2s}} \, dx \, dy \tag{35}$$

$$- \lambda \int_\Omega \frac{u\varphi}{|x|^{2s}} \, dx$$

$$= \int_\Omega u^{r-1} \varphi \, dx + \delta \int_\Omega g(u) \varphi \, dx.$$

We also need to consider the weak solution to problem (1).

Definition 3. We say that $u \in L^1(\Omega)$ is a weak solution to problem (1), if $u \geq 0$ a.e. in Ω, $u = 0$ in $\mathbb{R}^N \backslash \Omega$,

$$\int_\Omega \left(\lambda \frac{u}{|x|^{2s}} + u^{r-1} + \delta g(u) \right) \delta^s \, dx < \infty, \tag{36}$$

and for all $\varphi \in C^{2s+\beta}(\Omega) \cap C^s(\overline{\Omega})$, $\beta > 0$,

$$\int_\Omega u(-\Delta)^s \varphi \, dx = \int_\Omega \left(\lambda \frac{u}{|x|^{2s}} + u^{r-1} + \delta g(u) \right) \varphi \, dx, \tag{37}$$

where $\varphi = 0$ in $\mathbb{R}^N \backslash \Omega$ and $\delta(x) := \text{dist}(x, \partial\Omega)$.

Definition 4. If u satisfies

$$\begin{cases} (-\Delta)^s u - \lambda \dfrac{u}{|x|^{2s}} \geq u^{r-1} + \delta g(u), & \text{in } \Omega, \\[2mm] u \geq 0, & \text{in } \mathbb{R}^N \backslash \Omega, \end{cases} \tag{38}$$

in the weak sense, we say that u is a supersolution to problem (1).

If u satisfies

$$\begin{cases} (-\Delta)^s u - \lambda \dfrac{u}{|x|^{2s}} \leq u^{r-1} + \delta g(u), & \text{in } \Omega, \\[2mm] u \leq 0, & \text{in } \mathbb{R}^N \backslash \Omega, \end{cases} \tag{39}$$

in the weak sense, we say that u is a subsolution to problem (1).

Now, we recall the comparison lemma.

Lemma 1 (see [9]). *Let $u \in H^s(\mathbb{R}^N)$ and $v \in H^s(\mathbb{R}^N)$ be solutions, respectively, to*

$$\begin{cases} (-\Delta)^s u = f_1, & \text{in } \Omega, \\ u = g_1, & \text{in } \mathbb{R}^N \backslash \Omega, \\ (-\Delta)^s v = f_2, & \text{in } \Omega, \\ v = g_2, & \text{in } \mathbb{R}^N \backslash \Omega. \end{cases} \tag{40}$$

Then, $u(x) \leq v(x)$ for all $x \in \mathbb{R}^N$ if $f_1 \leq f_2$ and $g_1 \leq g_2$.

For the supercritical case, we need a prior regularity result, see [9], Lemma 2.2.

Lemma 2. *Given $f \in L^1(\Omega, \delta^s(x)dx)$, where $\delta(x) = \text{dist}(x, \partial\Omega)$. There exists a unique weak solution $v(x) \in L^1(\Omega)$ to*

$$\begin{cases} (-\Delta)^s v = f, & \text{in } \Omega, \\ v = 0, & \text{in } \mathbb{R}^N \backslash \Omega, \end{cases} \tag{41}$$

in the sense that

$$\int_\Omega v(-\Delta)^s \vartheta = \int_\Omega f\vartheta, \tag{42}$$

for all $\vartheta \in C^2(\overline{\Omega})$ with $\vartheta = 0$ in $\mathbb{R}^N \backslash \Omega$.

Moreover, $\|v\|_{L^1(\Omega)} \leq C \|f\|_{L^1(\Omega, \delta^s(x)dx)}$, for some constant C independent of f. In addition, if $f \geq 0$

$$\begin{cases} (-\Delta)^s v = f, & \text{in } \Omega, \\ v \geq 0, & \text{in } \mathbb{R}^N \setminus \Omega. \end{cases} \tag{43}$$

Then, $v \geq 0$ a.e. in Ω.

3. The Existence Result

We are now ready to prove Theorem 1 by employing the idea contained in [9, 15], whose proof will be split into several steps.

Proof of Theorem 1.

Step 1: subsolution to problem (1). We first consider the eigenvalue problem:

$$\begin{cases} (-\Delta)^s \varphi_1 = \lambda_1 \varphi_1, & \text{in } \Omega, \\ \varphi_1 = 0, & \text{in } \mathbb{R}^N \setminus \Omega. \end{cases} \tag{44}$$

Note that the eigenfunction $\varphi_1 \geq 0$ belongs to $X_0^s \cap L^\infty(\Omega)$.

Suppose $\delta M_0 > \lambda_1$, where M_0 is given in (12), by ($F4$), for all $\delta \in (\lambda_1/M_0, \delta_0]$, taking t small enough, we have

$$\frac{g(t\varphi_1)}{t\varphi_1} > \frac{\lambda_1}{\delta}. \tag{45}$$

Therefore, for $x \in \Omega$,

$$(-\Delta)^s (t\varphi_1) = \lambda_1 t\varphi_1 < \delta g(t\varphi_1) \leq \delta g(t\varphi_1) + (t\varphi_1)^{r-1} + \lambda \frac{t\varphi_1}{|x|^{2s}}. \tag{46}$$

Therefore,

$$\begin{cases} (-\Delta)^s (t\varphi_1) \leq \delta g(t\varphi_1) + (t\varphi_1)^{r-1} + \lambda \frac{t\varphi_1}{|x|^{2s}}, & \text{in } \Omega, \\ t\varphi_1 = 0, & \text{in } \mathbb{R}^N \setminus \Omega. \end{cases} \tag{47}$$

Thus, $\underline{u} := t\varphi_1$ is a subsolution to problem (1).

Next, we consider supersolution to problem (1) in the subcritical and supercritical case, respectively.

Step 2: supersolution for subcritical and critical case: $2 < r \leq 2_s^*$. We look for a supersolution of the form $w(x) := A|x|^{-\beta}$ with $A \geq 0$ and $\beta > 0$ as real parameters and verify

$$\beta < \frac{N - 2s}{2}. \tag{48}$$

Since $r \leq 2_s^*$, we obtain

$$(r - 1)\beta < \beta + 2s, \tag{49}$$

$$\beta r < N. \tag{50}$$

By (49), we deduce that

$$(-\Delta)^s w - \lambda \frac{w}{|x|^{2s}} \geq w^{r-1}, \quad \text{in } \Omega, \tag{51}$$

for the appropriate choice of A.

Let $\eta := \inf_\Omega w > 0$. Taking $\overline{u} = C_1 w$ with $0 < C_1 < 1$, which is a suitable constant such that, for δ small enough, and by (10) we have

$$\eta^{r-p} \geq \frac{\delta c_1}{C_1^{1-q}(C_1 - C_1^r)}, \tag{52}$$

where δ appears in (1).

By (52), we obtain

$$\begin{cases} (-\Delta^s)\overline{u} - \lambda \frac{\overline{u}}{|x|^{2s}} \geq \overline{u}^{r-1} + \delta g(\overline{u}), & \text{in } \Omega, \\ \overline{u} \geq 0, & \text{in } \mathbb{R}^N \setminus \Omega. \end{cases} \tag{53}$$

Thus, we have concluded that $C_1 w$ is a supersolution to (1) for $2 < r \leq 2_s^*$. Moreover, by (48) and (50), we obtain that

$$\overline{u} \in L^r(\Omega),$$
$$\frac{\overline{u}^2}{|x|^{2s}} \in L^1(\Omega). \tag{54}$$

Define $\{w_j\}$ in $L^1(\mathbb{R}^N)$ is the weak solution to

$$\begin{cases} (-\Delta)^s \omega_{j+1} = w_j^{r-1} + \lambda \frac{w_j}{|x|^{2s}} + \delta g(w_j), & \text{in } \Omega, \\ \omega_{j+1} = 0, & \text{in } \mathbb{R}^N \setminus \Omega, \end{cases} \tag{55}$$

for $j \geq 1$ and $w_0 := \underline{u}$. We now check that this definition makes sense and $\{w_j\}$ are monotone and satisfy

$$0 \leq \underline{u} \leq w_1 \leq w_2 \leq \cdots \leq w_j \leq w_{j+1} \leq \cdots \leq \overline{u} \text{ a.e. } \Omega. \tag{56}$$

For $\underline{u}$, there is nothing to prove. Suppose the result is true up to order j. Then,

$$
\begin{cases}
(-\Delta)^s w_{j+1} = w_j^{r-1} + \lambda \dfrac{w_j}{|x|^{2s}} + \delta g(w_j), \\[2mm]
\qquad \leq \overline{u}^{r-1} + \lambda \dfrac{\overline{u}}{|x|^{2s}} + \delta g(\overline{u}), \qquad \text{in } \Omega, \\[2mm]
\omega_{j+1} = 0, \qquad \text{in } \mathbb{R}^N \setminus \Omega.
\end{cases}
\tag{57}
$$

So $\{w_j\}$ is well-defined by (54) and Lemma 2. By the induction hypothesis, for $x \in \Omega$,

$$
(-\Delta)^s\big(w_{j+1} - w_j\big)
$$

$$
= \big(w_j^{r-1} - w_{j-1}^{r-1}\big) + \lambda \frac{\big(w_j - w_{j-1}\big)}{|x|^{2s}} + \delta\big(g(w_j) - g(w_{j-1})\big)
$$

$$
\geq 0,
\tag{58}
$$

and $w_{j+1} - w_j = 0$, in $\mathbb{R}^N \setminus \Omega$. Then, by Lemma 1, we obtain $w_{j+1} \geq w_j$ in Ω.

Similarly, for any $x \in \Omega$,

$$
(-\Delta)^s\big(\overline{u} - w_j\big) \geq \big(\overline{u}^{r-1} - w_j^{r-1}\big) + \lambda \frac{\big(\overline{u} - w_j\big)}{|x|^{2s}} + \delta\big(g(\overline{u})
$$

$$
- g(w_j)\big) \geq 0,
\tag{59}
$$

and $\overline{u} - w_{j+1} \geq 0$ in $\mathbb{R}^N \setminus \Omega$. Then, $w_{j+1} \leq \overline{u}$ a.e. in Ω. We conclude that (56) holds.

We can define $u_\delta := \lim_{j \to \infty} w_j$ in $L^1(\Omega)$. Moreover, by (9), (54), and (56),

$$
\big\| (-\Delta)^{s/2} w_j \big\|_{L^2(\mathbb{R}^N)} = \lambda \int_\Omega \frac{w_j w_{j-1}}{|x|^{2s}} dx + \int_\Omega w_j w_{j-1}^{r-1} dx
$$

$$
+ \delta \int_\Omega w_j g(w_{j-1}) dx
$$

$$
\leq \lambda \int_\Omega \frac{\overline{u}^2}{|x|^{2s}} dx + \int_\Omega \overline{u}^r dx
$$

$$
+ \delta c_1 \int_\Omega \overline{u}^q dx \leq C.
\tag{60}
$$

Hence, up to a subsequence, we know that $w_j \to u_\delta$ in $X_0^s(\Omega)$. By monotony, the whole sequence weakly converges. Therefore, we can pass to the limit in (55) and conclude that $u_\delta \geq 0$ is a minimal energy solution of (1).

Step 3: supersolution for supercritical case: $2_s^* < r < r(\lambda, s)$. If $r < r(\lambda, s)$, where $r(\lambda, s)$ is given in

(9). For constant $A \geq 0$, there exists a radial function $v(x) := A|x|^{-2s/(r-2)}$ such that

$$
(-\Delta)^s v - \lambda \frac{v}{|x|^{2s}} = v^{r-1}, \quad \text{in } \mathbb{R}^N.
\tag{61}
$$

Since $r > 2_s^* > ((2N - 2s)/(N - 2s))$, then

$$
v \in L_{\text{loc}}^{r-1}\big(\mathbb{R}^N\big),
$$

$$
\frac{v}{|x|^{2s}} \in L_{\text{loc}}^1\big(\mathbb{R}^N\big).
\tag{62}
$$

Taking $\overline{u} = C_1 v$, where the constant $C_1 > 0$ is given by (54), we obtain

$$
\begin{cases}
(-\Delta)^s \overline{u} - \lambda \dfrac{\overline{u}}{|x|^{2s}} \geq \overline{u}^{r-1} + \delta g(\overline{u}), & \text{in } \Omega, \\[2mm]
\overline{u} > 0, & \text{in } \mathbb{R}^N \setminus \Omega.
\end{cases}
\tag{63}
$$

Moreover by (62), $\overline{u} \geq 0$ satisfies (36). By Lemma 2, define $\{w_j\}$ to be the weak solutions of (55). Moreover, similarly, by the induction hypothesis, we can conclude that

$$
0 \leq \underline{u} \leq w_1 \leq w_2 \leq \cdots \leq w_j \leq w_{j+1} \leq \cdots \leq \overline{u} \text{ a.e. } \Omega.
\tag{64}
$$

Note that $(F2)$ and $(F4)$ hold, for all $\delta \in (\lambda_1/M_0, \delta_0]$, define w_1 as the solution of

$$
\begin{cases}
(-\Delta)^s w_1 = \underline{u}^{r-1} + \lambda \dfrac{\underline{u}}{|x|^{2s}} + \delta g(\underline{u}), & \text{in } \Omega, \\[2mm]
w_1 > 0, & \text{in } \Omega, \\[2mm]
w_1 = 0, & \text{in } \mathbb{R}^N \setminus \Omega.
\end{cases}
\tag{65}
$$

Set

$$
F(\underline{u}) = \underline{u}^{r-1} + \lambda \frac{\underline{u}}{|x|^{2s}} + \delta g(\underline{u}) = (t\varphi_1)^{r-1} + \lambda \frac{t\varphi_1}{|x|^{2s}} + \delta g(t\varphi_1).
\tag{66}
$$

Then, $w_1 \in W_0^{1,p} \cap L^\infty(\Omega)$. By (44), we obtain that

$$
\begin{cases}
(-\Delta)^s w_1 = F(\underline{u}) \geq (-\Delta)^s \underline{u}, & \text{in } \Omega, \\[2mm]
w_1 = 0, & \text{in } \mathbb{R}^N \setminus \Omega.
\end{cases}
\tag{67}
$$

We deduce from the comparison principle that $\underline{u} \leq w_1$ in Ω.

On the contrary, by (11), the function F is nondecreasing. Therefore,

$$\begin{cases} (-\Delta)^s \overline{u} \geq F(\overline{u}) \geq F(\underline{u}) = (-\Delta)^s w_1, & \text{in } \Omega, \\ \overline{u} \geq w_1, & \text{in } \mathbb{R}^N \setminus \Omega. \end{cases} \tag{68}$$

By the comparison principle we deduce that $w_1 \leq \overline{u}$ in Ω. In particular, for all $x \in \Omega$, $\{w_j\}$ is a nondecreasing sequence which is bounded. Therefore, $\{w_j\}$ monotone converges in $L^1(\mathbb{R}^N)$ to a weak nonnegative solution u_δ to (1) for $2_s^* < r < r(\lambda, s)$.

Therefore, for δ small enough, we have built a minimal solution in both subcritical and supercritical case. Let

$$M = \sup\{\delta > 0 : \text{problem (1) has a solution}\}, \tag{69}$$

that is, we show that $M > 0$.

Step 4: $M < \infty$, for $2 < r < r(\lambda, s)$. We consider the following eigenvalue problem with the Hardy potential:

$$\begin{cases} (-\Delta)^s \psi_1 - \lambda \dfrac{\psi_1}{|x|^{2s}} = \lambda_1 \psi_1, & \text{in } \Omega, \\ \\ \psi_1 = 0, & \text{in } \mathbb{R}^N \setminus \Omega. \end{cases} \tag{70}$$

Since $0 < \lambda < \Lambda_{N,s}$, problem (70) is well defined. Taking ψ_1 as a test function in problem (1), we obtain that

$$\frac{C(N,s)}{2} \int_Q \frac{(\psi_1(x) - \psi_1(y))(u(x) - u(y))}{|x - y|^{N+2s}} dx \, dy - \lambda \int_\Omega \frac{\psi_1 u}{|x|^{2s}} dx$$
$$= \int_\Omega u^{r-1} \psi_1 dx + \delta \int_\Omega g(u) \psi_1 dx. \tag{71}$$

Since ψ_1 is a solution to (70), it follows that

$$\int_\Omega \left(u^{r-1} + \delta g(u) \right) \psi_1 dx = \lambda_1 \int_\Omega u \psi_1 dx. \tag{72}$$

If $2_s^* < r < r(\lambda, s)$. Taking φ_1 as a test function in (1), where $\varphi_1 \geq 0$ is solution to problem (44), we have

$$\int_\Omega u(-\Delta)^s \varphi_1 dx = \int_\Omega \left(\lambda \frac{u}{|x|^{2s}} + u^{r-1} + \delta g(u) \right) \varphi_1 dx$$
$$\geq \int_\Omega \left(u^{r-1} + \delta g(u) \right) \varphi_1 dx. \tag{73}$$

Moreover, φ_1 is also a classical solution (see Remark 2.1 in [21]). From (72), we immediately deduce that

$$\lambda_1 \int_\Omega u \varphi_1 dx \geq \int_\Omega \left(u^{r-1} + \delta g(u) \right) \varphi_1 dx. \tag{74}$$

Since there exist structural positive constants b_0 and b_1 such that $|t|^{r-2} t + \delta g(t) > b_0 \delta^{b_1} t$, for any $t > 0$. From (70) and (73), we obtain that $b_0 \delta^{b_1} < \lambda_1$. This implies that $M < \infty$ for $r < r(\lambda, s)$.

We complete the Proof of Theorem 1. $\qquad \square$

4. Nonexistence Result

In this section, we consider the nonexistence of solution to problem (1) in H_0^s.

Proof of Theorem 2. Suppose that problem (1) has a solution $u \in H_0^s$ under the conditions of Theorem 2. Then, there exists a constant $\delta > 0$ such that $\delta \varphi_1 \leq u$ in Ω, where φ_1 is the first eigenfunction of $(-\Delta)^s$, that is, φ_1 satisfies (44).

Let $\mu \in (\lambda_1, \lambda_1 + \varepsilon)$, where $\varepsilon > 0$ is a small constant. Denote $\psi = \delta \varphi_1$. Then, we have

$$\begin{cases} (-\Delta)^s \psi = \lambda_1 \psi \leq \mu \psi < (\lambda_1 + \varepsilon) u, & \text{in } \Omega, \\ \psi = 0, & \text{in } \mathbb{R}^N \setminus \Omega. \end{cases} \tag{75}$$

Furthermore, for any $\tau > 1$, $\delta < \lambda_1 / M_1(\tau)$; then, for ε small enough, we deduce that

$$\begin{cases} (\lambda_1 + \varepsilon) u \leq u^{r-1} + \delta g(u) + \lambda \dfrac{u}{|x|^{2s}} \equiv (-\Delta)^s u, & \text{in } \Omega, \\ \\ u = 0, & \text{in } \mathbb{R}^N \setminus \Omega. \end{cases} \tag{76}$$

Thus, according to (75) and (76), we have

$$\begin{cases} (-\Delta)^s \psi \leq \mu \psi, & \text{in } \Omega, \\ (-\Delta)^s u \geq \mu u, & \text{in } \Omega, \\ u \geq \psi, & \text{in } \Omega, \\ u = \psi = 0, & \text{in } \mathbb{R}^N \setminus \Omega. \end{cases} \tag{77}$$

Hence, it is possible to construct the subsolution and supersolution to the problem:

$$\begin{cases} (-\Delta)^s u = \mu u, & \text{in } \Omega, \\ u = 0, & \text{in } \mathbb{R}^N \setminus \Omega, \end{cases} \tag{78}$$

with $\mu \in (\lambda_1, \lambda_1 + \varepsilon)$. However, this is impossible. $\qquad \square$

Data Availability

Data sharing not applicable to this article as no datasets were generated or analysed during the current study.

Conflicts of Interest

The authors declare that they have no conflicts of interest.

References

[1] S. Huang and Q. Tian, "Marcinkiewicz estimates for solution to fractional elliptic laplacian equation," *Computers & Mathematics with Applications*, vol. 78, no. 5, pp. 1732–1738, 2019.

[2] S. Huang and Q. Tian, "Harnack-type inequality for fractional elliptic equations with critical exponent," *Mathematical Methods in the Applied Sciences*, vol. 43, no. 8, pp. 5380–5397, 2020.

[3] M. Ri, S. Huang, and C. Huang, "Non-existence of solutions to some degenerate coercivity elliptic equations involving measures data," *Electronic Research Archive*, vol. 28, no. 1, pp. 165–182, 2020.

[4] L. Silvestre, "Regularity of the obstacle problem for a fractional power of the laplace operator," *Communications on Pure and Applied Mathematics*, vol. 60, no. 1, pp. 67–112, 2007.

[5] Q. Tian and Y. Xu, "Effect of the domain geometry on the solutions to fractional brezis-nirenberg problem," *Journal of Function Spaces*, vol. 2019, Article ID 1093804, 4 pages, 2019.

[6] Y. Ye, H. Liu, Y. Wei, M. Ma, and K. Zhang, "Dynamic study of a predator-prey model with weak Allee effect and delay," *Advances in Mathematical Physics*, vol. 2019, Article ID 7296461, 15 pages, 2019.

[7] B. Abdellaoui, M. Medina, I. Peral, and A. Primo, "The effect of the hardy potential in some Calderón-Zygmund properties for the fractional laplacian," *Journal of Differential Equations*, vol. 260, no. 11, pp. 8160–8206, 2016.

[8] Y. Mi, S. Huang, and C. Huang, "Combined effects of the hardy potential and lower order terms in fractional laplacian equations," *Boundary Value Problems*, vol. 2018, no. 1, p. 61, 2018.

[9] B. Barrios, M. Medina, and I. Peral, "Some remarks on the solvability of non-local elliptic problems with the hardy potential," *Communications in Contemporary Mathematics*, vol. 16, no. 4, Article ID 1350046, 2014.

[10] X. Shang, J. Zhang, and R. Yin, "Existence of positive solutions to fractional elliptic problems with hardy potential and critical growth," *Mathematical Methods in the Applied Sciences*, vol. 42, no. 1, pp. 115–136, 2019.

[11] K. Bogdan, T. Grzywny, T. Jakubowski, and D. Pilarczyk, "Fractional laplacian with hardy potential," *Communications in Partial Differential Equations*, vol. 44, no. 1, pp. 20–50, 2019.

[12] S. Dipierro, L. Montoro, I. Peral, and B. Sciunzi, "Qualitative properties of positive solutions to nonlocal critical problems involving the Hardy-Leray potential," *Calculus of Variations and Partial Differential Equations*, vol. 55, p. 99, 2016.

[13] N. Ghoussoub, F. Robert, S. Shakerian, and M. Zhao, "Mass and asymptotics associated to fractional Hardy-Schrödinger operators in critical regimes," *Communications in Partial Differential Equations*, vol. 43, no. 6, pp. 859–892, 2018.

[14] S. Rastegarzadeh and N. Nyamoradi, "Existence of positive solutions for hardy nonlocal fractional elliptic equations involving critical nonlinearities," *Topological Methods in Nonlinear Analysis*, vol. 53, pp. 731–746, 2019.

[15] L. Boccardo, M. Escobedo, and I. Peral, "A Dirichlet problem involving critical exponents," *Nonlinear Analysis: Theory, Methods & Applications*, vol. 24, no. 11, pp. 1639–1648, 1993.

[16] L. Caffarelli and L. Silvestre, "An extension problem related to the fractional laplacian," *Communications in Partial Differential Equations*, vol. 32, no. 8, pp. 1245–1260, 2007.

[17] J. Dávila, L. Dupaigne, L. Dupaigne, and M. Montenegro, "The extremal solution of a boundary reaction problem," *Communications on Pure & Applied Analysis*, vol. 7, no. 4, pp. 795–817, 2008.

[18] R. L. Frank, E. H. Lieb, and R. Seiringer, "Hardy-Lieb-thirring inequalities for fractional schrodinger operators," *Journal of the American Mathematical Society*, vol. 21, no. 4, pp. 925–950, 2008.

[19] R. Servadei and E. Valdinoci, "Mountain pass solutions for non-local elliptic operators," *Journal of Mathematical Analysis and Applications*, vol. 389, no. 2, pp. 887–898, 2012.

[20] E. Di Nezza, G. Palatucci, and E. Valdinoci, "Hitchhiker's guide to the fractional sobolev spaces," *Bulletin des Sciences Mathématiques*, vol. 136, no. 5, pp. 521–573, 2012.

[21] X. Ros-Oton and J. Serra, "The dirichlet problem for the fractional laplacian: regularity up to the boundary," *Journal de Mathématiques Pures et Appliquées*, vol. 101, no. 3, pp. 275–302, 2014.

WILEY | Hindawi

Research Article

Dynamic Analysis, Circuit Design, and Synchronization of a Novel 6D Memristive Four-Wing Hyperchaotic System with Multiple Coexisting Attractors

Fei Yu [iD],[1] **Li Liu** [iD],[1] **Hui Shen** [iD],[1] **Zinan Zhang** [iD],[1] **Yuanyuan Huang** [iD],[1] **Changqiong Shi** [iD],[1] **Shuo Cai** [iD],[1] **Xianming Wu** [iD],[2] **Sichun Du** [iD],[3] **and Qiuzhen Wan** [iD][4]

[1]*School of Computer and Communication Engineering, Changsha University of Science and Technology, Changsha 410114, China*
[2]*School of Mechanical and Electrical Engineering, Guizhou Normal University, Guiyang 550025, China*
[3]*College of Computer Science and Electronic Engineering, Hunan University, Changsha 410082, China*
[4]*College of Information Science and Engineering, Hunan Normal University, Changsha 410081, China*

Correspondence should be addressed to Fei Yu; yufeiyfyf@csust.edu.cn and Qiuzhen Wan; wanqiuzhen@sina.com

In this work, a novel 6D four-wing hyperchaotic system with a line equilibrium based on a flux-controlled memristor model is proposed. The novel system is inspired from an existing 5D four-wing hyperchaotic system introduced by Zarei (2015). Fundamental properties of the novel system are discussed, and its complex behaviors are characterized using phase portraits, Lyapunov exponential spectrum, bifurcation diagram, and spectral entropy. When a suitable set of parameters are chosen, the system exhibits a rich repertoire of dynamic behaviors including double-period bifurcation of the quasiperiod, a single two-wing, and four-wing chaotic attractors. Further analysis of the novel system shows that the multiple coexisting attractors can be observed with different system parameter values and initial values. Moreover, the feasibility of the proposed mathematical model is also presented by using Multisim simulations based on an electronic analog of the model. Finally, the active control method is used to design the appropriate controller to realize the synchronization between the proposed 6D memristive hyperchaotic system and the 6D hyperchaotic Yang system with different structures. The Routh–Hurwitz criterion is used to prove the rationality of the controller, and the feasibility and effectiveness of the proposed synchronization method are proved by numerical simulations.

1. Introduction

Since the 1960s, nonlinear science has developed rapidly in various branches of disciplines. The in-depth study of nonlinear science not only has important theoretical value to the academic community, but also has a broad prospect for the practical application in life [1]. Chaos is one of the most important subjects in nonlinear motion, which creates a new situation of nonlinear science. Since the discovery of chaotic motion, chaotic dynamics has made rapid progress, and scientists from all over the world have made in-depth analysis and research on the characteristics of chaos [2–7]. Chaotic motion is a random behavior occurring in a defined nonlinear system. It is highly sensitive to initial conditions, has complex dynamic properties, and is difficult to predict. At present, it is widely used in complex networks [8–11], electronic circuits [12–15], image processing [16–20], random number generator [21–23], secure communication [24, 25], and other engineering fields.

For the application of chaos in engineering, it is sometimes a key problem to generate a chaotic attractor with a complex topological structure. Most research in this field has been focused on the multiwing attractors [26–28], multiscroll attractors [29–32], and chaotic systems in the fractional-order form [33–35]. More and more articles are written on this topic every day, and numerous articles are devoted to explain the new high-dimensional chaotic systems and more complicated topological structure.

Compared with chaotic systems, hyperchaotic systems have more complex dynamic behaviors, which have two or more positive Lyapunov indices, more complex topological structures, and more unpredictable dynamic behaviors and are more difficult to crack. The most common method to construct hyperchaotic systems is to introduce new variables to the proposed chaotic systems to increase the dimensions of the differential equations and increase the nonlinear terms. Since the discovery of a first 4D hyperchaotic system by Rossler in 1979 [36], many 4D hyperchaotic systems have been found in the literature such as hyperchaotic Lorenz system [37], hyperchaotic Chen system [38], hyperchaotic Lü system [39], hyperchaotic Yu system [40], hyperchaotic Wang system [41], and hyperchaotic Vaidyanathan system [42]. Recently, people have developed a strong interest in searching for 5D and 6D hyperchaotic systems with more complex dynamic behavior and such 5D and 6D hyperchaotic systems have been found in the literature such as hyperchaotic Vaidyanathan system [43], hyperchaotic Kemih system [44], hyperchaotic Lorenz system [45], and hyperchaotic Yang system [46]. Hyperchaotic systems can also produce multiscroll or multiwing attractors, which is a very important phenomenon. In recent years, some four-wing hyperchaotic attractors have appeared [47, 48]. These attractors generally have five equilibrium points, and each wing hovers near a nonzero equilibrium point. The three or five equilibrium points of the chaotic system are very important, especially in the multiscroll or multiwing chaotic system, but the multiscroll or multiwing hyperchaotic attractor with a linear equilibrium point is exciting.

Memristor is a nonlinear passive element with nonlinearity and nonvolatility. In recent years, the research work has made gratifying progress, and the application of various memristors has become a research hotspot [49–51]. In 2008, scientists at HP LABS successfully built the first physically realized memristor [52], confirming the prediction of professor Chua in 1971 [53]. Since then, memristors have received extensive attention and research. Due to its small size and low power consumption, a memristor is an ideal choice for nonlinear circuits in chaos [54]. The common methods to produce hyperchaos are the linear feedback method and the nonlinear feedback method. Among them, the nonlinear feedback method is better than the linear feedback method. However, the product term of the nonlinear function makes the realization circuit more complex. If the memristor is used as the nonlinear feedback, it will greatly reduce the difficulty of circuit realization. At the same time, the memory ability of a memristor to flow through current is not possessed by conventional chaotic circuit elements [55]. Therefore, it is of practical significance to study the application of a memristor in a hyperchaotic system, and various hyperchaotic systems based on memristors have been paid close attention by researchers [56–59].

In order to construct memristive hyperchaotic systems with more complex dynamics, some kind of 5D and 6D memristive hyperchaotic systems have been proposed recently [60–62]. In [60], a novel 5D hyperchaotic four-wing memristive system (HFWMS) was proposed by introducing a flux-controlled memristor with quadratic nonlinearity into a 4D hyperchaotic system as a feedback term. The HFWMS with multiline equilibrium and three positive Lyapunov exponents presented very complex dynamic characteristics, such as the existence of chaos, hyperchaos, limit cycles, and periods. In [62], a 6D autonomous system was presented by introducing a flux-controlled memristor model into an existing 5D hyperchaotic autonomous system, which exhibited hyperchaotic under a line or a plane of equilibria. Some other attractive dynamics were also observed, like hidden extreme multistability, transient chaos, bursting, and offset boosting phenomenon. It can be seen that such super-high-dimensional attractors cannot be ignored. Because of their complexity, the generated signals are usually suitable for secure communication and random number generation, so the super-high-dimensional attractors will be an added value to their randomness.

Coexistence of multiple attractors is a kind of singular physical phenomenon often encountered in a nonlinear dynamic system. Under the condition of constant system parameters, when the initial state is changed, the trajectory of the system may asymptotically approach different stable states such as trend point, chaos, period, and quasiperiod [15, 23, 46]. In some special coupling systems and novel memristive chaotic systems, the coexistence of infinite number of attractors can also be observed [62]. Common multiple coexisting attractors generally have symmetry, and there is symmetric coexistence of left and right or upper and lower attractors. Recently, it has been found that the coexistence of asymmetric multiattractors also exists in some special systems, which is a new nonlinear phenomenon [61, 62]. Multiple coexisting attractors provide a great degree of freedom for the engineering application of nonlinear dynamic systems and also present a new challenge to the multistability state switching control technology. Therefore, the study of multiple coexisting attractors and their synchronization has important theoretical physical significance and engineering application value.

With the rapid development of network communication technology, the confidentiality of information and the security of the system is not considered complete, resulting in increasingly serious information security problems. Information security technology mainly includes monitoring, scanning, detection, encryption, authentication, and attack prevention [63–72]. Due to the characteristics of chaotic systems such as aperiodic, continuous wideband, and noise-like, the use of chaotic synchronization has more stringent communication confidentiality, so it has received great attention in the field of information security. Pecora and Carroll [73] first proposed the concept of chaotic synchronization in 1990 and observed the phenomenon of chaotic synchronization on electronic circuits. This pioneering work greatly promoted the study of chaotic synchronization theory. Since then, complete synchronization [74], antisynchronization [40], generalized synchronization [75], projection synchronization [76, 77], lag synchronization [78], function projection synchronization [79], and shape synchronization [80] methods have been widely studied in the literature.

In this paper, a novel 6D memristive hyperchaotic system is proposed based on a flux-controlled memristor model and the 5D hyperchaotic system introduced in [48]. Most importantly, the novel system generates the striking phenomenon of multiple coexisting chaotic attractors and exhibits hyperchaos with a line equilibrium. Under certain parameters and initial conditions, the system exits double-period bifurcation of the quasiperiod, which can produce four-wing hyperchaotic and chaotic attractors. A notable feature of the new system is the ability to generate two-wing and four-wing smooth chaotic attractors with special appearance. Then, an electronic circuit realization of the novel 6D memristive four-wing hyperchaotic system is presented to confirm the feasibility of the theoretical model. Finally, an adaptive active controller is designed to realize the global hyperchaos synchronization of the novel 6D memristive four-wing hyperchaotic systems and the 6D Yang hyperchaotic system with different structures.

The rest of this work is structured as follows: In Section 2, the mathematical model of the novel 6D memristive hyperchaotic system that can generate two-wing and four-wing attractors is introduced. Numerical findings of the novel 6D memristive hyperchaotic system are carried out in Section 3 by using classical nonlinear diagnostic tools. The multiple coexisting attractors of the system are investigated, and the spectral entropy complexity is also reported. Some Multisim simulations based on a suitable designed electronic analog circuit diagram of the model are carried out to show its feasibility in Section 4. In Section 5, the novel chaotic system's active control synchronization is derived. Finally, Section 6 draws the concluding remarks of this work.

2. A Novel 6D Memristive Four-Wing Hyperchaotic System

Recently, Zarei [48] proposed a 5D hyperchaotic system, whose differential equation can be described as

$$
\begin{cases}
\dot{x} = -ax + yz, \\
\dot{y} = -by + fu, \\
\dot{z} = -cz + xy + gw, \\
\dot{w} = dw - hz, \\
\dot{u} = eu - x^2 y,
\end{cases}
\tag{1}
$$

where $x, y, z, w,$ and u are the state variables of the system and $a, b, c, d, e, f, g,$ and h are the system parameters. The system has many interesting complex dynamical behaviors such as periodic orbit, chaos, and hyperchaos with only one equilibrium point. When proper system parameters and initial values are selected, the system can exhibit four-wing hyperchaotic attractors. The system has been well studied in [48], which shows the coexistence attractor and hyperchaotic attractor of two positive Lyapunov exponents. However, memristor chaos is not part of this feature. Our goal is to construct a high-dimensional system with coexistence attractors and memristor, thus forming a system of ordinary differential equations of memristive four-wing high-dimensional hyperchaos.

Memristor is a passive two-terminal device that describes the relationship between magnetic flux φ and charge q. The memristor used in this work is a flux-controlled memristor, which is described by the nonlinear constitutive relation between the terminal voltage u and the terminal current i of the device, i.e.,

$$
i = W(\varphi)u, \ \dot{\varphi} = u,
\tag{2}
$$

where $W(\varphi)$ is a memductance function which is called the incremental memductance, defined as $W(\varphi) \equiv dq(\varphi)/\varphi$.

In this paper, the $\varphi - q$ characteristic curve of the memristor is given by a smooth continuous cubic monotone-increasing nonlinearity, i.e., $q(\varphi) = m + n\varphi^3$, where $m, n > 0$. Thus, the memductance in this paper is given by

$$
W(\varphi) = m + 3n\varphi^2.
\tag{3}
$$

By introducing the lux-controlled memristor model (3) into the second equation of system (1), a novel 6D memristive autonomous hyperchaotic system is constructed

$$
\begin{cases}
\dot{x} = -ax + yz, \\
\dot{y} = -by + f(m + 3n\varphi^2)u, \\
\dot{z} = -cz + xy + gw, \\
\dot{w} = dw - hz, \\
\dot{u} = eu - x^2 y, \\
\dot{\varphi} = u,
\end{cases}
\tag{4}
$$

where $x, y, z, w, u,$ and φ are the state variables; $a, b, c, d, e, f, g, h, m,$ and n are the system parameters. When $a = 10, b = 60, c = 20, d = 15, e = 40, f = 1, g = 50, h = 10, m = 1, 3n = 0.02,$ and the initial condition is set to $[1, 1, 1, 1, 1, 1]$, we use the Runge–Kutta algorithm (RK45) to solve the differential equation. Figure 1 shows the phase portraits of system (4) obtained through MATLAB simulation. It can be seen from the figure that the proposed system presents four-wing chaos in different phase planes.

In general, symmetry is widespread in chaotic systems, and system (4) is invariant under the coordinate transformation $(x, y, z, w, u, \varphi) \longrightarrow (-x, -y, z, w, -u, -\varphi)$ and has the same symmetry as the original 5D system (1).

Let the six equations at the right end of system (4) be zero, and the equilibrium point of system (4) can be obtained by solving the following equations:

$$
\begin{cases}
-ax + yz = 0, \\
-by + f(m + 3n\varphi^2)u = 0, \\
-cz + xy + gw = 0, \\
dw - hz = 0, \\
eu - x^2 y = 0, \\
u = 0.
\end{cases}
\tag{5}
$$

According to equation (5), system (4) has a line equilibrium point $O = \{(x, y, z, w, u, \varphi) \mid x = y = z = w = 0, u = 0, \varphi = l\}$, which means that every point on the φ-axis is the system equilibrium point, where l is an arbitrary real

(a)

(b)

(c)

(d)
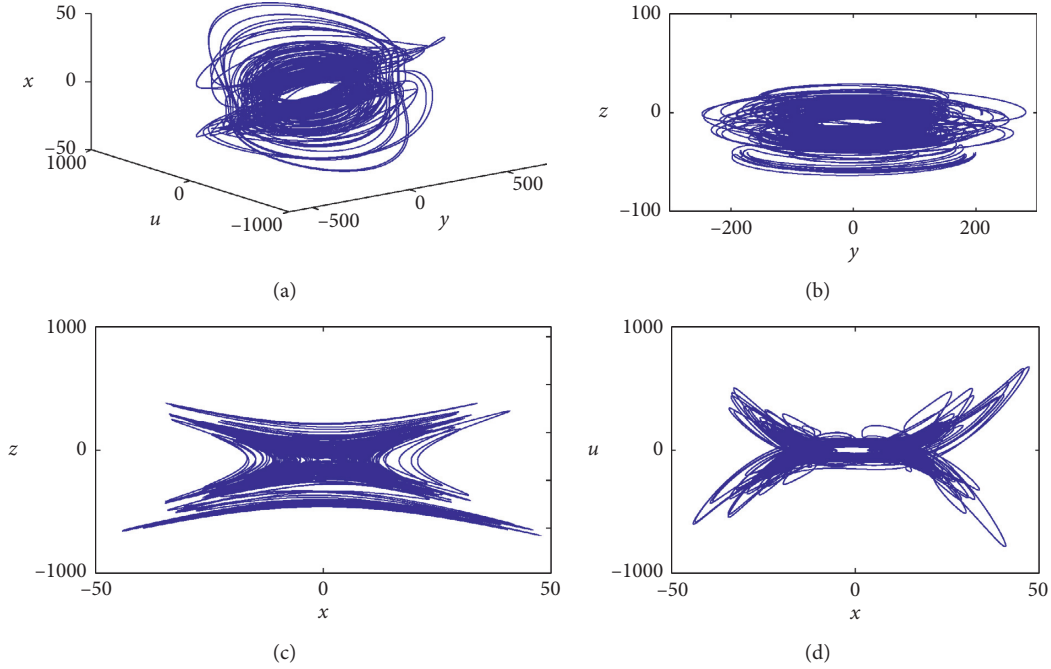
FIGURE 1: The four-wing chaotic attractor of system (4) in the (a) $y - u - x$ plane, (b) $y - z$ plane, (c) $x - z$ plane, and (d) time-domain waveform of $x - u$.

constant. The Jacobian matrix at the line equilibrium point O of system (4) is

$$J_o = \begin{bmatrix} -a & z & y & 0 & 0 & 0 \\ 0 & -b & 0 & 0 & f(m + 3n\varphi^2) & 6fn\varphi u \\ y & x & -c & g & 0 & 0 \\ 0 & 0 & -h & d & 0 & 0 \\ -2xy & -x^2 & 0 & 0 & e & 0 \\ 0 & 0 & 0 & 0 & 1 & 0 \end{bmatrix}. \quad (6)$$

According to (6), the characteristic equation can be obtained:

$$\lambda(\lambda - e)(\lambda + a)(\lambda + b)(\lambda - m_1)(\lambda - m_2) = 0, \quad (7)$$

where

$$m_1 = \frac{(d - c) + \sqrt{(c - d)^2 - 4(gh - cd)}}{2},$$

$$m_2 = \frac{(d - c) - \sqrt{(c - d)^2 - 4(gh - cd)}}{2}. \quad (8)$$

According to the characteristic equation and system parameters, $\lambda_1 = 0, \lambda_2 = 40, \lambda_3 = -10, \lambda_4 = -60, \lambda_5 = -2.5 + 13.9194i$, and $\lambda_6 = -2.5 - 13.9194i$ can be obtained. Therefore, there are one positive eigenvalue, one zero eigenvalue, and two negative eigenvalues, and the line equilibrium of system (4) is unstable saddle points.

The divergence of system (4) is given by

$$\nabla V = \frac{d\dot{x}}{dx} + \frac{d\dot{y}}{dy} + \frac{d\dot{z}}{dz} + \frac{d\dot{w}}{dw} + \frac{d\dot{u}}{du} + \frac{d\dot{\varphi}}{d\varphi} = -a - b - c + d + e, \quad (9)$$

since $-a + b - c - e = -35$ satisfies $\nabla V < 0$, system (4) is dissipative and converges exponentially.

3. Dynamic Analysis of the Novel 6D Memristive Chaotic System

In this section, with the help of a bifurcation diagram, Lyapunov exponent spectrum, and phase portraits, we will use the fourth-order Runge–Kutta algorithm to numerically study the complex dynamic behavior of system (4) by MATLAB.

3.1. Fix Other Parameters and Change Parameter a. Given parameters $b = 60, c = 20, d = 15, e = 40, f = 1, g = 50, h = 10, m = 1$, and $3n = 0.02$ and initial conditions $(0) = 1$, $y(0) = 1$, $z(0) = 1, w(0) = 1, u(0) = 1$, and $\varphi(0) = 1$, let parameter a be the bifurcation parameter of system (4), where Figure 2(a) shows the bifurcation diagram when system parameter a changes from 0 to 12, and Figure 2(b) shows the corresponding Lyapunov exponent spectrum. It can be seen from Figure 2 that the system is chaotic in $[0, 4.6]$ and hyperchaotic in $(4.6, 12]$. When $a = 12$, the value of the Lyapunov exponent is 12.56, which is the maximum value of the simulation interval and larger than the maximum Lyapunov exponent of system (1) $(LE_{max} = 9.979)$. Suffice it to say, the introduction of a memristor can make the system more complex. When $a = 10$, we use the famous wolf method to calculate the
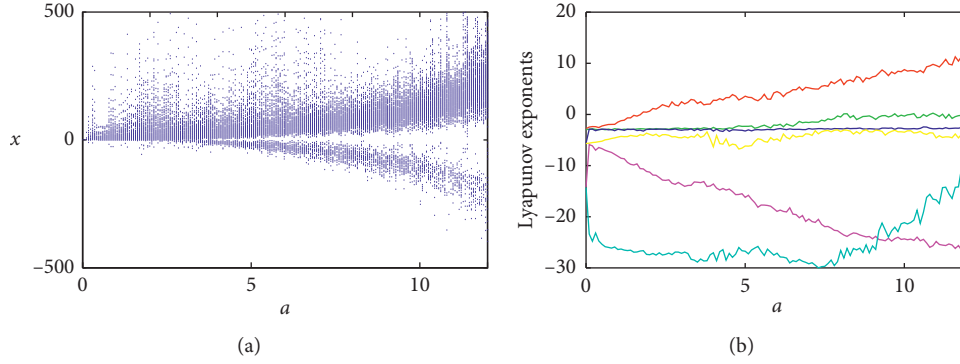
FIGURE 2: Lyapunov exponent spectrum and bifurcation diagram for parameter $a \in [0, 12]$: (a) bifurcation diagram; (b) Lyapunov exponent spectrum.

Lyapunov exponents. The LEs are $LE_1 = 10.16, LE_2 = 2.187$, $LE_3 = 0.0136$, $LE_4 = -0.5759$, $LE_5 = -16.08$, and $LE_6 = -18.86$. There are two positive Lyapunov exponents, so system (4) is hyperchaotic. Based on the Lyapunov exponents, we also get the Kaplan–Yorke dimension that describes the complexity of the attractor. It can be computed by

$$D_{KY} = D + \sum_{i=1}^{D} \frac{LE_i}{|LE_D|}, \tag{10}$$

where D is a constant satisfying $\sum_{i=1}^{D} LE_i \geq 0$ and $\sum_{i=1}^{D+1} LE_i < 0$. According to equation (10), the Kaplan–Yorke dimension of system (4) is 4.7723, so the attractors generated by the new system are strange attractors.

3.2. Fix Other Parameters and Change Parameter d.
Given parameters $a = 10, b = 60, c = 20, e = 40, f = 1$, $g = 50, h = 10, m = 1$, and $3n = 0.02$ and initial conditions $(0) = 1, y(0) = 1, z(0) = 1, w(0) = 1, u(0) = 1$, and $\varphi(0) = 1$, when parameter $d \in [-10, 20]$, Figure 3(a) shows the bifurcation diagram changing with parameter d, and Figure 3(b) shows the corresponding Lyapunov exponent spectrum. It can be seen from Figure 3 that the system has doubly periodic bifurcation, chaos, and hyperchaos phenomena. The double-period bifurcation simulated in this paper is different from the simulation results of most papers, which are double-period bifurcation of the period, while in this paper, it is the double-period bifurcation of the quasiperiod. Table 1 gives a summary of dynamic characteristics of parameter d. The following analysis shows the dynamic behavior with respect to parameter d:

(i) When $d = -2$, the maximum Lyapunov exponent of system (4) is zero ($LE_{1,2} = 0$, $LE_{3,4,5,6} < 0$), and the system is in a quasiperiodic 1 state. Figure 4(a) shows the corresponding phase portraits;

(ii) When $d = -1$, the maximum Lyapunov exponent of system (4) is zero ($LE_{1,2} = 0$, $LE_{3,4,5,6} < 0$), and the system is in a quasiperiodic 2 state. Figure 4(b) shows the corresponding phase portraits;

(iii) When $d = 0$, system (4) has a positive Lyapunov exponent ($LE_1 > 0$, $LE_2 = 0$, $LE_{3,4,5,6} < 0$), and the

system behaves as a two-wing chaotic attractor state. The corresponding phase portrait is shown in Figure 4(c);

(iv) When $d = 16$, system (4) has two positive Lyapunov exponents ($LE_{1,2} > 0$, $LE_3 = 0$, and $LE_{4,5,6} < 0$), and the system is in a four-wing hyperchaos state. The corresponding four-wing phase portrait is shown in Figure 4(d).

3.3. Multiple Coexisting Attractors.
In this section, we will study the multiple coexisting attractors of the proposed 6D memristive hyperchaotic system. Fixed system parameters are $a = 10, b = 60, c = 20, e = 40, f = 1, g = 50, h = 10, m = 1$, and $3n = 0.02$. When $d = -3$ and $d = -0.5$, two different initial conditions $[1, 1, 1, 1, 1, 1]$ and $[1, 1, -1, 1, 1, 1]$ are taken to observe the phenomenon of coexistence quasiperiodic 1 and coexistence quasiperiodic 2 as shown in Figures 5(a) and 5(b). When $d = 0$, two different initial conditions $[1, 1, 1, 1, 1, 1]$ and $[-1, 1, 1, 1, 1, 1]$ are taken to observe the coexistence of two-wing chaotic attractors presented in Figure 5(c). Choosing $d = 15$ and taking two different initial conditions $[1, 1, 0.001, 1, 1, 1]$ and $[1, 1, -0.001, 1, 1, 1]$, the coexistence of four-wing hyperchaotic attractors is observed in Figure 5(d). When $d = -7$ is selected, the initial conditions $[1, 1, 1, 1, 1, 1]$, $[-1, 1, 1, 1, 1, 1]$, $[20, 1, 1, 1, 1, 1]$, and $[-20, 1, 1, 1, 1, 1]$ are selected, as shown in Figure 5(e); there are four quasiperiodic attractors coexisting, and the four attractors are symmetric.

When the system parameters are selected as $a = 1, b = 8, c = 1, d = -20, e = 1, f = 2, g = 1, h = -1, m = 1$, and $3n = 0.02$, the phase portraits of system (4) under different initial conditions are shown in Figure 6. Figure 6(a) shows the coexistence of four one-wing period-1 attractors, Figure 6(b) shows the coexistence of four one-wing multiperiod attractors, Figure 6(c) shows the coexistence of two-wing multiperiod attractors, and Figure 6(d) shows the coexistence of four two-wing multiperiod attractors. When the system parameters are selected as $a = 1, b = 5, c = 1, d = -20, e = 1, f = 2, g = 1, h = -1, m = 1$, and $3n = 0.02$, the phase portraits of system (4) under different initial conditions are shown in Figure 7. In Figure 7(a), two-wing

(a)

(b)
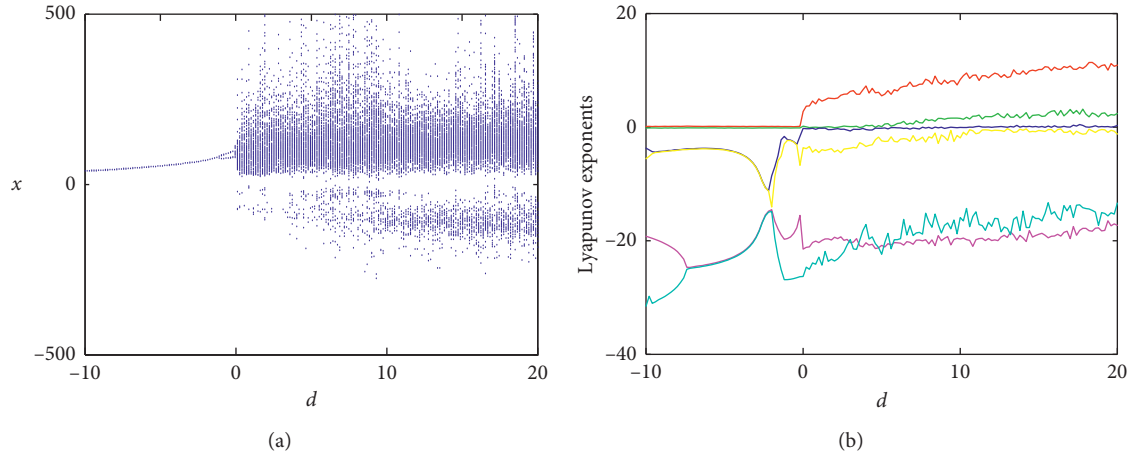
FIGURE 3: Lyapunov exponent spectrum and bifurcation diagram for parameter $d \in [-10, 20]$: (a) bifurcation diagram; (b) Lyapunov exponent spectrum.

TABLE 1: Dynamical behavior and Lyapunov exponents under different parameter range of d.

d	$(LE_1, LE_2, LE_3, LE_4, LE_5, LE_6)$	Dynamic	Figure
$[-10, -1.2]$	$(0, 0, -, -, -, -)$	Quasiperiodic 1	Figure 4(a)
$(-1.2, 0)$	$(0, 0, -, -, -, -)$	Quasiperiodic 2	Figure 4(b)
$[0, 5]$	$(+, 0, -, -, -, -)$	Chaotic	Figure 4(c)
$(5, 20]$	$(+, +, 0, -, -, -)$	Hyperchaotic	Figure 4(d)

(a)

(b)

(c)

(d)
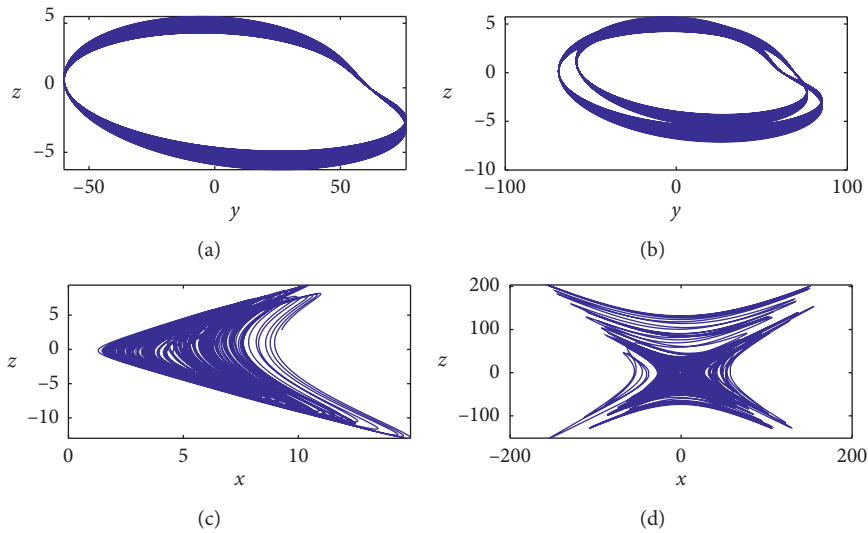
FIGURE 4: The phase portraits: (a) quasiperiodic 1, (b) quasiperiodic 2, (c) two-wing chaotic attractor, and (d) four-wing hyperchaotic attractor.

period-1 attractors coexist; in Figure 7(b), two-wing period-1 attractors coexist; in Figure 7(c), four-wing period-1 attractors coexist; in Figure 7(d), two-wing multiperiod attractors coexist, among which cyan, red, yellow, and earthy yellow are one group; black, green, blue, and magenta are the other. Figure 8 shows the phase portraits of different attractors when the initial conditions are $[1, 1, 1, 1, 1, 1]$ and $[1, 1, -1, 1, 1, 1]$, but the parameter values in Figures 8(a) and 8(b) are different. The parameter values in Figure 8(a) are

fixed to $a = 2, b = 6, c = 1, d = -20, e = 1, f = 2, g = 1, h = -1, m = 1$, and $3n = 0.02$. It can be seen from the figure that the system has the coexistence of two-wing chaotic attractors. The parameter values in Figure 8(b) are fixed to $a = 2, b = 6, c = 2, d = -2, e = 2, f = 2, g = -1, h = -1, m = 1$, and $3n = 0.02$. It can be seen from the Figure that the limit cycle presented by the system is completely symmetric. In conclusion, the attractors generated by the new system are symmetric with respect to different initial conditions.
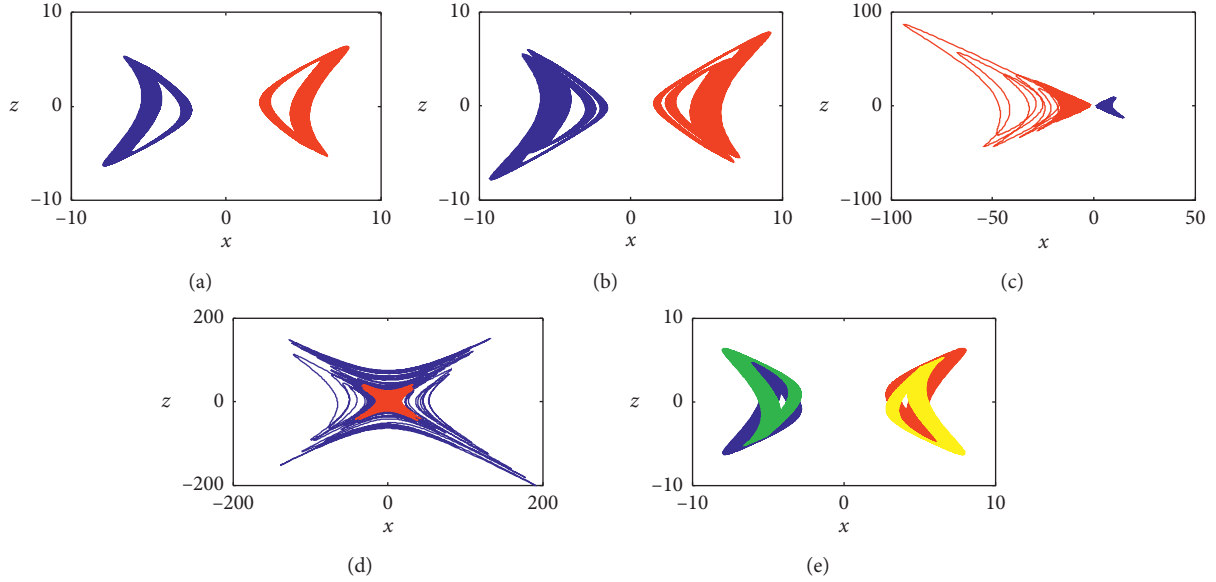
Figure 5: Various coexisting attractors with different values of parameter d in the $x - z$ plane: (a) $d = -3$, (b) $d = -0.5$, (c) $d = 0$, (d) $d = 15$, and (e) $d = -7$.
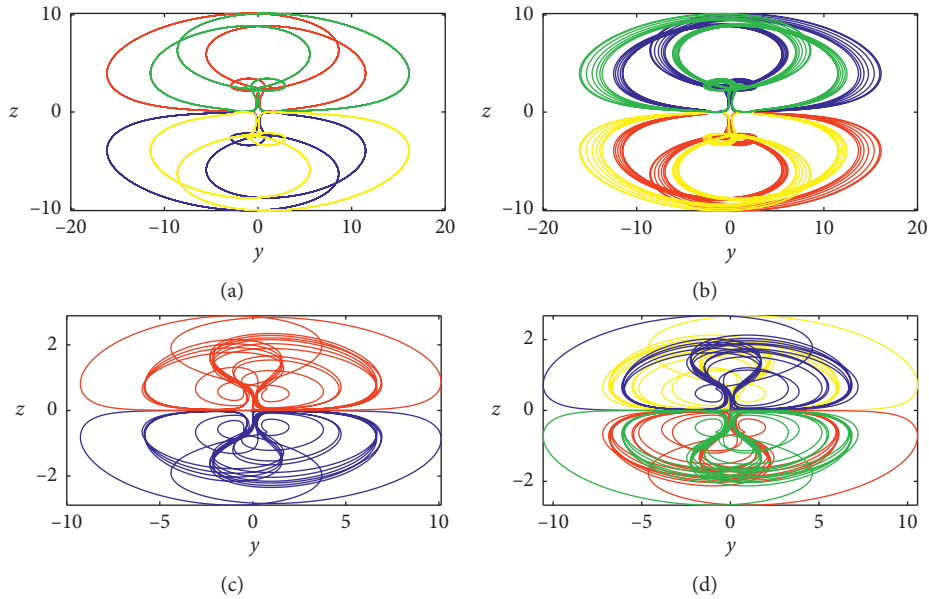
Figure 6: Coexisting attractors in the memristive hyperchaotic system: projections of different attractors on the $y - z$ plane for different initial conditions. (a) Symmetric period-1, $[1, 1, 1, 1, 1, 1]$ (red), $[-1, -1, -1, 1, 1, 1]$ (blue), $[-1, -1, 1, 1, -1, -1]$ (green), and $[1, 1, -1, -1, -1, 1]$ (yellow). (b) Symmetric one-wing multiperiod, $[-1, 1, 1, -1, 1, 1]$ (red), $[1, 1, -1, 1, 1, 1]$ (blue), $[-1, -1, -1, 1, -1, -1]$ (green), and $[1, -1, 1, -1, -1, -1]$ (yellow). (c) Symmetric two-wing multiperiod, $[-1, 1, 1, 1, 1, 1]$ (red) and $[1, 1, -1, -1, 1, 1]$ (blue). (d) Symmetric two-wing multiperiod, $[-1, 1, -1, 1, -1, -1]$ (red), $[-1, -1, 1, -1, 1, 1]$ (blue), $[1, -1, -1, 1, 1, 1]$ (green), and $[1, 1, 1, -1, -1, -1]$ (yellow).

3.4. Complexity Analysis of Spectral Entropy. Spectral entropy (SE) algorithm is based on the Fourier transform to calculate the relative power spectrum and the Shannon entropy to calculate the SE complexity of the sequence, which reflects the disorder of time series in the frequency domain [81]. If the spectrum of the sequence is more complex, the SE of the chaotic system will be larger, making the system more complex, otherwise the system complexity is low [82]. Generally, the SE algorithm can be described as follows: given a chaotic random sequence $\{x(n), n = 0, 1, 2, \ldots, N - 1\}$ of length N, $x(n) = x(n) - \overline{x}$ is adopted to remove the dc part, where $\overline{x}$ is the mean value of the given sequence, and discrete Fourier transform is performed on sequence $x(n)$:

(a)

(b)

(c)

(d)
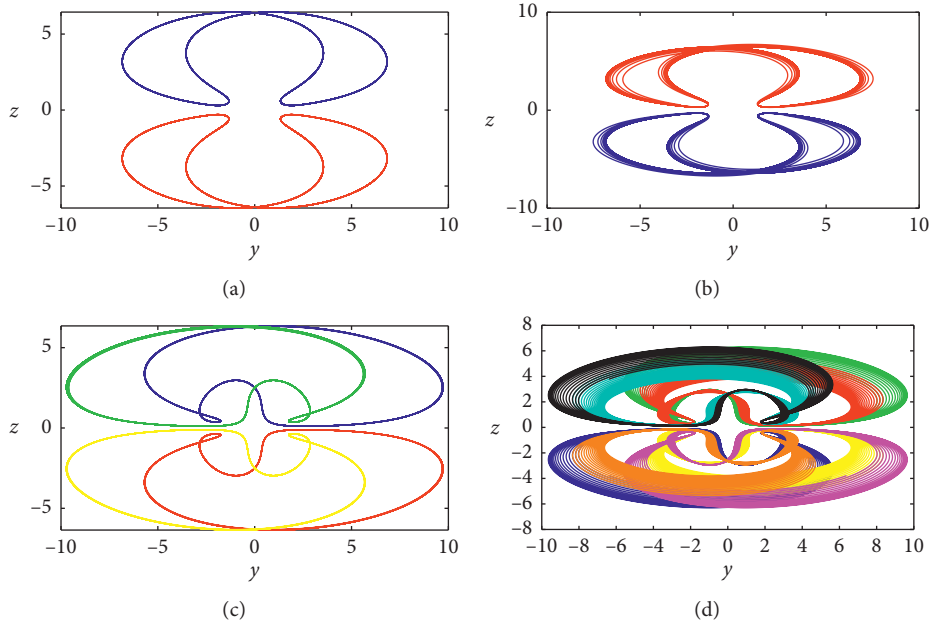
FIGURE 7: Coexisting attractors in the memristive hyperchaotic system: projections of different attractors on the $y - z$ plane for different initial conditions. (a) Symmetric two-wing period-1, $[1, 1, 1, 1, 1, 1]$ (blue) and $[1, -1, -1, 1, -1, 1]$ (red). (b) Symmetric two-wing multiperiod, $[-1, 1, 1, 1, 1, -1]$ (red) and $[-1, -1, -1, -1, -1, 1]$ (blue). (c) Symmetric one-wing period-1, $[-1, -1, -1, -1, -1, -1]$ (red), $[-1, 1, 1, 1, 1, 1]$ (blue), $[1, 1, 1, -1, -1, 1]$ (green), and $[-1, 1, -1, -1, -1, -1]$ (yellow). (d) Symmetric one-wing multiperiod, $[-1, -1, 1, -1, 1, 1]$ (red), $[1, -1, 1, -1, -1, -1]$ (blue), $[1, 1, -1, 1, 1, 1]$ (green), $[1, -1, -1, 1, 1, 1]$ (yellow), $[-1, -1, -1, 1, -1, -1]$ (black), $[-1, 1, -1, 1, -1, -1]$ (khaki), $[-1, 1, 1, -1, 1, 1]$ (magenta), and $[1, 1, 1, -1, -1, -1]$ (cyan).

(a)

(b)
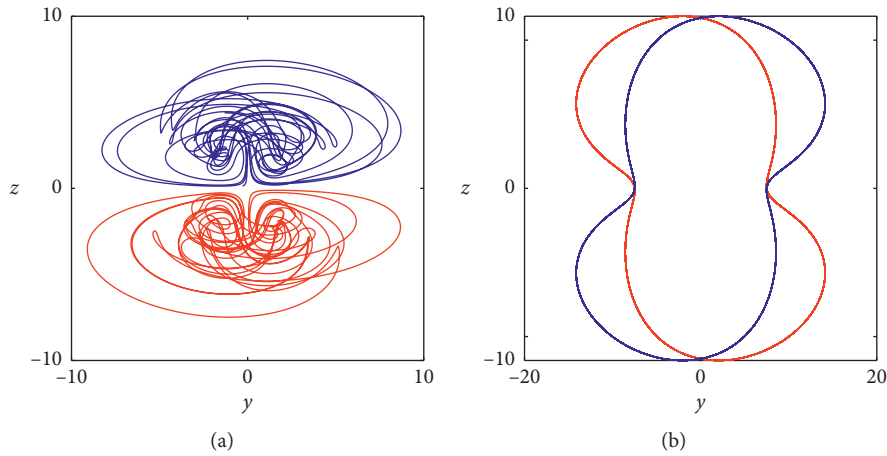
FIGURE 8: Various coexisting attractors in the $y - z$ plane under initial conditions $[1, 1, \pm 1, 1, 1, 1]$: (a) coexistence of two-wing chaotic attractors and (b) coexistence of limit cycles.

$$X(k) = \sum_{n=0}^{N-1} x(n) e^{-j2\pi nk/N}, \quad (11)$$

where $k = 0, 1, 2, \ldots, N - 1$. Taking half the total power of the calculation sequence for $X(k)$:

$$p_t = \frac{1}{N} \sum_{k=0}^{N/2-1} |X(k)|^2. \quad (12)$$

According to the total power of the sequence, the relative power spectrum probability of the sequence is obtained:

$$p_k = \frac{|X(k)|^2}{\sum_{k=0}^{N/2-1} |X(k)|^2}. \quad (13)$$

The normalized SE is

$$SE = \frac{se}{\ln(N/2)}, \quad (14)$$

where $se = -\sum_{k=0}^{N/2-1} P_k \ln P_k$. Using p_k and the Shannon entropy, the spectral entropy of the system is obtained.

The complexity of system (4) is analyzed by the SE algorithm. The control parameters a and d of the chaotic system

are divided into 101×101 parts, where $a \in [0, 12]$ and $d \in [-10, 20]$, and then the SE of each point (a, d) in the parameter space is calculated. Figure 7 shows the SE diagram of system (4) based on the previous algorithm. It can be seen from the figure that Figures 9(a) and 9(b) well correspond to the largest Lyapunov exponents in Figures 2 and 3. The results show that with the increase of parameters a and d, the higher the complexity of the chaotic system is, the higher the complexity of the system is mainly concentrated in $a \in [4.6, 12]$ and $d \in (0, 20]$. Figure 9(c) shows the SE complexity in control parameters a and d planes. It can be seen from the figure that the system has high complexity in a large range, which means chaos or hyperchaos in these ranges.

4. Circuit Design

In recent years, the implementation of a chaotic system by hardware mainly includes analog discrete component circuit, CMOS integrated circuit, and continuous chaotic signal by modern digital signal processing technology, such as FPGA. CMOS technology is used to realize the chaotic oscillator circuit, which has the characteristics of low power consumption and small area [12–14, 49], but the design needs a long period, high cost, and difficult tuning [83–85]. Because of its large capacity and high reliability, FPGA is widely used in modern digital signal processing. However, FPGA needs a discrete continuous system, writing the underlying hardware code and requiring the computational intensive reading [15, 21, 60]. It is the most common method to generate a chaotic signal by using discrete components to design an analog circuit with simple structure, low cost, and easy operation [26–28, 30–32, 57–59, 61]. To further verify the dynamic characteristics of system (4), the system circuit was designed using discrete components: resistors, capacitors, operational amplifiers, and multipliers. In the circuit design, LF347 is used as the operational amplifier, the multiplier is AD633JN, and the multiplication factor is 0.1/V. The operating voltage of operational amplifier is $\pm E = \pm 15\,\mathrm{V}$, and the saturation voltage measured by the operational amplifier and the multiplier is $\pm |\mathrm{Vsat}| \approx \pm 13.5\,\mathrm{V}$. The relevant circuit equations are as follows:

$$\begin{cases} \dot{v}_x = -\dfrac{1}{R_1 C_x} v_x + \dfrac{1}{10 \cdot R_2 C_x} v_y v_z, \\[2mm] \dot{v}_y = -\dfrac{1}{R_3 C_y} v_y + \dfrac{1}{R_4 C_y}\left(\dfrac{R v_u}{R_{13}} + \dfrac{R}{100 R_{14}} v_\varphi^2 v_u\right), \\[2mm] \dot{v}_z = \dfrac{1}{10 \cdot R_5 C_z} v_x v_y - \dfrac{1}{R_6 C_z} v_z + \dfrac{1}{R_7 C_z} v_w, \\[2mm] \dot{v}_w = \dfrac{1}{R_8 C_w} v_w - \dfrac{1}{R_9 C_w} v_z, \\[2mm] \dot{v}_u = \dfrac{1}{R_{10} C_u} v_u - \dfrac{1}{100 \cdot R_{11} C_u} v_x^2 v_y, \\[2mm] \dot{v}_\varphi = \dfrac{1}{R_{12} C_\varphi} v_u, \end{cases} \tag{15}$$

where $R_1 = R/a$, $R_3 = R/b$, $R_4 = R/f$, $R_6 = R/c$, $R_7 = R/g$, $R_8 = R/d$, $R_9 = R/h$, $R_{10} = R/e$, $R_{13} = R/fm$, and $R_{14} = R/(100 \cdot 3fn)$. The hardware experiment simulation circuit of system (4) is shown in Figure 10. According to the parameter values in the four cases given in Table 2, the resistance values of the parameters in the equation are calculated when $C_x = C_y = C_z = C_w = C_u = C_\varphi = 10\,\mathrm{nF}$, $R = 100\,\mathrm{k\Omega}$, $R_2 = R_5 = 10\,\mathrm{k\Omega}$, $R_{11} = 1\,\mathrm{k\Omega}$, and $R_{12} = 100\,\mathrm{k\Omega}$. Figure 11 shows a group of phase portraits obtained by the Multisim simulator, which is basically consistent with the MATLAB numerical simulation results in the previous dynamic analysis and verifies the correctness of the chaotic circuit.

5. Active Control Synchronization of the Novel 6D Memristive Hyperchaotic System

At present, many synchronization methods are based on the synchronization between two identical systems, but between practical engineering applications, many systems are of different structures, so it is very important to realize the synchronization between two systems with different structures. The system mainly consists of two parts: one is the main system and the other is the slave system. This section mainly uses the method of active control to realize the synchronization of system (4). Set the main system as

$$\begin{cases} \dot{x}_1 = a_1 x_1 + y_1 z_1, \\[1mm] \dot{y}_1 = -b_1 y_1 + f(m + 3n\varphi_1^2) l_1, \\[1mm] \dot{z}_1 = -c_1 z_1 + x_1 y_1 + g_1 w_1, \\[1mm] \dot{w}_1 = d_1 w_1 - h_1 z_1, \\[1mm] \dot{l}_1 = e l_1 - x_1^2 y_1, \\[1mm] \dot{\varphi}_1 = l_1. \end{cases} \tag{16}$$

The slave system is different from the main system in structure. The 6D hyperchaotic system designed by Yang et al. [46] is used as the slave system:

$$\begin{cases} \dot{x}_2 = a_2(y_2 - x_2) + w_2 + u_1, \\[1mm] \dot{y}_2 = c_2 x_2 - y_2 - x_2 z_2 + l_2 + u_2, \\[1mm] \dot{z}_2 = -b_2 z_2 - x_2 y_2 + u_3, \\[1mm] \dot{w}_2 = d_2 w_2 - x_2 z_2 + u_4, \\[1mm] \dot{l}_2 = -k y_2 + u_5, \\[1mm] \dot{\varphi}_2 = h_2 \varphi_2 + u_6, \end{cases} \tag{17}$$

where $u = [u_1, u_2, u_3, u_4, u_5, u_6]^T$ is the active controller of the synchronous system, which can make the main system and the slave system tend to be synchronous under different parameters and initial conditions. The error variable is made as shown in the following equation:
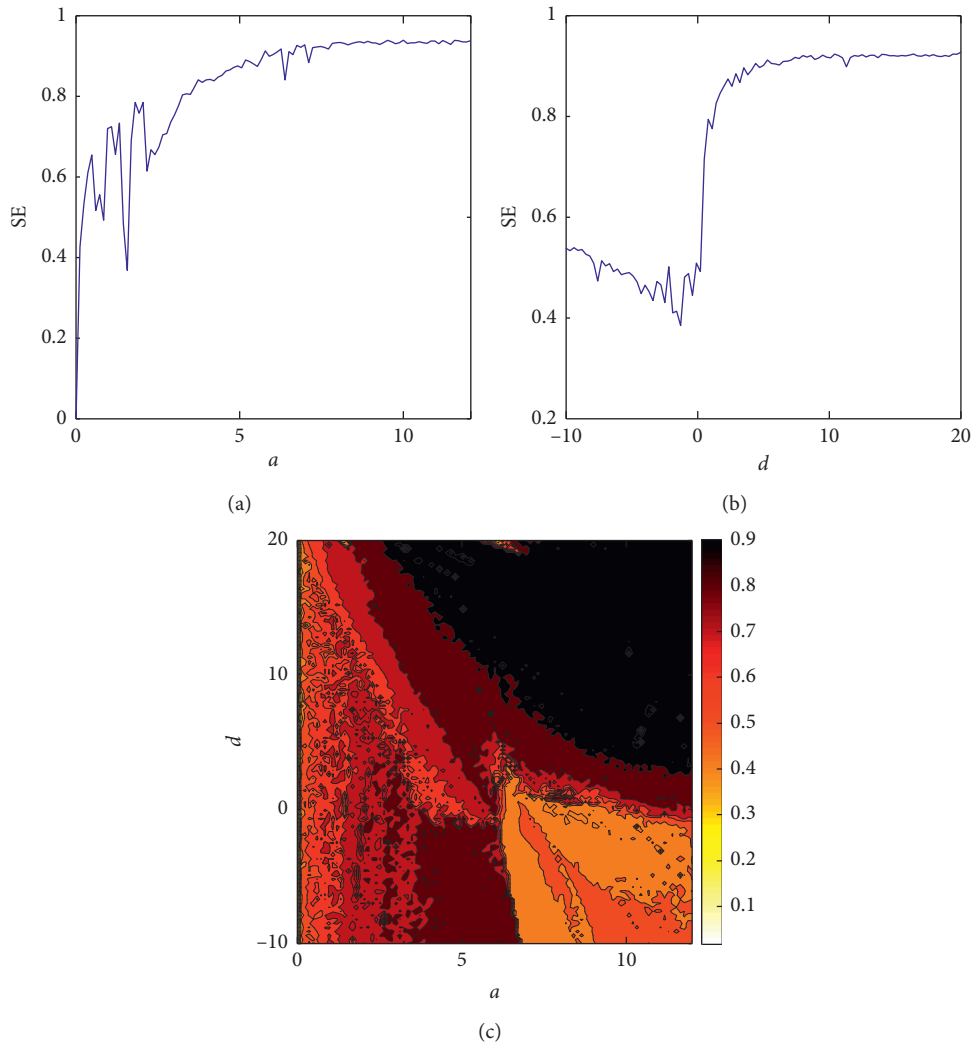
FIGURE 9: Spectral entropy (SE) complexity of system (4): (a) SE complexity versus a ($d = 15$); (b) SE complexity versus d ($a = 10$); (c) SE complexity in the $a - d$ plane.
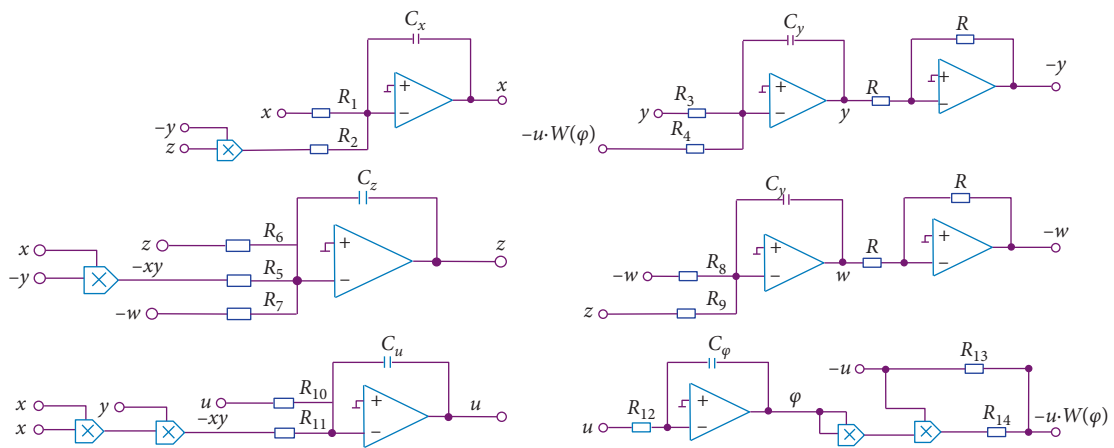
FIGURE 10: The circuit diagram of system (4).

TABLE 2: Resistance values corresponding to different parameter values and simulation Figure 11.

Case	Parameters	Resistor	Figure
Case 1	$a = 1, b = 8, c = 1, d = -20, e = 1,$ $f = 2, g = 1, h = -1, m = 1, 3n = 0.02$	$R_1 = 100 k\Omega, R_3 = 12.5 \, k\Omega, R_4 = 50 \, k\Omega, R_6 = 100 \, k\Omega,$ $R_7 = 100 \, k\Omega, R_8 = 5 \, k\Omega, R_9 = 100 \, k\Omega, R_{10} = 100 \, k\Omega$	Figure 11(a)
Case 2	$a = 1, b = 5, c = 1, d = -20, e = 1,$ $f = 2, g = 1, h = -1, m = 1, 3n = 0.02$	$R_1 = 100 \, k\Omega, R_3 = 20 \, k\Omega, R_4 = 50 \, k\Omega, R_6 = 100 \, k\Omega,$ $R_7 = 100 \, k\Omega, R_8 = 5 \, k\Omega, R_9 = 100 \, k\Omega, R_{10} = 100 \, k\Omega$	Figures 11(b) and 11(c)
Case 3	$a = 2, b = 6, c = 1, d = -20, e = 1,$ $f = 2, g = 1, h = -1, m = 1, 3n = 0.02$	$R_1 = 50 \, k\Omega, R_3 = 16.5 \, k\Omega, R_4 = 50 \, k\Omega, R_6 = 100 \, k\Omega,$ $R_7 = 100 \, k\Omega, R_8 = 5 \, k\Omega, R_9 = 100 \, k\Omega, R_{10} = 100 \, k\Omega$	Figures 11(d) and 11(e)
Case 4	$a = 2, b = 6, c = 2, d = -2, e = 2,$ $f = 2, g = -1, h = -1, m = 1, 3n = 0.02$	$R_1 = 50 \, k\Omega, R_3 = 16.5 \, k\Omega, R_4 = 50 \, k\Omega, R_6 = 50 \, k\Omega,$ $R_7 = 100 \, k\Omega, R_8 = 50 \, k\Omega, R_9 = 100 \, k\Omega, R_{10} = 50 \, k\Omega$	Figure 11(f)
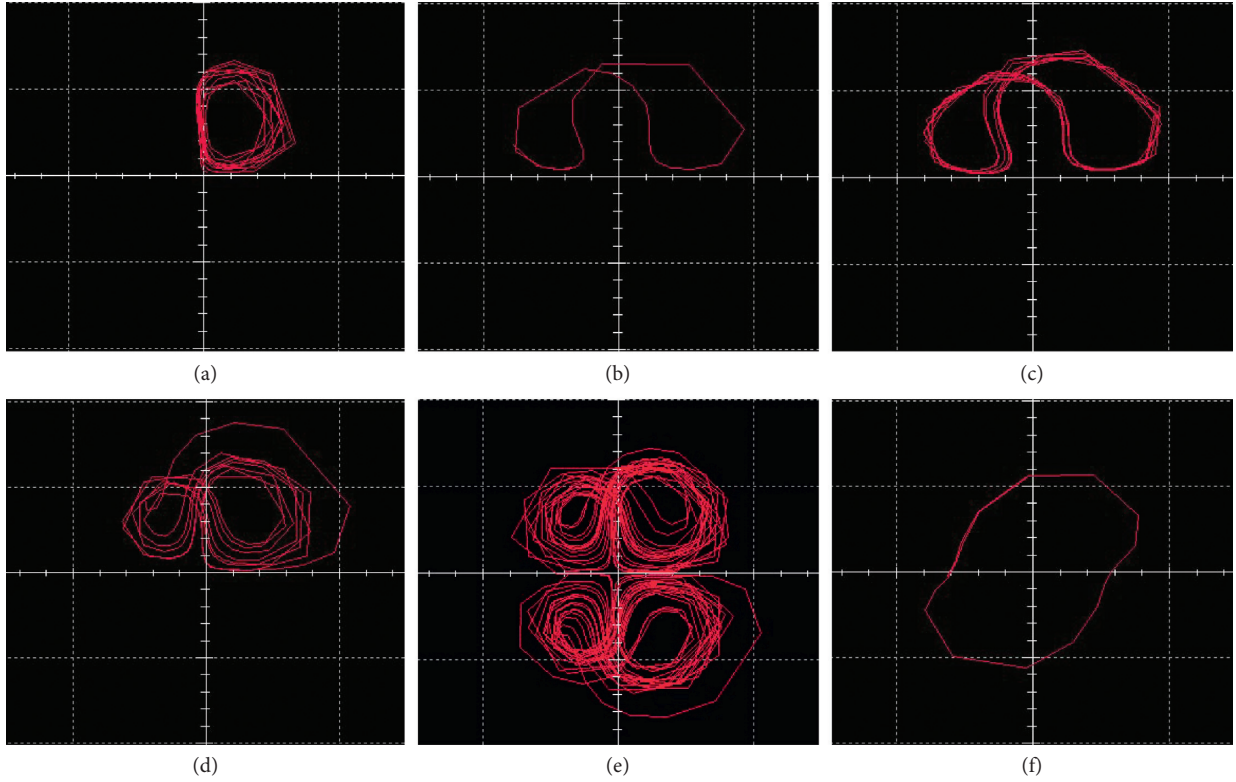
FIGURE 11: The circuit simulation diagram of system (4): (a) one-wing multiperiod, (b) period-1, (c) two-wing multiperiod, (d) two-wing, (e) four-wing, and (f) limit cycle.

$$\begin{cases} e_1 = x_2 - x_1, \\ e_2 = y_2 - y_1, \\ e_3 = z_2 - z_1, \\ e_4 = w_2 - w_1, \\ e_5 = l_2 - l_1, \\ e_6 = \varphi_2 - \varphi_1. \end{cases} \quad (18)$$

Therefore, from the error variable, the main system (16), and the slave system (17), the error system equation can be obtained:

$$\begin{cases} \dot{e}_1 = a_2 e_2 - (a_2 + a_1)e_1 + e_4 + a_2 y_1 - a_2 x_1 + a_1 x_2 - y_1 z_1 + w_1 + u_1, \\ \dot{e}_2 = c_2 e_1 + c_2 x_1 - (1 + b_1)e_2 - y_1 - x_2 z_2 + (1 + fm)e_5 + b_1 y_2 - fml_2 - 3nf\varphi_1^2 l_1 + l_1 + u_2, \\ \dot{e}_3 = (-b_2 - c_1)e_3 - b_2 z_1 + x_2 y_2 + c_1 z_2 - x_1 y_1 + g_1 e_4 - g_1 w_2 + u_3, \\ \dot{e}_4 = (d_2 + d_1)e_4 + d_2 w_1 - h_1 e_3 - x_2 z_2 - d_1 w_2 + h_1 z_2 + u_4, \\ \dot{e}_5 = -ke_2 + ee_5 - ky_1 - el_2 + x_1^2 y_1 + u_5, \\ \dot{e}_6 = h_2 e_6 + g_2 e_2 + e_5 + h_2 \varphi_1 + g_2 y_1 + u_6. \end{cases} \tag{19}$$

By simplifying the linear term of equation (19), the active control function is obtained:

$$\begin{cases} u_1 = -a_2 y_1 + a_2 x_1 - a_1 x_2 + y_1 z_1 - w_1 + v_1, \\ u_2 = -c_2 x_1 + y_1 + x_2 z_2 - b_1 y_2 + fml_2 + 3nf\varphi_1^2 l_1 - l_1 + v_2, \\ u_3 = b_2 z_1 - x_2 y_2 - c_1 z_2 + x_1 y_1 + g_1 w_2 + v_3, \\ u_4 = d_2 w_1 + x_2 z_2 + d_1 w_2 - h_1 z_2 + v_4, \\ u_5 = ky_1 + el_2 - x_1^2 y_1 + v_5, \\ u_6 = -h_2 \varphi_1 - g_2 y_1 + v_6, \end{cases} \tag{20}$$

where $v = [v_1, v_2, v_3, v_4, v_5, v_6]^T$ is the control input, and the linear error system without an active controller can be obtained by taking (20) into (19):

$$\begin{cases} \dot{e}_1 = a_2 e_2 - (a_2 + a_1)e_1 + e_4 + v_1, \\ \dot{e}_2 = c_2 e_1 + (1 + fm)e_5 - (1 + b_1)e_2 + v_2, \\ \dot{e}_3 = g_1 e_4 + (-b_2 - c_1)e_3 + v_3, \\ \dot{e}_4 = (d_2 + d_1)e_4 - h_1 e_3 + v_4, \\ \dot{e}_5 = -ke_2 + ee_5 + v_5, \\ \dot{e}_6 = h_2 e_6 + g_2 e_2 + e_5 + v_6. \end{cases} \tag{21}$$

To synchronize the system, we need to

$$\lim_{x \to \infty} e_i = 0, \quad (i = 1, 2, 3, 4, 5, 6). \tag{22}$$

The above formula shows that if system (21) tends to be stable with time and under the control input $v = [v_1, v_2, v_3, v_4, v_5, v_6]^T$, then the error variable $e = [e_1, e_2, e_3, e_4, e_5, e_6]^T$ tends to zero and then the main system (16) and the slave system (17) are synchronized. To achieve this goal, we define a matrix A to express the relationship between the error system and the control input, which can be expressed as

$$v = A \cdot e. \tag{23}$$

According to the criteria of Routh–Hurwitz, if equation (19) is stable, all eigenvalues of a matrix must be negative. Therefore, equation (19) can be expressed as

$$\begin{bmatrix} v_1 \\ v_2 \\ v_3 \\ v_4 \\ v_5 \\ v_6 \end{bmatrix} = \begin{bmatrix} a_1 + a_2 - 1 & -a_2 & 0 & 1 & 0 & 0 \\ -c_2 & b_1 & 0 & 0 & -fm - 1 & 0 \\ 0 & 0 & b_2 + c_1 - 1 & 0 & 0 & 0 \\ 0 & 0 & h_1 & -d_1 - d_2 - 1 & 0 & 0 \\ 0 & k & 0 & 0 & -e - 1 & 0 \\ 0 & -g_2 & 0 & 0 & -1 & -h_2 - 1 \end{bmatrix} \begin{bmatrix} e_1 \\ e_2 \\ e_3 \\ e_4 \\ e_5 \\ e_6 \end{bmatrix}. \tag{24}$$

Then, the eigenvalue of the error system (21) is $-1, -1,$ $-1, -1, -1,$ and -1, so equation (24) can be reduced to

$$\begin{cases} v_1 = (a_1 + a_2 - 1)(x_2 - x_1) + (w_2 - w_1) - a_2(y_2 - y_1), \\ v_2 = -c_2(x_2 - x_1) + b_1(y_2 - y_1) + (-fm - 1)(l_2 - l_1), \\ v_3 = (b_2 + c_1 - 1)(z_2 - z_1), \\ v_4 = h_1(z_2 - z_1) + (-d_1 - d_2 - 1)(w_2 - w_1), \\ v_5 = k(y_2 - y_1) + (-e - 1)(l_2 - l_1), \\ v_6 = -g_2(y_2 - y_1) - (l_2 - l_1) + (-h_2 - 1)(\varphi_2 - \varphi_1). \end{cases} \tag{25}$$
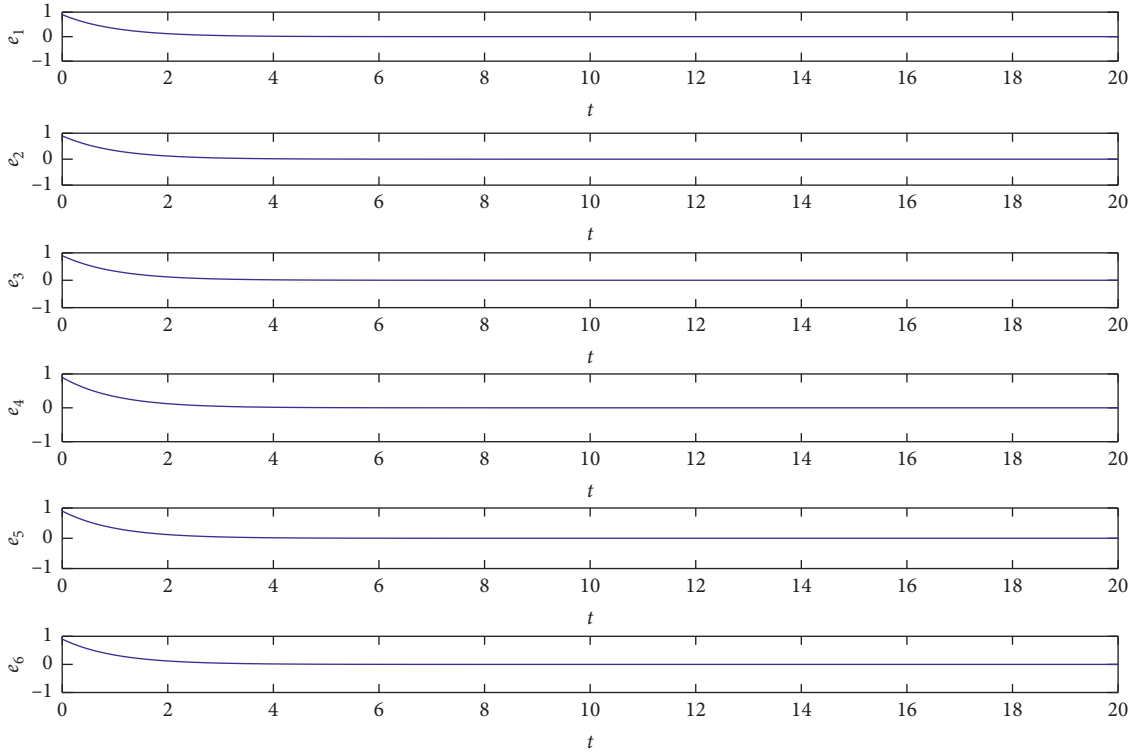
FIGURE 12: The trajectories of the synchronization errors e_1, e_2, e_3, e_4, e_5, and e_6.
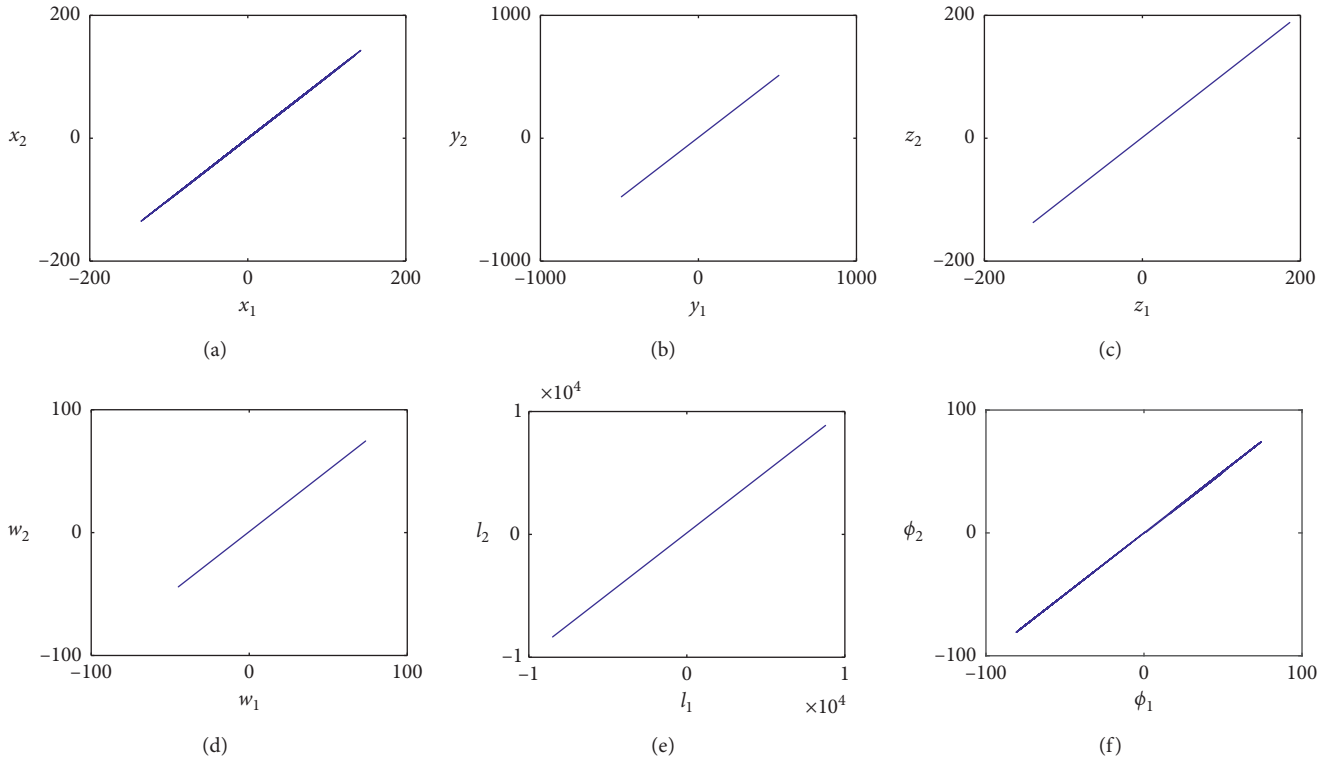
FIGURE 13: Synchronous phase diagram of two different structure systems in the corresponding plane. (a) $x_1 - x_2$, (b) $y_1 - y_2$, (c) $z_1 - z_2$, (d) $w_1 - w_2$, (e) $l_1 - l_2$, and (f) $\varphi_1 - \varphi_2$.

The main slave system is simulated by MATLAB to verify whether the proposed system can achieve synchronization. According to the system equation, the parameters of the main system (16) are given as $a_1 = 10, b_1 = 60, c_1 = 20, d_1 = 15, e = 40, f = 1, g_1 = 50, h_1 = 10, m = 1$, and $3n = 0.02$, the parameters of the slave system (17) are set as $a_2 = 10, b_2 = 8/3, c_2 = 28, \quad d_2 = 2, g_2 = 1, k = 8.4$, and $h_2 = 1$, and the initial conditions of the main slave system are set as $[1, 1, 1, 1, 1, 1]$ and $[0.1, 0.1, 0.1, 0.1, 0.1, 0.1]$, respectively. Figure 12 shows a simulation diagram of the system error. It can be seen from Figure 12 that when $t > 2$, two different structure hyperchaotic systems realize global synchronization. From Figure 13, it can also be seen from the six phase planes that the two systems realize synchronization.

6. Conclusion

This work presents a novel 6D memristive four-wing hyperchaotic system. Dynamical analysis and numerical simulation of the novel chaotic system were first carried out. Further analysis of the novel system shows that the multiple coexisting attractors can be observed with different system parameter values and initial values. Then, circuitry of the novel chaotic system was designed. The numerical and electronic circuit simulation results were found to be in good accordance. Besides, synchronization between the proposed 6D memristive hyperchaotic system and the 6D hyperchaotic Yang system with different structures was realized by an active control approach for secure communication applications, and the accuracy and validity of the results were verified by theoretical analysis and numerical simulations.

Data Availability

All data used to support the findings of this study are available from the corresponding author upon request.

Conflicts of Interest

The authors declare that they have no conflicts of interest.

Acknowledgments

References

[1] A. Dmitriev, V. Kornilov, and S. Maltseva, "Complexity of a microblogging social network in the framework of modern nonlinear science," *Complexity*, vol. 2018, Article ID 4732491, 11 pages, 2018.

[2] X. Zhang, C. Wang, W. Yao, and H. Lin, "Chaotic system with bondorbital attractors," *Nonlinear Dynamics*, vol. 97, no. 4, pp. 2159–2174, 2019.

[3] F. Wang, L. Zhang, S. Zhou, and Y. Huang, "Neural network-based finite-time control of quantized stochastic nonlinear systems," *Neurocomputing*, vol. 362, pp. 195–202, 2019.

[4] F. Yu, L. Liu, L. Xiao, K. Li, and S. Cai, "A robust and fixed-time zeroing neural dynamics for computing time-variant nonlinear equation using a novel nonlinear activation function," *Neurocomputing*, vol. 350, pp. 108–116, 2019.

[5] J. Jin, L. Zhao, M. Li, F. Yu, and Z. Xi, "Improved zeroing neural networks for finite time solving nonlinear equations," *Neural Computing and Applications*, vol. 32, no. 9, pp. 4151–4160, 2020.

[6] F. Tan, L. Zhou, F. Yu, and J. Lu, "Fixed-time continuous stochastic synchronisation of two-layer dynamical networks," *International Journal of Systems Science*, vol. 51, no. 2, pp. 242–257, 2020.

[7] M. Long, F. Peng, and Y. Zhu, "Identifying natural images and computer generated graphics based on binary similarity measures of PRNU," *Multimedia Tools and Applications*, vol. 78, no. 1, pp. 489–506, 2019.

[8] L. Zhou, F. Tan, F. Yu, and W. Liu, "Cluster synchronization of two-layer nonlinearly coupled multiplex networks with multi-links and time-delays," *Neurocomputing*, vol. 359, pp. 264–275, 2019.

[9] W. Yao, C. Wang, J. Cao, Y. Sun, and C. Zhou, "Hybrid multisynchronization of coupled multistable memristive neural networks with time delays," *Neurocomputing*, vol. 363, pp. 281–294, 2019.

[10] H. Lin and C. Wang, "Influences of electromagnetic radiation distribution on chaotic dynamics of a neural network," *Applied Mathematics and Computation*, vol. 369, Article ID 124840, 2020.

[11] L. Zhou and F. Tan, "A chaotic secure communication scheme based on synchronization of double-layered and multiple complex networks," *Nonlinear Dynamics*, vol. 96, no. 2, pp. 869–883, 2019.

[12] X. Zhang and C. Wang, "A novel multi-attractor period multi-scroll chaotic integrated circuit based on CMOS wide adjustable CCCII," *IEEE Access*, vol. 7, no. 1, pp. 16336–16350, 2019.

[13] J. Jin and L. Zhao, "Low voltage low power fully integrated chaos generator," *Journal of Circuits Systems and Computers*, vol. 27, no. 10, Article ID 1850155, 2018.

[14] J. Jin, "Programmable multi-direction fully integrated chaotic oscillator," *Microelectronics Journal*, vol. 75, pp. 27–34, 2018.

[15] F. Yu, H. Shen, L. Liu et al., "CCII and FPGA Realization: a multistable modified four-order autonomous Chua's chaotic system with coexisting multiple attractors," *Complexity*, vol. 2020, Article ID 5212601, 17 pages, 2020.

[16] Q. Yin and C. H. Wang, "A new chaotic image encryption scheme using breadth-first search and dynamic diffusion," *International Journal of Bifurcation and Chaos*, vol. 28, no. 4, Article ID 1850047, 2018.

[17] S. Wang, C. Wang, and C. Xu, "An image encryption algorithm based on a hidden attractor chaos system and the Knuth-Durstenfeld algorithm," *Optics and Lasers in Engineering*, vol. 128, Article ID 105995, 2020.

[18] G. Cheng, C. Wang, and H. Chen, "A novel color image encryption algorithm based on hyperchaotic system and permutation-diffusion architecture," *International Journal of Bifurcation and Chaos*, vol. 29, no. 9, Article ID 1950115, 2019.

[19] M. Long, F. Peng, and H.-y. Li, "Separable reversible data hiding and encryption for HEVC video," *Journal of Real-Time Image Processing*, vol. 14, no. 1, pp. 171–182, 2018.

[20] Y. Chen, J. Wang, R. Xia, Q. Zhang, Z. Cao, and K. Yang, "The visual object tracking algorithm research based on adaptive combination kernel," *Journal of Ambient Intelligence and Humanized Computing*, vol. 10, no. 12, pp. 4855–4867, 2019.

[21] F. Yu, Q. Wan, J. Jin et al., "Design and FPGA implementation of a pseudorandom number generator based on a four-wing memristive hyperchaotic system and Bernoulli map," *IEEE Access*, vol. 7, pp. 181884–181898, 2019.

[22] F. Yu, L. Li, Q. Tang, S. Cai, Y. Song, and Q. Xu, "A survey on true random number generators based on chaos," *Discrete Dynamics in Nature and Society*, vol. 2019, Article ID 2545123, 10 pages, 2019.

[23] F. Yu, L. Liu, S. Qian et al., "Chaos-based application of a novel multistable 5D memristive hyperchaotic system with coexisting multiple attractors," *Complexity*, vol. 2020, Article ID 8034196, 19 pages, 2020.

[24] F. Yu and C. Wang, "Secure communication based on a four-wing chaotic system subject to disturbance inputs," *Optik*, vol. 125, no. 20, pp. 5920–5925, 2014.

[25] L. L. Zhou, F. Tan, and F. Yu, "A robust synchronization-based chaotic secure communication scheme with double-layered and multiple hybrid networks," *IEEE Systems Journal*, pp. 1–12, 2019.

[26] F. Yu, L. Gao, K. Gu, B. Yin, Q. Wan, and Z. Zhou, "A fully qualified four-wing four-dimensional autonomous chaotic system and its synchronization," *Optik*, vol. 131, pp. 79–88, 2017.

[27] F. Yu, C. H. Wang, J. W. Yin et al., "Novel four-dimensional autonomous chaotic system generating one-, two-, three-and four-wing attractors," *Chinese Physics B*, vol. 20, no. 11, Article ID 110505, 2011.

[28] L. Zhou, C. Wang, and L. Zhou, "A novel no-equilibrium hyperchaotic multi-wing system via introducing memristor," *International Journal of Circuit Theory and Applications*, vol. 46, no. 1, pp. 84–98, 2018.

[29] Q. Deng and C. Wang, "Multi-scroll hidden attractors with two stable equilibrium points," *Chaos: An Interdisciplinary Journal of Nonlinear Science*, vol. 29, no. 9, Article ID 093112, 2019.

[30] F. Yu, P. Li, K. Gu, and B. Yin, "Research progress of multi-scroll chaotic oscillators based on current-mode devices," *Optik*, vol. 127, no. 13, pp. 5486–5490, 2016.

[31] C. Wang, X. Liu, and H. Xia, "Multi-piecewise quadratic nonlinearity memristor and its 2N-scroll and 2N+1-scroll chaotic attractors system," *Chaos: An Interdisciplinary Journal of Nonlinear Science*, vol. 27, no. 3, Article ID 033114, 2017.

[32] F. Yu, C. Wang, and H. He, "Grid multiscroll hyperchaotic attractors based on colpitts oscillator mode with controllable grid gradient and scroll numbers," *Journal of Applied Research and Technology*, vol. 11, no. 3, pp. 371–380, 2013.

[33] A. Lassoued and O. Boubaker, "Dynamic analysis and circuit design of a novel hyperchaotic system with fractional-order terms," *Complexity*, vol. 2017, Article ID 3273408, 10 pages, 2017.

[34] A. G. Radwan, A. T. Azar, S. Vaidyanathan, J. M. Munoz-Pacheco, and A. Ouannas, "Fractional-order and memristive nonlinear systems: advances and applications," *Complexity*, vol. 2017, Article ID 3760121, 2 pages, 2017.

[35] X. Zhang and Z. Li, "Hidden extreme multistability in a novel 4D fractional-order chaotic system," *International Journal of Non-linear Mechanics*, vol. 111, pp. 14–27, 2019.

[36] O. E. Rossler, "An equation for hyperchaos," *Physics Letters A*, vol. 71, no. 2-3, pp. 155–157, 1979.

[37] R. Barboza, "Dynamics of a hyperchaotic lorenz system," *International Journal of Bifurcation and Chaos*, vol. 17, no. 12, pp. 4285–4294, 2011.

[38] X. J. Wu and X. Y. Wang, "Chaos synchronization of a new hyperchaotic Chen system via nonlinear control," *Acta Physica Sinica*, vol. 55, no. 12, pp. 6261–6266, 2006.

[39] G. Wang, X. Zhang, Y. Zheng, and Y. Li, "A new modified hyperchaotic Lü system," *Physica A: Statistical Mechanics and its Applications*, vol. 371, no. 2, pp. 260–272, 2006.

[40] F. Yu, C. H. Wang, Y. Hu, and J. W. Yin, "Anti-synchronization of a novel hyperchaotic system with parameter mismatch and external disturbances," *Pramana*, vol. 79, no. 1, pp. 81–93, 2012.

[41] H. Wang and G. Dong, "New dynamics coined in a 4-D quadratic autonomous hyper-chaotic system," *Applied Mathematics and Computation*, vol. 346, no. 1, pp. 272–286, 2019.

[42] S. Vaidyanathan, "A ten-term novel 4-D hyperchaotic system with three quadratic nonlinearities and its control," *International Journal of Control Theory and Applications*, vol. 6, pp. 97–109, 2013.

[43] S. Vaidyanathan, C. Volos, and V.-T. Pham, "Hyperchaos, adaptive control and synchronization of a novel 5-D hyperchaotic system with three positive Lyapunov exponents and its SPICE implementation," *Archives of Control Sciences*, vol. 24, no. 4, pp. 409–446, 2014.

[44] K. Kemih, M. Ghanes, R. Remmouche, and A. Senouci, "A novel 5D-dimensional hyperchaotic system and its circuit simulation by EWB," *Mathematical Sciences Letters*, vol. 4, no. 1, pp. 1–4, 2015.

[45] M. M. Aziz and S. F. AL-Azzawi, "Chaos control and synchronization of a novel 5-D hyperchaotic lorenz system via nonlinear control," *International Journal of Modern Physics and Application*, vol. 2, no. 6, pp. 110–115, 2015.

[46] Q. Yang, W. M. Osman, and C. Chen, "A new 6D hyperchaotic system with four positive lyapunov exponents coined," *International Journal of Bifurcation and Chaos*, vol. 25, no. 4, Article ID 1550060, 2015.

[47] S. Cang, G. Qi, and Z. Chen, "A four-wing hyper-chaotic attractor and transient chaos generated from a new 4-D quadratic autonomous system," *Nonlinear Dynamics*, vol. 59, no. 3, pp. 515–527, 2010.

[48] A. Zarei, "Complex dynamics in a 5-D hyper-chaotic attractor with four-wing, one equilibrium and multiple chaotic attractors," *Nonlinear Dynamics*, vol. 81, no. 1-2, pp. 585–605, 2015.

[49] J. Jin and L. Cui, "Fully integrated memristor and its application on the scroll-controllable hyperchaotic system," *Complexity*, vol. 2019, Article ID 4106398, 2019.

[50] Q. Zhao, C. H. Wang, and X. Zhang, "A universal emulator for memristor, memcapacitor, and meminductor and its chaotic circuit," *Chaos: An Interdisciplinary Journal of Nonlinear Science*, vol. 29, no. 1, Article ID 013141, 2019.

[51] V. T. Pham, S. Vaidyanathan, E. Tlelo-Cuautle et al., "Memory circuit elements: complexity, complex systems, and applications," *Complexity*, vol. 2019, Article ID 4936123, 4 pages, 2019.

[52] D. B. Strukov, G. S. Snider, D. R. Stewart, and R. S. Williams, "The missing memristor found," *Nature*, vol. 453, no. 7191, pp. 80–83, 2008.

[53] L. Chua, "Memristor-the missing circuit element," *IEEE Transactions on Circuit Theory*, vol. 18, no. 5, pp. 507–519, 1971.

[54] M. Itoh and L. O. Chua, "Memristor oscillators," *International Journal of Bifurcation and Chaos*, vol. 18, no. 11, pp. 3183–3206, 2008.

[55] J.-Y. Ruan, K.-H. Sun, and J. Mou, "Memristor-based Lorenz hyper-chaotic system and its circuit implementation," *Acta Physica Sinica*, vol. 65, no. 19, Article ID 190502, 2016.

[56] L. Zhou, C. Wang, and L. Zhou, "Generating hyperchaotic multi-wing attractor in a 4D memristive circuit," *Nonlinear Dynamics*, vol. 85, no. 4, pp. 2653–2663, 2016.

[57] L. Zhou, C. Wang, and L. Zhou, "Generating four-wing hyperchaotic attractor and two-wing, three-wing, and four-wing chaotic attractors in 4D memristive system," *International Journal of Bifurcation and Chaos*, vol. 27, no. 2, Article ID 1750027, 2017.

[58] C. Wang, H. Xia, and L. Zhou, "A memristive hyperchaotic multiscroll Jerk system with controllable scroll numbers," *International Journal of Bifurcation and Chaos*, vol. 27, no. 6, Article ID 1750091, 2017.

[59] C. Wang, L. Zhou, and R. Wu, "The design and realization of a hyper-chaotic circuit based on a flux-controlled memristor with linear memductance," *Journal of Circuits, Systems and Computers*, vol. 27, no. 3, Article ID 1850038, 2018.

[60] F. Yu, L. Liu, B. He et al., "Analysis and FPGA realization of a novel 5D hyperchaotic four-wing memristive system, active control synchronization and secure communication application," *Complexity*, vol. 2019, Article ID 4047957, 18 pages, 2019.

[61] F. Yu, Z. Zhang, L. Liu et al., "Secure communication scheme based on a new 5D multistable four-wing memristive hyperchaotic system with disturbance inputs," *Complexity*, vol. 2020, Article ID 5859273, 16 pages, 2020.

[62] B. A. Mezatio, M. T. Motchongom, B. R. Wafo Tekam, R. Kengne, R. Tchitnga, and A. Fomethe, "A novel memristive 6D hyperchaotic autonomous system with hidden extreme multistability," *Chaos, Solitons and Fractals*, vol. 120, pp. 100–115, 2019.

[63] W. Li, Z. Chen, X. Gao, W. Liu, and J. Wang, "MultiModel framework for indoor localization under mobile edge computing environment," *IEEE Internet of Things Journal*, vol. 6, no. 3, pp. 4844–4853, 2019.

[64] K. Gu, X. Dong, and L. Wang, "Efficient traceable ring signature scheme without pairings," *Advances in Mathematics of Communications*, vol. 14, no. 2, pp. 207–232, 2020.

[65] W. Li, Y. Ding, Y. Yang et al., "Parameterized algorithms of fundamental NP-hard problems: a survey," *Human-Centric Computing and Information Sciences*, 2020.

[66] Y. Chen, W. Xu, J. Zuo, and K. Yang, "The fire recognition algorithm using dynamic feature fusion and IV-SVM classifier," *Cluster Computing*, vol. 22, no. S3, pp. 7665–7675, 2019.

[67] K. Gu, K. Wang, and L. Yang, "Traceable attribute-based signature," *Journal of Information Security and Applications*, vol. 49, pp. 102400–102416, 2019.

[68] L. Xiang, G. Guo, J. Yu, V. S. Sheng, and P. Yang, "A convolutional neural network-based linguistic steganalysis for synonym substitution steganography," *Mathematical Biosciences and Engineering*, vol. 17, no. 2, pp. 1041–1058, 2020.

[69] W. Li, H. Xu, H. Li et al., "Complexity and algorithms for superposed data uploading problem in networks with smart devices," *IEEE Internet of Things Journal*, p. 1, 2019.

[70] K. Gu, N. Wu, B. Yin, and W. Jia, "Secure data query framework for cloud and fog computing," *IEEE Transactions on Network and Service Management*, vol. 17, no. 1, pp. 332–345, 2020.

[71] Y. Chen, J. Wang, X. Chen et al., "Single-image super-resolution algorithm based on structural self-similarity and deformation block features," *IEEE Access*, vol. 7, pp. 58791–58801, 2019.

[72] K. Gu, W. Zhang, S.-J. Lim, P. K. Sharma, Z. Al-Makhadmeh, and A. Tolba, "Reusable mesh signature scheme for protecting identity privacy of IoT devices," *Sensors*, vol. 20, no. 3, p. 758, 2020.

[73] L. M. Pecora and T. L. Carroll, "Synchronization in chaotic systems," *Physical Review Letters*, vol. 64, no. 8, pp. 821–824, 1990.

[74] G. M. Mahmoud and E. E. Mahmoud, "Complete synchronization of chaotic complex nonlinear systems with uncertain parameters," *Nonlinear Dynamics*, vol. 62, no. 4, pp. 875–882, 2010.

[75] W. S. Sayed, M. M. R. Henein, S. K. Abd-El-Hafiz, and A. G. Radwan, "Generalized dynamic switched synchronization between combinations of fractional-order chaotic systems," *Complexity*, vol. 2017, Article ID 9189120, 17 pages, 2017.

[76] F. Yu, C.-H. Wang, Y. Hu, and J.-W. Yin, "Projective synchronization of a five-term hyperbolic-type chaotic system with fully uncertain parameters," *Acta Physica Sinica*, vol. 61, no. 6, Article ID 060505, 2012.

[77] C.-H. Wang, Y. Hu, F. Yu, and H. Xu, "Time-controllable projective synchronization of a class of chaotic systems based on adaptive method," *Acta Physica Sinica*, vol. 62, no. 11, Article ID 110509, 2013.

[78] X.-T. Tran and H.-J. Kang, "Fixed-time complex modified function projective lag synchronization of chaotic (hyperchaotic) complex systems," *Complexity*, vol. 2017, Article ID 4020548, 9 pages, 2017.

[79] F. Yu and Y. Song, "Complete switched generalized function projective synchronization of a class of hyperchaotic systems with unknown parameters and disturbance inputs," *Journal of Dynamic Systems, Measurement, and Control-Transactions of the ASME*, vol. 136, no. 1, Article ID 014505, 2014.

[80] F. Yu, S. Qian, X. Chen et al., "A new 4D four-wing memristive hyperchaotic system: dynamical analysis, electronic circuit design, shape synchronization and secure communication," *International Journal of Bifurcation and Chaos*, 2020.

[81] Y. Peng, K. Sun, D. Peng, and W. Ai, "Dynamics of a higher dimensional fractional-order chaotic map," *Physica A: Statistical Mechanics and its Applications*, vol. 525, pp. 96–107, 2019.

[82] S. He, N. A. A. Fataf, S. Banerjee, and K. Sun, "Complexity in the muscular blood vessel model with variable fractional derivative and external disturbances," *Physica A: Statistical Mechanics and its Applications*, vol. 526, Article ID 120904, 2019.

[83] F. Yu, L. Gao, L. Liu, S. Qian, S. Cai, and Y. Song, "A 1 V, 0.53 ns, 59 μW current comparator using standard 0.18 μm CMOS technology," *Wireless Personal Communications*, vol. 111, no. 2, pp. 843–851, 2020.

[84] F. Yu, "A low-voltage and low-power 3-GHz CMOS LC VCO for S-band wireless applications," *Wireless Personal Communications*, vol. 78, no. 2, pp. 905–914, 2014.

[85] F. Yu, Q. Tang, W. Wang, and H. Wu, "A 2.7 GHz low-phase-noise LC-QVCO using the gate-modulated coupling technique," *Wireless Personal Communications*, vol. 86, no. 2, pp. 671–681, 2016.

WILEY | Hindawi

Research Article

Global Existence and Decay of Solutions for Coupled Nondegenerate Kirchhoff System with a Time Varying Delay Term

Nadia Mezouar [ID],[1] **Salah Mahmoud Boulaaras** [ID],[2,3] **Sultan Alodhaibi** [ID],[2] **and Salem Alkhalaf** [ID][4]

[1]*Department of Commerce, Faculty of Economic, Mascara University, 29000 Mascara, Algeria*
[2]*Department of Mathematics, College of Sciences and Arts, Qassim University, Al-Rass, Saudi Arabia*
[3]*Laboratory of Fundamental and Applied Mathematics of Oran (LMFAO), University of Oran 1, Ahmed Benbella, Algeria*
[4]*Department of Computer, College of Sciences and Arts, Qassim University, Al-Rass, Saudi Arabia*

Correspondence should be addressed to Salah Mahmoud Boulaaras; s.boularas@qu.edu.sa

This paper deals with the global existence of solutions in a bounded domain for nonlinear viscoelastic Kirchhoff system with a time varying delay by using the energy and Faedo–Galerkin method with respect to the delay term weight condition in the feedback and the delay speed. Furthermore, by using some convex functions properties, we prove a uniform stability estimate.

1. Introduction

1.1. Model. Consider the following viscoelastic Kirchhoff system:

$$
\begin{cases}
|u_t|^l u_{tt} + \alpha v - M(\|\nabla u\|^2)\Delta u - \Delta u_{tt} + \int_0^t h_1(t-s)\Delta u(s)ds - \mu_1 \Delta u_t(x, t-\tau(t)) = 0, & \text{in } \Omega \times]0, +\infty[, \\[2mm]
|v_t|^l v_{tt} + \alpha u - M(\|\nabla v\|^2)\Delta v - \Delta v_{tt} + \int_0^t h_2(t-s)\Delta v(s)ds - \mu_2 \Delta v_t(x, t-\tau(t)) = 0, & \text{in } \Omega \times]0, +\infty[, \\[2mm]
u(x,t) = v(x,t) = 0, & \text{on } \partial\Omega \times]0, +\infty[, \\[2mm]
(u(x,0), v(x,0)) = (u_0(x), v_0(x)), (u_t(x,0), v_t(x,0)) = (u_1(x), v_1(x)), & \text{in } \Omega, \\[2mm]
(u_t(x, t-\tau(0)), v_t(x, t-((0)))) = (f_0(x, t-\tau(0)), g_0(x, t-\tau(0))), & \text{in } \Omega \times]0, \tau(0)[,
\end{cases}
\tag{1}
$$

where Ω is a bounded domain in IR^n, $n \in \mathrm{IN}^*$, with a smooth boundary $\partial\Omega$, $l > 0$, α, μ_1 and μ_2 are positive real numbers, h_1 and h_2 are positive functions which decay exponentially, $\tau(t) > 0$ is a time varying delay, and the initial data $(u_0, v_0, u_1, v_1, f_0, g_0)$ are in a suitable function space.

$M(r) = a + br^\gamma$ is a C^1-function for $r \geq 0$, with $a, b > 0$, and $\gamma \geq 1$.

Time delay is often present in applications and practical problems. In last few years, the control of PDEs with time delay effects has become an active area of research (see, for

example, [1–4] and the references therein). In [5], the authors showed that a small delay in a boundary control could turn a well-behaved hyperbolic system into a wild one and therefore delay becomes a source of instability. However, sometimes it can also improve the performance of the system.

By using the Faedo–Galerkin method, Wu in [6] proved the result of local existence and established the decay result by suitable Lyapunov functionals according to appropriate conditions on μ_1, μ_2 and on the kernel h.

Daewook [7] studied the following viscoelastic Kirchhoff equation with nonlinear source term and varying time delay:

$$
\begin{aligned}
& u_{tt} - M\big(x, t, \|\nabla u\|^2\big)\Delta u + \int_0^t h(t-s)\mathrm{div}\,(a(x)\nabla u(s))\mathrm{d}s \\
& \quad + |u|^m u + \mu_1 u_t(x, t) + \mu_2 u_t(x, t - \tau(t)) = 0, \\
& \quad \text{in } \Omega \times]0, +\infty[,
\end{aligned}
\tag{2}
$$

$$
\begin{cases}
|u_t|^l u_{tt} - M\big(\|\nabla u\|^2\big)\Delta u - \Delta u_{tt} + \int_0^t h(t-s)\Delta u(s)\mathrm{d}s + \mu_1 g_1\big(u_t(x, t)\big) + \mu_2 g_2\big(u_t(x, t - \tau(t))\big) = 0, & \text{in } \Omega \times]0, +\infty[, \\
u(x, t) = 0, & \text{on }]\partial\Omega \times [0, +\infty, \\
u(x, 0) = u_0(x), u_t(x, 0) = u_1(x), & \text{in } \Omega, \\
u_t(x, t - \tau(0)) = f_0(x, t - \tau(0)), & \text{in } \Omega \times]0, \tau(0)[,
\end{cases}
\tag{3}
$$

with respect to some proposed assumptions. Under assumption setting on g_1, g_2, σ, and τ, the authors have obtained the global existence of solution and the decay rate of energy.

Recently, Mezouar and Boulaaras [1] have studied viscoelastic nondegenerate Kirchhoff equation with varying delay term in the internal feedback.

In the present paper, we extent our recent published paper in [1] for a coupled system (3). The famous technique using the presence of delay in PDE's problem is to set a new variable defined by velocity depending on delay, which will give us new problem equivalent to our studied problem but the last one is a coupled system without delay. After this, we can prove the existence of global solutions in suitable Sobolev spaces by combining the energy method with the Faedo–Galerkin procedure, and under a choice of a suitable Lyapunov functional, we establish an exponential decay result.

The outline of the paper is as follows. In Section 2, some hypotheses related to problem are given and we state our main result. Then, in Section 3, the global existence of weak solutions is proven. Finally, in Section 4, we give the uniform energy decay.

which is a description of axially moving viscoelastic materials. According to the smallness condition taking into account of Kirchhoff coefficient and the relaxation function and by summing $0 \le m \le (2/(n-2))$ if $n > 2$ or $0 \le m$ if $n \le 2$, he got the uniform decay rate of the Kirchhoff type energy.

Very recently, in [1], we have proved the global existence and energy decay of solutions of the following viscoelastic nondegenerate Kirchhoff equation:

1.2. Preliminaries and Assumptions.
We denote by $(.,.)$ the inner product in $L^2(\Omega)$.

Now, we introduce, as in [8], the new variables

$$
\begin{aligned}
z_1(x, \rho, t) &= u_t(x, t - \rho\tau(t)), & x \in \Omega, \rho \in (0, 1), t > 0, \\
z_2(x, \rho, t) &= v_t(x, t - \rho\tau(t)), & x \in \Omega, \rho \in (0, 1), t > 0.
\end{aligned}
\tag{4}
$$

Then, we have

$$
\tau(t)z_1'(x, \rho, t) + \big(1 - \rho\tau'(t)\big)\frac{\partial}{\partial\rho}z_1(x, \rho, t) = 0,
\tag{5}
$$

$$
\text{in } \Omega \times (0, 1) \times (0, +\infty).
$$

Similarly, we have

$$
\tau(t)z_2'(x, \rho, t) + \big(1 - \rho\tau'(t)\big)\frac{\partial}{\partial\rho}z_2(x, \rho, t) = 0,
\tag{6}
$$

$$
\text{in } \Omega \times (0, 1) \times (0, +\infty).
$$

Therefore, problem (3) is equivalent to

$$\begin{cases} |u_t|^l u_{tt} + \alpha v - M(\|\nabla u\|^2)\Delta u - \Delta u_{tt} + \int_0^t h_1(t-s)\Delta u(s)ds - \mu_1 \Delta z_1(x,1,t) = 0, & \text{in } \Omega \times]0, +\infty[, \\[2ex] |v_t|^l u_{tt} + \alpha u - M(\|\nabla v\|^2)\Delta v - \Delta v_{tt} + \int_0^t h_2(t-s)\Delta v(s)ds - \mu_2 \Delta z_2(x,1,t) = 0, & \text{in } \Omega \times]0, +\infty[, \\[2ex] \tau(t)z_1'(x,\rho,t) + (1 - \rho\tau'(t))\dfrac{\partial}{\partial\rho}z_1(x,\rho,t) = 0, & \text{in } \Omega \times (0,1) \times (0,+\infty), \\[2ex] \tau(t)z_2'(x,\rho,t) + (1 - \rho\tau'(t))\dfrac{\partial}{\partial\rho}z_2(x,\rho,t) = 0, & \text{in } \Omega \times (0,1) \times (0,+\infty), \\[2ex] u(x,t) = v(x,t) = 0, & \text{on } [\partial\Omega \times [0,\infty, \\[2ex] (z_1(x,0,t), z_2(x,0,t)) = (u_t(x,t), v_t(x,t)), & \text{on } \Omega \times]0, \infty[, \\[2ex] (u(x,0), v(x,0)) = (u_0(x), v_0(x)), (u_t(x,0), (v_t(x,0)) = (u_1(x), v_1(x)), & \text{in } \Omega, \\[2ex] (z_1(x,\rho,0), z_2(x,\rho,0)) = (f_0(x,-\rho\tau(0)), g_0(x,-\rho\tau(0))), & \text{in } \Omega \times]0,1[. \end{cases} \quad (7)$$

To state and prove our result, we need some assumptions.

Assumption 1. Assume that $0 < l \leq \gamma$ satisfies

$$\begin{cases} \gamma \leq \dfrac{2}{n-2}, & \text{if } n > 2, \\[2ex] \gamma < \infty, & \text{if } n \leq 2. \end{cases} \quad (8)$$

Assumption 2. For the relaxation functions, $h_i : \mathrm{IR}_+ \longrightarrow \mathrm{IR}_+$ are bounded C^1 functions such that

$$a - \int_0^\infty h_i(s)ds \geq k > 0, \quad (9)$$

and suppose that there exist positive constants ζ_i satisfying

$$h_i'(t) \leq -\zeta_i h_i(t), \quad (10)$$

for $i = 1, 2$.

Assumption 3. τ is a function in $W^{2,\infty}([0,T])$, $T > 0$, such that

$$\begin{aligned} 0 < \tau_0 \leq \tau'(t) \leq \tau_1, & \quad \forall t > 0, \\ \tau'(t) \leq d < 1, & \quad \forall t > 0. \end{aligned} \quad (11)$$

We define the energy associated to the solution of system (7) by

$$\begin{aligned} E(t) = {}& \frac{1}{l+2}\left(\|u_t\|_{l+2}^{l+2} + \|v_t\|_{l+2}^{l+2}\right) + 2\alpha\int_\Omega u(x,t)v(x,t)dx \\ & + \frac{b}{2(\gamma+1)}\left(\|\nabla u\|^{2(\gamma+1)} + \|\nabla v\|^{2(\gamma+1)}\right) \\ & + \frac{1}{2}\left(a - \int_0^t h_1(s)ds\right)\|\nabla u\|^2 + \frac{1}{2}\left(a - \int_0^t h_2(s)ds\right) \\ & \cdot \|\nabla v\|^2 + \frac{1}{2}\left(\|\nabla u_t\|^2 + \|\nabla v_t\|^2\right) \\ & + \frac{1}{2}(h_1 o \nabla u)(t) + \frac{1}{2}(h_2 o \nabla v)(t) \\ & + \xi\tau(t)\int_0^1\left(\|\nabla z_1(x,\rho,t)\|^2 + \|\nabla z_2(x,\rho,t)\|^2\right)d\rho, \end{aligned} \quad (12)$$

where ξ is a positive constant such that

$$\frac{\max\{\mu_1, \mu_2\}}{2(1-d)} < \xi, \quad (13)$$

$$(h_i o w)(t) = \int_0^t h_i(t-s)\|w(.,t) - w(.,s)\|^2 ds, \quad \text{for } i = 1, 2. \quad (14)$$

Theorem 1 (global existence). *Let* $(u_0, v_0) \in (H^2(\Omega) \cap H_0^1(\Omega))^2$, *s, and* $(f_0, g_0) \in (H_0^1(\Omega, H^1(0,1)))^2$ *satisfy the compatibility condition*

$$(f_0(.,0), g_0(.,0)) = (u_1, v_1). \quad (15)$$

Assume that Assumptions 1–3 hold. Then, problem (3) admits a weak solution such that $u, v \in L^\infty$ $((0, \infty; H^2(\Omega) \cap H_0^1(\Omega)), \quad u_t, v_t \in L^\infty(0, \infty; H_0^1(\Omega)),$ and $u_{tt}, v_{tt} \in L^2(0, \infty, H_0^1(\Omega))$.

Theorem 2 (decay rates of energy). *Assume that Assumptions 1–3 hold. Then, for every $t_0 > 0$ there exist positive constants K and c' such that the energy defined by (12) possesses the following decay:*

$$E(t) \leq Ke^{-c't}, \quad \forall t \geq t_0. \tag{16}$$

2. Preliminaries

Lemma 1 (*Sobolev – Poincareinequality*). *Let q be a number with*

$$2 \leq q < +\infty (n = 1, 2) \text{ or } 2 \leq q \leq \frac{2n}{(n-2)(n \geq 3)}. \tag{17}$$

Then, there exists a constant $C_s = C_s(\Omega, q)$ such that

$$\|u\|_q \leq C_s \|\nabla u\|_2 \text{ for } u \in H_0^1(\Omega). \tag{18}$$

The following lemma states an important property of the convolution operator.

Lemma 2 (see [9]). *For $h, \varphi \in C^1([0, +\infty[, \text{IR}), \text{ we have}$*

$$\int_\Omega h * \varphi \varphi_t dx = -\frac{1}{2} h(t) \|\varphi(t)\|^2 + \frac{1}{2} (h' o \varphi)(t)$$
$$- \frac{1}{2} \frac{d}{dt} \left[(h o \varphi)(t) - \left(\int_0^t h(s) ds \right) \|\varphi\|^2 \right]. \tag{19}$$

Lemma 3. *Let (u, v, z_1, z_2) be a solution of problem (7). Then, the energy functional defined by (12) satisfies*

$$E(t) \leq -\beta \left(\|\nabla z_1(x, 1, t)\|^2 + \|\nabla z_2(x, 1, t)\|^2 \right)$$
$$+ \lambda \left(\|\nabla u_t(x, t)\|^2 + \|\nabla v_t(x, t)\|^2 \right) \tag{20}$$
$$+ \frac{1}{2} \left[(h_1' o \nabla u)(t) + (h_2' o \nabla v)(t) \right],$$

where $\lambda = \xi + (\mu/2), \beta = \xi(1-d) - \mu/2,$ and $\mu = \max\{\mu_1, \mu_2\}$ are positive.

Proof. Multiplying the first equation in (7) by u_t, integrating over Ω, and using integration by parts, we get

$$\frac{d}{dt} \left[\frac{1}{l+2} \|u_t\|_{l+2}^{l+2} + \frac{b}{2(\gamma+1)} \|\nabla u\|^{2(\gamma+1)} + \frac{1}{2} a \|\nabla u\|^2 + \frac{1}{2} \|\nabla u_t\|^2 \right]$$
$$- \int_\Omega \int_0^t h_1(t-s) \nabla u(s) \nabla u_t(t) ds \, dx$$
$$+ \alpha \int_\Omega u_t(x, t) v(x, t) dx + \mu_1 \int_\Omega \nabla u_t(x, t) \nabla z_1(x, 1, t) dx = 0. \tag{21}$$

Consequently, by applying Lemma 2, equation (21) becomes

$$\frac{d}{dt} \left[\frac{1}{l+2} \|u_t\|_{l+2}^{l+2} + \frac{b}{2(\gamma+1)} \|\nabla u\|^{2(\gamma+1)} + \frac{1}{2} \left(a - \int_0^t h_1(s) ds \right) \right.$$
$$\left. \cdot \|\nabla u\|^2 + \frac{1}{2} \|\nabla u_t\|^2 + \frac{1}{2} (h_1 o \nabla u)(t) \right]$$
$$+ \frac{1}{2} h_1(t) \|\nabla u(t)\|^2 - \frac{1}{2} (h_1' o \nabla u)(t) + \alpha \int_\Omega u_t(x, t) v(x, t) dx$$
$$+ \mu_1 \int_\Omega \nabla u_t(x, t) \nabla z_1(x, 1, t)) dx = 0. \tag{22}$$

Similarly by multiplying the second equation in (7) by v_t, integrating over Ω, and using integration by parts, we get

$$\frac{d}{dt} \left[\frac{1}{l+2} \|v_t\|_{l+2}^{l+2} + \frac{b}{2(\gamma+1)} \|\nabla v\|^{2(\gamma+1)} + \frac{1}{2} \left(a - \int_0^t h_2(s) ds \right) \right.$$
$$\left. \cdot \|\nabla v\|^2 + \frac{1}{2} \|\nabla v_t\|^2 + \frac{1}{2} (h_2 o \nabla v)(t) \right]$$
$$+ \frac{1}{2} h_2(t) \|\nabla v(t)\|^2 - \frac{1}{2} (h_2' o \nabla v)(t) + \alpha \int_\Omega u(x, t) v_t(x, t) dx$$
$$+ \mu_2 \int_\Omega \nabla v_t(x, t) \nabla z_2(x, 1, t) dx = 0. \tag{23}$$

Multiply the third equation in (7) by $\xi \Delta z_1$ and integrate the result over $\Omega \times (0, 1)$ to obtain

$$\xi \tau(t) \int_\Omega \int_0^1 z_1'(x, \rho, t) \Delta z_1(x, \rho, t) \Omega \times (0, 1) d\rho \, dx$$
$$= -\xi \int_\Omega \int_0^1 (1 - \rho \tau'(t)) \frac{\partial}{\partial \rho} z_1(x, \rho, t) \Delta z_1(x, \rho, t) d\rho \, dx. \tag{24}$$

Consequently,

$$\frac{d}{dt}\left(\xi\tau(t)\int_\Omega\int_0^1|\nabla z_1(x,\rho,t)|^2 d\rho dx\right)$$

$$= \xi\tau'(t)\int_\Omega\int_0^1|\nabla z_1(x,\rho,t)|^2 d\rho dx$$

$$- \xi\int_\Omega\int_0^1(1-\rho\tau'(t))\frac{\partial}{\partial\rho}|\nabla z_1(x,\rho,t)|^2 d\rho\,dx$$

$$= -\xi\int_\Omega\int_0^1\frac{\partial}{\partial\rho}\left((1-\rho\tau(t))|\nabla z_1(x,\rho,t)|^2\right)d\rho\,dx$$

$$= -\xi(1-\tau'(t))\int_\Omega|\nabla z_1(x,1,t)|^2 dx + \xi\int_\Omega|\nabla u_t(x,t)|^2 dx.$$

(25)

Similarly, we get

$$\frac{d}{dt}\left(\xi\tau(t)\int_\Omega\int_0^1|\nabla z_2(x,\rho,t)|^2 d\rho dx\right)$$

$$= -\xi(1-\tau'(t))\int_\Omega|\nabla z_2(x,1,t)|^2 dx + \xi\int_\Omega|\nabla v_t(x,t)|^2 dx.$$

(26)

Combining (22)–(26), we obtain

$$E'(t) = -\xi(1-\tau'(t))\int_\Omega\left(|\nabla z_1(x,1,t)|^2 + |\nabla z_2(x,1,t)|^2\right)dx$$

$$+ \xi\int_\Omega\left(|\nabla u_t(x,t)|^2 + |\nabla v_t(x,t)|^2\right)dx$$

$$- \frac{1}{2}\left[h_1(t)\|\nabla u(t)\|^2 + h_2(t)\|\nabla v(t)\|^2\right]$$

$$+ \frac{1}{2}\left[(h_1'o\nabla u)(t) + (h_2'o\nabla v)(t)\right]$$

$$- \mu_1\int_\Omega\nabla u_t(x,t)\nabla z_1(x,1,t)dx$$

$$- \mu_2\int_\Omega\nabla v_t(x,t)\nabla z_2(x,1,t)dx.$$

(27)

From Assumption 3, we get

$$E'(t) \le -\left(\xi(1-d)-\frac{\mu_1}{2}\right)\int_\Omega|\nabla z_1(x,1,t)|^2 dx$$

$$- \left(\xi(1-d)-\frac{\mu_2}{2}\right)\int_\Omega|\nabla z_2(x,1,t)|^2 dx$$

$$- \frac{1}{2}h_1(t)\|\nabla u_t(t)\|^2 + \left(\xi+\frac{\mu_1}{2}\right)\|\nabla u_t(t)\|^2$$

$$- \frac{1}{2}h_2(t)\|\nabla v(t)\|^2 + \left(\xi+\frac{\mu_2}{2}\right)\|\nabla v_t(t)\|^2$$

$$+ \frac{1}{2}\left[(h_1'o\nabla u)(t) + (h_2'o\nabla v)(t)\right].$$

(28)

Using (13), this completes the proof. □

3. Global Existence (Proof of Theorem 1)

Throughout this section we assume $u_0, v_0 \in H^2(\Omega)\cap H_0^1(\Omega)$, $u_1, v_1 \in H_0^1(\Omega)$, and $f_0, g_0 \in H_0^1(\Omega, H^1(0,1))$. We will use the Faedo–Galerkin method to prove the existence of global solutions. Let $T > 0$ be fixed and let $w^k, k \in IN$ be a basis of $H^2(\Omega)\cap H_0^1(\Omega)$ and V_k be the space generated by w^k. Now, we define, for $1 \le j \le k$, the sequence $\phi^j(x,\rho)$ as follows:

$$\phi^j(x,0) = w^j. \tag{29}$$

Then, we may extend $\phi^j(x,0)$ by $\phi^j(x,\rho)$ over $L^2(\Omega\times(0,1))$ such that $(\phi^j)_j$ forms a basis of $L^2(\Omega, H^1(0,1))$ and denote Z_k the space generated by $\{\phi^k\}$. We construct approximate solutions (u^k, v^k, z_1^k, z_2^k), $k = 1,2,3,\ldots$, in the form

$$u^k(t) = \sum_{j=1}^k a^{jk}(t)w^j,$$

$$v^k(t) = \sum_{j=1}^k b^{jk}(t)w^j,$$

$$z_1^k(t) = \sum_{j=1}^k c^{jk}(t)\phi^j,$$

$$z_2^k(t) = \sum_{j=1}^k d^{jk}(t)\phi^j,$$

(30)

where a^{jk}, b^{jk}, c^{jk}, and d^{jk} ($j = 1,2,\ldots,k$) are determined by the following ordinary differential equations:

$$\begin{cases} \left(|u_t^k|^l u_{tt}^k, w^j\right) + \alpha(v^k, w^j) + M\left(\|\nabla u^k(t)\|^2\right)(\nabla u^k, \nabla w^j) \\ \quad + (\nabla u_{tt}^k, \nabla w^j) - \int_0^t h_1(t-s)\left(\nabla u^k(s), \nabla w^j\right)ds \\ \quad + \mu_1\left(\nabla z_1^k(.,1), \nabla w^j\right) = 0, 1 \le j \le k, \\ \left(|v_t^k|^l v_{tt}^k, w^j\right) + \alpha(u^k, w^j) + M\left(\|\nabla v^k(t)\|^2\right)(\nabla v^k, \nabla w^j) \\ \quad + (\nabla v_{tt}^k, \nabla w^j) - \int_0^t h_2(t-s)\left(\nabla v^k(s), \nabla w^j\right)ds \\ \quad + \mu_2\left(\nabla z_2^k(.,1), \nabla w^j\right) = 0, 1 \le j \le k, \\ z_1^k(x,0,t) = u_t^k(x,t), z_2^k(x,0,t) = v_t^k(x,t), \end{cases}$$

(31)

$$u^k(0) = u_0^k = \sum_{j=1}^k (u_0, w^j)w^j \longrightarrow u_0, \text{in } H^2(\Omega)\cap H_0^1(\Omega) \text{ as } k$$

$$\longrightarrow +\infty,$$

(32)

$$v^k(0) = v_0^k = \sum_{j=1}^{k}(v_0, w^j)w^j \longrightarrow v_0,$$

$$\text{in } H^2(\Omega) \cap H_0^1(\Omega) \text{ as } k \longrightarrow +\infty, \tag{33}$$

$$u_t^k(0) = u_1^k = \sum_{j=1}^{k}(u_1, w^j)w^j \longrightarrow u_1,$$

$$\text{in } H_0^1(\Omega) \text{ as } k \longrightarrow +\infty, \tag{34}$$

$$v_t^k(0) = v_1^k = \sum_{j=1}^{k}(v_1, w^j)w^j \longrightarrow v_1,$$

$$\text{in } H_0^1(\Omega) \text{ as } k \longrightarrow +\infty, \tag{35}$$

$$\begin{cases} \left(\tau(t)\dfrac{\partial}{\partial t}z_1^k + (1 - \rho\tau'(t))\dfrac{\partial}{\partial \rho}z_1^k, \phi^j\right) = 0, & 1 \le j \le k, \\[2mm] \left(\tau(t)\dfrac{\partial}{\partial t}z_2^k + (1 - \rho\tau'(t))\dfrac{\partial}{\partial \rho}tz_2^k n, q\phi^j\right) = 0, & 1 \le j \le k, \end{cases} \tag{36}$$

$$z_1^k(\rho, 0) = \sum_{j=1}^{k}(f_0, \phi^j)\phi^j \longrightarrow f_0,$$

$$\text{in } H_0^1(\Omega, H^1(0,1)) \text{ as } k \longrightarrow +\infty, \tag{37}$$

$$z_2^k(\rho, 0) = \sum_{j=1}^{k}(g_0, \phi^j)\phi^j \longrightarrow g_0,$$

$$\text{in } H_0^1(\Omega, H^1(0,1)) \text{ as } k \longrightarrow +\infty. \tag{38}$$

Noting that $l/2(l+1) + 1/2(l+1) + 1/2 = 1$, from the generalized Hölder inequality, we obtain

$$\left(\left|u_t^k\right|^l u_{tt}^k, w_j\right) = \int_{\Omega}\left|u_t^k\right|^l u_{tt}^k w_j dx \le \left(\int_{\Omega}\left|u_t^k\right|^{2(l+1)}dx\right)^{l/(2(l+1))} \cdot \left\|u_{tt}^k\right\|_{2(l+1)}\left\|w_j\right\|_2. \tag{39}$$

Since Assumption 2 holds, according to Sobolev embedding, the nonlinear terms $(|u_t^k|^l u_{tt}^k, w_j)$ and $(|v_t^k|^l v_{tt}^k, w_j)$ in (31) make sense.

The standard theory of ODE guarantees that systems (31)–(38) have a unique solution in $[0, t_k)$, with $0 < t_k < T$. In the next step, we obtain a priori estimates for the solution of systems (31)–(38), so that it can be extended outside $[0, t_k)$ to obtain one solution defined for all $t > 0$, using a standard compactness argument for the limiting procedure.

3.1. First Estimate.

Since the sequences $u_0^k, v_0^k, u_1^k, v_1^k, z_1^k(\rho, 0)$, and $z_2^k(\rho, 0)$ converge and from Lemma 3 with employing Gronwall's lemma, we can find a positive constant C_1 independent of k such that

$$E^k(t) + \beta\int_0^t\left(\left\|\nabla z_1^k(x, 1, s)\right\|^2 + \left\|\nabla z_2^k(x, 1, s)\right\|^2\right)ds \le C_1, \tag{40}$$

where

$$E^k(t) = \frac{1}{l+2}\left(\left\|u_t^k\right\|_{l+2}^{l+2} + \left\|v_t^k\right\|_{l+2}^{l+2}\right) + 2\alpha\int_{\Omega}u^k v^k dx$$

$$+ \frac{b}{2(\gamma+1)}\left(\left\|\nabla u^k\right\|^{2(\gamma+1)} + \left\|\nabla v^k\right\|^{2(\gamma+1)}\right)$$

$$+ \frac{1}{2}\left(a - \int_0^t h_1(s)ds\right)\left\|\nabla u^k\right\|^2$$

$$+ \frac{1}{2}\left(a - \int_0^t h_2(s)ds\right)\left\|\nabla v^k\right\|^2 + \frac{1}{2}\left(\left\|\nabla u_t^k\right\|^2 + \left\|\nabla v_t^k\right\|^2\right)$$

$$+ \frac{1}{2}\left[(h_1 o \nabla u^k)(t) + (h_2 o \nabla v^k)(t)\right]$$

$$+ \xi\tau(t)\int_0^1\left(\left\|\nabla z_1^k(x, \rho, t)\right\|\right)^2 + \left(\left\|\nabla z_2^k(x, \rho, t)\right\|\right)^2 d\rho. \tag{41}$$

Noting Assumption 1 and estimate (40) yields that

$$u^k, v^k \text{ are bounded in } L_{loc}^{\infty}(0, \infty, H_0^1(\Omega)),$$

$$u_t^k, v_t^k \text{ are bounded in } L_{loc}^{\infty}(0, \infty, H_0^1(\Omega)),$$

$$z_1^k(x, \rho, t), z_2^k(x, \rho, t) \text{ are bounded in } L_{loc}^{\infty}(0, \infty, L^1(0, 1, H_0^1(\Omega))). \tag{42}$$

3.2. Second Estimate.

Multiplying the first equation (respectively, the second equation) in (31) by a_{tt}^{jk} (respectively, by b_{tt}^{jk}) and summing over j from 1 to k, it follows that

$$\begin{cases} \int_{\Omega}\left|u_t^k\right|^l\left|u_{tt}^k\right|^2 dx - \alpha\int_{\Omega}v_t^k u_t^k dx + \int_{\Omega}M\left(\left\|\nabla u^k\right\|^2\right)\nabla u^k\nabla u_{tt}^k dx \\[2mm] \quad + \left\|\nabla u_{tt}^k\right\|^2 = \int_0^t h_1(t-s)\int_{\Omega}\nabla u^k(s)\nabla u_{tt}^k(t)dxds \\[2mm] \quad - \mu_1\int_{\Omega}\nabla u_{tt}^k\nabla(z_1^k(x, 1, t))dx, \\[2mm] \int_{\Omega}\left|v_t^k\right|^l\left|v_{tt}^k\right|^2 dx - \alpha\int_{\Omega}v_t^k u_t^k dx + \int_{\Omega}M\left(\left\|\nabla v^k\right\|^2\right)\nabla v^k\nabla v_{tt}^k dx \\[2mm] \quad + \left\|\nabla v_{tt}^k\right\|^2 = \int_0^t h_2(t-s)\int_{\Omega}\nabla v^k(s)\nabla v_{tt}^k(t)dxds \\[2mm] \quad - \mu_2\int_{\Omega}\nabla v_{tt}^k\nabla(z_2^k(x, 1, t))dx. \end{cases} \tag{43}$$

Differentiating (36) with respect to t, we get

$$\begin{cases} \left(\left(\frac{\tau(t)}{(1-\rho\tau'(t))} \right)' \frac{\partial}{\partial t} z_1^k + \frac{\tau(t)}{(1-\rho\tau'(t))} \frac{\partial^2}{\partial t^2} z_1^k + \frac{\partial^2}{\partial t \partial \rho} z_1^k, \phi^j \right) = 0, \\[2mm] \left(\left(\frac{\tau(t)}{(1-\rho\tau'(t))} \right)' \frac{\partial}{\partial t} z_2^k + \frac{\tau(t)}{(1-\rho\tau'(t))} \frac{\partial^2}{\partial t^2} z_2^k + \frac{\partial^2}{\partial t \partial \rho} z_2^k, \phi^j \right) = 0. \end{cases}$$

$$(44)$$

Multiplying the first equation by c_t^{jk} (respectively, the second equation by d_t^{jk}) and summing over j from 1 to k, it follows that

$$\begin{cases} \left(\frac{\tau(t)}{(1-\rho\tau'(t))} \right)' \left\| \frac{\partial}{\partial t} z_1^k \right\|^2 + \frac{1}{2} \frac{\tau(t)}{(1-\rho\tau'(t))} \frac{d}{dt} \left\| \frac{\partial}{\partial t} z_1^k \right\|^2 + \frac{1}{2} \frac{d}{d\rho} \left\| \frac{\partial}{\partial t} z_1^k \right\|^2 = 0, \\[2mm] \left(\frac{\tau(t)}{(1-\rho\tau'(t))} \right)' \left\| \frac{\partial}{\partial t} z_2^k \right\|^2 + \frac{1}{2} \frac{\tau(t)}{(1-\rho\tau'(t))} \frac{d}{dt} \left\| \frac{\partial}{\partial t} z_2^k \right\|^2 + \frac{1}{2} \frac{d}{d\rho} \left\| \frac{\partial}{\partial t} z_2^k \right\|^2 = 0, \end{cases}$$

$$(45)$$

and then we have

$$\begin{cases} \frac{1}{2} \left(\frac{\tau(t)}{(1-\rho\tau'(t))} \right)' \left\| \frac{\partial}{\partial t} z_1^k \right\|^2 + \frac{1}{2} \frac{d}{dt} \left(\frac{\tau(t)}{(1-\rho\tau'(t))} \left\| \frac{\partial}{\partial t} z_1^k \right\|^2 \right) \\[2mm] \quad + \frac{1}{2} \frac{d}{d\rho} \left\| \frac{\partial}{\partial t} z_1^k \right\|^2 = 0, \\[3mm] \frac{1}{2} \left(\frac{\tau(t)}{(1-\rho\tau'(t))} \right)' \left\| \frac{\partial}{\partial t} z_2^k \right\|^2 + \frac{1}{2} \frac{d}{dt} \left(\frac{\tau(t)}{(1-\rho\tau'(t))} \left\| \frac{\partial}{\partial t} z_2^k \right\|^2 \right) \\[2mm] \quad + \frac{1}{2} \frac{d}{d\rho} \left\| \frac{\partial}{\partial t} z_2^k \right\|^2 = 0. \end{cases}$$

$$(46)$$

Integrating over $(0, 1)$ with respect to ρ, we obtain

$$\begin{cases} \frac{1}{2} \int_0^1 \left(\frac{\tau(t)}{(1-\rho\tau'(t))} \right)' \left\| \frac{\partial}{\partial t} z_1^k \right\|^2 d\rho + \frac{1}{2} \frac{d}{dt} \left(\int_0^1 \frac{\tau(t)}{(1-\rho\tau'(t))} \left\| \frac{\partial}{\partial t} z_1^k \right\|^2 d\rho \right) + \frac{1}{2} \left\| \frac{\partial}{\partial t} z_1^k(x,1,t) \right\|^2 - \frac{1}{2} \left\| u_{tt}^k(x,t) \right\|^2 = 0, \\[3mm] \frac{1}{2} \int_0^1 \left(\frac{\tau(t)}{(1-\rho\tau'(t))} \right)' \left\| \frac{\partial}{\partial t} z_2^k \right\|^2 d\rho + \frac{1}{2} \frac{d}{dt} \left(\int_0^1 \frac{\tau(t)}{(1-\rho\tau'(t))} \left\| \frac{\partial}{\partial t} z_2^k \right\|^2 d\rho \right) + \frac{1}{2} \left\| \frac{\partial}{\partial t} z_2^k(x,1,t) \right\|^2 - \frac{1}{2} \left\| v_{tt}^k(x,t) \right\|^2 = 0. \end{cases}$$

$$(47)$$

Summing (43) and (47) and as $M(r) \geq a$, we get

$$\begin{cases} \int_\Omega |u_t^k|^l |u_{tt}^k|^2 dx + \left\| \nabla u_{tt}^k \right\|^2 + \frac{1}{2} \frac{d}{dt} \left(\int_0^1 \frac{\tau(t)}{(1-\rho\tau'(t))} \left\| \frac{\partial}{\partial t} z_1^k \right\|^2 d\rho \right) + \frac{1}{2} \left\| \frac{\partial}{\partial t} z_1^k(x,1,t) \right\|^2 \leq -a \int_\Omega \nabla u^k \nabla u_{tt}^k dx + \frac{1}{2} \left\| u_{tt}^k(x,t) \right\|^2 \\[3mm] \quad + \alpha \int_\Omega v_t^k u_t^k dx - \frac{1}{2} \int_0^1 \left(\frac{\tau(t)}{(1-\rho\tau'(t))} \right)' \left\| \frac{\partial}{\partial t} z_1^k \right\|^2 d\rho + \int_0^t h_1(t-s) \int_\Omega \nabla u^k(s) \nabla u_{tt}^k(t) dx ds - \mu_1 \int_\Omega \nabla u_{tt}^k \nabla z_1^k(x,1,t) dx, \\[3mm] \int_\Omega |v_t^k|^l |v_{tt}^k|^2 dx + \left\| \nabla v_{tt}^k \right\|^2 + \frac{1}{2} \frac{d}{dt} \left(\int_0^1 \frac{\tau(t)}{(1-\rho\tau'(t))} \left\| \frac{\partial}{\partial t} z_2^k \right\|^2 d\rho \right) + \frac{1}{2} \left\| \frac{\partial}{\partial t} z_2^k(x,1,t) \right\|^2 \leq -a \int_\Omega \nabla v^k \nabla v_{tt}^k dx + \frac{1}{2} \left\| v_{tt}^k(x,t) \right\|^2 \\[3mm] \quad + \alpha \int_\Omega v_t^k u_t^k dx - \frac{1}{2} \int_0^1 \left(\frac{\tau(t)}{(1-\rho\tau'(t))} \right)' \left\| \frac{\partial}{\partial t} z_2^k \right\|^2 d\rho + \int_0^t h_2(t-s) \int_\Omega \nabla v^k(s) \nabla v_{tt}^k(t) dx ds - \mu_2 \int_\Omega \nabla v_{tt}^k \nabla z_2^k(x,1,t) dx. \end{cases}$$

$$(48)$$

By Young's inequality, the right hand side of (48) can be estimated as follows:

$$
\begin{cases}
\left| \int_\Omega a\nabla u^k \nabla u_{tt}^k \mathrm{d}x \right| \le \eta \left\| \nabla u_{tt}^k \right\|^2 + \dfrac{a^2}{4\eta} \left\| \nabla u^k \right\|^2, \\[3mm]
\left| \int_\Omega a\nabla v^k \nabla v_{tt}^k \mathrm{d}x \right| \le \eta \left\| \nabla v_{tt}^k \right\|^2 + \dfrac{a^2}{4\eta} \left\| \nabla v^k \right\|^2.
\end{cases}
\tag{49}
$$

Using Cauchy–Schwarz inequality and Sobolev–Poincare inequality, we obtain

$$
\alpha \int_\Omega v_t^k u_t^k \mathrm{d}x \le \frac{\alpha}{2}\left(\left\| v_t^k \right\|^2 + \left\| u_t^k \right\|^2 \right) \le \frac{C_s \alpha}{2}\left(\left\| \nabla v_t^k \right\|^2 + \left\| \nabla u_t^k \right\|^2 \right),
\tag{50}
$$

$$
\begin{aligned}
&\left| \int_0^t h_1(t-s) \int_\Omega \nabla u^k(s) \nabla u_{tt}^k(t) \mathrm{d}x\mathrm{d}s \right| \le \eta \left\| \nabla u_{tt}^k \right\|^2 \\
&\quad + \frac{1}{4\eta} \int_\Omega \left(\int_0^t h_1(t-s) \nabla u^k(s) \mathrm{d}s \right)^2 \mathrm{d}x \\
&\le \eta \left\| \nabla u_{tt}^k \right\|^2 + \frac{1}{4\eta} \int_0^t h(s)\mathrm{d}s \int_\Omega \int_0^t h_1(t-s) \left| \nabla u^k(s) \right|^2 \mathrm{d}s\,\mathrm{d}x \\
&\le \eta \left\| \nabla u_{tt}^k \right\|^2 + \frac{1}{4\eta}(a-k) \int_\Omega \int_0^t h_1(t-s) \left| \nabla u^k(s) \right|^2 \mathrm{d}s\,\mathrm{d}x \\
&\le \eta \left\| \nabla u_{tt}^k \right\|^2 + \frac{1}{4\eta}(a-k) \int_0^t h_1(t-s) \left\| \nabla u^k(s) \right\|^2 \mathrm{d}s \\
&\le \eta \left\| \nabla u_{tt}^k \right\|^2 + \frac{1}{4\eta}(a-k)h_1(0) \int_0^t \left\| \nabla u^k(s) \right\|^2 \mathrm{d}s.
\end{aligned}
\tag{51}
$$

Similarly,

$$
\begin{aligned}
&\left| \int_0^t h_2(t-s) \int_\Omega \nabla v^k(s) \nabla v^{k_{tt}}(t)\mathrm{d}x\,\mathrm{d}s \right| \le \eta \left\| \nabla v^{k_{tt}} \right\|^2 \\
&\quad + \frac{1}{4\eta}(a-k)h_2(0) \int_0^t \left(\nabla v^k(s) \right)^2 \mathrm{d}s,
\end{aligned}
\tag{52}
$$

$$
\begin{cases}
\left| \mu_1 \int_\Omega \nabla u_{tt}^k \nabla z_1^k(x,1,t)\mathrm{d}x \right| \le \eta\mu_1^2 \left\| \nabla u_{tt}^k \right\|^2 + \dfrac{1}{4\eta}\left\| \nabla z_1^k(x,1,t) \right\|^2, \\[3mm]
\left| \mu_2 \int_\Omega \nabla v_{tt}^k \nabla z_2^k(x,1,t)\mathrm{d}x \right| \le \eta\mu_2^2 \left\| \nabla v_{tt}^k \right\|^2 + \dfrac{1}{4\eta}\left\| \nabla z_2^k(x,1,t) \right\|^2.
\end{cases}
\tag{53}
$$

By using (49)–(53) in (48), we deduce

$$
\begin{cases}
\int_\Omega |u_t^k|^l |u_{tt}^k|^2 \mathrm{d}x + \left\| \nabla u_{tt}^k \right\|^2 + \dfrac{1}{2}\dfrac{\mathrm{d}}{\mathrm{d}t}\left(\int_0^1 \dfrac{\tau(t)}{1-\rho\tau'(t)} \left\| \dfrac{\partial}{\partial t} z_1^k \right\|^2 \mathrm{d}\rho \right) \\[4mm]
\quad + \dfrac{1}{2}\left\| \dfrac{\partial}{\partial t} z_1^k(x,1,t) \right\|^2 \le \left(\eta(\mu_1^2+2) + \dfrac{C_s^2}{2} \right) \left\| \nabla u_{tt}^k \right\|^2 \\[4mm]
\quad + \dfrac{C_s\alpha}{2}\left(\left\| \nabla v_t^k \right\|^2 + \left\| \nabla u_t^k \right\|^2 \right) + \dfrac{a^2}{4\eta}\left\| \nabla u^k \right\|^2 + \dfrac{1}{4\eta}\left\| \nabla z_1^k(x,1,t) \right\|^2 \\[4mm]
\quad + \dfrac{1}{4\eta}(a-k)h_1(0) \int_0^t \left\| \nabla u^k(s) \right\|^2 \mathrm{d}s \\[4mm]
\quad - \dfrac{1}{2}\int_0^1 \left(\dfrac{\tau(t)}{1-\rho\tau'(t)} \right)' \left\| \dfrac{\partial}{\partial t} z_1^k \right\|^2 \mathrm{d}\rho, \\[6mm]
\int_\Omega |v_t^k|^l |v_{tt}^k|^2 \mathrm{d}x + \left\| \nabla v_{tt}^k \right\|^2 + \dfrac{1}{2}\dfrac{\mathrm{d}}{\mathrm{d}t}\left(\int_0^1 \dfrac{\tau(t)}{1-\rho\tau'(t)} \left\| \dfrac{\partial}{\partial t} z_2^k \right\|^2 \mathrm{d}\rho \right) \\[4mm]
\quad + \dfrac{1}{2}\left\| \dfrac{\partial}{\partial t} z_2^k(x,1,t) \right\|^2 \le \left(\eta(\mu_2^2+2) + \dfrac{C_s^2}{2} \right) \left\| \nabla v_{tt}^k \right\|^2 \\[4mm]
\quad + \dfrac{C_s\alpha}{2}\left(\left\| \nabla v_t^k \right\|^2 + \left\| \nabla u_t^k \right\|^2 \right) + \dfrac{a^2}{4\eta}\left\| \nabla v^k \right\|^2 + \dfrac{1}{4\eta}\left\| \nabla z_2^k(x,1,t) \right\|^2 \\[4mm]
\quad + \dfrac{1}{4\eta}(a-k)h_2(0) \int_0^t \left\| \nabla v^k(s) \right\|^2 \mathrm{d}s \\[4mm]
\quad - \dfrac{1}{2}\int_0^1 \left(\dfrac{\tau(t)}{1-\rho\tau'(t)} \right)' \left\| \dfrac{\partial}{\partial t} z_2^k \right\|^2 \mathrm{d}\rho.
\end{cases}
\tag{54}
$$

By using Assumption 3 and taking the first estimate (40) into account, we infer

$$
\begin{cases}
\displaystyle \int_\Omega |u_t^k|^l |u_{tt}^k|^2 dx + \left(1 - \left(\eta(\mu_1^2 + 2) + \frac{C_s^2}{2}\right)\right)\|\nabla u_{tt}^k\|^2 \\[2mm]
\displaystyle + \frac{1}{2}\frac{d}{dt}\left(\int_0^1 \frac{\tau(t)}{1-\rho\tau'(t)}\left\|\frac{\partial}{\partial t}z_1^k\right\|^2 d\rho\right) \\[2mm]
\displaystyle + \frac{1}{2}\left\|\frac{\partial}{\partial t}z_1^k(x,1,t)\right\|^2 \le C_2 + \frac{1}{4\eta}(a-k_1)h_1(0)C_1 T \\[2mm]
\displaystyle + a_1 \int_0^1 \frac{\tau(t)}{1-\rho\tau'(t)}\left\|\frac{\partial}{\partial t}z_1^k\right\|^2 d\rho, \\[4mm]
\displaystyle \int_\Omega |v_t^k|^l |v_{tt}^k|^2 dx + \left(1 - \left(\eta(\mu_2^2 + 2) + \frac{C_s^2}{2}\right)\right)\|\nabla v_{tt}^k\|^2 \\[2mm]
\displaystyle + \frac{1}{2}\frac{d}{dt}\left(\int_0^1 \frac{\tau(t)}{1-\rho\tau'(t)}\left\|\frac{\partial}{\partial t}z_2^k\right\|^2 d\rho\right) \\[2mm]
\displaystyle + \frac{1}{2}\left\|\frac{\partial}{\partial t}z_2^k(x,1,t)\right\|^2 \le C_2 + \frac{1}{4\eta}(a-k_2)h_2(0)C_1 T \\[2mm]
\displaystyle + a_2 \int_0^1 \frac{\tau(t)}{1-\rho\tau'(t)}\left\|\frac{\partial}{\partial t}z_2^k\right\|^2 d\rho,
\end{cases}
\tag{55}
$$

where C_2 is a positive constant which depends on $\eta, a, C_1, C_s, \alpha$.

Integrating (55) over $(0, t)$, we obtain

$$
\begin{cases}
\displaystyle \int_0^t \int_\Omega |u_t^k|^l |u_{tt}^k|^2 dx dt + \left(1 - \left(\eta(\mu_1^2 + 2) + \frac{C_s^2}{2}\right)\right) \\[2mm]
\displaystyle \int_0^t \|\nabla u_{tt}^k(s)\|^2 ds + \int_0^1 \frac{\tau(t)}{1-\rho\tau'(t)}\left\|\frac{\partial}{\partial t}z_1^k\right\|^2 d\rho \\[2mm]
\displaystyle + \frac{1}{2}\int_0^t \left\|\frac{\partial}{\partial t}z_1^k(x,1,t)\right\|^2 dt \le C_2 T + \frac{1}{4\eta}(a-k)h_1(0)C_1 T^2 \\[2mm]
\displaystyle + a_1 \int_0^t \int_0^1 \frac{\tau(t)}{1-\rho\tau'(t)}\left\|\frac{\partial}{\partial s}z_1^k\right\|^2 d\rho ds, \\[4mm]
\displaystyle \int_0^t \int_\Omega |v_t^k|^l |v_{tt}^k|^2 dx dt + \left(1 - \left(\eta(\mu_2^2 + 2) + \frac{C_s^2}{2}\right)\right) \\[2mm]
\displaystyle \int_0^t \|\nabla v_{tt}^k(s)\|^2 ds + \int_0^1 \frac{\tau(t)}{1-\rho\tau'(t)}\left\|\frac{\partial}{\partial t}z_2^k\right\|^2 d\rho \\[2mm]
\displaystyle + \frac{1}{2}\int_0^t \left\|\frac{\partial}{\partial t}z_2^k(x,1,t)\right\|^2 dt \le C_2 T + \frac{1}{4\eta}(a-k)h_2(0)C_1 T^2 \\[2mm]
\displaystyle + + a_2 \int_0^t \int_0^1 \frac{\tau(s)}{1-\rho\tau'(s)}\left\|\frac{\partial}{\partial s}z_2^k\right\|^2 d\rho ds.
\end{cases}
\tag{56}
$$

For a suitable $\eta > 0$ such that $1 - (\eta(\mu_i^2 + 2)t + nC_s^2/2)) > 0$ for $i = 1, 2$ and using Gronwall's lemma, we obtain the second estimate

$$
\int_0^t \left(\|\nabla u^{k_{tt}}(s)\|^2 + \|\nabla v^{k_{tt}}(s)\|^2\right)ds + \int_0^1 \frac{\tau(t)}{1-\rho\tau'(t)}
$$
$$
\cdot\left(\left\|\frac{\partial}{\partial t}z_1^k\right\|^2 + \left\|\frac{\partial}{\partial t}z_2^k\right\|^2\right)d\rho \le C_3.
\tag{57}
$$

We observe from estimates (40) and (57) that there exist subsequences (u^m) of (u^k) and (v^m) of (v^k) such that

$$
(u^m, v^m) \longrightarrow (u, v) \text{ weakly star in } L^\infty\left(0, T, H_0^1(\Omega)\right),
\tag{58}
$$

$$
(u_t^m, v_t^m) \longrightarrow (u_t, v_t)) \text{ weakly star in } L^\infty\left(0, T, H_0^1(\Omega)\right),
\tag{59}
$$

$$
(u_{tt}^m, v_{tt}^m) \longrightarrow (u_{tt}, v_{tt}) \text{ weakly in } L^2\left(0, T, H_0^1(\Omega)\right),
\tag{60}
$$

$$
(z_1^m, z_1^m) \longrightarrow (z_1, z_2) \text{ weakly star in } L^\infty\left(0, T, H_0^1(\Omega, L^2(0,1))\right),
\tag{61}
$$

$$
\left(\frac{\partial}{\partial t}z_1^m, \frac{\partial}{\partial t}z_2^m\right) \longrightarrow \left(\frac{\partial}{\partial t}z_1, \frac{\partial}{\partial t}z_2\right) \text{ weakly star in}
$$
$$
\cdot L^\infty\left(0, T, L^2(\Omega \times (0,1))\right),
\tag{62}
$$

In the following, we will treat the nonlinear term. From the first estimate (40) and Lemma 1, we deduce

$$
\left\||u_t^k|^l u_t^k\right\|_{L^2(0,T,L^2(\Omega))} = \int_0^T \|u_t^k\|_{2(l+1)}^{2(l+1)} dt
$$
$$
\le C_s^{2(l+1)} \int_0^T \|\nabla u_t^k\|_2^{2(l+1)} dt \le C_s^{2(l+1)} C_1^{(l+1)} T.
\tag{63}
$$

On the other hand, from Aubin–Lions theorem (see [10]), we deduce that there exists a subsequence of (u^m), still denoted by (u^m) such that

$$
u_t^m \longrightarrow u_t \text{ strongly in } L^2\left(0, T, L^2(\Omega)\right),
\tag{64}
$$

which implies

$$
u_t^m \longrightarrow u_t \text{ almost everywhere in } \mathscr{A}.
\tag{65}
$$

Hence,

$$
|u_t^m|^l u_t^m \longrightarrow |u_t|^l u_t \text{ almost everywhere in } \mathscr{A},
\tag{66}
$$

where $\mathscr{A} = \Omega \times (0, T)$. Thus, using (64) and (66) and Lions lemma, we derive

$$
|u_t^m|^l u_t^m \longrightarrow |u_t|^l u_t \text{ weakly in } L^2\left(0, T, L^2(\Omega)\right).
\tag{67}
$$

Similarly,

$$
|v_t^m|^l v_t^m \longrightarrow |v_t|^l v_t \text{ weakly in } L^2\left(0, T, L^2(\Omega)\right),
\tag{68}
$$

$$
(z_1^m, z_2^m) \longrightarrow (z_1, z_2) \text{ strongly in } L^2\left(0, T, L^2(\Omega)\right),
\tag{69}
$$

which implies $(z_1^m, z_2^m) \longrightarrow (z_1, z_2)$ almost everywhere in $\mathscr{A}$.

By multiplying (31) and (36) by $\theta(t) \in \mathscr{D}(0, T)$ and by integrating over $(0, T)$, it follows that

$$
\left\{
\begin{aligned}
&-\frac{1}{l+1} \int_0^T \left(\left|u_t^k(t)\right|^l u_t^k(t), w^j\right)\theta'(t)\mathrm{d}t + \int_0^T M\left(\left\|\nabla u^k(t)\right\|^2\right)\left(\nabla u^k(t), \nabla w^j\right)\theta(t)\mathrm{d}t + \int_0^T \left(\nabla u_{tt}^k, \nabla w^j\right)\theta(t)\mathrm{d}t \\
&\quad -\int_0^T \int_0^t h_1(t-s)\left(\nabla u^k(s), \nabla w^j\right)\theta(t)\mathrm{d}s\mathrm{d}t + \mu_1 \int_0^T \left(\nabla z_1^k(.,1)\right), \nabla w^j \theta(t)\mathrm{d}t) = 0, \\[4pt]
&-\frac{1}{l+1} \int_0^T \left(\left|v_t^k(t)\right|^l v_t^k(t), w^j\right)\theta\prime(t)\mathrm{d}t + \int_0^T M\left(\left\|\nabla v^k(t)\right\|^2\right)\left(\nabla v^k(t), \nabla w^j\right)\theta(t)\mathrm{d}t + \int_0^T \left(\nabla v_{tt}^k, \nabla w^j\right)\theta(t)\mathrm{d}t \\[4pt]
&\quad -\int_0^T \int_0^t h_2(t-s)\left(\nabla v^k(s), \nabla w^j\right)\theta(t)\mathrm{d}s\mathrm{d}t + \mu_2 \int_0^T \left(\nabla z_2^k(.,1)\right), \nabla w^j \theta(t)\mathrm{d}t) = 0, \\[4pt]
&\int_0^T \int_0^1 \int_\Omega \left(\tau(t)\frac{\partial}{\partial t}z_1^k + (1 - \rho\tau'(t))\frac{\partial}{\partial \rho}z_1^k\right)\phi^j\theta(t)\mathrm{d}x\mathrm{d}\rho\mathrm{d}t = 0, \\[4pt]
&\int_0^T \int_0^1 \int_\Omega \left(\tau(t)\frac{\partial}{\partial t}z_2^k + (1 - \rho\tau'(t))\frac{\partial}{\partial \rho}z_2^k\right)\phi^j\theta(t)\mathrm{d}x\mathrm{d}\rho\mathrm{d}t = 0,
\end{aligned}
\right. \tag{70}
$$

for all $j = 1 \ldots k$.

The convergence condition in (58)–(62), (68) and (67) are sufficient, thus we can pass to the limit in (70). Then, we have

$$
\left\{
\begin{aligned}
&\int_0^T \int_\Omega \left(|u_t|^l u_{tt} - M\left(\|\nabla u(t)\|^2\right)\Delta u - \Delta u_{tt} + \int_0^t h_1(t-s)\Delta u(s)\mathrm{d}s - \mu_1 \Delta z_1(.,1)\right)w^j\theta(t)\mathrm{d}x\,\mathrm{d}t = 0, \\[4pt]
&\int_0^T \int_\Omega \left(|v_t|^l v_{tt} - M\left(\|\nabla v(t)\|^2\right)\Delta v - \Delta v_{tt} + \int_0^t h_2(t-s)\Delta u(s)\mathrm{d}s - \mu_2 \Delta z_2(.,1)\right)w^j\theta(t)\mathrm{d}x\,\mathrm{d}t = 0, \\[4pt]
&\int_0^T \int_0^1 \int_\Omega \left(\tau(t)\frac{\partial}{\partial t}z_1 + (1 - \rho\tau'(t))\frac{\partial}{\partial \rho}z_1\right)\phi^j\theta(t)\mathrm{d}x\,\mathrm{d}\rho\,\mathrm{d}t = 0, \\[4pt]
&\int_0^T \int_0^1 \int_\Omega \left(\tau(t)\frac{\partial}{\partial t}z_2 + (1 - \rho\tau'(t))\frac{\partial}{\partial \rho}z_2\right)\phi^j\theta(t)\mathrm{d}x\,\mathrm{d}\rho\,\mathrm{d}t = 0,
\end{aligned}
\right. \tag{71}
$$

for all $j = 1 \ldots k$. This completes the proof of Theorem 1.

4. Uniform Decay of the Energy (Proof of Theorem 2)

In this section we study the solution's asymptotic behavior of system (3).

To prove our main result, we construct a Lyapunov functional equivalent to E. For this, we define some functionals which allow us to obtain the desired estimate.

Lemma 4. *Let* (u, v, z_1, z_2) *be a solution of problem (7). Then, the functional*

$$
I(t) = \tau(t) \int_0^1 e^{-2\tau(t)\rho}\left(\left\|\nabla z_1(x, \rho, t)\right\|^2 + \left\|\nabla z_1(x, \rho, t)\right\|^2\right)\mathrm{d}\rho, \tag{72}
$$

satisfies the estimate

(i) $|I(t)| \le (1/\xi)E(t)$.

(ii) $I'(t) \le -2\tau(t)e^{-2\tau_1} \int_0^1 (\|\nabla z_1(x, \rho, t)\|^2 + \|\nabla z_2(x, \rho, t)\|^2)\mathrm{d}\rho - (1 - d)e^{-2\tau_1}(\|\nabla z_1(x, 1, t)\|^2 + \|\nabla z_2(x, 1, t)\|^2) + \|\nabla u_t(x, t)\|^2 + \|\nabla v_t(x, t)\|^2$.

Proof. (ii) Differentiating (72) with respect to t and using (5)-(6) and Assumption 3, we get

$$\frac{\mathrm{d}}{\mathrm{d}t} I(t) = \tau'(t) \int_0^1 e^{-2\tau(t)\rho} \left(\left\| \nabla z_1(x,\rho,t) \right\|^2 + \left\| \nabla z_2(x,\rho,t) \right\|^2 \right) \mathrm{d}\rho$$

$$+ \tau(t) \int_\Omega \int_0^1 \left[e^{-2\tau(t)\rho} \frac{\partial \left(\left| \nabla z_1(x,\rho,t) \right|^2 + \left| \nabla z_2(x,\rho,t) \right|^2 \right)}{\partial t} \right.$$

$$\left. -2\tau'(t)\rho e^{-2\tau(t)\rho} \left(\left| \nabla z_1(x,\rho,t) \right|^2 + \left| \nabla z_2(x,\rho,t) \right|^2 \right) \right] \mathrm{d}\rho \mathrm{d}x$$

$$= \int_\Omega \int_0^1 e^{-2\tau(t)\rho} \left[\tau'(t) \left(\left| \nabla z_1(x,\rho,t) \right|^2 + \left| \nabla z_2(x,\rho,t) \right|^2 \right) + \tau(t) \frac{\partial \left(\left| \nabla z_1(x,\rho,t) \right|^2 + \left| \nabla z_2(x,\rho,t) \right|^2 \right)}{\partial t} \right] \mathrm{d}\rho \mathrm{d}x$$

$$- 2 \int_\Omega \int_0^1 \tau(t)\tau'(t)\rho e^{-2\tau(t)\rho} \left(\left\| \nabla z_1(x,\rho,t) \right\|^2 + \left\| \nabla z_2(x,\rho,t) \right\|^2 \right) \mathrm{d}\rho \, \mathrm{d}x$$

$$= - \int_0^1 e^{-2\tau(t)\rho} \frac{\partial}{\partial \rho} \left((1 - \rho\tau'(t)) \left(\left\| \nabla z_1(x,\rho,t) \right\|^2 + \left\| \nabla z_2(x,\rho,t) \right\|^2 \right) \right) \mathrm{d}\rho$$

$$- 2 \int_0^1 \tau(t)\tau'(t)\rho e^{-2\tau(t)\rho} \left(\left\| \nabla z_1(x,\rho,t) \right\|^2 + \left\| \nabla z_2(x,\rho,t) \right\|^2 \right) \mathrm{d}\rho \tag{73}$$

$$= - \int_0^1 \left[\frac{\partial}{\partial \rho} \left(e^{-2\tau(t)\rho} (1 - \tau'(t)\rho) \left(\left\| \nabla z_1(x,\rho,t) \right\|^2 + \left\| \nabla z_2(x,\rho,t) \right\|^2 \right) \right) \right.$$

$$- 2\tau(t) e^{-2\tau(t)\rho} (1 - \tau'(t)\rho) \left(\left\| \nabla z_1(x,\rho,t) \right\|^2 + \left\| \nabla z_2(x,\rho,t) \right\|^2 \right) \mathrm{d}\rho$$

$$- 2\tau(t)\tau'(t) \int_0^1 \rho e^{-2\tau(t)\rho} \left(\left\| \nabla z_1(x,\rho,t) \right\|^2 + \left\| \nabla z_2(x,\rho,t) \right\|^2 \right) \mathrm{d}\rho$$

$$= \left(\left\| \nabla z_1(x,\rho,t) \right\|^2 + \left\| \nabla z_2(x,\rho,t) \right\|^2 \right) - e^{-2\tau(t)\rho} (1 - \tau'(t)) \left(\left\| \nabla z_1(x,\rho,t) \right\|^2 + \left\| \nabla z_2(x,\rho,t) \right\|^2 \right)$$

$$- 2\tau(t) \int_\Omega \int_0^1 \left[(1 - \tau'(t)\rho) + \tau'(t)\rho \right] e^{-2\tau(t)\rho} \left(\left| \nabla z_1(x,\rho,t) \right|^2 + \left| \nabla z_2(x,\rho,t) \right|^2 \right) \mathrm{d}\rho \, \mathrm{d}x$$

$$\leq -2I(t) + \left\| \nabla u_t(x,t) \right\|^2 + \left\| \nabla v_t(x,t) \right\|^2 - e^{-2\tau(t)\rho} (1 - d) \left(\left\| \nabla z_1(x,\rho,t) \right\|^2 + \left\| \nabla z_2(x,\rho,t) \right\|^2 \right).$$

Since $e^{-2\tau(t)\rho}$ is a decreasing function for $\rho \in [0,1]$ and $\tau(t) \in [\tau_0, \tau_1]$, we deduce

$$I(t) \geq \tau(t) \int_0^1 e^{-2\tau_1} \left(\left\| \nabla z_1(x,\rho,t) \right\|^2 + \left\| \nabla z_2(x,\rho,t) \right\|^2 \right) \mathrm{d}\rho. \tag{74}$$

Thus, our proof is completed. □

Lemma 5. Let (u, v, z_1, z_2) be a solution of problem (7). Then, the functional

$$\phi(t) = \frac{1}{l+1} \int_\Omega \left(\left| u_t \right|^l u_t u + \left| v_t \right|^l v_t v \right) \mathrm{d}x$$

$$+ \int_\Omega \nabla u_t \nabla u \mathrm{d}x + \int_\Omega \nabla v_t \nabla v \mathrm{d}x, \tag{75}$$

satisfies the estimate

(i) $|\phi(t)| \leq (1/(l+2)) (\|u_t\|_{l+2}^{l+2} + \|v_t\|_{l+2}^{l+2}) + (((l+1)^{-1}/(l+2))c_s^{l+2} + (c/2)) (\|\nabla u\|^{l+2} + \|\nabla v\|^{l+2}) + (1/2) (\|\nabla u\|^2 + \|\nabla v\|^2).$

(ii) $\phi'(t) \leq (1/(l+1)) (\|u_t\|_{l+2}^{l+2} + \|v_t\|_{l+2}^{l+2}) + (\eta(a - k + 1) + \alpha C_s - k) (\|\nabla u\|^2 + \|\nabla v\|^2) + (1/4\eta)[(h_1 o \nabla u)(t) + (h_1 o \nabla u)(t)] + (\mu_1^2/4\eta)\|\nabla z_1(x,1,t)\|^2 + (\mu_2^2/4\eta) \|\nabla z_2(x,1,t)\|^2 + \|\nabla u_t\|^2 + \|\nabla v_t\|^2.$

Proof

(i) From Young's inequality, the Sobolev embedding, and $L^{l+2} \longrightarrow L^2$, we deduce

$$|\phi(t)| \leq \frac{1}{l+2}\|u_t\|_{l+2}^{l+2} + \frac{(l+1)^{-1}}{l+2}\|u\|_{l+2}^{l+2} + \frac{1}{l+2}\|v_t\|_{l+2}^{l+2} + \frac{(l+1)^{-1}}{l+2}\|v\|_{l+2}^{l+2}$$

$$+ \frac{1}{2}\|\nabla u_t\|^2 + \frac{1}{2}\|\nabla u\|^2 + \frac{1}{2}\|\nabla v_t\|^2 + \frac{1}{2}\|\nabla v\|^2$$

$$\leq \frac{1}{l+2}\|u_t\|_{l+2}^{l+2} + \frac{(l+1)^{-1}}{l+2}c_s^{l+2}\|\nabla u\|^{l+2} + \frac{1}{l+2}\|v_t\|_{l+2}^{l+2} + \frac{(l+1)^{-1}}{l+2}c_s^{l+2}\|\nabla v\|^{l+2} \tag{76}$$

$$+ \frac{1}{2}\|\nabla u_t\|^2 + \frac{1}{2}\|\nabla u\|^2 + \frac{1}{2}\|\nabla v_t\|^2 + \frac{1}{2}\|\nabla v\|^2$$

$$\leq \frac{1}{l+2}\left(\|u_t\|_{l+2}^{l+2} + \|v_t\|_{l+2}^{l+2}\right) + \left(\frac{(l+1)^{-1}}{l+2}c_s^{l+2} + \frac{c}{2}\right)\left(\|\nabla u\|^{l+2} + \|\nabla v\|^{l+2}\right) + \frac{1}{2}\left(\|\nabla u_t\|^2 + \|\nabla v_t\|^2\right).$$

(i) Differentiating $\phi(t)$ with respect to t and using the first and second equations of (7), we get

$$\phi'(t) = \frac{1}{l+1}\int_\Omega \left(|u_t|^l u_t\right)' u dx + \frac{1}{l+1}\int_\Omega |u_t|^{l+2} dx + \frac{1}{l+1}\int_\Omega \left(|v_t|^l v_t\right)' v dx + \frac{1}{l+1}\int_\Omega |v_t|^{l+2} dx$$

$$+ \int_\Omega \nabla u_{tt}\nabla u dx + \int_\Omega \nabla u_t \nabla u_t dx + \int_\Omega \nabla v_{tt}\nabla v dx + \int_\Omega \nabla v_t \nabla v_t dx$$

$$= \int_\Omega \left[|u_t|^l u_t\right] u dx + \frac{1}{l+1}\|u_t\|_{l+2}^{l+2} + \int_\Omega \left[|v_t|^l v_t\right] v dx + \frac{1}{l+1}\|v_t\|_{l+2}^{l+2}$$

$$- \int_\Omega \nabla u_{tt} u dx + \|\nabla u_t\|^2 - \int_\Omega \nabla v_{tt}\nabla u dx + \|\nabla v_t\|^2$$

$$= \frac{1}{l+1}\left(\|u_t\|_{l+2}^{l+2} + \|u_t\|_{l+2}^{l+2}\right) + \int_\Omega \left[|u_t|^l u_t - \Delta u_{tt}\right] u dx + \int_\Omega \left[|v_t|^l v_t - \Delta v_{tt}\right] u dx + \|\nabla u_t\|^2 + \|\nabla v_t\|^2$$

$$= \frac{1}{l+1}\left(\|u_t\|_{l+2}^{l+2} + \|u_t\|_{l+2}^{l+2}\right) + \int_\Omega \left[-\alpha v + M\left(\|\nabla u\|^2\right)\Delta u - \int_0^t h_1(t-s)\Delta u(s)ds + \mu_1 \Delta z_1(x,1,t)\right] u dx$$

$$+ \int_\Omega \left[-\alpha u + M\left(\|\nabla v\|^2\right)\Delta v - \int_0^t h_1(t-s)\Delta v(s)ds + \mu_2 \Delta z_2(x,1,t)\right] u dx + \|\nabla u_t\|^2 + \|\nabla v_t\|^2$$

$$= \frac{1}{l+1}\left(\|u_t\|_{l+2}^{l+2} + \|u_t\|_{l+2}^{l+2}\right) - M\left(\|\nabla u\|^2\right)\|\nabla v\|^2 + \int_\Omega \nabla u(t)\int_0^t h_1(t-s)\Delta u(s)ds dx - \mu_1 \int_\Omega \nabla z_1(x,1,t)\nabla u dx$$

$$- M\left(\|\nabla v\|^2\right)\|\nabla v\|^2 + \int_\Omega \nabla v(t)\int_0^t h_2(t-s)\Delta v(s)ds dx - \mu_2 \int_\Omega \nabla z_2(x,1,t)\nabla v dx + \|\nabla u_t\|^2 + \|\nabla v_t\|^2 - 2\alpha \int_\Omega uv dx.$$

(77)

As $M(r) \geq a$ and making use Young's inequality, we obtain

$$\phi'(t) \leq \frac{1}{l+1}\left(\|u_t\|_{l+2}^{l+2} + \|v_t\|_{l+2}^{l+2}\right) - a\|\nabla u\|^2 + \int_\Omega \nabla u(t)\int_0^t h_1(t-s)\nabla u(s)ds dx + \frac{\mu_1^2}{4\eta}\|\nabla z_1(x,1,t)\|^2 + \eta\|\nabla u\|^2$$

$$- a\|\nabla v\|^2 + \int_\Omega \nabla v(t)\int_0^t h_2(t-s)\nabla v(s)ds\, dx + \frac{\mu_2^2}{4\eta}\|\nabla z_2(x,1,t)\|^2 + \eta\|\nabla v\|^2 + \|\nabla u_t\|^2 + \|\nabla v_t\|^2.$$

(78)

By use of Young's inequality, we can estimate the third term in the right side as follows:

$$\int_\Omega \nabla u(t) \int_0^t h_1(t-s)\nabla u(s)\mathrm{d}s\,\mathrm{d}x \le \int_0^t h(t-s)\int_\Omega |\nabla u(t)\nabla u(s) - \nabla u(t)|\mathrm{d}x\,\mathrm{d}s + \|\nabla u(t)\|^2 \int_0^t h_1(t-s)\mathrm{d}s$$

$$\le \eta\|\nabla u(t)\|^2 \int_0^t h_1(s)\mathrm{d}s + \frac{1}{4\eta}\int_0^t h_1(t-s)\|\nabla u(s) - \nabla u(t)\|^2\mathrm{d}s$$

$$+ \|\nabla u(t)\|^2 \int_0^t h_1(s)\mathrm{d}s$$

$$\le (1+\eta)(a-k)\|\nabla u(t)\|^2 + \frac{1}{4\eta}(h_1 o \nabla u)(t).$$

(79)

Similarly,

$$\int_\Omega \nabla v(t)\int_0^t h_2(t-s)\nabla v(s)\mathrm{d}s\mathrm{d}x \le (1+\eta)(a-k)\|\nabla v(t)\|^2 + \frac{1}{4\eta}(h_2 o \nabla v)(t),$$

(80)

$$-2\alpha\int_\Omega uv\mathrm{d}x \le \alpha C_s\left(\|\nabla u\|^2 + \|\nabla v\|^2\right).$$

Thus, our proof is completed. □

Lemma 6. *Let (u, z) be a solution of problem (7). Then, the functional*

$$\psi(t) = \int_\Omega \left(\Delta u_t - \frac{1}{l+1}|u_t|^l u_t\right)\int_0^t h_1(t-s)(u(t)-u(s))\mathrm{d}s\,\mathrm{d}x + \int_\Omega \left(\Delta v_t - \frac{1}{l+1}|v_t|^l v_t\right)\int_0^t h_2(t-s)(v(t)-v(s))\mathrm{d}s\,\mathrm{d}x,$$

(81)

satisfies the estimates

(i) $|\psi(t)| \le (1/2)(\|\nabla u_t\|^2 + \|\nabla v_t\|^2) + (1/2)(a-k)(1 + ((l+1)^{-1}/(l+2))(a-k)^l c_s^{l+2})[(h_1 o \nabla u)(t) + (h_2 o \nabla v)(t)] + ((l+1)^{-1}/(l+2))(a-k)^{l+2}c_s^{l+2}2^{2l+1}(\|\nabla u\|^{2(l+1)} + \|\nabla v\|^{2(l+1)}) + (1/(l+2))(\|u_t\|_{l+2}^{l+2} + \|v_t\|_{l+2}^{l+2}).$

(ii) $\psi(t) \le \delta[(a-k) + ((l+1)^{-1}/(l+2))(h_1(0))^{l+2}c_s^{l+2}2^{2(l+1)}]M(\|\nabla u\|^2)\|\nabla u\|^2 + ((\alpha C_s/2) + 2\delta(a-k)^2)\|\nabla u\|^2 + ((M(\|\nabla u\|^2)/4\delta) + ((\alpha C_s/2) + 2\delta + (1/2\delta))(a-k))(h_1 o \nabla v)(t) - (h_1(0)/4\delta)(1 + ((l+1)^{-1}/(l+2))(h_1(0))^l c_s^{l+2})(h_1' o \nabla v)(t) + (\delta - \int_0^t h_1(s)\mathrm{d}s)\|\nabla u_t\|^2 + \mu_1^2\delta\|\nabla z_1(x,1,t)\|^2 + (1/(l+1))(1 - \int_0^t h_1(s)\mathrm{d}s)\|u_t\|_{l+2}^{l+2} + \delta[(a-k) + ((l+1)^{-1}/(l+2))(h_2(0))^{l+2}c_s^{l+2}2^{2(l+1)}]M(\|\nabla v\|^2)\|\nabla v\|^2 + ((\alpha C_s/2) + 2\delta(a-k)^2)\|\nabla v\|^2 + ((M(\|\nabla u\|^2)/4\delta) + ((\alpha C_s/2) + 2\delta +$

$(1/2\delta))(a-k))(h_2 o \nabla v)(t) - (h_2(0)/4\delta)(1 + ((l+1)^{-1}/(l+2))(h_2(0))^l c_s^{l+2})(h_2' o \nabla v)(t) + (\delta - \int_0^t h_2(s)\mathrm{d}s)\|\nabla v_t\|^2 + \mu_2^2\delta\|\nabla z_2(x,1,t)\|^2 + (1/(l+1))(1 - \int_0^t h_2(s)\mathrm{d}s)\|v_t\|_{l+2}^{l+2},$

where $\delta > 0$ and c_s is the Sobolev embedding constant.

Proof

(i) $\psi(t) = -\int_\Omega \nabla u_t \int_0^t h_2(t-s)(\nabla u(t) - \nabla u(s))\,\mathrm{d}s\mathrm{d}x - \int_\Omega (1/(l+1))|u_t|^l u_t \int_0^t h_2(t-s)(u(t)-u(s))\,\mathrm{d}s\mathrm{d}x - \int_\Omega \nabla v_t \int_0^t h_2(t-s)(\nabla v(t) - \nabla v(s))\mathrm{d}s\mathrm{d}x - \int_\Omega (1/(l+1))|v_t|^l v_t \int_0^t h_2(t-s)(v(t)-v(s))\mathrm{d}s\mathrm{d}x.$

We use Young's inequality with the conjugate exponents $p = (l+2)/(l+1)$ and $q = l+2$, and the second term in the right hand side can be estimated as

$$\left|-\int_\Omega \frac{1}{l+1}|u_t|^l u_t \int_0^t h_1(t-s)(u(t)-u(s))ds dx\right| \le \frac{1}{l+1}\left|\int_\Omega \left(|u_t|^l u_t\right)\left(\int_0^t h_1((t-s)u(t)-u(s))ds\right)dx\right|$$

$$\le \frac{1}{l+1}\left[\frac{1}{p}\int_\Omega \left||u_t|^l u_t\right|^P dx + \frac{1}{q}\int_\Omega \left|\int_0^t h_1((t-s)u(t)-u(s))ds\right|^q dx\right]$$

$$\le \frac{1}{l+1}\left[\frac{1}{p}\int_\Omega \left||u_t|^{l+1}\right|^P dx + \frac{1}{q}\int_\Omega \int_0^t \left(h_1((t-s)u(t)-u(s))ds\right)^q dx\right]$$

$$\le \frac{1}{l+2}\|u_t\|_{l+2}^{l+2} + \frac{(l+1)^{-1}}{l+2}\int_\Omega \left[\int_0^t (h_1(t-s))^{\frac{l+1}{l+2}}\left((h_1(t-s))^{\frac{1}{l+2}}|u(t)-u(s)|\right)ds\right]^{l+2} dx.$$

$$(82)$$

We have by Hölder's inequality

$$\int_\Omega \left[\int_0^t (h_1(t-s))^{((l+1)/(l+2))}\left((h_1(t-s))^{(1/(l+2))}|u(t)-u(s)|\right)ds\right]^{l+2} dx$$

$$\le \int_\Omega \left[\left(\int_0^t \left((h_1(t-s))^{((l+1)/(l+2))}\right)^P ds\right)^{1/P}\left(\int_0^t \left((h_1(t-s))^{(1/(l+2))}|u(t)-u(s)|\right)^q ds\right)^{1/q}\right]^{l+2} dx$$

$$\le \int_\Omega \left(\int_0^t h_1(t-s)ds\right)^{((l+1)/(l+2))}\left[\left(\int_0^t h_1(t-s)ds|u(t)-u(s)|^{l+2}ds\right)^{1/l+2}\right]^{l+2} dx$$

$$\le \left(\int_0^t h_1(t-s)ds\right)^{l+1}\int_0^t h_1(t-s)\|u(t)-u(s)\|_{l+2}^{l+2}ds$$

$$\le (a-k)^{l+1}c_s^{l+2}\int_0^t \sqrt{h_1(t-s)}\sqrt{h_1(t-s)}\|\nabla u(t)-\nabla u(s)\|^{l+1}\|\nabla u(t)-\nabla u(s)\|ds$$

$$\le (a-k)^{l+1}c_s^{l+2}\left(\frac{1}{2}\int_0^t h_1(t-s)\|\nabla u(t)-\nabla u(s)\|^{2l+2}ds + \frac{1}{2}\int_0^t h_1(t-s)\|\nabla u(t)-\nabla u(s)\|^2 ds\right)$$

$$\le (a-k)^{l+1}c_s^{l+2}\left(\frac{1}{2}\int_0^t h_1(t-s)\|2\nabla u(t)\|^{2l+2}ds + \frac{1}{2}(h_1 o\nabla u)(t)\right)$$

$$\le (a-k)^{l+1}c_s^{l+2}\left(2^{2l+1}(a-k)\|\nabla u(t)\|^{2(l+1)} + \frac{1}{2}(h_1 o\nabla u)(t)\right).$$

$$(83)$$

Combining (83) with (82), we obtain

$$\left|-\int_\Omega \frac{1}{l+1}|u_t|^l u_t \int_0^t h_1(t-s)(u(t)-u(s))ds dx\right| \le \frac{1}{l+2}\|u_t\|_{l+2}^{l+2}$$

$$+ \frac{(l+1)^{-1}}{l+2}\left[(a-k)^{l+1}c_s^{l+2}\left(2^{2l+1}(a-k)\|\nabla u(t)\|^{2(l+1)} + \frac{1}{2}(h_1 o\nabla u)(t)\right)\right].$$

$$(84)$$

Similarly, we get

$$\left| -\int_\Omega \nabla u_t \int_0^t h_1(t-s)(\nabla u(t)-\nabla u(s))\mathrm{d}s\mathrm{d}x \right| \leq \frac{1}{2}\|\nabla u_t\|^2 + \frac{1}{2}\int_\Omega \left(\int_0^t h_1(t-s)|\nabla u(t)-\nabla u(s)|\mathrm{d}s \right)^2 \mathrm{d}x$$

$$\leq \frac{1}{2}\|\nabla u_t\|^2 + \frac{1}{2}(a-k)(h_1 o \nabla u)(t). \tag{85}$$

Similarly,

$$\begin{cases} \left| -\int_\Omega \dfrac{1}{l+1}|v_t|^l v_t \int_0^t h_2(t-s)(v(t)-v(s))\mathrm{d}s\mathrm{d}x \right| \leq \dfrac{1}{l+2}\|v_t\|^{l+2} \\[2mm] \quad +\dfrac{(l+1)^{-1}}{l+2}\left[(a-k)^{l+1}c_s^{l+2}\left(2^{2l+1}(a-k)\|\nabla v(t)\|^{2(l+1)} + \dfrac{1}{2}(h_2 o \nabla v)(t) \right) \right] \\[2mm] \left| -\int_\Omega \nabla v_t \int_0^t h_2(t-s)(\nabla v(t)-\nabla v(s))\mathrm{d}s\mathrm{d}x \right| \leq \dfrac{1}{2}\|\nabla v(t)\|^2 + \dfrac{1}{2}(a-k)(h_2 o \nabla v)(t). \end{cases} \tag{86}$$

Combining (84)–(86), we deduce (i).

(ii) Using the Leibniz formula and the first and second equations of (7), we have

$$\psi'(t) = \int_\Omega \left(\Delta u_{tt} - |u_t|^l u_{tt} \right) \int_0^t h_1(t-s)(u(t)-u(s))\mathrm{d}s\mathrm{d}x$$

$$+ \int_\Omega \left(\Delta u_t - \frac{1}{l+1}|u_t|^l u_t \right)\left(\int_0^t (h_1'(t-s)(u(t)-u(s))) + h_1(t-s)u_t(t)\mathrm{d}s \right)\mathrm{d}x$$

$$+ \int_\Omega \left(\Delta v_{tt} - |v_t|^l v_{tt} \right) \int_0^t h_2(t-s)(v(t)-v(s))\mathrm{d}s\mathrm{d}x$$

$$+ \int_\Omega \left(\Delta v_t - \frac{1}{l+1}|v_t|^l v_t \right)\left(\int_0^t (h_2'(t-s)(v(t)-v(s))) + h_2(t-s)v_t(t)\mathrm{d}s \right)\mathrm{d}x$$

$$= -\alpha \int_\Omega v(t) \int_0^t h_1(t-s)(u(t)-u(s))\mathrm{d}s\mathrm{d}x + \int_\Omega M(\|\nabla u\|)^2 \nabla u(t) \int_0^t h_1(t-s)(\nabla u(t)-\nabla u(s))\mathrm{d}s\mathrm{d}x$$

$$- \int_\Omega \int_0^t h_1(t-s)\nabla u(s)\mathrm{d}s \int_0^t h_1(t-s)(\nabla u(t)-\nabla u(s))\mathrm{d}s\mathrm{d}x$$

$$+ \mu_1 \int_\Omega \nabla z_1(x,1,t) \int_0^t h_1(t-s)(\nabla u(t)-\nabla u(s))\mathrm{d}s\mathrm{d}x$$

$$- \int_\Omega \nabla u_t \int_0^t h_1'(t-s)(\nabla u(t)-\nabla u(s))\mathrm{d}s\mathrm{d}x - \frac{1}{l+1}\int_\Omega |u_t|^l u_t \int_0^t h_1'(t-s)(\nabla u(t)-\nabla u(s))\mathrm{d}s\mathrm{d}x$$

$$- \|\nabla u_t\|^2 \int_0^t h_1(s)\mathrm{d}s - \frac{1}{l+1}\|u_t\|_{l+2}^{l+2} \int_0^t h_1(s)\mathrm{d}s$$

$$- \alpha \int_\Omega u(t) \int_0^t h_2(t-s)(v(t) - v(s)) \mathrm{d}s \mathrm{d}x + \int_\Omega M(\|\nabla v\|)^2 \nabla v(t) \int_0^t h_2(t-s)(\nabla v(t) - \nabla v(s)) \mathrm{d}s \, \mathrm{d}x$$

$$- \int_\Omega \int_0^t h_2(t-s) \nabla v(s) \mathrm{d}s \int_0^t h_2(t-s)(\nabla v(t) - \nabla v(s)) \mathrm{d}s \mathrm{d}x$$

$$+ \mu_2 \int_\Omega \nabla z_2(x,1,t) \int_0^t h_2(t-s)(\nabla v(t) - \nabla v(s)) \mathrm{d}s \mathrm{d}x$$

$$- \int_\Omega \nabla v_t \int_0^t h_2'(t-s)(\nabla v(t) - \nabla v(s)) \mathrm{d}s \mathrm{d}x - \frac{1}{l+1} \int_\Omega |v_t|^l v_t \int_0^t h_2'(t-s)(\nabla v(t) - \nabla v(s)) \mathrm{d}s \mathrm{d}x$$

$$- \|\nabla v_t\|^2 \int_0^t h_2(s) \mathrm{d}s - \frac{1}{l+1} \|v_t\|_{l+2}^{l+2} \int_0^t h_2(s) \mathrm{d}s$$

$$= I_1 + I_2 + I_3 + I_4 + I_5 + I_6 - \|\nabla u_t\|^2 \int_0^t h_1(s) \mathrm{d}s - \frac{1}{l+1} \|u_t\|^{l+2} \int_0^t h_1(s) \mathrm{d}s$$

$$- \|\nabla v_t\|^2 \int_0^t h_2(s) \mathrm{d}s - \frac{1}{l+1} \|v_t\|^{l+2} \int_0^t h_2(s) \mathrm{d}s,$$

$$\tag{87}$$

where

$$\begin{cases} I_1 = \int_\Omega M\left(\|\nabla u\|^2\right) \nabla u(t) \int_0^t h_1(t-s)(\nabla u(t) - \nabla u(s)) \mathrm{d}s \mathrm{d}x + \int_\Omega M\left(\|\nabla v\|^2\right) \nabla v(t) \int_0^t h_2(t-s)(\nabla v(t) - \nabla v(s)) \mathrm{d}s \mathrm{d}x \\[2mm]
I_2 = -\int_\Omega \int_0^t h_1(t-s) \nabla u(s) \mathrm{d}s \int_0^t h_1(t-s)(\nabla u(t) - \nabla u(s)) \mathrm{d}s \mathrm{d}x \\[2mm]
\quad - \int_\Omega \int_0^t h_2(t-s) \nabla v(s) \mathrm{d}s \int_0^t h_2(t-s)(\nabla v(t) - \nabla v(s)) \mathrm{d}s \mathrm{d}x \\[2mm]
I_3 = \mu_1 \int_\Omega \nabla z_1(x,1,t) \int_0^t h_1(t-s)(\nabla u(t) - \nabla u(s)) \mathrm{d}s \, \mathrm{d}x + \mu_2 \int_\Omega \nabla z_2(x,1,t) \int_0^t h_2(t-s)(\nabla v(t) - \nabla v(s)) \mathrm{d}s \, \mathrm{d}x \\[2mm]
I_4 = -\int_\Omega \nabla u_t \int_0^t h_1'(t-s)(\nabla u(t) - \nabla u(s)) \mathrm{d}s \, \mathrm{d}x - \int_\Omega \nabla v_t \int_0^t h_2'(t-s)(\nabla v(t) - \nabla v(s)) \mathrm{d}s \, \mathrm{d}x \\[2mm]
I_5 = -\frac{1}{l+1} \int_\Omega |u_t|^l u_t \int_0^t h_1'(t-s)(\nabla u(t) - \nabla u(s)) \mathrm{d}s \, \mathrm{d}x - \frac{1}{l+1} \int_\Omega |v_t|^l v_t \int_0^t h_2'(t-s)(\nabla v(t) - \nabla v(s)) \mathrm{d}s \, \mathrm{d}x \\[2mm]
I_6 = -\alpha \int_\Omega v(t) \int_0^t h_1'(t-s)(\nabla u(t) - \nabla u(s)) \mathrm{d}s \, \mathrm{d}x - \alpha \int_\Omega u(t) \int_0^t h_2'(t-s)(\nabla v(t) - \nabla v(s)) \mathrm{d}s \, \mathrm{d}x. \end{cases}$$

$$\tag{88}$$

In what follows we will estimate $I_1, \ldots, I_6$.

For I_1, we use Hölder and Young's inequalities with $p = q = 2$, and we get

$$|I_1| \leq M\left(\|\nabla u\|^2\right) \int_\Omega |\nabla u(t)| \left(\int_0^t h_1(s)ds\right)^{1/2} \left(\int_0^t h_1(s)|\nabla u(t) - \nabla u((s)|^2 ds\right)^{1/2} dx$$

$$+ M\left(\|\nabla v\|^2\right) \int_\Omega |\nabla v(t)| \left(\int_0^t h_2(s)ds\right)^{1/2} \left(\int_0^t h_2(t-s)|\nabla v(t) - \nabla v(s)|^2 ds\right)^{1/2} dx$$

$$\leq M\left(\|\nabla u\|^2\right)\left[\delta \int_\Omega |\nabla u(t)|^2 \left(\int_0^t h_1(s)ds\right)dx + \frac{1}{4\delta}\int_\Omega \int_0^t h_1(t-s)|\nabla u(t) - \nabla u(s)|^2 dsdx\right] \qquad (89)$$

$$+ M\left(\|\nabla v\|^2\right)\left[\delta \int_\Omega |\nabla v(t)|^2 \left(\int_0^t h_2(s)ds\right)dx + \frac{1}{4\delta}\int_\Omega \int_0^t h_2(t-s)|\nabla v(t) - \nabla v(s)|^2 dsdx\right]$$

$$\leq M\left(\|\nabla u\|^2\right)\left(\delta(a-k)\|\nabla u(t)\|^2 + \frac{1}{4\delta}(h_1 o \nabla u)(t)\right) + M\left(\|\nabla v\|^2\right)\left(\delta(a-k)\|\nabla v(t)\|^2 + \frac{1}{4\delta}(h_1 o \nabla v)(t)\right).$$

Similarly,

$$|I_2| \leq \delta \int_\Omega \left(\int_0^t h_1(t-s)|\nabla u(s)|ds\right)^2 dx + \frac{1}{4\delta}\int_\Omega \left(\int_0^t h_1(t-s)|\nabla u(t) - \nabla u(s)|ds\right)^2 dx$$

$$+ \delta \int_\Omega \left(\int_0^t h_2(t-s)|\nabla v(s)|ds\right)^2 dx + \frac{1}{4\delta}\int_\Omega \left(\int_0^t h_2(t-s)|\nabla v(t) - \nabla v(s)|ds\right)^2 dx$$

$$\leq \delta \int_\Omega \left(\int_0^t h_1(t-s)(|\nabla u(s) - \nabla u(t)| + |\nabla u(t)|)ds\right)^2 dx + \frac{1}{4\delta}\left(\int_0^t h_1(s)ds(h_1 o \nabla u)(t)\right)$$

$$+ \delta \int_\Omega \left(\int_0^t h_2(t-s)(|\nabla v(s) - \nabla v(t)| + |\nabla v(t)|)ds\right)^2 dx + \frac{1}{4\delta}\left(\int_0^t h_2(s)ds(h_2 o \nabla v)(t)\right) \qquad (90)$$

$$\leq 2\delta\|\nabla u(t)\|^2 \left(\int_0^t h_1(t)ds^2 dx + \left(2\delta + \frac{1}{4\delta}\right)\right)\int_0^t h_1((s)ds)(h_1 o \nabla u)(t)$$

$$+ 2\delta\|\nabla v(t)\|^2 \left(\int_0^t h_2(t)ds^2 dx + \left(2\delta + \frac{1}{4\delta}\right)\right)\int_0^t h_2((s)ds)(h_1 o \nabla v)(t)$$

$$\leq 2\delta\|\nabla u(t)\|^2(a-k)^2 + \left(2\delta + \frac{1}{4\delta}\right)(a-k)(h_1 o \nabla u)(t) + 2\delta\|\nabla v(t)\|^2(a-k)^2 + \left(2\delta + \frac{1}{4\delta}\right)(a-k)(h_2 o \nabla v)(t),$$

$$|I_3| \leq \delta\left(\mu_1^2\|\nabla z_1(x,1,t)\|^2 + \mu_2^2\|\nabla z_2(x,1,t)\|^2\right) + \frac{(a-k)}{4\delta}(h_1 o \nabla u)(t) + \frac{(a-k)}{4\delta}(h_2 o \nabla v)(t), \qquad (91)$$

$$|I_4| \leq \delta \int_\Omega |\nabla u_t|^2 dx + \frac{1}{4\delta}\int_\Omega \left(\int_0^t |h_1'(t-s)||\nabla u(t) - \nabla u(s)|ds\right)^2 dx$$

$$+ \delta \int_\Omega |\nabla v_t|^2 dx + \frac{1}{4\delta}\int_\Omega \left(\int_0^t |h_2'(t-s)||\nabla v(t) - \nabla v(s)|ds\right)^2 dx$$

$$\leq \delta\|\nabla u_t\|^2 + \frac{1}{4\delta}\int_0^t (-h_1'(t-s))ds \int_\Omega \int_0^t (-h_1'(t-s))|\nabla u(t) - \nabla u(s)|^2 dsdx \qquad (92)$$

$$+ \delta\|\nabla v_t\|^2 + \frac{1}{4\delta}\int_0^t (-h_2'(t-s))ds \int_\Omega \int_0^t (-h_2'(t-s))|\nabla v(t) - \nabla v(s)|^2 dsdx$$

$$\leq \delta\|\nabla u_t\|^2 - \frac{h_1(0)}{4\delta}(h_1' o \nabla u)(t) + \delta\|\nabla v_t\|^2 - \frac{h_2(0)}{4\delta}(h_2' o \nabla u)(t),$$

and since $l \leq \gamma$, we follow almost the same steps to obtain
$|\psi(t)|)$

$$|I_5| \leq \frac{1}{l+2}\left(\|u_t\|_{l+2}^{l+2} + \|v_t\|_{l+2}^{l+2}\right) + \frac{(l+1)^{-1}}{l+2}\left[(h_1(0))^{l+1}\int_0^t (-h_1'(t-s))\|u(t)-u(s)\|_{l+2}^{l+2}ds\right.$$

$$\left. + (h_2(0))^{l+1}\int_0^t (-h_2'(t-s))\|v(t)-v(s)\|_{l+2}^{l+2}ds\right.$$

$$\leq \frac{1}{l+2}\left(\|u_t\|_{l+2}^{l+2} + \|v_t\|_{l+2}^{l+2}\right) + \frac{(l+1)^{-1}}{l+2}c_s^{l+2}\left[(h_1(0))^{l+1}\int_0^t (-h_1'(t-s))\|\nabla u(t)-\nabla u(s)\|^{l+2}ds\right.$$

$$\left. + (h_2(0))^{l+1}\int_0^t (-h_2'(t-s))\|\nabla u(t)-\nabla u(s)\|^{l+2}ds\right.$$

$$\tag{93}$$

$$\leq \frac{1}{l+2}\left(\|u_t\|_{l+2}^{l+2} + \|v_t\|_{l+2}^{l+2}\right) + \frac{(l+1)^{-1}}{l+2}c_s^{l+2}(h_1(0))^{l+1}\left[\delta 2^{2(l+1)}h_1(0)\|\nabla u(t)\|^{2(l+1)} - \frac{1}{4\delta}(h_1'o\nabla u)(t)\right]$$

$$+ \frac{(l+1)^{-1}}{l+2}c_s^{l+2}(h_2(0))^{l+1}\left[\delta 2^{2(l+1)}h_2(0)\|\nabla v(t)\|^{2(l+1)} - \frac{1}{4\delta}(h_2'o\nabla v)(t)\right]$$

$$\leq \frac{1}{l+2}\left(\|u_t\|_{l+2}^{l+2} + \|v_t\|_{l+2}^{l+2}\right) + \frac{(l+1)^{-1}}{l+2}c_s^{l+2}(h_1(0))^{l+1}\left[\delta 2^{2(l+1)}h_1(0)M\left(\|\nabla u(t)\|^2\right)\|\nabla u(t)\|^2 - \frac{1}{4\delta}(h_1'o\nabla u)(t)\right]$$

$$+ \frac{(l+1)^{-1}}{l+2}c_s^{l+2}(h_2(0))^{l+1}\left[\delta 2^{2(l+1)}h_2(0)M\left(\|\nabla v(t)\|^2\right)\|\nabla v(t)\|^2 - \frac{1}{4\delta}(h_2'o\nabla v)(t)\right],$$

$$|I_6| \leq \frac{\alpha C_s}{2}\left(\|\nabla u(t)\|^2 + \|\nabla v(t)\|^2 + (a-k)\left[(h_1 o\nabla u)(t) + (h_2 o\nabla v)(t)\right]\right). \tag{94}$$

Combining (87) and (89)–(94), we finish the proof. □

Proof of Theorem 1.2. Now, for $M, \varepsilon_1 > 0$, we introduce the following functional:

$$F(t) = ME(t) + \varepsilon_1 \phi(t) + \psi(t) + I(t) \sim E(t). \tag{95}$$

Indeed, to prove $F(t) \sim E(t)$, we show that there exist two positive constants κ_1 and κ_2 such that

$$\kappa_1 E(t) \leq F(t) \leq \kappa_2 E(t). \tag{96}$$

From (i) of Lemmas 4–6 and recalling the fact that $l \leq \gamma$, we get

$$|\varepsilon_1\phi(t) + \psi(t) + I(t)| \leq \frac{\varepsilon_1+1}{l+2}\left(\|u_t\|_{l+2}^{l+2} + \|v_t\|_{l+2}^{l+2}\right) + \frac{\varepsilon_1+1}{2}\left(\|\nabla u_t\|^2\right) + \left(\|\nabla v_t\|^2\right)$$

$$+ \left(\frac{\varepsilon_1 c}{2} + \frac{(l+1)^{-1}}{(l+2)}c_s^{l+2}\left(\varepsilon_1 + 2^{2l+1}(a-k)^{l+2}\right)\right)\left(\|\nabla u\|^{2(\gamma+1)} + \|\nabla v\|^{2(\gamma+1)}\right)$$

$$\tag{97}$$

$$+ \frac{a-k}{2}\left(1 + \frac{(l+1)^{-1}}{(l+2)}(a-k)^l c_s^{l+2}\right)\left((h_1 o\nabla u)(t) + (h_2 o\nabla v)(t)\right) + \frac{1}{\xi}E(t)$$

$$\leq \kappa E(t),$$

where $\kappa > 0$ depending on $\varepsilon_1, a, b, l, c, c_s, k, \xi$. If we choose $M = \kappa + \epsilon$, we can obtain our result.

By recalling Lemmas 3–6 and by Assumption 2, we deduce that for $t \geq t_0 > 0$,

$$F'(t) = ME'(t) + \varepsilon_1 \phi'(t) + \psi'(t) + I'(t)$$

$$\leq \left(\mu^2 \delta + \varepsilon_1 \frac{\mu^2}{4\eta} - (1-d)e^{-2\tau_1} - M\beta \right) \left(\left\| \nabla z_1(x,1,t) \right\|^2 + \left\| \nabla z_2(x,1,t) \right\|^2 \right)$$

$$- 2\tau(t)e^{-2\tau_1} \int_0^1 \left(\left\| \nabla z_1(x,p,t) \right\|^2 + \left\| \nabla z_2(x,p,t) \right\|^2 \right) d\rho$$

$$- \left(\varepsilon_1 [k - \eta(a-k+1)] - \frac{\alpha C_S}{2} - 2\delta(a-k)^2 - \delta \left[(a-k) + \frac{(l+1)^{-1}}{(l+2)} (h_2 c_s)^{l+2} 2^{2(l+1)} \right] M_0 \right) \left(\left\| \nabla u \right\|^2 + \left\| \nabla v \right\|^2 \right)$$

$$+ \left[\left(\frac{M}{2} - \frac{h_1}{4\delta} \left(1 + \frac{(l+1)^{-1}}{(l+2)} h_1^l c_s^{l+2} \right) - \frac{1}{\zeta} \left(\frac{\varepsilon_1}{4\eta} + \frac{M_0}{4\delta} + \left(\frac{\alpha C_S}{2} + 2\delta + \frac{1}{2\delta} \right) (a-k) \right) \right] (h_1' o \nabla u)(t) + (h_2' o \nabla u)(t)$$

$$- \frac{1}{l+1} (h_0 - 1 - \varepsilon_1) \left(\left\| u_t \right\|_{l+2}^{l+2} + \left\| v_t \right\|_{l+2}^{l+2} \right) - (h_0 - \delta - M\lambda - 1 - \varepsilon_1) \left(\left\| \nabla u_t \right\|^2 + \left\| \nabla v_t \right\|^2 \right),$$

(98)

where $M_0 = \max\{ M(\|\nabla u\|^2), M(\|\nabla v\|^2) \}$, $h_0 = \min \{ \int_0^{t_0} h_1(s)ds, \int_0^{t_0} h_2(s)ds \}$, $h_1 = \min\{h_1(0), h_2(0)\}$, $h_2 = \min \{h_1(0), h_2(0)\}$, and $\zeta = \max\{\zeta_1, \zeta_1\}$.

Let $\epsilon > 0$ be sufficiently small so M is fixed; we take $h_0 - M\lambda - 1 > \varepsilon_1$ and δ small enough such that

$$a_3 = h_0 - 1 - \varepsilon_1 > 0,$$
$$a_4 = h_0 - \delta - M\lambda - 1 - \varepsilon_1.$$

(99)

Further, we choose η, α small enough such that

$$a_1 = \mu_1^2 \delta + \varepsilon_1 \frac{\mu^2}{4\eta} - (1-d)e^{-2\tau_1} - M\beta > 0,$$

$$a_2 = \varepsilon_1 [k - \eta[a-k+1]] - \frac{\alpha C_S}{2} - 2\delta(a-k)^2 - \delta \left((a-k) + \frac{(l+1)^{-1}}{(l+2)} (h_2 c_s)^{l+2} 2^{2(l+1)} \right) M_0 > 0,$$

(100)

$$a_5 = \frac{M}{2} - \frac{h_1}{4\delta} \left(1 + \frac{(l+1)^{-1}}{(l+2)} h_1^l c_s^{l+2} \right) - \frac{1}{\zeta} \left(\frac{\varepsilon_1}{4\eta} + \frac{M_0}{4\delta} + \left(\frac{\alpha C_S}{2} + 2\delta + \frac{1}{2\delta} \right) (a-k) \right) < 0.$$

Thus,

$$F'(t) \leq -a_3 \frac{1}{l+2} \left(\left\| u_t \right\|_{l+2}^{l+2} + \left\| v_t \right\|_{l+2}^{l+2} \right) - a_2 \left(\|\nabla u\|^2 + \|\nabla v\|^2 \right) - 2\tau(t)e^{-2\tau_1} \int_0^1 \left(\left\| \nabla z_1(x,\rho,t) \right\|^2 + \left\| \nabla z_2(x,\rho,t) \right\|^2 \right) d\rho$$

$$+ a_1 \left(\left\| \nabla z_1(x,1,t) \right\|^2 + \left\| \nabla z_2(x,1,t) \right\|^2 \right) - a_4 \left(\left\| \nabla u_t \right\|^2 + \left\| \nabla v_t \right\|^2 \right) + a_5 [(h_1' o \nabla u)(t) + (h_2' o \nabla v)(t)]$$

(101)

$$\leq -mE(t) - cE'(t),$$

where $m = \min\{(2e^{-2\tau_1}/\xi), 2(a_2/a), a_3\}$ and $(a_1/\beta) \leq c \leq \min\{(a_4/\lambda), -2a_5\}$.

Let $L(t) = F(t) + cE(t) \sim E(t)$. From (101), we get

$$L'(t) \leq -c'L(t), \quad \forall t \geq t_0, \qquad (102)$$

for some $c' > 0$. A simple integration over (t_0, t) yields

$$L(t) \leq L(t_0)e^{-c'(t-t_0)}, \quad \forall t \geq t_0. \qquad (103)$$

Thanks to equivalence between L and E, we obtain (16). □

Data Availability

No data were used to support this study.

Conflicts of Interest

The authors declare that there are no conflicts of interest regarding the publication of this paper.

Authors' Contributions

All authors contributed equally to this study. All authors read and approved the final manuscript.

References

[1] N. Mezouar and S. Boulaaras, "Global existence and decay of solutions for a class of viscoelastic Kirchhoff equation," *Bulletin of the Malaysian Mathematical Sciences Society*, vol. 43, no. 1, pp. 725–755, 2020.

[2] N. Mezouar and S. Boulaaras, "Global existence of solutions to a viscoelastic non-degenerate Kirchhoff equation," *Applicable Analysis*, 2018, in Press.

[3] S. Nicaise and C. Pignotti, "Interior feedback stabilization of wave equations with time dependent delay," *Electronic Journal of Differential Equations*, vol. 41, pp. 1–20, 2011.

[4] Q. C. Zhong, *Robust Control of Time-Delay Systems*, Springer, London, UK, 2006.

[5] E. Fridman, S. Nicaise, and J. Valein, "Stabilization of second order evolution equations with unbounded feedback with time-dependent delay," *SIAM Journal on Control and Optimization*, vol. 48, no. 8, pp. 5028–5052, 2010.

[6] S.-T. Wu, "Asymptotic behavior for a viscoelastic wave equation with a delay term," *Taiwanese Journal of Mathematics*, vol. 17, no. 3, pp. 765–784, 2013.

[7] K. Daewook, "Asymptiotic behavior for the viscoelastic Kirchhoff type equation with an internal time varying delay term," *East Asian Mathematical Journal*, vol. 32, no. 3, pp. 399–412, 2016.

[8] S. Nicaise and C. Pignotti, "Stability and instability results of the wave equation with a delay term in the boundary or internal feedbacks," *SIAM Journal on Control and Optimization*, vol. 45, no. 5, pp. 1561–1585, 2006.

[9] J. Y. Park and J. R. Kang, "Global existence and uniform decay for a nonlinear viscoelastic equation with damping," *Acta Applicandae Mathematicae*, vol. 110, no. 3, pp. 1393–1406, 2010.

[10] J. L. Lions, *Quelques Methodes de Resolution des Problemes Aux Limites Non Lineaires*, Dunod, Paris, France, in French, 1969.

Research Article

Hyperchaotic Oscillation in the Deformed Rikitake Two-Disc Dynamo System Induced by Memory Effect

Yanling Wang,[1] **Tengfei Lei,**[1] **Xin Zhang** ®**,**[2] **Chunbiao Li** ®**,**[1,2] **and Sajad Jafari** ®[3]

[1]*Collaborative Innovation Center of Memristive Computing Application (CICMCA), Qilu Institute of Technology, Jinan 250200, China*
[2]*Jiangsu Collaborative Innovation Center of Atmospheric Environment and Equipment Technology, Nanjing University of Information Science & Technology, Nanjing 210044, China*
[3]*Biomedical Engineering Faculty, Amirkabir University of Technology, 424 Hafez Ave, Tehran 15875-4413, Iran*

Correspondence should be addressed to Chunbiao Li; goontry@126.com

The fundamental dynamics of the deformed Rikitake two-disc dynamo system is explored in this paper. Memory effect on the dynamical behavior of the generator system is studied by introducing a quadratic flux-controlled memristor. Hyperchaotic oscillation in the deformed Rikitake two-disk coupled generator is therefore firstly found. Lyapunov exponents, bifurcation diagram, and phase portraits prove the abundant dynamic behavior consistently.

1. Introduction

Memristor is a passive element with nonlinearity and nonvolatility. According to the completeness of basic circuit components, in 1971, Chua first predicted the existence of the fourth circuit component, which describes the relationship between charge and flux [1]. In 2008, Hewlett–Packard Laboratory successfully fabricated the nanoscale memristor based on metal and metal oxides [2], which aroused great interest in the scientific and technological community. Recently, great progress has been made in the research of memristors, and the application of memristoralso has become a hot focus. Because of the small size, low power consumption, nonlinearity, and non-volatility, the memristor can be applied in many areas such as nonlinear chaotic circuits [3–6], electronic engineering [7–9], artificial intelligence [10–12], and neural networks [13–15].

It is considered that the geomagnetic field is associated with the conductive outer core, which has been proved by some dynamical models. In 1958, T. Rikitake firstly proposed a Two-Disc Dynamo System (RTDDS) and observed this physical law [16]. RTDDS is a simple model to demonstrate the polarity reversal of the earth's magnetic field, in which the current from each disc excites the coil of the other [17]. In fact, it is a chaotic system [18] and exhibits abundant dynamical behavior [19–21].

Recently, much attention has been paid to the RTDDS. A new attractor synthesis algorithm was applied to model the attractors in the Rikitake system [22]. By applying synchronization technique based on control theory, an active controller was designed for the synchronization of two identical RTDDS [19]. A method to stabilize asymptotically the nontrivial Lyapunov stable states of Rikitake two-disk dynamo dynamics was given in [23]. It was proven that the two non-hyperbolic equilibrium points of the Rikitake system are all stable for all positive parameters [24]. A simple realization of the symmetric Rikitake system was given in [25]. A reduced-order projective synchronization system was designed for the Rikitake system without any equilibria or with two non-hyperbolic equilibrium points in [26]. In [27], a 4-D hyperchaotic Rikitake dynamo system without any equilibria was proposed. In [28], a 5-D hyperchaotic Rikitake dynamo system with three positive Lyapunov exponents was proposed, which has a hidden attractor without any equilibrium point. From aforementioned references, the

hyperchaotic system of RTDDS was constructed by artificial numerical methods directly through feedback and other means.

With the continuous development of industrial automation, intelligent motors with control and learning capabilities have also been realized. In this paper, a deformed RTDDS is constructed by introducing an extra flux-controlled memristor. The motor can be controlled to avoid the chaotic region through the combination of memristors and memristor control parameters. After the memristor is added, the bifurcation point of the system is changed, and the original behavior state of the RTDDS is also changed. Therefore, the research in this paper provides an important idea for the control of the double-disk motor. This system is proven with abundant dynamical behaviors, including a line of equilibria and hyperchaos [29–33]. In Section 2, the brief introduction of the flux-controlled memristor is given, thereafter a new lossy RTDDS is given, and the deformed RTDDS is constructed by adding one extra flux-controlled memristor. Rich dynamics of the presented system are analyzed in Section 3. In Section 4, the analog circuit of the new memristive hyperchaotic system is implemented based on Multisim simulation. Some conclusions are finally drawn in Section 5.

2. Modeling of the Deformed Two-Disc Generator

2.1. Memristor Model. According to the relationship between voltage v and current of a flux-controlled memristor [1, 34, 35], choose a cubic nonlinearity to describe the q function [36–38], and then, $W(\varphi)$ is

$$\begin{cases} i = W(\varphi)y, \\ W(\varphi) = \alpha + 3\beta\varphi^2, \\ \dot{\varphi} = y, \end{cases} \tag{1}$$

where α and β are two positive constants. Figure 1 shows the voltage-current relationship of the memristor with $\alpha = 2$ and $\beta = 0.1$ under the frequency $f = 1$ Hz. The hysteresis curve agrees the inherent characteristics of the memristor.

In the following, the above memristor is applied to study the memory effect of the deformed RTDDS.

2.2. Description of the Deformed RTDDS. In 1958, Rikitake first proposed a two-disc generator, in which the dimensionless equations are [16, 18]

$$\begin{cases} \dot{x}_1 = -\mu x_1 + x_2 x_3, \\ \dot{x}_2 = -\mu x_2 + x_1 [x_3 - \mu(\sigma^2 - \sigma^{-2})], \\ \dot{x}_3 = 1 - x_1 x_2, \end{cases} \tag{2}$$

where x_1 and x_2 are dimensionless currents, x_3 is the angular velocity of the two discs, μ and σ are adjustable parameters.

In the chaotic double-disk generator, considering the wear rate of the double-disk generator, the model of the deformed double-disk coupled generator is constructed under electromechanical coupling. The new deformed RTDDS is proposed as
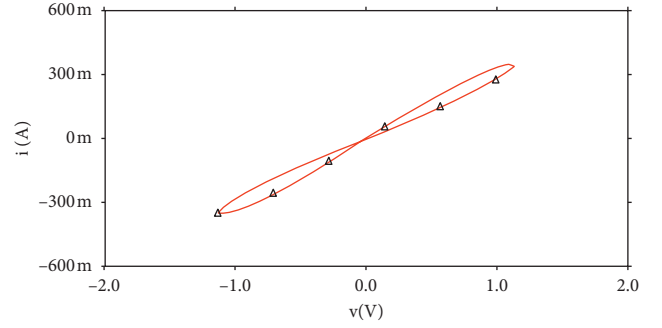
FIGURE 1: Pinched hysteresis loop of the memristor with $\alpha = 2$ and $\beta = 0.1$ ($f = 1$ Hz).

$$\begin{cases} \dot{x} = -ax + y(z + c), \\ \dot{y} = -by + x(z - c), \\ \dot{z} = dz - xy, \end{cases} \tag{3}$$

where a and b are the ratio of resistance to self-inductance of the two loops, which represent the dissipative performance of the generator, and are closely related to the working conditions of the generator. Here, c is the difference in angular velocity between two rotors of the coupled generators, d is the wear parameter, x and y represent the current across the two loops, and z is the angular velocity of the double discs. System (3) with $a = 2$, $b = 3$, $c = 5$, and $d = 0.75$ has a chaotic solution with Lyapunov exponents: $LE_1 = 0.2825$, $LE_2 = 0$, and $LE_3 = -4.4179$ under the initial condition $(0.1, 0.1, 0.1)$, as shown in Figure 2. System (3) shows rotational symmetry since it is recovered by the transformation $(x, y, z) \longrightarrow (-x, -y, z)$.

2.3. Memristive Deformed RTDDS. In RTDDS, assume that the loop current of the first disc depends on the change of the current of the other disc, and the memory effect can be indicated by the memristor. A flux-controlled memristor is applied in RTDDS with $\alpha = 2$ and $\beta = 0.1$, and the memristive deformed RTDDS is

$$\begin{cases} \dot{x} = -ax + yz + kW(\varphi)y, \\ \dot{y} = -by + x(z - c), \\ \dot{z} = dz - xy, \\ \dot{\varphi} = y, \end{cases} \tag{4}$$

where a, b, c, and d are positive parameters, and k is a positive parameter representing the strength of the memristor. System (4) with $a = 2$, $b = 3$, $c = 5$, $d = 0.75$, and $k = 1$ has a hyperchaotic attractor with Lyapunov exponents $LE_1 = 0.3784$, $LE_2 = 0.0218$, $LE_3 = 0.0000$, and $LE_4 = -4.6503$, two of which are positive indicating hyperchaos, as shown in Figure 3. The Kaplan–York dimension is $D_{KY} = 3.0861$. Poincaré map is a line representing chaos if the surface represents hyperchaos, and the Poincaré map of the system is shown in Figure 4; in this system, Poincaré map is surface, so it is hyperchaos. The invariance of system (4) under the transformation $(x, y, z, \varphi) \longrightarrow (-x, -y, z, -\varphi)$ shows the
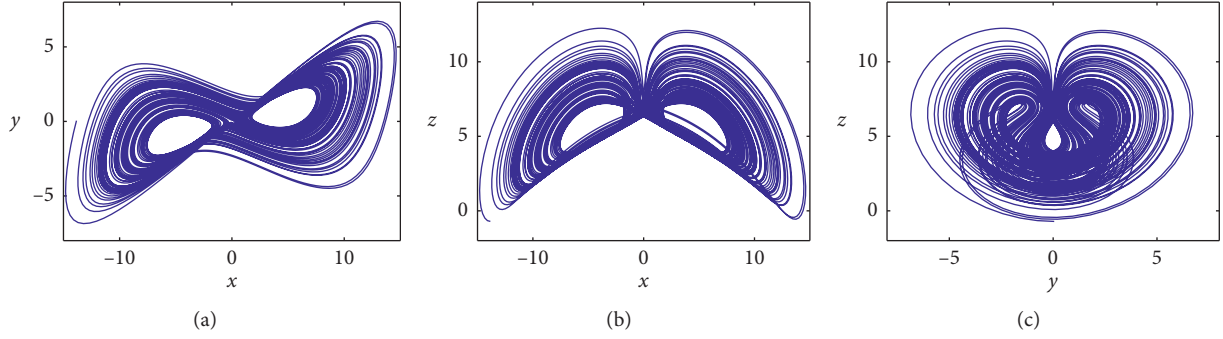
FIGURE 2: Phase portraits of system (3) with $a = 2$, $b = 3$, $c = 5$, and $d = 0.75$: (a) x-y plane, (b) x-z plane, and (c) y-z plane.
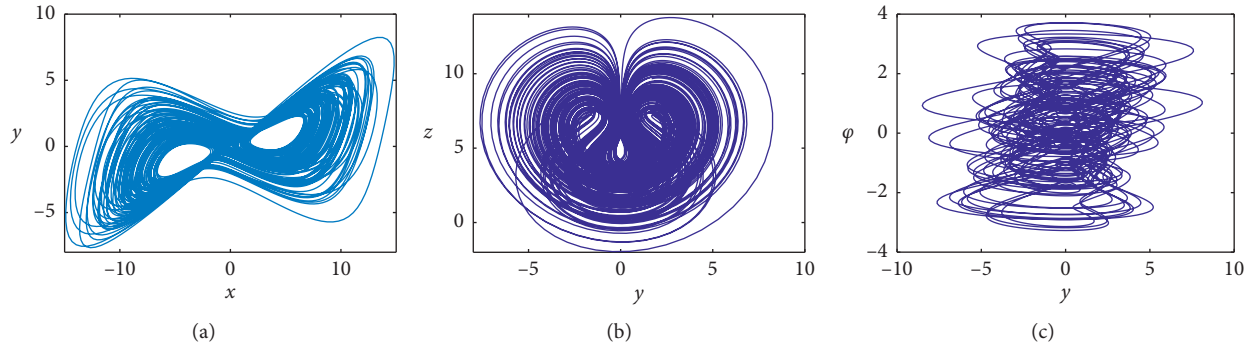
FIGURE 3: Phase portraits of system (4) with $a = 2$, $b = 3$, $c = 5$, $d = 0.75$, and $k = 1$: (a) x-y plane, (b) y-z plane, and (c) y-φ plane.
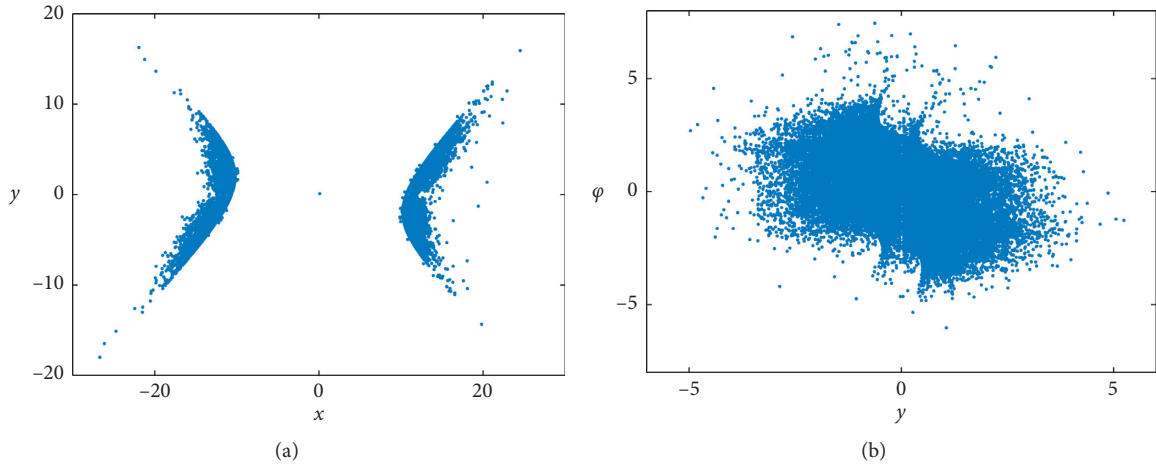
FIGURE 4: Poincaré map of system (4) with $a = 2$, $b = 3$, $c = 5$, $d = 0.75$, and $k = 1$: (a) x-y plane; (b) y-φ plane.

rotational symmetric structure. Therefore, newly introduced memristor transforms the system to be a hyperchaotic one.

3. Dynamical Behaviours of the Proposed Chaotic System

3.1. Line of Equilibria and Stability Analysis. The equilibrium points of system (4) can be derived by solving the following equations:

$$\begin{cases} -ax + yz + kW(\varphi)y = 0, \\ -by + x(z - c) = 0, \\ dz - xy = 0, \\ y = 0. \end{cases} \tag{5}$$

System (5) has a line of equilibria $[0, 0, 0, \varphi]$, where φ is a real variable. By linearizing system (5) at the equilibria, the Jacobian matrix can be obtained:

(a)

(b)
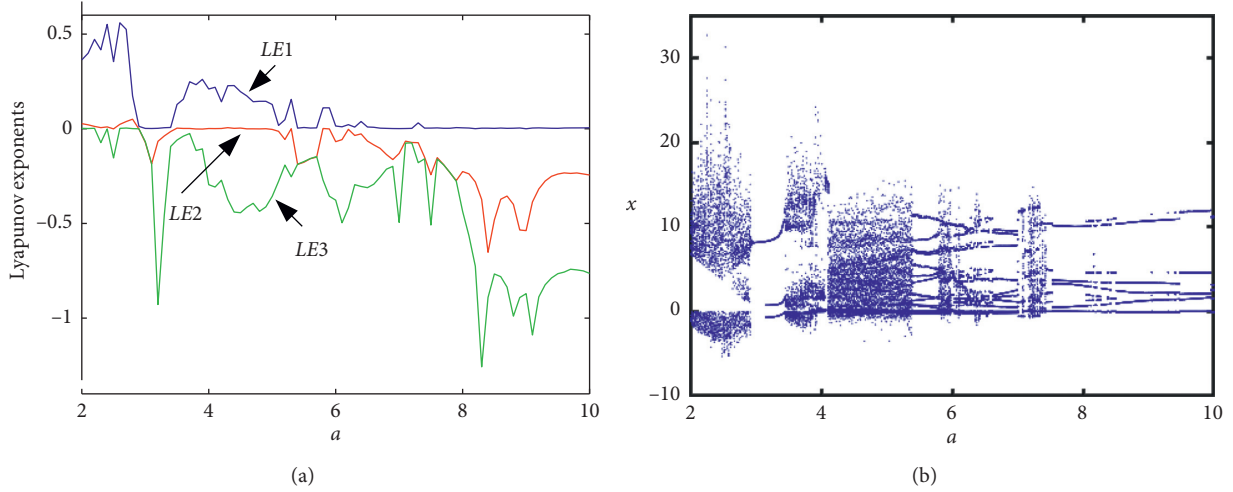
FIGURE 5: Lyapunov exponent spectra and bifurcation of system (4) with $b = 3$, $c = 5$, $d = 0.75$, and $k = 1$, and a varies in [2, 10]: (a) Lyapunov exponent spectra: LE_1 is blue, LE_2 is red, and LE_3 is green; (b) bifurcation diagram.

$$Jo = \begin{bmatrix} -a & kW(\varphi) & 0 & 0 \\ -c & -b & 0 & 0 \\ 0 & 0 & d & 0 \\ 0 & 1 & 0 & 0 \end{bmatrix}. \quad (6)$$

According to equation (6), the characteristic equation can be obtained as

$$\lambda(\lambda - d)\left[\lambda^2 + (a + b)\lambda + ab + ckW(\varphi)\right] = 0. \quad (7)$$

So, the eigenvalues are

$$\lambda_1 = 0,$$

$$\lambda_2 = d,$$

$$\lambda_{3,4} = \frac{-(a + b) \pm \sqrt{(a - b)^2 - 4ckW(\varphi)}}{2}. \quad (8)$$

Therefore, the stability of the line equilibria is associated with the values of a, b, c, k, and $W(\varphi)$. From λ_2 and $\lambda_{3,4}$, it can be seen that when a, b, and d are positive, the line equilibria point is unstable, command $\Delta_k = (a - b)^2 - 4ckW(\varphi)$, where if $\Delta_k > 0$, and the line equilibria are unstable nodes or else if $\Delta_k < 0$, the line equilibria are unstable saddle foci. Specifically, when $a = 2$, $b = 3$, $c = 5$, $d = 0.75$, and $k = 1$, the line equilibria are unstable saddle focus.

3.2. Dynamical Analysis. The dynamic behavior of system (4) will be further investigated with Lyapunov exponent spectra and bifurcation diagram.

When $b = 3$, $c = 5$, $d = 0.75$, $k = 1$, and a varies in [2, 10], set the initial condition $IC = (0.1, 0.1, 0.1, 0.1)$, step size of a is 0.01, time step is 0.01 s, and running time is 300 s; the corresponding Lyapunov exponent spectra and bifurcation diagram are obtained as shown in Figure 5. As shown in Figure 5(a), when $a \in [0, 2.58]$, the largest Lyapunov exponent is positive, so system (4) is chaotic; when $a \in [2.58, 2.9]$, two of

the Lyapunov exponents are positive. Thus, system (4) is hyperchaotic; thereafter, system (4) enters into the periodic mode at $a = 2.9$. It remains periodic when $a \in [2.9, 3.42)$. When $a \in [3.42, 5.33) \cup [5.81, 6.4) \cup [7.24, 7.6)$, it stays in chaos; system (4) drops in the periodic state occasionally when $a \in [5.33, 5.81) \cup [6.4, 7.24) \cup [7.6, 10)$. Bifurcation diagram shown in Figure 5(b) agrees with the Lyapunov exponents. Specific periodic oscillations are shown Figure 6, and the detail information of Lyapunov exponents is shown in Table 1. We noticed that system (4) sometimes provides a symmetric oscillation and sometimes gives a symmetric pair of limit cycles.

The memristor bridges the loop current of two disks. Different phase portraits can be obtained under different initial values, as shown in Figure 7. A symmetric oscillation or a symmetric pair of limit cycles is found simultaneously.

Let $a = 2$, $b = 3$, $d = 0.75$, and $k = 1$, while c varies from 0 to 10, and the initial condition $IC = (0.1, 0.1, 0.1, 0.1)$, the Lyapunov exponent spectra, and the corresponding bifurcation diagram are shown in Figure 8. As shown in Figure 8, when $c \in [0, 1.9) \cup [4.6, 8) \cup [8.24, 10]$, system (4) is chaotic; when $c \in [2.7, 4.6)$, system (4) is hyperchaotic; and when $c \in [1.9, 2.64) \cup [8, 8.42)$, system (4) is periodic. Let $a = 2$, $b = 3$, $c = 5$, and $d = 0.75$, while k varies in [0, 5], set the initial condition $IC = (0.1, 0.1, 0.1, 0.1)$, and the Lyapunov exponent spectra and the corresponding bifurcation diagram are shown in Figure 9, showing system (4) stays in chaos robustly. Usually, a memristive system shows multistability induced by the memory effect, however when $a = 2$, $b = 3$, $c = 5$, $d = 0.75$, and $k = 1$, let the initial condition $IC = (0.1, 0.1, 0.1, \varphi)$, φ varies from −5 to 5, the Lyapunov exponent spectra and the corresponding bifurcation diagram are shown in Figure 10, showing system (4) stays in chaotic orbit.

4. Circuit Simulation Based on Multisim

In order to further observe the specific hyperchaotic oscillation behavior induced from the memory effect, a circuit
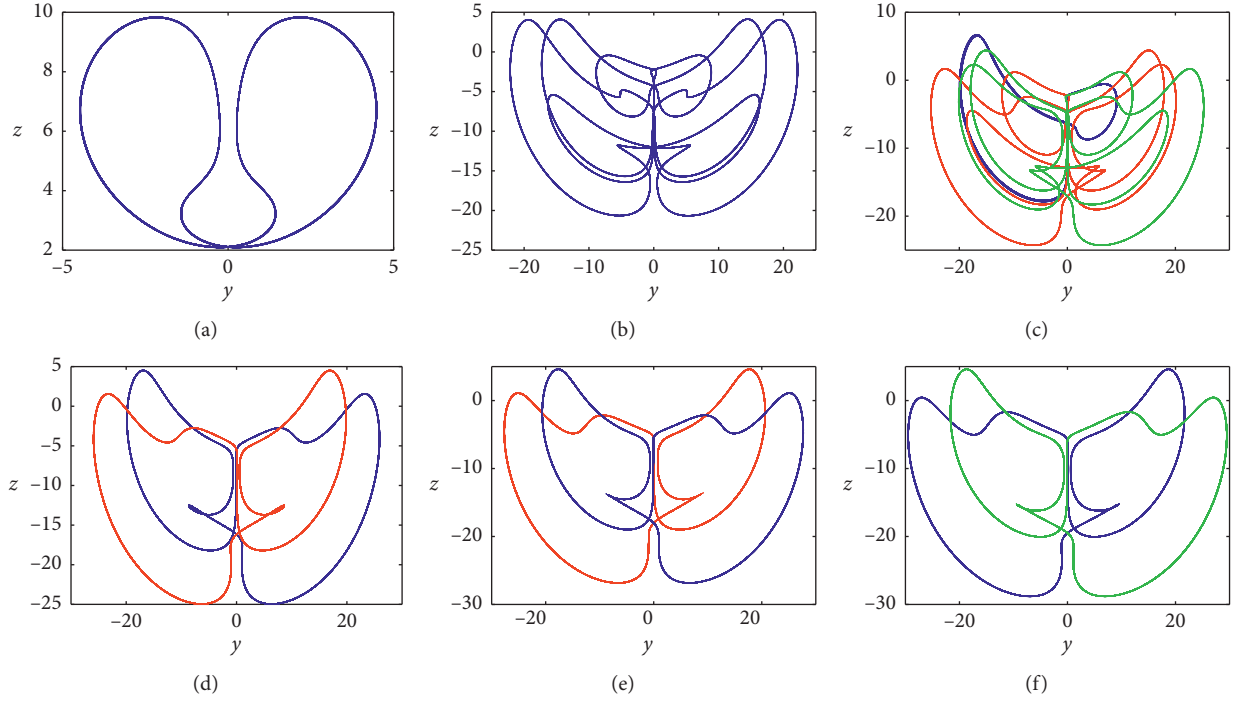
FIGURE 6: Various periodic oscillations in system (4) with $b = 2$, $c = 5$, $d = 0.75$, and $k = 1$ and (a) $a = 3.2$, (b) $a = 5.8$, (c) $a = 7$, (d) $a = 8.5$, (e) $a = 9$, and (f) $a = 9.8$, $IC = (0.1, 0.1, 0.1, 0.1)$ is blue, $(-0 \ 1, 0.1, 0.1, 0.1)$ is red, and $(0.1, 0.1, -0.1, 0.1)$ is green.

TABLE 1: Periodic oscillations in system (4) under different parameters of a.

Cases	Parameter a	Lyapunov exponents	Solution type of system (4)
A	$a = 3.2$	0.0002 −0.0665 −0.9399 −4.4432	Symmetric attractor
B	$a = 5.8$	0.1214 0.0000 −0.3017 −7.8699	Symmetric attractor
C	$a = 7$	0.0005 −0.1337 −0.5036 −8.6132	Asymmetric attractor
D	$a = 8.5$	0.0000 −0.4863 −0.7792 −9.4844	Asymmetric attractor
E	$a = 9$	0.0014 −0.5440 −0.8858 −9.8216	Asymmetric attractor
F	$a = 9.8$	0.0006 −0.2361 −0.7574 −11.0571	Asymmetric attractor
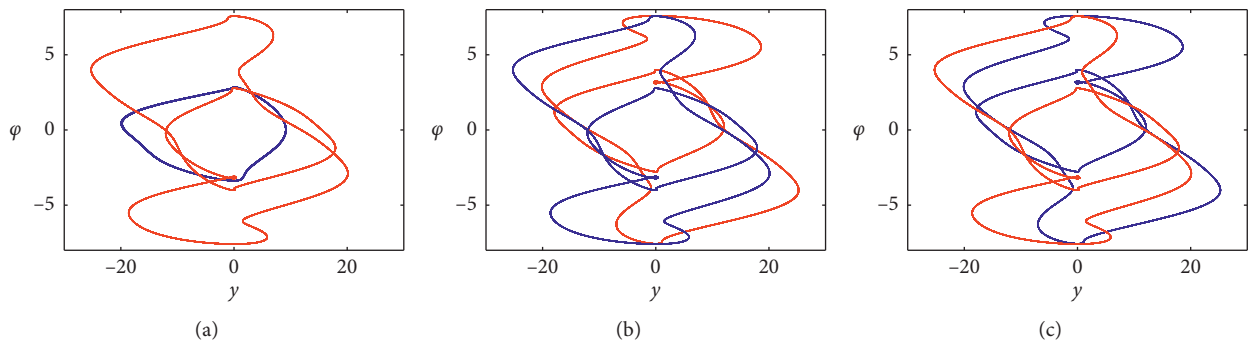
FIGURE 7: Various periodic oscillations in system (4) with $a = 7$, $b = 3$, $c = 5$, $d = 0.75$, and $k = 1$: (a) $IC = (0.1, 0.1, 0.1, 0.1)$ is blue, $(0.1, -0.1, 0.1, 0.1)$ is red, (b) $IC = (0.1, 5, 0.1, 0.1)$ is blue, $(0.1, -5, 0.1, 0.1)$ is red, and (c) $IC = (0.1, 10, 0.1, 0.1)$ is blue, $(0.1, -10, 0.1, 0.1)$ is red.

simulation is realized based on Multisim software [39]. In the circuit design, resistors, capacitors, operational amplifiers (OPA404AG), analog multipliers, and other elements are applied. The supply voltages for OPA404AG operational amplifiers (with saturated voltages $V_{sat} \approx \pm 13.5$ V) are ± 15 V. In fact, the variable z is beyond the normal operating range

of the device. Therefore, here, the variables are transformed by proportional compression, that is, $v_x = 10v_{x1}$, $v_y = 10v_{y1}$, $v_z = 10v_{z1}$, and $v_\varphi = 10v_{\varphi 1}$, where v_{x1}, v_{y1}, v_{z1}, and $v_{\varphi 1}$ are the voltages on the integral capacitor, respectively. By time rescaling of system (4), the equations can be obtained as follows:

(a)

(b)
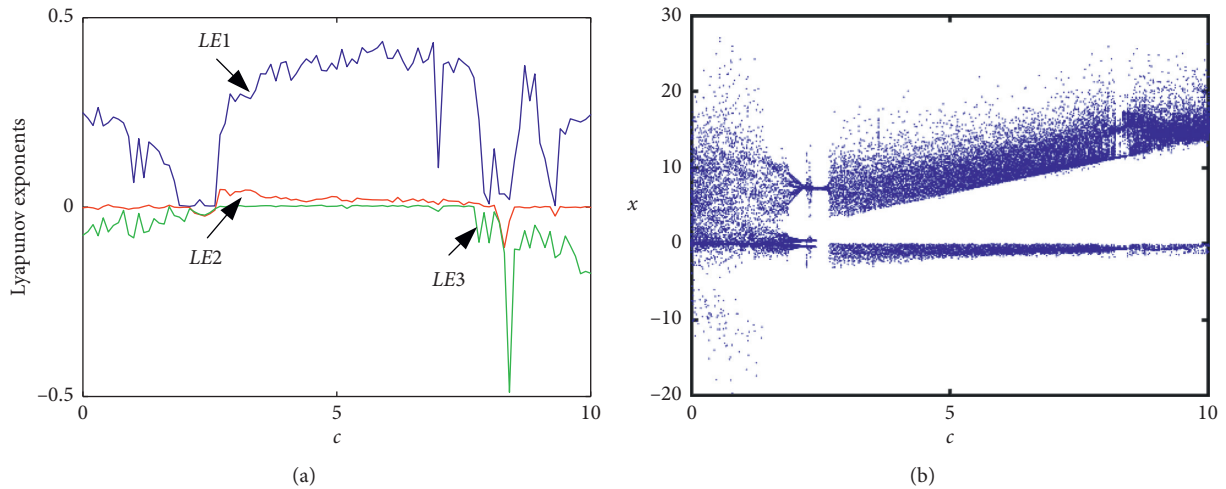
Figure 8: Lyapunov exponent spectra and bifurcation diagram of system (4) with $a = 2$, $b = 3$, $d = 0.75$, and $k = 1$, while c varies in [1, 10]: (a) Lyapunov exponent spectra: LE_1 is blue, LE_2 is red, and LE_3 is green; (b) bifurcation diagram.

(a)

(b)
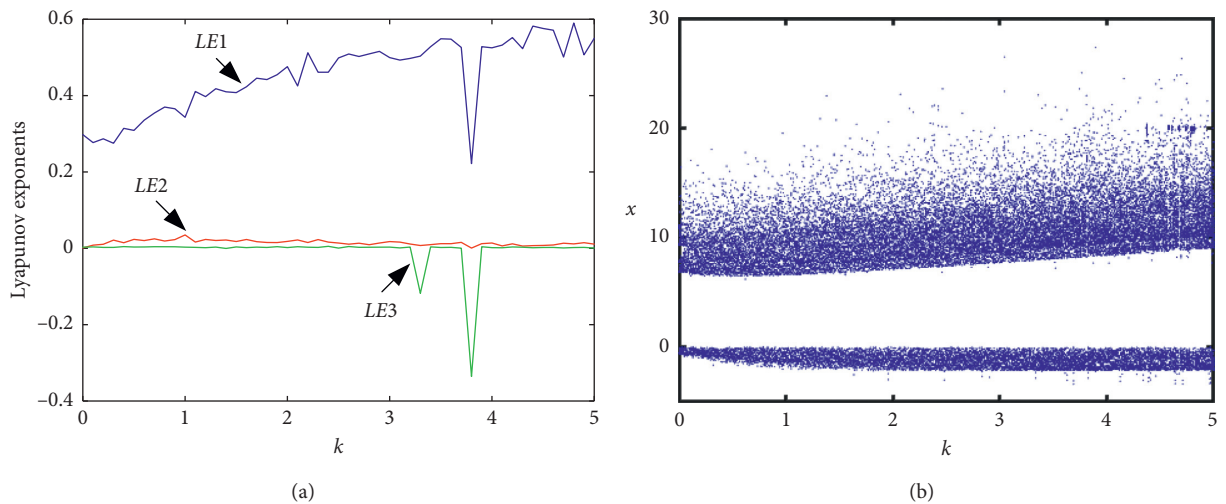
Figure 9: Lyapunov exponent spectra and bifurcation diagram of system (4) with $a = 2$, $b = 3$, $c = 5$, and $d = 0.75$, while k varies in [0, 5]: (a) Lyapunov exponent spectra: LE_1 is blue, LE_2 is red, and LE_3 is green; (b) bifurcation diagram.
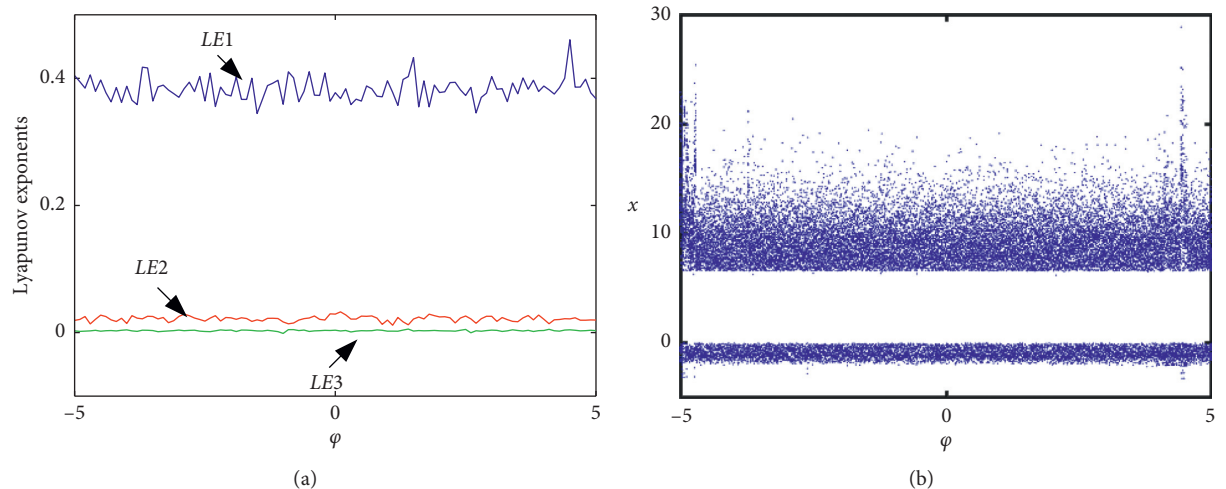
(a)

(b)

Figure 10: Lyapunov exponent spectra and bifurcation diagram of system (4) with $a = 2$, $b = 3$, $c = 5$, $d = 0.75$, and $k = 1$, while φ varies in [−5, 5]: (a) Lyapunov exponent spectra: LE_1 is blue, LE_2 is red, and LE_3 is green; (b) bifurcation diagram.

(a)

(b)
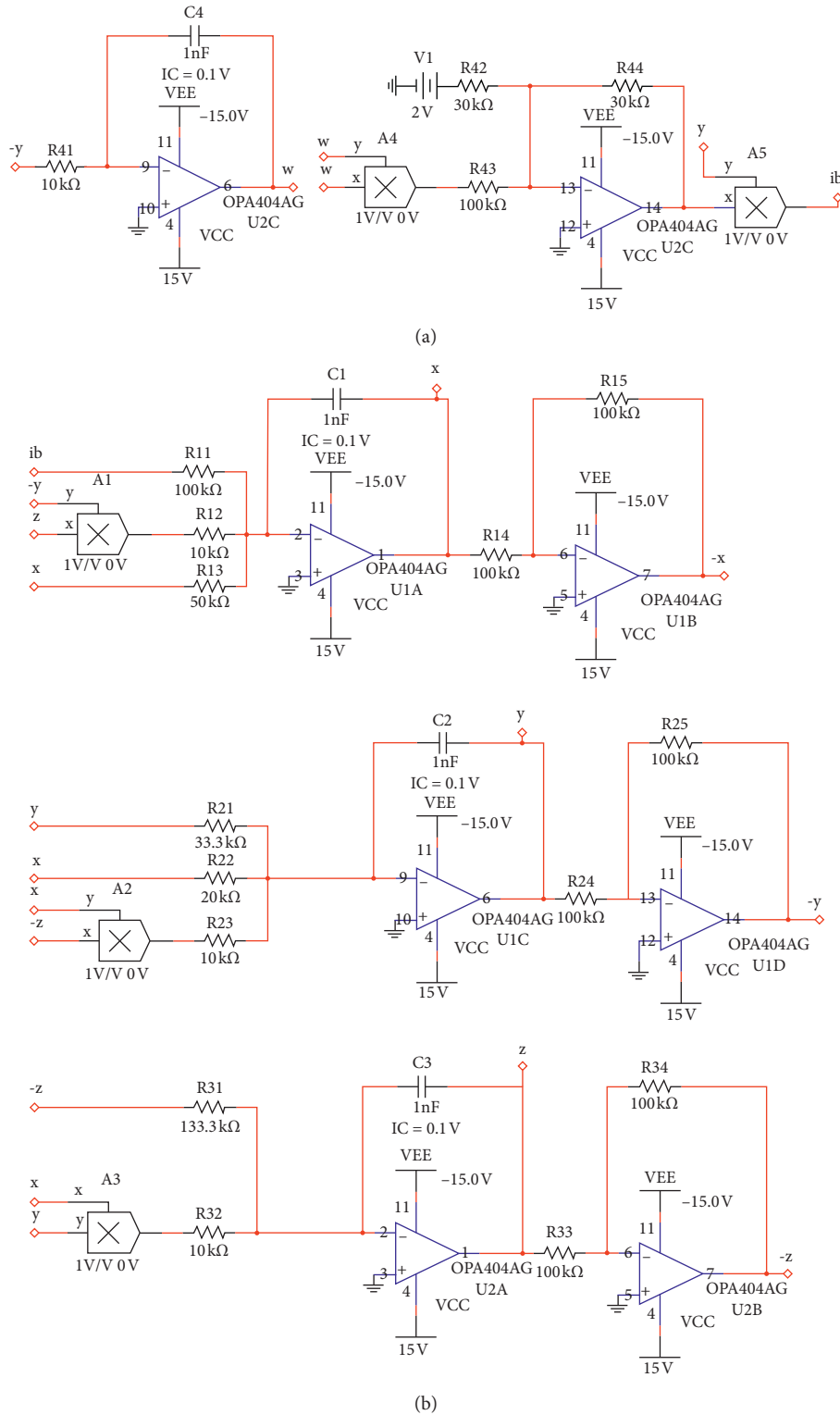
FIGURE 11: The analog circuit of the deformed RTDDS.
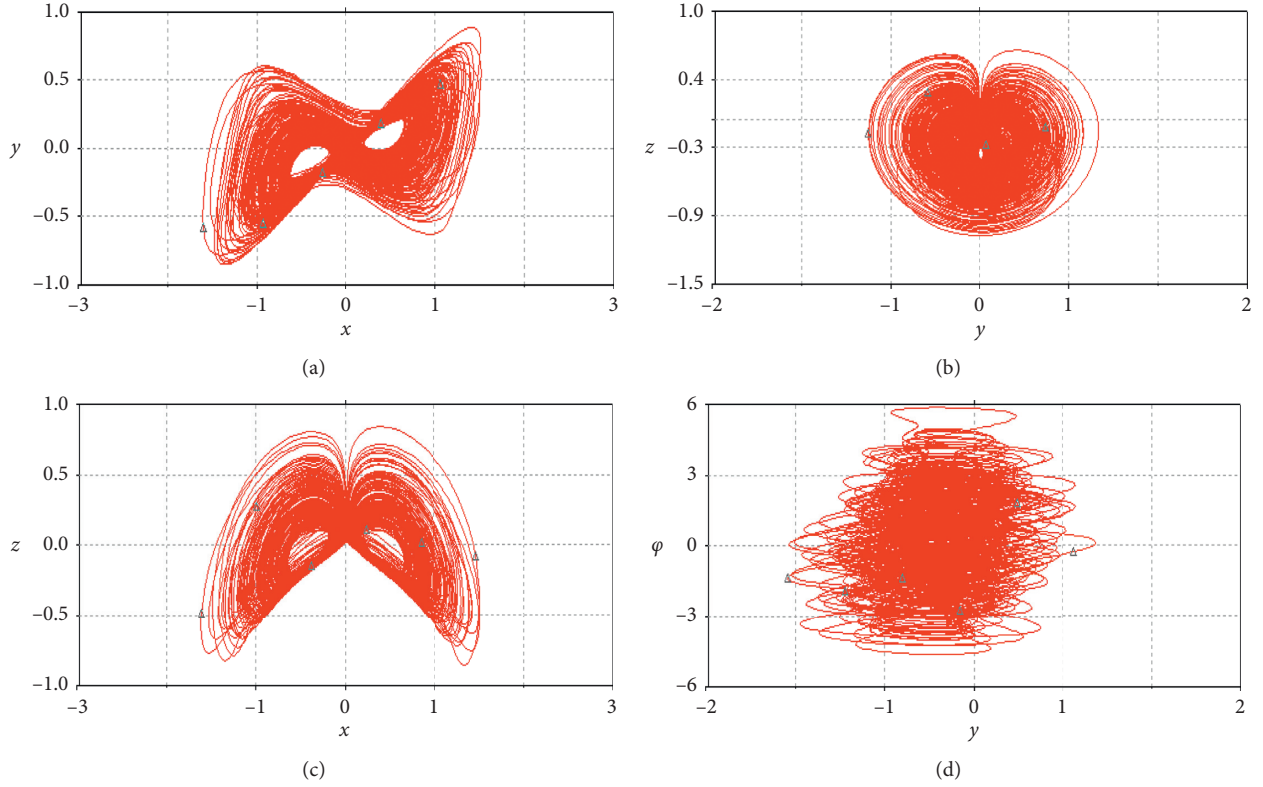
Figure 12: Simulation results obtained from Multisim software: (a) attractor on the x-y plane, (b) attractor on the y-z plane, (c) attractor on the x-z plane, and (d) attractor on the y-φ plane.
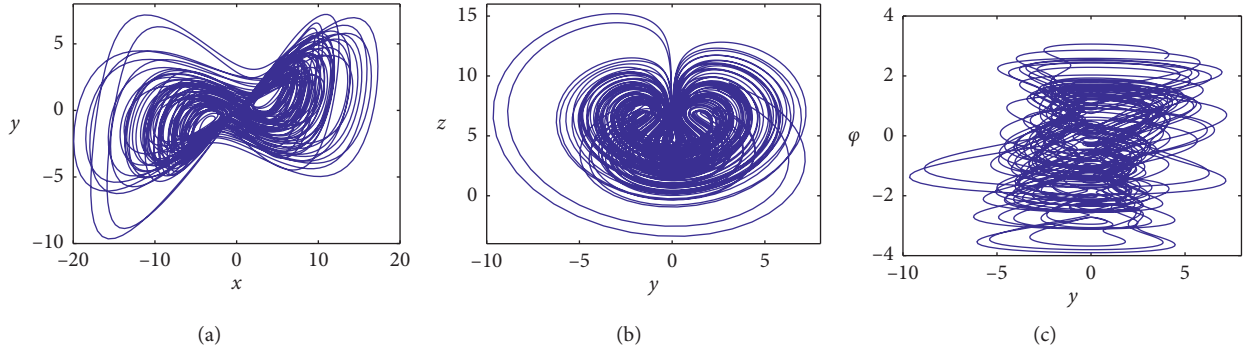
Figure 13: Phase portraits of system (4) with memristor $W(\varphi) = -m + n|\varphi|$, $m = 2$, $n = 5$, and $a = 2$, $b = 3$, $c = 5$, $d = 0.75$, and $k = 1$: (a) x-y plane, (b) y-z plane, and (c) y-φ plane.

$$
\begin{cases}
C_1 \dot{v}_x = -\dfrac{1}{R_{13}} v_x + \dfrac{1}{R_{12}} v_y v_z + \dfrac{1}{R_{11}} W(\varphi) v_y, \\[2mm]
C_2 \dot{v}_y = -\dfrac{1}{R_{21}} v_y + \dfrac{1}{R_{22}} v_x v_z - \dfrac{1}{R_{23}} v_x, \\[2mm]
C_3 \dot{v}_z = \dfrac{1}{R_{31}} v_z - \dfrac{1}{R_{32}} v_x v_y, \\[2mm]
C_4 \dot{v}_\varphi = \dfrac{1}{R_{41}} v_y.
\end{cases}
\tag{9}
$$

The corresponding analog circuit is shown in Figure 11. The circuit in Figure 11(a) represents the quadratic nonlinear flux-controlled memristor, which consists of an integration circuit and a proportional circuit. Resistor R41, operational amplifier U2C, and capacitor C4 constitute an integral circuit, which integrates the voltage v across the memristor giving the magnetic flux through the memristor.

In Figure 11, the capacitances and resistances are $C_1 = C_2 = C_3 = C_4 = 1 \text{ nF}$, $R_{12} = R_{23} = R_{32} = R_{41} = 10 \text{ k}\Omega$, $R_{13} = 50 \text{ k}\Omega$, $R_{21} = 33.3 \text{ k}\Omega$, $R_{22} = 20 \text{ k}\Omega$, $R_{31} = 133.3 \text{ k}\Omega$, $R_{42} = R_{44} = 30 \text{ k}\Omega$, and $R_{14} = R_{15} = R_{24} = R_{25} = R_{33} = R_{34} = R_{43} = R_{11} = 100 \text{ k}\Omega$. Figure 12 gives the phase trajectories shown in the oscilloscopes.

In order to verify the memory effect in RTDDS, a new flux-controlled memristor $W(\varphi) = -m + n|\varphi|$, with $m = 2$ and $n = 5$, is introduced. System (4) has a hyperchaotic attractor with Lyapunov exponents $LE_1 = 0.3225$, $LE_2 = 0.0554$, $LE_3 = 0.0000$, and $LE_4 = -4.6309$ when $a = 2$, $b = 3$, $c = 5$, $d = 0.75$, and $k = 1$, two of which are positive indicating hyperchaos, as shown in Figure 13.

5. Conclusions and Discussion

The deformed Rikitake two-disc dynamo system possesses rich dynamics including chaos, hyperchaos, and different periodic oscillations. A memristive deformed RTDDS was constructed for observing the memory effect. Consequently, an analog circuit based on the flux-controlled memristor was designed for further verification. Circuit simulation agrees with the theoretical analysis and numerical simulation. By the memristor model built the control circuit, through memristor and matching parameters of the memristor, the RTDDS can be controlled to avoid the chaotic region and realize the smooth operation. This research provides a meaningful reference for motor design and control.

Data Availability

The data used to support the findings of this study are available from the corresponding author upon request.

Conflicts of Interest

The authors declare that they have no conflicts of interest.

Acknowledgments

References

[1] L. Chua, "Memristor-The missing circuit element," *IEEE Transactions on Circuit Theory*, vol. 18, no. 5, pp. 507–519, 1971.

[2] D. B. Stukov, G. S. Snider, D. R. Stewart et al., "The missing memristor found," *Nature*, vol. 453, pp. 80–83, 2008.

[3] B. C. Bao, Z. Liu, and J. P. Xu, "Steady periodic memristor oscillator with transient chaotic behaviours," *Electronics Letters*, vol. 46, no. 3, p. 228, 2010.

[4] C. Li, W. Joo-Chen Thio, H. Ho-Ching Iu, and T. Lu, "A memristive chaotic oscillator with increasing amplitude and frequency," *IEEE Access*, vol. 6, pp. 12945–12950, 2018.

[5] J. Wang, G. Iu, and T. Fernando, *IEEE Transactions on Circuits System*, vol. 28, 2018.

[6] G. Ella, *International Journal of Bifurcation and Chaos in Applied Sciences and Engineering*, vol. 29, pp. 246–250, 2014.

[7] H. Chang, Z. Wang, Y. Li, and G. Chen, *Semiconductor Science and Technology*, vol. 65, pp. 104004–104014, 2017.

[8] L. Xie, H. A. D. Nguyen, M. Taouil, S. Hamdioui, and K. Bertels, "A mapping methodology of boolean logic circuits on memristor crossbar," *IEEE Transactions on Computer-Aided Design of Integrated Circuits and Systems*, vol. 37, no. 2, pp. 311–323, 2018.

[9] X. Wang, Q. Wu, Q. Chen, and Z. Zeng, "A novel design for memristor-based multiplexer via NOT-material implication," *IEEE Transactions on Computer-Aided Design of Integrated Circuits and Systems*, vol. 37, no. 7, pp. 1436–1444, 2018.

[10] M. Vaynshteyn and A. Lanis, "Applications of electrochemical elements in systems of artificial intelligence," *Natural Science*, vol. 11, pp. 45–51, 2013.

[11] S. Liu, Y. Wang, M. Fardad, and P. K. Varshney, "A memristor-based optimization framework for artificial intelligence applications," *IEEE Circuits and Systems Magazine*, vol. 18, no. 1, pp. 29–44, 2018.

[12] J. H. Yoon, Z. Wang, K. M. Kim et al., "An artificial nociceptor based on a diffusive memristor," *Nature Communications*, vol. 9, p. 417, 2018.

[13] I. E. Ebong and P. Mazumder, "CMOS and memristor-based neural network design for position detection," *Proceedings of the IEEE*, vol. 100, no. 6, pp. 2050–2060, 2012.

[14] B. Bao, H. Qian, J. Wang et al., "Numerical analyses and experimental validations of coexisting multiple attractors in Hopfield neural network," *Nonlinear Dynamics*, vol. 90, no. 4, pp. 2359–2369, 2017.

[15] M. Di Marco, M. Forti, and L. Pancioni, "New conditions for global asymptotic stability of memristor neural networks," *IEEE Transactions on Neural Networks and Learning Systems*, vol. 29, no. 5, pp. 1822–1834, 2018.

[16] T. Rikitake, "Oscillations of a system of disk dynamos," *Mathematical Proceedings of the Cambridge Philosophical Society*, vol. 54, 1958.

[17] A. E. Cook and P. H. Roberts, "The Rikitake two-disc dynamo system," *Mathematical Proceedings of the Cambridge Philosophical Society*, vol. 68, no. 2, pp. 547–569, 1970.

[18] I. Keisuke, "Chaos in the Rikitake two-disc dynamo system," *Earth and Planetary Science Letters*, vol. 51, pp. 451–456, 1980.

[19] U. E. Vincent, "Synchronization of Rikitake chaotic attractor using active control," *Physics Letters A*, vol. 343, no. 1–3, pp. 133–138, 2005.

[20] M. T. Răzvan and A. Gîrban, *Nonlinear Analysis: Real World Applications*, vol. 11, pp. 2888–2895, ScienceDirect, Edinburgh, London, 2009.

[21] J. Llibre and M. Messias, "Global dynamics of the Rikitake system," *Physica D: Nonlinear Phenomena*, vol. 238, no. 3, pp. 241–252, 2009.

[22] M.-F. Danca and S. Codreanu, "Modeling numerically the Rikitake's attractors by parameter switching," *Journal of the Franklin Institute*, vol. 349, no. 3, pp. 861–878, 2012.

[23] R. A. Tudoran, *Nonlinear Analysis: Real World Applications*, vol. 12, pp. 2505–2510, Elsevier, Oxford, UK, 2011.

[24] D. C. Braga, F. S. Dias, and L. F. Mello, "On the stability of the equilibria of the Rikitake system," *Physics Letters A*, vol. 374, pp. 4316–4320, 2010.

[25] C. Lăzureanu and T. Bînzar, "On the symmetries of a Rikitake type system," *Comptes Rendus-Mathématique*, vol. 350, pp. 529–533, 2012.

[26] F. Yu and W. Q. Pan, "Hidden attractors without equilibrium and adaptive reduced-order function projective synchronization from hyperchaotic Rikitake system," *Pramana*, vol. 88, pp. 1–6, 2017.

[27] S. Vaidyanathan, C. K. Volos, and V.-T. Pham, "Analysis, adaptive control and adaptive synchronization of a nine-term novel 3-D chaotic system with four quadratic nonlinearities and its circuit simulation," *Journal of Engineering Science and Technology Review*, vol. 8, pp. 232–244, 2015.

[28] S. Vaidyanathan, V.-T. Pham, and C. K. Volos, "A 5-D hyperchaotic Rikitake dynamo system with hidden attractors," *The European Physical Journal Special Topics*, vol. 224, no. 8, pp. 1575–1592, 2015.

[29] S. Jafari and J. C. Sprott, "Simple chaotic flows with a line equilibrium," *Chaos, Solitons & Fractals*, vol. 57, pp. 79–84, 2013.

[30] K. Sun, X. Wang, and J. C. Sprott, "Bifurcations and chaos in fractional-order simplified lorenz system," *International Journal of Bifurcation and Chaos*, vol. 20, no. 4, pp. 1209–1219, 2010.

[31] G. Zhang, P. Qian, and Z. Su, "Evolution of fractional-order chaotic economic systems based on non-degenerate equilibrium points," *Chaos, Solitons & Fractals*, vol. 128, pp. 219–228, 2019.

[32] C. B. Li, J. C. Sprott, W. Thio, and H. Q. Zhu, "A new piecewise linear hyperchaotic circuit," *IEEE Transaction on Circuits and System II Express Briefs*, vol. 61, p. 977C981, 2014.

[33] B. Bao, P. Jiang, H. Wu, and F. Hu, "Complex transient dynamics in periodically forced memristive Chua's circuit," *Nonlinear Dynamics*, vol. 79, no. 4, pp. 2333–2343, 2015.

[34] L. O. Chua and S. M. Sung Mo Kang, "Memristive devices and systems," *Proceedings of the IEEE*, vol. 64, no. 2, pp. 209–223, 1976.

[35] M. D. Ventra, Y. V. Pershin, and L. O. Chua, "Circuit elements with memory: Memristors, memcapacitors, and meminductors," *Proceedings of the IEEE*, vol. 97, pp. 1717–1724, 2009.

[36] B. Muthuswamy, "Implementing memristor based chaotic circuits," *International Journal of Bifurcation and Chaos*, vol. 20, no. 5, pp. 1335–1350, 2010.

[37] H. H. C. Iu, D. S. Yu, A. L. Fitch, V. Sreeram, and H. Chen, "Controlling chaos in a memristor based circuit using a twin-T notch filter," *IEEE Transactions on Circuits and Systems I: Regular Papers*, vol. 58, no. 6, pp. 1337–1344, 2011.

[38] B. C. Bao, J. P. Xu, G. H. Zhou, Z. H. Ma, and L. Zou, "Chaotic memristive circuit: equivalent circuit realization and dynamical analysis," *Chinese Physics B*, vol. 20, 2011.

[39] Y. Sui, Y. He, W. Yu, and Y. Li, "Design and circuit implementation of a five-dimensional hyperchaotic system with linear parameter," *International Journal of Circuit Theory and Applications*, vol. 46, no. 8, pp. 1503–1515, 2018.

Research Article

Existence of Positive Weak Solutions for a New Class of (p, q) Laplacian Nonlinear Elliptic System with Sign-Changing Weights

Rafik Guefaifia [ID],[1] Salah Mahmoud Boulaaras [ID],[2,3] Sultan Alodhaibi,[2] and Salem Alkhalaf [ID][4]

[1]*Department of Mathematics, Faculty of Exact Sciences, Larbi Tebessi University, Tebessa 12002, Algeria*
[2]*Department of Mathematics, College of Sciences and Arts, Al-Rass, Qassim University, Saudi Arabia*
[3]*Laboratory of Fundamental and Applied Mathematics of Oran (LMFAO), University of Oran 1, Ahmed Benbella, Algeria*
[4]*Department of Computer, College of Sciences and Arts, Al-Rass, Qassim University, Saudi Arabia*

Correspondence should be addressed to Salah Mahmoud Boulaaras; s.boularas@qu.edu.sa

In this paper, by using subsuper solutions method, we study the existence of weak positive solutions for a new class of (p, q) Laplacian nonlinear elliptic system in bounded domains, when $a(x), b(x), \alpha(x),$ and $\beta(x)$ are sign-changing functions that maybe negative near the boundary, without assuming sign conditions on $f(0), g(0), h(0),$ and $\gamma(0)$.

1. Introduction

The study of differential equations and variational problems with nonstandard $p(x)$–growth conditions is a new and interesting topic. It arises from nonlinear elasticity theory, electrorheological fluids, etc. (see [1–15]). Many existence results have been obtained on this kind of problems, see, for example [10, 12, 16–18] and [19–30]. In [31, 32], Fan et al. studied the regularity of solutions for differential equations with nonstandard $p(x)$--growth conditions.

In this article, we consider the following system:

$$\begin{cases} -\triangle_p u - |u|^{p-2} u = \lambda_1 a(x) f(v) + \mu_1 \alpha(x) h(u) \text{ in } \Omega, \\ -\triangle_q v - |v|^{q-2} v = \lambda_2 b(x) g(u) + \mu_2 \beta(x) \gamma(v) \text{ in } \Omega, \\ u = v = 0 \text{ on } \partial\Omega, \end{cases}$$

(1)

where $\Delta_s z = \text{div}(|\nabla z|^{s-2}\nabla z)$, $s > 1, \Omega \subset \mathbb{R}^N$ $(N \geq 3)$ is a bounded domain with smooth boundary $\partial\Omega, a(x), b(x),$ $\alpha(x), \beta(x) \in C(\overline{\Omega})$, and $\lambda_1, \lambda_2, \mu_1,$ and μ_2 are nonnegative parameters.

In fact, we study the existence of positive solutions to system (1) with sign-changing weight functions $a(x), b(x),$ $\alpha(x),$ and $\beta(x)$. Due to these weight functions, the extensions are challenging and nontrivial.

These problems arise in some physical models and are interesting in applications at combustion, mathematical biology, and chemical reactions. Our approach is based on the method of sub- and supersolutions (see [6, 23–25, 27, 30]).

We make the following assumptions:

$(H1) f, g, h, \gamma \in C^1([0, \infty))$ are nondecreasing functions such that $\lim_{s \to +\infty} f(s) = \lim_{s \to +\infty} g(s) = \lim_{s \to +\infty} h(s) = \lim_{s \to +\infty} \gamma(s) = +\infty$

$(H2) \lim_{s \to +\infty} ((f(M(g(s)^{(1/q-1)}))/s^{p-1}) = 0, \forall M > 0$

$(H3) \lim_{s \to +\infty} (h(s)/s^{p-1}) = \lim_{s \to +\infty} (\gamma(s)/s^{q-1}) = 0$

Let σ_r be the first eigenvalue of $-\Delta_r$ with Dirichlet boundary conditions and ϕ_r be the corresponding eigenfunction with $\phi_r > 0$ in Ω and $\|\phi_r\| = 1$ for $r = p, q$. Let $m, \eta, \delta > 0$ be such that $(|\nabla\phi_r|^r - \sigma_r\phi_r \geq m)$ on

$\overline{\Omega_\delta} = \{x \in \Omega, d(x, \partial\Omega) \le \delta\}$ and $\phi_r \ge \eta$ on $(\Omega/\overline{\Omega_\delta})$ for $r = p, q$.

Here, we assume that the weights $a(x)$, $b(x)$, $\alpha(x)$, and $\beta(x)$ take negative values in $\overline{\Omega_\delta}$ but require $a(x)$, $b(x)$, $\alpha(x)$, and $\beta(x)$ to be strictly positive in $(\Omega/\overline{\Omega_\delta})$. To be precise, we assume that there exist positive constants $a_0, a_1, b_0, b_1, \alpha_0, \alpha_1, \beta_0,$ and β_1 such that

$$
\begin{aligned}
a(x) &\ge -a_0, \\
b(x) &\ge -b_0, \\
\alpha(x) &\ge -\alpha_0, \\
\beta(x) &\ge -\beta_0, \\
&\quad x \in \overline{\Omega_\delta}, \\
a(x) &\ge a_1, \\
b(x) &\ge b_1, \\
\alpha(x) &\ge \alpha_1, \\
\beta(x) &\ge \beta_1, \\
&\quad x \in (\Omega/\overline{\Omega_\delta}).
\end{aligned}
\tag{2}
$$

Also, let $s_0 \ge 0$ be such that $f(s_0), g(s_0), h(s_0), \gamma(s_0) > 0$, and

$$
\begin{aligned}
K_1 &= \left(\frac{p-1}{p}\right)\eta^{p/(p-1)}, \\
K_2 &= \left(\frac{q-1}{q}\right)\eta^{q/(q-1)}, \\
\theta_0 &= \max\left\{\left(\frac{s_0}{K_1}\right)^{1/(p-1)}, \left(\frac{s_0}{K_2}\right)^{q/(q-1)}\right\}.
\end{aligned}
\tag{3}
$$

For $\theta > \theta_0$, we define

$$
\lambda_{1*}(\theta) := \frac{\theta\sigma_p}{d a_1 f\left(\theta^{1/(q-1)}K_2\right)},
$$

$$
\lambda_1^*(\theta) := \frac{\theta m}{d a_0 f\left(\theta^{1/(q-1)}\right)},
$$

$$
\mu_{1*}(\theta) := \frac{\theta\sigma_p}{d'\alpha_1 h\left(\theta^{1/(p-1)}K_1\right)},
$$

$$
\mu_1^*(\theta) := \frac{\theta m}{d'\alpha_0 h\left(\theta^{1/(q-1)}\right)},
$$

$$
\lambda_{2*}(\theta) := \frac{\theta\sigma_q}{d b_1 g\left(\theta^{1/(p-1)}K_1\right)},
\tag{4}
$$

$$
\lambda_2^*(\theta) := \frac{\theta m}{d b_0 g\left(\theta^{1/(p-1)}\right)},
$$

$$
\mu_{2*}(\theta) := \frac{\theta\sigma_q}{d'\beta_1 \gamma\left(\theta^{1/(q-1)}K_2\right)},
$$

$$
\mu_2^*(\theta) := \frac{\theta m}{d'\beta_0 \gamma\left(\theta^{1/(q-1)}\right)},
$$

where $d > 1$ and $(1/d) + (1/d') = 1$; also assume

$$
\begin{aligned}
\Lambda = \{\theta > \theta_0 : {} &\lambda_{1*}(\theta) < \lambda_1^*(\theta), \mu_{1*}(\theta) < \mu_1^*(\theta), \lambda_{2*}(\theta) \\
&< \lambda_2^*(\theta), \mu_{2*}(\theta) < \mu_2^*(\theta)\}.
\end{aligned}
\tag{5}
$$

2. Existence Result

We give the following two definitions before we give our main result.

Definition 1. Let $(u, v) \in W^{1,p}(\Omega) \cap C(\overline{\Omega}) \times W^{1,q}(\Omega) \cap C(\overline{\Omega})$, (u, v) be said a weak solution of (1) if it satisfies

$$
\begin{aligned}
\int_\Omega |\nabla u|^{p-2}\nabla u \cdot \nabla\xi \, dx - \int_\Omega |u|^{p-2}u \cdot \xi \, dx &= \lambda_1 \int_\Omega a(x)f(v)\xi \, dx + \mu_1 \int_\Omega \alpha(x)h(u)\xi \, dx \text{ in } \Omega, \\
\int_\Omega |\nabla v|^{q-2}\nabla v \cdot \nabla\zeta \, dx - \int_\Omega |v|^{q-2}v \cdot \zeta \, dx &= \lambda_2 \int_\Omega b(x)g(u)\zeta \, dx + \mu_2 \int_\Omega \beta(x)\gamma(v)\zeta \, dx \text{ in } \Omega,
\end{aligned}
\tag{6}
$$

for all $(\xi, \zeta) \in W_0^{1,p}(\Omega) \times W_0^{1,q}(\Omega)$.

Definition 2. A pair of nonnegative functions $(\underline{u}, \underline{v}), (\overline{u}, \overline{v})$ in $W^{1,p}(\Omega) \cap C(\overline{\Omega}) \times W^{1,q}(\Omega) \cap C(\overline{\Omega})$ is called a weak subsolution and supersolution of (1) if they satisfy $(\underline{u}, \underline{v}), (\overline{u}, \overline{v}) = (0, 0)$ on $\partial\Omega$:

$$
\begin{aligned}
\int_\Omega |\nabla \underline{u}|^{p-2}\nabla \underline{u} \cdot \nabla\xi \, dx - \int_\Omega |\underline{u}|^{p-2}\underline{u} \cdot \xi \, dx &\le \lambda_1 \int_\Omega a(x)f(\underline{v})\xi \, dx + \mu_1 \int_\Omega \alpha(x)h(\underline{u})\xi \, dx \text{ in } \Omega, \\
\int_\Omega |\nabla \underline{v}|^{q-2}\nabla \underline{v} \cdot \nabla\zeta \, dx - \int_\Omega |\underline{v}|^{q-2}\underline{v} \cdot \zeta \, dx &\le \lambda_2 \int_\Omega b(x)g(\underline{u})\zeta \, dx + \mu_2 \int_\Omega \beta(x)\gamma(\underline{v})\zeta \, dx \text{ in } \Omega, \\
\int_\Omega |\nabla\overline{u}|^{p-2}\nabla\overline{u} \cdot \nabla\xi \, dx - \int_\Omega |\overline{u}|^{p-2}\overline{u} \cdot \xi \, dx &\ge \lambda_1 \int_\Omega a(x)f(\overline{v})\xi \, dx + \mu_1 \int_\Omega \alpha(x)h(\overline{u})\xi \, dx \text{ in } \Omega, \\
\int_\Omega |\nabla\overline{v}|^{q-2}\nabla\overline{v} \cdot \nabla\zeta \, dx - \int_\Omega |\overline{v}|^{q-2}\overline{v} \cdot \zeta \, dx &\ge \lambda_2 \int_\Omega b(x)g(\overline{u})\zeta \, dx + \mu_2 \int_\Omega \beta(x)\gamma(\overline{v})\zeta \, dx \text{ in } \Omega,
\end{aligned}
\tag{7}
$$

for all $(\xi, \zeta) \in W_0^{1,p}(\Omega) \times W_0^{1,q}(\Omega)$.

We shall establish the following result.

Theorem 1. *Assume that the conditions* $(H1) - (H3)$ *hold,* $a(x)$, $b(x)$, $\alpha(x)$, *and* $\beta(x)$ *are in* $L^\infty(\Omega)$ *and* $\Lambda \neq \varnothing$. *Let*

$$I = \cup_{\theta \in \Lambda} [\lambda_{1*}(\theta), \lambda_1^*(\theta)] \times [\mu_{1*}(\theta), \mu_1^*(\theta)] \times [\lambda_{2*}(\theta), \lambda_2^*(\theta)] \times [\mu_{2*}(\theta), \mu_2^*(\theta)].$$

(8)

Then, problem (1) has a positive weak solution for each $(\lambda_1, \mu_1, \lambda_2, \mu_2) \in I$.

Proof of Theorem 1. Let $(\lambda_1, \mu_1, \lambda_2, \mu_2) \in I$ and $\theta > \theta_0$ be such that $(\lambda_1, \mu_1, \lambda_2, \mu_2) \in [\lambda_{1*}(\theta), \lambda_1^*(\theta)] \times [\mu_{1*}(\theta), \mu_1^*(\theta)] \times [\lambda_{2*}(\theta), \lambda_2^*(\theta)] \times [\mu_{2*}(\theta), \mu_2^*(\theta)]$.

We shall verify that

$$\underline{u} = \theta^{1/(p-1)}\left(\frac{p-1}{p}\right)\phi_p^{p/(p-1)},$$

$$\underline{v} = \theta^{1/(q-1)}\left(\frac{q-1}{q}\right)\phi_q^{q/(q-1)},$$

(9)

is a subsolution of (1). Let the test function $\xi(x) \in W_0^{1,p}(\Omega)$ with $\xi(x) \geq 0$. We have

$$\int_\Omega |\nabla \underline{u}|^{p-2}\nabla \underline{u} \cdot \nabla \xi \mathrm{d}x - \int_\Omega |\underline{u}|^{p-2}\underline{u} \cdot \xi \mathrm{d}x \leq \int_\Omega |\nabla \underline{u}|^{p-2}\nabla \underline{u} \cdot \nabla \xi \mathrm{d}x$$
$$= \theta \int_\Omega \phi_p |\nabla \phi_p|^{p-2}\nabla \phi_p \cdot \nabla \xi \mathrm{d}x$$
$$= \theta \int_\Omega \left[|\nabla \phi_p|^{p-2}\nabla \phi_p \cdot \nabla(\phi_p \xi) - |\nabla \phi_p|^p \xi\right]\mathrm{d}x$$
$$= \theta \int_\Omega \left(\sigma_p \phi_p^p - |\nabla \phi_p|^p\right)\xi \mathrm{d}x.$$

(10)

Similarly,

$$\int_\Omega |\nabla \underline{v}|^{q-2}\nabla \underline{v} \cdot \nabla \zeta \mathrm{d}x - \int_\Omega |\underline{v}|^{q-2}\underline{v} \cdot \zeta \mathrm{d}x \leq \theta \int_\Omega \left(\sigma_q \phi_q^q - |\nabla \phi_q|^q\right)\zeta \mathrm{d}x.$$

(11)

For all $\zeta(x) \in W_0^{1,q}(\Omega)$ with $\zeta(x) \geq 0$.

Now, on $\overline{\Omega_\delta}$ we have

$$\theta \int_{\overline{\Omega_\delta}} \left(\sigma_p \phi_p^p - |\nabla \phi_p|^p\right)\xi \mathrm{d}x \leq -\theta m \int_{\overline{\Omega_\delta}} \xi \mathrm{d}x$$
$$= -\theta m \left(\frac{1}{d} + \frac{1d}{d'}\right)\int_{\overline{\Omega_\delta}} \xi \mathrm{d}x$$
$$\leq \left[-\lambda_1 a_0 f\left(\theta^{(1/q-1)}\right) - \mu_1 \alpha_0 h\left(\theta^{(1/p-1)}\right)\right]\int_{\overline{\Omega_\delta}} \xi \mathrm{d}x$$
$$\leq \int_{\overline{\Omega_\delta}} \left[-\lambda_1 a_0 f\left(\theta^{(1/q-1)}\left(\frac{q-1}{q}\right)\phi_q^{q/q-1}\right) - \mu_1 \alpha_0 h\left(\theta^{(1/p-1)}\left(\frac{p-1}{p}\right)\phi_p^{p/p-1}\right)\right]\xi \mathrm{d}x$$
$$\leq \int_{\overline{\Omega_\delta}} [\lambda_1 a(x)f(\underline{v}) + \mu_1 \alpha(x)h(\underline{u})]\xi \mathrm{d}x$$

$$\theta \int_{\overline{\Omega_\delta}} \left(\sigma_q \phi_q^q - |\nabla \phi_q|^q\right)\zeta \mathrm{d}x \leq -\theta m \int_{\overline{\Omega_\delta}} \zeta \mathrm{d}x,$$
$$= \left(\frac{-\theta m}{d} - \frac{\theta m}{d'}\right)\int_{\overline{\Omega_\delta}} \zeta \mathrm{d}x$$
$$\leq \left[-\lambda_2 b_0 g\left(\theta^{(1/p-1)}\right) - \mu_2 \beta_0 \gamma\left(\theta^{(1/q-1)}\right)\right]\int_{\overline{\Omega_\delta}} \zeta \mathrm{d}x$$
$$\leq \int_{\overline{\Omega_\delta}} \left[-\lambda_2 b_0 g\left(\theta^{(1/p-1)}\left(\frac{p-1}{p}\right)\phi_p^{p/p-1}\right) - \mu_2 \beta_0 \gamma\left(\theta^{(1/q-1)}\left(\frac{q-1}{q}\right)\phi_q^{q/q-1}\right)\right]\zeta \mathrm{d}x$$
$$\leq \int_{\overline{\Omega_\delta}} [\lambda_2 b(x)g(\underline{u}) + \mu_2 \beta(x)\gamma(\underline{v})]\zeta \mathrm{d}x.$$

(12)

On the contrary, on $(\Omega/\overline{\Omega}_\delta)$ we have

$$
\begin{aligned}
\theta \int_{(\Omega/\overline{\Omega}_\delta)} \left(\sigma_p \phi_p^p - \left|\nabla\phi_p\right|^p\right)\xi \mathrm{d}x &\leq \theta\sigma_p \int_{(\Omega/\overline{\Omega}_\delta)} \xi \mathrm{d}x, \\
&= \theta\sigma_p\left(\frac{1}{d}+\frac{1}{d'}\right)\int_{(\Omega/\overline{\Omega}_\delta)} \xi \mathrm{d}x \\
&\leq \left[\lambda_1 a_1 f\left(\theta^{(1/q-1)}K_2\right) + \mu_1\alpha_0 h\left(\theta^{(1/p-1)}K_1\right)\right]\int_{(\Omega/\overline{\Omega}_\delta)} \xi \mathrm{d}x \\
&\leq \int_{(\Omega/\overline{\Omega}_\delta)} \left[\lambda_1 a(x)f(\underline{v}) + \mu_1\alpha(x)h(\underline{u})\right]\xi \mathrm{d}x,
\end{aligned}
\tag{13}
$$

and similarly,

$$
\theta \int_{(\Omega/\overline{\Omega}_\delta)} \left(\sigma_q \phi_q^q - \left|\nabla\phi_q\right|^q\right)\zeta \mathrm{d}x \leq \int_{(\Omega/\overline{\Omega}_\delta)} \left[\lambda_2 b(x)g(\underline{u}) + \mu_2\beta(x)\gamma(\underline{v})\right]\zeta \mathrm{d}x.
\tag{14}
$$

Therefore, $(\underline{u},\underline{v})$ is subsolution of problem (1).

Next, we construct a supersolution of (1). Let ω_r be a unique positive solution of

$$
\begin{cases}
-\triangle_r \omega_r = 1 \text{ in } \Omega, \\
\omega_r = 0 \text{ on } \partial\Omega,
\end{cases}
\tag{15}
$$

for $r = p, q$. We denote

$$
\begin{aligned}
\overline{u} &= \frac{C}{\nu_p}\left(\frac{\lambda_1\|a\|_\infty + \mu_1\|\alpha\|_\infty}{1 - \nu_p^{p-1}}\right)^{1/(p-1)} \omega_p, \\
\overline{v} &= \left[\left(\frac{\lambda_2\|b\|_\infty + \mu_2\|\beta\|_\infty}{1 - \nu_q^{q-1}}\right)g\left(C\left(\frac{\lambda_1\|a\|_\infty + \mu_1\|\alpha\|_\infty}{1 - \nu_p^{p-1}}\right)^{1/(p-1)}\right)^{1/(q-1)}\right]\omega_q,
\end{aligned}
\tag{16}
$$

where $\nu_r = \|\omega_r\|_\infty$, $r = p, q$, and $C > 0$ is a large number to be chosen later. We shall verify that $(\overline{u}, \overline{v})$ is a supersolution of (1) such that $(\overline{u}, \overline{v}) \geq (\underline{u}, \underline{v})$. By $(H2) - (H3)$, we can choose C large enough so that

$$
\begin{aligned}
\left(\frac{C}{\nu_p}\right)^{p-1} &\geq f\left(\left[\left(\frac{\lambda_2\|b\|_\infty + \mu_2\|\beta\|_\infty}{1 - \nu_q^{q-1}}\right)g\left(C\left(\frac{\lambda_1\|a\|_\infty + \mu_1\|\alpha\|_\infty}{1 - \nu_p^{p-1}}\right)^{(1/p-1)}\right)^{(1/q-1)}\right]\omega_q\right) \\
&\quad + \mu_1 h\left(\frac{\lambda_1\|a\|_\infty + \mu_1\|\alpha\|_\infty}{1 - \nu_p^{p-1}}\right)^{(1/p-1)} \omega_p.
\end{aligned}
\tag{17}
$$

Hence,

$$
\begin{aligned}
&\int_\Omega |\nabla\overline{u}|^{p-2}\nabla\overline{u} \cdot \nabla\xi \mathrm{d}x - \int_\Omega |\overline{u}|^{p-2}\overline{u}\cdot\xi \mathrm{d}x \\
&= \left(\frac{C}{\nu_p}\right)^{p-1}(\lambda_1\|a\|_\infty + \mu_1\|\alpha\|_\infty)\int_\Omega \xi \mathrm{d}x.
\end{aligned}
\tag{18}
$$

Using (17),

$$
\begin{aligned}
&\int_\Omega |\nabla\overline{u}|^{p-2}\nabla\overline{u} \cdot \nabla\xi \mathrm{d}x - \int_\Omega |\overline{u}|^{p-2}\overline{u}\cdot\xi \mathrm{d}x \\
&\geq \lambda_1\|a\|_\infty f\left(\left[\left(\frac{\lambda_2\|b\|_\infty + \mu_2\|\beta\|_\infty}{1 - \nu_q^{q-1}}\right)g\left(C\left(\frac{\lambda_1\|a\|_\infty + \mu_1\|\alpha\|_\infty}{1 - \nu_p^{p-1}}\right)^{1/(p-1)}\right)^{1/(q-1)}\right]\omega_q\right)\int_\Omega \xi \mathrm{d}x \\
&\quad + \mu_1\|\alpha\|_\infty \int_\Omega h\left(C\left(\frac{\lambda_1\|a\|_\infty + \mu_1\|\alpha\|_\infty}{1 - \nu_p^{p-1}}\right)^{1/(p-1)}\right)\xi \mathrm{d}x \\
&\geq \int_\Omega \left[\lambda_1 a(x)f(\overline{v}) + \mu_1\alpha(x)h(\overline{u})\right]\xi \mathrm{d}x.
\end{aligned}
\tag{19}
$$

Next

$$\int_\Omega |\nabla \overline{v}|^{q-2} \nabla \overline{v} \nabla \zeta \mathrm{d}x - \int_\Omega |\overline{v}|^{q-2} \overline{v} . \zeta \mathrm{d}x$$

$$= \left\{ (\lambda_2 \|b\|_\infty + \mu_2 \|\beta\|_\infty) g\left(C\left(\frac{\lambda_1 \|a\|_\infty + \mu_1 \|\alpha\|_\infty}{1 - v_p^{p-1}}\right)^{1/(p-1)} \right) \right\} \omega_q \int_\Omega \xi \mathrm{d}x$$

$$\geq \left[\begin{array}{c} \lambda_2 \|b\|_\infty g\left(C\left(\frac{\lambda_1 \|a\|_\infty + \mu_1 \|\alpha\|_\infty}{1 - v_p^{p-1}}\right)^{1/(p-1)} \right) \\ \\ + \mu_2 \|\beta\|_\infty g\left(C\left(\frac{\lambda_1 \|a\|_\infty + \mu_1 \|\alpha\|_\infty}{1 - v_p^{p-1}}\right)^{1/(p-1)} \right) \end{array} \right] \int_\Omega \xi \mathrm{d}x. \tag{20}$$

By (H3), choose C large so that

$$g\left(C\left(\frac{\lambda_1 \|a\|_\infty + \mu_1 \|\alpha\|_\infty}{1 - v_p^{p-1}}\right)^{1/(p-1)} \right)$$

$$\geq \gamma \left(\left[\left(\frac{\lambda_2 \|b\|_\infty + \mu_2 \|\beta\|_\infty}{1 - v_q^{q-1}}\right) g\left(C\left(\frac{\lambda_1 \|a\|_\infty + \mu_1 \|\alpha\|_\infty}{1 - v_p^{p-1}}\right)^{1/(p-1)} \right)^{1/(q-1)} \right] \|\omega_q\|_\infty \right). \tag{21}$$

Then, from (19), we have

$$\int_\Omega |\nabla \overline{v}|^{q-2} \nabla \overline{v} \cdot \nabla \zeta \mathrm{d}x - \int_\Omega |\overline{v}|^{q-2} \overline{v} \cdot \zeta \mathrm{d}x$$

$$\geq \lambda_2 \|b\|_\infty g\left(C\left(\frac{\lambda_1 \|a\|_\infty + \mu_1 \|\alpha\|_\infty}{1 - v_p^{p-1}}\right)^{1/(p-1)} \right)$$

$$+ \mu_2 \|\beta\|_\infty \gamma \left(\left\{ \left(\frac{\lambda_2 \|b\|_\infty + \mu_2 \|\beta\|_\infty}{1 - v_q^{q-1}}\right) g\left(C\left(\frac{\lambda_1 \|a\|_\infty + \mu_1 \|\alpha\|_\infty}{1 - v_p^{p-1}}\right)^{1/(p-1)} \right) \right\}^{1/(q-1)} \|\omega_q\|_\infty \right)$$

$$\geq \int_\Omega [b(x) g(\overline{u}) + \mu_2 \beta(x) \gamma(\overline{v})] \zeta \mathrm{d}x. \tag{22}$$

According to (19) and (20), we can conclude that $(\overline{u}, \overline{v})$ is a supersolution of (1). Furthermore, $\overline{u} \geq \underline{u}$ and $\overline{v} \geq \underline{v}$ for C large, Thus, there exists a solution $(u, v) \in W^{1,p}(\Omega) \cap C(\overline{\Omega}) \times W^{1,q}(\Omega) \cap C(\overline{\Omega})$ of (1) with $\underline{u} \leq u \leq \overline{u}$ and $\underline{v} \leq v \leq \overline{v}$. This completes the Proof of Theorem 1. □

Data Availability

The data used to support the findings of this study are available from the corresponding author upon request.

Conflicts of Interest

The authors declare that there are no conflicts of interest regarding the publication of this manuscript.

Authors' Contributions

All authors contributed equally to this work. They have all read and approved the final manuscript.

References

[1] G. A. Afrouzi and K. J. Brown, "Positive solutions for a semilinear elliptic problem with sign-changing nonlinearity," *Nonlinear Analysis: Theory, Methods & Applications*, vol. 36, no. 4, pp. 507–510, 1999.

[2] J. Ali and R. Shivaji, "Existence results for classes of Laplacian systems with sign-changing weight," *Applied Mathematics Letters*, vol. 20, no. 5, pp. 558–562, 2007.

[3] S. Boulaaras, M. S. Touati Brahim, S. Bouzenada, and A. Zarai, "An asymptotic behavior and a posteriori error estimates for the generalized Schwartz method of advection-diffusion equation," *Acta Mathematica Scientia*, vol. 38, no. 4, pp. 1227–1244, 2018.

[4] N. Boumaaza and S. Boulaaras, "General decay for Kirchhoff type in viscoelasticity with not necessarily decreasing kernel," *Mathematical Methods in the Applied Sciences*, vol. 41, no. 16, pp. 6050–6069, 2018.

[5] N. Mezouar and S. Boulaaras, "Global existence of solutions to a viscoelastic non-degenerate Kirchhoff equation," *Applicable Analysis*, pp. 1–25, 2018, In press.

[6] Y. Bouizem, S. Boulaaras, and B. Djebbar, "Some existence results for an elliptic equation of Kirchhoff-type with changing sign data and a logarithmic nonlinearity," *Mathematical Methods in the Applied Sciences*, vol. 42, no. 7, pp. 2465–2474, 2019.

[7] D. D. Hai and R. Shivaji, "An existence result on positive solutions for a class of p-Laplacian systems," *Nonlinear Analysis: Theory, Methods & Applications*, vol. 56, no. 7, pp. 1007–1010, 2004.

[8] N. Mezouar and S. Boulaaras, "Global existence and decay of solutions for a class of viscoelastic Kirchhoff equation," *Bulletin of the Malaysian Mathematical Sciences Society*, vol. 43, no. 1, pp. 725–755, 2020.

[9] S. H. Rasouli, Z. Halimi, and Z. Mashhadban, "A remark on the existence of positive weak solution for a class of -Laplacian nonlinear system with sign-changing weight," *Nonlinear Analysis: Theory, Methods & Applications*, vol. 73, no. 2, pp. 385–389, 2010.

[10] S. Boulaaras and A. Allahem, "Existence of positive solutions of nonlocal $p(x)$-Kirchhoff evolutionary systems via sub-super solutions concept," *Symmetry*, vol. 11, no. 2, p. 253, 2019.

[11] G. A. Afrouzi, N. T. Chung, and S. Shakeri, "Existence of positive solutions for Kirchhoff type equations," *Electronic Journal of Differential Equations*, vol. 2013, pp. 1–8, 2013.

[12] S. Boulaaras and R. Guefaifia, "Existence of positive weak solutions for a class of Kirrchoff elliptic systems with multiple parameters," *Mathematical Methods in the Applied Sciences*, vol. 41, no. 13, pp. 5203–5210, 2018.

[13] Y. Chen, S. Levine, and M. Rao, "Variable exponent, linear growth functionals in image restoration," *SIAM Journal on Applied Mathematics*, vol. 66, no. 4, pp. 1383–1406, 2006.

[14] M. Ruzicka, *Electrorheological Fluids: Modeling and Mathematical Theory*, Springer-Verlag, Berlin, Germany, 2002.

[15] V. V. Zhikov, "Averaging of functionals of the calculus of variations and elasticity theory," *Mathematics of the USSR-Izvestiya*, vol. 29, no. 1, pp. 33–66, 1987.

[16] G. A. Afrouzi, S. Shakeri, and N. T. Chung, "Existence of positive solutions for variable exponent elliptic systems with multiple parameters," *Afrika Matematika*, vol. 26, no. 1-2, pp. 159–168, 2015.

[17] S. Boulaaras, "A well-posedness and exponential decay of solutions for a coupled Lamé system with viscoelastic term and logarithmic source terms," *Applicable Analysis*, pp. 1–19, 2019, In press.

[18] S. Boulaaras, Y. Bouizem, and R. Guefaifia, "Existence of positive solutions of $(p(x), q(x))$-Laplacian parabolic systems with right hand side defined as a multiplication of two separate functions," *Mathematical Methods in the Applied Sciences*, vol. 43, no. 5, pp. 2615–2625, 2020.

[19] S. Boulaaras, "Some existence results for a new class of elliptic Kirchhoff equation with logarithmic source terms," *Journal of Intelligent & Fuzzy Systems*, vol. 37, no. 6, pp. 8335–8344, 2019, In press.

[20] Y. Bouizem, S. Boulaaras, and A. Ali, "Existence of positive solutions for a class of $(p(x), q(x))$-Laplacian elliptic systems with multiplication of two separate functions," *Complexity*, vol. 2020, Article ID 3756406, 10 pages, 2020.

[21] N. T. Chung, "Multiple solutions for a $p(x)$-Kirchhoff-type equation with sign-changing nonlinearities," *Complex Variables and Elliptic Equations*, vol. 58, no. 12, pp. 1637–1646, 2013.

[22] S. Boulaaras and N. Mezouar, "Global existence and decay of solutions of a singular nonlocal viscoelastic system with a nonlinear source term, nonlocal boundary condition, and localized damping term," *Mathematical Methods in the Applied Sciences*, 2020, In press.

[23] S. Boulaaras, "Existence of positive solutions of nonlocal $p(x)$-Kirchhoff hyperbolic systems via sub-super solutions concept," *Journal of Intelligent & Fuzzy Systems*, pp. 1–13, 2020.

[24] R. Guefaifia and S. Boulaaras, "Sub-super solutions method for elliptic systems involving $(p_1, \ldots, p_m)$ Laplacian operator," *Mathematical Methods in the Applied Sciences*, vol. 43, no. 7, pp. 4191–4199, 2020.

[25] R. Guefaifia and S. Boulaaras, "Existence of positive solution for a class of $(p(x), q(x))$-Laplacian systems," *Rendiconti del Circolo Matematico di Palermo Series 2*, vol. 67, pp. 93–103, 2018.

[26] S. Boulaaras and D. Ouchenane, "General decay for a coupled Lamé system of nonlinear viscoelastic equations," *Mathematical Methods in the Applied Sciences*, vol. 43, no. 4, pp. 1717–1735, 2020.

[27] A. Menaceur, S. Boulaaras, R. Guefafia, and A. Alharbi, "Existence of positive weak solutions for quasilinear Kirchhoff elliptic systems via sub-super solutions concept," *Mathematical Problems in Engineering*, vol. 2020, Article ID 6527672, 6 pages, 2020.

[28] N. Mezouar, S. Boulaaras, and A. Alahem, "Global existence of solutions for the viscoelastic Kirchhoff equation with logarithmic source terms," *Complexity*, vol. 2020, Article ID 7105387, 25 pages, 2020.

[29] Q. H. Zhang, "Existence of positive solutions for a class of $p(x)$−Laplacian systems," *Journal of Mathematical Analysis and Applications*, vol. 333, pp. 591–603, 2007.

[30] F. Kamache, R. Guefaifia, S. Boulaaras, and A. Alharbi, "Existence of weak solutions for a new class of fractional p-Laplacian boundary value systems," *Mathematics*, vol. 8, no. 4, p. 475, 2020.

[31] X. L. Fan, "On the sub-supersolution method for $p(x)$−Laplacian equations," *Journal of Mathematical Analysis and Applications*, vol. 330, pp. 665–682, 2007.

[32] X. Fan and D. Zhao, "On the Spaces $L^{p(x)}(\Omega)$ and $W^{m,p(x)}(\Omega)$," *Journal of Mathematical Analysis and Applications*, vol. 263, no. 2, pp. 424–446, 2001.

WILEY | Hindawi

Research Article

Modeling, Synchronization, and FPGA Implementation of Hamiltonian Conservative Hyperchaos

Enzeng Dong [ID],[1] **Xiaodong Jiao**,[1] **Shengzhi Du** [ID],[2] **Zengqiang Chen** [ID],[3] **and Guoyuan Qi** [ID][4]

[1]*Key Laboratory for Control Theory & Applications in Complicated Systems, Tianjin University of Technology, Tianjin 300384, China*
[2]*Department of Mechanical Engineering, Tshwane University of Technology, Pretoria 0001, South Africa*
[3]*Department of Automation, Nankai University, Tianjin 300071, China*
[4]*Tianjin Key Laboratory of Advanced Technology of Electrical Engineering and Energy, Tiangong University, Tianjin 300387, China*

Correspondence should be addressed to Enzeng Dong; dongenzeng@163.com

Conservative chaotic systems have potentials in engineering application because of their superiority over the dissipative systems in terms of ergodicity and integer dimension. In this paper, five-dimension Euler equations are constructed by integrating two of sub-Euler equations, which are contributory to the exploration of higher-dimensional systems. These Euler equations compose the conservative parts from their antisymmetric structure, which have been proved to be both Hamiltonian and Casimir energy conservative. Furthermore, a family of Hamiltonian conservative hyperchaotic systems are proposed by breaking the conservation of Casimir energy. The numerical analysis shows that the system displays some interesting behaviors, such as the coexistence of quasi-periodic, chaotic, and hyperchaotic behaviors. Adaptive synchronization method is used to realize the hyperchaos synchronization. Finally, the system passed the NIST tests successfully. Field programmable gate array (FPGA) platform is used to implement the proposed Hamiltonian conservative hyperchaos.

1. Introduction

Since the discovery of Lorenz attractor in 1963 [1], the interesting dynamic behavior of chaotic attractors has attracted intensive attention, with various mathematical analyses. Conventional analyses on the chaotic system include the determination of Lyapunov exponents (LEs), bifurcation diagram [2], phase portrait, ultimate boundary estimation, and topological horseshoe analysis [3, 4], which illustrate the chaotic state intuitively. LEs are commonly used as an indicator of chaotic systems. The bifurcation diagram focuses on the evolution of the dynamics of a chaotic system when parameters or initial values are changed. The phase portrait describes the phase space trajectory of a chaotic system. The ultimate boundary estimation and topological horseshoe analysis [3, 4] reveal the abundant characteristics of a chaotic system.

Generally, chaotic systems can be categorized into dissipative or conservative chaotic systems. A dissipative chaotic system (DCS) owns strange attractor that has sensitive dependence on initial conditions. A conservative chaotic system (CCS) does not even have any attractor with integer dimension. The ergodicity of CCS is usually greater than DCS. According to the sign of the coefficients in the dissipation term, the DCS can be further divided into two types: Rayleigh and non-Rayleigh DCSs [5, 6], as there must be at least one positive dissipation term in a non-Rayleigh DCS [5]. There are two types of CCSs too. A Hamiltonian CCS (HCCS) meets conditions of zero-sum LEs, and the Hamiltonian energy and the phase space volume are both conservative, while a non-Hamiltonian CCS (non-HCCS) only meets zero-sum LE condition, such as Sprott A system in [7] and Cang-case B system in [8]. HCCSs are further categorized to traditional HCCS (traditional-HCCS) [9, 10]

and generalized HCCS (generalized-HCCS) [11]. DCS has received intensive attention but much little for CCS. In the early stage of chaos research, there are few reports on the mechanism of chaos. Recently, analyses on energy cycling in chaotic systems have made some progresses. For instance, Vinicio Pelino, Filippo Maimone, and Pasini described the energy cycle of Lorenz attractor [12]. The energy cycle of the Qi four-wing chaotic system [5] was explained by using the system entropy and the Casimir function as the kernel of Lie–Poisson bracket. In this process, the concerned system was converted to Kolmogorov form containing the conservative term, dissipative term, and an external force [5, 12]. As a measuring index of the orbital mode, the rate of change of Casimir energy, Casimir power, is analyzed in detail. The conservative term is interpreted by Euler equations. As a basic equation in inviscid hydrodynamics, Euler equation gives a Hamiltonian description in 3D form. However, higher-dimensional Euler equations (such as 4D and 5D) are essential to be studied.

In research of chaotic systems, an important and useful implementation is encryption algorithms [13–16] because of the complex properties, such as extremely sensitive dependency on initial conditions, topologically mixing and density of periodic orbits, broadband, pseudo-randomness, and white-noise-like phenomenon [16]. Since the first four-dimensional hyperchaotic system [17] was proposed, researchers found that a hyperchaotic system has potential in engineering applications, especially in control [18, 19], encryption [20, 21], communication [22], synchronization [23], optical system [24], and biological network [25]. Research on hyperchaotic systems has become a hot topic. One of the most important phenomena in these dynamical systems [26–28] is the multistability occurring in physics, chemistry, biology [29], economics [30], and nature. There are two kinds of systems with multistability including hidden attractors [31] and infinite attractors [32, 33]. Both display complex dynamical behavior such as the coexistence attractor [11, 34]. All CCSs do not have attractors, but some have line equilibrium which is referred as hidden attractors. Therefore, it is interesting to test whether CCSs can show multistability behavior as well. For application, chaos can be controlled and synchronized, usually including designing a controller to stabilize the chaotic system and tracking the chaotic system. Chaos synchronization is of vital significance to the practical application of chaos. Important works in chaos synchronization for the chaotic system and its applications in control and tracking have been done recently and in the past [35, 36]. Design and implementation of the pseudo-random digital signal generator is one of the most important chaos-based application. With the advantages of digital integrated circuits, superior computing power, and reconfigurable designs [37], FPGA is considered as one of the most suitable platforms to implement a chaotic system.

While intensive research studies were made on 3D and 4D chaotic systems, this paper focuses on the vital importance to expand the research to higher-dimensional systems, for instance, 5D systems, which display rich dynamics and lay an important foundation for higher-dimensional chaotic systems' study.

The rest of this paper is listed as follows: in Section 2, five 5D Euler equations are constructed, and a family of HCCSs are proposed; in Section 3, the nonconservation property of the proposed HCCS and dynamics are analyzed in detail by numerical simulation; in Section 4, adaptive synchronization is achieved for system Σ_3^H; in Section 5, FPGA digital development platform is used to generate the pseudo-random number generator; and Section 6 concludes the paper.

2. Modeling of HCCS

2.1. Model of 5D Euler Equations. Euler equations govern the rotation of a rigid body and control the motion of an inviscid fluid, which are also applicable to incompressible fluid. 5D Euler equations are imperative to satisfy the Lie–Poisson structure. Thus, from the view point of the 3D free rotational rigid body, 5D Euler equations governing the 5D rigid body or fluid systems can be constructed satisfying the Lie–Poisson bracket for the generalized Hamiltonian systems or Kolmogorov systems. In [10], six types Euler equations are proposed but the modeling work just considering the four-dimensional case. On the contrary, only the system dimension of a conservative chaotic system is greater than or equal to 5, and the dynamics of the system may be hyperchaotic state according to the requirements of LEs.

To construct the 5D Euler equations, the following 3D rigid subbodies are considered: subbody S_{ijk} defined in the space spanned from the axes ijk (taking the values of 123, 124, 125, 145, 245, and 345). Suppose there is a 5D rigid body with five axes, with the principle moment of inertia I_i, $\Pi_i = I_i^{-1}$, and angular momentum $x_i = I_i \omega_i$, ω_i is the angular velocity, $i = 1, 2, 3, 4, 5$. Then, the six 3D rigid subbodies can be extended to 5D by leaving another two dimensions uncoupled, and one gets the generalized 5D sub-Euler equations; these six 5D sub-Euler equations can be used to construct the five types of 5D Euler equations as summarized in Table 1.

As an example of Table 1, by coupling subbody S_{123} and subbody S_{345} with the third common axis, the 5D Euler equation of body $\sum_3$ is demonstrated in a Hamiltonian vector field form as equation (1). Bodies $\sum_1$, $\sum_2$, $\sum_4$, and $\sum_5$ can be developed in the similar way. The general form of the five 5D Euler equations is $\sum_i \dot{x} = J_i(x)\nabla H(x)$, where $i = 1, 2, 3, 4,$ and 5.

$$\sum_3 \dot{x} = J_3(x)\nabla H(x), \tag{1}$$

with

$$
J_3(x) = \begin{bmatrix} 0 & -x_3 & x_2 & 0 & 0 \\ x_3 & 0 & -x_1 & 0 & 0 \\ -x_2 & x_1 & 0 & 0 & 0 \\ 0 & 0 & 0 & 0 & 0 \\ 0 & 0 & 0 & 0 & 0 \end{bmatrix} + \begin{bmatrix} 0 & 0 & 0 & 0 & 0 \\ 0 & 0 & 0 & 0 & 0 \\ 0 & 0 & 0 & -x_5 & x_4 \\ 0 & 0 & x_5 & 0 & -x_3 \\ 0 & 0 & -x_4 & x_3 & 0 \end{bmatrix}
$$

$$
= \begin{bmatrix} 0 & -x_3 & x_2 & 0 & 0 \\ x_3 & 0 & -x_1 & 0 & 0 \\ -x_2 & x_1 & 0 & -x_5 & x_4 \\ 0 & 0 & x_5 & 0 & -x_3 \\ 0 & 0 & -x_4 & x_3 & 0 \end{bmatrix}, \tag{2}
$$

and its cross-product form is

TABLE 1: Modeling coupling mode.

Type	Subbody A	Subbody B	Common axis	Coupled rigid body
1	Subbody S_{123}	Subbody S_{145}	First axis	Body $\sum_1$
2	Subbody S_{123}	Subbody S_{245}	Second axis	Body $\sum_2$
3	Subbody S_{123}	Subbody S_{345}	Third axis	Body $\sum_3$
4	Subbody S_{124}	Subbody S_{345}	Fourth axis	Body $\sum_4$
5	Subbody S_{125}	Subbody S_{345}	Fifth axis	Body $\sum_5$

$$\sum_3 \dot{x} = x_{123} \times \nabla H(x_{123}) + x_{345} \times \nabla H(x_{345}). \quad (3)$$

The Hamiltonian energy of these 5D systems is

$$H(x) = \frac{1}{2}\left(\Pi_1 x_1^2 + \Pi_2 x_2^2 + \Pi_3 x_3^2 + \Pi_4 x_4^2 + \Pi_5 x_5^2\right). \quad (4)$$

As a significant physical quantity, similiar to the enstrophy or potential vorticity in the context of hydrodynamics, the Casimir function, C, is a valid way in globally describing a dynamical system and analyzing stability conditions. The Casimir function is defined as the kernel of the Lie–Poisson bracket [38]:

$$\{F, H\} = [\nabla F(x)]^T J(x)\nabla H(x), \quad (5)$$

in which $J(x)$ is the structural matrix of a generalized Hamiltonian system, which meets $J(x) = -J^T(x)$, i.e., $\{C, G\} = 0, \forall G \in C^\infty(g^*)$.

For a Hamiltonian system with a constant of the motion, one gets $\{C, H\} = 0$. The Casimir energy is conservative when there is no dissipative torque and external torque [5, 39]. The Casimir function (energy) of a generalized 5D Euler equations can be defined as

$$C(x) = \frac{1}{2}\left(x_1^2 + x_2^2 + x_3^2 + x_4^2 + x_5^2\right). \quad (6)$$

The rate of change of the Casimir energy is called the Casimir power [10], which is defined as

$$\dot{C} = x^T \cdot \dot{x} = x^T \cdot J(x)\nabla H(x), \quad (7)$$

in which $J(x)$ is an antisymmetric matrix, which represents the energy conservative part of a system.

Remark 1. The constructed 5D Euler equations (Tex translation failed) ($i = 1, 2, 3, 4, 5$) are both Hamiltonian and Casimir energy conservative.

The proposed five 5D Euler equations satisfy the vector field shown in equation (1), which provides the symplectic structure. Because the proposed 5D Euler equations are conservative for both the Hamiltonian and Casimir energy, they cannot produce chaos. However, they can be used as the basic framework to construct the HCCS.

2.2. The Proposed 5D HCCS. To generate chaotic behavior, conservation of the proposed generalized 5D Euler equations has to be broken. Replace one zero element by a in the upper triangle and $-a$ in the lower triangle of $J_i(x)$, respectively. Because $J_i^H(x)$ still keeps the skew-symmetric form, the conservations of Hamiltonian are preserved, but the

Casimir energy is broken. Correspondingly, the five systems $\sum_i$ generate a family of Hamiltonian conservative chaotic systems:

$$\sum_i^H \dot{x} = J_i^H(x)\nabla H(x). \quad (8)$$

As an example, for $J_3^H(x)$, one gets

$$J_3^H(x) = \begin{bmatrix} 0 & -x_3 & x_2 & 0 & 0 \\ x_3 & 0 & -x_1 & a & 0 \\ -x_2 & x_1 & 0 & -x_5 & x_4 \\ 0 & -a & x_5 & 0 & -x_3 \\ 0 & 0 & -x_4 & x_3 & 0 \end{bmatrix}, \quad (9)$$

with a is a constant. The resulting system is a HCCS.

Force and energy analysis can be used to explain the mechanism underlying chaos and its dynamic states [5]. For system Σ_3^H, the Casimir energy is not conservative, which means there must exist an external torque that breaks the conservation. According to Kolmogorov–Arnold–Moser perturbation theorem [10], when a Hamiltonian system whose $H(x)$ function is perturbed by the inclusion of an interaction term $H_1(x)$, the coupled Hamiltonian system probably generates conservative chaos with Hamilton function $H_2(x) = H(x) + \varepsilon H_1(x)$ because of the energy exchange between the two Hamiltonian functions ($H(x)$ and $H_1(x)$).

From equations (8) and (9), we have

$$\sum_3^H \dot{x} = J_3(x)\nabla H(x) + J^H(x)\nabla H_1(x), \quad (10)$$

with

$$J^H(x) = \begin{bmatrix} 0 & 0 & 0 & 0 & 0 \\ 0 & 0 & 0 & a & 0 \\ 0 & 0 & 0 & 0 & 0 \\ 0 & -a & 0 & 0 & 0 \\ 0 & 0 & 0 & 0 & 0 \end{bmatrix}, \quad (11)$$

$$H_1(x) = \frac{1}{2}\left(\Pi_2 x_2^2 + \Pi_4 x_4^2\right).$$

Consider $H_1(x)$ as a perturbation term, which represents a kind of external torque. According to equation (7), the Casimir power of system Σ_3^H is

$$\begin{aligned} \dot{C} &= x^T \cdot \dot{x} \\ &= x^T \cdot J_3(x)\nabla H(x) + x^T \cdot J^H(x)\nabla H_1(x) \quad (12) \\ &= a(\Pi_4 - \Pi_2)x_2 x_4. \end{aligned}$$

The term $J_3(x)\nabla H(x)$ of system Σ_3^H is conservative in both Hamiltonian and Casimir energy. Therefore, this term is an inertial torque, which can be a kind of fictitious torque generated by a free rotational rigid body without external torque [5, 38]. But, the term $J^H(x)\nabla H_1(x) = \begin{bmatrix} 0 & \Pi_4 x_4 & 0 & \Pi_2 x_2 & 0 \end{bmatrix}^T$ is a nonconservative torque and

leads to the loss of Casimir energy conservation. Rewrite system Σ_3^H in vector form to illustrate the conservative and nonconservative torque as

$$
\begin{bmatrix} \dot{x}_1 \\ \dot{x}_2 \\ \dot{x}_3 \\ \dot{x}_4 \\ \dot{x}_5 \end{bmatrix} = \begin{bmatrix} (\Pi_3 - \Pi_2)x_2 x_3 \\ (\Pi_1 - \Pi_3)x_1 x_3 \\ (\Pi_2 - \Pi_1)x_1 x_2 + (\Pi_5 - \Pi_4)x_4 x_5 \\ (\Pi_3 - \Pi_5)x_3 x_5 \\ (\Pi_4 - \Pi_3)x_3 x_4 \end{bmatrix} + \begin{bmatrix} 0 \\ a\Pi_4 x_4 \\ 0 \\ -a\Pi_2 x_2 \\ 0 \end{bmatrix},
$$

(13)

where the first vector term on the right is the initial torque, and the second vector term is the external term causing the energy exchanges between dissipative and supplied energy.

3. Dynamic Analysis on the Proposed 5D HCCS

For simplicity, we only analyze system $\sum_3^H$:

$$
\sum_3^H: \begin{aligned} \dot{x}_1 &= (\Pi_3 - \Pi_2)x_2 x_3 \\ \dot{x}_2 &= (\Pi_1 - \Pi_3)x_1 x_3 + a\Pi_4 x_4 \\ \dot{x}_3 &= (\Pi_2 - \Pi_1)x_1 x_2 + (\Pi_5 - \Pi_4)x_4 x_5 \\ \dot{x}_4 &= (\Pi_3 - \Pi_5)x_3 x_5 - a\Pi_2 x_2 \\ \dot{x}_5 &= (\Pi_4 - \Pi_3)x_3 x_4 \end{aligned}
$$

(14)

System has six adjustable parameters: Π_i ($i = 1$, 2, 3, 4, and 5) and a having influences on the system dynamic motion. The initial values x_{i0} determine Hamiltonian equation (4) when Π_i is fixed. From equation (12), parameters a and Π_i determine the change rate of Casimir energy, which will impact the degree of chaos with fixed x_{i0}.

3.1. Equilibrium Point Analysis on System Σ_3^H.
With $(\Pi_1, \Pi_2, \Pi_3, \Pi_4, \Pi_5, a) = (14, 20, 10, 5, 30, 0.1)$, the equilibrium points of system Σ_3^H are $(p, 0, 0, 0, 0)$, $(0, 0, r, 0, 0)$, $(0, 0, 0, 0, q)$, and $(p, 0, 0, 0, q)$, in which $p, q, r \in R$. Thus, the equilibrium points of system Σ_3^H are in the form of three lines and one plane. Substituting equilibrium points $(0, 0, 0, 0, 0)$, $(p, 0, 0, 0, 0)$, $(0, 0, r, 0, 0)$, $(0, 0, 0, 0, q)$, and $(p, 0, 0, 0, q)$ into the Jacobian matrix and calculating the characteristic polynomial, one gets

$$
f_1(\lambda) = \lambda^3 \cdot (\lambda^2 + 1),
$$

(15)

$$
f_2(\lambda) = \lambda^3 \cdot [\lambda^2 + (1 - 24 \cdot x_1^2)],
$$

(16)

$$
f_3(\lambda) = \lambda \cdot [\lambda^4 + (1 - 60 \cdot x_3^2) \cdot \lambda^2 - 4000 \cdot x_3^4],
$$

(17)

$$
f_4(\lambda) = \lambda^3 \cdot [\lambda^2 + (1 + 500 \cdot x_5^2)],
$$

(18)

$$
f_5(\lambda) = \lambda^2 \cdot [\lambda^3 + (1 + 500 \cdot x_5^2 - 24 \cdot x_1^2) \cdot \lambda + 260 \cdot x_1 \cdot x_5],
$$

(19)

respectively. Let these characteristic polynomials equal to zero; then, we obtain the eigenvalues of these polynomials, as shown in Table 2.

System Σ_3^H has nonhyperbolic equilibrium points, which are rare in chaotic systems [8]. Another finding from Table 2 is that different kinds of equilibrium points all have zero eigenvalues, so the equilibrium points of Σ_3^H are all unstable (exponential) [40].

3.2. Numerical Investigations.
Let $(\Pi_1, \Pi_2, \Pi_3, \Pi_4, \Pi_5) = (14, 20, 10, 5, 30)$ and initial values $(x_{10}, x_{20}, x_{30}, x_{40}, x_{50}) = (0.1, 0.5, 0.5, 0.5, 0.1)$. When $a = 0$, system Σ_3^H becomes (Tex translation failed), it is both Hamiltonian energy ($H(t) = 4.595$) and Casimir energy ($C(t) = 0.385$) conservative with a periodic trajectory (the red curve shown in Figure 1), and the Casimir power is zero (the red line in Figure 2). When $a = 0.1$, Σ_3^H is still Hamiltonian conservative ($H(t) = 4.595$) but not Casimir energy, and the Casimir power is not zero as the blue curve shown in Figure 2. The orbit becomes chaotic as shown by the blue trajectory in Figure 1.

Usually, the bifurcation diagram evolution process is "source—periodic orbit—double periodic orbits—multiperiodic orbits—chaos." However, system Σ_3^H does not. It enters the chaotic orbit almost immediately when the parameter $a > 0$, as shown in the bifurcation diagram in Figure 3(a), $a \in [0, 0.01]$; correspondingly, Figure 3(b) shows the Lyapunov exponent spectrum as a increases, in which there are two LEs greater than 0.

Remark 2. When the Casimir energy is conservative, the system may be either periodic or quasi-periodic states.

Considering $\Pi_2 = \Pi_4$ with $a \neq 0$, we have $\dot{C} = a(\Pi_4 - \Pi_2)x_2 x_4 = 0$; hence, the system remains conservative both in the Hamiltonian and the Casimir energy with $H(t) = 2.72$ and $C(t) = 0.385$, where $\Pi_2 = \Pi_4 = 5$, $a = 0.1$, and the system is quasi-periodic state with five zero Les; the corresponding phase portrait and Poincare section are shown in Figure 4.

3.3. Coexistence of System Σ_3^H.
The dynamics of classical chaotic systems contain periodic motion, quasi-periodic motion, chaos, and hyperchaos, which can be verified by LEs [41, 42]. A hyperchaotic system is characterized by the presence of two or more positive LEs [41, 43]. For a dynamical system with conservative flows, the sum of all LEs must be zero [43]. There must be two positive LEs for a 5D autonomous conservative hyperchaotic system.

Basin of attraction is an important tool for analyzing the dissipative coexisting attractors [44, 45], which change with initial values. Various initial values can be used to get full information about the typical regimes and their localization; as the same idea of the basin of attraction, the dynamical evolution map is used for this purpose.

The dynamical evolution map is generated for system Σ_3^H to study the coexistence phenomenon. Fixed system parameters $(\Pi_1, \Pi_2, \Pi_3, \Pi_4, \Pi_5, a) = (14, 20, 10, 5, 30, 1.5)$, the sampling period $= 0.1$ s, and changed the third and fourth initial values, i.e., $(0.1, 0.5, x_{30}, x_{40}, 0.1)$, where $x_{30} \in [-8, 8]$ and $x_{40} \in [-5, 5]$, the step of the initial values changing is 0.05. The dynamical evolution map is shown in Figure 5, which shows LE_1, LE_2, LE_4, and LE_5 of each point with

TABLE 2: Σ_3^H Hamiltonian conservative chaotic system.

System	Equilibrium $(p, q, r \in \mathbb{R})$	$f(\lambda)$	Eigenvalue $(\sigma, \omega > 0)$	Hyperbolic or not
	$(0, 0, 0, 0, 0)$	$f_1(\lambda)$	$(0, 0, 0, j, -j)$	Nonhyperbolic
			$(0, 0, 0, j\omega_1, -j\omega_1)$	Nonhyperbolic
	$(p, 0, 0, 0, 0)$	$f_2(\lambda)$	$(0, 0, 0, \sigma_1, -\sigma_1)$	Hyperbolic
	$(0, 0, r, 0, 0)$	$f_3(\lambda)$	$(0, \sigma_2, -\sigma_2, j\omega_2, -j\omega_2)$	Nonhyperbolic
Σ_3^H			$(0, 0, 0, j\omega_3, -j\omega_3)$	Nonhyperbolic
	$(0, 0, 0, 0, q)$	$f_4(\lambda)$	$(0, 0, \sigma_3, -\sigma_4 + j\omega_1, -\sigma_4 - j\omega_1)$	Hyperbolic
			$(0, 0, \sigma_3, \sigma_4 + j\omega_1, \sigma_4 - j\omega_1)$	Hyperbolic
			$(0, 0, 0, j\omega_4, -j\omega_4)$	Nonhyperbolic
	$(p, 0, 0, 0, q)$	$f_5(\lambda)$	$(0, 0, +\sigma_5, -\sigma_6, -\sigma_7)$	Hyperbolic
			$(0, 0, -\sigma_5, +\sigma_6, +\sigma_7)$	Nonhyperbolic
			$(0, 0, 0, \sigma_8, -\sigma_8)$	Nonhyperbolic
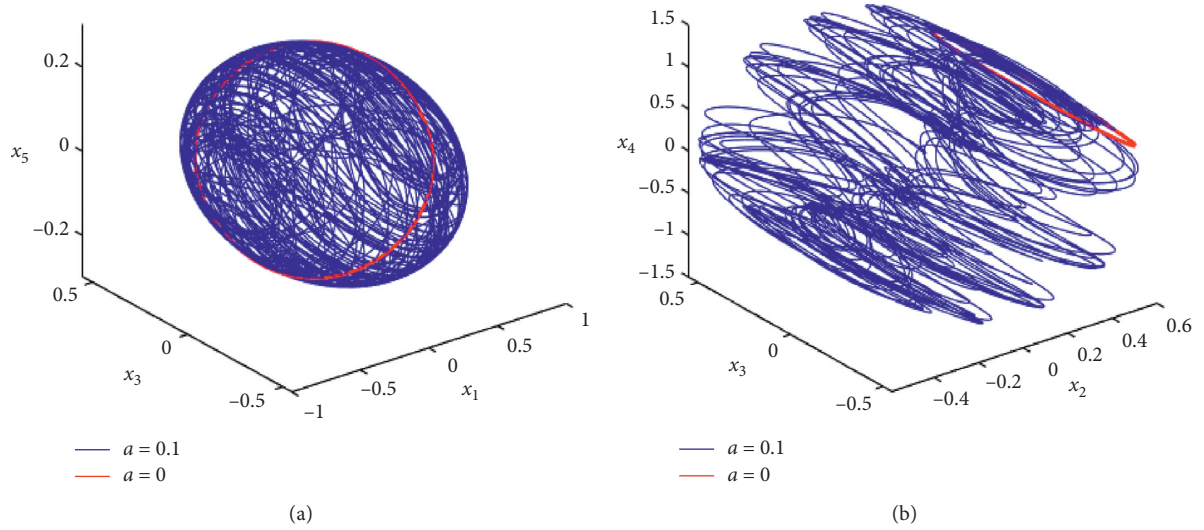
FIGURE 1: Phase portraits of (a) $x_1 - x_3 - x_5$ and (b) $x_2 - x_3 - x_4$ with $a = 0$ (red orbit) and $a = 0.1$ (blue orbit).
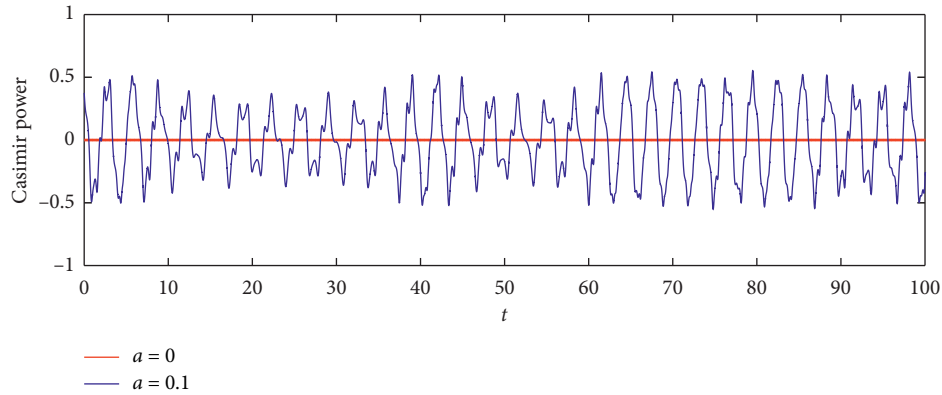
FIGURE 2: Time series of Casimir power with $(\Pi_1, \Pi_2, \Pi_3, \Pi_4, \Pi_5) = (14, 20, 10, 5, 30)$.

$LE_3 = 0$, respectively. Various coexisting orbits are highlighted with different colors in Figure 4. The values of region A are close to zero. The rest area is denoted as region B, where the values of LEs are greater than zero.

Comparing the dynamical evolution map, one finds that the LEs are symmetric about their 0 LE, and the dynamics of system switch among hyperchaos, chaos, and quasi-periodic motion. When the initial values of x_{30} and x_{40} are located in region A, all of the five LEs are approximating to zero, which indicates the system undergoes a quasi-periodic motion. When the initial values of x_{30} and x_{40} are located in region B, the largest LE is greater larger than zero, and the second one is greater than or equal to zero, which means the system is chaotic or hyperchaotic. As a demonstration, Figures 6 and 7
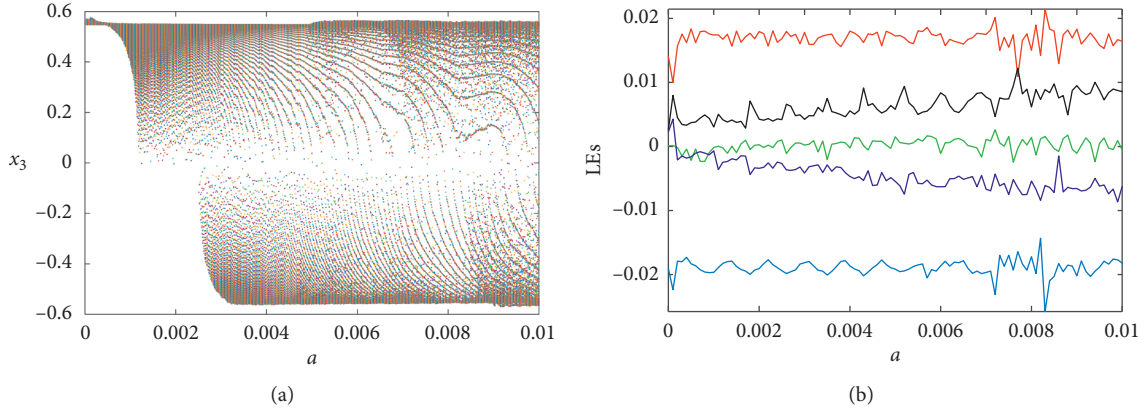
(a)

(b)

FIGURE 3: (a) Bifurcation diagram of x_3; (b) Lyapunov exponent spectrum with increase in a.

(a)

(b)
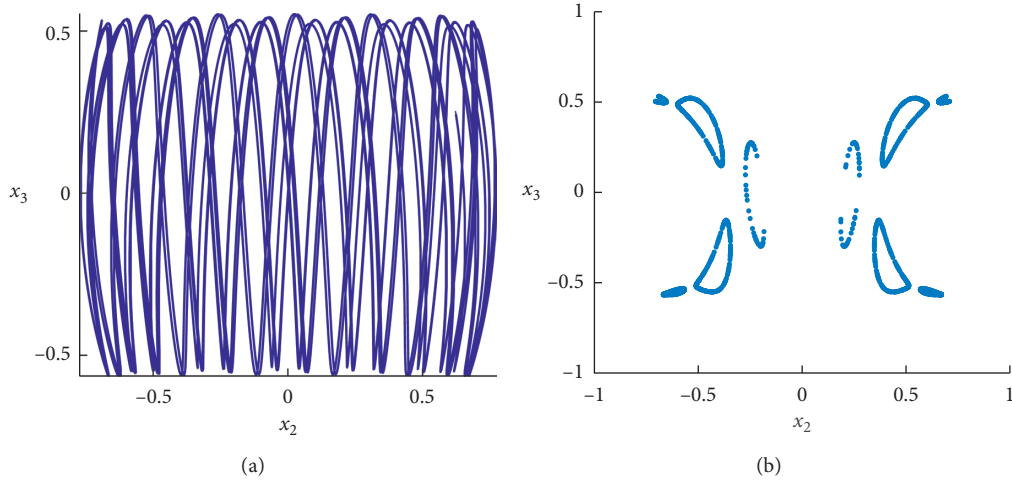
FIGURE 4: (a) Phase portrait with $\Pi_2 = \Pi_4 = 5, a = 0.1$; (b) Poincare section with $\Pi_2 = \Pi_4 = 5, a = 0.1$.

show the coexistence of quasi-periodic state with $x_{30} = 0.9$, $x_{40} = -3.6$, and hyperchaotic state (with the five LEs 4.4358, 0.1288, 0, −0.1288, and −4.4358) for $x_{30} = 5.5$ and $x_{40} = 0.3$.

When system Σ_3^H evolves into the hyperchaotic state, the system is still Hamiltonian conservative but not in Casimir energy. The phase portraits with Hamiltonian and Casimir energy represented by color are shown in Figures 8(a) and 8(b) which confirm this point. Therefore, the break of the conservation of Casimir energy is an effective indicator of the chaos-generating mechanism.

4. Adaptive Synchronization of System Σ_3^H

The property of chaotic synchronization gives the ability to exercise control over the dynamics of the chaotic system. As a result, such systems are of vital importance for secure communication. In this part, the adaptive synchronization method is used to realize the synchronization. The adaptive synchronization method has a mature theoretical and application basis, which is widely used in the electronic field [36, 46, 47]. This method has the following advantages: small synchronization error, the control intensity can be adjusted

adaptively according to the error, and if it is applied to chaotic communication, the security is strong.

Relabeling system Σ_3^H as the master system, one gets

$$\begin{cases} \dot{x}_1 = c_1 x_2 x_3, \\ \dot{x}_2 = c_2 x_1 x_3 + a x_4, \\ \dot{x}_3 = c_3 x_1 x_2 + c_4 x_4 x_5, \\ \dot{x}_4 = c_5 x_3 x_5 - b x_2, \\ \dot{x}_5 = c_6 x_3 x_4, \end{cases} \tag{20}$$

where x_1, x_2, x_3, x_4, x_5 are state variables and $c_1, c_2, c_3, c_4, c_5, c_6, a, b$ are parameters. Consider the slave system as

$$\begin{cases} \dot{y}_1 = c_1 y_2 y_3 + u_1, \\ \dot{y}_2 = c_2 y_1 y_3 + a y_4 + u_2, \\ \dot{y}_3 = c_3 y_1 y_2 + c_4 y_4 y_5 + u_3, \\ \dot{y}_4 = c_5 y_3 y_5 - b y_2 + u_4, \\ \dot{y}_5 = c_6 y_3 y_4 + u_5, \end{cases} \tag{21}$$
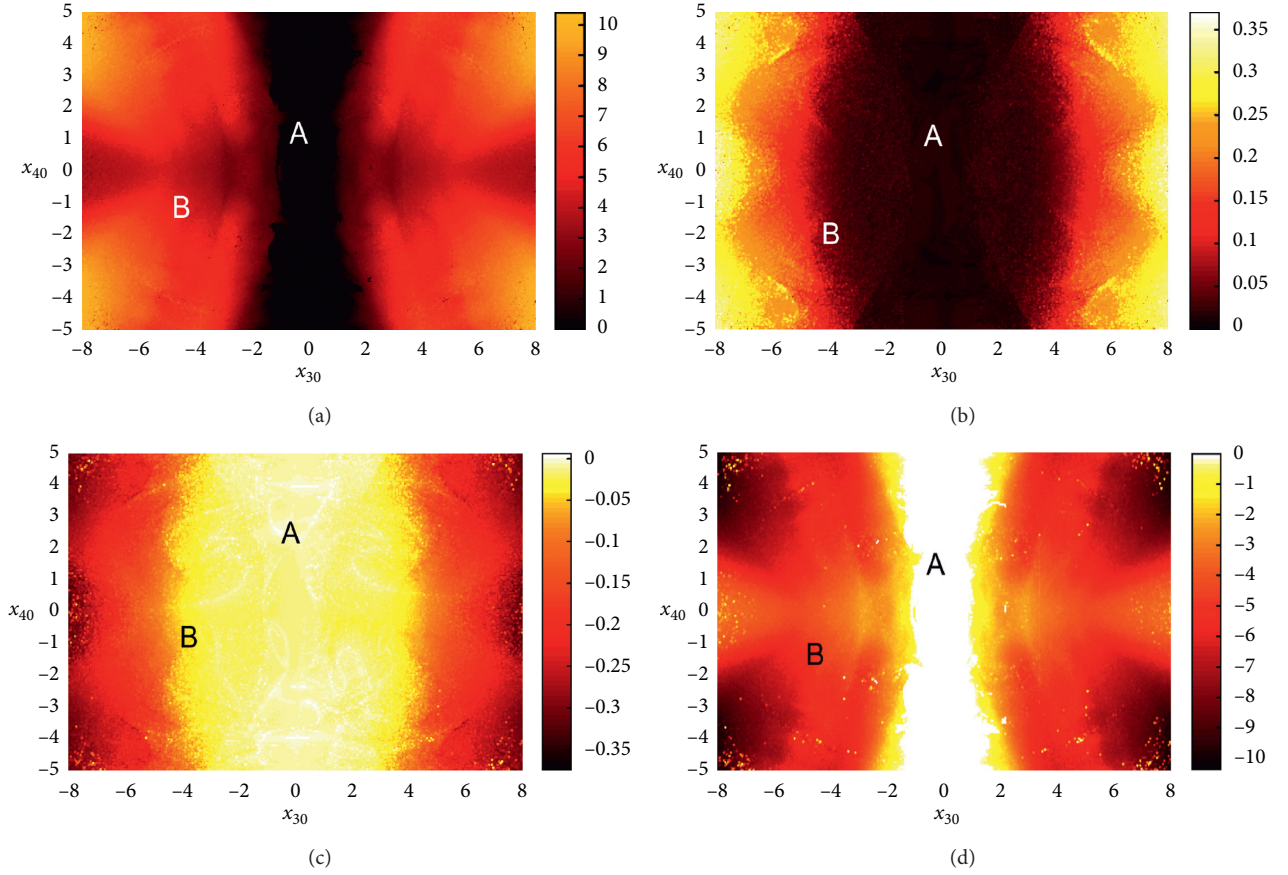
Figure 5: Dynamical evolution map in the (x_{30}, x_{40}) plane. (a) LE$_1$. (b) LE$_2$. (c) LE$_4$. (d) LE$_5$.
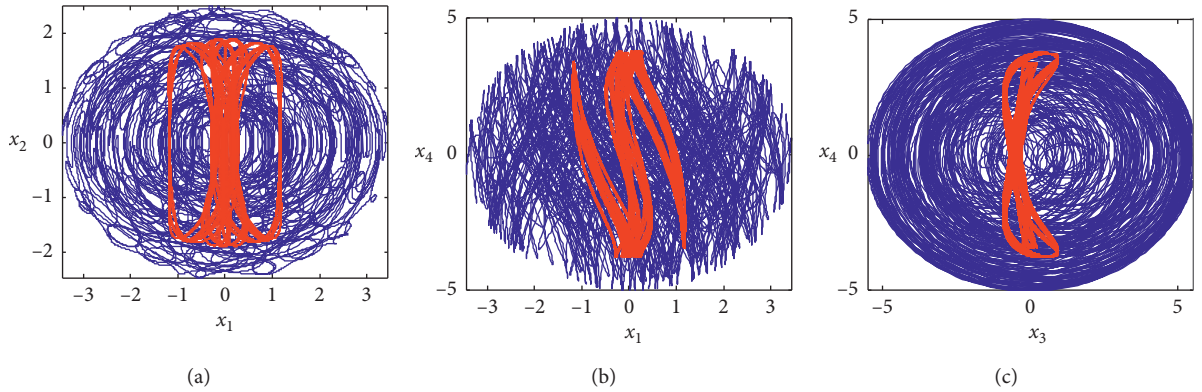
Figure 6: Coexistence of the quasi-periodic orbit with $x_{30} = 0.9$ and $x_{40} = -3.6$ (red) and the hyperchaotic orbit with $x_{30} = 5.5$ and $x_{40} = 0.3$ (blue). (a) (x_1, x_2) plane. (b) (x_1, x_4) plane. (c) (x_3, x_4) plane.

where y_1, y_2, y_3, y_4, y_5 are state variables and u_1, u_2, u_3, u_4, u_5 are controllers to be configured. The synchronization errors are determined by $e_i(t) = y_i(t) - x_i(t)$, $i = 1, 2, \ldots, 5$, and the adaptive controllers are set as $u_i = -k_i(y_i - x_i)$, $i = 1, 2, \ldots, 5$, in which $\dot{k}_i = -(y_i - x_i)^2$.

Lyapunov function is constructed as the following form:

$$V = \frac{1}{2} \sum_{i=1}^{5} \left(e_i^2 + k_i^2 \right), \quad i = 1, 2, \ldots, 5, \tag{22}$$

and one gets

(a)

(b)
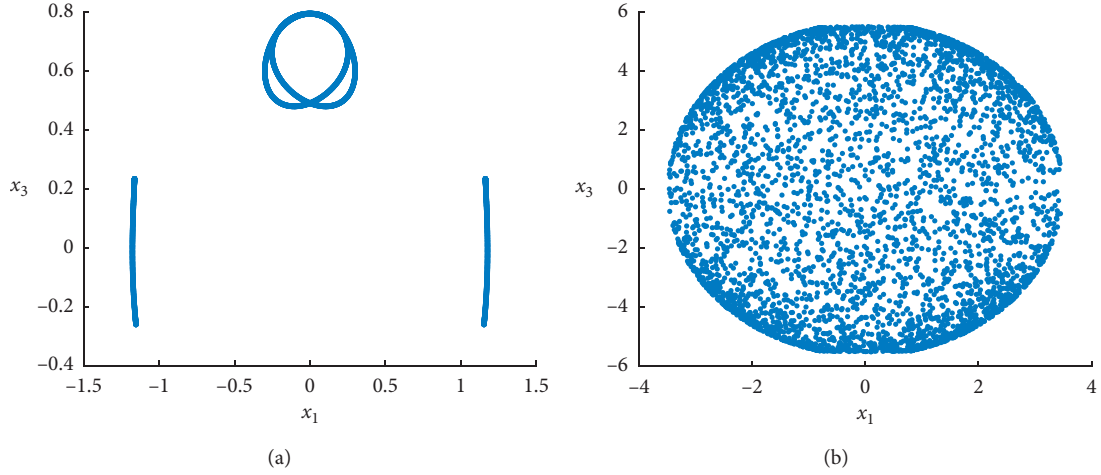
FIGURE 7: (a) Poincare section of the quasi-periodic orbit with $x_{30} = 0.9$ and $x_{40} = -3.6$; (b) Poincare section of the conservative hyperchaotic orbit with $x_{30} = 5.5$ and $x_{40} = 0.3$.

(a)

(b)
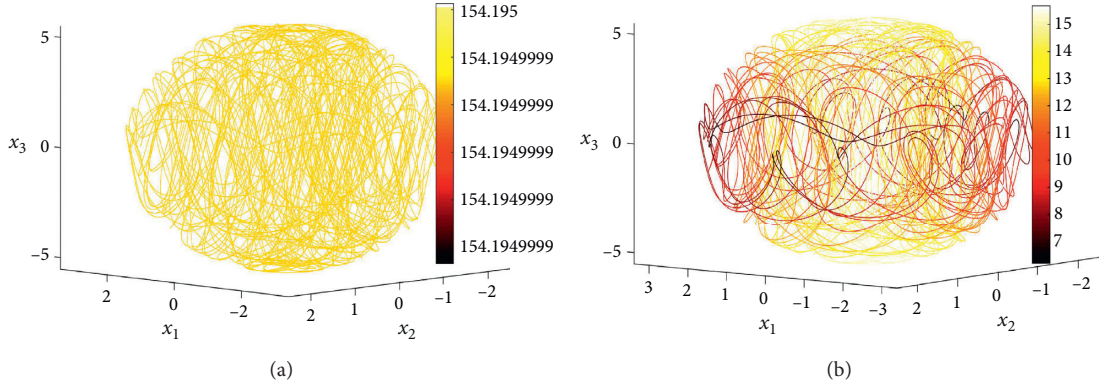
FIGURE 8: (a) Phase portrait with constant Hamiltonian; (b) phase portrait with varying Casimir energy.

$$\dot{V} = (c_1 + c_2)x_3e_1e_2 + (c_2 + c_3)x_1e_2e_3 + (c_1 + c_3)x_2e_1e_3$$
$$+ (c_4 + c_5)x_5e_3e_4$$
$$+ (c_5 + c_6)x_3e_4e_5 + (c_4 + c_6)x_4e_3e_5 + (a-b)e_2e_4 - 2\sum_{i=1}^{5}\left(k_ie_i^2\right)$$
$$\leq (c_1 + c_2)M_{x_3}e_1e_2 + (c_2 + c_3)M_{x_1}e_2e_3 + (c_1 + c_3)M_{x_2}e_1e_3$$
$$+ (c_4 + c_5)M_{x_5}e_3e_4$$
$$+ (c_5 + c_6)M_{x_3}e_4e_5 + (c_4 + c_6)M_{x_4}e_3e_5 + (a-b)e_2e_4 - 2\sum_{i=1}^{5}\left(k_ie_i^2\right)$$
$$= -e^T Pe,$$
$$(23)$$

in which $M_{x_i}, i = 1, 2, \ldots, 5$, are the upper bound of the corresponding state variables, $e = [e_1, e_2, e_3, e_4, e_5]^T$, and P is the matrix corresponding to quadric form $\dot{V}$. Hence, to guarantee the asymptotic stability of synchronization errors, P must be a positive definite matrix, that is to say, $\dot{V}$ is a negative definite quadratic form, which means $e_i \longrightarrow 0, i = 1, 2 \ldots 5$ exponentially as times goes on.

Set the control parameters for master system (22) and slave system (23) as $c_1 = -10, c_2 = 4, c_3 = -6, c_4 = 25, c_5 = -20, c_6 = -5, a = 7.5, b = 30$, the gains $k_1 = 40, k_2 = 40, k_3 = 40, k_4 = 45, k_5 = 50$, and the initial values are

$(x_{10}, x_{20}, x_{30}, x_{40}, x_{50}) = (0.1, 0.5, 5.5, 0.3, 0.1)$, under which the master system keeps hyperchaotic states, $(y_{10}, y_{20}, y_{30}, y_{40}, y_{50}) = (1, 0.5, 5, 3, 1)$, respectively. By calculation, matrix P has five positive characteristic roots, and $\dot{V}$ is a negative definite quadratic form. To test the validity of synchronization, simulations are implemented, and the first 5 seconds are time sequences of master and slave systems without synchronization. From the 5th second, synchronization is achieved, see Figures 9(a)–9(c); for the first 5 seconds, x_i and y_i conduct different time evolution, and after synchronization is achieved, x_i and y_i carry on synchronous evolution, and other two variables proceed the similar evolution. Figure 9(d) depicts the time history of e_1, e_2, e_3, e_4, e_5, which converge to 0 quickly, and the state variables move to be synchronized.

5. NIST Test and FPGA Implementation

5.1. NIST Test of System Σ_3^H. The National Institute of Standards and Technology (NIST) provides 15 statistical tests for random or pseudo-random generators, namely, the SP800-22 standard. Widely used in the test of pseudo-random sequences, the SP800-22 standard is considered as a

FIGURE 9: Adaptive synchronization simulation results. (a) State variables of x_1(blue); y_1(red). (b) State variables of x_2(blue); y_2(red). (c) State variables of x_3(blue); y_3(red). (d) Time series of synchronization errors.
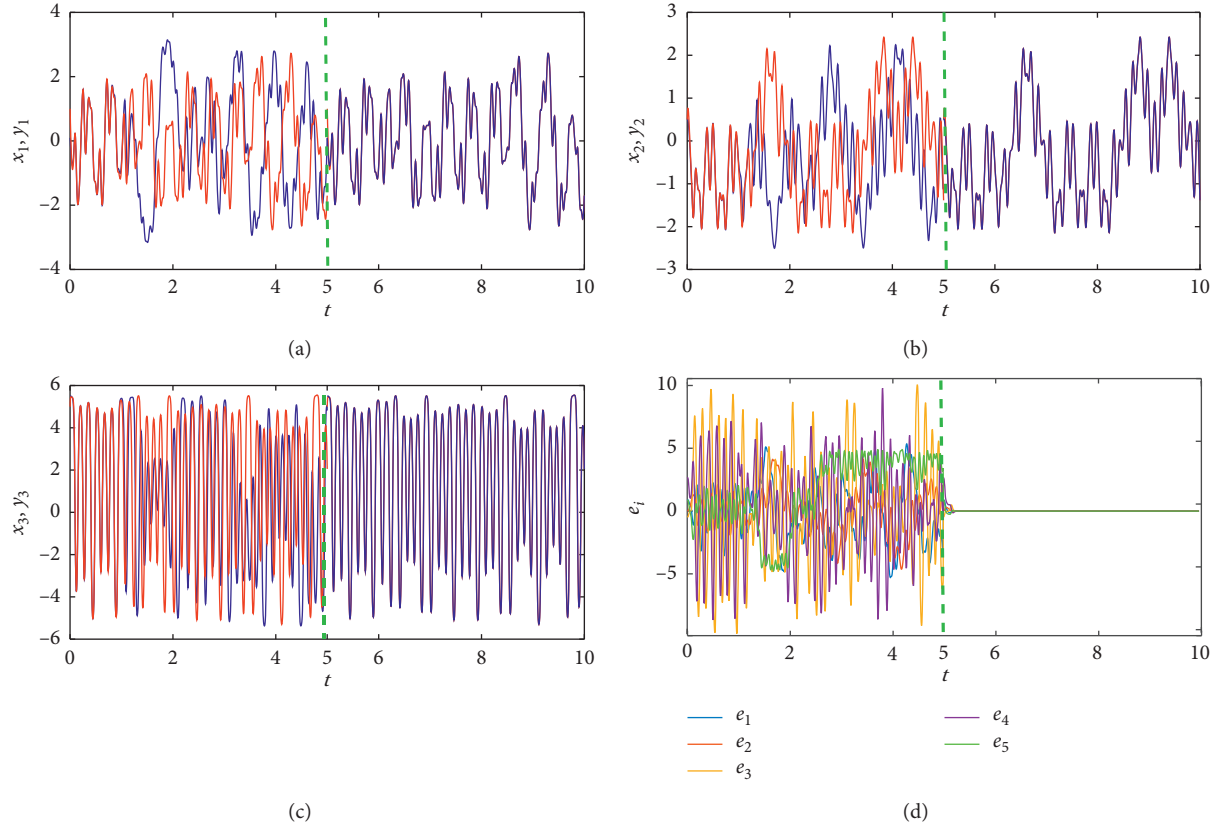
criterion for evaluating the statistical performance of pseudo-random sequences [48, 49]. The tests comprehensively analyze the performance of the pseudo-random sequence. A sequence passes the test only when the following conditions are satisfied: all P values are greater than the significance level, $\alpha = 0.01$; the relevant proportions are within the acceptance interval $[0.9601, 1.0298]$; and the distribution of P values obeys the uniformity.

From Table 3, all P values obtained in the statistical tests are greater than the significance level, $\alpha = 0.01$, so condition one is met. The relevant proportions lie within the acceptance interval $[0.9601, 1.0298]$, and hence, the second condition holds. In addition, the distribution of P values must pass the uniformity test. For simplicity, we consider the nonoverlapping template (Test No. 8 in Table 3) as an example. The distribution of P values is examined to validate the uniformity which can be visually illustrated using the histogram. Figure 10 shows the distribution of P values for the nonoverlapping template which is uniform. Other 14 tests obtained a similar uniformity. Therefore, the third condition is also satisfied. The conclusion is that the proposed Hamiltonian conservative hyperchaotic system Σ_3^H is suitable as a pseudo-random generator.

5.2. FPGA Implementation for System Σ_3^H. Although some important works have been implemented on FPGA [37, 50],

TABLE 3: NIST test results of hyperchaotic system Σ_3^H.

No.	Statistical test	P value	Proportion
1	Frequency	0.334538	0.99
2	Block frequency	0.883171	1
3	Cumulative sums	0.637119	0.99
4	Runs	0.798139	1
5	Longest run	0.719747	0.98
6	Rank	0.153763	1
7	FFT	0.096578	0.98
8	Nonoverlapping template	0.437274	0.99
9	Overlapping template	0.595549	0.97
10	Universal	0.955835	1
11	Approximate entropy	0.181557	1
12	Random excursions	0.834308	1
13	Random excursion variant	0.671779	1
14	Serial	0.494392	0.98
15	Linear complexity	0.851383	0.99

hardware implementation of conservative chaotic systems is more difficult than common dissipative chaotic systems since the former is highly sensitive to initial conditions and computational errors. In this section, we perform the implementation of system Σ_3^H, as an example, based on the FPGA platform. In order to accommodate digital computers, the first-order difference algorithm is used to discrete the system [51]. For system Σ_3^H with $(\Pi_1, \Pi_2, \Pi_3, \Pi_4, \Pi_5, a) = (14, 20, 10, 5, 30, 1.5)$, one obtains
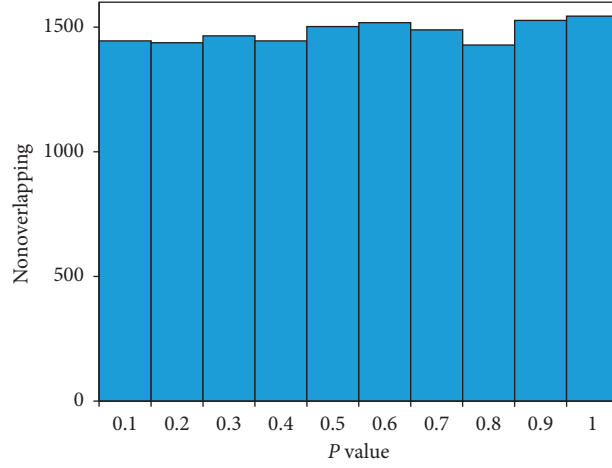
FIGURE 10: Probability distribution of P value for the nonoverlapping template.

(a)   (b)   (c)
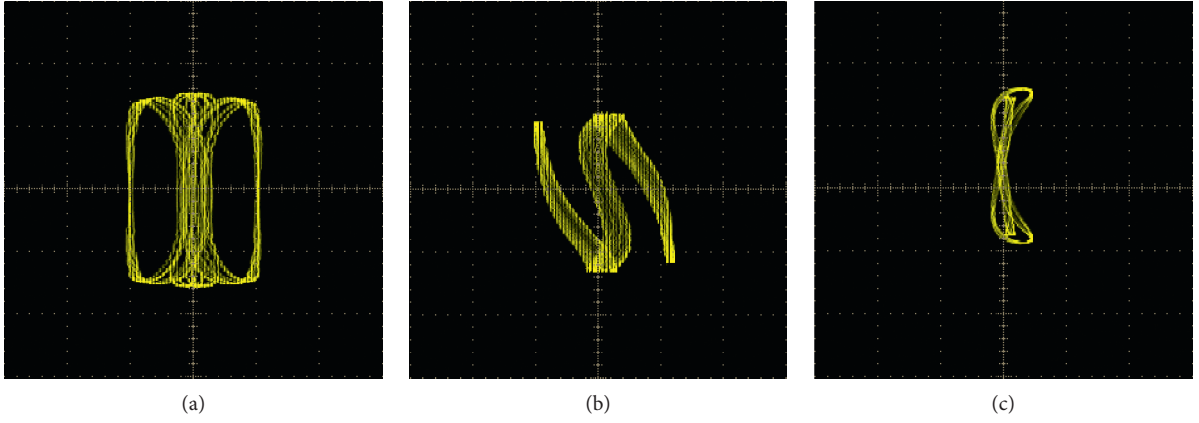
FIGURE 11: Quasi-periodic orbit of system Σ_3^H generated by FPGA. (a) (x_1, x_2) plane. (b) (x_1, x_4) plane. (c) (x_3, x_4) plane.

(a)   (b)   (c)
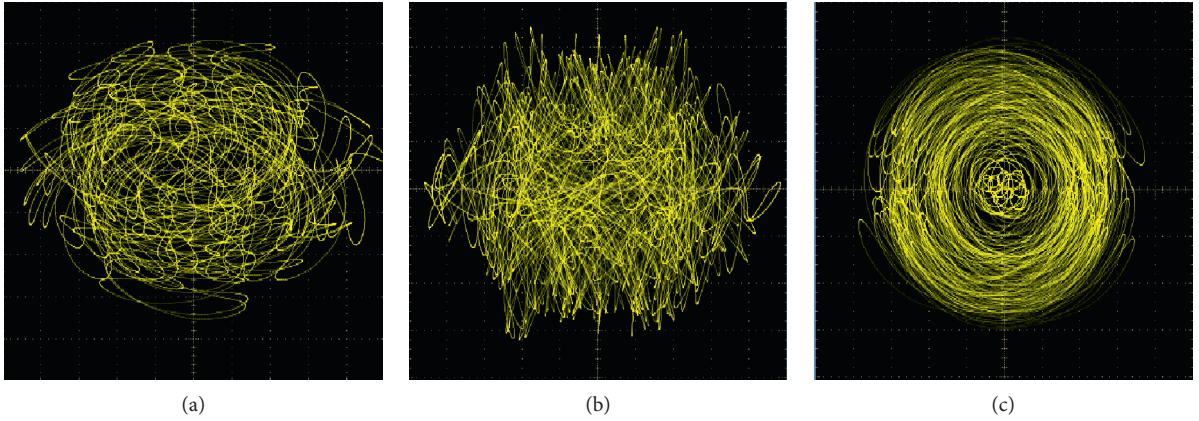
FIGURE 12: Hyperchaotic attractor of system Σ_3^H generated by FPGA. (a) (x_1, x_2) plane. (b) (x_1, x_4) plane. (c) (x_3, x_4) plane.

$$\begin{cases} \begin{cases} x_1(k+1) = \left[(\Pi_3 - \Pi_2)x_2(k)x_3(k)\right]\Delta T + x_1(k), \\ x_2(k+1) = \left[(\Pi_1 - \Pi_3)x_1(k)x_3(k) + a\Pi_4 x_4(k)\right]\Delta T + x_2(k), \\ x_3(k+1) = \left[(\Pi_2 - \Pi_1)x_1(k)x_2(k) + (\Pi_5 - \Pi_4)x_4(k)x_5(k)\right]\Delta T + x_3(k), \\ x_4(k+1) = \left[(\Pi_3 - \Pi_5)x_3(k)x_5(k) - a\Pi_2 x_2(k)\right]\Delta T + x_4(k), \\ x_5(k+1) = \left[(\Pi_4 - \Pi_3)x_3(k)x_4(k)\right]\Delta T + x_5(k). \end{cases} \end{cases} \tag{24}$$

The discrete model was built by DSP-builder in MATLAB (R2015b). Then, system (24) is solved by the fourth-order the Runge–Kutta method in Matlab/Simulink/DSP-builder, with the fixed step of 10^{-8} s, initial values set as Section 3.3, and sampling time of 10^{-6} s. The system models in equation (24) are converted to the VHDL code (Verilog hardware description language), synthesized, and compiled to the RTL (register transfer level) code.

To compare the results of computer simulation with digital circuit implementation, the phase portraits of system Σ_3^H are shown in Figures 11 and 12. It shows that the phase portraits of system Σ_3^H implemented by FPGA are roughly consistent with the computer simulation (shown in Figure 5), which means the conservative hyperchaotic system is implemented in the digital circuit with an acceptable error level.

6. Conclusions

This paper constructed a family of 5D Hamiltonian conservative hyperchaotic systems. Some interesting properties are revealed by theoretical and numerical analyses. The paper started from extending the 3D Euler equations of rigid bodies to generalized 5D sub-Euler equations. Five 5D Euler equations were then obtained by combining any two of the generalized 5D sub-Euler equations that with one common axis. These 5D Euler equations were proved to be both Hamiltonian and Casimir energy conservative, which can be regarded as the conservative term in a Kolmogorov system or a 5D generalized Hamiltonian system because of their antisymmetric structure matrix. So, these generalized 5D Euler equations are useful to study the dynamics of inviscid fluid and quantum mechanics and rigid body dynamics systems.

The mechanism of the proposed 5D Hamiltonian conservative chaotic systems was found by analyzing the Casimir energy and the Casimir power, which is an effective indicator of chaos generating. Using the dynamical evolution map, the coexistence of quasi-periodic and hyperchaotic was revealed, which showed the abundant dynamic characteristics of the proposed 5D Hamiltonian conservative chaotic systems. By the adaptive synchronization method, the hyperchaotic system was synchronized effectively.

To validate the application value of the proposed systems, NIST tests on system Σ_3^H were performed to verify the feasibility as a random number sequence generator. The system is implemented based on FPGA digital development platform, which was a contributing work for this field due to the difficulties of hardware implementation of conservative hyperchaos. These proposed systems are expected to be further helpfully applied to secure communication, neural network, and economics.

Data Availability

The data used to support the conclusions of this article can be computed by the relative equations and parameters given in the article using ODE45 solver in Matlab.

Conflicts of Interest

The authors declare that there are no conflicts of interest regarding the publication of this paper.

Authors' Contributions

Enzeng Dong and Xiaodong Jiao contributed equally to this work.

Acknowledgments

References

[1] E. N. Lorenz, "Deterministic nonperiodic flow," *Journal of the Atmospheric Sciences*, vol. 20, no. 2, pp. 130–141, 1963.

[2] A. Gragnani and S. Rinaldi, "A universal bifurcation diagram for seasonally perturbed predator-prey models," *Bulletin of Mathematical Biology*, vol. 57, no. 5, pp. 701–712, 1995.

[3] E. Dong, M. Yuan, C. Zhang, J. Tong, Z. Chen, and S. Du, "Topological horseshoe analysis, ultimate boundary estimations of a new 4D hyperchaotic system and its fpga implementation," *International Journal of Bifurcation and Chaos*, vol. 28, no. 7, Article ID 1850081, 2018.

[4] E. Dong, Z. Zhang, M. Yuan, Y. Ji, X. Zhou, and Z. Wang, "Ultimate boundary estimation and topological horseshoe analysis on a parallel 4D hyperchaotic system with any number of attractors and its multi-scroll," *Nonlinear Dynamics*, vol. 95, no. 4, pp. 3219–3236, 2019.

[5] H. Jia, Z. Guo, S. Wang, and Z. Chen, "Mechanics analysis and hardware implementation of a new 3D chaotic system," *International Journal of Bifurcation and Chaos*, vol. 28, no. 13, Article ID 1850161, 2019.

[6] G. Qi and X. Liang, "Mechanism and energy cycling of the Qi four-wing chaotic system," *International Journal of Bifurcation and Chaos*, vol. 27, no. 12, Article ID 1750180, 2017.

[7] W. G. Hoover, "Remark on some simple chaotic flows," *Physical Review E*, vol. 51, no. 1, pp. 759-760, 1995.

[8] A. G. Wu, S. J. Cang, R. Zhang, Z. Wang, and Z. Chen, "Hyperchaos in a conservative system with nonhyperbolic fixed points," *Complexity*, vol. 2018, Article ID 9430637, 8 pages, 2018.

[9] E. Ott, *Chaos in Dynamical Systems*, Cambridge University Press, Cambridge, UK, 2002.

[10] G. Qi, "Modelings and mechanism analysis underlying both the 4D euler equations and Hamiltonian conservative chaotic systems," *Nonlinear Dynamics*, vol. 95, no. 3, pp. 2063–2077, 2018.

[11] E. Dong, M. Yuan, S. Du, and Z. Chen, "A new class of Hamiltonian conservative chaotic systems with multistability and design of pseudo-random number generator," *Applied Mathematical Modelling*, vol. 73, no. 9, pp. 40–71, 2019.

[12] V. Pelino, F. Maimone, and A. Pasini, "Energy cycle for the lorenz attractor," *Chaos, Solitons & Fractals*, vol. 64, no. 1, pp. 67–77, 2014.

[13] F. Sun, S. Liu, Z. Li, and Z. Lü, "A novel image encryption scheme based on spatial chaos map," *Chaos, Solitons & Fractals*, vol. 38, no. 3, pp. 631–640, 2008.

[14] Z. Guan, F. Huang, and W. Guan, "Chaos-based image encryption algorithm," *Physics Letters A*, vol. 346, no. 1–3, pp. 153–157, 2005.

[15] G. Chen, Y. Mao, and C. K. Chui, "A symmetric image encryption scheme based on 3d chaotic cat maps," *Chaos, Solitons & Fractals*, vol. 21, no. 3, pp. 749–761, 2004.

[16] Q. H. Zhang, H. Zhang, and Z.-H. Li, "One-way hash function construction based on conservative chaotic systems," in *Proceedings of the International Conference on Information Assurance Security*, IEEE, Xi'an, China, August 2009.

[17] O. E. Rossler, "An equation for hyperchaos," *Physics Letters A*, vol. 71, no. 2-3, pp. 155–157, 1979.

[18] J. Zheng, "A simple universal adaptive feedback controller for chaos and hyperchaos control," *Computers & Mathematics with Applications*, vol. 61, no. 8, pp. 2000–2004, 2011.

[19] H. Yu, G. Cai, and G. Li, "Dynamic analysis and control of a new hyperchaotic finance system," *Nonlinear Dynamics*, vol. 67, no. 3, pp. 2171–2182, 2012.

[20] G. Qi and S. B. Matondo, "Hyper-chaos encryption using convolutional masking and model free unmasking," *Chinese Physics B*, vol. 23, no. 5, Article ID 050507, 2014.

[21] D. P. Rosin, *Dynamics of Complex Autonomous Boolean Networks*, Springer International Publishing, Berlin, Germany, 2015.

[22] F. Yu, Z. N. Zhang, L. Liu et al., "Secure communication scheme based on a new 5D multistable four-wing memristive hyperchaotic system with disturbance inputs," *Complexity*, vol. 2020, Article ID 5859273, 16 pages, 2020.

[23] S. Vaidyanathan and S. Sampath, "Hybrid synchronization of hyperchaotic chen systems via sliding mode control," in *Lecture Notes of the Institute for Computer Sciences, Social Informatics and Telecommunications Engineering*, vol. 85, pp. 257–266, Springer, Berlin, Germany, 2012.

[24] M. Zhang, T. Liu, P. Li, A. Wang, J. Zhang, and Y. Wang, "Generation of broadband chaotic laser using dual-wavelength optically injected fabry-pérot laser diode with optical feedback," *IEEE Photonics Technology Letters*, vol. 23, no. 24, pp. 1872–1874, 2011.

[25] A. V. Holden and L. F. Olsen, "Exploring nature's roulette wheel: chaos in biological systems," in *Cell to Cell Signals in Plants and Animals*, vol. 51, pp. 173–185, Springer, Berlin, Germany, 1991.

[26] A. Silchenko, T. Kapitaniak, and V. Anishchenko, "Noise-enhanced phase locking in a stochastic bistable system driven by a chaotic signal," *Physical Review E*, vol. 59, no. 2, pp. 1593–1599, 1999.

[27] V. T. Pham, S. Jafari, C. Volos, X. Wang, and S. M. R. H. Golpayegani, "Is that really hidden? The presence of complex fixed-points in chaotic flows with no equilibria," *International Journal of Bifurcation and Chaos*, vol. 24, no. 11, Article ID 1450146, 2015.

[28] P. Jaros, P. Perlikowski, and T. Kapitaniak, "Synchronization and multistability in the ring of modified Rössler oscillators," *The European Physical Journal Special Topics*, vol. 224, no. 8, pp. 1541–1552, 2015.

[29] D. Angeli, J. E. Ferrell, and E. D. Sontag, "Detection of multistability, bifurcations, and hysteresis in a large class of biological positive-feedback systems," *Proceedings of the National Academy of Sciences*, vol. 101, no. 7, pp. 1822–1827, 2004.

[30] M. Peng, Z. Jiang, X. Jiang, J. Hu, and Y. Qu, "Multistability and complex dynamics in a simple discrete economic model," *Chaos, Solitons & Fractals*, vol. 41, no. 2, pp. 671–687, 2009.

[31] V.-T. Pham, S. Jafari, C. Volos, and T. Kapitaniak, "Different families of hidden attractors in a new chaotic system with

[32] J. C. Sprott, S. Jafari, A. J. M. Khalaf, and T. Kapitaniak, "Megastability: coexistence of a countable infinity of nested attractors in a periodically-forced oscillator with spatially-periodic damping," *The European Physical Journal Special Topics*, vol. 226, no. 9, pp. 1979–1985, 2017.

[33] S. Cang, Y. Li, R. Zhang, and Z. Wang, "Hidden and self-excited coexisting attractors in a lorenz-like system with two equilibrium points," *Nonlinear Dynamics*, vol. 95, no. 1, pp. 381–390, 2019.

[34] J. C. Sprott, X. Wang, and G. Chen, "Coexistence of point, periodic and strange attractors," *International Journal of Bifurcation and Chaos*, vol. 23, no. 5, Article ID 1350093, 2013.

[35] L. Ren and G. Zhang, "Adaptive projective synchronization for a class of switched chaotic systems," *Mathematical Methods in the Applied Sciences*, vol. 42, no. 18, pp. 6192–6204, 2019.

[36] T.-L. Liao and S.-H. Tsai, "Adaptive synchronization of chaotic systems and its application to secure communications," *Chaos, Solitons & Fractals*, vol. 11, no. 9, pp. 1387–1396, 2000.

[37] I. Koyuncu, A. T. Ozcerit, and I. Pehlivan, "Implementation of FPGA-based real time novel chaotic oscillator," *Nonlinear Dynamics*, vol. 77, no. 1-2, pp. 49–59, 2014.

[38] J. E. Marsden and T. S. Ratiu, *Introduction to Mechanics and Symmetry: A Basic Exposition of Classical Mechanical Systems*, Springer, Berlin, Germany, 2008.

[39] G. Qi and J. Hu, "Force analysis and energy operation of chaotic system of permanent-magnet synchronous motor," *International Journal of Bifurcation and Chaos*, vol. 27, no. 14, Article ID 1750216, 2017.

[40] Y. A. Kuznetsov, "Elements of applied bifurcation theory," *Applied Mathematical Sciences*, vol. 288, no. 2, pp. 715–730, 2004.

[41] A. Wolf, J. B. Swift, H. L. Swinney, and J. A. Vastano, "Determining lyapunov exponents from a time series," *Physica D: Nonlinear Phenomena*, vol. 16, no. 3, pp. 285–317, 1985.

[42] S. Vaidyanathan and A. T. Azar, *Analysis and Control of a 4-D Novel Hyperchaotic System: Chaos Modeling and Control Systems Design*, Springer International Publishing, Berlin, Germany, 2015.

[43] A. T. Azar, S. Vaidyanathan, and A. Ouannas, *Fractional Order Control and Synchronization of Chaotic Systems: Studies in Computational Intelligence*, Springer, Berlin, Germany, 2017.

[44] C. A. Jousseph, T. S. Kruger, C. Manchein, S. R. Lopes, and M. W. Beims, "Weak dissipative effects on trajectories from the edge of basins of attraction," *Physica A: Statistical Mechanics and Its Applications*, vol. 456, pp. 68–74, 2016.

[45] J. Aguirre, J. C. Vallejo, and M. A. F. Sanjuan, "Wada basins and unpredictability in Hamiltonian and dissipative systems," *International Journal of Modern Physics B*, vol. 17, no. 22, pp. 4171–4175, 2003.

[46] Y. Hong, H. Qin, and G. Chen, "Adaptive synchronization of chaotic systems via state or output feedback control," *International Journal of Bifurcation and Chaos*, vol. 11, no. 4, pp. 1149–1158, 2001.

[47] S. Vaidyanathan, "Qualitative analysis, adaptive control and synchronization of a seven-term novel 3-D chaotic system with a quartic nonlinearity," *International Journal of Control Theory and Applications*, vol. 7, no. 1, pp. 1–20, 2014.

[48] O. Y. Lui, C. H. Yuen, and K. W. Wong, "A pseudo-random number generator employing multiple RNYI maps,"

International Journal of Modern Physics C, vol. 24, no. 11, pp. 44–54, 2013.

[49] A. Rukhin, J. Soto, N. James et al., "A statistical test suite for random and pseudorandom number generators for cryptographic applications," *Applied Physics Letters*, vol. 22, no. 7, pp. 1645–1579, 2001.

[50] G. Y. Wang, X. L. Bao, and Z. L. Wang, "Design and FPGA Implementation of a new hyperchaotic system," *Chinese Physics B*, vol. 17, no. 10, pp. 3596–3602, 2008.

[51] E. Dong, Z. Liang, S. Du, and Z. Chen, "Topological horseshoe analysis on a four-wing chaotic attractor and its FPGA implement," *Nonlinear Dynamics*, vol. 83, no. 1-2, pp. 623–630, 2016.

WILEY | Hindawi

Research Article

Study on Intelligent Compaction-Equipment Logistics Scheduling and Propagation Characteristics of Vibration Wave in Nonlinear Systems with Multistability Based on Field Test

Yixuan Han [1], **Changwei Yang** [2], **Degou Cai** [3], **Hongye Yan** [3], **and Hailing Zeng** [3]

[1]*Beijing Jiaotong University, 100044 Beijing, China*
[2]*Southwest Jiaotong University Sichuan, 610031 Chengdu, China*
[3]*Railway Engineering Research Institute,*
 China Academy of Railway Sciences China Academy of Railway Sciences Corporation Limited, 100044 Beijing, China

Correspondence should be addressed to Changwei Yang; yangchangwei56@163.com

The equipment scheduling and propagation characteristics of vibration wave from vibratory roller ⟶ filling material nonlinear systems with multistability are the core problems of subgrade intelligent construction technology, and the logistics scheduling of the equipment is directly related to the construction efficiency. Aiming at the shortages, one typical subgrade located at the Gu'an station of Beijing-Xiong'an city railway is selected to research and finish the field tests; some findings are shown as follows: first, some valuable suggestions about the logistics scheduling of intelligent equipment are proposed, which can break the barriers between the organizations and improve construction efficiency; second, when the vibration wave propagates from the vibratory roller ⟶ surface of filling material ⟶ different buried depths of filling material, the peak acceleration of vibration wave gradually decreases and is hyperbolic distribution approximately. At the same time, the sensitive of attenuation is shown as follows: Z<X ≈ Y, and the critical depth of vibration energy propagation is about 1.0 m. At the same time, the peak acceleration of vibration wave at the interface of different filling material layers exists in steps and is "side clock" distribution approximately with the increase in buried depth. Third, in the propagation process, with the increase in buried depth, the amplitude of fundamental, primary, secondary, until fifth harmonics decreases exponentially (R^2>0.9), and the concrete functional relationship among different amplitudes of harmonics can be summarized as $y = Ae^{-BX}$; fourth, the vibration energy is mainly concentrated near 10–30 Hz in the vibratory roller, but when the vibration wave propagates from vibratory roller ⟶ filling material, the vibration energy gradually decreases with the increase in depth, and the marginal spectrum gradually changes from one peak to two peaks, that is, 30–50 Hz and 50–100 Hz; fifth, the vibration energy in the vibrational wheel is distributed averagely in the compaction process, and the effective compaction time is two seconds, which will be helpful for revealing the propagation characteristics of vibration wave, optimizing the compaction quality control models and providing some support for the development of intelligent compaction theory of railway subgrade.

1. Introduction

China has built the world's largest high-speed rail network whose operating mileage reaches 22,000 kilometers and it will be expected to reach 38,000 kilometers in 2030, which will form a high-speed railway network with "eight-vertical and eight-horizontal" as the main channel. The ratio of length of subgrade to total mileage of high-speed railway is more than 30%, which has been an important part of railway infrastructure and the basis for carrying the track structure and trains. In recent years, intelligent compaction technology [1–3] is more and more widely used in practical projects, such as Jingxiong high-speed railway.

Significant engineering achievements have been made in terms of intelligent compaction, but its research on the basic theory has just started; the propagation characteristics of

vibration wave in the compaction process are still not clear enough, and a lot of research studies mainly focus on numerical simulation, theoretical analysis, and laboratory test [4–11] [12].

At the same time, the recent research focuses on two aspects, such as time domain and frequency, but there are little studies on the joint time-frequency domain. However, the vibration wave is a complex nonlinear signal; amplitude and frequency of the vibration gradually change with time, which will affect the reasonability of analysis results if it is analyzed from the time domain or the frequency domain alone. Therefore, the propagation characteristics of vibration wave should be studied from time domain, frequency domain, and joint time-frequency domain by some new signal analysis technology.

Based on this, one typical subgrade section of Beijing-Xiong'an Railway in Gu'an Station is selected to finish the field test, and the intelligent compaction and the logistics scheduling of equipment used in the typical subgrade section are introduced briefly. And then, some valuable test data are used to study the propagation characteristics among soil layers in different depths during the vibration compaction process from time domain, frequency domain, and joint time-frequency domain by Hilbert–Huang transform, which will be helpful for optimizing the compaction quality control models and providing some support for the development of intelligent compaction theory of railway subgrade.

2. Intelligent Compaction and Equipment Deployment Technology

Subgrade intelligent compaction technology mainly integrates automatic monitoring and control, satellite positioning, and information management, as shown in Figure 1.

2.1. Intelligent Compaction Technology. During the construction process, the vibration characteristics of compaction machinery and the compressed filling material are collected in real time by control system, and the main parameters of vibratory roller are continuously adjusted based on the collected information which can reflect the compaction quality in order to optimize compaction and meet the required conditions, such as vibration amplitude, frequency, excitation force, and walking speed. At the same time, the satellite positioning system can accurately determine the position of vibratory roller and feedback the parameters such as modulus, stiffness, and resistance, which is directly related to the compaction quality of filling material to the control system in real time, so as to identify weak areas of subgrade compaction, and then take targeted remedial measures.

2.2. Logistics Scheduling of Intelligent Equipment. In actual operations, the logistics scheduling of intelligent equipment by relevant departments is still in a backward stage. In the construction, because of the lack of modern logistics management knowledge, the integration level in the current construction departments is low, and the

management implementation is weak so that the relevant departments often have low utilization rates of resources such as distribution of idle equipment, operations of smart rollers, and dispatch of materials such as machinery and equipment. Aiming at this practical operation problem, this article proposes a scientific logistics scheduling management method. The key to effective scheduling and configuration of intelligent vibratory rollers and other equipment is the establishment of tacit cooperation between all parties, including numerous suppliers, different contractors, and information supporters, connected with the construction project. Due to the particularity of project construction, a temporary and high-efficient material scheduling center should be established, and the collaboration of different organizations is supported by a cross-organizational information platform, as shown in Figure 2.

In the organizational logistics scheduling network, the coordination mechanism is similar to the supply chain network, that is, "To be flexible and rigidly both" [13]. First, each organization node should establish a trusting and harmonious organizational environment. Second, the authority of each organization should be appropriately decentralized; meanwhile, the penetration and connection between different organization subjects should be strengthened via various levels of communication, including information platforms and social network. Third, cross-organizational contracts and agreements in the organizational logistics scheduling network should be finished. Fourth, establishing a sophisticated talent selection system and completing the assessment system are extremely necessary, where both valuing practical skills and academic qualifications, rather than considering merely one.

Based on this, the barriers between the organizations can be broken, completely changing the state of "a pool of standing water" of important materials. Relying on a fast and efficient organizational logistics scheduling network, materials and information flows can quickly transmit and respond between nodes, becoming "live water" where there is demand, and other nodes respond quickly. Whether it is the contradiction between subjective organizations or the contradiction that too many sudden factors cause the failure of resource allocation, it can be solved fundamentally.

3. Test Design

The test site is located in the subgrade section about 200 m by 100 m near the Gu'an Station of the Beijing-Xiong'an Intercity Railway as the test section, as shown in Figure 3. The whole height compacted filling is 1.5 m, which is divided into five layers. The subgrade filling material is the AB group coarse breccia, which is the mixture of A group material and B group material, and the concrete parameters are regulated in detail in the 《high-speed railway design specification》 (TB10621-2014). Its particle grading curves of five test results are shown in Figure 4. Figure 4 shows the test data have good consistency.
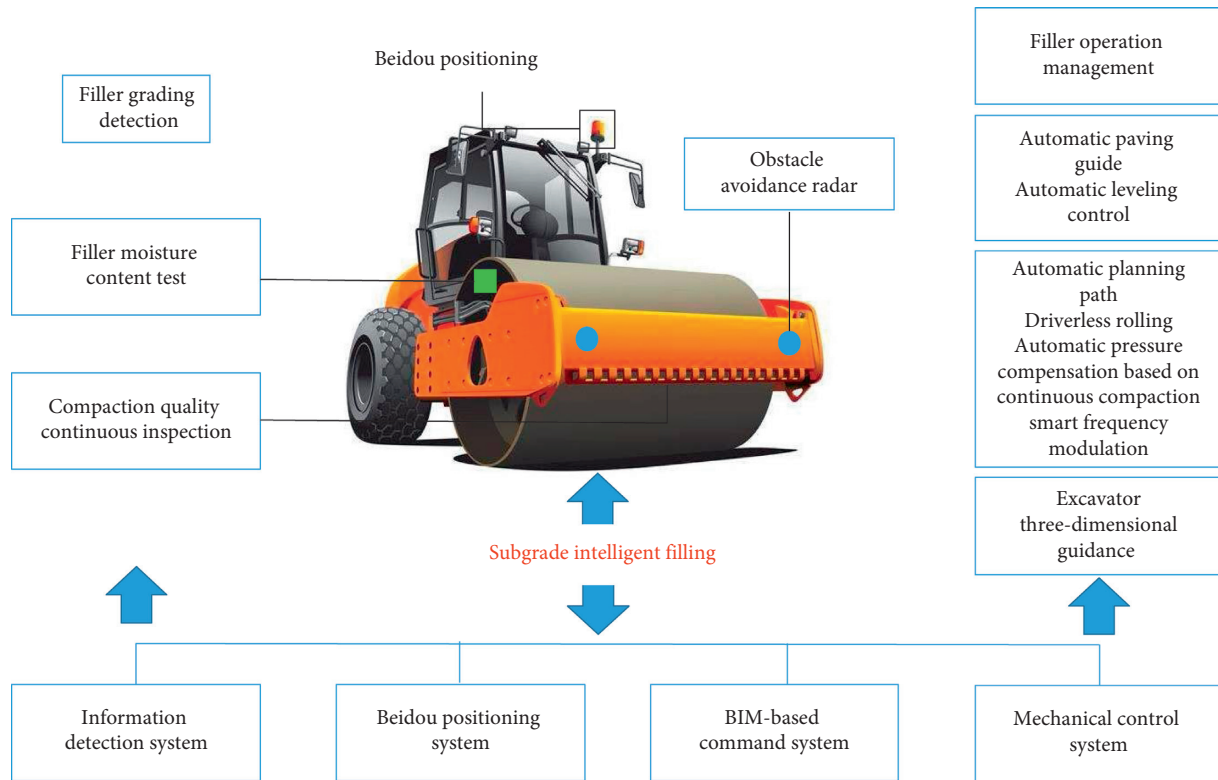
FIGURE 1: Schematic diagram of the intelligent road roller in the Gu'an section of Beijing-Xiong'an Railway.
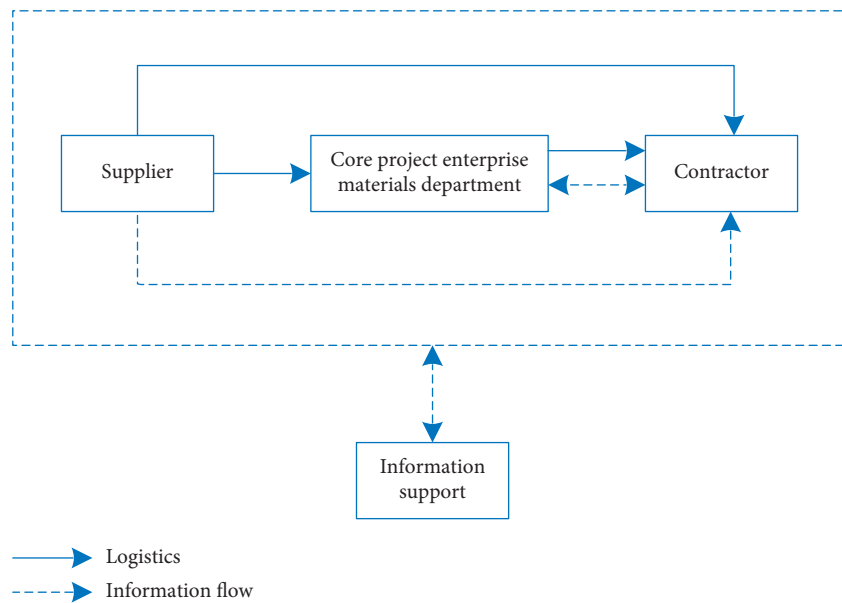
FIGURE 2: Project organizational logistics scheduling network.

3.1. Test Equipment. The vibratory compaction equipment adopts Sany Heavy Industry Vibratory Roller (No. SSR260C-6), the whole machine quality is 26.7 t, and its rated power is 180 kW. The weak vibration parameters: vibration frequency is 31 Hz, and vibration amplitude is 1.03 mm; the strong vibration parameters: vibration frequency is 27 Hz, and vibration amplitude is 2.05 mm. Based on a large number of actual projects in the early stage, it is found that the weak vibration is more conducive to the subgrade compaction after its filler is loosely laid and statically pressed. Consequently, the test adopts weak vibration conditions for research. At the same time, the data acquisition adopts 64-channel Donghua dynamic data acquisition equipment DH3823 and the acceleration sensor adopts Donghua three-way acceleration sensor 1C302 with a range of ±5.0 g. In order to ensure the fit between the collected signal and the original signal, the

FIGURE 3: Field test environment.
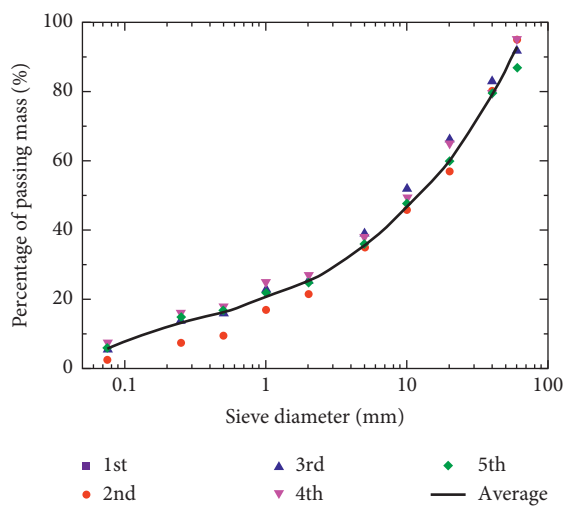
FIGURE 4: Particle grading curves of five tests.

sampling frequency of acceleration sensors was set to 2000 Hz. And all the data acquisition system and sensors were calibrated before the test.

3.2. Distribution of Acceleration Measuring Points in the Filler Material. The correct installation and embedment of sensors is decisive for the accuracy of test data. Before the sensors are buried, some work should be finished, as shown in Figure 5. At the same time, in order to study the vibration characteristics in different depths in the compaction process, the sensors are set on the vibratory wheel and its following five layers. The concrete distribution of acceleration measuring points in the filler material and the overall coordinate system in the field test are shown in Figures 6 and 7.

4. Test Results

In order to systematically analyse the propagation characteristics of vibration wave in the vertical direction, this paper will carry out the research from four aspects: time domain, frequency domain, joint time-frequency domain, and energy domain.

4.1. Propagation Characteristics of Peak Acceleration in the Vertical Direction. The duration of measured vibrational signal is nearly 10 seconds, so 10 second time-history curve is selected for analysis. The peak acceleration of vibration wave at each measuring point in the compaction process is shown in Figure 8.

Figure 8 shows that when vibration wave propagates from vibratory roller ⟶ filler surface ⟶ deep filler, the shape of peak acceleration is hyperbolic with the increase in buried depth and is also inversely proportional to buried depth. When the vibration wave propagates from frame ⟶ filler surface, the peak acceleration in the Z, Y, and X directions is, respectively, attenuated by 56.7%, 83.7%, and 85.1% and, respectively, attenuated by 94.5%, 98.6%, and 98.4% at a buried depth of 0.9 m, which is basically stable after that, and then, the vibration energy is nearly zero at a buried depth of 1.50 m in which the vibrational energy is, respectively, attenuated by 96.1%, 99.3%, and 98.7%. The above phenomenon may be caused by the dissipation of energy by the damping of the filler itself, and it can be seen that the critical depth of vibration energy propagation during the vibration compaction process is about 1.0 m. At the same time, at the interface of the filler, the vibration accelerations in different directions are stepped, which is mainly caused by the differences in physical and mechanical parameters between adjacent

(a)

(b)

FIGURE 5: (a) Installation and embedment of sensors and (b) data acquisition in the field test.
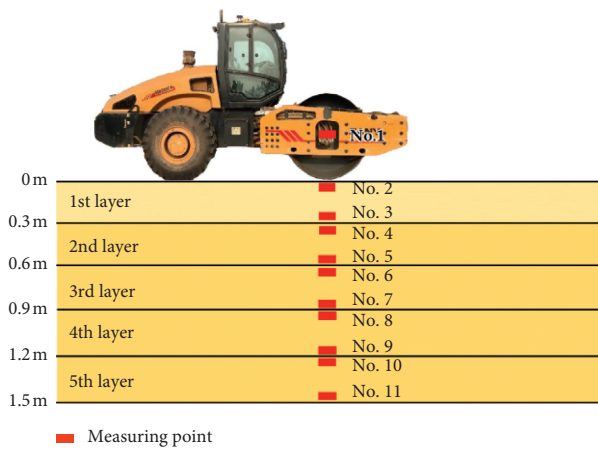
FIGURE 6: Acceleration measuring points in the filler material.

FIGURE 7: Schematic diagram of overall coordinate system in the field test.

FIGURE 8: Distribution of peak acceleration at each measuring point in different directions.
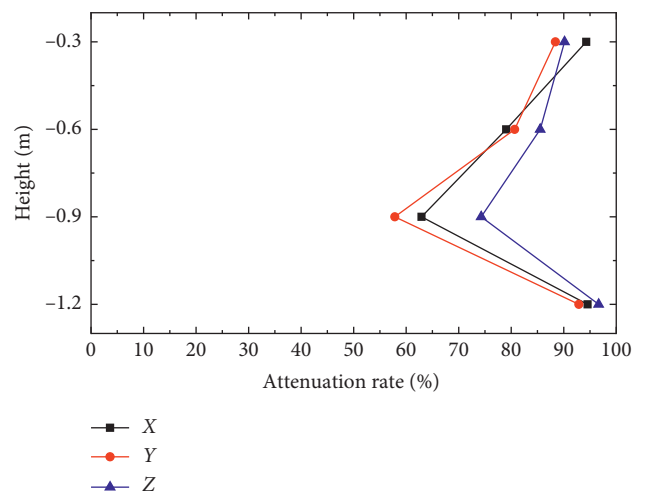
FIGURE 9: Attenuation of acceleration at different interfaces.

filling material, especially the difference in wave impedance between the two sides of interface, which causes a large amount of reflection, transmission, and other scattering phenomenon at the interface, which weakens the downward propagation of vibration energy. Based on this, in order to analyze the influence of the filler interface on the vibration acceleration quantitatively, this paper assumes that the measurement point on the upper surface of each interface is used as the benchmark and uses the ratio of the acceleration amplitude of the lower surface to the benchmark as acceleration peak attenuation percentage, and the result is shown in Figure 9.

Figure 9 shows that the attenuation characteristics of vibration acceleration in different directions with the increase in buried depth is basically consistent, showing a "side clock" shape, the attenuation in the X direction is more serious than the Y direction, and the Z direction is the smallest. At the same time, due to the increase in buried depth, the attenuation percentage at different interfaces decreases firstly, reaching minimum when the buried depth is 0.9 m, about 55%, and then gradually increases. The reason of the above phenomenon may be that the propagation depth of vibration energy is about 1.0 m, which can cause the secondary compaction within 1 m filling material in the compaction process, whose density and rigidity can gradually increase, and the compaction parts more than 1.0 m mainly depend on the inertial force generated by the vibration of upper filler and the upper heaped load. Consequently, the soil buried depth (0.6 m–0.9 m) realizes secondary compaction by vibration and that more than 0.9 m is compacted by inertia force and heaped load, and then, the acceleration attenuation is the largest, which is mainly due to the larger differences in the degree of compaction, and the density and stiffness of soil on both sides cause a large wave impedance and reflection of vibration energy, so the acceleration peak attenuation is small at the interface of 1.2 m buried depth (the soil within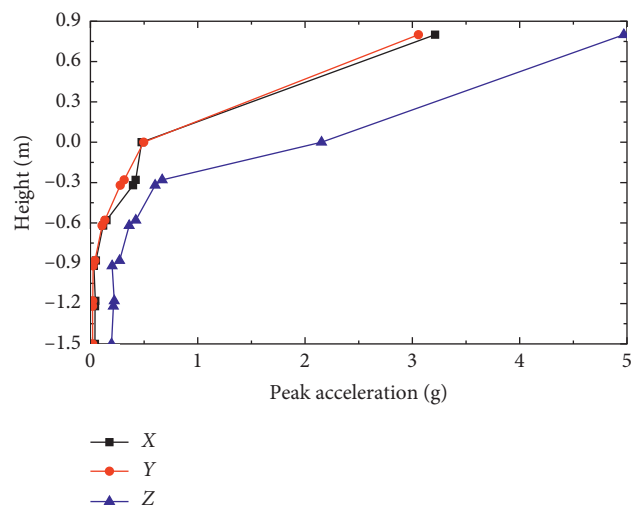 the range of 0.9 m–1.2 m/more than 1.2 m), which is for the reason that the soil density and stiffness on both sides of interface are basically consistent, so the reflection for vibration wave is small.

4.2. Propagation Characteristics of Acceleration Spectrum in the Vertical Direction.

In order to research the propagation characteristics of acceleration spectrum in the vertical direction, the vertical acceleration data of #1, #3, #5, #7, #9, and #11 measuring points are selected for analysis. The results are shown in Figure 10.

Figure 10 shows that the frequency of fundamental wave in the #1 measuring point is near 21 Hz. When the vibration wave propagates in the filling material, the first harmonic is near 42 Hz, the second harmonic is near 63 Hz, the third harmonic is near 84 Hz, the fourth harmonic is near 105 Hz, and the fifth harmonic is stable at 130 Hz. At the same time, the dominant frequency of first harmonic is basic consistent, but that of the other harmonics gradually increase, as shown in Figure 11.

The above phenomenon may be for the reason that the density and stiffness of the filler gradually increase with the increase in the buried depth, which causes the high-frequency component of the vibration wave to gradually increase and the low-frequency component to appropriately lower, thereby causing the main frequency of the harmonic to gradually change to a high frequency, and the ratio of the amplitude of the harmonic wave to the fundamental wave is also gradually increasing.

4.3. Propagation Characteristics of Vibration Wave Energy in the Vertical Direction.

In order to accurately describe the propagation characteristics of vibration wave energy in the vertical direction as shown in Figure 12, the measured acceleration time-history curves at the monitoring points #1–#11 are selected to calculate the acceleration marginal spectrum at different depths, and the calculation results are shown in Figures 13 and 14.

Figures 13 and 14 show that the vibration wave energy is mainly concentrated near 10–30 Hz in the vibratory roller, which is basically consistent with the fundamental wave frequency. However, the peak values of marginal spectrum gradually change from one to two. The vibration wave energy is mainly concentrated near 30–50 Hz and 50–100 Hz, and the energy of signal gradually decreases with the increase in buried depth. The test phenomenon fully shows that the vibration energy in the frequency appears as large change with the increase in buried depth, and the percentage of higher harmonic energy in the total energy gradually increases. When the vibration energy is transmitted from the roller to the surface of the filler, the vibration energy is dissipated, and the transmission efficiency is low; therefore, how to improve the energy transfer efficiency is essential for energy saving and efficiency improvement.

4.4. Three-Dimensional Propagation Characteristics of Vibration Wave in Vertical Direction.

In order to fully describe the propagation characteristics of vibration wave in the vertical direction, the Hilbert–Huang spectrum at different buried depths is calculated by using Hilbert–Huang transform.

4.4.1. Introduction to Hilbert–Huang Transform.

The HHT transform is an autoadaptive time-frequency analysis method proposed by Norden E. Huang in 1998 for nonlinear and unstable signal processing, which mainly includes empirical mode decomposition and Hilbert spectrum analysis [14]. The EMD algorithm (Formula (1)) can decompose the complex vibration wave signal into multiple intrinsic mode functions IMF, and the distribution law of time-frequency-energy of each IMF signal can be obtained by HHT transform (Formula (2)), that is, Hilbert spectrum, and it is worth noting that the relevant parameters in equations (1) and (2) are found in [15]:

$$c_j(t) = \frac{1}{N} \sum_{i=1}^{N} c_{ij}(t). \tag{1}$$

$$H(w,t) = \text{Re} \sum_{i=1}^{n+1} a_i(t) \cdot e^j \int w_i(t) dt. \tag{2}$$

4.4.2. Empirical Mode Decomposition of Vibration Wave.

The measured acceleration time-history is selected to introduce. First, EMD is performed on the original wave, and several IMF signals and one residual moisture are obtained. IMF4, IMF5, and IMF6 are selected to illustrate the frequency component of measured acceleration time-history, as shown in Figures 15–17.
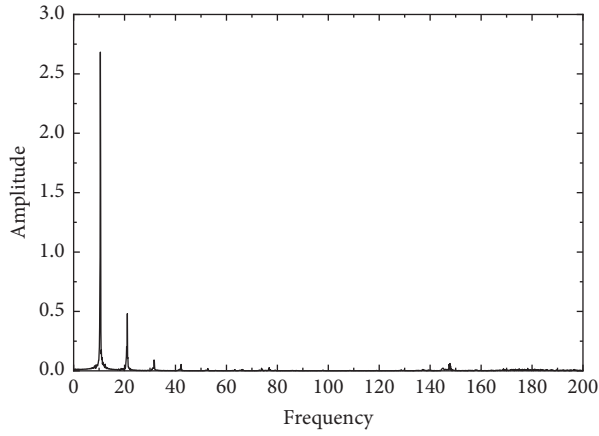
(a)
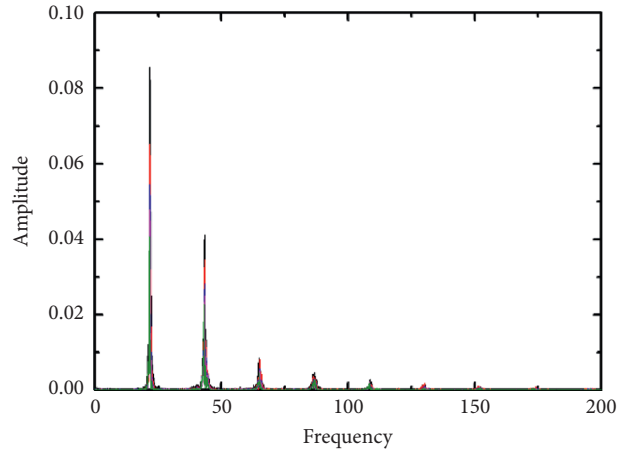
(b)

FIGURE 10: Distribution of Fourier spectrum in vertical direction: (a) Fourier spectrum of #1 measuring point; (b) Fourier spectrum of #3, #5, #7, #9, and #11 measuring points.
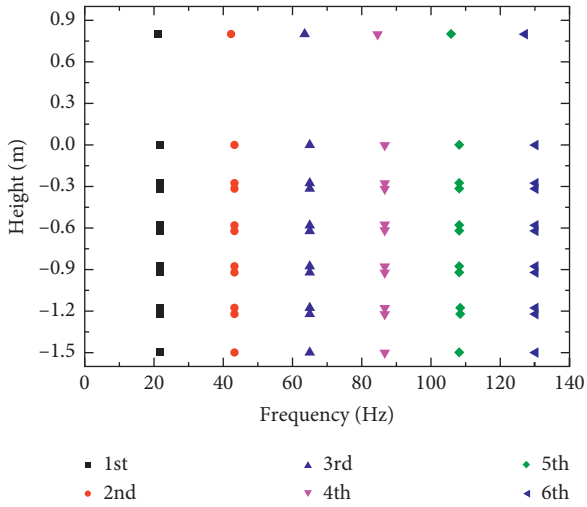
FIGURE 11: Evolution law of harmonic frequency along buried depth.
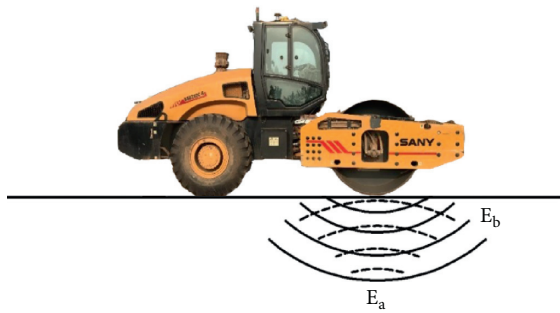
E_a — Compaction energy produced by vibratory roller
E_b — Compaction energy returned to vibratory roller

FIGURE 12: Energy interaction between vibratory roller and surface of filling material.
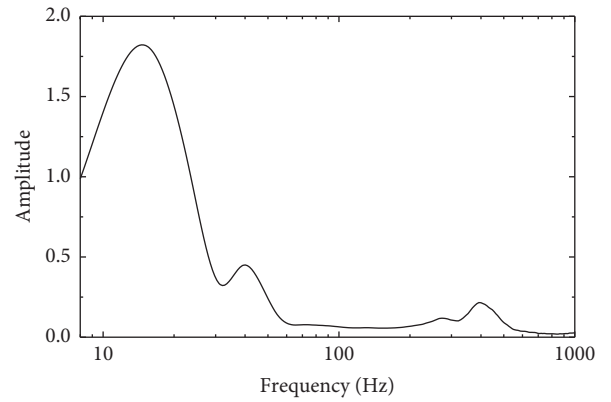
FIGURE 13: Distribution of vibration wave energy in vibrational wheel.
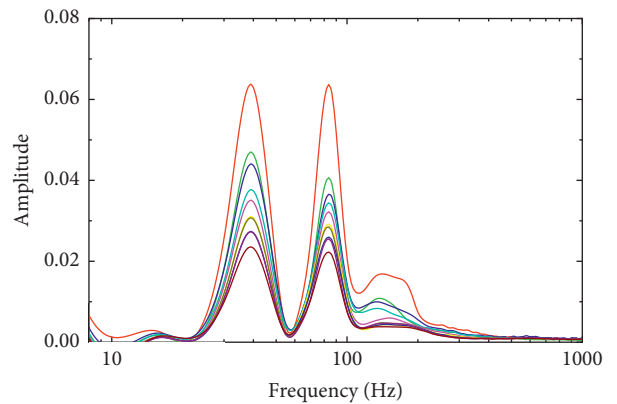
FIGURE 14: Distribution of vibration wave energy in different buried depths.
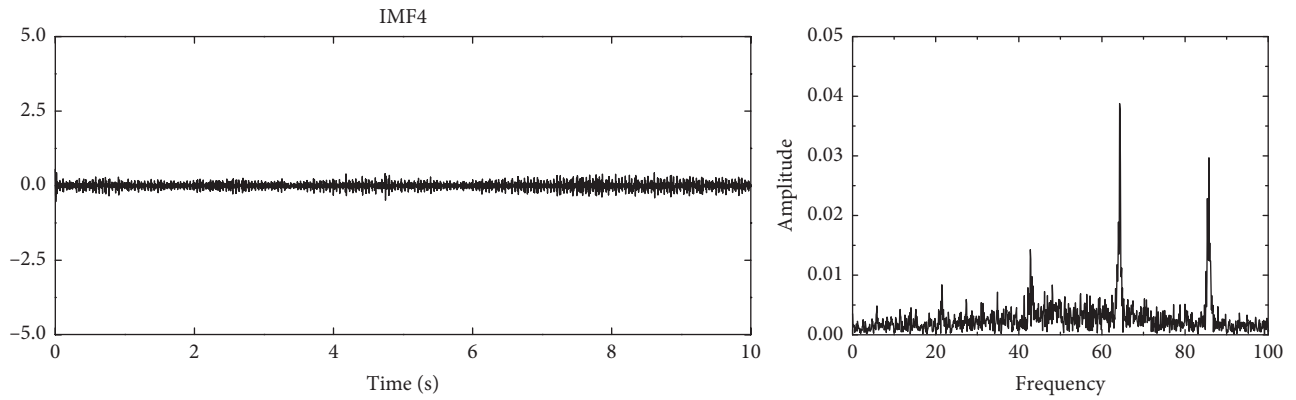
Figure 15: IMF4 and its FFT spectrum.
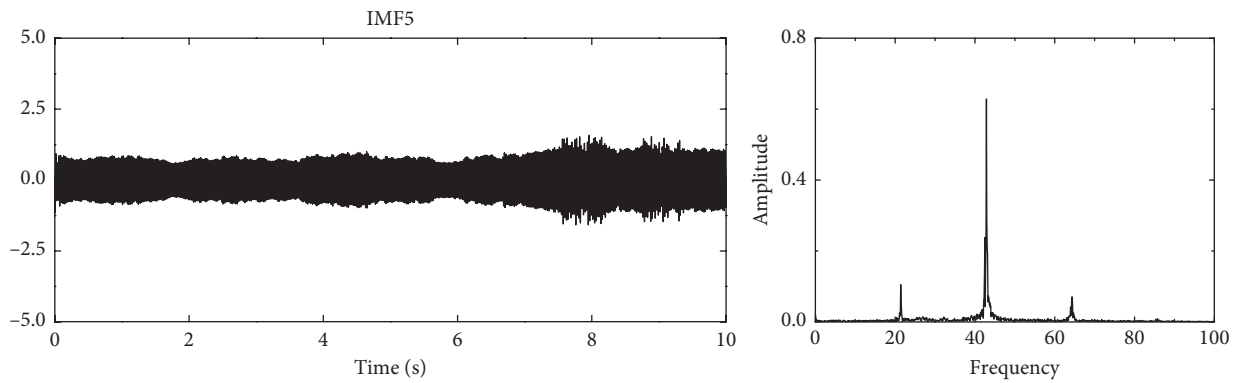
Figure 16: IMF5 and its FFT spectrum.
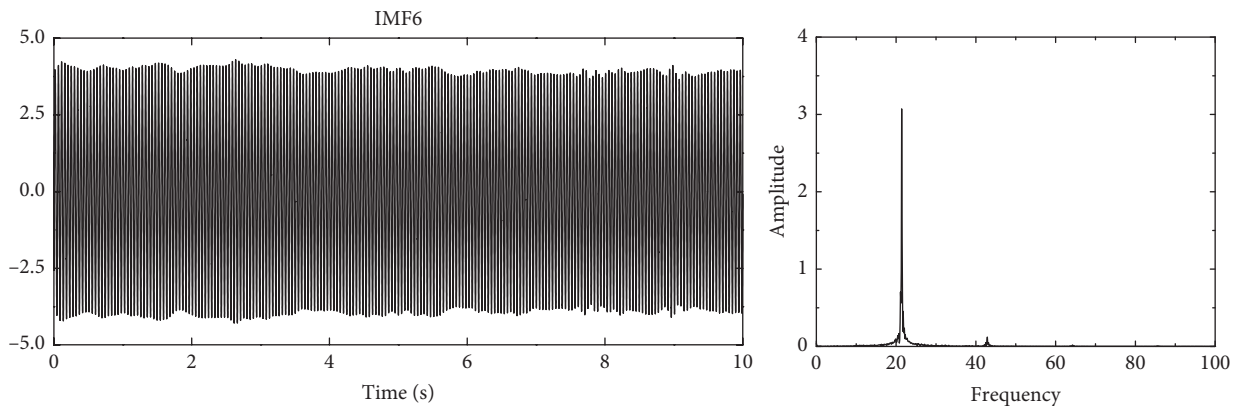
Figure 17: IMF6 and its FFT spectrum.

Among the abovementioned IMF components, the peak value of IMF6 is biggest. Its waveform and dominant frequency are consistent with that of original signal; IMF5 dominant frequency is the closest to the first harmonic. The frequencies with the largest amplitude of IMF4 are basically consistent with that of second and third harmonic waves of original vibration signal, and the remaining components are high-frequency or low-frequency interference signals. Therefore, the waveform of wheel is composed of IMF6, IMF5, and IMF4. To some extent, EMD can identify the fundamental and harmonic components of vibration signals and remove the mechanical and environmental noise interference.

(a)

(b)

FIGURE 18: Continued.

(c)
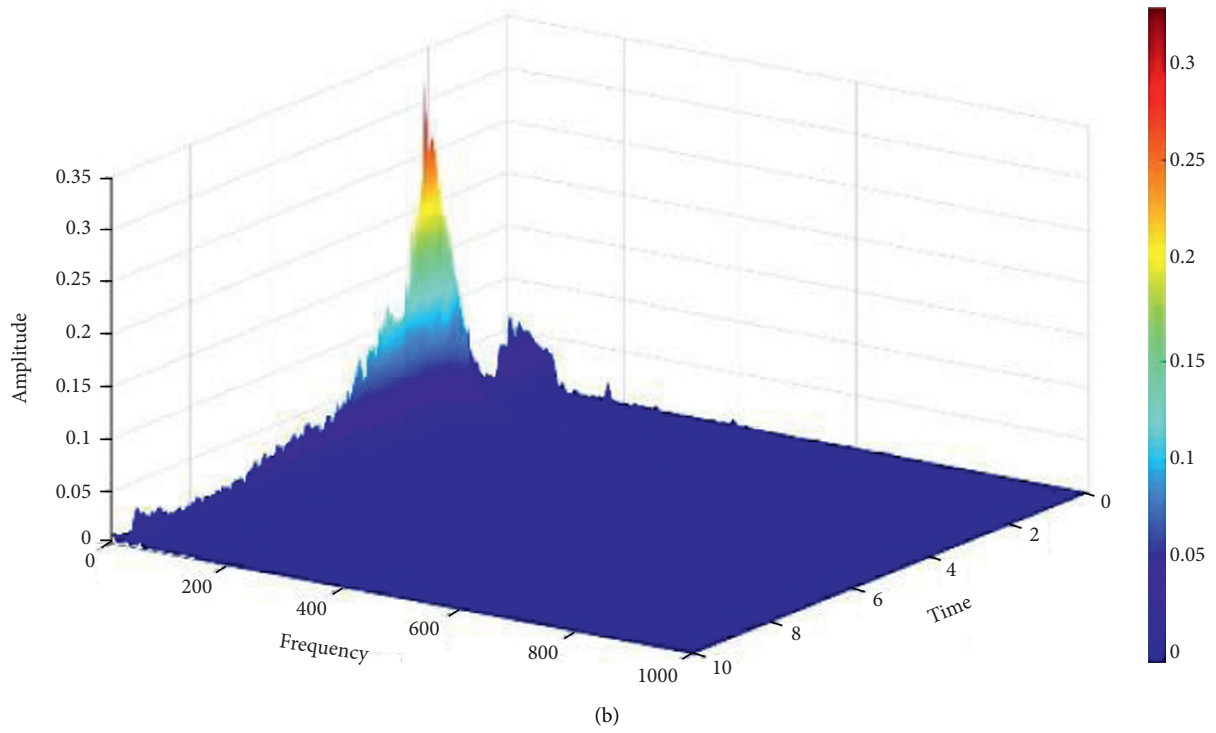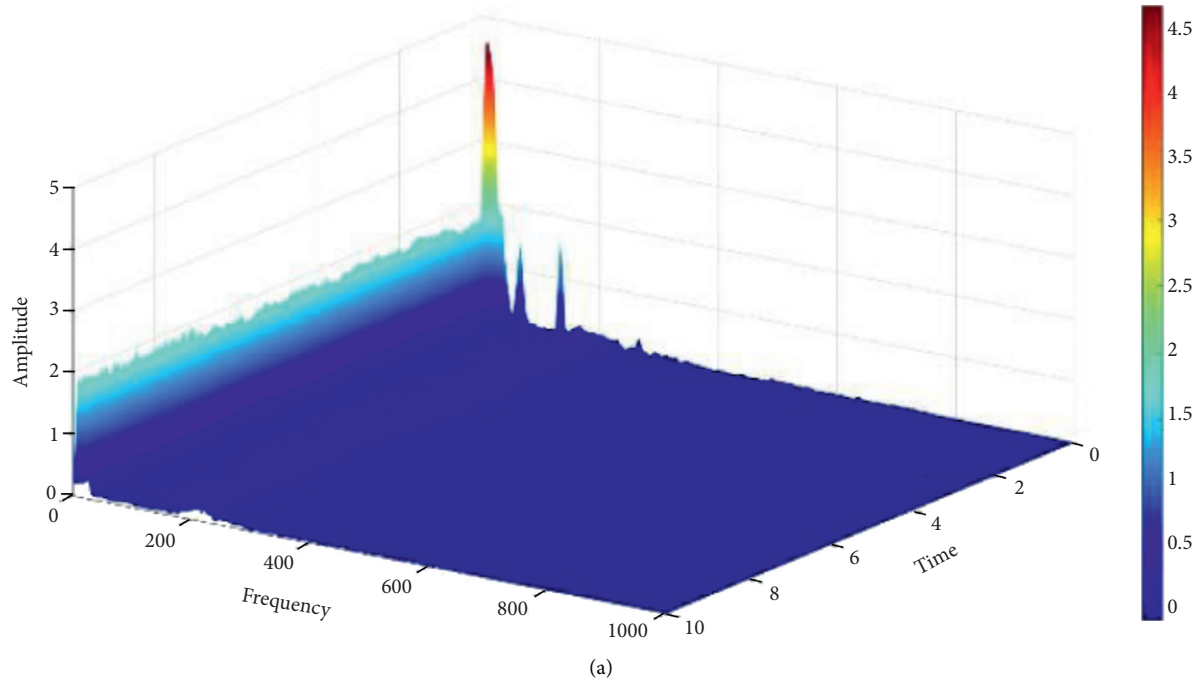
(d)

FIGURE 18: Continued.

(e)

(f)
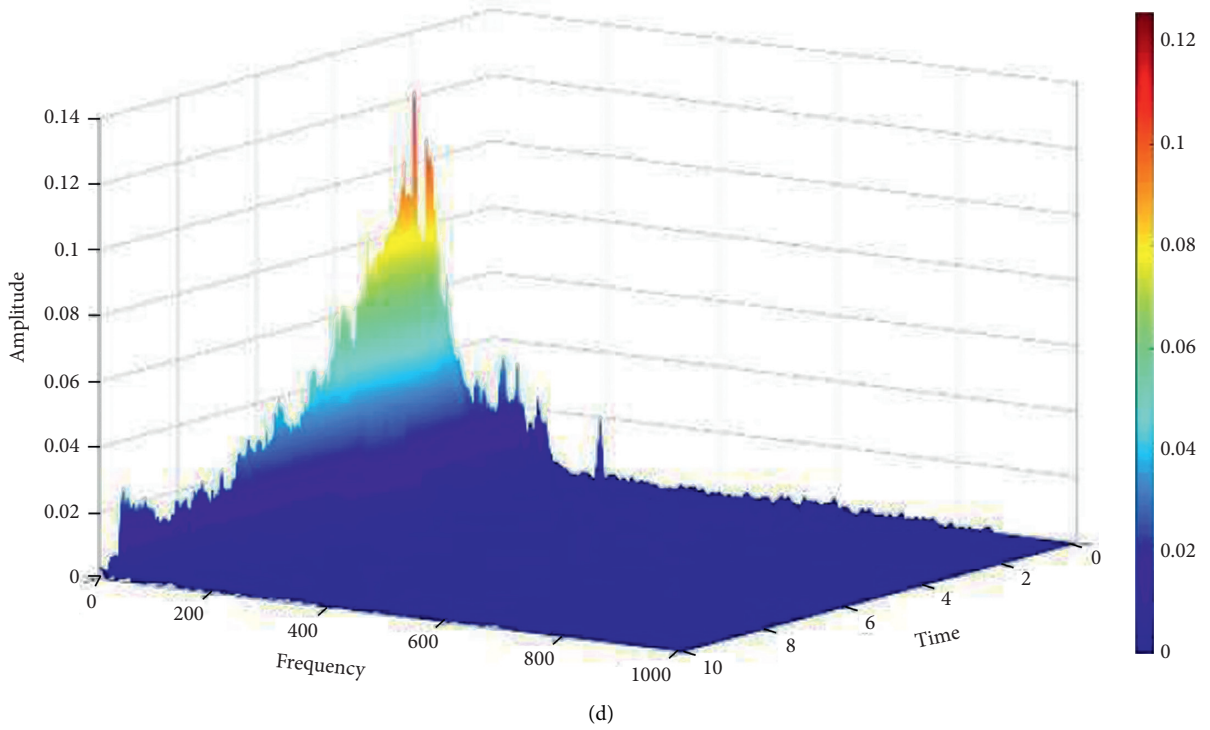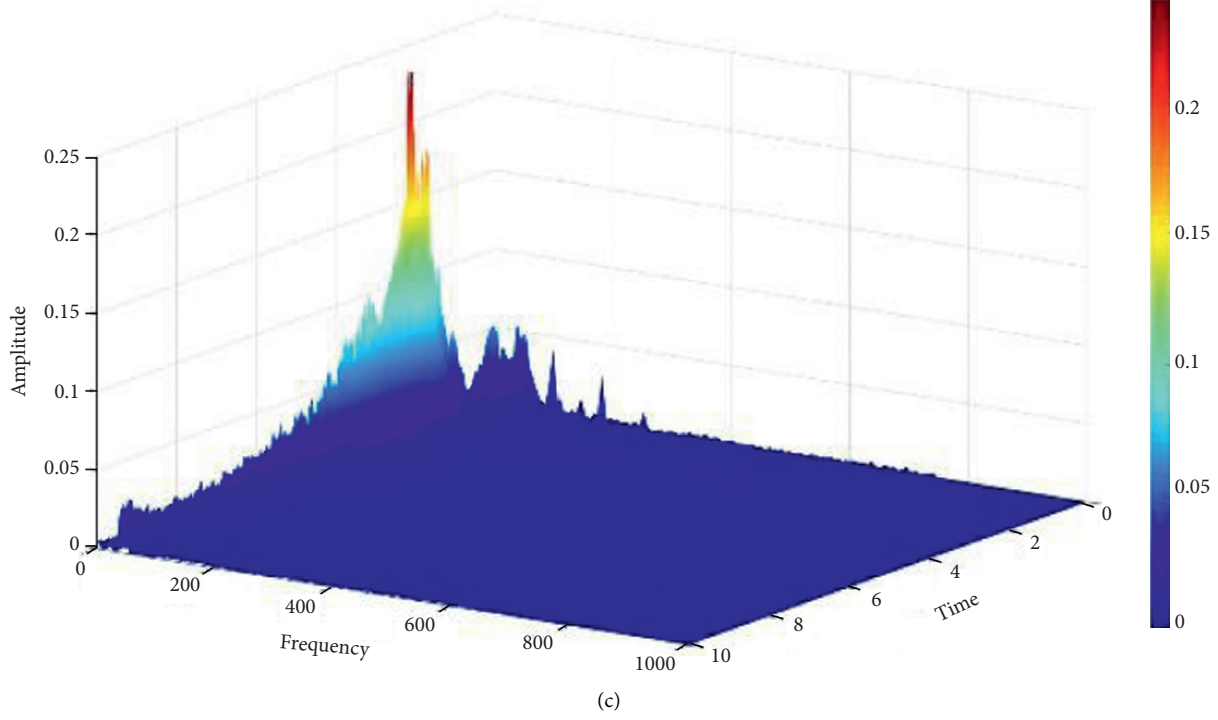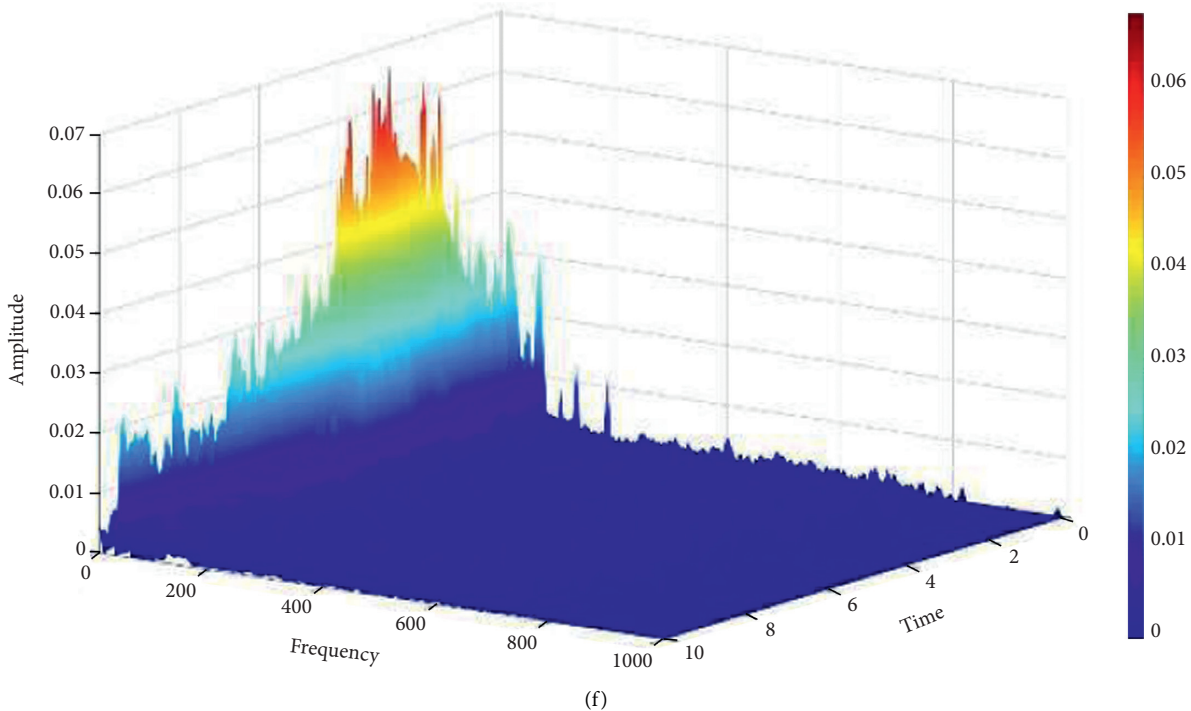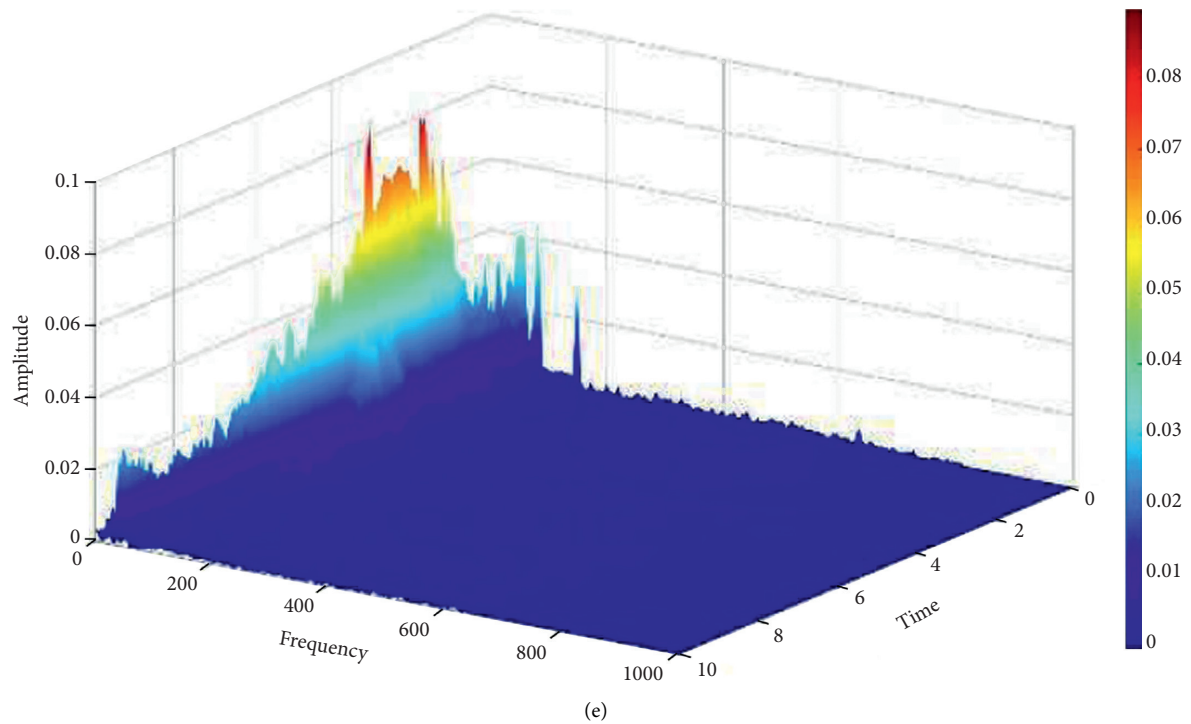
FIGURE 18: Hilbert–Huang spectrums at points (a) #1, (b) #3, (c) #5, (d) #7, (e) #9, and (f) #11.

4.4.3. Hilbert–Huang Spectrum of Vibrational Wave. In order to systematically analyze the propagation characteristics of Hilbert spectrum in the different buried depths, this paper selects the Hilbert–Huang spectrums of #1, #3, #5, #7, #9, and #11 measuring points, as shown in Figure 18.

Figure 18 shows that the vibration energy in the vibratory roller is distributed averagely in the compaction process, and the corresponding frequency is between 10 Hz and 30 Hz. The vibration energy in the subgrade filling mainly concentrates between $T = 2.0$ s and $T = 4.0$ s, and the corresponding frequency is between 30 Hz and 100 Hz. Therefore, the effective compaction time is two seconds. Consequently, the Hilbert spectrum of vibration wave signal can comprehensively and systematically reflect the spectral characteristics and time-domain characteristics of the signal at any time.
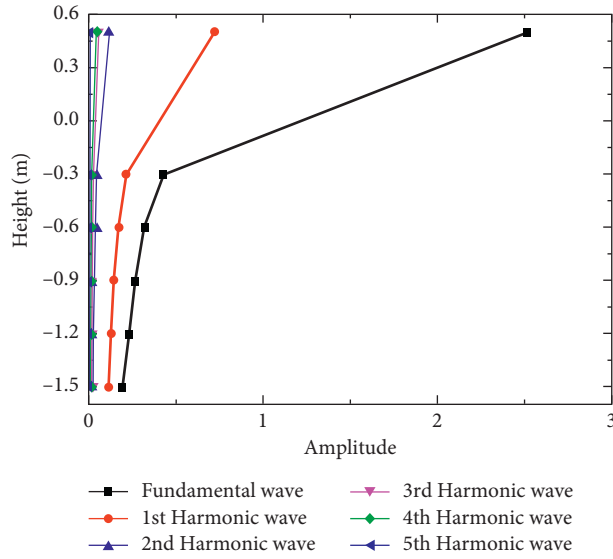
FIGURE 19: Different harmonic wave amplitudes in different buried depths.
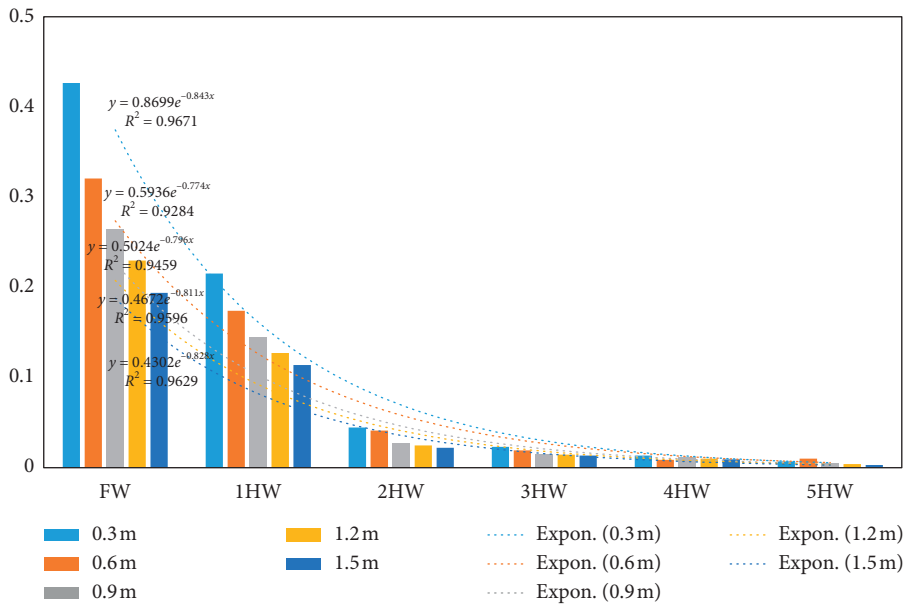
FIGURE 20: Concrete functional relationship among different amplitudes of harmonics.

4.5. Propagation Characteristics of Vibration Harmonic Wave in the Vertical Direction. In order to comprehensively study the propagation characteristics of vibration harmonic wave in the vertical direction, the frequency and amplitude of first, second, third, fourth, and fifth harmonic waves in the vertical direction are selected, as shown in Figures 19 and 20.

Figure 19 shows that, with the increase in buried depth, the amplitude of every harmonic gradually decreases. At the same time, the amplitude of fundamental, primary, secondary, until fifth harmonics decreases exponentially with the order of harmonic ($R^2 > 0.9$), and the attenuation models are shown in Figure 20. The concrete functional relationship among different amplitudes of harmonics can be summarized, as shown in $y = Ae^{-BX}$; in formula, A and B represent the coefficient, X represents the order of harmonic, and Y represents the amplitude of harmonic when its order is X.

5. Conclusion

Aiming at the shortages, one typical subgrade located at the Gu'an station of Beijing-Xiong'an city railway is selected to research and finish the field tests, and some research results are shown as follows.

First, when the vibration wave propagates from the vibratory roller $\longrightarrow$ surface of filling material $\longrightarrow$ different buried depths of filling material, the peak acceleration of vibration wave gradually decreases and is hyperbolic distribution approximately. At the same time, the sensitive of

attenuation is shown as follows: $Z < X \approx Y$, and the critical depth of vibration energy propagation is about 1.0 m. At the same time, the peak acceleration of vibration wave at the interface of different filling material layers exists in steps and is "side clock" distribution approximately with the increase in buried depth.

Second, in the propagation process, with the increase in buried depth, the amplitude of fundamental, primary, secondary, until fifth harmonics decreases exponentially ($R^2 > 0.9$), and the concrete functional relationship among different amplitudes of harmonics can be summarized as $y = Ae^{-BX}$.

Third, the vibration energy is mainly concentrated near 10–30 Hz in the vibratory roller, but when the vibration wave propagates from vibratory roller $\longrightarrow$ filling material, the vibration energy gradually decreases with the increase in depth, and the marginal spectrum gradually changes from one peak to two peaks that 30–50 Hz and 50–100 Hz; fourth, the waveform of vibratory roller is composed of IMF6, IMF5, and IMF4. At the same time, EMD can identify the fundamental and harmonic components of vibration signals and remove the mechanical and environmental noise interference. The vibration energy in the vibrational wheel is distributed averagely in the compaction process, and the effective compaction time is two seconds, which will be helpful for optimizing the compaction quality control models of railway subgrade.

Data Availability

The data used to support the findings of this study are available from the corresponding author upon request.

Conflicts of Interest

The authors declare that there are no conflicts of interest regarding the publication of this article.

Acknowledgments

References

[1] R. Anderegg and K. Kaufmann, "Intelligent compaction with vibratory rollers: feedback control systems in automatic compaction and compaction control," *Transportation Research Record: Journal of the Transportation Research Board*, vol. 1868, no. 1, pp. 124–134, 2004.

[2] L. Dong, D. Sun, X. Li, J. Ma, L. Zhang, and X. Tong, "Interval non-probabilistic reliability of surrounding jointed rockmass considering microseismic loads in mining tunnels," *Tunnelling and Underground Space Technology*, vol. 81, pp. 326–335, 2018.

[3] M. A. Mooney, *Intelligent Soil Compaction Systems*, Transportation Research Board, Washington, D. C., USA, 2010.

[4] D. Adam, "Roller-integrated continuous compaction control (CCC) Technical Contractual Provisions & Recommendations," *Design and Construction of Pavements and Rail Tracks*, vol. 10, pp. 111–138, 2007.

[5] S. A. Kumar, R. Aldouri, S. Nazarian et al., "Accelerated assessment of quality of compacted geomaterials with intelligent compaction technology," *Construction and Building Materials*, vol. 113, pp. 824–834, 2016.

[6] D. Liu, M. Lin, and S. Li, "Real-time quality monitoring and control of Highway compaction," *Automation in Construction*, vol. 62, pp. 114–123, 2016.

[7] L. Dong, X. Tong, X. Li, J. Zhou, S. Wang, and B. Liu, "Some developments and new insights of environmental problems and deep mining strategy for cleaner production in mines," *Journal of Cleaner Production*, vol. 210, pp. 1562–1578, 2019.

[8] M. A. Mooney and R. V. Rinehart, "Field monitoring of roller vibration during compaction of subgrade soil," *Journal of Geotechnical and Geoenvironmental Engineering*, vol. 133, no. 3, pp. 257–265, 2007.

[9] J. Pistrol, S. Villwock, W. Völkel, F. Kopf, and D. Adam, "Continuous compaction control (CCC) with Oscillating rollers," *Procedia Engineering*, vol. 143, pp. 514–521, 2016.

[10] M. Thompson and D. White, "Field calibration and Spatial analysis of compaction-monitoring technology measurements," *Journal of the Transportation Research Board*, vol. 2004, pp. 69–79, 2007.

[11] T. S. Yoo, *A Theory for Vibratory Compaction of Soils*, pp. 44–52, State university of New York at Buffalo, Buffalo, New York, USA, 1975.

[12] C. Herrera, P. Alves Costa, and B. Caicedo, "Numerical modelling and inverse analysis of continuous compaction control," *Transportation Geotechnics*, vol. 17, pp. 165–177, 2018.

[13] J. Xu, "Research on network structure and operation of logistics organization," Ph.D. thesis, Beijing Jiaotong University, Beijing, China, 2007.

[14] N. E. Huang, Z. Shen, S. R. Long et al., "The empirical mode decomposition and the Hilbert spectrum for nonlinear and non-stationary time series analysis," *Proceedings of the Royal Society of London. Series A: Mathematical, Physical and Engineering Sciences*, vol. 454, no. 1971, pp. 903–995, 1998.

[15] N. E. Huang, M.-L. C. Wu, S. R. Long et al., "A confidence limit for the empirical mode decomposition and Hilbert spectral analysis," *Proceedings of the Royal Society of London. Series A: Mathematical, Physical and Engineering Sciences*, vol. 459, no. 2037, pp. 2317–2345, 2003.

WILEY | Hindawi

Research Article

Global Existence of Solutions for the Viscoelastic Kirchhoff Equation with Logarithmic Source Terms

Nadia Mezouar,[1] Salah Mahmoud Boulaaras [ID],[2,3] and Ali Allahem[4]

[1]*Faculty of Sciences Economics, Mustapha Stambouli University, Mascara 29000, Algeria*
[2]*Department of Mathematics, College of Sciences and Arts, Qassim University, Al-Rass, Saudi Arabia*
[3]*Laboratory of Fundamental and Applied Mathematics of Oran (LMFAO), University of Oran 1, Oran, Algeria*
[4]*Department of Mathematics, College of Sciences, Qassim University, Buraydah, Saudi Arabia*

Correspondence should be addressed to Salah Mahmoud Boulaaras; s.boularas@qu.edu.sa

In this paper, a nonlinear viscoelastic Kirchhoff equation in a bounded domain with a time-varying delay term and logarithmic nonlinearity in the weakly nonlinear internal feedback is considered, where the global and local existence of solutions in suitable Sobolev spaces by means of the energy method combined with Faedo-Galerkin procedure is proved with respect to the condition of the weight of the delay term in the feedback and the weight of the term without delay and the speed of delay. Furthermore, a general stability estimate using some properties of convex functions is given. These results extend and improve many results in the literature.

1. Introduction

1.1. Model. In this paper, we consider the global existence and decay properties of solutions for the initial boundary value problem of the following viscoelastic nondegenerate Kirchhoff equation of the form:

$$
\begin{cases}
\left|u_t\right|^l u_{tt} - M\left(\|\nabla u\|^2\right)\Delta u - \Delta u_{tt} + \displaystyle\int_0^t h(t-s)\Delta u(s)\mathrm{d}s \\
\quad + \mu_1 g_1\left(u_t(x,t)\right) + \mu_2 g_2\left(u_t(x,t-\tau(t))\right) = \nu u \ln|u|, & \text{in } \Omega \times\ ]0,+\infty[, \\
u(x,t) = 0, & \text{on } \partial\Omega \times [0,+\infty[, \\
u(x,0) = u_0(x), u_t(x,0) = u_1(x), & \text{in } \Omega, \\
u_t(x,t-\tau(0)) = f_0(x,t-\tau(0)), & \text{in } \Omega \times\ ]0,\tau(0)[,
\end{cases}
\tag{1}
$$

where Ω is a bounded domain in $\mathbb{R}^n$, $n \in \mathbb{N}^*$, with a smooth boundary $\partial\Omega$, $l > 0$, ν, μ_1, and μ_2 are positive real numbers, h is a positive function which decays exponentially, $\tau(t) > 0$ is a time-varying delay, g_1 and g_2 are two functions, and the initial data (u_0, u_1, f_0) are in a suitable function space. $M(r) = a + br^\gamma$ is a C^1-function for $r \geq 0$, with $a, b > 0$ and $\gamma \geq 1$.

In the absence of delay term (i.e., $\mu_2 = 0$), Han and Wang in [1] considered the following nonlinear viscoelastic equation with damping:

$$|u_t|^l u_{tt} - \Delta u - \Delta u_{tt} + \int_0^t h(t-s)\Delta u(s)\mathrm{d}s$$
$$+ u_t(x,t) = 0, \text{ in } \Omega \times]0, +\infty[. \tag{2}$$

Time delay is often present in applications and practical problems. In recent years, the control of PDEs with time delay effects has become an active area of research (see, for example, [2–4]). For example, in [5], it has been proven that a small delay in a boundary control could turn a well-behaved hyperbolic system into a wild one, thus showing that delay can be a source of instability.

Wu [6] treated problem (1) for a constant time delay τ and $g_1(x) = g_2(x) = x$. He proved the local existence result using the Faedo-Galerkin method and established the decay result employing suitable Lyapunov functionals under appropriate conditions on μ_1 and μ_2 and on the kernel h.

Benaissa et al. [7] considered the case of constant time delay τ, with $l = 0$ and $M(r) = 1$. They proved the global existence and uniform decay for the following problem:

$$u_{tt} - \Delta u + \int_0^t h(t-s)\Delta u(s)\mathrm{d}s + \mu_1 g_1(u_t(x,t))$$
$$+ \mu_2 g_2(u_t(x, t - \tau)) = 0, \text{ in } \Omega \times]0, +\infty[. \tag{3}$$

The same problem (3) was also treated by Kirane and Said-Houari [8] for $g_1(x) = g_2(x) = x$ and a homogeneous right hand side with τ, a constant time delay. Daewook [9] considered a viscoelastic Kirchhoff equation, with a time-varying delay and a nonlinear source term, given as

$$u_{tt} - M\left(x, t, \|\nabla u\|^2\right)\Delta u + \int_0^t h(t-s)\mathrm{div}\left(a(x)\nabla u(s)\right)\mathrm{d}s + |u|^m u$$
$$+ \mu_1 u_t(x,t) + \mu_2 u_t(x, t - \tau(t)) = 0, \text{ in } \Omega \times]0, +\infty[, \tag{4}$$

This equation describes axially moving viscoelastic materials. Using the smallness condition with respect to Kirchhoff coefficient and the relaxation function and by assuming $0 \le m \le (2/(n-2))$ if $n > 2$ or $0 \le m$ if $n \le 2$, he obtained the uniform decay rate of the Kirchhoff-type energy.

In [10], the authors studied homogeneous problem (1) without the viscoelastic term, with $l = 0$ and $M(r) = 1$. In addition, $\mu_1 g_1$ and $\mu_2 g_2$ are multiplied by a positive non-increasing function σ of $C^1(R_+)$ satisfying $\int_0^{+\infty} \sigma(s)\mathrm{d}s = +\infty$ and $|\sigma'(t)| \le c\sigma(t)$. They proved the global existence, and using a multiplier method with some properties of convex functions to get decay rate of the energy (when t goes to infinity) depends on the function σ and on the function H which represents the growth at the origin of g_1.

Apart from the aforesaid attention given to polynomial nonlinear terms, logarithmic nonlinearity has also received a great deal of interest from both physicists and mathematicians. This type of nonlinearity was introduced in the nonrelativistic wave equations describing spinning particles moving in an external electromagnetic field and also in the relativistic wave equation for spinless particles [11]. Moreover, the logarithmic nonlinearity appears in several branches of physics such as inflationary cosmology [12], nuclear physics [13], optics [14], and geophysics [15]. With all this specific underlying meaning in physics, the global-in-time well-posedness of solution to the problem of evolution equation with such logarithmic-type nonlinearity captures lots of attention. Birula and Mycielski [16, 17] studied the following problem:

$$\begin{cases} u_{tt} - u_{xx} + u - \varepsilon u \ln|u|^2 = 0, & \text{in } [a, b] \times (0, T), \\ u(a, t) = u(b, t) = 0, & (0, T), \\ u(x, 0) = u_0(x), u_t(x, 0) = u_1(x), & \text{in } [a, b], \end{cases} \tag{5}$$

which is a relativistic version of logarithmic quantum mechanics and can also be obtained by taking the limit p goes to 1 for the p-adic string equation [18, 19]. In [20], Cazenave and Haraux considered

$$u_{tt} - \Delta u = u \ln |u|^k, \quad \text{in } \mathbb{R}^3, \tag{6}$$

and they established the existence and uniqueness of the solution for the Cauchy problem. Gorka [21] used some compactness arguments and obtained the global existence of weak solutions, for all

$$(u_0, u_1) \in H_0^1(\Omega) \times L^2([a, b]), \tag{7}$$

to initial boundary value problem (5) in the one-dimensional case. Bartkowski and Górka [22] proved the existence of classical solutions and investigated the weak solutions for the corresponding one-dimensional Cauchy problem for equation (6). Hiramatsu et al. [23] introduced the following equation:

$$u_{tt} - \Delta u + u + u_t + |u|^2 u = u \ln|u|, \tag{8}$$

to study the dynamics of Q-ball in theoretical physics and presented a numerical study. However, there was no theoretical analysis for the problem. In [24], Han proved the global existence of weak solutions, for all

$$(u_0, u_1) \in H_0^1(\Omega) \times L^2(\Omega), \tag{9}$$

to initial boundary value problem (8) in $\mathbb{R}^3$.

In the present paper, we investigate the stabilization of a dynamic model describing a string with a rigid surface and an interior somehow permissive to slight deformations. This leads to a varying material density $|u_t|^l$ and a Kirchhoff term $M(\|\nabla u\|^2)$ that depends on $\|\nabla u\|^2$. We prove the existence of global solutions in suitable Sobolev spaces by combining the energy method with the Fadeo-Galerkin procedure. We also establish an explicit and general decay result using a perturbed energy method with some techniques due to Mustafa and Messaoudi [25], as well as some properties of convex functions. These convexity arguments were introduced and developed by Lasiecka et al. [26–28] and used, with appropriate modifications, by Liu and Zuazua [29], Alabau-Boussouira [30], and others.

The paper is organized as follows: In Section 2, we give some hypotheses and state our main result. Then, in Section 3,

we prove the global existence of weak solutions. Furthermore, in Section 4, the uniform decay of the energy is derived.

1.2. Formulation of the Results. We denote by $(.,.)$ the inner product in $L^2(\Omega)$ and the corresponding norm by $\|.\|^2$. Now, we introduce, as in [31], the new variable:

$$z(x,\rho,t) = u_t(x,t-\rho\tau(t)), \quad x \in \Omega, \rho \in (0,1), t > 0. \tag{10}$$

Then, we have

$$\tau(t)z_t(x,\rho,t) + (1-\rho\tau'(t))z_\rho(x,\rho,t) = 0,$$
$$\text{in } \Omega \times (0,1) \times (0,+\infty). \tag{11}$$

Therefore, problem (1) is equivalent to

$$\begin{cases} |u_t|^l u_{tt} - M(\|\nabla u\|^2)\Delta u - \Delta u_{tt} + \int_0^t h(t-s)\Delta u(s)\mathrm{d}s \\ \quad + \mu_1 g_1(u_t(x,t)) + \mu_2 g_2(z(x,1,t)) = \nu u \ln|u| & \text{in } \Omega \times]0,+\infty[, \\ \tau(t)z_t(x,\rho,t) + (1-\rho\tau'(t))z_\rho(x,\rho,t) = 0, & \text{in } \Omega \times]0,1[\times]0,+\infty[, \\ u(x,t) = 0, & \text{on } \partial\Omega \times [0,\infty[, \\ z(x,0,t) = u_t(x,t), & \text{on } \Omega \times [0,\infty[, \\ u(x,0) = u_0(x), u_t(x,0) = u_1(x), & \text{in } \Omega, \\ z(x,\rho,0) = f_0(x,-\rho\tau(0)), & \text{in } \Omega \times]0,1[. \end{cases} \tag{12}$$

To state and prove our result, we need some assumptions.

(A1) Assume that l satisfies

$$\begin{cases} 0 < l \le \dfrac{2}{n-2}, & \text{if } n > 2, \\ 0 < l < \infty, & \text{if } n \le 2. \end{cases} \tag{13}$$

(A2) The relaxation function $h: \mathbb{R}_+ \longrightarrow \mathbb{R}_+$ is a bounded C^1 function, such that

$$a - \int_0^\infty h(s)\mathrm{d}s = k > 0, \quad h(0) > 0, \tag{14}$$

and suppose that there exists a positive constant ζ satisfying

$$h'(t) \le -\zeta h(t). \tag{15}$$

(A3) $g_1: \mathbb{R} \longrightarrow \mathbb{R}$ is a nondecreasing function of class C^1 and $H: \mathbb{R}_+ \longrightarrow \mathbb{R}_+$ is convex, increasing and of class $C^1(\mathbb{R}_+) \cap C^2(]0,+\infty[)$, satisfying

$$\begin{cases} H(0) = 0 \text{ and } H \text{ is linear}, & \text{on } [0,\varepsilon] \text{ or} \\ H'(0) = 0 \text{ and } H'' > 0, & \text{on }]0,\varepsilon] \text{ such that} \\ c_1|s| \le |g_1(s)| \le c_2|s|, & \text{if } |s| \ge \varepsilon \\ s^2 + g_1(s)^2 \le H^{-1}(sg_1(s)), & \text{if } |s| \le \varepsilon, \end{cases} \tag{16}$$

where $\varepsilon, c_1,$ and c_2 are positive constants. $g_2: \mathbb{R} \longrightarrow \mathbb{R}$ is an odd nondecreasing function of class $C^1(\mathbb{R})$ such that there exist $c_3, \alpha_1,$ and $\alpha_2 > 0$,

$$|g_2'(s)| \le c_3, \tag{17}$$

$$\begin{cases} \alpha_1 sg_2(s) \le G(s) \le \alpha_2 sg_1(s), \\ G(s) = \displaystyle\int_0^s g_2(r)\mathrm{d}r. \end{cases} \tag{18}$$

(A4) τ is a function in $W^{2,\infty}([0,T]), T > 0$, such that

$$\begin{cases} 0 < \tau_0 \le \tau(t) \le \tau_1, & \forall t > 0, \\ \tau'(t) \le d < 1, & \forall t > 0, \end{cases} \tag{19}$$

where τ_0 and τ_1 are positive numbers.

(A5) We also assume that

$$\mu_2 < \frac{\alpha_1(1-d)}{\alpha_2(1-\alpha_1 d)}\mu_1. \tag{20}$$

(A6)

$$1 < \nu < 2\pi k e^3. \tag{21}$$

We define the energy associated to the solution of system (12) by

$$E(t) = \frac{1}{l+2}\|u_t\|_{l+2}^{l+2} + \frac{b}{2(\gamma+1)}\|\nabla u\|^{2(\gamma+1)}$$

$$+ \frac{1}{2}\left(a - \int_0^t h(s)\mathrm{d}s\right)\|\nabla u\|^2 + \frac{1}{2}\|\nabla u_t\|^2$$

$$- \frac{\nu}{2}\int_\Omega u^2 \ln|u|\mathrm{d}x + \frac{\nu}{4}\|u\|^2 + \frac{1}{2}(h\circ\nabla u)(t) \tag{22}$$

$$+ \xi\tau(t)\int_\Omega \int_0^1 G(z(x,\rho,t))\mathrm{d}\rho\,\mathrm{d}x,$$

where ξ is a positive constant such that

$$\frac{\mu_2(1-\alpha_1)}{\alpha_1(1-d)} < \xi < \frac{\mu_1 - \alpha_2\mu_2}{\alpha_2}, \tag{23}$$

$$(hov)(t) = \int_0^t h(t-s)\|(v.,t) - v(.,s)\|^2 ds. \tag{24}$$

Theorem 1 (Global Existence). Let $(u_0, u_1, f_0) \in H^2(\Omega) \cap H_0^1(\Omega) \times H_0^1(\Omega) \times H_0^1((\Omega), H^1(0,1))$ satisfy the compatibility condition:

$$f_0(.,0) = u_1. \tag{25}$$

Assume that (A1)–(A6) hold under smallness condition on the initial data (u_0, u_1). Then, problem (1) admits a weak solution:

$$u \in L^\infty\big([0,\infty); H^2(\Omega) \cap H_0^1(\Omega)\big),$$

$$u_t \in L^\infty\big([0,\infty); H_0^1(\Omega)\big), u_{tt} \in L^\infty\big([0,\infty); L^2(\Omega)\big) \tag{26}$$

Theorem 2 (Uniform Decay Rates of Energy). Assume that (A1)–(A6) hold and if $E(0)$ is positive and bounded, then for every $t_0 > 0$, there exist positive constants w_1, w_2, w_3, and ε_0 such that the solution energy of (1) satisfies

$$E(t) \le w_3 H_1^{-1}(w_1 t + w_2), \quad \forall t \ge t_0, \tag{27}$$

where

$$H_1(t) = \int_t^1 \frac{1}{H_2(s)} ds, \tag{28}$$

$$H_2(t) = tH'(\varepsilon_0 t).$$

Here, H_1 is strictly decreasing and convex on $(0,1]$ with $\lim_{t\to 0} H_1(t) = +\infty$.

2. Preliminaries

Lemma 1 (Sobolev–Poincaré's Inequality). *Let q be a number with*

$$2 \le q \le +\infty \ (n = 1,2)$$

$$\text{or} \ \frac{2 \le q \le 2n}{((n-2)(n \ge 3))}. \tag{29}$$

Then, there exists a constant $C_s = C_s(\Omega, q)$ such that

$$\|u\|_q \le C_s \|\nabla u\|, \quad \text{for } u \in H_0^1(\Omega). \tag{30}$$

Lemma 2 (see [32, 33]) (Logarithmic Sobolev Inequality). *Let u be any function in $H_0^1(\Omega)$ and $\sigma > 0$ be any number. Then,*

$$\int_\Omega u^2 \ln|u| dx \le \frac{1}{2}\|u\|^2 \ln\|u\|^2 + \frac{\sigma^2}{2\pi}\|\nabla u\|^2 - (1+\ln\sigma)\|u\|^2. \tag{31}$$

Lemma 3 (see [20]) (Logarithmic Gronwall Inequality). *Let $C > 0$ and $\varphi \in L^1(0,T;\mathbb{R}^+)$ and assume that the function $w: [0,T] \longrightarrow [1,\infty)$ satisfies*

$$w(t) \le C\left(1 + \int_0^t \varphi(s)w(s)\ln(w(s))ds\right), \quad \forall t \in [0,T]. \tag{32}$$

Then,

$$w(t) \le C\exp\left(C\int_0^t \varphi(s)ds\right), \quad \forall t \in [0,T]. \tag{33}$$

Lemma 4. *Let $\epsilon_0 \in (0,1)$. Then, there exists $d_{\epsilon_0} > 0$ such that*

$$s|\ln s| \le s^2 + d_{\epsilon_0} s^{1-\epsilon_0}, \quad \forall s > 0. \tag{34}$$

Proof. Let $r(s) = s^{\epsilon_0}(|\ln s| - s)$. Notice that r is continuous on $(0,\infty)$, and its limit at 0^+ is 0^+ and its limit at ∞ is $-\infty$. Then, r has a maximum d_{ϵ_0} on $(0,\infty)$, so the proof is complete.

The following lemma states an important property of the convolution operator. $\square$

Lemma 5 (see [34]). *For $h, \varphi \in C^1([0,+\infty[, \mathbb{R})$, we have*

$$\int_\Omega (h*\varphi)\varphi_t dx = -\frac{1}{2}h(t)\|\varphi(t)\|^2 + \frac{1}{2}(h'o\varphi)(t)$$

$$- \frac{1}{2}\frac{d}{dt}\left[(ho\varphi)(t) - \left(\int_0^t h(s)ds\right)\|\varphi\|^2\right]. \tag{35}$$

Remark 1. Let us denote by Φ^* the conjugate function of the differentiable convex function Φ, i.e.,

$$\Phi^*(s) = \sup_{t\in\mathbb{R}^+}(st - \Phi(t)). \tag{36}$$

Then, Φ^* is the Legendre transform of Φ, which is given by (see Arnold [35], p. 61-62)

$$\Phi^*(s) = s\left(\Phi'^{-1}(s)\right) - \Phi\left[\left(\Phi'^{-1}(s)\right)\right], \quad \text{if } s \in (0, \Phi'(r)], \tag{37}$$

and Φ^* satisfies the generalized Young inequality:

$$AB \le \Phi^*(A) + \Phi(B), \quad \text{if } A \in (0, \Phi'(r)] B \in (0, r]. \tag{38}$$

Lemma 6. *Let (u, z) be a solution of problem (12). Then, the energy functional defined by (22) satisfies*

$$E'(t) \le -\lambda\int_\Omega u_t g_1(u_t)dx - \beta\int_\Omega z(x,1,t)g_2(z(x,1,t))dx$$

$$- \frac{1}{2}h(t)\|\nabla u(t)\|^2 + \frac{1}{2}(h'o\nabla u)(t) \le 0, \tag{39}$$

where $\lambda = \mu_1 - \xi\alpha_2 - \mu_2\alpha_2$ and $\beta = \xi(1-d)\alpha_1 - \mu_2(1-\alpha_1)$.

Proof. Multiplying the first equation in (12) by u_t, integrating over Ω, and using integration by parts, we get

$$\frac{\mathrm{d}}{\mathrm{d}t}\left[\frac{1}{l+2}\|u_t\|_{l+2}^{l+2} + \frac{b}{2(\gamma+1)}\|\nabla u\|^{2(\gamma+1)} + \frac{1}{2}a\|\nabla u\|^2 + \frac{1}{2}\|\nabla u_t\|^2\right.$$
$$-\frac{\gamma}{2}\int_\Omega |u|^2 \ln|u|\mathrm{d}x + \frac{\gamma}{4}\|u\|^2\right] + \int_\Omega \int_0^t h(t-s)\nabla u(s)\nabla u_t(t)\mathrm{d}s\,\mathrm{d}x$$
$$+\mu_1 \int_\Omega u_t(x,t)g_1(u_t(x,t))\mathrm{d}x + \mu_2 \int_\Omega u_t(x,t)g_2(z(x,1,t))\mathrm{d}x = 0. \tag{40}$$

Consequently, by applying Lemma 5, equation (40) becomes

$$\frac{\mathrm{d}}{\mathrm{d}t}\left[\frac{1}{l+2}\|u_t\|_{l+2}^{l+2} + \frac{b}{2(\gamma+1)}\|\nabla u\|^{2(\gamma+1)}\right.$$
$$+\frac{1}{2}\left(a - \int_0^t h(s)\mathrm{d}s\right)\|\nabla u\|^2 + \frac{1}{2}\|\nabla u_t\|^2 - \frac{\gamma}{2}\int_\Omega |u|^2 \ln|u|\mathrm{d}x$$
$$+\frac{\gamma}{4}\|u\|^2 + \frac{1}{2}(h\circ\nabla u)(t)\right] + \frac{1}{2}h(t)\|\nabla u(t)\|^2 - \frac{1}{2}(h'\circ\nabla u)(t)$$
$$+\mu_1 \int_\Omega u_t(x,t)g_1(u_t(x,t))\mathrm{d}x + \mu_2 \int_\Omega u_t(x,t)g_2(z(x,1,t))\mathrm{d}x = 0. \tag{41}$$

Multiplying the second equation in (12) by $\xi g_2(z)$ and integrating the result over $\Omega \times (0,1)$, we obtain

$$\xi\tau(t)\int_\Omega \int_0^1 z_t(x,\rho,t)g_2(z(x,\rho,t))\mathrm{d}\rho\,\mathrm{d}x$$
$$= -\xi\int_\Omega \int_0^1 (1-\rho\tau'(t))\frac{\partial}{\partial\rho}G(z(x,\rho,t))\mathrm{d}\rho\,\mathrm{d}x. \tag{42}$$

Consequently,

$$\frac{\mathrm{d}}{\mathrm{d}t}\left(\xi\tau(t)\int_\Omega \int_0^1 G(z(x,\rho,t))\mathrm{d}\rho\,\mathrm{d}x\right)$$
$$= \xi\tau'(t)\int_\Omega \int_0^1 G(z(x,\rho,t))\mathrm{d}\rho\,\mathrm{d}x$$
$$\quad -\xi\int_\Omega \int_0^1 (1-\rho\tau'(t))\frac{\partial}{\partial\rho}G(z(x,\rho,t))\mathrm{d}\rho\,\mathrm{d}x$$
$$= -\xi\int_\Omega \int_0^1 \frac{\partial}{\partial\rho}\left((1-\rho\tau'(t))G(z(x,\rho,t))\right)\mathrm{d}\rho\,\mathrm{d}x$$
$$= -\xi(1-\tau'(t))\int_\Omega G(z(x,1,t))\mathrm{d}x + \xi\int_\Omega G(u_t(x,t))\mathrm{d}x. \tag{43}$$

Combining (41) and (43), we obtain

$$E'(t) = -\xi(1-\tau'(t))\int_\Omega G(z(x,1,t))\mathrm{d}x$$
$$\quad +\xi\int_\Omega G(u_t(x,t))\mathrm{d}x - \frac{1}{2}h(t)\|\nabla u(t)\|^2$$
$$\quad +\frac{1}{2}(h'\circ\nabla u)(t) - \mu_1 \int_\Omega u_t(x,t)g_1(u_t(x,t))\mathrm{d}x$$
$$\quad -\mu_2 \int_\Omega u_t(x,t)g_2(z(x,1,t))\mathrm{d}x. \tag{44}$$

From (18) and (A4), we get

$$E'(t) \le -(\mu_1 - \xi\alpha_2)\int_\Omega u_t(x,t)g_1(u_t(x,t))\mathrm{d}x$$
$$\quad -\xi(1-d)\alpha_1 \int_\Omega z(x,1,t)g_2(z(x,1,t))\mathrm{d}x$$
$$\quad -\mu_2 \int_\Omega u_t(x,t)g_2(z(x,1,t))\mathrm{d}x - \frac{1}{2}h(t)\|\nabla u(t)\|^2$$
$$\quad +\frac{1}{2}(h'\circ\nabla u)(t). \tag{45}$$

Using (18) and Remark 1, we obtain

$$G^*(s) = sg_2^{-1}(s) - G(g_2^{-1}(s)), \quad \forall s \ge 0. \tag{46}$$

Hence,

$$G^*(g_2(z(x,1,t))) = z(x,1,t)g_2((x,1,t)) - G(z(x,1,t))$$
$$\le (1-\alpha_1)z(x,1,t)g_2(z(x,1,t)). \tag{47}$$

Using (18) and (38) with $A = g_2(z(x,1,t))$ and $B = u_t(x,t)$, we have from (45) that

$$E'(t) \le -(\mu_1 - \xi\alpha_2)\int_\Omega u_t(x,t)g_1(u_t(x,t))\mathrm{d}x$$
$$\quad -\xi(1-d)\alpha_1 \int_\Omega z(x,1,t)g_2(z(x,1,t))\mathrm{d}x$$
$$\quad +\mu_2 \int_\Omega \left(G(u_t(x,t)) + G^*(g_2(z(x,1,t)))\right)\mathrm{d}x$$
$$\quad -\frac{1}{2}h(t)\|\nabla u(t)\|^2 + \frac{1}{2}(h'\circ\nabla u)(t)$$
$$\le -(\mu_1 - \xi\alpha_2 - \mu_2\alpha_2)\int_\Omega u_t(x,t)g_1(u_t(x,t))\mathrm{d}x$$
$$\quad -(\xi(1-d)\alpha_1 - \mu_2(1-\alpha_1))\int_\Omega z(x,1,t)g_2(z(x,1,t))\mathrm{d}x$$
$$\quad -\frac{1}{2}h(t)\|\nabla u(t)\|^2 + \frac{1}{2}(h'\circ\nabla u)(t). \tag{48}$$

This completes the proof. □

3. Proof of Theorem 1

3.1. Local Existence. Throughout this section, we assume $u_0 \in H^2(\Omega) \cap H_0^1(\Omega)$, $u_1 \in H_0^1(\Omega)$ and $f_0 \in H_0^1(\Omega, H^1(0,1))$. We will use the Faedo-Galerkin method to prove the existence of a solution to problem (1). Let $T > 0$ be fixed and let $w^k, k \in \mathbb{N}$, be a basis of $H^2(\Omega) \cap H_0^1(\Omega)$, and let V_k be the space generated by $\{w^k\}$. Now, we define, for $1 \le j \le k$, the sequence $\phi^j(x,\rho)$ as follows:

$$\phi^j(x,0) = w^j. \tag{49}$$

Then, we may extend $\phi^j(x, 0)$ by $\phi^j(x, \rho)$ over $L^2(\Omega \times (0, 1))$ such that $(\phi^j)_j$ forms a basis of $L^2(\Omega, H^1(0, 1))$ and denote Z_k as the space generated by $\{\phi^k\}$. We construct approximate solutions (u^k, z^k), $k = 1, 2, 3, \ldots$, in the form

$$
\begin{aligned}
u^k(t) &= \sum_{j=1}^{k} c^{jk}(t) w^j, \\
z^k(t) &= \sum_{j=1}^{k} d^{jk}(t) \phi^j,
\end{aligned}
\tag{50}
$$

where c^{jk} and d^{jk} ($j = 1, 2, \ldots, k$) are determined by the following ordinary differential equations:

$$
\begin{cases}
\left(|u_t^k|^l u_{tt}^k, w^j\right) + M\left(\left\|\nabla u^k(t)\right\|^2\right)(\nabla u^k, \nabla w^j) + (\nabla u_{tt}^k, \nabla w^j) \\
\quad - \int_0^t h(t-s)(\nabla u^k(s), \nabla w^j) ds + \mu_1\left(g_1\left(u_t^k\right), w^j\right) \\
\quad + \mu_2\left(g_2\left(z^k(., 1)\right), w^j\right) = \nu \int_\Omega w^j u^k \ln|u^k| dx, \\
1 \le j \le k, \\
z^k(x, 0, t) = u_t^k(x, t),
\end{cases}
\tag{51}
$$

$$
\begin{aligned}
u^k(0) = u_0^k &= \sum_{j=1}^{k} (u_0, w^j) w^j \longrightarrow u_0, \\
&\text{in } H^2(\Omega) \cap H_0^1(\Omega) \text{ as } k \longrightarrow +\infty,
\end{aligned}
\tag{52}
$$

$$
\begin{aligned}
u_t^k(0) = u_1^k &= \sum_{j=1}^{k} (u_1, w^j) w^j \longrightarrow u_1, \\
&\text{in } H_0^1(\Omega) \text{ as } k \longrightarrow +\infty,
\end{aligned}
\tag{53}
$$

$$
\begin{cases}
\left(\tau(t) z_t^k\right) + \left(1 - \rho \tau_\rho^{'k}, \phi^j\right) = 0, \\
1 \le j \le k,
\end{cases}
\tag{54}
$$

$$
\begin{aligned}
z^k(\rho, 0) = z_0^k &= \sum_{j=1}^{k} (f_0, \phi^j) \phi^j \longrightarrow f_0, \\
&\text{in } H_0^1\left(\Omega, H^1(0, 1)\right) \text{ as } k \longrightarrow +\infty.
\end{aligned}
\tag{55}
$$

Noting that $(l/(2(l+1))) + (1/(2(l+1))) + (1/2) = 1$, from the generalized Hölder inequality, we obtain

$$
\begin{aligned}
\left(|u_t^k|^l u_t^k, w_j\right) &= \int_\Omega |u_t^k|^l u_{tt}^k w_j dx \\
&\le \left(\int_\Omega |u_t^k|^{2(l+1)} dx\right)^{(l/2(l+1))} \left\|u_{tt}^k\right\|_{2(l+1)} \left\|w_j\right\|_2.
\end{aligned}
\tag{56}
$$

Since (A1) holds, according to Sobolev, embedding the nonlinear term $(|u_t^k|^l u_{tt}^k, w_j)$ in (51) makes sense.

The standard theory of ODE guarantees that systems (51)–(55) have a unique solution in $[0, t_k)$, with $0 < t_k < T$, by Zorn lemma since the nonlinear terms in (51) are locally Lipschitz continuous. Note that $u^k(t)$ is of class C^2. In the next step, we obtain a priori estimate for the solution of

systems (51)–(55), so that it can be extended to $[0, T]$ and that the local solution is uniformly bounded independently of k and t.

3.1.1. The First Estimate. Since the sequences $u_0^k, u_1^k,$ and z_0^k converge and from Lemma 6, we can find a positive constant C_1 independent of k such that

$$
\begin{aligned}
E^k(t) - E^k(0) &\le -\lambda \int_0^t \int_\Omega u_t^k g_1\left(u_t^k\right) dx \, ds \\
&\quad - \beta \int_0^t \int_\Omega z^k(x, 1, s) g_2\left(z^k(x, 1, s)\right) dx \, ds \\
&\quad - \frac{1}{2} \int_0^t h(s) \left\|\nabla u^k(s)\right\|^2 ds + \frac{1}{2} \int_0^t \left(h' o \nabla u^k\right)(s) ds \\
&\le -\lambda \int_0^t \int_\Omega u_t^k g_1\left(u_t^k\right) dx \, ds \\
&\quad - \beta \int_0^t \int_\Omega z^k(x, 1, s) g_2\left(z^k(x, 1, s)\right) dx \, ds.
\end{aligned}
\tag{57}
$$

As h is a positive nonincreasing function, we get

$$
\begin{aligned}
&E^k(t) + \lambda \int_0^t \int_\Omega u_t^k g_1\left(u_t^k\right) dx \, ds \\
&\quad + \beta \int_0^t \int_\Omega z^k(x, 1, s) g_2\left(z^k(x, 1, s)\right) dx \, ds \le E^k(0) \le C_1,
\end{aligned}
\tag{58}
$$

where

$$
\begin{aligned}
E^k(t) &= \frac{1}{l+2} \left\|u_t^k\right\|_{l+2}^{l+2} + \frac{b}{2(\gamma+1)} \left\|\nabla u^k\right\|^{2(\gamma+1)} \\
&\quad + \frac{1}{2}\left(a - \int_0^t h(s) ds\right) \left\|\nabla u^k\right\|^2 + \frac{1}{2}\left\|\nabla u_t^k\right\|^2 + \frac{1}{2}\left(h o \nabla u^k\right)(t) \\
&\quad - \frac{\nu}{2} \int_\Omega |u^k|^2 \ln|u^k| dx + \frac{\nu}{4}\left\|u^k\right\|^2 \\
&\quad + \xi \tau(t) \int_\Omega \int_0^1 G\left(z^k(x, \rho, t)\right) d\rho \, dx.
\end{aligned}
\tag{59}
$$

By applying the Logarithmic Sobolev inequality, (58) yields

$$
\begin{aligned}
&\left\|u_t^k\right\|_{l+2}^{l+2} + \left(k - \frac{\nu \sigma^2}{2\pi}\right)\left\|\nabla u^k\right\|^2 + \left\|\nabla u_t^k\right\|^2 + \left[\frac{\nu}{2} + \nu(1 + \ln \sigma)\right]\left\|u^k\right\|^2 \\
&\quad + \left(h \circ \nabla u^k\right)(t) + \int_\Omega \int_0^1 G\left(z^k(x, \rho, t)\right) d\rho \, dx \\
&\quad + \int_0^t \int_\Omega u_t^k g_1\left(u_t^k\right) dx \, ds + \int_0^t \int_\Omega z^k(x, 1, s) g_2\left(z^k(x, 1, s)\right) dx \, ds \\
&\le C_2 + \left\|u^k\right\|^2 \ln\left\|u^k\right\|^2,
\end{aligned}
\tag{60}
$$

where C_2 is a positive constant depending only on $\|u_0\|_{H_0^1}, \|u_1\|_{H_0^1}, l, \gamma, \xi, \tau_1, \lambda$, and β.

By choosing

$$e^{(-3/2)} < \sigma < \sqrt{\frac{2\pi k}{\nu}}, \tag{61}$$

we obtain $k - (\nu\sigma^2/2\pi) > 0$ and $(\nu/2) + (\nu(1 + \ln\sigma)) > 0$.

This selection is possible thanks to (A6). So we get

$$
\begin{aligned}
& \left\|u_t^k\right\|_{l+2}^{l+2} + \left\|\nabla u^k\right\|^2 + \left\|\nabla u_t^k\right\|^2 + \left\|u^k\right\|^2 + \left(h \circ \nabla u^k\right)(t) \\
& + \int_\Omega \int_0^1 G\left(z^k(x,\rho,t)\right) d\rho\, dx + \int_0^t \int_\Omega u_t^k g_1\left(u_t^k\right) dx\, ds \\
& + \int_0^t \int_\Omega z^k(x,1,s) g_2\left(z^k(x,1,s)\right) dx\, ds \\
& \leq c\left(1 + \left\|u^k\right\|^2 \ln\left\|u^k\right\|^2\right).
\end{aligned}
\tag{62}
$$

Let us note that

$$u^k(t) = u^k(0) + \int_0^t u_s^k(s) ds. \tag{63}$$

Then, by using Cauchy Schwarz's inequality, we get

$$
\begin{aligned}
\left\|u^k\right\|^2 & \leq \left\|u^k(0)\right\|^2 + 2\left\|\int_0^t u_s^k(s) ds\right\|^2 \\
& \leq \left\|u^k(0)\right\|^2 + 2T \int_0^t \left\|u_s^k(s)\right\|^2 ds.
\end{aligned}
\tag{64}
$$

Hence, (62) gives

$$\left\|u^k\right\|^2 \leq C\left(1 + \int_0^t \left\|u^k\right\|^2 \ln\left\|u^k\right\|^2 ds\right), \tag{65}$$

where $C = \max\left\{2Tc, 2\|u^k(0)\|^2\right\}$. Applying the Logarithmic Gronwall inequality to (65), we obtain

$$\left\|u^k\right\|^2 \leq Ce^{CT}. \tag{66}$$

Hence, from (58), we obtain the first estimate:

$$
\begin{aligned}
& \left\|u_t^k\right\|_{l+2}^{l+2} + \left\|\nabla u^k\right\|^2 + \left\|\nabla u_t^k\right\|^2 + \left\|u^k\right\|^2 + \left(h \circ \nabla u^k\right)(t) \\
& + \int_\Omega \int_0^1 G\left(z^k(x,\rho,t)\right) d\rho\, dx + \int_0^t \int_\Omega u_t^k g_1\left(u_t^k\right) dx\, ds \\
& + \int_0^t \int_\Omega z^k(x,1,s) g_2\left(z^k(x,1,s)\right) dx\, ds \\
& \leq c\left(1 + Ce^{CT} \ln\left(Ce^{CT}\right)\right) = A_1,
\end{aligned}
\tag{67}
$$

The estimate implies that the solution (u^k, z^k) exists in $[0,T)$ and it yields

$$u^k \text{ is bounded in } L_{loc}^\infty\left(0,\infty,H^1(\Omega)\right), \tag{68}$$

$$u_t^k \text{ is bounded in } L_{loc}^\infty\left(0,\infty,H_0^1(\Omega)\right), \tag{69}$$

$$G\left(z^k(x,\rho,t)\right) \text{ is bounded in } L_{loc}^\infty\left(0,\infty,L^1(\Omega \times (0,1))\right), \tag{70}$$

$$u_t^k(t) g_1\left(u_t^k(t)\right) \text{ is bounded in } L^1(\Omega \times (0,T)), \tag{71}$$

$$z^k(x,1,t) g_2\left(z^k(x,1,t)\right) \text{ is bounded in}\left(L^1(\Omega \times (0,T))\right). \tag{72}$$

3.1.2. The Second Estimate. Replacing w^j by $-\Delta w^j$ in (51), multiplying by c_t^{jk}, and summing over j from 1 to k, it follows that

$$
\begin{aligned}
& \int_\Omega \left|u_t^k(t)\right|^l u_{tt}^k(t)\left(-\Delta u_t^k\right) dx + \int_\Omega M\left(\left\|\nabla u^k\right\|^2\right)\Delta u^k \Delta u_t^k dx \\
& + \int_\Omega \Delta u_{tt}^k \Delta u_t^k dx - \int_0^t h(t-s) \int_\Omega \Delta u^k \Delta u_t^k dx\, ds \\
& - \mu_1 \int_\Omega \Delta u_t^k g_1\left(u_t^k\right) dx - \mu_2 \int_\Omega \Delta u_t^k g_2\left(z^k(x,1,t)\right) dx \\
& = -\nu \int_\Omega \Delta u_t^k u^k \ln\left|u^k\right| dx.
\end{aligned}
\tag{73}
$$

Noting that $M\left(\|\nabla u^k\|^2\right) \geq a$ and by using Lemma 5, we obtain

$$
\begin{aligned}
& -\int_\Omega \left|u_t^k(t)\right|^l u_{tt}^k(t) \Delta u_t^k dx \\
& + \frac{1}{2}\frac{d}{dt}\left[\left(a - \int_0^t h(s) ds\right)\left\|\Delta u^k\right\|^2 + \left\|\Delta u_t^k\right\|^2 + \left(h \circ \Delta u^k\right)\right] \\
& + \frac{1}{2}h(t)\left\|\Delta u^k\right\|^2 - \frac{1}{2}\left(h' \circ \Delta u^k\right) + \mu_1 \int_\Omega \left|\nabla u_t^k\right|^2 g_1'\left(u_t^k\right) dx \\
& + \mu_2 \int_\Omega \nabla u_t^k \nabla z^k(x,1,t) g_2'\left(z^k(x,1,t)\right) dx \\
& \leq -\nu \int_\Omega \Delta u_t^k u^k \ln\left|u^k\right| dx.
\end{aligned}
\tag{74}
$$

By using the Green formula, we have

$$
\begin{aligned}
-\int_\Omega \left|u_t^k(t)\right|^l u_{tt}^k \Delta u_t^k dx = {} & \frac{d}{dt}\left[\int_\Omega \left|u_t^k(t)\right|^l \left|\nabla\left|u_t^{k2}\right|\right| dx\right] \\
& - (l+1) \int_\Omega \left|u_t^k(t)\right|^l \nabla u_{tt}^k \nabla u_t^k dx.
\end{aligned}
\tag{75}
$$

Consequently, equation (74) yields

$$
\begin{aligned}
& \frac{1}{2}\frac{d}{dt}\left[2\int_\Omega \left|u_t^k(t)\right|^l \left|\nabla u_t^k\right|^2 dx + \left(a - \int_0^t h(s) ds\right)\left\|\Delta u^k\right\|^2\right. \\
& \left. + \left\|\Delta u_t^k\right\|^2 + \left(h \circ \Delta u^k\right)\right] \\
& - (l+1) \int_\Omega \left|u_t^k(t)\right|^l \nabla u_{tt}^k \nabla u_t^k dx + \frac{1}{2}h(t)\left\|\Delta u^k\right\|^2 \\
& - \frac{1}{2}\left(h' \circ \Delta u^k\right) + \mu_1 \int_\Omega \left|\nabla u_t^k\right|^2 g_1'\left(u_t^k\right) dx + \\
& \mu_2 \int_\Omega \nabla u_t^k \nabla z^k(x,1,t) g_2'\left(z^k(x,1,t)\right) dx \\
& \leq -\nu \int_\Omega \Delta u_t^k u^k \ln\left|u^k\right| dx.
\end{aligned}
\tag{76}
$$

To estimate the term on the right-hand side of (76), we apply Lemma 4 with $\epsilon_0 = (1/2)$ and use repeatedly Young's, Cauchy-Schwartz's, and the embedding inequalities as follows:

$$
\begin{aligned}
\left| \nu \int_\Omega \Delta u_t^k u^k \ln |u^k| \mathrm{d}x \right| &\leq \nu \int_\Omega |\Delta u_t^k| \left(|u^k|^2 + \mathrm{d}_{\epsilon_0} \sqrt{|u^k|} \right) \mathrm{d}x \\
&\leq \nu \left(\eta \int_\Omega |\Delta u_t^k|^2 \mathrm{d}x + \frac{1}{4\eta} \int_\Omega \left(|u^k|^2 + \mathrm{d}_{\epsilon_0} \sqrt{|u^k|} \right)^2 \mathrm{d}x \right) \\
&\leq \nu \eta \int_\Omega |\Delta u_t^k|^2 \mathrm{d}x + \frac{c}{4\eta} \left(\int_\Omega |u^k|^4 \mathrm{d}x + \int_\Omega |u^k| \mathrm{d}x \right) \\
&\leq \nu \eta \|\Delta u_t^k\|^2 + \frac{c}{4\eta} \left(\|\nabla u^k\|^4 + \|u^k\| \right), \quad \eta > 0.
\end{aligned}
\tag{77}
$$

Combining (76) and (77) to have

$$
\begin{aligned}
&\frac{1}{2} \frac{\mathrm{d}}{\mathrm{d}t} \left[2 \int_\Omega |u_t^k(t)|^l |\nabla u_t^k|^2 \mathrm{d}x + \left(a - \int_0^t h(s) \mathrm{d}s \right) \|\Delta u^k\|^2 + \|\Delta u_t^k\|^2 + (h \circ \Delta u^k) \right] \\
&- (l+1) \int_\Omega |u_t^k(t)|^l \nabla u_{tt}^k \nabla u_t^k \mathrm{d}x + \frac{1}{2} h(t) \|\Delta u^k\|^2 - \frac{1}{2} (h' \circ \Delta u^k) + \mu_1 \int_\Omega |\nabla u_t^k|^2 g_1'(u_t^k) \mathrm{d}x \\
&+ \mu_2 \int_\Omega \nabla u_t^k \nabla z^k(x,1,t) g_2'(z^k(x,1,t)) \mathrm{d}x \leq \nu \eta \|\Delta u_t^k\|^2 + \frac{c}{4\eta} \left(\|\nabla u^k\|^4 + \|u^k\| \right).
\end{aligned}
\tag{78}
$$

Replacing ϕ^j by $-\Delta \phi^j$ in (54), multiplying by d^{jk}, and summing over j from 1 to k, it follows that

$$
\frac{\tau(t)}{1 - \tau'(t)\rho} \int_\Omega \nabla z_t^k \nabla z^k \mathrm{d}x + \int_\Omega \nabla z_\rho^k \nabla z^k \mathrm{d}x = 0.
\tag{79}
$$

Then, we get

$$
\begin{aligned}
&\frac{1}{2} \left[\frac{\mathrm{d}}{\mathrm{d}t} \left(\frac{\tau(t)}{1 - \tau'(t)\rho} \|\nabla z^k\|^2 \right) - \left(\frac{\tau(t)}{1 - \tau'(t)\rho} \right)' \|\nabla z^k\|^2 \right] \\
&+ \frac{1}{2} \frac{\mathrm{d}}{\mathrm{d}\rho} \|\nabla z^k\|^2 = 0.
\end{aligned}
\tag{80}
$$

We integrate over $(0,1)$, and we find

$$
\begin{aligned}
&\frac{1}{2} \frac{\mathrm{d}}{\mathrm{d}t} \int_0^1 \frac{\tau(t)}{1 - \tau'(t)\rho} \|\nabla z^k(x,\rho,t)\|^2 \mathrm{d}\rho + \frac{1}{2} \|\nabla z^k(x,1,t)\|^2 \\
&= \frac{1}{2} \int_0^1 \left(\frac{\tau(t)}{1 - \tau'(t)\rho} \right)' \|\nabla z^k(x,\rho,t)\|^2 \mathrm{d}\rho + \frac{1}{2} \|\nabla u_t^k(t)\|^2.
\end{aligned}
\tag{81}
$$

Combining (78) and (81) and using (A2), we get

$$
\begin{aligned}
&\frac{1}{2} \frac{\mathrm{d}}{\mathrm{d}t} \left[2 \int_\Omega |u_t^k(t)|^l |\nabla u_t^k|^2 \mathrm{d}x + \left(a - \int_0^t h(s) \mathrm{d}s \right) \|\Delta u^k\|^2 + \|\Delta u_t^k\|^2 + (h \circ \Delta u^k) \right. \\
&\left. + \int_0^1 \frac{\tau(t)}{1 - \tau'(t)\rho} \|\nabla z^k(x,\rho,t)\|^2 \mathrm{d}\rho \right] + \mu_1 \int_\Omega |\nabla u_t^k|^2 g_1'(u_t^k) \mathrm{d}x + \frac{1}{2} \|\nabla z^k(x,1,t)\|^2 \\
&\leq (l+1) \int_\Omega |u_t^k(t)|^l \nabla u_{tt}^k \nabla u_t^k \mathrm{d}x - \mu_2 \int_\Omega \nabla u_t^k \nabla z^k(x,1,t) g_2'(z^k(x,1,t)) \mathrm{d}x \\
&+ \frac{1}{2} \int_0^1 \left(\frac{\tau(t)}{1 - \tau'(t)\rho} \right)' \|\nabla z^k(x,\rho,t)\|^2 \mathrm{d}\rho + \frac{1}{2} \|\nabla u_t^k(t)\|^2 \\
&+ \nu \eta \|\Delta u_t^k\|^2 + \frac{c}{4\eta} \left(\|\nabla u^k\|^4 + \|u^k\| \right).
\end{aligned}
\tag{82}
$$

From the first estimate (67) and Young's inequality, we get

$$\int_\Omega \left| u_t^k \right|^l \nabla u_{tt}^k(t) \nabla u_t^k \mathrm{d}x \leq A_1^{(l/(l+2))+(1/2)} \left\| \nabla u_{tt}^k \right\|_2$$

$$\leq \eta \left\| \nabla u_{tt}^k \right\|^2 + \frac{A_1^{(2l/(l+2))+1}}{4\eta}. \tag{83}$$

Using (17) and Chaucy-Schwarz's inequality, we obtain

$$\left| \int_\Omega \nabla u_t^k \nabla z^k(x,1,t) g_2'\big(z^k(x,1,t)\big) \mathrm{d}x \right|$$

$$\leq c_3^2 \frac{\varepsilon}{2} \int_\Omega \left| \nabla u_t^k \right|^2 \mathrm{d}x + \frac{\varepsilon}{2} \int_\Omega \left| \nabla z^k(x,1,t) \right|^2 \mathrm{d}x. \tag{84}$$

Taking into account (83) and (84) into (82) yields

$$\frac{1}{2} \frac{\mathrm{d}}{\mathrm{d}t} 2 \int_\Omega \left| u_t^k(t) \right|^l \left| \nabla u_t^k \right|^2 \mathrm{d}x + \left(a - \int_0^t h(s) \mathrm{d}s \right) \left\| \Delta u^k \right\|^2 + \left\| \Delta u_t^k \right\|^2 + \big(ho\Delta u^k \big)$$

$$+ \int_0^1 \frac{\tau(t)}{1 - \tau'(t)\rho} \left\| \nabla z^k(x,\rho,t) \right\|^2 \mathrm{d}\rho \right] + \mu_1 \int_\Omega \left| \nabla u_t^k \right|^2 g_1'\big(u_t^k\big) \mathrm{d}x + c \left\| \nabla z^k(x,1,t) \right\|^2$$

$$\leq (l+1)\eta \left\| \nabla u_{tt}^k \right\|^2 + C_\eta' A_1 + \frac{1}{2} \int_0^1 \left(\frac{\tau(t)}{1 - \tau'(t)\rho} \right)' \left\| \nabla z^k(x,\rho,t) \right\|^2 \mathrm{d}\rho + c' \left\| \nabla u_t^k \right\|^2$$

$$+ v\eta \left\| \Delta u_t^k \right\|^2 + \frac{c}{4\eta} \Big(\|\theta\|^4 + \|u^k\| \Big). \tag{85}$$

Multiplying (51) by c_{tt}^{jk} and summing over j from 1 to k, it follows that

$$\int_\Omega \left| u_t^k \right|^l \left| u_{tt}^k \right|^2 \mathrm{d}x + \int_\Omega M\big(\left\| \nabla u^k \right\|^2 \big) \nabla u^k \nabla u_{tt}^k \mathrm{d}x + \left\| \nabla u_{tt}^k \right\|^2 - \int_0^t h(t-s) \int_\Omega \nabla u^k(s) \nabla u_{tt}^k(t) \mathrm{d}x \, \mathrm{d}s$$

$$+ \mu_1 \int_\Omega u_{tt}^k g_1\big(u_t^k\big) \mathrm{d}x + \mu_2 \int_\Omega u_{tt}^k g_2\big(z^k(x,1,t)\big) \mathrm{d}x = v \int_\Omega u_{tt}^k u^k \ln |u^k| \mathrm{d}x. \tag{86}$$

Then,

$$\int_\Omega \left| u_t^k \right|^l \left| u_{tt}^k \right|^2 \mathrm{d}x + \left\| \nabla u_{tt}^k \right\|^2 = - \int_\Omega M\big(\left\| \nabla u^k \right\|^2 \big) \nabla u^k \nabla u_{tt}^k \mathrm{d}x + \int_0^t h(t-s) \int_\Omega \nabla u^k(s) \nabla u_{tt}^k(t) \mathrm{d}x \, \mathrm{d}s$$

$$- \mu_1 \int_\Omega u_{tt}^k g_1\big(u_t^k\big) \mathrm{d}x - \mu_2 \int_\Omega u_{tt}^k g_2\big(z^k(x,1,t)\big) \mathrm{d}x + v \int_\Omega u_{tt}^k u^k \ln |u^k| \mathrm{d}x. \tag{87}$$

Differentiating (54) with respect to t, we get

$$\left(\left(\frac{\tau(t)}{1 - \rho\tau'(t)} \right)' z_t^k + \frac{\tau(t)}{1 - \rho\tau'(t)} z_{tt}^k + z_{t\rho}^k, \phi^j \right) = 0. \tag{88}$$

Multiplying by d_t^{jk} and summing over j from 1 to k, it follows that

$$\left(\frac{\tau(t)}{1 - \rho\tau'(t)} \right)' \left\| z_t^k \right\|^2 + \frac{1}{2} \frac{\tau(t)}{1 - \rho\tau'(t)} \frac{\mathrm{d}}{\mathrm{d}t} \left\| z_t^k \right\|^2 + \frac{1}{2} \frac{\mathrm{d}}{\mathrm{d}\rho} \left\| z_t^k \right\|^2 = 0. \tag{89}$$

Then, we have

$$\frac{1}{2} \left(\frac{\tau(t)}{1 - \rho\tau'(t)} \right)' \left\| z_t^k \right\|^2 + \frac{1}{2} \frac{\mathrm{d}}{\mathrm{d}t} \left(\frac{\tau(t)}{1 - \rho\tau'(t)} \left\| z_t^k \right\|^2 \right) + \frac{1}{2} \frac{\mathrm{d}}{\mathrm{d}\rho} \left\| z_t^k \right\|^2 = 0. \tag{90}$$

Integrating over $(0,1)$ with respect to ρ, we obtain

$$\frac{1}{2} \int_0^1 \left(\frac{\tau(t)}{1 - \rho\tau'(t)} \right)' \left\| z_t^k \right\|^2 \mathrm{d}\rho + \frac{1}{2} \frac{\mathrm{d}}{\mathrm{d}t} \int_0^1 \frac{\tau(t)}{1 - \rho\tau'(t)} \left\| z_t^k \right\|^2 \mathrm{d}\rho$$

$$+ \frac{1}{2} \left\| z_t^k(x,1,t) \right\|^2 - \frac{1}{2} \left\| u_{tt}^k(x,t) \right\|^2 = 0. \tag{91}$$

Summing (87) and (91), we get

$$\int_\Omega \left|u_t^k\right|^l \left|u_{tt}^k\right|^2 \mathrm{d}x + \left\|\nabla u_{tt}^k\right\|^2 + \frac{1}{2}\frac{\mathrm{d}}{\mathrm{d}t}\int_0^1 \frac{\tau(t)}{1-\rho\tau'(t)}\left\|z_t^k\right\|^2 \mathrm{d}\rho + \frac{1}{2}\left\|z_t^k(x,1,t)\right\|^2$$

$$= \frac{1}{2}\left\|u_{tt}^k(x,t)\right\|^2 - \frac{1}{2}\int_0^1 \left(\frac{\tau(t)}{1-\rho\tau'(t)}\right)'\left\|z_t^k\right\|^2 \mathrm{d}\rho - \int_\Omega M\left(\left\|\nabla u^k\right\|^2\right)\nabla u^k \nabla u_{tt}^k \mathrm{d}x$$

$$+ \int_0^t h(t-s)\int_\Omega \nabla u^k(s)\nabla u_{tt}^k(t)\mathrm{d}x\,\mathrm{d}s + \nu\int_\Omega u_{tt}^k u^k \ln\left|u^k\right|\mathrm{d}x - \mu_1\int_\Omega u_{tt}^k g_1\left(u_t^k\right)\mathrm{d}x$$

$$- \mu_2\int_\Omega u_{tt}^k g_2\left(z^k(x,1,t)\right)\mathrm{d}x. \tag{92}$$

By Cauchy-Schwarz's, Sobolev's, and Young's inequalities, the right hand side of (92) can be estimated as follows:

$$\left|\int_\Omega M\left(\left\|\nabla u^k\right\|^2\right)\nabla u^k \nabla u_{tt}^k \mathrm{d}x\right| \leq \left(a + b\left\|\nabla u^k\right\|^{2\gamma}\right)\int_\Omega \nabla u^k \nabla u_{tt}^k \mathrm{d}x$$

$$\leq \left(a + bE(0)^{(2\gamma/2(\gamma+1))}\right)\int_\Omega \nabla u^k \nabla u_{tt}^k \mathrm{d}x \tag{93}$$

$$\leq \eta\left\|\nabla u_{tt}^k\right\|^2 + \frac{m_0^2}{4\eta}\left\|\nabla u^k\right\|^2,$$

$$\left|\int_0^t h(t-s)\int_\Omega \nabla u^k(s)\nabla u_{tt}^k(t)\mathrm{d}x\,\mathrm{d}s\right| \leq \eta\left\|\nabla u_{tt}^k\right\|^2 + \frac{1}{4\eta}\int_\Omega\left(\int_0^t h(t-s)\nabla u^k(s)\mathrm{d}s\right)^2 \mathrm{d}x$$

$$\leq \eta\left\|\nabla u_{tt}^k\right\|^2 + \frac{1}{4\eta}\int_0^t h(s)\mathrm{d}s\int_\Omega\int_0^t h(t-s)\left|\nabla u^k(s)\right|^2 \mathrm{d}s\,\mathrm{d}x$$

$$\leq \eta\left\|\nabla u_{tt}^k\right\|^2 + \frac{1}{4\eta}(a-k)\int_\Omega\int_0^t h(t-s)\left|\nabla u^k(s)\right|^2 \mathrm{d}s\,\mathrm{d}x \tag{94}$$

$$\leq \eta\left\|\nabla u_{tt}^k\right\|^2 + \frac{1}{4\eta}(a-k)\int_0^t h(t-s)\left\|\nabla u^k(s)\right\|^2 \mathrm{d}s$$

$$\leq \eta\left\|\nabla u_{tt}^k\right\|^2 + \frac{1}{4\eta}(a-k)h(0)\int_0^t\left\|\nabla u^k(s)\right\|^2 \mathrm{d}s,$$

and from (16),

$$\left|\int_\Omega u_{tt}^k g_1\left(u_t^k\right)\mathrm{d}x\right| \leq \frac{1}{2}\int_\Omega\left|u_{tt}^k\right|^2 \mathrm{d}x + \frac{1}{2}\int_\Omega\left|g_1\left(u_t^k\right)\right|\mathrm{d}x$$

$$\leq \frac{1}{2}\int_\Omega\left|u_{tt}^k\right|^2 \mathrm{d}x + \frac{1}{2}\int_{\left|u_t^k\right|\geq\varepsilon}\left|g_1\left(u_t^k\right)\right|^2 \mathrm{d}x + \frac{1}{2}\int_{\left|u_t^k\right|\leq\varepsilon}\left|g_1\left(u_t^k\right)\right|^2 \mathrm{d}x \tag{95}$$

$$\leq \frac{1}{2}\int_\Omega\left|u_{tt}^k\right|^2 \mathrm{d}x + \frac{1}{2}\int_{\left|u_t^k\right|\geq\varepsilon} u_t^k g_1\left(u_t^k\right)\mathrm{d}x + \frac{1}{2}\int_\Omega H^{-1}\left(u_t^k g_1\left(u_t^k\right)\right)\mathrm{d}x.$$

Using Lemma 6, Jensen's inequality, and the concavity of H^{-1}, we obtain

$$
\left| \int_\Omega u_{tt}^k g_1(u_t^k) dx \right| \leq \frac{1}{2} \int_\Omega \left| u_{tt}^k \right|^2 dx + \frac{1}{2} \int_{|u_t^k| \geq \varepsilon} u_t^k g_1(u_t^k) dx + cH^{-1} \left(\int_\Omega u_t^k g_1(u_t^k) dx \right) + k \int_\Omega u_{tt}^k u^k \ln |u^k| dx
$$

$$
\leq \frac{1}{2} \int_\Omega \left| u_{tt}^k \right|^2 dx + \frac{1}{2} \int_{|u_t^k| \geq \varepsilon} u_t^k g_1(u_t^k) dx + c' H^*(1) + c'' \int_\Omega u_t^k g_1(u_t^k) dx
$$

$$
\leq \frac{1}{2} \left\| u_{tt}^k \right\|^2 dx + c' H^*(1) + c'' \int_\Omega u_t^k g_1(u_t^k) dx
$$

$$
\leq C_s \left\| \nabla u_{tt}^k \right\|^2 + c' H^*(1) + c(-E').
$$
(96)

From (17) (that is, $|g_2(s)| \leq c|s|, \forall s \in \mathbb{R}$), we get

$$
\left| \int_\Omega u_{tt}^k g_2(z^k(x,1,t)) dx \right|
$$

$$
\leq \frac{1}{2} \int_\Omega \left| u_{tt}^k \right|^2 dx + \frac{1}{2} \int_\Omega \left| g_2(z^k(x,1,t)) \right|^2 dx
$$

$$
\leq \frac{1}{2} \left\| u_{tt}^k \right\|^2 + c_3 \int_\Omega z^k(x,1,t) g_2(z^k(x,1,t)) dx
$$
(97)

$$
\leq C_s \left\| \nabla u_{tt}^k \right\|^2 + c'(-E').
$$

Similar to (77), we get

$$
\nu \int_\Omega u_{tt}^k u^k \ln |u^k| dx \leq c\eta \left\| \nabla u_{tt}^k \right\|^2 + \frac{c}{4\eta} \left(\left\| \nabla u^k \right\|^4 + \left\| u^k \right\| \right).
$$
(98)

Substituting (93)–(98) into (92) yields

$$
\int_\Omega |u_t^k|^l |u_{tt}^k|^2 dx + \left\| \nabla u_{tt}^k \right\|^2 + \frac{1}{2} \frac{d}{dt} \int_0^1 \frac{\tau(t)}{1 - \rho\tau'(t)} \left\| z_t^k \right\|^2 d\rho
$$

$$
+ \frac{1}{2} \left\| z_t^k(x,1,t) \right\|^2 \leq (2\eta + 3C_s) \left\| \nabla u_{tt}^k \right\|^2 +
$$

$$
+ \frac{m_0^2}{4\eta} \left\| \nabla u^k \right\|^2 + \frac{1}{4\eta} (a-k) h(0) \int_0^t \left\| \nabla u^k(s) \right\|^2 ds
$$

$$
+ c(-E') - \frac{1}{2} \int_0^1 \left(\frac{\tau(t)}{1 - \rho\tau'(t)} \right)' \left\| z_t^k \right\|^2 d\rho
$$

$$
+ c\eta \left\| \nabla u_{tt}^k \right\|^2 + \frac{c}{4\eta} \left(\left\| \nabla u^k \right\|^4 + \left\| u^k \right\| \right).
$$
(99)

Combining (85) and (99), we get

$$
\frac{1}{2} \frac{d}{dt} \left[2 \int_\Omega \left| u_t^k(t) \right|^l \left| \nabla u_t^k \right|^2 dx + \left(a - \int_0^t h(s) ds \right) \left\| \Delta u^k \right\|^2 + \left\| \Delta u_t^k \right\|^2 + (h o \Delta u^k) \right.
$$

$$
+ \int_0^1 \frac{\tau(t)}{1 - \tau'(t)\rho} \left\| \nabla z^k(x,\rho,t) \right\|^2 d\rho + \int_0^1 \frac{\tau(t)}{1 - \rho\tau'(t)} \left\| z_t^k \right\|^2 d\rho + cE(t) \right] + \int_\Omega \left| u_t^k \right|^l \left| u_{tt}^k \right|^2 dx
$$

$$
+ \frac{1}{2} \left\| z_t^k(x,1,t) \right\|^2 + (1 - (l+3)\eta - 3C_s) \left\| \nabla u_{tt}^k \right\|^2 + \mu_1 \int_\Omega \left| \nabla u_t^k \right|^2 g_1'(u_t^k) dx + c \left\| \nabla z^k(x,1,t) \right\|^2
$$
(100)

$$
\leq C_\eta' A_1 + \frac{1}{2} \int_0^1 \left(\frac{\tau(t)}{1 - \rho\tau'(t)} \right)' \left\| \nabla z^k(x,\rho,t) \right\|^2 d\rho + c' \left\| \nabla u_t^k \right\|^2 + \frac{m_0^2}{4\eta} \left\| \nabla u^k \right\|^2
$$

$$
+ c\eta \left\| \nabla u_{tt}^k \right\|^2 + \frac{c_4}{4\eta} \left(\left\| \nabla u^k \right\|^4 + \left\| u^k \right\| \right) + \nu\eta \left\| \Delta u_t^k \right\|^2.
$$

Then, from (67) and by integration over $(0, t)$, (100) yields

$$\left(a - \int_0^t h(s)\mathrm{d}s \right)\left\| \Delta u^k \right\|^2 + \left\| \Delta u_t^k \right\|^2 + \left(ho\Delta u^k \right) + \int_0^1 \frac{\tau(t)}{1 - \tau'(t)\rho}\left\| \nabla z^k(x, \rho, t) \right\|^2 \mathrm{d}\rho + \int_0^1 \frac{\tau(t)}{1 - \rho\tau'(t)}\left\| z_t^k \right\|^2 \mathrm{d}\rho$$

$$+ cE(t) + 2\int_\Omega \left| u_t^k(t) \right|^l \left| \nabla u_t^k \right|^2 \mathrm{d}x + 2\int_0^t \int_\Omega \left| u_t^k \right|^l \left| u_{tt}^k \right|^2 \mathrm{d}x\, \mathrm{d}s + c\int_0^t \left\| z_t^k(x, 1, t) \right\|^2 \mathrm{d}s$$

$$+ 2\left(1 - (l + 3 - c)\eta - 3C_s \right)\int_0^t \left\| \nabla u_{tt}^k \right\|^2 \mathrm{d}s + c_*\int_0^t \left\| \nabla z^k(x, 1, t) \right\|^2 \mathrm{d}s \tag{101}$$

$$\leq \left(C_\eta' A_1 + c' + \frac{m_0^2}{2\eta} + \frac{1}{2\eta}(a - k)h(0)T \right)T + E(0) + A_2 + \nu\eta\int_0^t \left\| \Delta u_t^k \right\|^2 \mathrm{d}s$$

$$+ c_*'' \int_0^t \int_0^1 \left(\frac{\tau(t)}{1 - \tau'(t)\rho} \right)' \left\| \nabla z^k(x, \rho, t) \right\|^2 \mathrm{d}\rho\, \mathrm{d}s + c'' \int_0^t \int_0^1 \left(\frac{\tau(t)}{1 - \rho\tau'(t)} \right)' \left\| z_t^k \right\|^2 \mathrm{d}\rho\, \mathrm{d}s.$$

For a suitable η, we get

$$\left\| \Delta u^k \right\|^2 + \left\| \Delta u_t^k \right\|^2 + \left(ho\Delta u^k \right) + \int_0^1 \frac{\tau(t)}{1 - \tau'(t)\rho}\left\| \nabla z^k(x, \rho, t) \right\|^2 \mathrm{d}\rho + \int_0^1 \frac{\tau(t)}{1 - \rho\tau'(t)}\left\| z_t^k \right\|^2 \mathrm{d}\rho + \int_0^t \left\| \nabla u_{tt}^k \right\|^2 \mathrm{d}s$$

$$\leq (C_\delta' A_1 + A_1')T + A_2' + c_*'' \int_0^t \int_0^1 \left(\frac{\tau(t)}{1 - \rho\tau'(t)} \right)' \left\| \nabla z^k(x, \rho, t) \right\|^2 \mathrm{d}\rho\, \mathrm{d}s \tag{102}$$

$$+ c'' \int_0^1 \left(\frac{\tau(t)}{1 - \rho\tau'(t)} \right)' \left\| z_t^k \right\|^2 \mathrm{d}\rho + c\int_0^t \left\| \Delta u_t^k \right\|^2 \mathrm{d}s.$$

Using Gronwall lemma, we obtain

$$\left\| \Delta u^k \right\|^2 + \left\| \Delta u_t^k \right\|^2 + \left(ho\Delta u^k \right) + \int_0^1 \frac{\tau(t)}{1 - \tau'(t)\rho}\left\| \nabla z^k(x, \rho, t) \right\|^2 \mathrm{d}\rho$$

$$+ \int_0^1 \frac{\tau(t)}{(1 - \rho\tau'(t))}\left\| z_t^k \right\|^2 \mathrm{d}\rho + \int_0^t \left\| \nabla u_{tt}^k \right\|^2 \mathrm{d}s \leq C_3. \tag{103}$$

We observe from the estimates (67) and (103) that there exists a subsequence $\{u^m\}$ of $\{u^k\}$ and functions u, z, χ, and ψ such that

$$u^m \rightharpoonup u \text{ weakly star in } L^\infty\left(0, T, H^2(\Omega) \cap H_0^1(\Omega) \right), \tag{104}$$

$$u_t^m \rightharpoonup u_t \text{ weakly star in } L^\infty\left(0, T, H_0^2(\Omega) \right), \tag{105}$$

$$g_1(u_t^m) \rightharpoonup \chi \text{ weakly star in } L^2\left(\Omega \times (0, T) \right), \tag{106}$$

$$u_{tt}^m \rightharpoonup u_{tt} \text{ weakly star in } L^2\left(0, T, H_0^1(\Omega) \right), \tag{107}$$

$$z^m \rightharpoonup z \text{ weakly star in } L^\infty\left(0, T, H_0^1(\Omega, L^2(0, 1)) \right), \tag{108}$$

$$z_t^m \rightharpoonup z_t \text{ weakly star in } L^\infty\left(0, T, L^2(\Omega \times (0, 1)) \right), \tag{109}$$

$$g_2(z^m(x, 1, t)) \rightharpoonup \psi \text{ weakly star in } L^2\left(\Omega \times (0, T) \right). \tag{110}$$

Now, we will prove that u is the solution of (1). First, we will treat the nonlinear terms.

(1) Term $|u_t^k|^l u_t^k$: from the first estimate (67) and Lemma 1, we deduce

$$\left\| |u_t^k|^l u_t^k \right\|_{L^2(0, T, L^2(\Omega))} = \int_0^T \left\| u_t^k \right\|_{2(l+1)}^{2(l+1)} \mathrm{d}t$$

$$\leq C_s^{2(l+1)} \int_0^T \left\| \nabla u_t^k \right\|^{2(l+1)} \mathrm{d}t \leq C_s^{2(l+1)} A_1^{2(l+1)} T. \tag{111}$$

On the other hand, from Aubin-Lions theorem (see Lions [36]), we deduce that there exists a subsequence of $\{u^m\}$, still denoted by $\{u^m\}$ such that

$$u_t^m \longrightarrow u_t \text{ strongly in } L^2\left(0, T, L^2(\Omega) \right), \tag{112}$$

which implies that

$$u_t^m \longrightarrow u_t \text{ almost everywhere in } \mathscr{A}. \tag{113}$$

Hence,

$$\left| u_t^m \right|^l u_t^m \longrightarrow \left| u_t \right|^l u_t \text{ almost everywhere in } \mathscr{A}, \tag{114}$$

where $\mathscr{A} = \Omega \times (0, T)$. Thus, using (117), (114), and Lions Lemma, we derive

$$|u_t^m|^l u_t^m \rightharpoonup |u_t|^l u_t \text{ weakly in } L^2\left(0, T, L^2\left(\Omega\right)\right), \qquad (115)$$

$$z^m \longrightarrow z \text{ strongly in } L^2\left(0, T, L^2\left(\Omega\right)\right), \qquad (116)$$

which implies $z^m \longrightarrow z$ almost everywhere in $\mathscr{A}$.

(2) Term $u^k \ln|u^k|$: using (103), we have $\{u^k\}$ being bounded in $L^\infty\left(0, T, H_0^2\left(\Omega\right)\right)$ which implies the boundedness of $\{u^k\}$ in $L^2\left(\mathscr{A}\right)$. Similarly, $\{u_t^k\}$ is bounded in $L^2\left(\mathscr{A}\right)$. Then, from Aubin-Lions theorem, we find a subsequence such that

$$u^m \longrightarrow u \text{ strongly in } L^2\left(\mathscr{A}\right), \qquad (117)$$

which implies

$$u^m \longrightarrow u \text{ almost everywhere in } \mathscr{A}. \qquad (118)$$

Since the map $s \longrightarrow \nu s \ln|s|$ is continuous, we have the following convergence:

$$\nu u^m \ln|u^m| \longrightarrow \nu u \ln|u| \text{ almost every where in } \mathscr{A}. \qquad (119)$$

Using the embedding of $H_0^1\left(\Omega\right)$ in $L^\infty\left(\Omega\right)$, it is clear that $\nu(u^m \ln|u^m|)$ is bounded in $L^\infty\left(\Omega \times (0, T)\right)$. Next, taking into account the Lebesgue bounded convergence theorem (Ω is bounded), we get

$$\nu u^m \ln|u^m| \longrightarrow \nu u \ln|u| \text{ strongly in } L^2\left(0, T; L^2\left(\Omega\right)\right). \qquad (120)$$

Lemma 7. *For each $T > 0$, $g_1(u_t), g_2(z(x, 1, t)) \in L^1\left(\mathscr{A}\right)$, and $\|g_1(u')\|_{L^1\left(\mathscr{A}\right)}, \|g_2(z(x, 1, t))\|_{L^1\left(\mathscr{A}\right)} \le K$, where K is a constant independent of t.*

Proof. By (A2) and (118), we have

$$g_1\left(u_t^m(x, t)\right) \longrightarrow g_1\left(u_t(x, t)\right) \text{ almost everywhere in } \mathscr{A},$$
$$0 \le u_t^k(x, t) g_1\left(u_t^m(x, t)\right) \longrightarrow u_t(x, t) g_1\left(u_t(x, t)\right)$$
$$\text{almost everywhere in } \mathscr{A}. \qquad (121)$$

Hence, by (71) and Fatou's Lemma, we have

$$\int_0^T \int_\Omega u_t(x, t) g_1\left(u_t(x, t)\right) dx dt \le K_1, \quad \text{for } T > 0. \qquad (122)$$

By using Cauchy-Schwarz's inequality, (96), and (122), we have

$$\int_0^T \int_\Omega |g_1\left(u_t(x, t)\right)| dx dt$$
$$\le c|\mathscr{A}|^{(1/2)} \left(\int_0^T \int_\Omega u_t(x, t) g_1\left(u_t(x, t)\right) dx dt\right)^{(1/2)}$$
$$\le c|\mathscr{A}|^{(1/2)} K_1^{(1/2)} \equiv K. \qquad (123)$$

$\square$

Lemma 8. *We have $g_1(u_t^k) \rightharpoonup g_1(u_t)$ weak in $L^2\left(\Omega \times (0, T)\right)$ and $g_2(z^k) \rightharpoonup g_2(z)$ weak in $L^2\left(\Omega \times (0, T)\right)$.*

Proof. Let $E \subset \Omega \times [0, T]$ and set

$$E_1 = \left\{(x, t) \in E, \left|g_1\left(u_t^k(x, t)\right)\right| \le \frac{1}{\sqrt{|E|}}\right\}, E_2 = \frac{E}{E_1}, \qquad (124)$$

where $|E|$ is the measure of E. If $M(r) = \inf\{|s|, s \in \mathbb{R} \text{ and } |g(s)| \ge r\}$,

$$\int_E |g_1\left(u_t^k\right)| dx dt \le c\sqrt{|E|} + \left(M\left(\frac{1}{\sqrt{|E|}}\right)\right)^{-1} \int_{E_2} |u_t^k g_1\left(u_t^k\right)| dx dt. \qquad (125)$$

By applying (71), we deduce that $\sup_k \int_E |g_1\left(u_t^k\right)| dx dt \longrightarrow 0$ as $|E| \longrightarrow 0$. From Vitali's convergence theorem, we deduce that

$$g_1\left(u_t^k\right) \longrightarrow g_1\left(u_t\right) \text{ in } L^1\left(\Omega \times (0, T)\right). \qquad (126)$$

Hence,

$$g_1\left(u_t^k\right) \rightharpoonup g_1\left(u_t\right) \text{ weak in } L^2\left(\Omega \times (0, T)\right). \qquad (127)$$

Similarly, we have

$$g_2\left(z^k\right) \rightharpoonup g_2\left(z\right) \text{ weak in } L^2\left(\Omega \times (0, T)\right). \qquad (128)$$

$\square$

Remark 2. By using (103) and from (104) and (105) combined with the Aubin-Lions compactness lemma, we deduce

$$\int_0^T \left(M\left(\left\|\nabla u^k(t)\right\|\right)^2 \Delta u^k(t), w\theta(t)\right) dt$$
$$\longrightarrow \int_0^T \left(M\|\nabla u(t)\|^2 \Delta u(t), w\right)\theta(t) dt, \quad \text{as } k \longrightarrow \infty. \qquad (129)$$

By multiplying (51) and (54) by $\theta(t) \in \mathscr{D}(0, T)$ and by integrating over $(0, T)$, it follows that

$$
\begin{cases}
\displaystyle\int_0^T \left(\left| u_t^k(t) \right|^l u_{tt}^k(t), w^j \right) \theta(t)\mathrm{d}t + \int_0^T \left(M\left(\left\| \nabla u^k(t) \right\|^2 \right) \left(\nabla u^k(t), \nabla w^j \right) \theta(t) \right) \mathrm{d}t \\[4mm]
\displaystyle\quad + \int_0^T \left(\nabla u_{tt}^k, \nabla w^j \right) \theta(t)\mathrm{d}t - \int_0^T \int_0^t h(t-s) \left(\nabla u^k(s), \nabla w^j \right) \theta(t)\mathrm{d}s\,\mathrm{d}t + \mu_1 \int_0^T \left(g_1\left(u_t^k \right), w^j \right) \theta(t)\mathrm{d}t \\[4mm]
\displaystyle\quad + \mu_2 \int_0^T \left(g_2\left(z^k(.,1) \right), w^j \theta(t) \right) \mathrm{d}t = \nu \int_0^T \left(u^k(s)\ln\left| u^k(s) \right|, w^j \right) \theta(t)\mathrm{d}t, \\[4mm]
\displaystyle\int_0^T \int_0^1 \int_\Omega \left(\tau(t) z_t^k + \left((1 - \rho\tau'(t)) z_\rho^k \right) \phi^j \right) \theta(t)\mathrm{d}x\,\mathrm{d}\rho\,\mathrm{d}t = 0,
\end{cases}
\tag{130}
$$

for all $j = 1, \ldots, k$.

The convergence of (104)–(110), (115), and (124)–(129) is sufficient to pass to the limit in (130) in order to obtain

$$
\int_0^T \int_\Omega \left(\left| u_t \right|^l u_{tt} - M\left(\| \nabla u(t) \|^2 \right) \Delta u - \Delta u_{tt} + \int_0^t h(t-s)\Delta u(s)\mathrm{d}s + \mu_1 g_1(u_t) \right.
$$

$$
\left. + \mu_2 g_2(z(.,1)) \right) w\theta(t)\mathrm{d}s\,\mathrm{d}t = \nu \int_0^T (u(s)\ln|u(s)|, w)\theta(t)\mathrm{d}t,
\tag{131}
$$

$$
\int_0^T \int_0^1 \int_\Omega \left(\tau(t) z_t + (1 - \rho\tau'(t)) z_\rho \right) \phi^j \theta(t)\mathrm{d}x\,\mathrm{d}\rho\,\mathrm{d}t = 0.
$$

Then, problem (1) has a weak solution on $[0, T]$, $T > 0$.

3.2. Global Existence.

To state and prove our global existence, we introduce the following functionals:

$$
I(t) = \left(a - \int_0^t h(s)\mathrm{d}s \right) \| \nabla u \|^2 + \left\| \nabla u_t \right\|^2 + (h \circ \nabla u)(t)
$$

$$
- 3\nu \int_\Omega u^2 \ln|u|\mathrm{d}x,
\tag{132}
$$

$$
J(t) = \frac{1}{2} \left(a - \int_0^t h(s)\mathrm{d}s \right) \| \nabla u \|^2 + \frac{1}{2} \left\| \nabla u_t \right\|^2 + \frac{1}{2} (h\circ\nabla u)(t)
$$

$$
\quad - \frac{\nu}{2} \int_\Omega u^2 \ln|u|\mathrm{d}x + \frac{\nu}{4} \| u \|^2
$$

$$
= \frac{1}{3} \left[\left(a - \int_0^t h(s)\mathrm{d}s \right) \| \nabla u \|^2 + \left\| \nabla u_t \right\|^2 \right.
$$

$$
\left. + (h\circ\nabla u)(t) \right] + \frac{\nu}{4} \| u \|^2 + \frac{1}{6} I(t).
\tag{133}
$$

We note that

$$
E(t) = \frac{1}{l+2} \| u_t \|_{l+2}^{l+2} + \frac{b}{2(\gamma+1)} \| \nabla u \|^{2(\gamma+1)} + J(t)
\tag{134}
$$

$$
\quad + \xi\tau(t) \int_\Omega \int_0^1 G(z(x,\rho,t))\mathrm{d}\rho\,\mathrm{d}x.
$$

Lemma 9. *The following inequalities hold:*

$$
-d_0 \sqrt{|\Omega| c_s^3 \| \nabla u \|}^{(3/2)} \leq \int_\Omega u^2 \ln|u|\mathrm{d}x \leq c_s^3 \| \nabla u \|^3,
\tag{135}
$$

$$
\forall u \in H_0^1(\Omega),
$$

where $d_0 = \sup_{0 < s < 1} \sqrt{s}|\ln s| = (2/e)$, $|\Omega|$ is the Lesbegue measure of Ω, and c_s is the smallest embedding constant:

$$
\| u \|_3 \leq c_s \| \nabla u \|, \quad \forall u \in H_0^1(\Omega).
\tag{136}
$$

Proof. Let $\Omega_1 = \{ x \in \Omega : |u| \leq 1 \}$ and $\Omega_2 = \{ x \in \Omega : |u_t| > 1 \}$. By using (136), we have

$$
\int_\Omega u^2 \ln|u|\mathrm{d}x = \int_{\Omega_1} u^2 \ln|u|\mathrm{d}x + \int_{\Omega_2} u^2 \ln|u|\mathrm{d}x
$$

$$
\leq \int_{\Omega_2} u^2 \ln|u|\mathrm{d}x \leq \int_{\Omega_2} |u|^3 \mathrm{d}x
\tag{137}
$$

$$
\leq \int_{\Omega_2} |u|^3 \mathrm{d}x \leq c_s^3 \| \nabla u \|^3.
$$

On the other hand, using Hölder's inequality and (136), we get

$$-\int_\Omega u^2 \ln|u| dx = -\int_{\Omega_1} u^2 \ln|u| dx - \int_{\Omega_2} u^2 \ln|u| dx$$

$$\leq -\int_{\Omega_1} u^2 \ln|u| dx = \int_{\Omega_1} u^2 |\ln|u|| dx$$

$$\leq d_0 \int_{\Omega_1} |u|^{(3/2)} dx \leq d_0 \sqrt{|\Omega|} \left(\int_{\Omega_1} |u|^3 dx\right)^{(1/2)}$$

$$\leq d_0 \sqrt{|\Omega| c_s^3} \|\nabla u\|^{(3/2)}.$$

$$(138)$$

Hence, (135) is obtained. □

Lemma 10. *Assume that (A1)–(A6) hold. Let* $(u_0, u_1) \in H^2(\Omega) \cap H_0^1(\Omega) \times H_0^1(\Omega)$ *such that*

$$I(0) > 0,$$

$$\sqrt{27} \nu c_s^3 \left(\frac{E(0)}{k}\right)^{(1/2)} \leq k. \qquad (139)$$

Then,

$$I(t) > 0, \quad \forall t \in [0, T). \qquad (140)$$

Proof. Since $I(0) > 0$ and I is continuous on $[0, T]$, there exists $t_* \in (0, T]$ such that $I(t) > 0$, for all $t \in [0, t_*]$. Let us denote by t_0 the largest real number in $(0, T]$ such that $I > 0$ on $[0, t_0)$. We assume by contradiction that $t_0 \neq T$, so we have $I(t_0) = 0$ and from (133), we have

$$\|\nabla u(t)\|^2 \leq \frac{3}{k} J(t) \leq \frac{3}{k} E(t) \leq \frac{3}{k} E(0), \quad \forall t \in [0, t_0). \quad (141)$$

The last inequality is obtained from Lemma 6. If $\|\nabla u(t_0)\|^2 = 0$, then (132) and (135) give

$$0 = I(t_0) = \left(a - \int_0^{t_0} h(s) ds\right) \|\nabla u(t_0)\|^2$$

$$+ \|\nabla u_t(t_0)\|^2 + (ho\nabla u)(t_0)$$

$$- 3\nu \int_\Omega u^2(t_0) \ln|u(t_0)| dx = (ho\nabla u)(t_0)$$

$$= \int_0^{t_0} h(s) \|\nabla u(s)\|^2 ds. \qquad (142)$$

Consequently, if $h > 0$ on $[0, t_0)$, we get

$$\|\nabla u(s)\|^2 = 0, \quad \forall s \in [0, t_0). \qquad (143)$$

Then,

$$I(t) = 0, \quad \forall s \in [0, t_0), \qquad (144)$$

which is not true since $I > 0$ on $[0, t_0)$. If there exists t^* in $[0, t_0)$ such that $h(t^*) = 0$, then let $t_1 \in [0, t_0)$ be the smallest real number such that $h(t_1) = 0$. Because $h(0) > 0$ and h is

positive, nonincreasing, and continuous on $\mathbb{R}_+$, then $t_1 > 0$ and $h = 0$ on $[t_1, +\infty)$. Therefore, from (142), we deduce that

$$0 = \int_0^{t_0} h(s) \|\nabla u(s)\|^2 ds = \int_0^{t_1} h(s) \|\nabla u(s)\|^2 ds. \qquad (145)$$

Then,

$$\|\nabla u(s)\|^2 = 0, \quad \forall s \in [0, t_1). \qquad (146)$$

As given above, we get a contradiction with the fact that $I > 0$ on $[0, t_0)$. Then, we conclude that $\|\nabla u(t_0)\|^2 > 0$. From (132), we have

$$I(t_0) \geq k \|\nabla u(t_0)\|^2 - 3\nu \int_\Omega |u(t_0)|^2 \ln|u(t_0)| dx. \qquad (147)$$

By using (135) and (141), we have

$$I(t_0) \geq \left(k - 3\nu \left(\frac{3}{k} E(0)\right)^{(1/2)}\right) \|\nabla u(t_0)\|^2. \qquad (148)$$

By recalling (139), we arrive at $I(t_0) > 0$, which contradicts the assumption that $I(t_0) = 0$. Hence, $t_0 = T$ and then $I > 0$ on $[0, T)$.

This completes the proof of Theorem 1. □

4. Uniform Decay of the Energy Proof of Theorem 2

In this section, we study the solution's asymptotic behavior of system (1).

To prove our main result, we construct a Lyapunov functional F equivalent to E. For this, we define some functionals which allow us to obtain the desired estimate.

Lemma 11. *Let* (u, z) *be a solution of problem (12). Then, the functional*

$$\chi(t) = \tau(t) \int_\Omega \int_0^1 e^{-2\tau(t)\rho} G(z(x, \rho, t)) d\rho \, dx \qquad (149)$$

satisfies the estimates

(i) $|\chi(t)| \leq \dfrac{1}{\xi} E(t)$,

(ii) $\chi'(t) \leq -2\tau(t) e^{-2\tau_1} \displaystyle\int_\Omega \int_0^1 G(z(x, \rho, t)) d\rho \, dx$

$$-\alpha_1(1-d) e^{-2\tau_1} \int_\Omega z(x, 1, t) g_2(z(x, 1, t)) dx$$

$$+\alpha_2 \int_\Omega u_t(x, t) g_1(u_t(x, t)) dx.$$

$$(150)$$

Proof.

(ii) Differentiating (149) with respect to t and using (16), (11), and (A4), we get

$$\frac{\mathrm{d}}{\mathrm{d}t}\chi(t) = \tau'(t)\int_\Omega \int_0^1 e^{-2\tau(t)\rho}\left(Gz(x,\rho,t)\right)\mathrm{d}\rho\,\mathrm{d}x$$

$$+ \tau(t)\int_\Omega \int_0^1 \left[e^{-2\tau(t)\rho}\frac{\partial G(z(x,\rho,t))}{\partial t} - 2\tau'(t)\rho e^{-2\tau(t)\rho}G(z(x,\rho,t))\right]\mathrm{d}\rho\,\mathrm{d}x$$

$$= \int_\Omega \int_0^1 e^{-2\tau(t)\rho}\left[\tau'(t)G(z(x,\rho,t)) + \tau(t)\frac{\partial G(z(x,\rho,t))}{\partial t}\right]\mathrm{d}\rho\,\mathrm{d}x$$

$$- 2\int_\Omega \int_0^1 \tau(t)\tau'(t)\rho e^{-2\tau(t)\rho}G(z(x,\rho,t))\mathrm{d}\rho\,\mathrm{d}x$$

$$= -\int_\Omega \int_0^1 e^{-2\tau(t)\rho}\frac{\partial}{\partial\rho}\left((1-\rho\tau'(t))G(z(x,\rho,t))\right)\mathrm{d}\rho\,\mathrm{d}x$$

$$- 2\int_\Omega \int_0^1 \tau(t)\tau'(t)\rho e^{-2\tau(t)\rho}G(z(x,\rho,t))\mathrm{d}\rho\,\mathrm{d}x$$

$$= -\int_\Omega \int_0^1 \left(\frac{\partial}{\partial\rho}\left(e^{-2\tau(t)\rho}\left(1-\tau'(t)\rho\right)G(z(x,\rho,t))\right)\right.$$

$$\left. +2\tau(t)e^{-2\tau(t)\rho}\left(1-\tau'(t)\rho\right)G(z(x,\rho,t))\right)\mathrm{d}\rho\,\mathrm{d}x$$

$$- 2\tau(t)\tau'(t)\int_\Omega \int_0^1 \rho e^{-2\tau(t)\rho}G(z(x,\rho,t))\mathrm{d}\rho\,\mathrm{d}x$$

$$= \int_\Omega G(u_t(x,t))\mathrm{d}x - e^{-2\tau(t)}(1-\tau'(t))\int_\Omega G(z(x,1,t))\mathrm{d}x \qquad (151)$$

$$- 2\tau(t)\int_\Omega \int_0^1 [(1-\tau'(t)\rho) + \tau'(t)]\rho e^{-2\tau(t)\rho}G(z(x,\rho,t))\mathrm{d}\rho\,\mathrm{d}x$$

$$\leq -2\chi(t) + \alpha_2\int_\Omega u_t(x,t)g_1(u_t(x,t))\mathrm{d}x$$

$$- e^{-2\tau(t)}(1-d)\alpha_1\int_\Omega z(x,1,t)g_2(z(x,1,t))\mathrm{d}x.$$

Since $e^{-2\tau(t)\rho}$ is a decreasing function for $\rho \in [0,1]$ and $\tau(t) \in [\tau_0, \tau_1]$, we deduce

$$\chi(t) \geq \tau(t)\int_\Omega \int_0^1 e^{-2\tau_1}G(z(x,\rho,t))\mathrm{d}\rho\,\mathrm{d}x. \qquad (152)$$

Thus, our proof is completed.

$\square$

Lemma 12. *Let (u,z) be a solution of problem (12). Then, the functional*

$$\phi(t) = \frac{1}{l+1}\int_\Omega |u_t|^l u_t u\,\mathrm{d}x + \int_\Omega \nabla u_t \nabla u\,\mathrm{d}x \qquad (153)$$

satisfies the estimates

$$(\mathrm{i})\ |\phi(t)| \leq \frac{1}{l+2}\|u_t\|_{l+2}^{l+2} + \left(\frac{(l+1)^{-1}}{(l+2)}c_s^{l+2}\left(\frac{2E(0)}{a}\right)^{(l/2)} + \frac{1}{2}\right)\|\nabla u\|^2 + \frac{1}{2}\|\nabla u_t\|^2,$$

$$(\mathrm{ii})\ \phi'(t) \leq \frac{1}{l+1}\|u_t\|_{l+2}^{l+2} - \mathrm{Ma}\left(\|\nabla u\|^2\right)\|\nabla u\|^2 + (1+\eta)(a-k)\|\nabla u\|^2 \qquad (154)$$

$$+ \frac{1}{4\eta}(ho\nabla u)(t) + \|\nabla u_t\|^2 - \mu_1\int_\Omega u(x,t)g_1(u_t(x,t))\mathrm{d}x$$

$$- \mu_2\int_\Omega u(x,t)g_2(z(x,1,t))\mathrm{d}x + \nu\int_\Omega u^2\ln|u|\mathrm{d}x,$$

where $\eta > 0$ and c_s is the Sobolev embedding constant.

Proof.

(i) From Young's inequality, Sobolev embedding, and Lemma 6, we deduce

$$
\begin{aligned}
|\phi(t)| &\leq \frac{1}{l+2}\|u_t\|_{l+2}^{l+2} + \frac{(l+1)^{-1}}{l+2}\|u\|_{l+2}^{l+2} + \frac{1}{2}\|\nabla u_t\|^2 + \frac{1}{2}\|\nabla u\|^2 \\
&\leq \frac{1}{l+2}\|u_t\|_{l+2}^{l+2} + \frac{(l+1)^{-1}}{l+2}c_s^{l+2}\|\nabla u\|^{l+2} + \frac{1}{2}\|\nabla u_t\|^2 + \frac{1}{2}\|\nabla u\|^2 \\
&\leq \frac{1}{l+2}\|u_t\|_{l+2}^{l+2} + \left(\frac{(l+1)^{-1}}{l+2}c_s^{l+2}\left(\frac{2E(0)}{a}\right)^{(l/2)} + \frac{1}{2}\right)\|\nabla u\|^2 + \frac{1}{2}\|\nabla u_t\|^2.
\end{aligned}
\tag{155}
$$

(ii) Differentiating $\phi(t)$ with respect to t and using the first equation of (12), we get

$$
\begin{aligned}
\phi'(t) &= \frac{1}{l+1}\int_\Omega \left(|u_t|^l u_t\right)' u\,dx + \frac{1}{l+1}\int_\Omega |u_t|^{l+2}dx + \int_\Omega \nabla u_{tt}\nabla u\,dx + \int_\Omega \nabla u_t\nabla u_t\,dx \\
&= \int_\Omega \left[|u_t|^l u_{tt}\right]u\,dx + \frac{1}{l+1}\|u_t\|_{l+2}^{l+2} - \int_\Omega \Delta u_{tt}u\,dx + \|\nabla u_t\|^2 \\
&= \frac{1}{l+1}\|u_t\|_{l+2}^{l+2} + \int_\Omega \left[|u_t|^l u_{tt} - \Delta u_{tt}\right]u\,dx + \|\nabla u_t\|^2 \\
&= \frac{1}{l+1}\|u_t\|_{l+2}^{l+2} + \int_\Omega \left[M\left(\|\nabla u\|^2\right)\Delta u - \int_0^t h(t-s)\Delta u(s)ds - \mu_1 g_1\left(u_t(x,t)\right) - \mu_2 g_2\left(z(x,1,t)\right)\right. \\
&\quad \left. + \nu u\ln|u|\right]u\,dx + \|\nabla u_t\|^2 \\
&= \frac{1}{l+1}\|u_t\|_{l+2}^{l+2} - M\left(\|\nabla u^2\|\right)\|\nabla u\|^2 + \int_\Omega \nabla u(t)\int_0^t h(t-s)\nabla u(s)ds\,dx - \mu_1\int_\Omega u g_1\left(u_t(x,t)\right)dx \\
&\quad - \mu_2\int_\Omega u g_2\left(z(x,1,t)\right)dx + \|\nabla u_t\|^2 + \nu\int_\Omega u^2\ln|u|dx.
\end{aligned}
\tag{156}
$$

By using Young's inequality and Sobolev embedding, we can estimate the third term in the right side as follows:

$$
\begin{aligned}
\int_\Omega \nabla u(t)\int_0^t h(t-s)\nabla u(s)ds\,dx &\leq \int_0^t h(t-s)\int_\Omega |\nabla u(t)(\nabla u(s) - \nabla u(t))|dx\,ds + \|\nabla u(t)\|^2\int_0^t h(t-s)ds \\
&\leq \eta\|\nabla u(t)\|^2\int_0^t h(s)ds + \frac{1}{4\eta}\int_0^t h(t-s)\|(\nabla u(s) - \nabla u(t))\|^2ds \\
&\quad + \|\nabla u(t)\|^2\int_0^t h(s)ds \\
&\leq (1+\eta)(a-k)\|\nabla u(t)\|^2 + \frac{1}{4\eta}(h o \nabla u)(t).
\end{aligned}
\tag{157}
$$

Thus, our proof is completed. $\qquad\square$

Lemma 13. *Let (u, z) be a solution of problem (12). Then, the* *satisfies the estimates*
functional

$$\psi(t) = \int_\Omega \left(\Delta u_t - \frac{1}{l+1}|u_t|^l u_t\right) \int_0^t h(t-s)(u(t) - u(s))\mathrm{d}s\,\mathrm{d}x$$

$$(158)$$

(i) $|\psi(t)| \le \dfrac{1}{2}\|\nabla u_t\|^2 + \left(\dfrac{1}{2}(a-k) + \dfrac{(l+1)^{-1}}{(l+2)}(a-k)^{l+2}c_s^{l+2}\left(\dfrac{4E(0)}{a}\right)^{(l/2)}\right)(ho\nabla u)(t) + \dfrac{1}{l+2}\|u_t\|_{l+2}^{l+2},$

(ii) $\psi'(t) \le \delta((a-k) + b_0)M\big(\|\nabla u\|^2\big)\|\nabla u\|^2 + 2\delta(a-k)^2\|\nabla u\|^2$

$$(159)$$

$$+ \left(\frac{M_0}{4\delta} + \left(2\delta + \frac{1}{4\delta} + (\mu_1 + \mu_2 + \nu)\frac{c_s^2}{4\delta}\right)(a-k)\right)(ho\nabla u)(t) - \frac{h(0)}{4\delta}\left(1 + \frac{c_s^2}{l+1}\right)(h'o\nabla u)(t)$$

$$+ \left(\delta + \frac{\delta a_0}{l+1} - \int_0^t h(s)\mathrm{d}s\right)\|\nabla u_t\|^2 + \mu_1\delta\|g_1(u_t(x,t))\|^2 + \mu_2\delta\|g_2(z(x,1,t))\|^2 - \frac{1}{l+1}\int_0^t h(s)\mathrm{d}s\|u_t\|_{l+2}^{l+2},$$

where

$$M_0 = a + b\left(\frac{2E(0)}{a}\right)^\gamma,$$

$$a_0 = c_s^{2(l+1)}\left(\frac{2E(0)}{a}\right)^l, \quad \eta > 0, b_0 = \frac{\nu}{2}c_s^2 \max\left\{\frac{\sqrt{|\Omega|}}{a}, \frac{c_s^2}{b}\right\},$$

$$(160)$$

and c_s is the Sobolev embedding constant.

Proof.
(i) We have

$$\psi(t) = -\int_\Omega \nabla u_t \int_0^t h(t-s)(\nabla u(t) - \nabla u(s))\mathrm{d}s\,\mathrm{d}x$$

$$- \int_\Omega \frac{1}{l+1}|u_t|^l u_t \int_0^t h(t-s)(u(t) - u(s))\mathrm{d}s\,\mathrm{d}x.$$

$$(161)$$

We use Young's and Hölder's inequalities with the conjugate exponents $p = ((l+2)/(l+1))$ and $q = l+2$; the second term in the right hand side can be estimated as

$$\left|-\int_\Omega \frac{1}{l+1}|u_t|^l u_t \int_0^t h(t-s)(u(t) - u(s))\mathrm{d}s\,\mathrm{d}x\right|$$

$$\le \frac{1}{l+2}\|u_t\|_{l+2}^{l+2} + \frac{(l+1)^{-1}}{l+2}\int_\Omega\left[\int_0^t (h(t-s))^{((l+1)/(l+2))}\left((h(t-s))^{1/(l+2)}|u(t) - u(s)|\right)\mathrm{d}s\right]^{l+2}\mathrm{d}x$$

$$\le \frac{1}{l+2}\|u_t\|_{l+2}^{l+2} + \frac{(l+1)^{-1}}{l+2}\left(\int_0^t h(t-s)\mathrm{d}s\right)^{l+1}\int_\Omega\int_0^t h(t-s)|u(t) - u(s)|^{l+2}\mathrm{d}s\,\mathrm{d}x$$

$$\le \frac{1}{l+2}\|u_t\|_{l+2}^{l+2} + \frac{(l+1)^{-1}}{l+2}(a-k)^{l+1}c_s^{l+2}\left(4\frac{E(0)}{a}\right)^{(l/2)}(ho\nabla u)(t).$$

$$(162)$$

We get the last inequality from (22) and Lemma 6. Similarly, we use Young's and Hölder's inequalities with $p = q = 2$, we get

$$\left|-\int_\Omega \nabla u_t \int_0^t h(t-s)(\nabla u(t) - \nabla u(s))\mathrm{d}s\,\mathrm{d}x\right| \le \frac{1}{2}\|\nabla u_t\|^2 + \frac{1}{2}\int_\Omega\left(\int_0^t h(t-s)|\nabla u(t) - \nabla u(s)|\mathrm{d}s\right)^2\mathrm{d}x$$

$$\le \frac{1}{2}\|\nabla u_t\|^2 + \frac{1}{2}(a-k)(ho\nabla u)(t).$$

$$(163)$$

Combining (162) and (163), we deduce

$$|\psi(t)| \leq \frac{1}{2}\|\nabla u_t\|^2 + \left(\frac{1}{2}(a-k) + \frac{(l+1)^{-1}}{(l+2)}(a-k)^{l+2}c_s^{l+2}\left(\frac{4E(0)}{a}\right)^{(l/2)}\right)(ho\nabla u)(t) + \frac{1}{l+2}\|u_t\|_{l+2}^{l+2}. \tag{164}$$

(ii) We use the Leibniz formula and the first equation of (12), and we have

$$\begin{aligned}
\psi'(t) &= \int_\Omega \left(\Delta u_{tt} - |u_t|^l u_{tt}\right) \int_0^t h(t-s)(u(t)-u(s))ds\,dx \\
&\quad + \int_\Omega \left(\Delta u_t - \frac{1}{l+1}|u_t|^l u_t\right)\left(\int_0^t (h'(t-s)(u(t)-u(s)) + h(t-s)u_t(t))ds\right)dx \\
&= \int_\Omega M\left(\|\nabla u\|^2\right)\nabla u(t) \int_0^t h(t-s)(\nabla u(t)-\nabla u(s))ds\,dx \\
&\quad - \int_\Omega \int_0^t h(t-s)\nabla u(s)ds \int_0^t h(t-s)(\nabla u(t)-\nabla u(s))ds\,dx \\
&\quad + \mu_1\int_\Omega g_1(u_t(x,t)) \int_0^t h(t-s)(u(t)-u(s))ds\,dx + \mu_2\int_\Omega g_2(z(x,1,t)) \int_0^t h(t-s)(u(t)-u(s))ds\,dx \\
&\quad - \nu\int_\Omega u\ln|u| \int_0^t h(t-s)(u(t)-u(s))ds\,dx - \int_\Omega \nabla u_t \int_0^t h'(t-s)(\nabla u(t)-\nabla u(s))ds\,dx \\
&\quad - \frac{1}{l+1}\int_\Omega |u_t|^l u_t \int_0^t h'(t-s)(u(t)-u(s))ds\,dx - \|\nabla u_t\|^2 \int_0^t h(s)ds - \frac{1}{l+1}\|u_t\|_{l+2}^{l+2} \int_0^t h(s)ds \\
&= I_1 + I_2 + \mu_1 I_3 + \mu_2 I_4 + I_5 + I_6 + I_7 - \|\nabla u_t\|^2 \int_0^t h(s)ds - \frac{1}{l+1}\|u_t\|_{l+2}^{l+2} \int_0^t h(s)ds.
\end{aligned} \tag{165}$$

In what follows, we will estimate $I_1, \ldots, I_7$. For I_1, we use Hölder's and Young's inequalities with $p = q = 2$, and we get

$$\begin{aligned}
|I_1| &\leq M\left(\|\nabla u\|^2\right) \int_\Omega |\nabla u(t)|\left(\int_0^t h(s)ds\right)^{(1/2)}\left(\int_0^t h(t-s)|\nabla u(t)-\nabla u(s)|^2 ds\right)^{(1/2)}dx \\
&\leq M\left(\|\nabla u\|^2\right)\left[\delta\int_\Omega |\nabla u(t)|^2 \int_0^t h(s)ds\,dx + \frac{1}{4\delta}\int_\Omega \int_0^t h(t-s)|\nabla u(t)-\nabla u(s)|^2 ds\,dx\right] \\
&\leq M\left(\|\nabla u\|^2\right)\left(\delta\|\nabla u(t)\|^2 \int_0^t h(s)ds + \frac{1}{4\delta}(ho\nabla u)(t)\right) \\
&\leq \delta M\left(\|\nabla u\|^2\right)\|\nabla u(t)\|^2(a-k) + \frac{M_0}{4\delta}(ho\nabla u)(t),
\end{aligned} \tag{166}$$

where $M_0 = (a+b)(2E(0)/a)^\gamma$ obtained by recalling (22) and Lemma 6. Similarly,

$$|I_2| \le \delta \int_\Omega \left(\int_0^t h(t-s)|\nabla u(s)|ds \right)^2 dx + \frac{1}{4\delta} \int_\Omega \left(\int_0^t h(t-s)|\nabla u(t) - \nabla u(s)|ds \right)^2 dx$$

$$\le \delta \int_\Omega \left(\int_0^t h(t-s)(|\nabla u(s) - \nabla u(t)| + |\nabla u(t)|)ds \right)^2 dx + \frac{1}{4\delta} \left(\int_0^t h(s)ds \right)(ho\nabla u)(t)$$

$$\le 2\delta \|\nabla u(t)\|^2 \left(\int_0^t h(s)ds \right)^2 dx + \left(2\delta + \frac{1}{4\delta} \right) \left(\int_0^t h(s)ds \right)(ho\nabla u)(t) \tag{167}$$

$$\le 2\delta \|\nabla u(t)\|^2 (a-k)^2 + \left(2\delta + \frac{1}{4\delta} \right)(a-k)(ho\nabla u)(t),$$

$$|I_3| \le \delta \|g_1(u_t(x,t))\|^2 + \frac{c_s^2}{4\delta}(a-k)(ho\nabla u)(t), \tag{168}$$

$$|I_4| \le \delta \|g_2(z(x,1,t))\|^2 + \frac{c_s^2}{4\delta}(a-k)(ho\nabla u)(t). \tag{169}$$

To estimate I_5, we apply Lemma 4 with $\epsilon_0 = (1/2)$ and use repeatedly Young's, Cauchy-Schwartz's, and the embedding inequalities, as follows:

$$|I_5| \le \nu \int_\Omega \left(u^2 + d_{\epsilon_0}\sqrt{|u|} \right) \left| \int_0^t h(t-s)(u(t) - u(s))ds \right| dx$$

$$\le \nu \left(\frac{1}{4\delta} \int_\Omega \left| \int_0^t h(t-s)(u(t) - u(s))ds \right|^2 dx + \delta \int_\Omega \left(u^2 + d_{\epsilon_0}\sqrt{|u|} \right)^2 dx \right)$$

$$\le \frac{c_s^2(a-k)\nu}{4\delta}(ho\nabla u)(t) + \frac{\nu}{2}\delta \left(\int_\Omega |u|^4 dx + \int_\Omega |u|dx \right) \tag{170}$$

$$\le \frac{c_s^2(a-k)\nu}{4\delta}(ho\nabla u)(t) + \frac{\nu}{2}\delta \left(\|\nabla u\|^4 + \sqrt{|\Omega|}\|u\| \right)$$

$$\le \frac{c_s^2(a-k)\nu}{4\delta}(ho\nabla u)(t) + b_0 \delta M\left(\|\nabla u\|^2 \right)\|\nabla u\|^2,$$

where $b_0 = (\nu/2)c_s^2 \max\{(\sqrt{|\Omega|}/a), (c_s^2/b)\}$. Also,

$$|I_6| \le \delta \int_\Omega |\nabla u_t|^2 dx + \frac{1}{4\delta} \int_\Omega \left(\int_0^t |h'(t-s)| \|\nabla u(t) - \nabla u(s)|ds \right)^2 dx$$

$$\le \delta \|\nabla u_t\|^2 + \frac{1}{4\delta} \int_0^t |h'(t-s)|ds \int_\Omega \int_0^t |h'(t-s)|\|\nabla u(t) - \nabla u(s)|^2 ds\, dx. \tag{171}$$

As h is a positive decreasing function, $|h'(t-s)| = -h'(t-s)$ and then,

$$|I_6| \leq \delta \|\nabla u_t\|^2 + \frac{1}{4\delta} \int_0^t (-h'(t-s)) \mathrm{d}s \int_\Omega \int_0^t (-h'(t-s))|\nabla u(t) - \nabla u(s)|^2 \mathrm{d}s \, \mathrm{d}x$$

$$\leq \delta \|\nabla u_t\|^2 - \frac{h(0)}{4\delta} (h'o\nabla u)(t), \tag{172}$$

$$|I_7| \leq \frac{1}{l+1} \left[\delta \int_\Omega |u_t|^l |u_t||^2 \mathrm{d}x + \frac{1}{4\delta} \int_\Omega \left(\int_0^t |h'(t-s)||u(t) - u(s)| \mathrm{d}s \right)^2 \mathrm{d}x \right]$$

$$\leq \frac{1}{l+1} \left[\delta \|u_t\|_{2(l+1)}^{2(l+1)} - \frac{h(0)c_s^2}{4\delta} (h'o\nabla u)(t) \right]$$

$$\leq \frac{\delta c_s^{2(l+1)}}{l+1} \|\nabla u_t\|^{2(l+1)} - \frac{h(0)c_s^2}{4\delta(l+1)} (h'o\nabla u)(t) \tag{173}$$

$$\leq \frac{\delta a_0}{l+1} \|\nabla u_t\|^2 - \frac{h(0)c_s^2}{4\delta(l+1)} (h'o\nabla u)(t),$$

where $a_0 = c_s^{2(l+1)}(2E(0)/a)^l$ obtained by recalling (22) and Lemma 6. Combining (165) and (166)–(173), we finish the proof. Now, for $M, \varepsilon_1 > 0$, we introduce the following functional:

$$F(t) = ME(t) + \varepsilon_1 \phi(t) + \psi(t) + \chi(t). \tag{174}$$

□

Lemma 14. *Let* (u,z) *be a solution of problem (12). Assume that (A1)–(A6) hold and*

$$0 < E(0) < \min \left\{ \frac{ek\pi}{4}, \frac{k^3}{27\nu^2 c_*^6} \right\}. \tag{175}$$

Then, $F(t)$ *satisfies, along the solution and for some positive constants* $m, c > 0$*, the following estimate:*

$$F'(t) \leq -mE(t) + c \left[\|g_1(u_t(x,t))\|^2 + \|g_2(z(x,1,t))\|^2 \right.$$

$$+ \int_\Omega |u(x,t)g_1(u_t(x,t))| \mathrm{d}x$$

$$\left. + \int_\Omega |u(x,t)g_2(z(x,1,t))| \mathrm{d}x \right] \tag{176}$$

and $F(t) \sim E(t)$.

Proof. By (ii) of Lemmas 11–13 and Lemma 6 and by (A2), we deduce that for $t \geq t_0 > 0$:

$$F'(t) = ME'(t) + \varepsilon_1 \phi'(t) + \psi'(t) + \chi'(t)$$

$$\leq -(M\lambda - \alpha_2) \int_\Omega u_t(x,t) g_1(u_t(x,t)) \mathrm{d}x - \left(M\beta + \alpha_1(1-d)e^{-2\tau_1} \right) \int_\Omega z(x,1,t) g_2(z(x,1,t)) \mathrm{d}x$$

$$- 2\tau(t)e^{-2\tau_1} \int_\Omega \int_0^1 G(z(x,\rho,t)) \mathrm{d}\rho \, \mathrm{d}x - (\varepsilon_1 - \delta(a-k+b_0)) M(\|\nabla u\|^2) \|\nabla u\|^2 - \frac{1}{l+1} (h_0 - \varepsilon_1) \|u_t\|_{l+2}^{l+2}$$

$$- \left(h_0 - \delta \left(1 + \frac{a_0}{l+1} \right) - \varepsilon_1 \right) \|\nabla u_t\|^2 - \left(\frac{Mh_1}{2} - \varepsilon_1(1+\eta)(a-k) - 2\delta(a-k)^2 \right) \|\nabla u(t)\|^2$$

$$- \left[\zeta \left(\frac{M}{2} - \frac{h(0)}{4\delta} \left(1 + \frac{c_s^2}{l+1} \right) \right) - \left(\frac{\varepsilon_1}{4\eta} + \frac{M_0}{4\delta} + \left(2\delta + \frac{1}{4\delta} + (\mu_1 + \mu_2 + \nu) \frac{c_s^2}{4\delta} \right) (a-k) \right) \right] (ho\nabla u)(t)$$

$$+ \mu_1 \delta \|g_1(u_t(x,t))\|^2 + \mu_2 \delta \|g_2(z(x,1,t))\|^2 - \varepsilon_1 \mu_1 \int_\Omega u(x,t) g_1(u_t(x,t)) \mathrm{d}x - \varepsilon_1 \mu_2 \int_\Omega u(x,t) g_2(z(x,1,t)) \mathrm{d}x$$

$$+ \varepsilon_1 \nu \int_\Omega u^2 \ln|u| \mathrm{d}x, \tag{177}$$

where

$$h_0 = \int_0^{t_0} h(s)\mathrm{d}s,$$
$$h_1 = \min\{h(t), t \ge t_0 > 0\}.$$

(178)

We take $h_0 > \varepsilon_1$ and $\delta > 0$ sufficiently small such that

$$a_4 = h_0 - \delta\left(1 + \frac{a_0}{l+1}\right) - \varepsilon_1 > 0,$$
$$a_2 = \varepsilon_1 - \delta(a - k + b_0) > 0.$$

(179)

As long as ε_1 and δ are fixed, we choose M large enough such that

$$a_1 = M\lambda - \alpha_2 > 0,$$

$$a_5 = \frac{Mh_1}{2} - \varepsilon_1(1 + \eta)(a - k) - 2\delta(a - k)^2 > 0,$$

(180)

$$a_6 = \zeta\left(\frac{M}{2} - \frac{h(0)}{4\delta}\left(1 + \frac{c_s^2}{l+1}\right)\right) - \left(\frac{\varepsilon_1}{4\eta} + \frac{M_0}{4\delta} + \left(2\delta + \frac{1}{4\delta} + (\mu_1 + \mu_2 + \nu)\frac{c_s^2}{4\delta}\right)(a - k)\right) > 0.$$

Thus,

$$F'(t) \le - a_3\frac{1}{l+1}\|u_t\|_{l+2}^{l+2} - a_2 M\left(\|\nabla u\|^2\right)\|\nabla u\|^2 - a_4\|\nabla u_t\|^2$$

$$- a_6(ho\nabla u)(t) - 2\tau(t)e^{-2\tau_1}\int_\Omega\int_0^1 G(z(x, \rho, t))\mathrm{d}\rho\,\mathrm{d}x$$

$$+ c\left[\|g_1(u_t(x, t))\|^2 + \|g_2(z(x, 1, t))\|^2 + \int_\Omega |u(x, t)g_1(u_t(x, t))|\mathrm{d}x\right.$$

(181)

$$\left. + \int_\Omega |u(x, t)g_2(z(x, 1, t))|\mathrm{d}x\right] + \varepsilon_1\nu\int_\Omega u^2\ln|u|\mathrm{d}x$$

$$\le - m_1 E(t) + \left(\varepsilon_1 - \frac{m_1}{2}\right)\nu\int_\Omega u^2\ln|u|\mathrm{d}x + \frac{m_1\nu}{4}\|u\|_2^2$$

$$+ c\left[\|g_1(u_t(x, t))\|^2 + \|g_2(z(x, 1, t))\|^2 + \int_\Omega |u(x, t)g_1(u_t(x, t))|\mathrm{d}x + \int_\Omega |u(x, t)g_2(z(x, 1, t))|\mathrm{d}x\right],$$

where

$$m_1 = \min\{2a_2, 2e^{-2\tau_1}\xi, 2a_4, a_3\}.$$

(182)

Using the Logarithmic Sobolev inequality, we get

$$F'(t) \le - m_1 E(t) - \left(\varepsilon_1 - \frac{m_1}{2}\right)\frac{\nu}{2}\left(2(1 + \ln\sigma) - \ln\|u\|^2\right)\|u\|^2 + \left(\varepsilon_1 - \frac{m_1}{2}\right)\frac{\sigma^2}{2\pi}\|\nabla u\|^2 + \frac{m_1\nu}{4}\|u\|^2$$

$$+ c\left[\|g_1(u_t(x, t))\|^2 + \|g_2(z(x, 1, t))\|^2\right.$$

(183)

$$\left. + \int_\Omega |u(x, t)g_1(u_t(x, t))|\mathrm{d}x + \int_\Omega |u(x, t)g_2(z(x, 1, t))|\mathrm{d}x\right].$$

From (61) and for

$$m_1 \le \varepsilon_1 \le \frac{m_1}{2}(\nu + 1),\tag{184}$$

we have

$$m_2 = \frac{m_1}{2}\left(a - \int_0^t h(s)\mathrm{d}s\right) - \left(\varepsilon_1 - \frac{m_1}{2}\right)\frac{\sigma^2}{2\pi}$$

$$\ge \frac{m_1}{2}k - \left(\varepsilon_1 - \frac{m_1}{2}\right)\frac{k}{\nu} > 0 \tag{185}$$

$$\frac{m_1 \nu}{4} \le \left(\varepsilon_1 - \frac{m_1}{2}\right)\frac{\nu}{2}.$$

This selection is possible thanks to (A6). So we get

$$F'(t) \le -mE(t) - \left(\varepsilon_1 - \frac{m_1}{2}\right)\frac{\nu}{2}\left(1 + 2\ln\sigma - \ln\|u\|^2\right)\|u\|^2$$

$$F'(t) \le -mE(t) - \left(\varepsilon_1 - \frac{m_1}{2}\right)\frac{\nu}{2}\left(1 + 2\ln\sigma - \ln\|u\|^2\right)\|u\|^2$$

$$+ \int_\Omega |u(x,t)g_1(u_t(x,t))|\mathrm{d}x + \int_\Omega |u(x,t)g_2(z(x,1,t))|\mathrm{d}x\Big], \tag{186}$$

where $m = \min\{m_1, m_2\}$. By recalling that $E' \le 0$ and $I(t) > 0$ and using (133), (134), and (175), we obtain

$$\ln\|u\|_2^2 \le \ln\left(\frac{4}{\nu}J(t)\right) \le \ln\left(\frac{4}{\nu}E(t)\right)$$

$$\le \ln\left(\frac{4}{\nu}E(0)\right) \le \ln\left(\frac{ek\pi}{\nu}\right). \tag{187}$$

Taking σ satisfies

$$\max\left\{e^{-3/2}, \sqrt{\frac{k\pi}{\nu}}\right\} \le \sigma \le \sqrt{\frac{2k\pi}{\nu}}. \tag{188}$$

(So (61) is satisfied), and we guarantee

$$1 + 2\ln\sigma - \ln\|u\|^2 \ge 0, \tag{189}$$

twhich completes the proof of (176). To prove $F(t) \sim E(t)$, we show that there exist two positive constants κ_1 and κ_2 such that

$$\kappa_1 E(t) \le F(t) \le \kappa_2 E(t). \tag{190}$$

From (i) of Lemmas 11–13, (140), (133), and (134), we get $\kappa > 0$ depending on $\varepsilon_1, a, l, c_s, E(0), k$, and ξ such that

$$|\varepsilon_1 \phi(t) + \psi(t) + \chi(t)| \le \kappa E(t). \tag{191}$$

For a choice of M large enough such that $\kappa_1 = M - \kappa > 0$ and $\kappa_2 = M + \kappa > 0$, we get our result. By the proof of Theorem 2 as given by Komornik [37], we consider the following partition of Ω:

$$\Omega_1 = \{x \in \Omega : |u_t| \le \varepsilon\},$$
$$\Omega_2 = \{x \in \Omega : |u_t| > \varepsilon\}. \tag{192}$$

We use Young's inequality (with $p = q = 2$), (22), and Lemma 6, and we have

$$\int_\Omega |ug_1(u_t)|\mathrm{d}x + \|g_1(u_t)\|^2 \le \delta\|u\|^2 + \left(\frac{1}{4\delta} + 1\right)\|g_1(u_t)\|^2$$

$$\le \delta C_s^2 \|\nabla u\|^2 + \left(\frac{1}{4\delta} + 1\right)\left(\int_{\Omega_1} H^{-1}(u_t g_1(u_t))\mathrm{d}x + c_2 \int_{\Omega_2} u_t g_1(u_t)\mathrm{d}x\right) \tag{193}$$

$$\le \frac{2\delta C_s^2}{a}E(t) + c_\delta \int_{\Omega_1} H^{-1}(u_t g_1(u_t))\mathrm{d}x - C_\delta E'(t).$$

Similarly and by application of (17), we obtain

$$\int_\Omega |ug_2(z(x,1,t))|\mathrm{d}x + \|g_2(z(x,1,t))\|^2 \le \delta C_s^2 \|\nabla u\|^2$$

$$+ \left(\frac{1}{4\delta} + 1\right)c_3 \int_\Omega z(x,1,t)g_2(z(x,1,t))\mathrm{d}x$$

$$\le \frac{2\delta C_s^2}{a}E(t) - C_\delta' E'(t). \tag{194}$$

Combining (193) and (194), (176) becomes

$$F'(t) \le -\left(m - \frac{4\delta C_s}{a}\right)E(t) - C_\delta'' E'(t) + c_\delta \int_{\Omega_1} H^{-1}(u_t g_1(u_t))\mathrm{d}x, \tag{195}$$

where $C_\delta'' = C_\delta' + C_\delta$. Now, for δ small enough such that $d = m - (4\delta C_s/a) > 0$, the function $L(t) = F(t) + C_\delta'' E(t)$ satisfies

$$L'(t) \le -dE(t) + c \int_{\Omega_1} H^{-1}(u_t g_1(u_t))\mathrm{d}x, \tag{196}$$

$$L(t) \sim E(t). \tag{197}$$

$\square$

Case 1. H is linear on $[0, \varepsilon]$; using (16) and Lemma 6, we deduce that

$$L'(t) \leq -\mathrm{d}E(t) - cE'(t). \tag{198}$$

Thus, $R = L + cE \sim E$ satisfies

$$R(t) \leq R(0)e^{-c't}. \tag{199}$$

Hence,

$$E(t) \leq C(E(0))e^{-c't}. \tag{200}$$

Case 2. H is nonlinear on $[0, \varepsilon]$; so we exploit Jensen's inequality (see [2]) and the concavity of H^{-1} to obtain

$$H^{-1}\left(\frac{1}{|\Omega_1|}\int_{\Omega_1} u_t g_1(u_t)\mathrm{d}x\right) \geq c\int_{\Omega_1} H^{-1}(u_t g_1(u_t))\mathrm{d}x. \tag{201}$$

Then, (196) becomes

$$L'(t) \leq -\mathrm{d}E(t) + H^{-1}\left(\frac{1}{|\Omega_1|}\int_{\Omega_1} u_t g_1(u_t)\mathrm{d}x\right). \tag{202}$$

For $\varepsilon_0 < \varepsilon$ and $w_0 > 0$, we define L_0 by

$$L_0(t) = H'\left(\varepsilon_0 \frac{E(t)}{E(0)}\right)L(t) + w_0 E(t). \tag{203}$$

Then, we easily see that for $b_1, b_2 > 0$,

$$b_1 L_0(t) \leq E(t) \leq b_2 L_0(t). \tag{204}$$

By recalling that $E' \leq 0$, $H' > 0$, and $H'' > 0$ on $(0, \varepsilon]$ and using (202), we obtain

$$L_0'(t) = \varepsilon_0 \frac{E'(t)}{E(0)}H''\left(\varepsilon_0\frac{E(t)}{E(0)}\right)L(t) + H'\left(\varepsilon_0\frac{E(t)}{E(0)}\right)L'(t) + w_0 E'(t)$$

$$\leq -\mathrm{d}E(t)H'\left(\varepsilon_0\frac{E(t)}{E(0)}\right) + cH'\left(\varepsilon_0\frac{E(t)}{E(0)}\right)H^{-1}\left(\frac{1}{|\Omega_1|}\int_{\Omega_1} u_t g_1(u_t)\mathrm{d}x\right) + w_0 E'(t). \tag{205}$$

Using Remark 1 with H^*, the convex conjugate of H in the sense of Young, we obtain

$$L_0'(t) \leq -\mathrm{d}E(t)H'\left(\varepsilon_0\frac{E(t)}{E(0)}\right) + cH^*\left(H'\left(\varepsilon_0\frac{E(t)}{E(0)}\right)\right)$$

$$L_0'(t) \leq -\mathrm{d}E(t)H'\left(\varepsilon_0\frac{E(t)}{E(0)}\right) + cH^*\left(H'\left(\varepsilon_0\frac{E(t)}{E(0)}\right)\right)$$

$$\leq -\mathrm{d}E(t)H'\left(\varepsilon_0\frac{E(t)}{E(0)}\right) + c\varepsilon_0\frac{E(t)}{E(0)}H'\left(\varepsilon_0\frac{E(t)}{E(0)}\right)$$

$$- w_1 E'(t) + w_0 E'(t), \tag{206}$$

where w_1 is a positive constant depending of Ω_1 and α_2. By taking ε_0 small enough such that $\mathrm{d}E(0) - c\varepsilon_0 > 0$ and $w_0 > w_1$, we obtain

$$L_0'(t) \leq -w\frac{E(t)}{E(0)}H'\left(\varepsilon_0\frac{E(t)}{E(0)}\right) = -wH_2\left(\frac{E(t)}{E(0)}\right), \tag{207}$$

where $H_2(t) = tH'(\varepsilon_0 t)$ a positive increasing function on $(0, 1]$. By setting $L_1(t) = (b_1 L_0(t)/E(0))$, we easily see that, by (204), we have

$$L_1(t) \sim E(t). \tag{208}$$

Using (207), we arrive at

$$L_1'(t) \leq -w_1 H_2(L_1(t)). \tag{209}$$

By recalling (28), we deduce

$$L_1'(t) \leq w_1\frac{1}{H_1'(L_1(t))}, \tag{210}$$

which gives

$$[H_1(L_1(t))]' \leq w_1. \tag{211}$$

A simple integration leads to

$$H_1(L_1(t)) \leq w_1 t + H_1(L_1(0)). \tag{212}$$

Consequently,

$$L_1(t) \leq H_1^{-1}(w_1 t + w_2). \tag{213}$$

Using (208) and (213), we obtain (27). The proof is completed.

Data Availability

No data were used to support this study.

Conflicts of Interest

The authors declare that there are no conflicts of interest regarding the publication of this manuscript.

Authors' Contributions

All authors contributed equally to this article. They have all read and approved the final manuscript.

References

[1] X. Han and M. Wang, "Global existence and uniform decay for a nonlinear viscoelastic equation with damping," *Nonlinear Analysis: Theory, Methods & Applications*, vol. 70, no. 9, pp. 3090–3098, 2009.

[2] N. Mezouar and S. Boulaaras, "Global existence and decay of solutions for a class of viscoelastic Kirchhoff equation," *Bulletin of the Malaysian Mathematical Sciences Society*, vol. 43, no. 1, pp. 725–755, 2020.

[3] S. Nicaise and C. Pignotti, "Interior feedback stabilization of wave equations with time dependent delay," *Electronic Journal of Differential Equations*, vol. 41, pp. 1–20, 2011.

[4] N. Mezouar and S. Boulaaras, "Global existence of solutions to a viscoelastic non-degenerate Kirchhoff equation," *Applicable Analysis*pp. 1–25, 2018, In press.

[5] E. Fridman, S. Nicaise, and J. Valein, "Stabilization of second order evolution equations with unbounded feedback with time-dependent delay," *SIAM Journal on Control and Optimization*, vol. 48, no. 8, pp. 5028–5052, 2010.

[6] S.-T. Wu, "Asymptotic behavior for a viscoelastic wave equation with a delay term," *Taiwanese Journal of Mathematics*, vol. 17, no. 3, pp. 765–784, 2013.

[7] A. Benaissa, A. Benguessoum, and S. A. Messaoudi, "Global existence and energy decay of solutions to a viscoelastic wave equation with a delay term in the non-linear internal feedback," *International Journal of Dynamical Systems and Differential Equations*, vol. 5, no. 1, pp. 1–13, 2014.

[8] M. Kirane and B. Said-Houari, "Existence and asymptotic stability of a viscoelastic wave equation with a delay," *Zeitschrift für angewandte Mathematik und Physik*, vol. 62, no. 6, pp. 1065–1082, 2011.

[9] D. Kim, "Asymptiotic behavior for the viscoelastic Kirchhoff type equation with an internal time varying delay term," *East Asian Mathematical Journal*, vol. 32, no. 3, pp. 399–412, 2016.

[10] A. Benaissa, A. Benaissa, and S. A. Messaoudi, "Global existence and energy decay of solutions for the wave equation with a time varying delay term in the weakly nonlinear internal feedbacks," *Journal of Mathematical Physics*, vol. 53, no. 12, Article ID 123514, 2012.

[11] B. Hu and H. M. Yin, "Semilinear parabolic equations with prescribed energy," *Rendiconti del Circolo Matematico di Palermo*, vol. 44, no. 3, pp. 479–505, 1995.

[12] C. Qu, X. Bai, and S. Zheng, "Blow-up versus extinction in a nonlocal p -Laplace equation with Neumann boundary conditions," *Journal of Mathematical Analysis and Applications*, vol. 412, no. 1, pp. 326–333, 2014.

[13] L. Yan and Z. Yong, "Blow-up and non-extinction for a nonlocal parabolic equation with logarithmic nonlinearity," *Boundary Value Problems*, vol. 2018, no. 1, 2018.

[14] K. Enqvist and J. McDonald, "Q-balls and baryogenesis in the MSSM," *Physics Letters B*, vol. 425, no. 3-4, pp. 309–321, 1998.

[15] N. Ioku, "The Cauchy problem for heat equations with exponential nonlinearity," *Journal of Differential Equations*, vol. 251, no. 4-5, pp. 1172–1194, 2011.

[16] I. Bialynicki-Birula and J. Mycielski, "Wave equations with logarithmic nonlinearities," *Bulletin L'Académie Polonaise des Science Mathematics, Astronomy and Physics*, vol. 23, no. 4, pp. 461–466, 1975.

[17] I. Bialynicki-Birula and J. Mycielski, "Nonlinear wave mechanics," *Annals of Physics*, vol. 100, no. 1-2, pp. 62–93, 1976.

[18] P. Górka, H. Prado, and E. G. Reyes, "Nonlinear equations with infinitely many derivatives," *Complex Analysis and Operator Theory*, vol. 5, no. 1, pp. 313–323, 2011.

[19] V. S. Vladimirov, "The equation of the p-adic open string for the scalar tachyon field," *Izvestiya: Mathematics*, vol. 69, no. 3, pp. 487–512, 2005.

[20] T. Cazenave and A. Haraux, "Équations d'évolution avec non linéarité logarithmique," *Annales de la faculté des sciences de Toulouse Mathématiques*, vol. 2, no. 1, pp. 21–51, 1980.

[21] P. Gorka, "Logarithmic klein-gordon equation," *Acta Physica Polonica B*, vol. 40, no. 1, pp. 59–66, 2009.

[22] K. Bartkowski and P. Górka, "One-dimensional Klein-Gordon equation with logarithmic nonlinearities," *Journal of Physics A: Mathematical and Theoretical*, vol. 41, no. 35, Article ID 355201, 2008.

[23] T. Hiramatsu, M. Kawasaki, and F. Takahashi, "Numerical study of Q-ball formation in gravity mediation," *Journal of Cosmology and Astroparticle Physics*, vol. 2010, no. 6, p. 8, 2010.

[24] X. Han, "Global existence of weak solutions for a logarithmic wave equation arising from Q-ball dynamics," *Bulletin of the Korean Mathematical Society*, vol. 50, no. 1, pp. 275–283, 2013.

[25] M. I. Mustafa and S. A. Messaoudi, "General energy decay for a weakly damped wave equation," *Communications in Mathematical Analysis*, vol. 9, pp. 1938–9787, 2010.

[26] I. Lasiecka, "Stabilization of wave and plate-like equations with nonlinear dissipation on the boundary," *Journal of Differential Equations*, vol. 79, no. 2, pp. 340–381, 1989.

[27] I. Lasiecka and D. Toundykov, "Energy decay rates for the semilinear wave equation with nonlinear localized damping and source terms," *Nonlinear Analysis: Theory, Methods & Applications*, vol. 64, no. 8, pp. 1757–1797, 2006.

[28] I. Lasiecka and D. Toundykov, "Regularity of higher energies of wave equation with nonlinear localized damping and a nonlinear source," *Nonlinear Analysis: Theory, Methods & Applications*, vol. 69, no. 3, pp. 898–910, 2008.

[29] W. J. Liu and E. Zuazua, "Decay rates for dissipative wave equations," *Search Results*, vol. 48, pp. 61–75, 1999.

[30] F. Alabau-Boussouira, "Convexity and weighted integral inequalities for energy decay rates of nonlinear dissipative hyperbolic systems," *Applied Mathematics and Optimization*, vol. 51, no. 1, pp. 61–105, 2005.

[31] S. Nicaise and C. Pignotti, "Stability and instability results of the wave equation with a delay term in the boundary or internal feedbacks," *SIAM Journal on Control and Optimization*, vol. 45, no. 5, pp. 1561–1585, 2006.

[32] H. Chen, P. Luo, and G. Liu, "Global solution and blow-up of a semilinear heat equation with logarithmic nonlinearity," *Journal of Mathematical Analysis and Applications*, vol. 422, no. 1, pp. 84–98, 2015.

[33] L. Gross, "Logarithmic Sobolev inequalities," *American Journal of Mathematics*, vol. 97, no. 4, pp. 1061–1083, 1975.

[34] J. Y. Park and J. R. Kang, "Global existence and uniform decay for a nonlinear viscoelastic equation with damping," *Acta Applicandae Mathematicae*, vol. 110, no. 3, pp. 1393–1406, 2010.

[35] V. I. Arnold, *Mathematical Methods of Classical Mechanics*, Springer-Verlag, New York, USA, 1989.

[36] J. L. Lions, *Quelques Methodes de Resolution des Problemes aux Limites Non Lineaires*, Dunod, Paris, France, in French, 1969.

[37] V. Yin, *Exact Controllability and Stabilization The Multiplier Method*, Masson Wiley, Paris, France, 1994.

Research Article

Infinitely Many Coexisting Attractors in No-Equilibrium Chaotic System

Qiang Lai [ID],[1] **Paul Didier Kamdem Kuate** [ID],[2] **Huiqin Pei** [ID],[1] **and Hilaire Fotsin** [ID][2]

[1]*School of Electrical and Automation Engineering, East China Jiaotong University, Nanchang 330013, China*
[2]*Laboratory of Condensed Matter, Electronics and Signal Processing Department of Physics, University of Dschang, P.O. Box 067, Dschang, Cameroon*

Correspondence should be addressed to Qiang Lai; laiqiang87@126.com

This paper proposes a new no-equilibrium chaotic system that has the ability to yield infinitely many coexisting hidden attractors. Dynamic behaviors of the system with respect to the parameters and initial conditions are numerically studied. It shows that the system has chaotic, quasiperiodic, and periodic motions for different parameters and coexists with a large number of hidden attractors for different initial conditions. The circuit and microcontroller implementations of the system are given for illustrating its physical meaning. Also, the synchronization conditions of the system are established based on the adaptive control method.

1. Introduction

Encouraging progress has been made on chaos in the past few decades. An important change is to recognize the great application potential of chaos in engineering. Nowadays, chaos generation has become an important research issue arousing constant concern. Inspired by the well-known Lorenz system [1], many different chaotic systems have been created [2–7]. There are two interesting directions in generating new chaotic systems. One is to discover chaos in nonlinear systems with very simple mathematical models. The most representative work was made by Sprott who established nineteen polynomial chaotic systems with either five terms and two nonlinear terms or six terms and one nonlinear term [8]. The other is to construct chaotic systems with special strange attractors including butterfly attractor, multiscroll attractor, multiwing attractor, hidden attractor, and coexisting attractors [9–14]. The number and type of equilibria play a decisive role in the dynamic properties of chaotic system to some extent. A classic argument is that a dynamic system with one saddle focus connected by homoclinic orbit or two saddle foci connected by heteroclinic orbit generates horseshoe chaos [15]. It is generally recognized that no equilibrium chaotic

system may generate hidden attractor. Also, a lot of previous studies have shown that chaotic systems with multiple unstable equilibria usually have richer dynamic behaviors and are more likely to produce coexisting attractors. Therefore, many scholars tend to construct chaotic systems and distinguish their dynamic properties by configuring different quantities and types of equilibria. Chaotic systems with no equilibrium, one stable equilibrium, one unstable node, two saddle foci, circular equilibria, a line equilibria, and other types of equilibria have been reported [16–19].

Recently, the study of coexisting attractors and hidden attractors in chaotic systems has aroused great enthusiasm among scholars. Li et al. studied the coexisting attractors in Lorenz systems by some numerical experiments and proposed the conditional symmetry method to yield any number of coexisting attractors [20, 21]. Kengne et al. put forward some simple jerk systems with coexisting attractors [22]. Lai et al. introduced some effective methods to construct chaotic systems with infinitely many coexisting strange attractors [23, 24]. Li et al. designed a programmable chaotic circuit with infinitely many chaotic attractors and established the coexistence of multiple attractors by simulation methods [25]. Bao et al. found that memristor-based

chaotic systems can generate different types of coexisting attractors [26, 27]. Li et al. studied the coexisting attractors in memristor-based chaotic circuit in depth and considered its application in image encryption [28, 29]. Wei et al. studied the nonstationary chimeras in Hindmarsh–Rose neuronal network and found that the network coexists with periodic and chaotic states [30]. The history of studying the hidden attractors in dynamical systems without equilibria dates back to the well-known Sommerfeld effect, arising from feedback in the energy exchange between vibrating systems [31]. The electromechanical and drilling systems without equilibria have the ability to yield multiple hidden attractors [32, 33]. It is very interesting to generate as many hidden attractors as possible in chaotic system via some periodic functions which can continuously replicate the attractors in phase space. The attractors produced by this method usually have the same properties. Another interesting question is how many nontrivial attractors can be coexist in phase space of nonlinear system, which corresponds to a chaotic generalization [34] of the second part of Hilbert's 16th problem. Recently, the study of hidden attractors in chaotic systems has received increasing concern. Wei et al. generated an extended Rikitake system with hidden attractors [35] and investigated the hidden hyperchaos of five-dimensional self-exciting homopolar disc dynamo via analytical and numerical approaches [36]. Pham et al. did many important works on hidden attractors and first showed different families of hidden attractors in chaotic systems [37, 38]. Danca et al. discovered the hidden attractors of the classic Rabinovich–Fabrikant system [39]. Hidden attractor that refers to attractor whose basin of attraction does not intersect with small neighborhoods of equilibria [40] embodies some mysterious unknown dynamic behaviors of the system. The phenomenon of coexisting attractors that corresponds to the generation of multiple attractors with independent basins of attractions implies the strong influence of initial conditions on the final state of system. Both hidden attractors and coexisting attractors are interesting nonlinear dynamics worthy of further study. The construction of simple no-equilibrium chaotic system with an infinite number of hidden attractors is an interesting and challenging thing. It will be of great significance to reveal the complex behaviors of simple systems. However, most existing systems can generate a limited number of attractors. So this paper aims to present a new autonomous chaotic system with infinitely many coexisting hidden attractors from the perspective of building complex behavior of simple system. Necessary theoretical and experimental researches are given to illustrate the dynamic properties of the proposed system. The circuit and microcontroller implementations and synchronization control of the system are studied. The paper is organized as follows. Section 2 derives the model of the new system. Section 3 presents the coexisting hidden attractors of the system. Section 4 implements the system for physically illustrating its dynamics. Section 5 considers its synchronization problem. Section 6 summarizes the conclusions.

2. New Chaotic System

Looking back, an augmented Sprott B system is described by the following differential equations [41]:

$$
\begin{cases}
\dot{x}_1 = a(x_2 - x_1), \\
\dot{x}_2 = x_1 x_3 + x_4, \\
\dot{x}_3 = b - x_1 x_2, \\
\dot{x}_4 = -c x_2,
\end{cases}
\tag{1}
$$

where x_1, x_2, x_3, and x_4 are state variables and a, b, and c are parameters. The previous study has shown that system (1) has no equilibrium and coexists with two symmetric strange attractors. Replacing the nonlinear term $x_1 x_3$ of system (1) with $k x_1 \sin(x_3)$ ($k > 0$ is a real number), then the following new chaotic system is established:

$$
\begin{cases}
\dot{x}_1 = a(x_2 - x_1), \\
\dot{x}_2 = k x_1 \sin(x_3) + x_4, \\
\dot{x}_3 = b - x_1 x_2, \\
\dot{x}_4 = -c x_2.
\end{cases}
\tag{2}
$$

System (2) and system (1) have some similar properties including the following: (i) they have no equilibrium because there exists no point that satisfies $\dot{x}_1 = \dot{x}_2 = \dot{x}_3 = \dot{x}_4 = 0$; (ii) they are dissipative with the divergence $\nabla V = \partial \dot{x}_1/\partial x_1 + \partial \dot{x}_2/\partial x_2 + \partial \dot{x}_3/\partial x_3 + \partial \dot{x}_4/\partial x_4 = -a < 0$ for $a > 0$; (iii) they have the symmetry under the transformation $(x_1, x_2, x_3, x_4) \longrightarrow (-x_1, -x_2, x_3, -x_4)$; and (iv) they have hidden attractors whose basins of attraction do not intersect with small neighborhoods of any equilibria. However, the remarkable difference between them is that system (2) can generate infinitely many coexisting hidden attractors while system (1) only generates no more than three attractors for given parameters. Also, to our best knowledge, system (2) has never been reported before. Thus, system (2) can be classified as a new chaotic system. The following section will give an intuitive observation of the dynamic properties of system (2).

3. Coexisting Hidden Attractors

Here, we will investigate the influence of the parameters and initial conditions on the dynamic behaviors of system (2) by simulation experiments, emphasizing the existence of infinitely many hidden chaotic and periodic attractors in system (2). We apply the well-known fourth-fifth-order Runge–Kutta method to numerically solved system (2) on Matlab platform. All the simulation results are obtained by fixing the step size $\Delta t = 0.01$ and time region $t \in [0, 300]$. The Lyapunov exponents are calculated along the trajectories of system (2) by using the Wolf method [42]. We also can further consider the Lyapunov exponents by using the method proposed in literature [43]. Here, the Lyapunov exponents are used to distinguish the chaotic, periodic, and stable states of system (2). So, we use the conventional method to calculate them. There is no doubt that a system with the positive largest Lyapunov exponent cannot be

judged to be chaotic directly. It also requires that the system is bounded. However, it is difficult to quantitatively establish the boundedness of the system by using the analytical method. In our simulations, we try many experiments to demonstrate the boundedness of system (2). It shows that all the state variables remain in a bounded range for a long enough time in our simulations, which partially implies the boundedness of system (2). Actually, the dissipativity of system (2) for $a > 0$ can partially determine its boundedness. Also, the literature [44] gives an interesting work corresponding to a new idea on the boundedness of chaotic systems.

Firstly, we study the dynamic evolution of system (2) with respect to the parameters. It is easy to generate the bifurcation diagram and Lyapunov exponents of system (2) for the parameters $a \in [4, 20]$, $b = c = 1$, and $k = 12$ and initial value $(1, 1, 1, 1)$. From Figure 1, we get that system (2) makes chaotic, quasiperiodic, and periodic motions for different values of a. When $a = 4$, system (2) has a strange attractor shown in Figure 2. The positive maximum Lyapunov exponent $L_1 \approx 0.4456$ and fractal Lyapunov dimension $D_L \approx 3.0996$ imply the chaotic feature of the attractor. When $a = 12$, system (2) performs quasiperiodic motion as its first two Lyapunov exponents $L_1 = L_2 \approx 0$. The phase portraits of the quasiperiodic attractor are given in Figure 3. When $a = 20$, system (2) performs periodic motion as illustrated in Figure 4.

We also can illustrate the dynamic evolution of system (2) corresponding to the parameters $a = 4$, $b = 1$, $c \in [1, 12]$, and $k = 12$ and initial value $(1, 1, 1, 1)$ via the bifurcation diagram and Lyapunov exponents in Figure 5. It indicates that the chaotic, quasiperiodic, and periodic motions will generate with the variation of c. Figure 6 shows the chaotic and quasiperiodic motions of system (2) with $c = 6, 12$.

Secondly, we will consider the influence of initial value on the final state of system (2). Let the parameters $a = 4$, $b = c = 1$, and $k = 12$ and initial value $x_0 = (x_{10}, x_{20}, x_{30}, x_{40})$ with $x_{10} = x_{20} = x_{40} = 1$; then we can plot the bifurcation diagram and Lyapunov exponents of system (2) for $x_{30} \in [0, 35]$, as given in Figure 7. It is easy to know that system (2) coexists with six chaotic attractors for $x_{30} \in [0, 35]$ from Figure 7. We can obtain the attractors by plotting the phase portraits of system (2) from initial values $(1, 1, 2j\pi, 1)$, $j = 0, 1, 2, , 3, 4, 5$. As shown in Figure 8, the attractors are generated along the x_3-axis and all these attractors have the same nature. Also, the coexisting quasiperiodic (or periodic) attractors can be obtained in system (2) by fixing $a = 12$, $b = c = 1$, and $k = 12$ (or $a = 20$, $b = c = 1$, and $k = 12$). Figure 9 shows six quasiperiodic (or periodic) attractors of system (2) yielded from initial values $(1, 1, 2j\pi, 1)$, $j = 0, 1, 2, 3, 4, 5$. As a matter of fact, system (2) has the ability to generate infinitely many hidden attractors from initial values $(1, 1, 2j\pi, 1)$, $j = 0, \pm 1, \pm 2, \ldots, \pm n$ along the x_3-axis.

4. Circuit and Microcontroller Realization

From the theoretical study presented above, it is predicted that system (2) exhibits a plethora of interesting dynamic behaviors for suitable sets of parameters and initial conditions. The goal of this section is to investigate the practical implementation of system (2). The corresponding circuit in Figure 10 is designed using commercially available off-the-shelf electronic components, operational amplifiers, and analog multipliers AD633 integrated circuits, all powered by $\pm 18 \, \text{V}$ symmetric voltages.

The state variables x_1, x_2, x_3, and x_4 are emulated by output signals of integrators. Using the basic electrical circuit's laws, system (2) can be rewritten as

$$
\begin{cases}
x_1 = \dfrac{R_4}{R_1} \dfrac{1}{RC_1} \int \left(\dfrac{R}{R_2} x_2 - \dfrac{R}{R_1} x_1 \right) dt, \\[2ex]
x_2 = \dfrac{R_8}{R_7} \dfrac{1}{RC_2} \int \left(\dfrac{R}{R_5} x_1 \sin(x_3) - \dfrac{R}{R_6} x_4 \right) dt, \\[2ex]
x_3 = \dfrac{R_{12}}{R_{11}} \dfrac{1}{RC_3} \int \left(\dfrac{R}{R_{10}} V_b - \dfrac{R}{R_9} x_1 x_2 \right) dt, \\[2ex]
x_4 = \dfrac{1}{RC_4} \int \left(\dfrac{R}{R_{13}} x_2 \right) dt.
\end{cases}
\tag{3}
$$

By taking $C_1 = C_2 = C_3 = C_4 = C$, $R_6 = R_9 = R_{10} = R$, $R_3 = R_4 = R_7 = R_8 = R_{11} = R_{12} = 10 \, k\Omega$, and $R_1 = R_2 = R_a$, we have the parameters $a = R/R_a$, $k = R/R_5$, $b = V_b$, and $c = R/R_{13}$ and the time scaling factor $\tau = t/RC$. From this point, it is easy to demonstrate that the differentiation of system (3) is equivalent to the original system (2). Let $C = 10 \, \text{nF}$, $R = 100 \, k\Omega$, $R_a = 25 \, k\Omega$, $R_5 = 8.3333 \, k\Omega$, $R_{13} = 100 \, k\Omega$, and $V_b = 1 \, \text{V}$; a chaotic behavior is observed in Figure 11. Periodic and quasiperiodic orbits are also noticed from the analog circuit; see Figure 12. Other cases of chaotic and quasiperiodic behaviors are also observed from the analog circuit, as illustrated in Figures 13 and 14.

Up to five coexisting chaotic attractors, five coexisting limit cycles, and five coexisting quasiperiodic orbits are noticed for the initial voltage of the capacitor C_3 successively fixed as $(1, 1, -6\pi)$, $(1, 1, -4\pi)$, $(1, 1, -2\pi)$, $(1, 1, 0)$, $(1, 1, 2\pi)$, and $(1, 1, 4\pi)$ as illustrated in Figure 15.

Next, we will present the microcontroller-based implementation of system (2) by using an Arduino Mega 2650 board. It is a low-cost open-source and easy-to-use electronic board based on the ATMEGA2560 microcontroller. The designed system is simulated and realized using the scheme on Figure 16. The digital outputs of the microcontroller board are connected to two R-2R ladders acting here as Digital-to-Analog Converters (DAC). The converted analog signals corresponding to the state variables of system (2) are simultaneously visualized on an oscilloscope and a computer through a low-cost data acquisition module. The program is written in such a way that the magnitude of the output signals can be adjusted within the voltage range $0 - 5 \, \text{V}$. Figure 17 shows the practical setup of the experiment on the microcontroller-based implementation of system (2).
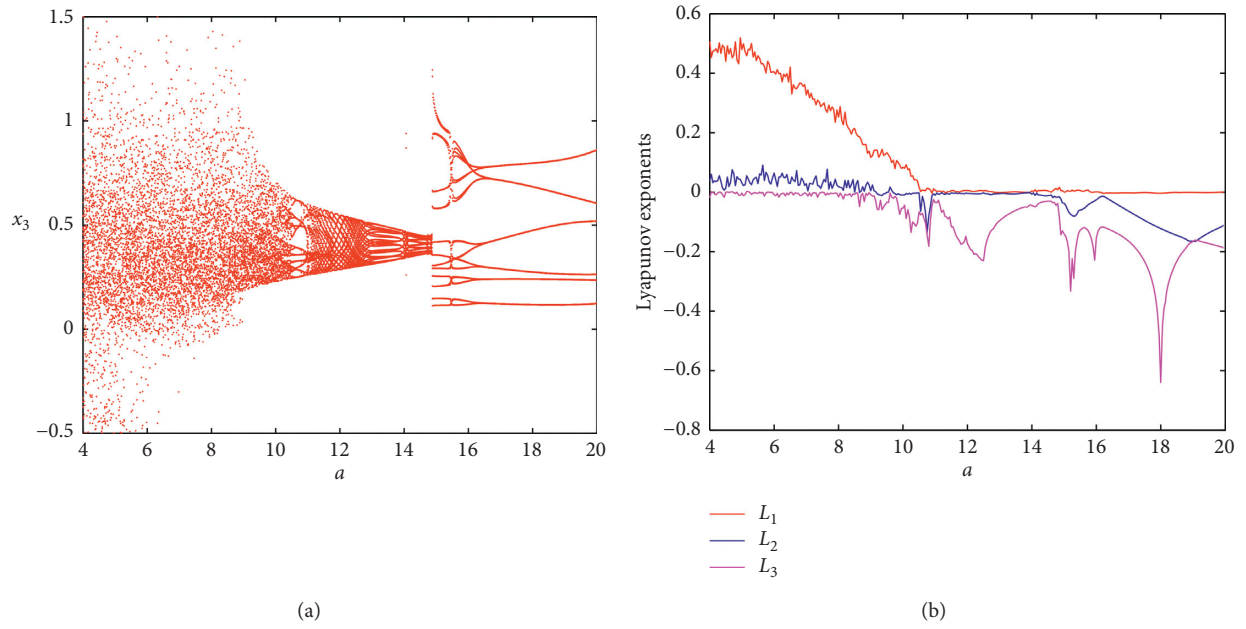
(a)

(b)

FIGURE 1: Bifurcation diagram and Lyapunov exponent of system (2) versus $a \in [4, 20]$ from initial value $(1, 1, 1, 1)$, where $L_1 > L_2 > L_3 > L_4$ are Lyapunov exponents of system (2) and L_4 is always less than -4.
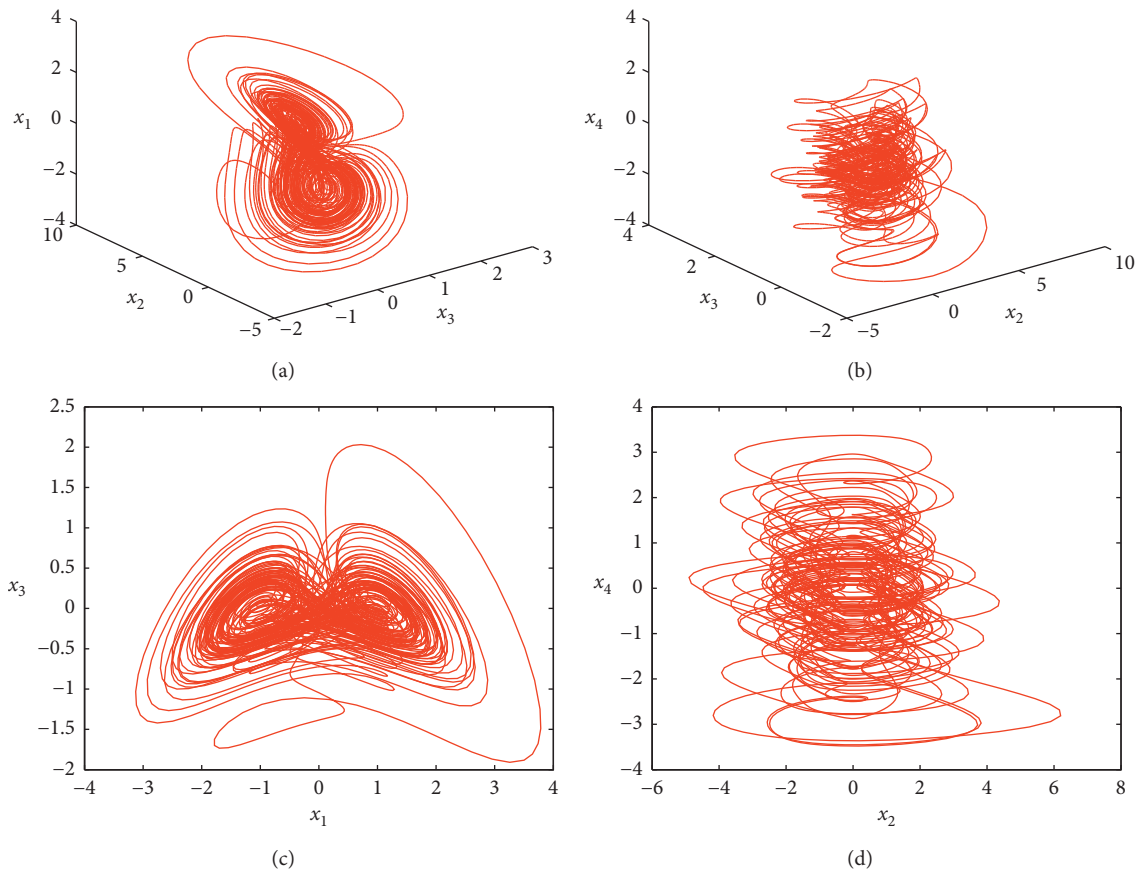

(a)

(b)

(c)

(d)

FIGURE 2: Chaotic attractor of system (2) with $a = 4$, $b = c = 1$, and $k = 12$: (a) $x_3 - x_2 - x_1$; (b) $x_2 - x_3 - x_4$; (c) $x_1 - x_3$; (d) $x_2 - x_4$.
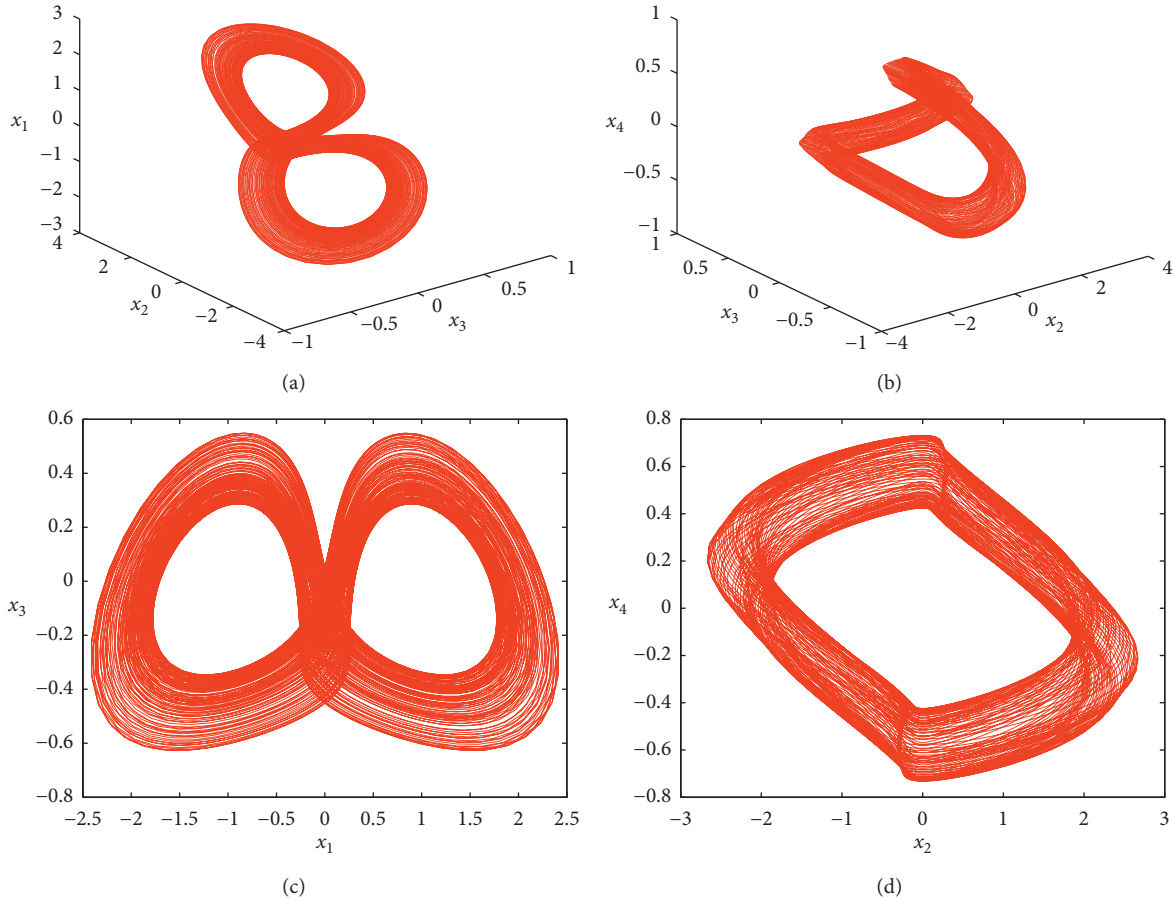
(a)

(b)

(c)

(d)

FIGURE 3: Quasiperiodic motion of system (2) with $a = 12$, $b = c = 1$, and $k = 12$: (a) $x_3 - x_2 - x_1$; (b) $x_2 - x_3 - x_4$; (c) $x_1 - x_3$; (d) $x_2 - x_4$.

The phase portraits and time series obtained from the microcontroller-based implementation of system (2) confirm all the predicted dynamic behaviors. Chaotic, periodic, and quasiperiodic motions are all observed as illustrated in Figure 18. Other cases of chaotic and quasiperiodic motions are also observed for appropriated sets of parameters, as illustrated in Figure 19.

The phase portraits obtained from the microcontroller-based implementation, the analog circuit, and the numerical study are all in accordance. The new chaotic system is able to generate a multitude of coexisting attractors under various types of dynamic behaviors.

5. Synchronization Control

In various chaos-based technological applications like secure communication or cryptography, synchronization is needed between a master system (sender) and a slave system (receiver). The practical realization of such mechanisms is subject to many challenges. In electronic implementations, the ageing, the temperature effects, the electromagnetic activity of the environment, and the nonideal behavior of the channel are some of the various factors which can induce huge errors and undesirable consequences. This is why it is important to design an adaptive synchronization scheme for chaotic system with unknown parameters. The adaptive

synchronization of chaotic system has important practical significance. It extends the engineering applications of chaotic system and shows the ability of chaotic system to change its own characteristics or use the external control input to achieve synchronization when the information of the system and environment has some uncertainty. Among the several synchronization techniques, the adaptive method appears to be one of the most interesting because of its robustness and its simplicity of implementation. It has proved to be an effective method to synchronize the chaotic system with unknown parameters [45, 46]. In many practical systems, the parameters of systems are probably unknown or change from time to time. For such systems, the adaptive control is a better choice to realize the synchronization. Also, the adaptive control can be used in combination with other control methods. In addition, no prior knowledge of parameters is needed for master system and slave system to be synchronized [47, 48]. Because of these advantages, the adaptive control is widely accepted in academic circles and its application on synchronization has been reported by many scholars [49, 50]. This section will consider the adaptive synchronization problem of system (2). The result is based on the Lyapunov stability theory. All the parameters of the master system are accessible to measurements and those of the slave system are unknown. Consider the following master system:
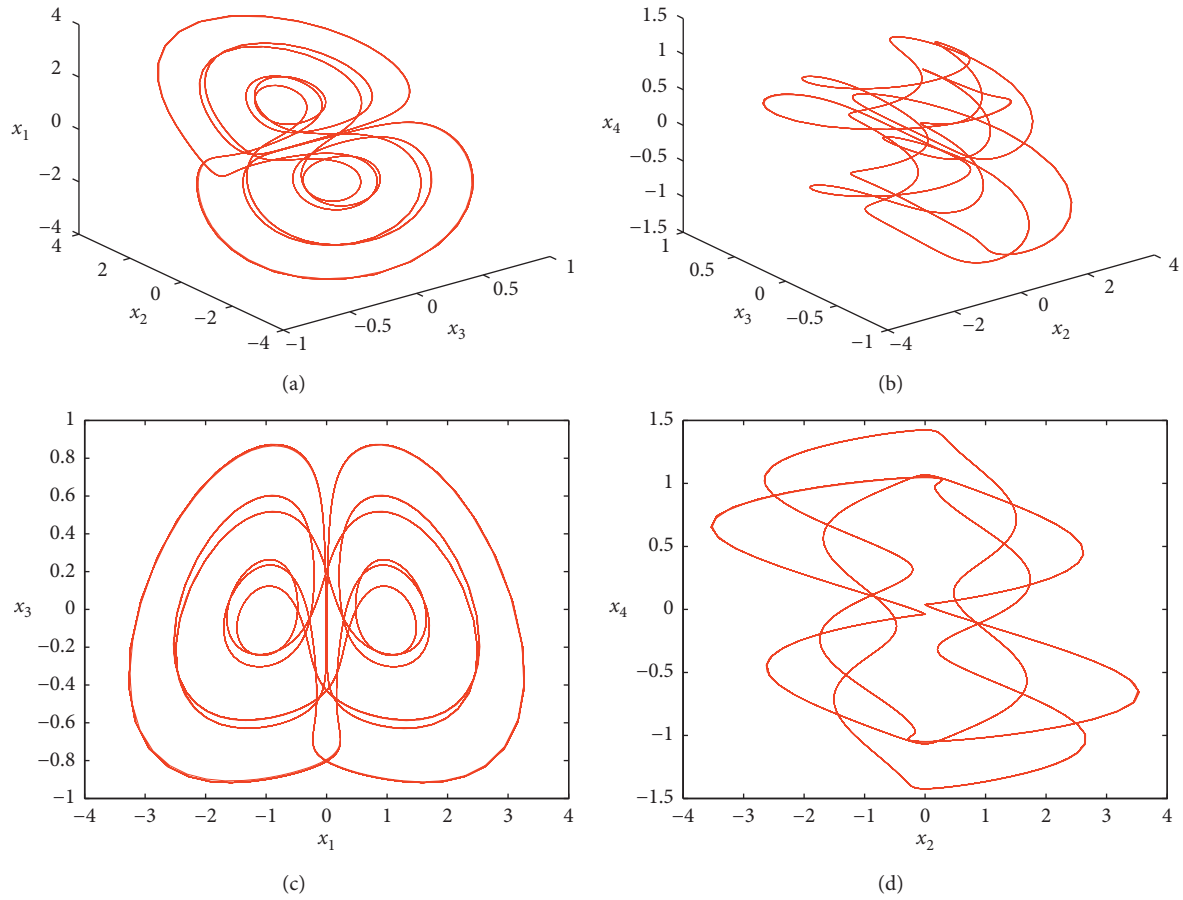
(a)

(b)

(c)

(d)

Figure 4: Periodic motion of system (2) with $a = 20$, $b = c = 1$, and $k = 12$: (a) $x_3 - x_2 - x_1$; (b) $x_2 - x_3 - x_4$; (c) $x_1 - x_3$; (d) $x_2 - x_4$.
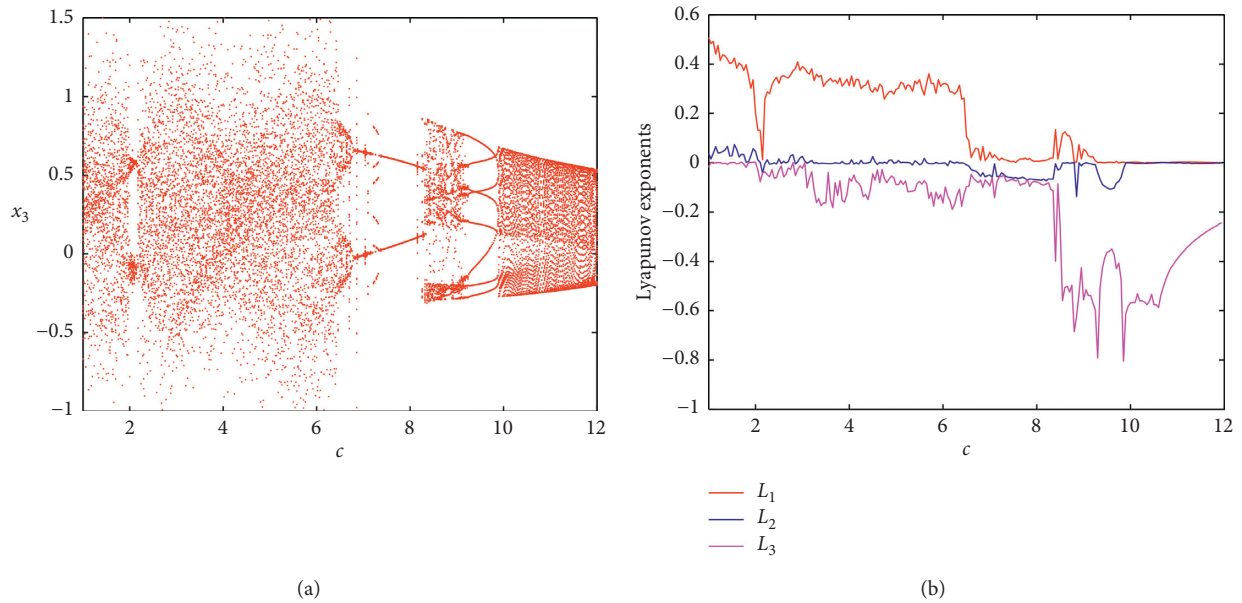

(a)

(b)

Figure 5: Bifurcation diagram and Lyapunov exponents of system (2) versus $c \in [1, 12]$ from initial value $(1, 1, 1, 1)$, where $L_1 > L_2 > L_3 > L_4$ are Lyapunov exponents of system (2) and L_4 is always less than -4.
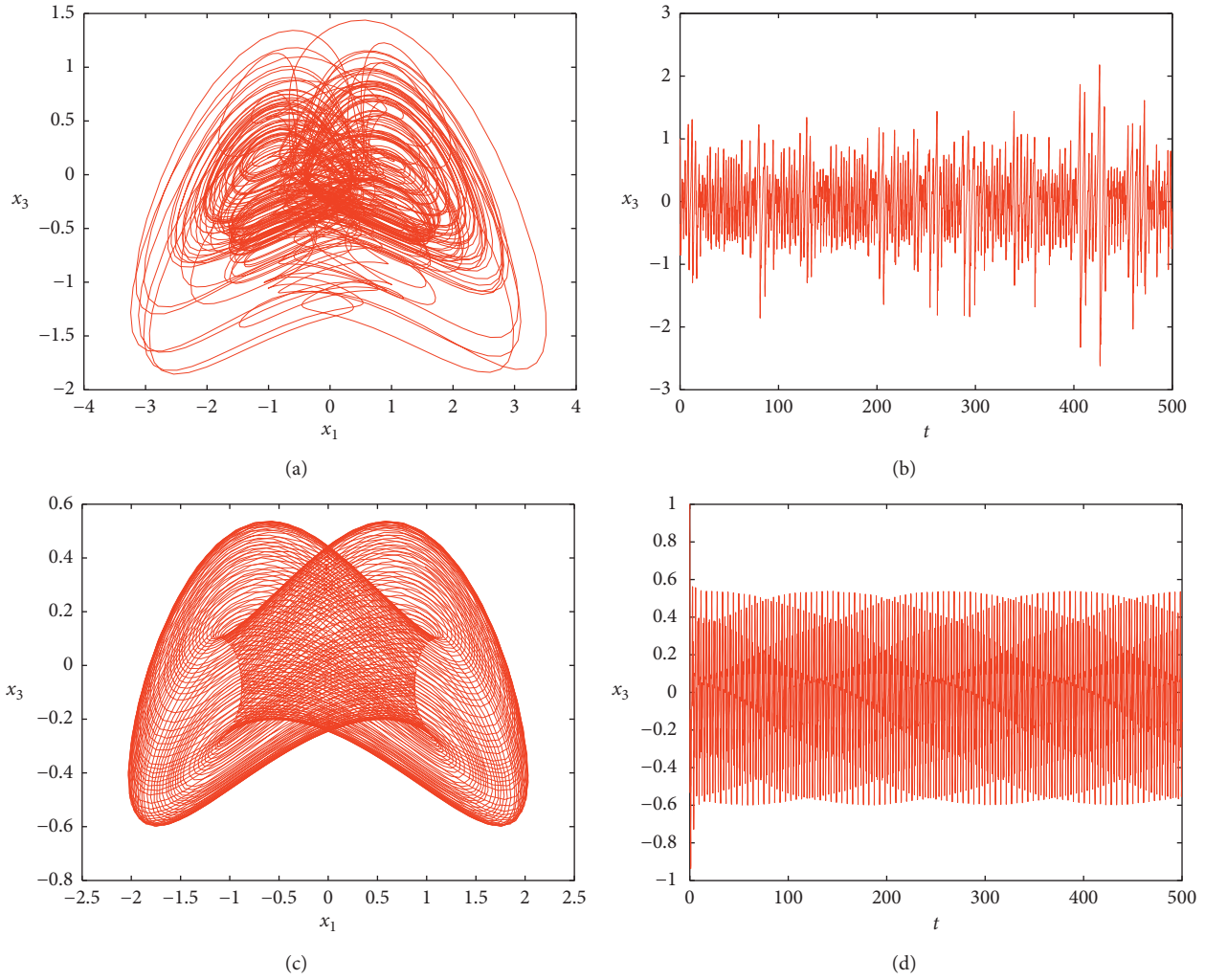
(a)

(b)

(c)

(d)

FIGURE 6: Chaotic and quasiperiodic motions of system (2) with $a = 4$ and $b = 1$: (a, b) $c = 6$; (c, d) $c = 12$.

(a)

(b)
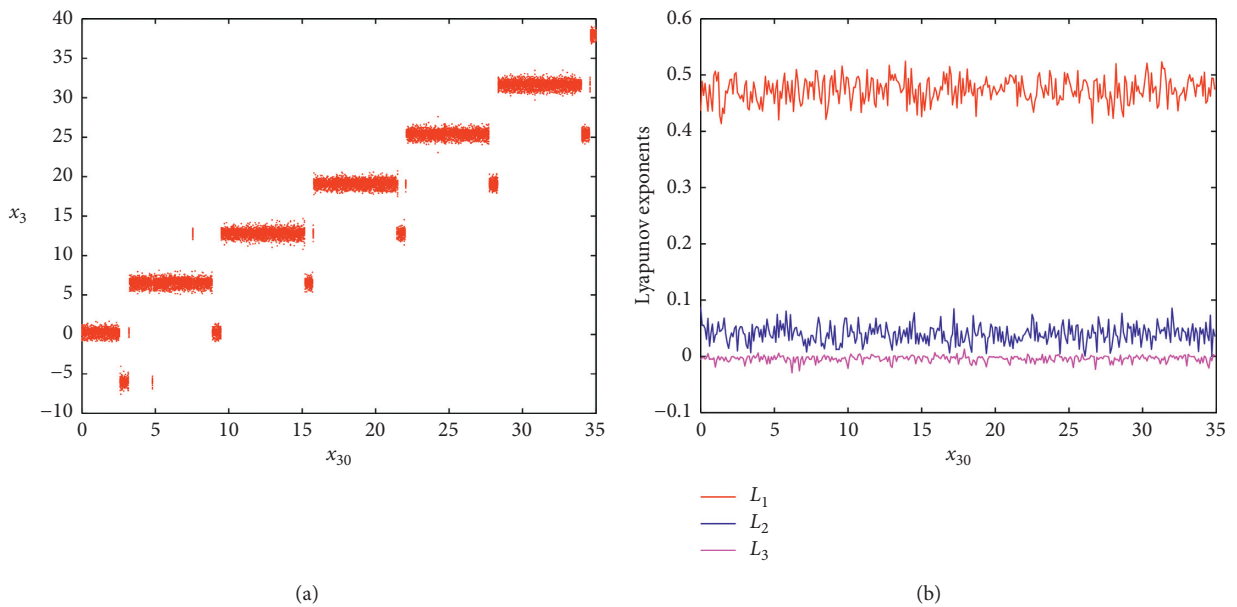
FIGURE 7: Bifurcation diagram and Lyapunov exponent of system (2) with $a = 4$, $b = c = 1$, $k = 12$, and $x_{30} \in [0, 35]$, where $L_1 > L_2 > L_3 > L_4$ are Lyapunov exponents of system (2) and L_4 is always less than -4.

(a)

(b)
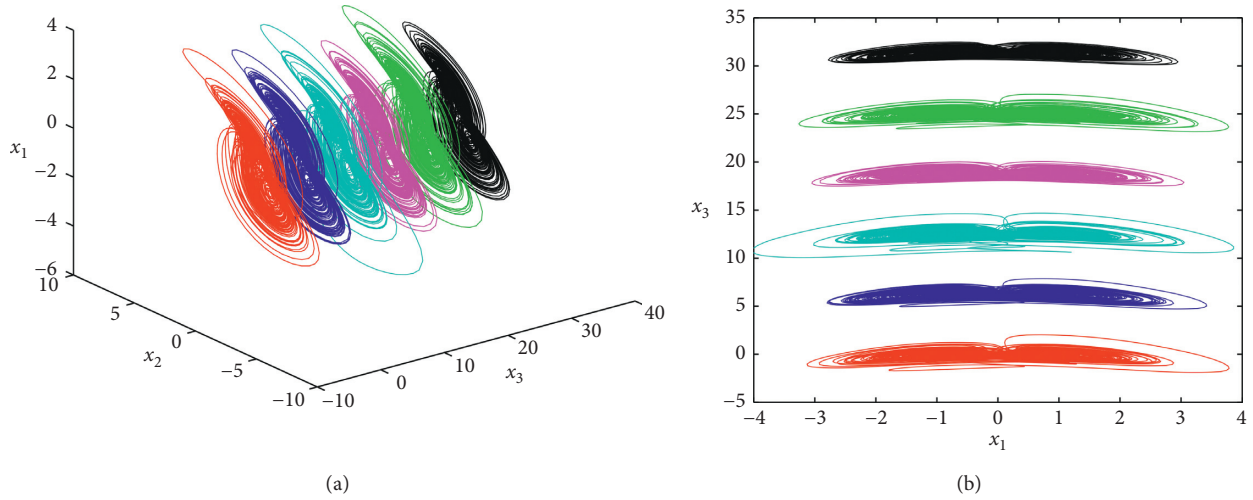
FIGURE 8: Coexisting six hidden strange attractors of system (2) with $a = 4$, $b = c = 1$, and $k = 12$ and initial values $(1, 1, 2j\pi, 1)$, $j = 0, 1, 2, 3, 4, 5$.

(a)

(b)
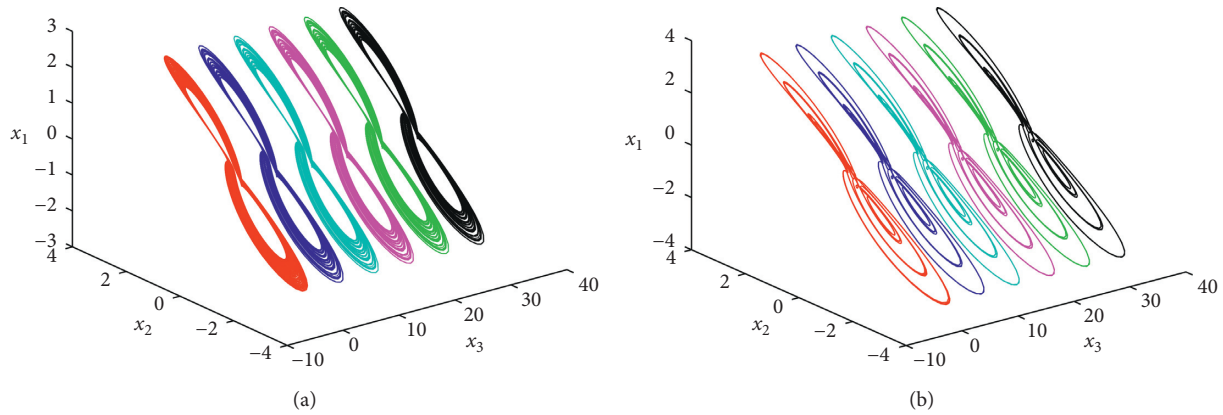
FIGURE 9: Coexisting six hidden attractors of system (2) from initial values $(1, 1, 2j\pi, 1)$, $j = 0, 1, 2, 3, 4, 5$. (a) Quasiperiodic attractors for $a = 12$, $b = c = 1$, and $k = 12$. (b) Periodic attractors for $a = 20$, $b = c = 1$, and $k = 12$.
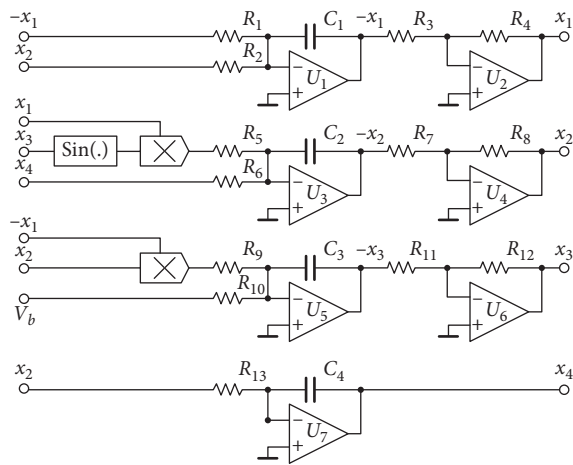
FIGURE 10: Analog circuit of system (2).

$$\begin{cases} \dot{x}_1 = a(x_2 - x_1), \\ \dot{x}_2 = kx_1 \sin(x_3) + x_4, \\ \dot{x}_3 = b - x_1 x_2, \\ \dot{x}_4 = -cx_2, \end{cases} \quad (4)$$

and the slave system is given by

$$\begin{cases} \dot{y}_1 = a(y_2 - y_1) + u_1, \\ \dot{y}_2 = ky_1 \sin(y_3) + y_4 + u_2, \\ \dot{y}_3 = b - y_1 y_2 + u_3, \\ \dot{y}_4 = -cy_2 + u_4, \end{cases} \quad (5)$$

where $u = (u_1, u_2, u_3, u_4)^T$ is the adaptive control law to be designed. The parameters of the slave system are all unknown and the design goal is to find the control feedback law
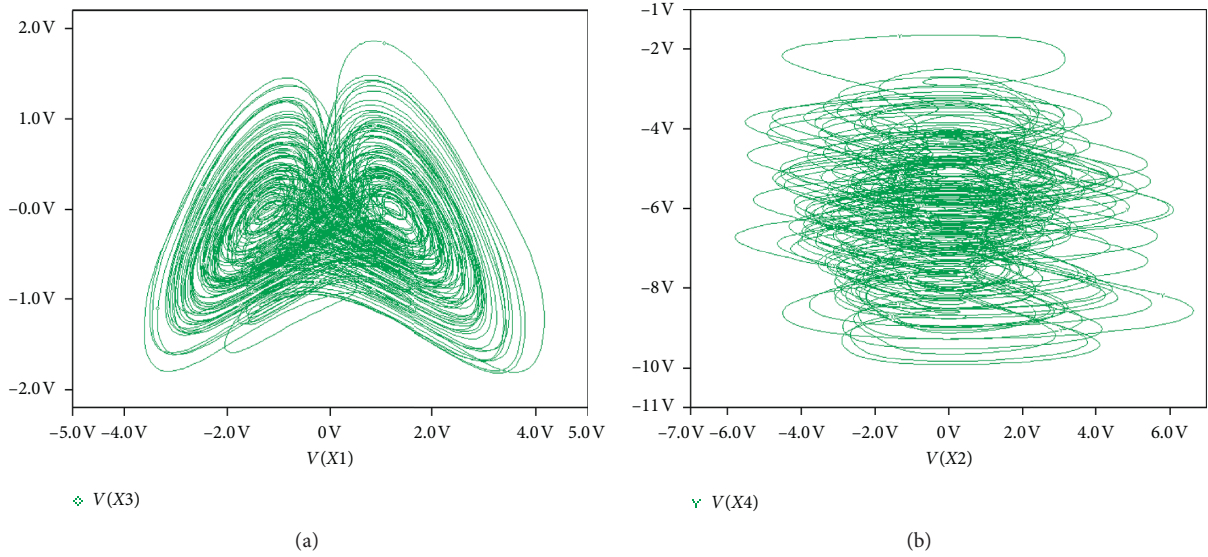
FIGURE 11: A chaotic attractor of system (2) obtained from the analog circuit for $R_a = 25\,k\Omega$, $R_5 = 8.3333\,k\Omega$, $R_{13} = 100\,k\Omega$, and $V_b = 1$ V: (a)$x_1 - x_3$; (b)$x_2 - x_4$.

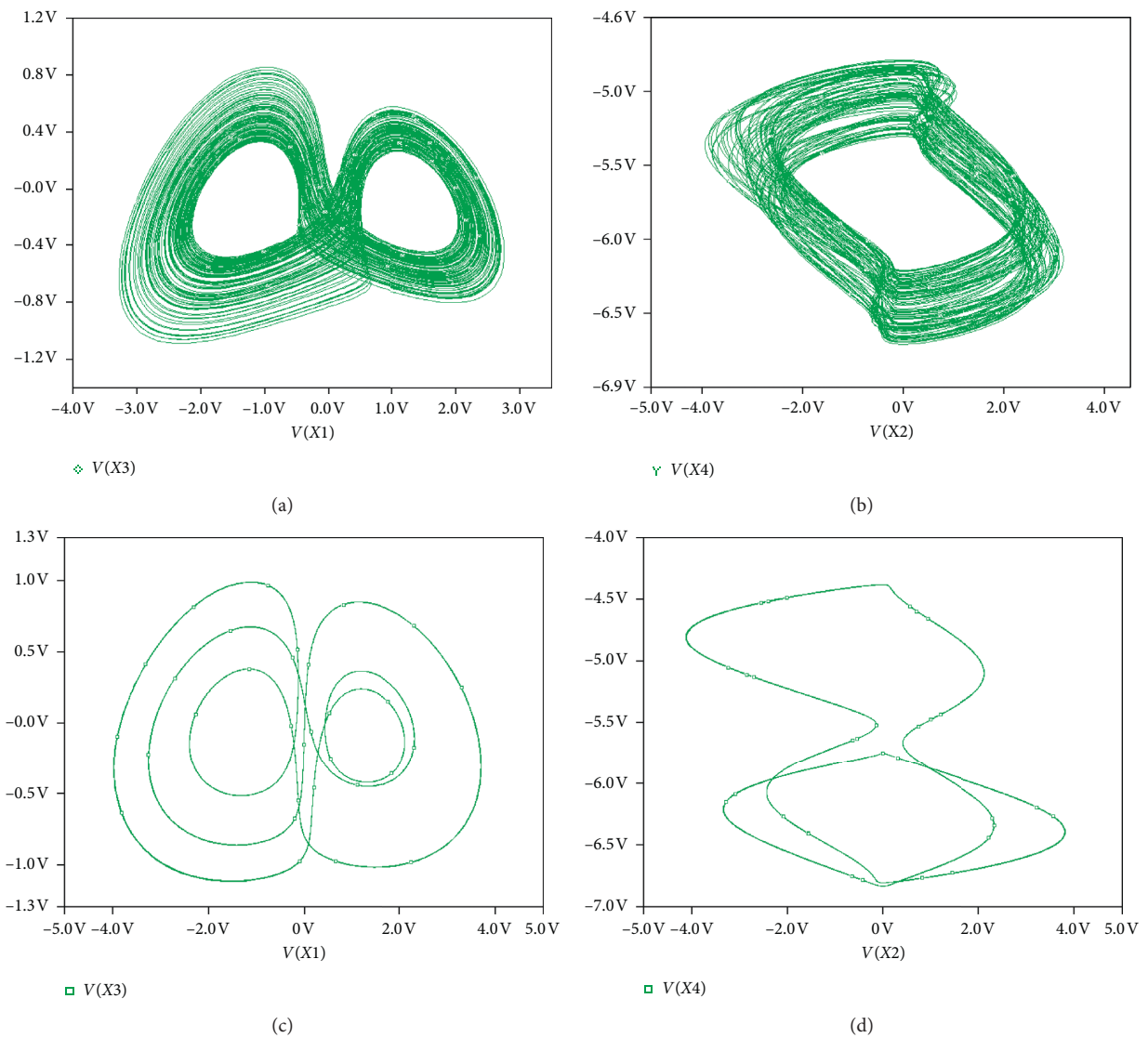FIGURE 12: Quasiperiodic motion observed for $R_a = 10\,k\Omega$, $R_5 = 8.3333\,k\Omega$, $R_{13} = 100\,k\Omega$, and $V_b = 1$ V: (a)$x_1 - x_3$; (b)$x_2 - x_4$. Periodic motion observed for $R_a = 2.65\,k\Omega$, $R_5 = 8.3333\,k\Omega$, $R_{13} = 100\,k\Omega$, and $V_b = 1$ V: (c)$x_1 - x_3$; (d)$x_2 - x_4$.

(a)

(b)
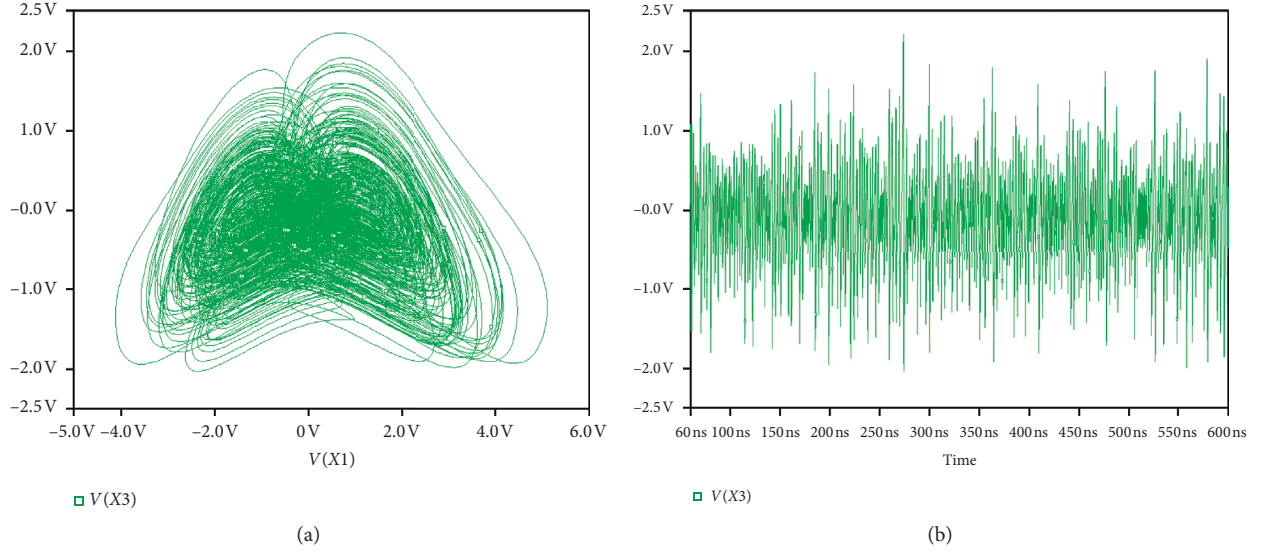
Figure 13: Chaotic behavior of system (2) observed for $R_a = 25\,k\Omega$, $R_5 = 8.3333\,k\Omega$, $R_{13} = 8.333\,k\Omega$, and $V_b = 0.8$ V: (a)$x_1 - x_3$; (b)$x_2 - x_4$.
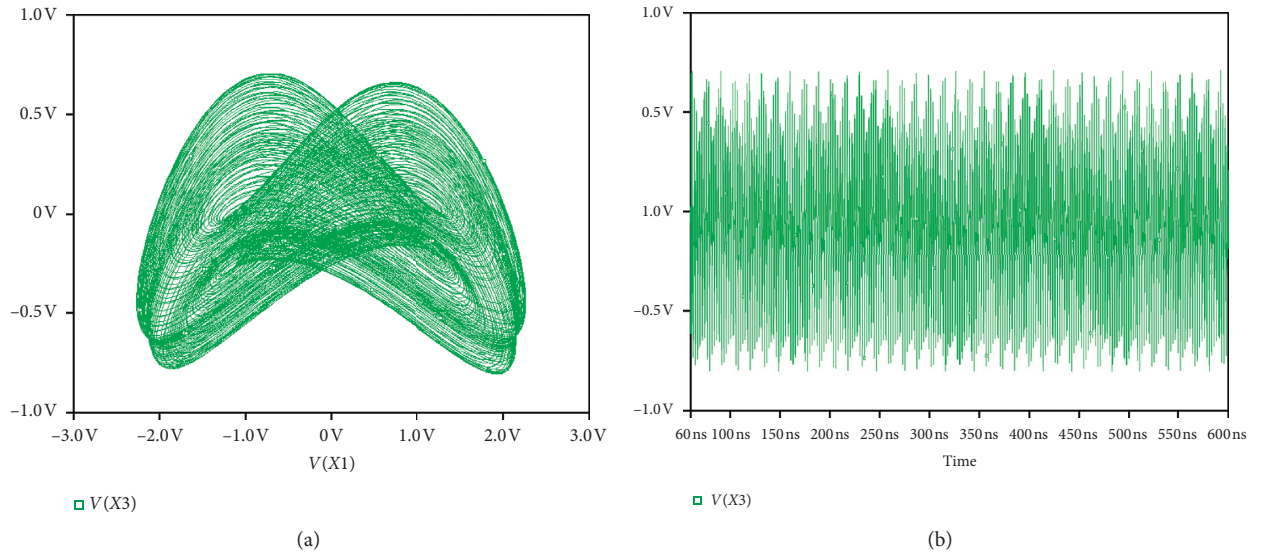

(a)

(b)

Figure 14: Periodic orbit observed from the analog circuit of the novel system for $R_a = 25\,k\Omega$, $R_5 = 8.33334\,k\Omega$, $R_{13} = 16.6667\,k\Omega$, and $V_b = 0.8$ V: (a)$x_1 - x_3$; (b)$x_2 - x_4$.

u to eliminate the error between the master system and the slave system. The synchronization error is defined as follows:

$$\begin{cases} e_1 = y_1 - x_1, \\ e_2 = y_2 - x_2, \\ e_3 = y_3 - x_3, \\ e_4 = y_4 - x_4. \end{cases} \tag{6}$$

The corresponding error system is written as

$$\begin{cases} \dot{e}_1 = a(e_2 - e_1) + u_1, \\ \dot{e}_2 = k(y_1 \sin(y_3) - x_1 \sin(x_3)) + e_4 + u_2, \\ \dot{e}_3 = x_1 x_2 - y_1 y_2 + u_3, \\ \dot{e}_4 = -ce_2 + u_4. \end{cases} \tag{7}$$

Give the adaptive feedback control laws as follows:

$$\begin{cases} u_1 = -\hat{a}(t)(e_2 - e_1) - g_1 e_1, \\ u_2 = -\hat{k}(t)(y_1 \sin(y_3) - x_1 \sin(x_3)) - e_4 - g_2 e_2, \\ u_3 = -x_1 x_2 + y_1 y_2 - g_3 e_3, \\ u_4 = \hat{c}(t)e_2 - g_4 e_4, \end{cases} \tag{8}$$
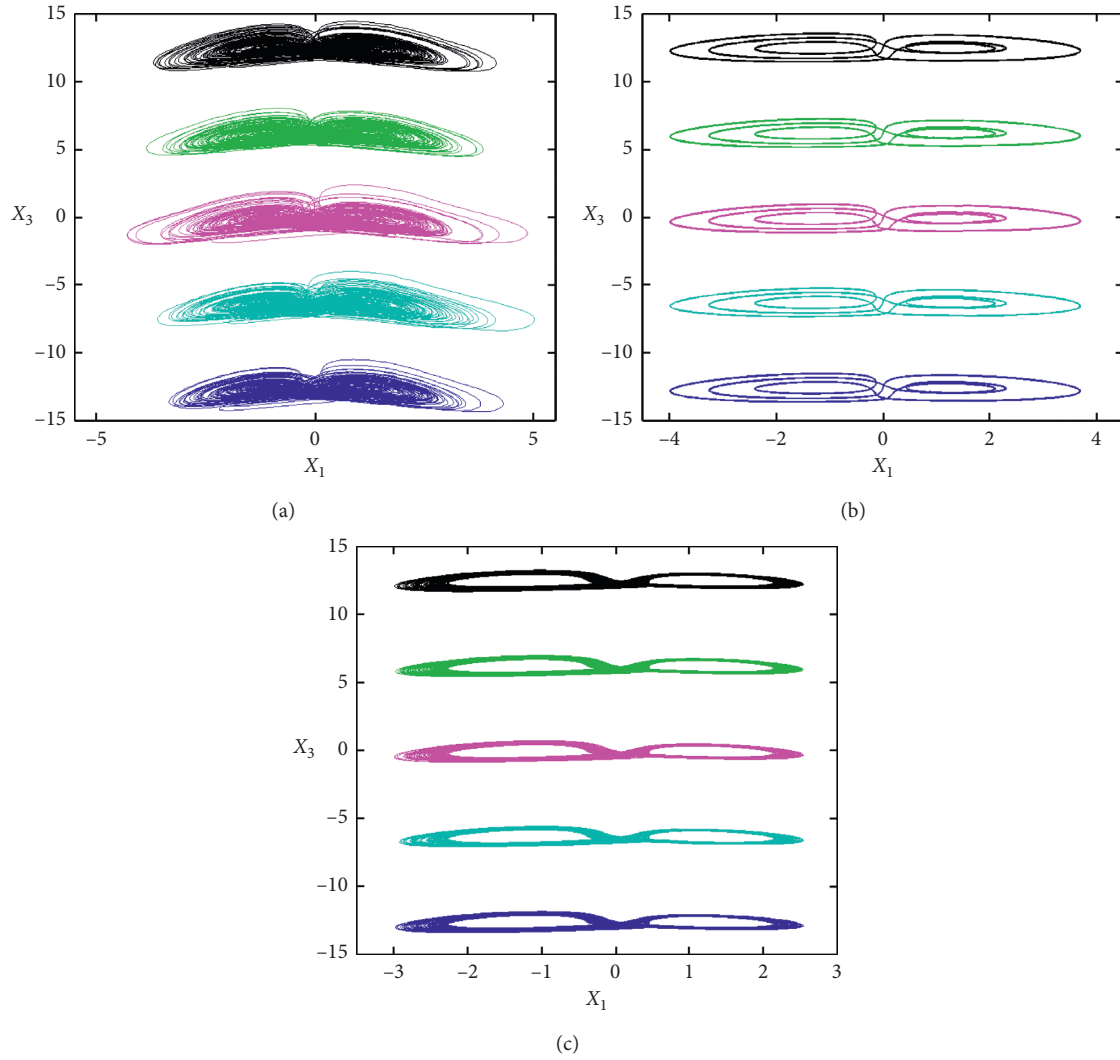
(a)

(b)

(c)

FIGURE 15: Projections on $x_1 - x_3$ plane of coexisting attractors obtained from the analog circuit of system (2) for initial voltage of capacitor C_3 fixed as $(1, 1, -6\pi)$, $(1, 1, -4\pi)$, $(1, 1, -2\pi)$, $(1, 1, 0)$, $(1, 1, 2\pi)$, and $(1, 1, 4\pi)$: (a) coexisting five chaotic attractors; (b) coexisting five periodic attractors; (c) coexisting five quasiperiodic attractors.
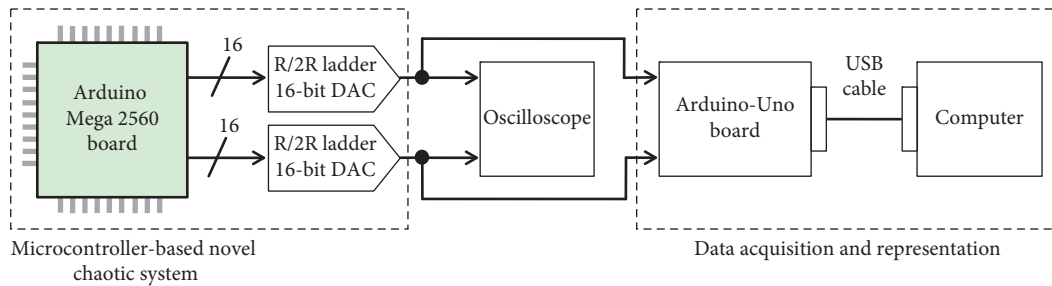

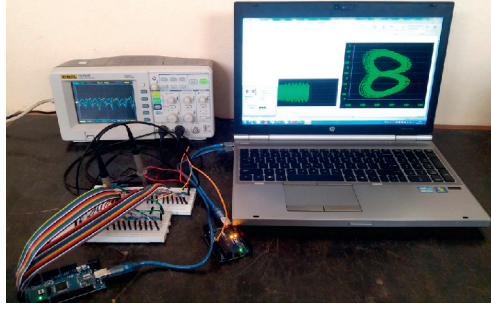FIGURE 16: Scheme of the experiment on microcontroller-based implementation of system (2).

FIGURE 17: Practical setup for the experiment on the microcontroller-based on the implementation of system (2).
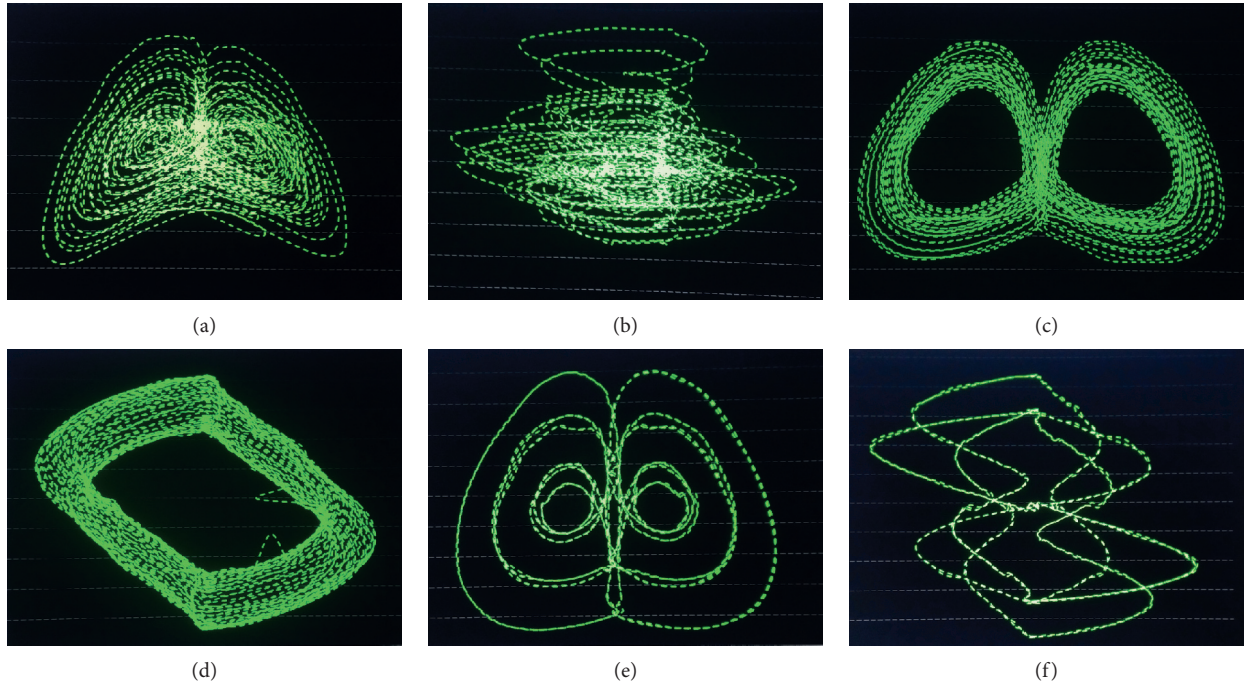

(a)

(b)

(c)

(d)

(e)

(f)

FIGURE 18: Experimental phase portraits from the microcontroller-based implementation of system (2): (a, b) projections on $x_1 - x_3$ and $x_2 - x_4$ planes for chaotic attractor; (c, d) projections on $x_1 - x_3$ and $x_2 - x_4$ planes for quasiperiodic attractor; (e, f) projections on $x_1 - x_3$ and $x_2 - x_4$ planes for periodic attractor.

where g_1, g_2, g_3, and g_4 are positive gain constants. By substituting the control laws u_1, u_2, u_3, and u_4 into system (7), we get

$$\begin{cases} \dot{e}_1 = (a - \widehat{a}(t))(e_2 - e_1) - g_1 e_1, \\ \dot{e}_2 = (k - \widehat{k}(t))(y_1 \sin(y_3) - x_1 \sin(x_3)) - g_2 e_2, \\ \dot{e}_3 = -g_3 e_3, \\ \dot{e}_4 = -(c - \widehat{c}(t))e_2 - g_4 e_4. \end{cases} \quad (9)$$

The errors in system (9) can be simplified by taking the parameter estimation errors as

$$\begin{cases} e_a(t) = a - \widehat{a}(t), \\ e_b(t) = b - \widehat{b}(t), \\ e_c(t) = c - \widehat{c}(t), \\ e_k(t) = k - \widehat{k}(t). \end{cases} \quad (10)$$

It follows that

$$\begin{cases} \dot{e}_a = -\widehat{a}(t), \\ \dot{e}_b = -\widehat{b}(t), \\ \dot{e}_c = -\widehat{c}(t), \\ \dot{e}_k = -\widehat{k}(t). \end{cases} \quad (11)$$

Thus, system (9) can be rewritten as

$$\begin{cases} \dot{e}_1 = e_a(e_2 - e_1) - k_1 e_1, \\ \dot{e}_2 = e_k(y_1 \sin(y_3) - x_1 \sin(x_3)) - k_2 e_2, \\ \dot{e}_3 = -k_3 e_3, \\ \dot{e}_4 = -e_c e_2 - k_4 e_4. \end{cases} \quad (12)$$

Next we will establish the synchronization conditions by using the Lyapunov function. Consider the Lyapunov function
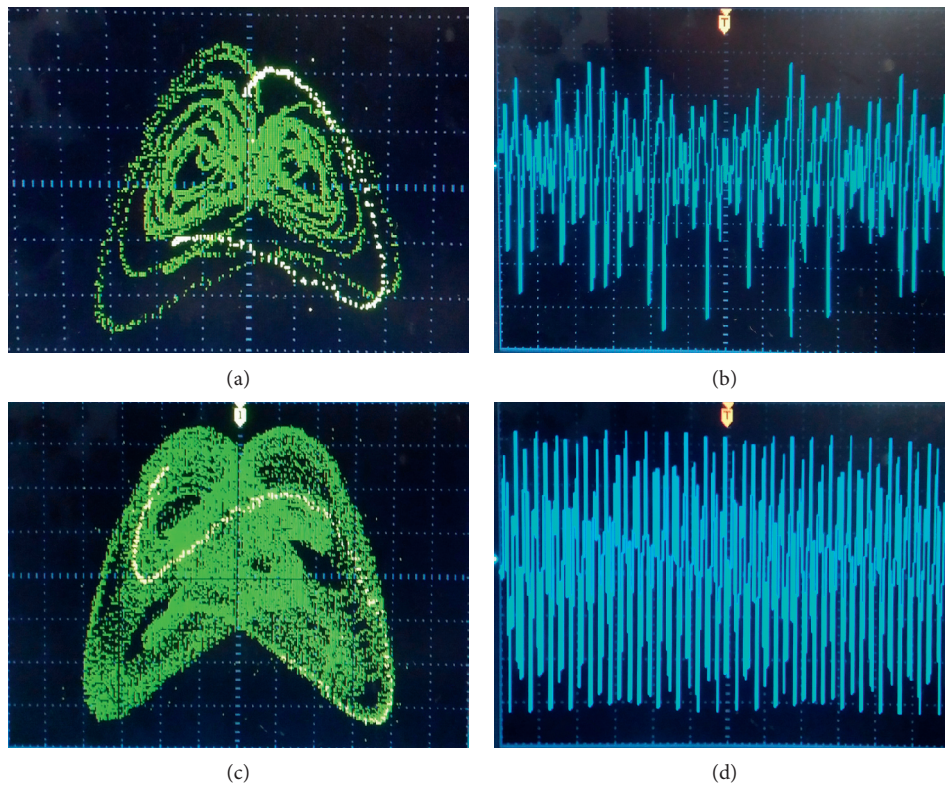
(a)

(b)

(c)

(d)

FIGURE 19: Chaotic and quasiperiodic attractors from the microcontroller-based implementation of system (2).
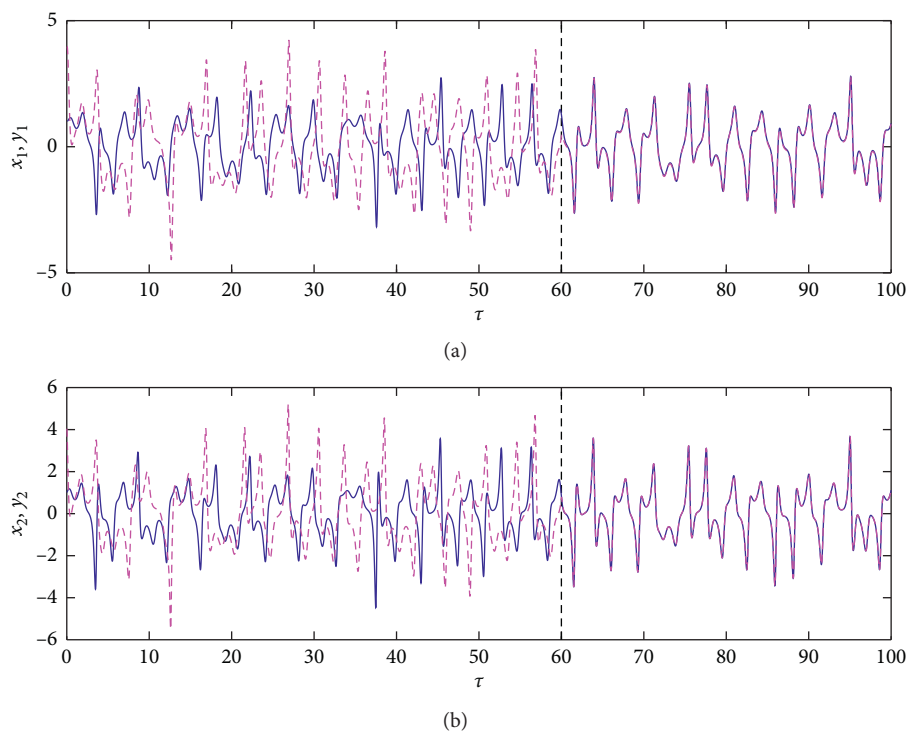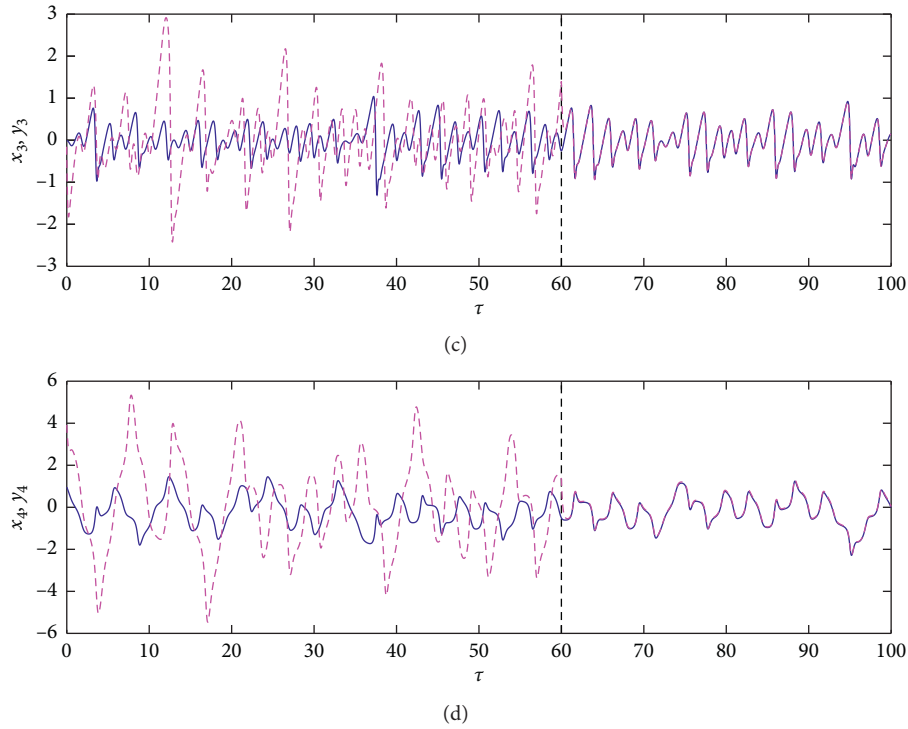

(a)

(b)

FIGURE 20: Continued.

(c)

(d)

FIGURE 20: Time series $x_1(\tau)$, $x_2(\tau)$, $x_3(\tau)$, and $x_4(\tau)$ of master and slave systems showing the result of the adaptive law activated at $\tau = 60$.
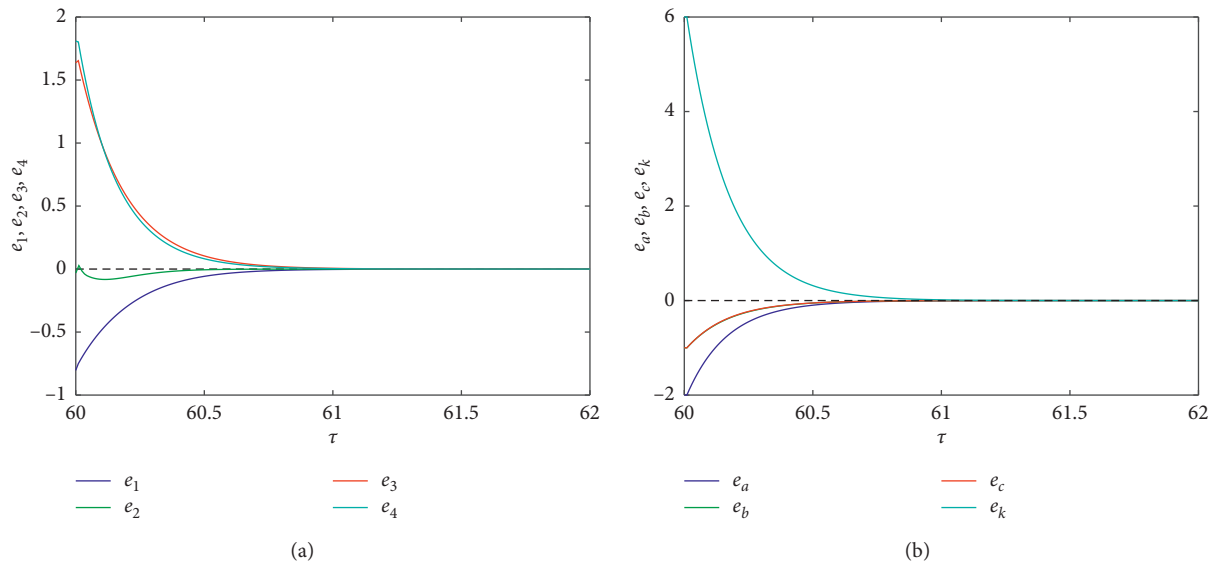

(a)

(b)

FIGURE 21: Time evolution of the synchronization errors e_1, e_2, e_3, and e_4 and the parameter estimation errors e_a, e_b, e_c, and e_k directly after the activation of the adaptive control law.

$$V = \frac{1}{2}\left(e_1^2 + e_2^2 + e_3^2 + e_4^2 + e_a^2 + e_b^2 + e_c^2 + e_k^2\right). \quad (13)$$

Differentiating V along the trajectories, we have

$$\dot{V} = -g_1 e_1^2 - g_2 e_2^2 - g_3 e_3^2 - g_4 e_4^2 + e_a\left[e_1\left(e_2 - e_1\right) - \dot{\hat{a}}\right]$$
$$- e_b \dot{\hat{b}} - e_c\left(e_2 e_4 + \dot{\hat{c}}\right) + e_k\left[e_2\left(y_1 \sin\left(y_3\right) - x_1 \sin\left(x_3\right)\right) - \dot{\hat{k}}\right].$$

$$(14)$$

Here, the parameter update laws are

$$
\begin{cases}
\dot{\hat{a}} = e_1 (e_2 - e_1) + g_5 e_a, \\
\dot{\hat{b}} = g_6 e_b, \\
\dot{\hat{c}} = -e_2 e_4 + g_7 e_c, \\
\dot{\hat{k}} = e_2 (y_1 \sin(y_3) - x_1 \sin(x_3)) + g_8 e_k,
\end{cases}
\tag{15}
$$

with positive gain constants g_5, g_6, g_7, and g_8. By substituting the parameter update law (15) into (14), we have

$$
\dot{V} = -g_1 e_1^2 - g_2 e_2^2 - g_3 e_3^2 - g_4 e_4^2 - g_5 e_a^2 - g_6 e_b^2 - g_7 e_c^2 - g_8 e_k^2.
\tag{16}
$$

Based on the Lyapunov stability theory, we can derive that the synchronization errors e_1, e_2, e_3, and e_4 and the parameter estimation errors e_a, e_b, e_c, and e_k globally and exponentially converge to zero with time increasing. Thus, we obtained the following theorem.

Theorem 1. *The systems in (4) and (5) with unknown parameters are globally and exponentially synchronized for all initial conditions by the adaptive feedback control law (8) and the parameter update law (15), where g_i, $(i = 1, 2, \ldots, 8)$ are positive constants. The parameter estimation errors e_a, e_b, e_c, and e_k globally and exponentially converge to zero with time.*

Next, we will verify the effectiveness of Theorem 1 via numerical simulation. Suppose the parameters $a = 6, b = 1$, $c = 1$, and $k = 12$ of system (4) and system (5). The systems are integrated via the fourth order Runge–Kutta method from 0 to 100 with a time step $\Delta t = 0.001$. The control law (8) is exactly applied at $\tau = 60$. Initial values are randomly taken as $(1, 1, 0, 1)$ for system (4) and $(4, 4, 0, 4)$ for system (5). The initial values of parameters are selected randomly as $\hat{a}(0) = 8, \hat{b}(0) = 2, \hat{c}(0) = 2$, and $\hat{k}(0) = 6$. The time series of signals from the master and slave systems are shown in Figure 19. The synchronization errors and the parameters estimations are also presented in Figure 20. From the numerical simulations, one can see that the adaptive synchronization between master system (4) and slave system (5) is successfully achieved and the error signals asymptotically approach zero. The time evolution of the synchronization errors and the parameter estimation errors is presented in Figure 21. As one can see, after the activation of the control law, the errors all converge to zero, showing that the parameters meet the instructed value and the master and slave systems exhibit the same dynamic behavior.

6. Conclusions

This paper focuses on the dynamic analysis, circuit, and microcontroller realization and synchronization control of a new chaotic system with infinite many coexisting hidden attractors. The system generated from an augmented Sprott B system has no equilibrium. Its distinct feature is that it can generate any number of hidden attractors for selecting different initial values. Also, it exhibits chaotic, periodic, and quasiperiodic motion with the variation of parameters. The circuit and microcontroller realization is given for illustrating the dynamic behaviors of the system. Moreover, the adaptive synchronization conditions of the system are theoretically and numerically established.

Data Availability

The data used to support the findings of this study are available from the corresponding author upon request.

Conflicts of Interest

The authors declare that there are no conflicts of interest regarding the publication of this paper.

Acknowledgments

References

[1] E. N. Lorenz, "Deterministic nonperiodic flow," *Journal of the Atmospheric Sciences*, vol. 20, no. 2, pp. 130–141, 1963.

[2] O. E. Rössler, "An equation for continuous chaos," *Physics Letters A*, vol. 57, no. 5, pp. 397-398, 1976.

[3] G. Chen and T. Ueta, "Yet another chaotic attractor," *International Journal of Bifurcation and Chaos*, vol. 9, no. 7, pp. 1465-1466, 1999.

[4] C. Li, W. Joo-Chen Thio, H. H. C. Iu, and L. Tian, "A memristive chaotic oscillator with increasing amplitude and frequency," *IEEE Access*, vol. 6, pp. 12945–12950, 2018.

[5] Q. Lai, P. D. Kamdem Kuate, F. Liu, and H. H. C. Iu, "An extremely simple chaotic system with infinitely many coexisting attractors," *IEEE Transactions on Circuits and Systems II: Express Briefs*, vol. 68, 2019.

[6] C.-L. Li, H.-M. Li, W. Li et al., "Dynamics, implementation and stability of a chaotic system with coexistence of hyperbolic and non-hyperbolic equilibria," *AEU - International Journal of Electronics and Communications*, vol. 84, pp. 199–205, 2018.

[7] C. Li, K. Qian, S. He, H. Li, and W. Feng, "Dynamics and optimization control of a robust chaotic map," *IEEE Access*, vol. 7, pp. 160072–160081, 2019.

[8] J. C. Sprott, "Some simple chaotic flows," *Physical Review E*, vol. 50, no. 2, pp. 647–650, 1994.

[9] S. Dadras and H. R. Momeni, "A novel three-dimensional autonomous chaotic system generating two, three and four-scroll attractors," *Physics Letters A*, vol. 373, no. 40, pp. 3637–3642, 2009.

[10] N. B. Slimane, K. Bouallegue, and M. Machhout, "Designing a multi-scroll chaotic system by operating Logistic map with fractal process," *Nonlinear Dynamics*, vol. 88, no. 3, pp. 1655–1675, 2017.

[11] C. Zhang, S. Yu, Q. He, and J. Ruan, "On constructing complex grid multiwing chaotic system by switching control and mirror symmetry conversion," *International Journal of Bifurcation and Chaos*, vol. 23, no. 7, Article ID 1350115, 2013.

[12] Q. Lai, A. Akgul, C. B. Li, G. Xu, and U. Cavusoglu, "A new chaotic system with multiple attractors: dynamic analysis,

circuit realization and S-Box design," *Entropy*, vol. 20, no. 1, p. 12, 2017.

[13] Q. Lai, B. Norouzi, and F. Liu, "Dynamic analysis, circuit realization, control design and image encryption application of an extended Lü system with coexisting attractors," *Chaos, Solitons & Fractals*, vol. 114, pp. 230–245, 2018.

[14] H. Wu, H. Bao, Q. Xu, and M. Chen, "Abundant coexisting multiple attractors' behaviors in three-dimensional sine chaotic system," *Complexity*, vol. 2019, Article ID 3687635, 11 pages, 2019.

[15] C. P. Silva, "Shil'nikov's theorem-a tutorial," *IEEE Transactions on Circuits and Systems I: Fundamental Theory and Applications*, vol. 40, no. 10, pp. 675–682, 1993.

[16] S. Jafari and J. C. Sprott, "Simple chaotic flows with a line equilibrium," *Chaos, Solitons & Fractals*, vol. 57, no. 4, pp. 79–84, 2013.

[17] S. Jafari, J. C. Sprott, and S. M. R. Hashemi Golpayegani, "Elementary quadratic chaotic flows with no equilibria," *Physics Letters A*, vol. 377, no. 9, pp. 699–702, 2013.

[18] T. Gotthans and J. Petrzela, "New class of chaotic systems with circular equilibrium," *Nonlinear Dynamics*, vol. 81, no. 33, pp. 1143–1149, 2015.

[19] J. C. Sprott, S. Jafari, V.-T. Pham, and Z. S. Hosseini, "A chaotic system with a single unstable node," *Physics Letters A*, vol. 379, no. 36, pp. 2030–2036, 2015.

[20] C. Li and J. C. Sprott, "Multistability in the Lorenz system: a broken butterfly," *International Journal of Bifurcation and Chaos*, vol. 24, no. 10, Article ID 1450131, 2014.

[21] C. Li, J. C. Sprott, and H. Xing, "Constructing chaotic systems with conditional symmetry," *Nonlinear Dynamics*, vol. 87, no. 2, pp. 1351–1358, 2017.

[22] J. Kengne, Z. T. Njitacke, and H. B. Fotsin, "Dynamical analysis of a simple autonomous jerk system with multiple attractors," *Nonlinear Dynamics*, vol. 83, no. 1-2, pp. 751–765, 2016.

[23] Q. Lai and S. Chen, "Generating multiple chaotic attractors from Sprott B system," *International Journal of Bifurcation and Chaos*, vol. 26, no. 11, Article ID 1650177, 2016.

[24] Q. Lai, C. Chen, X.-W. Zhao, J. Kengne, and C. Volos, "Constructing chaotic system with multiple coexisting attractors," *IEEE Access*, vol. 7, no. 1, pp. 24051–24056, 2019.

[25] C. Li, W. Joo-Chen Thio, J. C. Sprott, H. H.-C. Iu, and Y. Xu, "Constructing infinitely many attractors in a programmable chaotic circuit," *IEEE Access*, vol. 6, pp. 29003–29012, 2018.

[26] B. C. Bao, P. Y. Wu, H. Bao, H. G. Wu, X. Zhang, and M. Chen, "Symmetric periodic bursting behavior and bifurcation mechanism in a third-order memristive diode bridge-based oscillator," *Chaos, Solitons & Fractals*, vol. 109, pp. 146–153, 2018.

[27] B. Bao, L. Xu, Z. Wu, M. Chen, and H. Wu, "Coexistence of multiple bifurcation modes in memristive diode-bridge-based canonical Chua's circuit," *International Journal of Electronics*, vol. 105, no. 7, pp. 1159–1169, 2018.

[28] C. Li, Y. Zhou, Y. Yang et al., "Complicated dynamics in a memristor-based RLC circuit," *The European Physical Journal Special Topics*, vol. 228, no. 10, pp. 1925–1941, 2019.

[29] C.-L. Li, Z.-Y. Li, W. Feng, Y.-N. Tong, J.-R. Du, and D.-Q. Wei, "Dynamical behavior and image encryption application of a memristor-based circuit system," *AEU—International Journal of Electronics and Communications*, vol. 110, p. 152861, 2019.

[30] Z. Wei, F. Parastesh, H. Azarnoush et al., "Nonstationary chimeras in a neuronal network," *EPL (Europhysics Letters)*, vol. 123, no. 4, p. 48003, 2018.

[31] D. Dudkowski, S. Jafari, T. Kapitaniak, N. V. Kuznetsov, G. A. Leonov, and A. Prasad, "Hidden attractors in dynamical systems," *Physics Reports*, vol. 637, pp. 1–50, 2016.

[32] M. A. Kiseleva, N. V. Kuznetsov, and G. A. Leonov, "Hidden attractors in electromechanical systems with and without equilibria," *IFAC-PapersOnLine*, vol. 49, no. 14, pp. 51–55, 2016.

[33] G. A. Leonov, N. V. Kuznetsov, M. A. Kiseleva, E. P. Solovyeva, and A. M. Zaretskiy, "Hidden oscillations in mathematical model of drilling system actuated by induction motor with a wound rotor," *Nonlinear Dynamics*, vol. 77, no. 1-2, pp. 277–288, 2014.

[34] G. A. Leonov and N. V. Kuznetsov, "On differences and similarities in the analysis of Lorenz, Chen, and Lu systems," *Applied Mathematics and Computation*, vol. 256, pp. 334–343, 2015.

[35] Z. Wei, W. Zhang, Z. Wang, and M. Yao, "Hidden attractors and dynamical behaviors in an extended Rikitake system," *International Journal of Bifurcation and Chaos*, vol. 25, no. 2, Article ID 1550028, 2015.

[36] Z. C. Wei, I. Moroz, J. C. Sprott, A. Akgul, and W. Zhang, "Hidden hyperchaos and electronic circuit application in a 5D self-exciting homopolar disc dynamo," *Chaos*, vol. 27, no. 3, Article ID 033101, 2017.

[37] V.-T. Pham, C. Volos, S. Jafari, S. Vaidyanathan, T. Kapitaniak, and X. Wang, "A chaotic system with different families of hidden attractors," *International Journal of Bifurcation and Chaos*, vol. 26, no. 8, Article ID 1650139, 2016.

[38] V. T. Pham, C. Volos, S. Jafari, and T. Kapitaniak, "Coexistence of hidden chaotic attractors in a novel no-equilibrium system," *Nonlinear Dynamics*, vol. 87, no. 3, pp. 2001–2010, 2017.

[39] M.-F. Danca, N. Kuznetsov, and G. Chen, "Unusual dynamics and hidden attractors of the Rabinovich-Fabrikant system," *Nonlinear Dynamics*, vol. 88, no. 1, pp. 791–805, 2017.

[40] G. A. Leonov and N. V. Kuznetsov, "Hidden attractors in dynamical systems. From hidden oscillations in Hilbert-Kolmogorov, aizerman, and kalman problems to hidden chaotic attractor in chua circuits," *International Journal of Bifurcation and Chaos*, vol. 23, no. 1, Article ID 1330002, 2013.

[41] C. Li and J. C. Sprott, "Coexisting hidden attractors in a 4-D simplified Lorenz system," *International Journal of Bifurcation and Chaos*, vol. 24, no. 3, p. 1450034, 2014.

[42] A. Wolf, J. B. Swift, H. L. Swinney, and J. A. Vastano, "Determining lyapunov exponents from a time series," *Physica D: Nonlinear Phenomena*, vol. 16, no. 3, pp. 285–317, 1985.

[43] N. V. Kuznetsov, G. A. Leonov, T. N. Mokaev, A. Prasad, and M. D. Shrimali, "Finite-time Lyapunov dimension and hidden attractor of the Rabinovich system," *Nonlinear Dynamics*, vol. 92, no. 2, pp. 267–285, 2018.

[44] G. A. Leonov, N. V. Kuznetsov, and T. N. Mokaev, "Homoclinic orbits, and self-excited and hidden attractors in a Lorenz-like system describing convective fluid motion," *The European Physical Journal Special Topics*, vol. 224, no. 8, pp. 1421–1458, 2015.

[45] B. Zhang, Y. Jia, and J. Du, "Adaptive synchronization control of networked robot systems without velocity measurements," *International Journal of Robust and Nonlinear Control*, vol. 28, no. 11, pp. 3606–3622, 2018.

[46] S. Vaidyanathan and C. Volos, "Analysis and adaptive control of a novel 3-D conservative no-equilibrium chaotic system," *Archives of Control Sciences*, vol. 25, no. 3, pp. 333–353, 2015.

[47] H. B. Fotsin and J. Daafouz, "Adaptive synchronization of uncertain chaotic colpitts oscillators based on parameter

identification," *Physics Letters A*, vol. 339, no. 3–5, pp. 304–315, 2005.

[48] T.-L. Liao and S.-H. Tsai, "Adaptive synchronization of chaotic systems and its application to secure communications," *Chaos, Solitons & Fractals*, vol. 11, no. 9, pp. 1387–1396, 2000.

[49] S. Chen and J. Lü, "Synchronization of an uncertain unified chaotic system via adaptive control," *Chaos, Solitons & Fractals*, vol. 14, no. 4, pp. 643–647, 2002.

[50] O. Mofid and S. Mobayen, "Adaptive synchronization of fractional-order quadratic chaotic flows with nonhyperbolic equilibrium," *Journal of Vibration and Control*, vol. 24, no. 21, pp. 4971–4987, 2018.